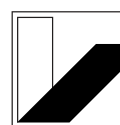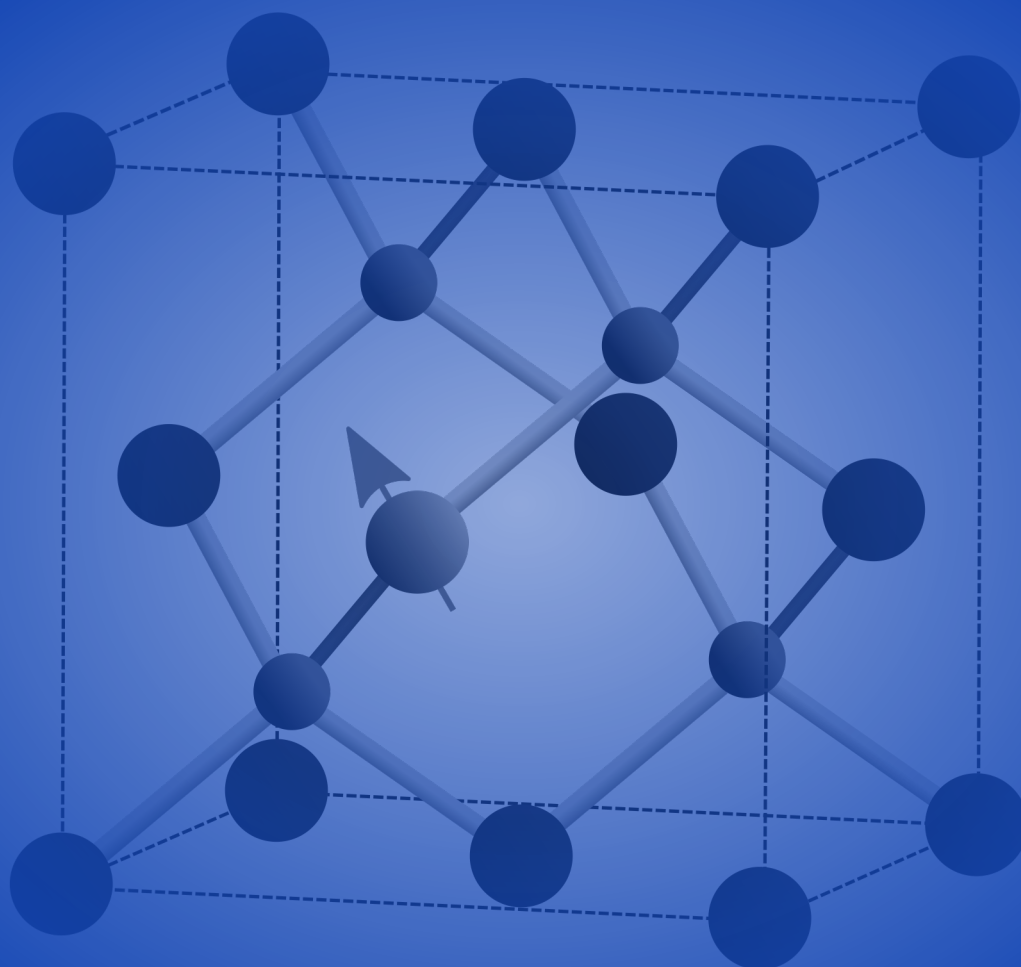# Ultrafast correlated many-body dynamics in magnetic and nonmagnetic quantum nanostructures

Florian Roland Ungar

UNIVERSITÄT BAYREUTH

Ultrafast correlated many-body dynamics in magnetic and nonmagnetic quantum nanostructures

Von der Universität Bayreuth
zur Erlangung des Grades eines
Doktors der Naturwissenschaften (Dr. rer. nat.)
genehmigte Abhandlung

von

Florian Roland Ungar

geboren in Rotthalmünster

1. Gutachter: Prof. Dr. Vollrath Martin Axt
2. Gutachter: Prof. Dr. Doris Reiter
3. Gutachter: Prof. Dr. Paweł Machnikowski

Tag der Einreichung: 22.08.2019
Tag des Kolloquiums: 07.01.2020

Abstract

In a time where CPU frequencies have stagnated and a limit to shrinking transistor sizes is within reach, the exploration of novel computing methods in terms of new materials as well as fundamentally different computing techniques becomes ever more important. In this cumulative thesis, two possible avenues are explored in that regard which fall into the category of spintronics and photon-based quantum computing realized in magnetic and nonmagnetic quantum nanostructures, respectively. While the former seeks to combine the spin and charge degrees of freedom of carriers to achieve a more robust fundamental logical unit, the latter approach aims to explicitly harness superpositions of quantum states using nonclassical quantum algorithms.

Both of these approaches require a thorough theoretical understanding of ultrafast processes to which this thesis contributes by theoretically investigating the correlated many-body dynamics in diluted magnetic semiconductors and nonmagnetic quantum dots on a level beyond the effective single-particle approximation. Since two distinct types of materials are investigated, this thesis is divided into two parts, each of which focuses on the influence of many-body correlations on typical observables of interest. In diluted magnetic semiconductors, the many-body physics is due to the interaction between the magnetic doping atoms and the carriers in the material, whereas the many-body problem in quantum dots originates from the carrier-phonon coupling.

Part I of this thesis introduces the material system of diluted magnetic semiconductors and specifically focuses on the ultrafast spin dynamics of excitons in the presence of magnetic impurities in quantum-well nanostructures. To this end, a quantum kinetic theory is developed that allows an explicit treatment of exciton-impurity correlations based on a previously studied model for quasi-free particles. In contrast to the predominant theoretical description in the literature, the predicted spin-decay rates agree well with experimental findings and their dependence on an external magnetic field features similar nonmonotonic tendencies.

Furthermore, it is shown how the correlation energy indicative for the deviation from the bare exciton picture can be extracted from the linear absorption spectrum and how the presence of correlations affects the occupation of excited exciton states. To highlight non-Markovian effects, the quantum kinetic results are generally compared with the Markov limit of the theory, which corresponds to vanishing correlations and agrees with standard theoretical models based on Fermi's golden rule.

After extending the theory by also accounting for carrier-phonon scattering, its impact on the spin dynamics of optically generated excitons as well as a highly nonequilibrium distribution of hot excitons is investigated. Albeit the scattering with magnetic impurities is found to dominate the spin dynamics, phonons do have a significant impact on the exciton distribution and can even cause a ratchet-like dynamics at low temperatures in suitably high magnetic fields. Finally, it is shown that radiative decay as well as correlations can

lead to significant spin overshoots and that, depending on the specific semiconductor, spin-orbit interaction in the conduction band can have a pronounced impact on the spin dynamics of hot excitons.

Part II of this thesis focuses on semiconductor quantum dots embedded in a cavity and makes use of a real-time path-integral description to fully account for the phonon coupling in terms of a pure-dephasing model. First, an existing version of the algorithm is refined by grouping all states with the same phonon coupling, thereby reducing the numerical demand by several orders of magnitude and paving the way towards a study of many-level systems, which have so far been out of reach due to their high numerical demand. Specifically, the modified algorithm is applied to a 41-level system with up to twenty photons in the cavity, revealing highly unconventional photon statistics as a function of time.

Since multitime correlation functions are an important tool in the characterization of photon states in general, it is also shown how such quantities can be evaluated within the path-integral framework without relying on additional approximations and, most importantly, without neglecting the phonon-induced memory. Applying this scheme to calculate the single-photon purity after pulsed excitation of the quantum dot, it is shown that a high-quality single-photon source whose emission frequency is spectrally separated from the laser frequency can be achieved by off-resonant phonon-assisted excitation.

Finally, the biexciton cascade in quantum-dot cavity systems is discussed regarding the generation of entangled photon pairs. Due to the somewhat ambiguous way of quantifying entanglement via properties of the reduced two-photon density matrix using the notion of concurrence, this quantity is first analyzed with respect to its different appearances throughout the literature. Subsequently, the concurrence of simultaneously-emitted photon pairs is compared for different quantum-dot cavity configurations and it is shown that, quite contrary to the general belief that phonons always lead to a degradation of entanglement, phonon-enhanced entanglement can occur for certain parameters.

Kurzfassung

In einer Zeit, in der CPU-Frequenzen stagniert sind sowie das Erreichen der unteren Strukturgrenze von Transistoren absehbar ist, werden die Entwicklung und Erforschung neuartiger Computersysteme immer wichtiger, sowohl in Bezug auf neue Materialien als auch auf fundamental neuartige logische Grundbausteine. In der vorliegenden kumulativen Dissertation werden zwei verschiedene Zugänge zu diesem Thema untersucht, wobei die magnetischen Nanostrukturen in die Kategorie der Spintronik und die nichtmagnetischen Systeme in das Gebiet Photon-basierter Quantencomputer eingeteilt werden können. Während in den erstgenannten Systemen die Kombination des Spin- und Ladungsfreiheitsgrades in Halbleitern zur Schaffung eines robusteren logischen Grundbausteins im Vordergrund steht, zielt der zweite Themenbereich auf die explizite Ausnutzung der Superposition von Quantenzuständen durch neuartige nichtklassische Algorithmen ab.

Beide Zugänge setzen ein tiefgehendes theoretisches Verständnis der benötigten Prozesse auf ultrakurzen Zeitskalen voraus. Mit der theoretischen Untersuchung der korrelierten Vielteilchendynamik in verdünnten magnetischen Halbleitern einerseits sowie in nichtmagnetischen Quantenpunkten andererseits, welche jeweils über eine effektive Einteilchenbeschreibung hinausgeht, trägt diese Arbeit zu einem solchen Verständnis bei. Aufgrund der Behandlung zweier unterschiedlicher Materialsysteme wird dabei eine entsprechende Aufteilung vorgenommen, wobei jeder Teil insbesondere den Einfluss von Vielteilchenkorrelationen auf typische Observablen beleuchtet. In verdünnten magnetischen Halbleitern kommen diese Korrelationen dabei durch die Wechselwirkung der Ladungsträger mit den magnetischen Dotieratomen zustande, wohingegen das Vielteilchenproblem in Quantenpunkten auf die Kopplung an Phononen zurückgeht.

Der erste Teil der Dissertation stellt zunächst die Eigenschaften verdünnter magnetischer Halbleiter vor und konzentriert sich anschließend auf die Beschreibung der Ultrakurzzeitdynamik von Exzitonen sowie deren Spins unter Berücksichtigung der Wechselwirkung mit den magnetischen Störstellen in zweidimensionalen Nanostrukturen. Hierzu wird eine quantenkinetische Theorie entwickelt, die eine explizite Berücksichtigung von Korrelationen zwischen Exzitonen und Störstellen ermöglicht und auf einer existierenden Theorie zur Beschreibung quasifreier Ladungsträger basiert. Im Gegensatz zu den in der Literatur vorherrschenden Modellen liefert die hier entwickelte Theorie Spinzerfallsraten, welche gut mit experimentellen Daten übereinstimmen und zudem eine ähnliche nichtmonotone Tendenz in einem äußeren Magnetfeld aufweisen.

Überdies wird gezeigt, wie die für die Abweichung von der Beschreibungsstufe unabhängiger Exzitonen aussagekräftige Korrelationsenergie direkt aus dem linearen Absorptionsspektrum gewonnen werden kann und wie sich die Korrelationen auf die Besetzung höherer Exzitonzustände auswirken. Dabei werden die Ergebnisse der quantenkinetischen Theorie stets mit denen im Markovgrenzfall verglichen, wobei letzterer dem Grenzfall verschwindender Korrelationen entspricht und mit der üblichen Beschreibungs-

stufe auf Basis von Fermis goldener Regel zusammenfällt.

Nachdem die Theorie um die Phononstreuung erweitert wird, kann deren Einfluss auf die Spindynamik optisch angeregter sowie heißer Exzitonen, welche sich durch ein hohes thermisches Nichtgleichgewicht auszeichnen, untersucht werden. Obwohl die Streuung an den magnetische Störstellen den wesentlichen Einfluss auf die Spindynamik darstellt, führen Phononen doch zu einer deutlichen Veränderung der Exzitonverteilung und können insbesondere eine stark gerichtete Dynamik bei tiefen Temperaturen und ausreichend hohen Magnetfeldern verursachen. Schließlich wird gezeigt, dass sowohl strahlender Zerfall als auch Korrelationen zu ausgeprägten Überschwingern in der Spinpolarisation führen können und dass, abhängig vom vorliegenden Halbleiter, die Spindynamik signifikant von der Spin-Bahn-Kopplung im Leitungsband beeinflusst wird.

Der zweite Teil der Dissertation befasst sich mit Halbleiter-Quantenpunkten in Resonatoren, wobei zur theoretischen Beschreibung eine Echtzeit-Pfadintegralmethode gewählt wird, die eine vollständige Berücksichtigung der Phononkopplung im Rahmen eines reinen Dephasierungsmodells erlaubt. Zuallererst wird dieser Algorithmus durch die Gruppierung von Zuständen mit identischer Phononkopplung modifiziert, was eine Reduktion des numerischen Aufwands um mehrere Größenordnungen zur Folge hat und damit die Untersuchung von Systemen mit weitaus mehr Niveaus ermöglicht, als bisher mit dieser Methode zugänglich waren. Beispielhaft wird der so modifizierte Algorithmus auf ein System mit 41 Niveaus angewandt, wobei bis zu zwanzig Photonen im Resonator berücksichtigt werden können und eine in hohem Maße unkonventionelle Photonstatistik als Funktion der Zeit beobachtet wird.

Da Korrelationsfunktionen mit mehreren Zeitargumenten ein wichtiges Mittel zur Charakterisierung von Photonzuständen im Allgemeinen sind, wird zudem gezeigt, wie solche Größen mit Hilfe des Pfadintegralalgorithmus berechnet werden können. Dabei muss weder auf weitere Näherungen zurückgegriffen noch das Phonon-induzierte Gedächtnis vernachlässigt werden. Verwendet man dieses Schema zur Berechnung der Reinheit des Ein-Photon-Zustandes im Resonator bei gepulster Anregung des Quantenpunktes, so zeigt sich, dass man mittels Phonon-assistierter Anregung eine Ein-Photon-Quelle hoher Güte realisieren kann, deren Emissionsfrequenz spektral von der Frequenz des anregenden Lasers getrennt ist.

Abschließend wird die Biexzitonkaskade in Quantenpunkt-Resonator-Systemen im Hinblick auf die Erzeugung verschränkter Photonpaare untersucht. Aufgrund der nicht einheitlichen Charakterisierung des Verschränkungsgrades basierend auf Eigenschaften der reduzierten Dichtematrix im zwei-Photon-Zustandsraum mit Hilfe der *concurrence* werden zunächst die in der Literatur verwendeten verschiedenen Berechnungsmethoden dieser Größe verglichen. Im Falle von gleichzeitig emittierten Photonpaaren wird die *concurrence* dann für verschiedene Quantenpunkt-Resonator-Konfigurationen berechnet und verglichen. Entgegen der allgemeinen Erwartung, dass der Phononeinfluss stets eine Abnahme des Verschränkungsgrades zur Folge hat, kann für geeignete Parameter sogar eine Phonon-induzierte Steigerung der Verschränkung gezeigt werden.

Contents

1 Introduction & outline

Starting with the first demonstration of a semiconductor transistor by Bardeen and Brattain in 1947 [1] and its subsequent refinement by their supervisor Shockley in 1950 [2], electronic devices have operated based on the same fundamental principle: controlling the flow of charges in a device. And although our modern-day devices are approaching the limit of Moore's law with transistor counts in the billions and structure sizes of merely a few nanometers [3], they still follow the efforts that culminated in the 1956 Nobel prize in physics [4]. But since the early 2000s, it has become more and more clear that a completely new type of device will be necessary to enable the next big leap in computing performance. Processor clock speeds have remained on a similar level for more than a decade due to the increased heat output that goes hand in hand with shrinking devices, a trend that even the ubiquitous CMOS transistor architecture appearing in the early 1990s was unable to counter [5]. This is why nowadays there is a big focus on multi-core architecture and GPU computing, with the aim to increase computing power by parallelizing the workload [3]. However, such an approach requires more sophisticated algorithms and software designs to fully leverage its benefits, which can be either difficult or outright impossible, depending on the task in question.

All in all, this illustrates the demand for novel computing methods on the hardware level, which has become an active area of research in physics over the past few decades. From a physics perspective, this also requires a profound theoretical understanding of materials that could act as possible candidates for the enhancement or outright replacement of existing semiconductor technology. In this thesis, two prominent yet entirely different material systems are investigated in this context, namely diluted magnetic semiconductors (DMSs) and quantum dots (QDs). While applications using the former are aimed at augmenting existing semiconductor devices or can be at least straightforwardly integrated into state-of-the-art circuits, the latter are building blocks for a fundamentally different approach to computing that relies on optical quantum networks.

Turning first to DMSs, these are either III-V or II-VI semiconductor compounds such as $Ga_{1-x}Mn_xAs$ or $Cd_{1-x}Mn_xTe$, respectively, where a small percentage x of magnetic impurity ions, most commonly manganese, is incorporated into a host lattice [6–10]. Intensively studied since the late 1970s when they were still referred to as semimagnetic semiconductors [6], DMSs arguably attracted considerable attention in 1996 when Ohno et al. first demonstrated ferromagnetism in Mn-doped GaAs with a Curie temperature of about $60\,K$ [11], a discovery that sparked a search for ever higher transition temperatures [9, 12]. Nowadays, through careful optimization of crystal growth parameters and the application of post-growth annealing, Curie temperatures have been pushed as high as $185\,K$ [13]. The magnetic properties of DMSs are a consequence of the partially filled d shell of the introduced impurities, resulting in localized magnetic moments that can interact with each other via the carrier-mediated Ruderman-Kittel-Kasuya-Yosida mechanism

[14, 15]. To be specific, the strong ferromagnetism observed in III-V DMSs is believed to be a hole-mediated effect stemming from the strong p doping when transition metals such as Mn are incorporated in the lattice [8], an effect that is theoretically described by the Zener model [16]. Nevertheless, a complete understanding of the ferromagnetic impurity interaction on the microscopic level remains elusive [17] and is still actively investigated [18].

In the context of this thesis, however, the main attraction of DMSs consists of their being promising candidates for spintronic devices, which aim to augment existing semiconductor technology by not only focusing on carrier charges but also manipulating their spins [19–23]. In fact, harvesting magnetic properties of materials for applications is no new concept and, owing to the discovery of the giant magnetoresistance in the late 1980s [24, 25], has become a key building block of modern data storage. But the spintronics paradigm goes further than that by aiming to actively make use of the spin degree of freedom also in logic circuits themselves, as is probably best exemplified by the famous suggestion of a spin transistor by Datta and Das [26]. Although considerable effort has been devoted to such devices, industrial applications are still lacking and only proofs of concept relying on spintronics exist in laboratories [27, 28].

Evidently, further research and an improved theoretical understanding of ultrafast processes in DMSs are required to advance spintronics into a viable alternative for existing device architectures. The fact that carrier spin-transfer rates in DMSs and their magnetic field dependence are insufficiently described by standard theoretical models only highlights this statement [29]. Therefore, in part I of this thesis, an advanced theoretical description of the carrier dynamics in DMSs is presented which not only accounts for the Coulomb interaction between the carriers, leading to the formation of electron-hole pairs known as excitons, but is also based on a recently developed quantum kinetic treatment of the carrier-impurity exchange interaction that explicitly takes dynamic correlations between carriers and impurities into account [30]. Thus, the approach aims to capture the many-body nature of this interaction beyond the usually employed independent-particle picture. Apart from predicting new features and effects in the exciton dynamics, most notably the emergence of correlations in linear absorption spectra presented in Pub. 3, the spin-transfer rates obtained by this quantum kinetic theory (QKT) are indeed close to the experimental values, as shown in Pub. 1. The QKT also offers an explanation for their unusual dependence on an external magnetic field discussed in Pub. 2. After a brief introduction to DMSs and the spin dynamics in these materials in chapter 2, the main results of the publications on these magnetic systems are presented in chapter 3.

While the first part of this work is devoted to magnetic systems aiming to augment existing semiconductor circuitry, part II is motivated by an entirely different approach to revolutionizing modern computing that relies on interconnecting quantum few-level systems such as found in trapped ions [31–33], nitrogen-vacancy centers in diamonds [34–37] or, in the case of semiconductors, quantum dots [38–44]. The original idea of the so-called quantum computer is typically ascribed to Feynman, although his argument rather deals with the fact that, instead of a classical computer, a quantum system is required to simulate quantum physics [45]. Made concrete by Deutsch et al. [46] and arguably boosted by Shor's proposal of an algorithm to quickly and efficiently factorize large numbers using quantum computers [47] as well as Grover's efficient search algorithm a few years later

[48], the field of quantum information in general continues to receive a massive amount of attention and resources today. Although companies like D-Wave claim to have already built a fully-functioning quantum computer, such machines are only capable of performing a quantum-annealing process, which means preparing the system in an excited state and letting it relax to its ground state [49]. A quantum computer as such does still not exist and some even argue that it never will because of the overwhelming amount of degrees of freedom that need to be controlled [50]. Despite facing many experimental challenges, applications such as the key distribution for quantum cryptography have been successfully realized [51, 52], the most recent example being the establishment of a satellite-relayed quantum network between China and Austria [53].

A fundamental ingredient for quantum protocols are single photons, the generation of which requires efficient and reliable single-photon sources. In contrast to superconducting Josephson junctions, which are based on charge tunneling [54], single-photon emitters have the great advantage that their signals can be transmitted over relatively large distances using optical fibers. The focus in this thesis lies on the properties of photons emitted by semiconductor QDs, which are nanometer-sized structures with quasi-atomic spectra due to a strong confinement of the charge carriers in all spatial directions [55]. In contrast to trapped ions, however, QDs are still influenced by vibrations of the surrounding crystal lattice in the form of phonons [56–61], which also translates to a phonon influence on photonic properties of QDs. To enhance the emission from such devices, the QDs are typically placed inside semiconductor or photonic-crystal microcavities [62–64] which make use of the Purcell effect [65]. Furthermore, the direction of photon emission can be controlled by placing the QD at a chiral point in a nanophotonic waveguide [66].

Although many theoretical models take the phonon influence on QDs into account, most of them do so at an approximate level which is often only valid for a limited choice of parameters [67–70]. In contrast, using a path-integral (PI) approach [71] to deal with the coupling of the QD to the bosonic phonon modes represents a versatile alternative which, due to the finite memory depth induced by the carrier-phonon interaction, enables a numerically complete solution of the equations of motion only limited by the time discretization [61, 72–74] and even allows for a straightforward integration of non-Hamiltonian dissipative dynamics [75]. Part II of this work presents an advanced version of this algorithm with significantly less numerical demand, opening up the possibility to study systems beyond the few-level regime as addressed in Pub. 9 as well as the calculation of multi-time correlation functions discussed in Pub. 10 while including the many-body interaction with phonons. Following a brief introduction to the physics of QDs in cavities and an explanation of the real-time PI method in chapter 5, the main findings laid out in the corresponding publications are summarized in chapter 6.

Part I

Magnetic systems – quantum kinetic description of excitons in diluted magnetic semiconductors

2 Diluted magnetic semiconductors & spin dynamics

In this chapter, the material system of DMSs is discussed regarding its basic properties and theoretical description. Later sections introduce excitons and the spin dynamics in DMSs and recapitulate selected results from the literature.

2.1 The DMS material system

DMSs are ternary II-VI or III-V semiconductor alloys where a small fraction of the group II or group-III elements is replaced by transition metal ions, typically manganese [76]. Owing to the partly-filled $3d$ shell of the doping ions, the resulting material effectively contains localized magnetic moments that can drastically change its magnetic properties even on a macroscopic scale. The crystals are typically grown by either the thermal-equilibrium Bridgman method or using methods which are far from thermal equilibrium, such as molecular beam epitaxy or metalorganic vapor-phase epitaxy [10]. In fact, using growth techniques beyond thermal equilibrium as well as subsequent annealing are crucial to achieve a higher solubility of magnetic impurities and to remove unwanted interstitial Mn ions that reside in between atoms of the host lattice [8, 13]. The most widely studied materials are arguably $Ga_{1-x}Mn_xAs$ and $Cd_{1-x}Mn_xTe$ which, like typical DMSs, crystallize in the zinc-blende structure with a lattice parameter that depends only weakly on the impurity content [7]. A sketch of the typical DMS crystal structure is depicted in Fig. 2.1(a).

While $Ga_{1-x}Mn_xAs$ or other III-V DMSs display strong ferromagnetism with high Curie temperatures [13], II-VI DMSs such as $Cd_{1-x}Mn_xTe$ are paramagnetic in the dilute limit ($x \lesssim 1\%$) and have an antiferromagnetic tendency at higher doping fractions in the high-temperature limit [7]. The main reason for this is the strong p doping in III-V DMSs introduced by the magnetic impurities, which means that holes play a much more important role in these systems and are also responsible for the carrier-mediated ferromagnetism [8]. In contrast, II-VI DMSs can incorporate Mn ions isoelectronically so no excess charge doping occurs [7]. This makes these systems ideal candidates to study the physics of excitons since screening effects are minor and the formation of trions or other exciton complexes can also be neglected. In part I of this work, the focus therefore lies on II-VI DMSs. Specifically, DMSs quantum wells (QWs) are investigated where electrons and holes are confined within a two-dimensional plane with a width of a few nanometers.

The schematic band structure of a zinc-blende DMS QW is depicted in Fig. 2.1(b) and shows the six most important bands in these crystals around the Γ point, which is the center of the Brillouin zone. In the $\mathbf{k} \cdot \mathbf{p}$ framework one typically starts with the Kane model, which takes the lowest antibonding s-like conduction band as well as the highest bonding p-like valence band into account [77]. But instead of using the carrier spin to
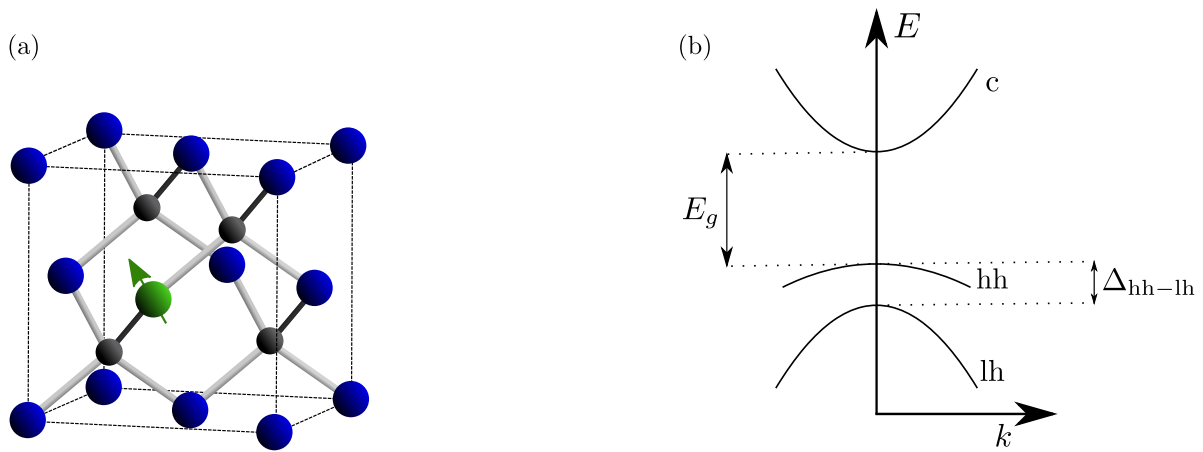
Figure 2.1: (a) Sketch of a typical zinc-blende DMS where an ion in a unit cell is replaced by a magnetic ion, whose spin is indicated by an arrow. (b) Typical band structure of a DMS QW with conduction (c), heavy hole (hh), and light-hole (lh) band around the center of the Brillouin zone with a direct band gap E_g. The hh-lh splitting $\Delta_{\text{hh-lh}}$ at the Γ point is caused by confinement and strain.

label the bands, which is not a good quantum number due to spin-orbit coupling, the total angular momentum $\mathbf{j} = \mathbf{l} + \mathbf{s}$ consisting of the orbital angular momentum $\mathbf{l}$ and the spin $\mathbf{s}$ is considered [78]. In quasi two-dimensional structures such as QWs, this yields a total of four bands which are each twofold degenerate: the conduction band with $j_z = s_z = \pm\frac{1}{2}$, the heavy-hole (hh) band with $j_z = \pm\frac{3}{2}$, the light-hole (lh) band with $j_z = \pm\frac{1}{2}$, and a split-off band with $j_z = \pm\frac{1}{2}$. Since the latter is energetically far removed from the other bands, the split-off band does not play a role for the excitations considered here and is not shown in Fig. 2.1(b).

2.2 Excitons in quantum wells

The basic optical excitation in semiconductors consists of promoting an electron from the topmost valence to the lowest conduction band in accordance with momentum and angular-momentum conservation. In the quasiparticle picture typically used in semiconductor physics, this means that the excitation generates a hole in the valence band and an electron in the conduction band that interact with one another via the Coulomb interaction due to their opposite charges [79]. The resulting two-particle state, the exciton, is a concept which has first been described by Frenkel for excitations in molecules [80] and has later been formulated for semiconductors by Wannier [81]. Today, Frenkel excitons commonly refer to electron-hole pairs in organic molecules which either reside in one molecule or are a few molecules apart and Wannier excitons describe the delocalized electron-hole pairs found in typical semiconductors, where the corresponding exciton wave function extends over many unit cells in the crystal lattice.

Although the exciton problem is fundamentally a many-body problem that involves starting from the Hartree-Fock ground state of the semiconductor and finding the energetically lowest excitation [82], it is often sufficient to calculate exciton wave functions and energies using the much simpler two-particle picture of electrons and holes bound

by the Coulomb interaction. The resulting Hamiltonian closely resembles the hydrogen problem, except that one has to account for the dielectric screening in a semiconductor as well as the modification of the Coulomb potential in quantum nanostructures [78]. In the effective-mass approximation and the strong-confinement limit, excitons in a QW with a width d can be described by

$$
\left(-\frac{\hbar^2}{2M}\Delta_{\mathbf{R}} - \frac{\hbar^2}{2\mu}\Delta_{\mathbf{r}} - \underbrace{\int_{-\frac{d}{2}}^{\frac{d}{2}} dz \int_{-\frac{d}{2}}^{\frac{d}{2}} dz' \frac{e^2\,|u_0^{\mathrm{e}}(z)|^2\,|u_0^{\mathrm{h}}(z')|^2}{4\pi\epsilon\epsilon_0\sqrt{\mathbf{r}^2 + (z-z')^2}}}_{=:V^{\mathrm{eff}}(\mathbf{r})} \right)\psi_{x\mathbf{K}}(\mathbf{R},\mathbf{r}) = E_{x\mathbf{K}}\,\psi_{x\mathbf{K}}(\mathbf{R},\mathbf{r})
$$

$$(2.1)$$

with the total exciton mass $M = m_{\mathrm{e}} + m_{\mathrm{h}}$, the reduced exciton mass $\mu = \frac{m_{\mathrm{e}}m_{\mathrm{h}}}{M}$, and the two-dimensional Laplacians $\Delta_{\mathbf{R}}$ and $\Delta_{\mathbf{r}}$ for the center of mass (CoM) and relative motion, respectively. The effective Coulomb potential $V^{\mathrm{eff}}(\mathbf{r})$ with the elementary charge e, the vacuum permittivity ϵ_0, and the dielectric constant ϵ is obtained by projecting the standard screened Coulomb potential down to the lowest confinement state $u_0^{\mathrm{e/h}}(z)$ for electrons and holes, respectively. This is a good approximation as long as the confinement is strong, i.e., as long as the QW is sufficiently narrow so that transitions to higher confinement states can be disregarded, as is the case for $d \lesssim 30\,\mathrm{nm}$ [78, 83]. Since this is a two-particle problem, it is convenient to decompose the exciton wave functions

$$
\psi_{x\mathbf{K}}(\mathbf{R},\mathbf{r}) = \frac{1}{\sqrt{A}}e^{i\mathbf{K}\cdot\mathbf{R}}\phi_x(\mathbf{r})
$$

$$(2.2)$$

into a CoM motion described by a plane wave and the relative part $\phi_x(\mathbf{r}) = \frac{1}{\sqrt{2\pi}}R_n(r)e^{il\varphi}$, where $x \in \{1s, 2s, 2p, \dots\}$ denotes the exciton state which is composed of a principal quantum number $n \in \mathbb{N}$ and an angular-momentum quantum number $l \in \{0, \pm 1, \dots, \pm(n-1)\}$ [78, 84]. In contrast to the hydrogen atom in free space or excitons in bulk, excitons in QWs are sufficiently described by only two quantum numbers, reflecting the reduction in dimensionality. Together with the CoM momentum $\mathbf{K}$, which follows a parabolic dispersion $\omega = \frac{\hbar K^2}{2M}$ similar to quasi-free carriers but with a larger mass, the exciton state x for the relative motion fully describes the bound electron-hole pair.

There are numerous methods to solve Eq. (2.1), such as a variational approach in terms of an ansatz with a free parameter for $R_n(r)$ [85, 86] or using Greens functions [87]. Here, a direct numerical discretization and subsequent diagonalization of the Hamiltonian in Eq. (2.1) is performed to obtain the exciton wave functions and energies. In contrast to the variational approach, which requires a suitable ansatz for different exciton states, the approach taken here allows a straightforward calculation of an arbitrary number of exciton states. A similar procedure is used to solve the confinement problem which yields the envelope functions $u_i^{\mathrm{e/h}}(z)$.

As an example, the radial part of the wave functions of the three energetically lowest exciton states in a 10-nm-wide ZnSe QW is shown in Fig. 2.2(a). Although calculated using the effective two-dimensional potential $V^{\mathrm{eff}}(\mathbf{r})$, the ground state qualitatively resembles the one obtained for the hydrogen atom in free space and only the Bohr radius differs. As shown in Fig. 2.2(b), the exciton binding energy in smaller nanostructures is typically much larger than in bulk crystals [88], although there are exceptions such as cuprous
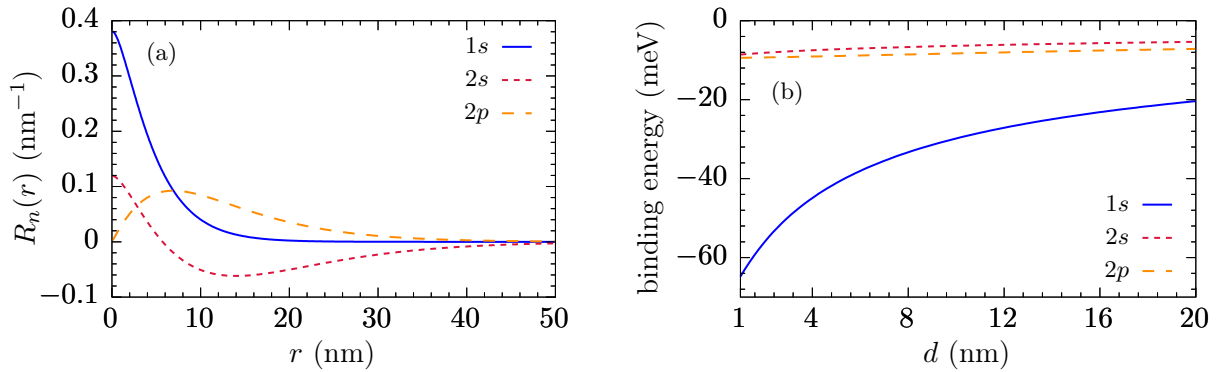
Figure 2.2: (a) Radial part of the exciton wave function in a 10-nm-wide ZnSe QW for the three energetically lowest states and (b) their calculated binding energy with respect to the band gap as a function of the well width d. The parameters of Table I in Pub. 1 are used for the simulations.

oxide with exciton binding energies of about $100\,\mathrm{meV}$ in bulk [89]. As of today, in the monolayer limit, binding energies of several hundred meV can be reached in the prominent material class of transition-metal dichalcogenides [90–92]. Note that the $2p$ state is doubly degenerate as its energy does not depend on the angular-momentum quantum number. In contrast to the bulk limit, where the exciton binding energy depends solely on the principal quantum number n, going over to nanostructures causes an energy splitting between the $2p$ and $2s$ state, as can be seen in Fig. 2.2(b). Since part I of this thesis focuses on DMSs with small doping fractions of maximally a few percent and the crystal parameters depend only weakly on the impurity content [93], the exciton states calculated for the bare II-VI semiconductor material can also be used for the corresponding DMS.

2.3 Spin dynamics in DMSs

As pointed out in Sec. 2.1, the interaction that typically defines the physics in DMSs is the carrier-impurity exchange interaction, which can be written as [30, 76, 94]

$$H_{sd/pd} = J_{sd/pd} \sum_{iI} \mathbf{S}_I \cdot \mathbf{s}_i^{\mathrm{e/h}} \, \delta(\mathbf{R}_I - \mathbf{r}_i^{\mathrm{e/h}}) \qquad (2.3)$$

for s-type electrons and p-type holes, respectively, and which describes the scattering with the localized d-shell electrons of the impurities. Here, $J_{sd/pd}$ is the coupling constant, $\mathbf{S}_I$ denotes the operator for the Ith impurity spin at the position $\mathbf{R}_I$, and $\mathbf{s}_i^{\mathrm{e/h}}$ is the corresponding spin operator for the ith carrier at the position $\mathbf{r}_i^{\mathrm{e/h}}$. Note that, throughout this work, the spin operators are taken to be dimensionless and the usually appearing constant $\hbar$ is incorporated into the coupling constant instead. With values on the order of $10\,\mathrm{meV}$ for typical II-VI DMSs, the exchange integral J_{sd} in the conduction band is quite strong, and the corresponding valence-band constant is typically even four times larger than that [7]. The values of these exchange integrals, which are often given as $N_0\alpha$ and $N_0\beta$ with N_0 being the number of unit cells per volume, are well established in the literature and can be measured, e.g., via excitonic Zeeman splittings or spin-flip Raman

scattering [95]. These measurements exploit the so-called giant Zeeman effect in DMSs, which describes the back action of the mean impurity magnetization onto the carrier spin resulting from the alignment of the impurity spins in an external magnetic field [76].

This effect is perhaps best understood in the simplest approximation for the carrier-impurity exchange interaction, which is the combination of the mean field and the virtual-crystal approach. To this end, the impurity spin operators in Eq. (2.3) are replaced by their thermal average and it is assumed that the impurities are distributed regularly instead of randomly throughout the crystal lattice, resulting in the replacement $\delta(\mathbf{R}_I - \mathbf{r}_i^{\mathrm{e/h}}) \to \frac{1}{V}$ for a crystal with volume V. Then, Eq. (2.3) simplifies to

$$H_{sd/pd} = n_{\mathrm{Mn}} J_{sd/pd} \sum_i \langle \mathbf{S} \rangle \cdot \mathbf{s}_i^{\mathrm{e/h}} \tag{2.4}$$

with the impurity density n_{Mn}. Equation (2.4) thus has the same form as a standard Zeeman term for the carriers but, due to the magnitude of $J_{sd/pd}$, the resulting Zeeman splittings can reach values exceeding $100\,\mathrm{meV}$ at liquid-helium temperatures and magnetic fields of a few Tesla [76]. However, it should be pointed out that this approximation prohibits a description of exciton-impurity correlations [30] and is thus insufficient for the purposes of this thesis.

In contrast to nonmagnetic semiconductors, where the most common spin relaxation mechanisms can either be traced back to spin-orbit coupling or electron-hole exchange [96], the spin dynamics in DMSs is typically dominated by the carrier-impurity exchange interaction [29, 97–103]. Since the standard theoretical models are based on the application of Fermi's golden rule to obtain a spin-transfer rate from the carrier to the impurity subsystem [29, 94, 100, 104–109], they fail to take effects beyond the mean-field approximation into account and predict a dynamics that is strictly exponential with a single decay rate. For quasi-free electrons in a DMS QW at zero magnetic field, this rate reads

$$\tau_{\mathrm{e}}^{-1} = \frac{I J_{sd}^2 n_{\mathrm{Mn}} m_{\mathrm{e}}}{\hbar^3 d} \langle S^2 \rangle, \tag{2.5}$$

where $I = d \int_{-\frac{d}{2}}^{\frac{d}{2}} dz \, |u_0^{\mathrm{e}}(z)|^4$ is the envelope integral. In particular, the rate does not depend on the carrier momentum and scales linearly with the doping fraction in the DMS. Note the dependence on the second moment of the impurity spin, which can be substituted by $\langle S^2 \rangle = \frac{1}{3} \langle \mathbf{S}^2 \rangle$ if no preferred direction exists in the system.

Although other approaches such as the projection operator formalism [110] or the so-called kinetic spin-Bloch equations [111] have been discussed in the literature on spin dynamics in DMSs, these theories still coincide with Fermi's golden rule at zero magnetic field and only yield different rates for finite fields. The need for a theory beyond the rate-equation level is probably best exemplified in a recent publication by Ben Cheikh et al. [29], where measured spin-decay rates of different groups on different samples have been collected and compared with the results of Eq. (2.5), which are found to severely underestimate the experimental values by a factor of five. Despite the argument that most experiments probe excitons rather than quasi-free electrons [100], which is certainly true when looking at the literature [99–101, 112–115], calculating the spin-decay rate for excitons does not solve this problem. Since m_{e} in Eq. (2.5) would have to be replaced by the exciton mass in this case [104], one instead faces theoretical rates which overestimate

the experimental values due to the fact that exciton masses are roughly eight times larger than the effective electron masses in typical II-VI DMSs [7]. In addition, considering excitons instead of quasi-free carriers does not explain experimental observations of a nonmonotonic magnetic-field dependence of the rates [103].

All in all, these observations suggest that a novel theoretical model for the spin dynamics in DMSs is needed. For quasi-free electrons, such an approach in terms of a correlation expansion of carrier-impurity density matrices has been worked out by Thurn et al. [30] and subsequently expanded by Cygorek et al. to also include nonmagnetic scattering [116]. The most prominent findings of this QKT are a time-dependent redistribution of electron kinetic energies and the possibility of a nonexponential spin dynamics that shows an overshooting behavior for short times [117]. The former can be understood in terms of a finite negative correlation energy in DMSs which can be used to increase the average carrier kinetic energy in accordance with energy conservation [118]. From a different perspective, the correlations captured in the QKT can also be understood in terms of a finite memory in the spin dynamics, which is in contrast to the Markov theory (MT) commonly used in the theoretical description of the spin dynamics in DMSs. In fact, performing the Markov limit of the QKT, which is equivalent to the assumption of a vanishing memory, yields the same exponential spin dynamics as predicted by Fermi's golden rule [119]. Thus, comparing results of the MT with those of the QKT allows one to pinpoint non-Markovian effects, which is also an important aspect of this thesis. In part I, the methods involved in the derivation of the QKT for quasi-free carriers are used as a starting point to develop a QKT that also takes the Coulomb interaction between carriers into account so that a description of the exciton dynamics in DMSs beyond the mean-field approximation becomes possible. The developed theory, its predictions, and its expansion in terms of carrier-phonon scattering and spin-orbit coupling are published in several papers, an introduction to which is given in the following chapter.

3 Introduction to the publications on magnetic systems

Concerning magnetic systems in the form of DMSs, the work carried out over the course of this thesis has resulted in eight publications listed in part III. This chapter provides an overview of these papers and is divided into four sections. After sketching out the derivation of the QKT in Sec. 3.1, which mainly contains results published in Pub. 1, Sec. 3.2 summarizes the main consequences of exciton-impurity correlations for resonantly excited excitons in DMSs and is mainly based on Pub. 2, Pub. 3, and Pub. 4. In Sec. 3.3, the QKT is extended to include carrier-phonon scattering as detailed in Pub. 5, which also enables the description of highly nonequilibrium exciton distributions away from the optically accessible bottom of the exciton parabola. Furthermore, the phonon influence on the long-time behavior of the exciton spin is discussed in Pub. 6. The combined influence of phonon scattering and radiative decay in DMSs also leads to new physical insights, which have been explored in Pub. 7 and are summarized in section 3.4. Finally, in Sec. 3.5, a simple model for the incorporation of spin-orbit interaction (SOI) in the conduction band developed in Pub. 8 is discussed.

3.1 Development of the QKT

First, the derivation of the quantum kinetic equations in Pub. 1 is discussed and the employed truncation methods are explained. Subsequently, reduced equations are presented for a subclass of DMS samples where the treatment of the hole spins is facilitated. The Markov limit of the equations is sketched in a final section.

3.1.1 Derivation of the equations

The starting point for the derivation of quantum kinetic equations for the exciton dynamics in DMSs consists of specifying the Hamiltonian H of the system to be studied and setting up the Heisenberg equation of motion

$$i\hbar\frac{\partial}{\partial t}\langle c^\dagger_{l_1\mathbf{k}_1} d^\dagger_{v_1-\mathbf{k}_2} d_{v_2-\mathbf{k}_3} c_{l_2\mathbf{k}_4}\rangle = \langle\left[c^\dagger_{l_1\mathbf{k}_1} d^\dagger_{v_1-\mathbf{k}_2} d_{v_2-\mathbf{k}_3} c_{l_2\mathbf{k}_4}, H\right]\rangle \tag{3.1}$$

for the four-point density matrix $\langle c^\dagger_{l_1\mathbf{k}_1} d^\dagger_{v_1-\mathbf{k}_2} d_{v_2-\mathbf{k}_3} c_{l_2\mathbf{k}_4}\rangle$, from which the carrier densities and spins can be extracted [120]. Here, $c^\dagger_{l\mathbf{k}}$ ($c_{l\mathbf{k}}$) denotes the creation (annihilation) operator of an electron in the conduction band l with wave vector $\mathbf{k}$ and $d^\dagger_{v-\mathbf{k}}$ ($d_{v-\mathbf{k}}$) is the analogous operator for a hole in the valence band v. Similarly, all contributions to H are written in electron-hole representation in order to evaluate the commutator $[.,.]$ appearing in Eq. (3.1).

To model the optical excitation of electron-hole pairs in DMSs and their subsequent spin dynamics, the Hamiltonian can be decomposed according to

$$H = \underbrace{H_0^{\mathrm{e}} + H_0^{\mathrm{h}} + H_{\mathrm{C}} + H_{\mathrm{conf}}}_{\text{excitons}} + \underbrace{H_{\mathrm{Z}}^{\mathrm{e}} + H_{\mathrm{Z}}^{\mathrm{h}} + H_{\mathrm{Z}}^{\mathrm{Mn}}}_{\text{magnetic field}} + H_{\mathrm{lm}} + \underbrace{H_{sd} + H_{pd} + H_{\mathrm{nm}}^{\mathrm{e}} + H_{\mathrm{nm}}^{\mathrm{h}}}_{\text{exciton-impurity scattering}}. \quad (3.2)$$

First of all, H contains the free propagation of the carriers through the crystal ($H_0^{\mathrm{e}}+H_0^{\mathrm{h}}$) as well as the Coulomb potential (H_{C}) which, combined with the confinement due to the QW (H_{conf}), can be diagonalized to obtain the exciton states (cf. Sec. 2.2). A homogeneous external magnetic field is accounted for by adding the relevant Zeeman terms for electrons ($H_{\mathrm{Z}}^{\mathrm{e}}$), holes ($H_{\mathrm{Z}}^{\mathrm{h}}$), and magnetic impurities ($H_{\mathrm{Z}}^{\mathrm{Mn}}$). For the optical excitations considered in this work, it is sufficient to take only the conduction, hh, and lh bands in DMSs into account, as sketched in Fig. 2.1(b). Due to the additional spin degree of freedom, the conduction band can be conveniently represented in terms of 2×2 Pauli matrices, whereas 4×4 angular-momentum matrices can be used for the valence bands. To directly model the laser excitation (H_{lm}), the standard dipole approximation is employed so that only interband transitions with vanishing CoM momentum are considered [121]. Apart from the signature interaction in DMSs, which is the carrier-impurity exchange interaction given by Eq. (2.3) ($H_{sd}+H_{pd}$), also a nonmagnetic-scattering contribution of carriers at the localized impurities ($H_{\mathrm{nm}}^{\mathrm{e}} + H_{\mathrm{nm}}^{\mathrm{h}}$) is considered here. This interaction can be understood in terms of a local change in the bandstructure of the DMS due to the incorporation of foreign atoms into the lattice, which is modeled here as a localized scattering potential that does not depend on the carrier-spin orientation and is thus nonmagnetic in nature. Such a scattering has been investigated for quasi-free electrons, where it significantly influences the spin dynamics as well as the carrier distribution in **k** space [116]. The explicit expressions of all contributions to the Hamiltonian are given in Pub. 1.

Since H contains many-body interactions such as the carrier-impurity scattering, evaluating the commutator in Eq. (3.1) leads to the appearance of higher-order density matrices on the right-hand side for which the time evolution must also be calculated. This procedure evidently leads to an infinite hierarchy of equations of motion that needs to be truncated in a suitable manner to obtain a closed and solvable set of differential equations. In fact, one faces two distinct hierarchies in the model under discussion: One is caused by the Coulomb interaction and another is due to the carrier-impurity scattering, where the latter is characterized by the appearance of multiple impurity-spin operators. The simplest way to deal with the latter hierarchy would be to use the mean-field approach for the exchange interaction, resulting in Eq. (2.4). However, this also means that the many-body nature of the scattering is disregarded and correlations between carriers and impurities cannot be captured. This is why the correlation expansion developed in Ref. [30] is adopted here to construct a theory beyond the mean-field level, which leverages the fact that impurities in DMSs are far apart so that correlations involving Mn ions on different sites can be expected to be small. In addition, a dynamics-controlled truncation (DCT) is performed for the Coulomb hierarchy. This allows one to classify all expectation values in a semiconductor in terms of their order in the generating laser field **E**, which means that higher-order expectation values can be disregarded when focusing on the low-density regime [122]. Here, density matrices up to second order in the laser field are kept.

To apply the correlation expansion for the impurity operators and the corresponding carrier-assisted density matrices, it is advantageous to represent the impurity spins as $\mathbf{S}_I = \sum_{nn'} S_{nn'} \hat{P}^I_{nn'}$ in terms of the projection operators $\hat{P}^I_{nn'} = |I, n\rangle\langle I, n'|$. Here, $|I, n\rangle$ are the eigenstates to the spin operator S^z_I with the eigenvalues $n \in \{-\frac{5}{2}, -\frac{3}{2}, \ldots, \frac{5}{2}\}$. Keeping in mind that impurities in DMSs are far apart, this enables a factorization according to [30]

$$\langle \hat{P}^I_{n_1 n_2} \hat{P}^{I' \neq I}_{n_3 n_4} \rangle \approx \langle \hat{P}^I_{n_1 n_2} \rangle \langle \hat{P}^{I' \neq I}_{n_3 n_4} \rangle, \tag{3.3a}$$

$$\langle \hat{P}^I_{n_1 n_2} \hat{P}^I_{n_3 n_4} \rangle = \langle \hat{P}^I_{n_1 n_4} \rangle \delta_{n_2, n_3} \tag{3.3b}$$

and also allows one to conveniently deal with impurity operators on the same site. Note that Eq. (3.3b) is exact and also holds for impurity-assisted expectation values. However, the Hamiltonian for the magnetic and the nonmagnetic carrier-impurity interaction still explicitly depends on the impurity positions $\mathbf{R}_I$. In $\mathbf{k}$ space, this leads to the appearance of a factor $e^{i\Delta\mathbf{k}\cdot\mathbf{R}_I}$, which contains the difference $\Delta\mathbf{k}$ of carrier wave vectors before and after the scattering event as well as the impurity position. Due to the random nature of the impurity positions in the DMS crystal lattice, this exponential function effectively becomes a classical random variable that must be treated accordingly within a correlation expansion.

Having applied the DCT, one is then left with expectation values of the form

$$S_Q = \langle X e^{i\Delta\mathbf{k}\cdot\mathbf{R}_I} e^{i\Delta\mathbf{k}'\cdot\mathbf{R}_{I'}} \hat{P}^I_{n_1 n_2} \hat{P}^{I'}_{n_1' n_2'} \rangle, \tag{3.4}$$

where X may contain up to four Fermi operators such that $\langle X \rangle \leq \mathcal{O}(E^2)$. The expectation value in the above equation now also contains an average over the impurity positions in the DMS. Assuming a random but on average homogeneous distribution of impurities then implies that $\langle e^{i\Delta\mathbf{k}\cdot\mathbf{R}_I} \rangle = \delta_{\Delta\mathbf{k},\mathbf{0}}$ [30]. Clearly, Eq. (3.4) can be straightforwardly simplified if $I = I'$ with the help of Eq. (3.3b). In addition, the special cases where either $\Delta\mathbf{k} = 0$ or $\Delta\mathbf{k}' = 0$ have to be treated separately since then either one or both complex exponentials are equal to unity, thus reducing the number of operators that need to be accounted for in a correlation expansion. In the most general case given by $I \neq I'$, $\Delta\mathbf{k} \neq 0$, and $\Delta\mathbf{k}' \neq 0$, Eq. (3.4) is decomposed according to

$$S_Q = \delta\langle X e^{i\Delta\mathbf{k}\cdot\mathbf{R}_I} \hat{P}^I_{n_1 n_2} \rangle \langle e^{i\Delta\mathbf{k}'\cdot\mathbf{R}_{I'}} \rangle \langle \hat{P}^{I'}_{n_1' n_2'} \rangle + \delta\langle X e^{i\Delta\mathbf{k}\cdot\mathbf{R}_I} \rangle \langle \hat{P}^I_{n_1 n_2} \rangle \langle e^{i\Delta\mathbf{k}'\cdot\mathbf{R}_{I'}} \rangle \langle \hat{P}^{I'}_{n_1' n_2'} \rangle. \tag{3.5}$$

The true correlations are denoted by $\delta\langle \ldots \rangle$ and, for the sake of brevity, only the nonvanishing terms in the correlation expansion are written down. First, correlations evaluated at different sites or those containing two or more impurity operators are neglected since impurities in DMSs are far apart so correlations between them are expected to be small. Second, one can show analytically that correlations of the form $\langle e^{i\Delta\mathbf{k}\cdot\mathbf{R}_I} \hat{P}^I_{n_1 n_2} \rangle$ are not driven if they are initially zero and can thus be disregarded in the equations of motion. From a physical point of view, such quantities could be used to model impurity-spin waves in DMSs, a topic which is, however, beyond the scope of this work.

Having performed all of the steps described above, a closed set of equations can be obtained involving density matrices with only Fermi operators as well as carrier-impurity correlations, which are given explicitly in Pub. 1. But since the focus here lies on bound electron-hole pairs and not on quasi-free carriers, it is much more convenient and numer-
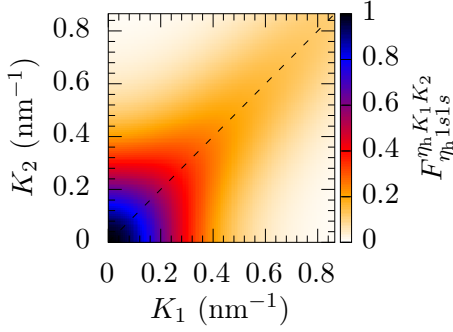
Figure 3.1: Angle-averaged exciton form factor $F_{\eta_{\mathrm{h}}1s1s}^{\eta_{\mathrm{h}}K_1K_2}$ as a function of the exciton CoM momenta K_1 and K_2 evaluated using the parameters for a 15-nm-wide $\mathrm{Zn}_{1-x}\mathrm{Mn}_x\mathrm{Se}$ QW. Only the $1s$ exciton state is considered and the diagonal elements with $K_1 = K_2$ are indicated by a dashed line.

ically efficient to switch to a two-particle basis [120]. Using the exciton wave functions given by Eq. (2.2), a transformation between the corresponding exciton creation operator and the Fermi operators can be readily obtained and carried out, leading to new dynamical variables that depend on the exciton state x as well as the CoM momentum $\mathbf{K}$. These variables along with the resulting equations of motion can be found in Pub. 1. Although the structure of the equations is similar to what has been found for quasi-free electrons in Ref. [30], the fact that excitons rather than free carriers are excited causes the appearance of exciton form factors

$$
F_{\eta_1 x_1 x_2}^{\eta_2 \mathbf{K}_1 \mathbf{K}_2} = 4\pi^2 \int_0^\infty dr\, r\, R_{n_1}(r) R_{n_2}(r)\, J_{l_2 - l_1}\big(\eta_1 |\mathbf{K}_1 - \mathbf{K}_2| r\big)
$$
$$
\times \int_0^\infty dr'\, r'\, R_{n_1}(r') R_{n_2}(r')\, J_{l_2 - l_1}\big(\eta_2 |\mathbf{K}_1 - \mathbf{K}_2| r'\big). \tag{3.6}
$$

The form factors contain the radial part of the exciton wave function $R_n(r)$ as introduced in Sec. 2.2 and the angular-momentum quantum number l enters via cylindrical Bessel functions $J_{\Delta l}\big(\eta_1 |\mathbf{K}_1 - \mathbf{K}_2| r\big)$. Furthermore, $\eta \in \{\eta_{\mathrm{e}}, \eta_{\mathrm{h}}\}$ denotes the mass ratio between carriers and excitons given by either $\eta_{\mathrm{e}} = \frac{m_{\mathrm{e}}}{M}$ or $\eta_{\mathrm{h}} = \frac{m_{\mathrm{h}}}{M}$.

Averaged over the polar angles in $\mathbf{K}$ space, the exciton form factor for the $1s$ ground state is plotted in Fig. 3.1 for the case of a 15-nm-wide $\mathrm{Zn}_{1-x}\mathrm{Mn}_x\mathrm{Se}$ QW. As can be seen, $F_{\eta_{\mathrm{h}}1s1s}^{\eta_{\mathrm{h}}K_1K_2}$ decays with increasing CoM momenta and can have values between zero and unity. Whereas the decay is most pronounced when either K_1 or K_2 vanishes and only one of the arguments is varied, the form factor decreases more gradually along the diagonal line characterized by $K_1 = K_2$. As will be seen later on, these form factors have a significant impact on the dynamics and even change the spin-decay rate on the Markov level, leading to an explicit dependence on the exciton CoM momentum.

Of course, it is a valid question to ask why H has not been immediately projected onto the exciton basis to calculate the equations of motion from there, instead of using the much more lengthy and cumbersome electron-hole representation for the Hamiltonian and the density matrices and switching to the exciton basis afterwards. However, this approach has the fundamental drawback that the representation of the electron-hole continuum is lost and cannot be recovered. Furthermore, the electron-hole representation is actually much more convenient for the application of the DCT, which provides a clear physical justification to neglect higher-order density matrices.

3.1.2 Reduced equations of motion

Instead of discussing the full quantum kinetic equations, the remainder of this thesis focuses on reduced equations applicable to a subclass of DMS nanostructures with large hh-lh splitting $\Delta_{\text{hh-lh}}$ in the valence band. Considering an optical excitation with σ^- polarization resonant with the 1s-hh exciton, one obtains an electron with $s_z = \frac{1}{2}$ bound to a hh with $j_z = -\frac{3}{2}$. Since there is no direct matrix element of H_{pd} between the two hh states, the hh spins have to pass through the lh states in order to reach the opposite spin orientation. However, for systems with large hh-lh splitting, this process is off-resonant on the order of $\Delta_{\text{hh-lh}}$, resulting in an effectively pinned hh spin [99, 104, 123, 124]. This greatly reduces the number of variables that need to be accounted for since the spin degree of freedom in the valence band is eliminated. Thus, only two possible exciton spin states remain: A bright state with $s_z = \frac{1}{2}$, $j_z = -\frac{3}{2}$ and a dark state with $s_z = -\frac{1}{2}$, $j_z = -\frac{3}{2}$, which can be conveniently denoted by $\uparrow$ and $\downarrow$, respectively, by only referring to the spin state of the exciton-bound electron. The situation is sketched in Fig. 3.2.

It should be noted that transitions between the two hh spin states become allowed in the presence of a hh-lh mixing, such as provided by the long-range part of the Coulomb interaction [125, 126]. However, in Pub. 2, the typical energy of this interaction is estimated to be on the order of $10\,\mu\text{eV}$, which is orders of magnitude smaller compared with the typical energy scale of the magnetic exchange interaction in DMSs and is therefore neglected here.

In addition to the assumption of a pinned hh spin, the equations of motion can be considerably simplified for the excitation scenarios considered in this work since, in the limit of low excitation power, the exciton density n_x is much lower than the impurity density n_{Mn} in the DMS. Hence, due to spin conservation, the total change of the impurity spin is proportional to $n_x/n_{\text{Mn}} \ll 1$ and can be effectively disregarded. This is why the
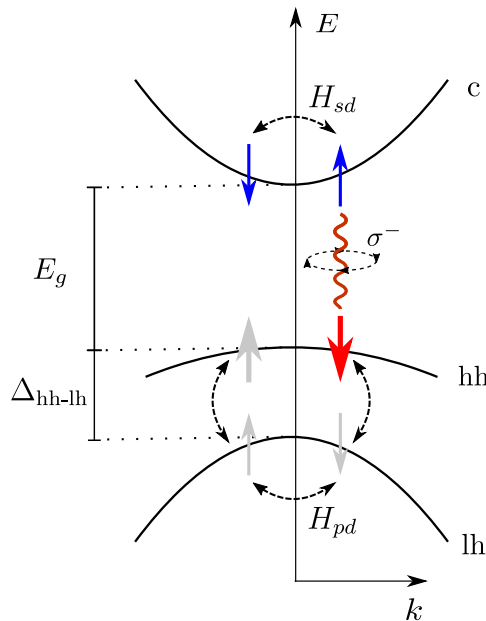
Figure 3.2: [taken from Pub. 7] Sketch of an optical excitation with σ^- polarization of the 1s-hh exciton. The small arrows denote spins with $s_z = \pm\frac{1}{2}$ in the conduction band and $j_z = \pm\frac{1}{2}$ in the lh band, respectively, while the larger arrows depict hh spins with $j_z = \pm\frac{3}{2}$. Spin-flips in the conduction band are mediated by H_{sd}, while H_{pd} acts on spins in the valence band. Inaccessible spin states are indicated by grayed-out arrows.

equation of motion for the impurity spin can be dropped and the corresponding density matrix can be replaced by its thermal equilibrium value instead [117]. Since the system under consideration is isotropic in $\mathbf{k}$ space, an average over the polar angles of the exciton CoM wave vectors does not introduce further approximations but is in fact essential in reducing the numerical demand of the quantum kinetic equations. However, note that any kind of spin-orbit coupling breaks this symmetry and therefore requires an explicit treatment of wave-vector angles.

Using the assumptions above, the QKT for the time-dependent spin up and spin-down exciton density can be condensed into the equation

$$
\begin{aligned}
\frac{\partial}{\partial t} n_{x_1 K_1}^{\uparrow/\downarrow} ={} & \frac{2}{\hbar} \mathbf{E}(t) \cdot \mathbf{M}_{\uparrow/\downarrow} \mathrm{Im}\big[y_{x_1}^{\uparrow} \phi_{x_1}\big] \delta_{K_1,0} \pm \frac{J_{pd} n_{\mathrm{Mn}}}{\hbar V} \sum_{x'K'} \Big(\mathrm{Im}\big[Q_{\eta_{\mathrm{e}} 3 x' K'}^{3 x_1 K_1}\big] \pm \frac{1}{2} \mathrm{Im}\big[Q_{\eta_{\mathrm{e}} 3 x' K'}^{0 x_1 K_1}\big] \Big) \\
& \pm \frac{J_{sd} n_{\mathrm{Mn}}}{\hbar V} \sum_{x'K'} \Big(\sum_{jl} \epsilon_{jl3} \mathrm{Re}\big[Q_{-\eta_{\mathrm{h}} j x' K'}^{l x_1 K_1}\big] - \frac{1}{2} \mathrm{Im}\big[Q_{-\eta_{\mathrm{h}} 3 x' K'}^{0 x_1 K_1}\big] \mp \sum_j \mathrm{Im}\big[Q_{-\eta_{\mathrm{h}} j x' K'}^{j x_1 K_1}\big] \Big) \\
& \mp \frac{J_0^{\mathrm{e}} n_{\mathrm{Mn}}}{\hbar V} \sum_{x'K'} \Big(2 \mathrm{Im}\big[Z_{-\eta_{\mathrm{h}} \ x' K'}^{3 x_1 K_1}\big] \pm \mathrm{Im}\big[Z_{-\eta_{\mathrm{h}} \ x' K'}^{0 x_1 K_1}\big] \Big) \\
& \mp \frac{J_0^{\mathrm{h}} n_{\mathrm{Mn}}}{\hbar V} \sum_{x'K'} \Big(2 \mathrm{Im}\big[Z_{\eta_{\mathrm{e}} \ x' K'}^{3 x_1 K_1}\big] \pm \mathrm{Im}\big[Z_{\eta_{\mathrm{e}} \ x' K'}^{0 x_1 K_1}\big] \Big).
\end{aligned}
\tag{3.7}
$$

Apart from the laser driving that enters via the time-dependent pulse $\mathbf{E}(t)$ and the transition-dipole matrix element $\mathbf{M}_{\uparrow/\downarrow}$, the dynamics is driven by the magnetic and non-magnetic correlations $Q_{\eta j x K}^{\alpha x' K'}$ and $Z_{\eta \ x K}^{\alpha x' K'}$, respectively, which explicitly depend on time. Here, Latin indices $j \in \{1, 2, 3\}$ correspond to the spatial directions and $\alpha \in \{0, 1, 2, 3\}$. The origin of the correlations can be determined from the corresponding coupling constants acting as prefactors of the individual contributions in Eq. (3.7), where along with the previously introduced J_{sd} and J_{pd} also the nonmagnetic coupling constants J_0^{e} and J_0^{h} appear. The latter stem from the local potential mismatch in the bandstructure of electrons and holes, respectively, due to the impurity doping. Only the real or imaginary part of the correlations enters since the spin-dependent exciton density is an observable quantity. The first term on the right-hand side of Eq. (3.7) additionally contains the interband coherence $y_x^{\uparrow}$, where the index $\uparrow$ characterizes the optically active spin state, together with the radial part of the exciton wave function evaluated at the origin, which is abbreviated by ϕ_x. Due to momentum conservation, excitons are optically generated with quasi-vanishing CoM momentum, as can be seen by $\delta_{K,0}$. The influence of an external magnetic field is contained in the equations of motion for the correlations and it is assumed that the field is oriented along the z direction perpendicular to the QW plane. The relevant exciton spin component can be recovered from Eq. (3.7) using the relation $s_{xK}^z = \frac{1}{2}(n_{xK}^{\uparrow} - n_{xK}^{\downarrow})$.

For the propagation of the coherence and the correlations, which is rather lengthy and intricate, the reader is referred to Appendix B of Pub. 1. Here, only the general form of the corresponding equations is of interest to gain insight into their role for the exciton dynamics. The equation of motion for a time-dependent correlation $Q(t)$ has the general

form

$$\frac{\partial}{\partial t}Q(t) = -i\omega_Q Q(t) + b(t), \qquad (3.8)$$

where ω_Q contains a difference of exciton frequencies and is also influenced by Zeeman splittings in case of an external magnetic field. Additionally, the source term $b(t)$ depends on the exciton density or the exciton spin and is thus explicitly time dependent. Whereas only the exciton eigenenergies enter in a mean-field model of the spin dynamics, the explicit presence of dynamic **K**-dependent correlations in Eq. (3.7) reflects the breaking of the translational invariance and the resulting momentum nonconservation due to the random positions of impurities in DMSs. Since the correlations oscillate with energy differences rather than exciton energies and also contain inhomogeneities, it is clear that the equilibrium value of $n_{xK}^{\uparrow/\downarrow}$ will be affected by the correlations. In other words, the correlations are expected to influence the exciton occupation, causing a deviation from the mean-field expectation where momentum conservation is strictly enforced. Thus, the presence of the correlations in the QKT accounts for the fact that the independent-particle exciton states are actually not the proper eigenstates of the system in the presence of the exciton-impurity interaction.

3.1.3 Markov limit

To identify quantum kinetic features and many-body effects in the exciton dynamics, it is important to have a theory which does not account for exciton-impurity correlations in DMSs. In this context, the Markov limit is considered, a concept which is typically associated with the assumption of an infinitely short memory in a system. Indeed, formally integrating Eq. (3.8) reveals a memory induced by the correlations, which means that the exciton-impurity interaction in DMSs can also be considered in terms of introducing a finite memory. Then, the Markov limit is established by

$$Q(t) = \int_0^t d\tau\, e^{-i\omega_Q(t-\tau)} b(\tau) \approx b(t) \underbrace{\int_0^t d\tau\, e^{-i\omega_Q(t-\tau)} e^{-i\omega_b(\tau-t)}}_{\to\, \pi\delta(\omega_Q-\omega_b)-\mathcal{P}\frac{i}{\omega_Q-\omega_b}}, \qquad (3.9)$$

which basically amounts to neglecting the values of the independent-particle quantities $b(\tau)$ for past times $\tau < t$ and effectively replacing it by $b(t)$.

However, in a magnetic field, $b(\tau)$ actually has a time dependence which is in part determined by the external field and which must not be neglected. This is why one has to split off any possible fast-rotating components first, resulting in the additional complex exponential with the frequency ω_b in Eq. (3.9). This process is similar to a rotating-wave approximation and it has been shown that, for quasi-free electrons, missing these oscillations neglects energy shifts that are required for the energy conservation in an external magnetic field [119]. The final memory integral can be calculated analytically in the limit $t \to \infty$ and yields a delta function as well as a principal value, where the latter is typically disregarded.

Inserting the Markov limit of the correlations into Eq. (3.7), one obtains the desired MT to which the results of the QKT can be compared. For zero magnetic field and considering

only the $1s$ exciton ground state, the resulting equations can be solved analytically and one obtains the spin-decay rate

$$\tau_{1sK}^{-1} = \frac{IJ_{sd}^2 n_{\mathrm{Mn}} M}{\hbar^3 d} \langle S^2 \rangle F_{\eta_{\mathrm{h}} 1s1s}^{\eta_{\mathrm{h}} KK}, \tag{3.10}$$

which corresponds to the result of Fermi's golden rule. Comparing Eq. (3.10) with the rate for quasi-free electrons given by Eq. (2.5), it becomes clear that, apart from the replacement of the electron effective mass by the exciton mass M, the K-dependent form factor $F_{\eta_{\mathrm{h}} 1s1s}^{\eta_{\mathrm{h}} KK}$ introduced in Eq. (3.6) appears in the rate. Thus, in contrast to quasi-free electrons, the spin-decay rate for excitons decreases with increasing K due to the form factor, where the decrease follows the diagonal dashed line in Fig. 3.1. Note that $F_{\eta_{\mathrm{h}} 1s1s}^{\eta_{\mathrm{h}} KK}\big|_{K=0} = 1$ for optically generated excitons with $K = 0$ so that only the change of the effective mass is important in that case.

Although an analytic decay rate can still be found for fields perpendicular to the QW plane, the spin no longer decays to zero for this configuration and reaches a finite equilibrium value instead that depends on the magnitude of the applied field. However, if the magnetic field lies in the QW plane, the equations are more complicated due to the influence of the hh spins, which are still pinned along the growth direction and thus break the symmetry of the system so that an analytic solution can no longer be obtained. Both cases are discussed in Pub. 2.

3.2 Impact of exciton-impurity correlations

In this section, the developed QKT is applied to typical DMS QWs and the impact of exciton-impurity correlations on the spin dynamics is investigated for vanishing as well as finite magnetic fields. Additionally, it is shown how the correlations manifest in the linear absorption and how they affect transitions to excited exciton states.

3.2.1 Spin dynamics without magnetic field

Starting with the case when no magnetic field is applied, the exciton spin dynamics has been investigated in Pub. 1. Using a slightly larger QW thickness and a lower doping fraction, the exciton spin dynamics in a 15-nm-wide $\mathrm{Zn}_{0.975}\mathrm{Mn}_{0.025}\mathrm{Se}$ QW is depicted in Fig. 3.3(a). If not specified otherwise, a Gaussian laser pulse with a full width at half maximum of $100\,\mathrm{fs}$ is considered throughout part I of this thesis and the sample is assumed to be at $2\,\mathrm{K}$.

First of all, one notices that the spin decay in the QKT is initially slowed down compared with the MT. In fact, for the first few picoseconds of the dynamics, the result of the QKT actually follows a calculation where artificially only half the spin-decay rate obtained in the MT is used. In Pub. 1, this behavior is traced back to the memory kernel introduced by the correlations, which can be understood as follows. Looking again at Eq. (3.9), the final integral can be evaluated up to a finite time t, which yields a time-dependent memory kernel $\sim \frac{\sin(\omega t)}{\omega}$ that depends on the exciton frequency ω. As explained in Sec. 3.1.3, the Markov limit is obtained by taking the limit $t \to \infty$ of the memory kernel, where it retracts to the δ function appearing in Fermi's golden rule. However, since excitons are
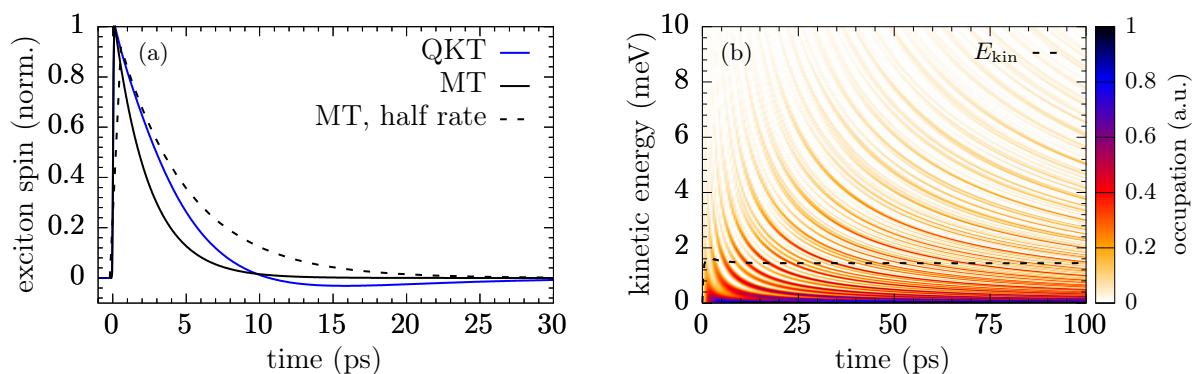
Figure 3.3: (a) Exciton spin dynamics in a 15-nm-wide $Zn_{0.975}Mn_{0.025}Se$ QW calculated with the QKT and the MT. Additionally, results of the MT are shown using only half the decay rate. (b) Time- and energy-resolved exciton occupation along with the average kinetic energy per exciton (E_{kin}).

optically generated with nearly vanishing CoM momentum and, thus, are excited close to $\omega = 0$, half of the memory kernel is effectively cut off as there are no exciton states below the bottom of the exciton parabola. As a consequence, this causes a deviation of the predictions obtained by the QKT compared with those of the standard MT for short times in the form of a slower decay.

The initial slowdown of the spin decay is a crucial feature of the theory which, for the first time, provides an explanation for an inconsistency of theoretical spin-decay rates with experimentally observed results collected in Ref. [29]. There, spin-decay rates for different samples measured by various groups are collected and compared with the standard theoretical model for quasi-free electrons given by Eq. (2.5), which turns out to significantly underestimate the spin decay by a factor of five. The argument that excitons instead of quasi-free electrons should be considered since the experiments probe the exciton resonance is unable to rectify this issue because of the much larger exciton mass $M \approx 8m_e$. However, if one extracts a spin-decay rate from the QKT result in Fig. 3.3(a), which can be done by taking the inverse of the time where the spin has reached $\frac{1}{e}$ of its maximum value, a smaller rate compared to the MT is obtained. In combination with the overestimation of the experimental observations, the QKT thus offers predictions which are much closer to the measurements in Ref. [29].

Combing back to Fig. 3.3(a), one also observes an overall nonmonotonic time evolution due to an overshoot of the spin after approximately 10 ps which is completely absent in the exponential dynamics predicted by the MT. Such features are signatures of a coherent dynamics that cannot be described on the Markov level and which have also been investigated in terms of a QKT for quasi-free electrons [117]. The overshoot can be understood as yet another consequence of the sinc-like memory kernel or, to be specific, its decaying oscillations [127]. Since the oscillations of the memory kernel depend on the exciton frequency, which is close to zero in case of optical excitation, one would expect that they can have a marginal impact on the spin dynamics at best, let alone causing an overshoot. However, Fig. 3.3(b) reveals that the presence of exciton-impurity correlations also directly impacts the occupation of the exciton parabola. Immediately after the optical excitation, excitons are scattered towards states with kinetic energies of

up to several meV, causing the kinetic energy per exciton to increase to about $1.5\,\mathrm{meV}$ already during the finite pulse width. Note that the redistribution of excitons to higher kinetic energies is not caused by energy-time uncertainty since it can only act on short timescales of a few picoseconds here. Instead, states with finite kinetic energies remain populated even at long times. For the evaluation of the memory kernel, this means that a multitude of different frequencies has to be considered so that, on average, an overshoot remains.

3.2.2 Spin dynamics in a finite magnetic field

Whereas up to this point only situations without an external magnetic field have been considered, this section focuses on the exciton spin dynamics in a finite magnetic field. Although a field can be applied in arbitrary orientations, the two most commonly studied cases are the Faraday and the Voigt configuration. While the magnetic field is oriented perpendicular to the QW in the first case, the Voigt configuration describes the case where it is flipped by 90° and lies in the quantum-well plane [76]. The first configuration is sketched in Fig. 3.4(a) along with the spin orientations of the impurities as well as the exciton-bound carriers.

In case of the Faraday configuration, the formerly spin-degenerate exciton parabolas now show a giant Zeeman splitting given by

$$\hbar\omega_{\mathrm{e}} = g_{\mathrm{e}}\mu_B B^z + J_{sd}n_{\mathrm{Mn}}\langle S^z\rangle, \tag{3.11}$$

where g_{e} is the electron g factor and μ_B denotes the Bohr magneton. Note that the hh Zeeman splitting does not enter since only DMSs with a large hh-lh splitting are considered so the hh spin is pinned. Due to the second term in Eq. (3.11), which is proportional to the average impurity spin polarization $\langle S^z\rangle$ in the z direction, splittings exceeding $100\,\mathrm{meV}$ can be reached at liquid-helium temperatures and fields of a few Tesla [76].
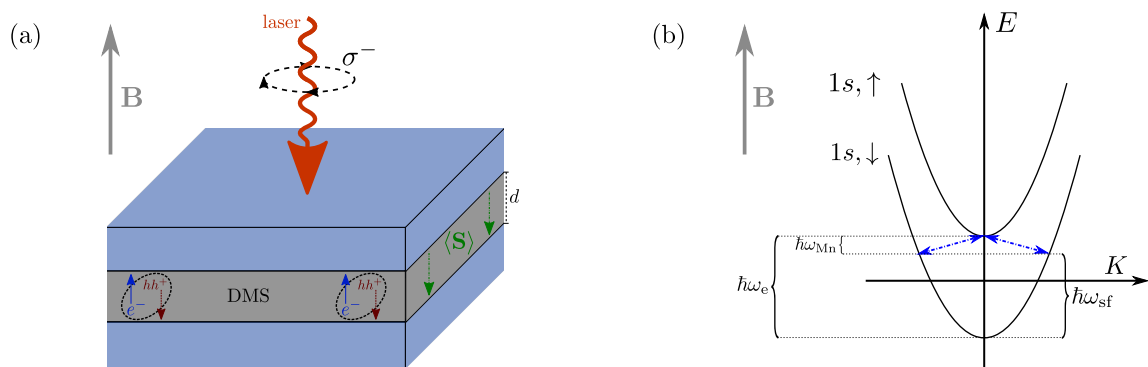

Figure 3.4: (a) Sketch of a DMS QW with thickness d in the Faraday configuration under σ^--polarized optical excitation. Green arrows indicate the average Mn spin polarization $\langle\mathbf{S}\rangle$ in the DMS, whereas blue and red arrows indicate the spin orientation of exciton-bound electrons and heavy holes, respectively. The magnetic field is denoted by $\mathbf{B}$. (b) Giant Zeeman splitting $\hbar\omega_{\mathrm{e}}$ of the $1s$ exciton parabolas with spin-flip transitions indicated by blue arrows. Also shown is the spin-flip scattering shift $\hbar\omega_{\mathrm{sf}}$ and the Mn Zeeman splitting $\hbar\omega_{\mathrm{Mn}}$.
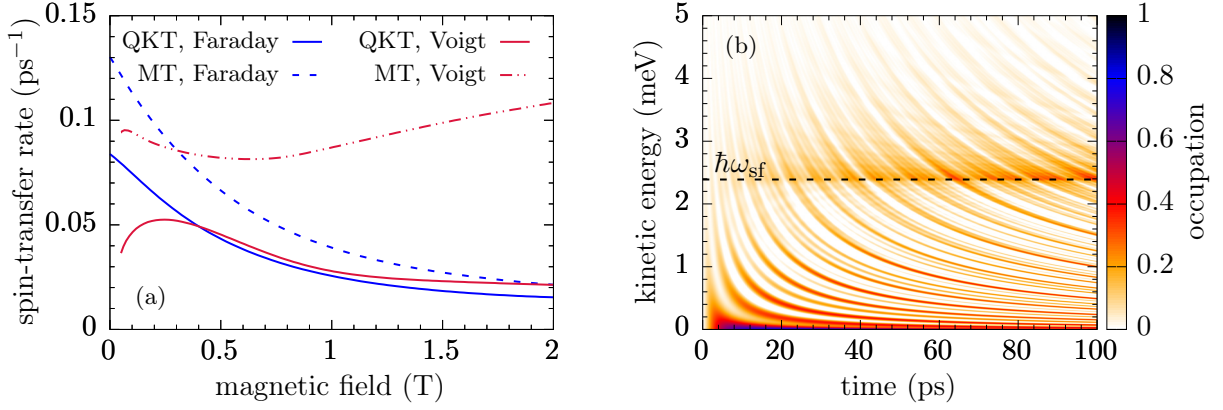
Figure 3.5: (a) Spin-transfer rates for a 20-nm-wide $Zn_{0.99}Mn_{0.01}Se$ QW as a function of the external magnetic field in Faraday and Voigt configuration. (b) Time- and energy-resolved exciton occupation with respect to the bottom of the exciton parabola for a magnetic field $B = 0.5\,T$ in Faraday configuration. The spin-flip scattering shift $\hbar\omega_{sf}$ is indicated by a dashed line.

This is why DMSs exhibit a giant Zeeman shift much larger compared with nonmagnetic semiconductors. The $1s$ exciton parabolas for this case are depicted in Fig. 3.4(b).

In Pub. 2, the exciton spin dynamics is investigated using the QKT for both, Faraday and Voigt configuration. To compare the data for magnetic fields of different magnitudes, a spin-transfer rate is numerically extracted from the simulations in a similar fashion to the case without magnetic field. However, since a preferred direction is imposed on the system by the external field, the exciton spin no longer decays to zero and reaches a finite equilibrium value instead. Thus, the rate is taken to be the inverse time where the envelope of the spin has decayed to $\frac{1}{e}$ times the difference between the maximum spin and the equilibrium value. Considering the envelope of the spin also allows for an analogous treatment of the Voigt configuration, where the exciton spin precesses around the magnetic field. For the Faraday case, the scattering in terms of the MT is illustrated in Fig. 3.4(b) by blue arrows. The excitons are optically excited at the bottom of the $1s,\uparrow$ parabola and, due to the magnetic exchange interaction, a spin-flip scattering towards the $1s,\downarrow$ parabola and vice versa takes place. However, the transitions are not horizontal since flipping an exciton spin requires a corresponding decrease of the Mn spin proportional to the Mn Zeeman splitting $\hbar\omega_{Mn}$. This is why a scattering from $E = 0$ of $1s,\uparrow$ excitons towards $E = \hbar\omega_{sf} := \hbar\omega_e - \hbar\omega_{Mn}$ of $1s,\downarrow$ excitons is expected. The introduced quantity $\hbar\omega_{sf}$ is referred to as the spin-flip scattering shift.

Plotting the spin-transfer rates for the Faraday configuration as a function of the magnetic field in Fig. 3.5(a), one again notices the slower decay predicted by the QKT compared with MT discussed in the previous section. For higher fields, the rate monotonically decreases and the results of the QKT and the MT approach one another. The decrease of the rate is a consequence of the decreasing exciton form factor evaluated for larger spin-flip scattering shifts and, consequently, larger CoM momenta, as shown in Fig. 3.1. As discussed in the previous section, the QKT also predicts a redistribution of exciton kinetic energies in the presence of a magnetic field. In contrast to the MT, where only a scattering between $E = 0$ and $E = \hbar\omega_{sf}$ can occur, Fig. 3.5(b) reveals the distinct

signatures of the quantum-kinetic broadening. Although the regions around $E = 0$ and $E = \hbar\omega_{\text{sf}}$ still show the highest occupations, a significant percentage of excitons occupies states with other energies.

Quite unexpectedly, however, the predictions of the QKT and the MT differ not only quantitatively for the Voigt configuration, but the QKT shows a completely reversed trend. In the Voigt configuration, instead of a giant Zeeman splitting and the previously discussed spin-flip scattering, the exciton spins perform a precession around the axis of the magnetic field so that the observed decay of the spin polarization is a consequence of an ensemble average and not a scattering between states with different energies. The nonmagnetic impurity scattering, which yields no contribution on the Markov level but significantly contributes to the redistribution of exciton kinetic energies in the QKT, turns out to be the main culprit behind this trend reversal. Similar to the Dyakonov-Perel mechanism, which describes a spin decay that is inversely proportional to the momentum-scattering rate, here the nonmagnetic scattering of excitons at the impurities inhibits the spin precession and causes a slower dephasing, leading to a significantly smaller spin-transfer rate. The pronounced nonmonotonic behavior of the spin-transfer rate as a function of the magnetic field in the Voigt configuration may also contribute to similar nonmonotonic tendencies observed in experiments [29].

It is also interesting to note that, in the QKT, the spin-transfer rates in the Faraday and the Voigt configuration for magnetic fields larger than a few $100\,\text{mT}$ are very similar. This observation suggests that the spin transfer in the DMSs studied here is dominated by nonmagnetic impurity scattering, which does not depend on the orientation of the field. In this context, one should also be aware that the magnetic pd exchange interaction effectively becomes a nonmagnetic interaction with a large coupling constant $J_{pd} = 50\,\text{meV}$ in ZnSe-based DMSs due to the pinned hh spins. Pub. 2 provides further details on the impact of nonmagnetic scattering on the redistribution of exciton kinetic energies for the Voigt configuration similar to Fig. 3.5(b).

3.2.3 Linear absorption

From another point of view, the impact of exciton-impurity correlations on the temporal behavior of the exciton kinetic energy shown in Figs. 3.3(b) and 3.5(b) can be seen as a consequence of the underlying many-body nature of the exciton dynamics in DMSs. Accounting for the exciton-impurity interaction beyond the Markov level via the correlations included in the QKT means that the eigenstates of the problem are no longer given by those obtained in a model of independent excitons. Rather, in the presence of the interaction, the eigenstates are a linear combination of the ones obtained by solving the independent-exciton problem given by Eq. (2.1). As a consequence, the fact that the QKT predicts a linear combination of exciton states should also have an impact on the linear absorption of DMSs, which is indeed the case and is the main topic of Pub. 3.

Calculating the linear absorption for 15-nm-wide $\text{Zn}_{1-x}\text{Mn}_x\text{Se}$ QWs for various doping fractions reveals a redshift of the main $1s$ exciton resonance with increasing impurity content which is accompanied by the emergence of a second feature to the right of the peak, as can be seen in Fig. 3.6(a). The second feature is split off from the exciton resonance for larger doping fractions and becomes increasingly smeared out with an exponentially decaying tail on the high-energy side. Comparing the distance between the maximum of
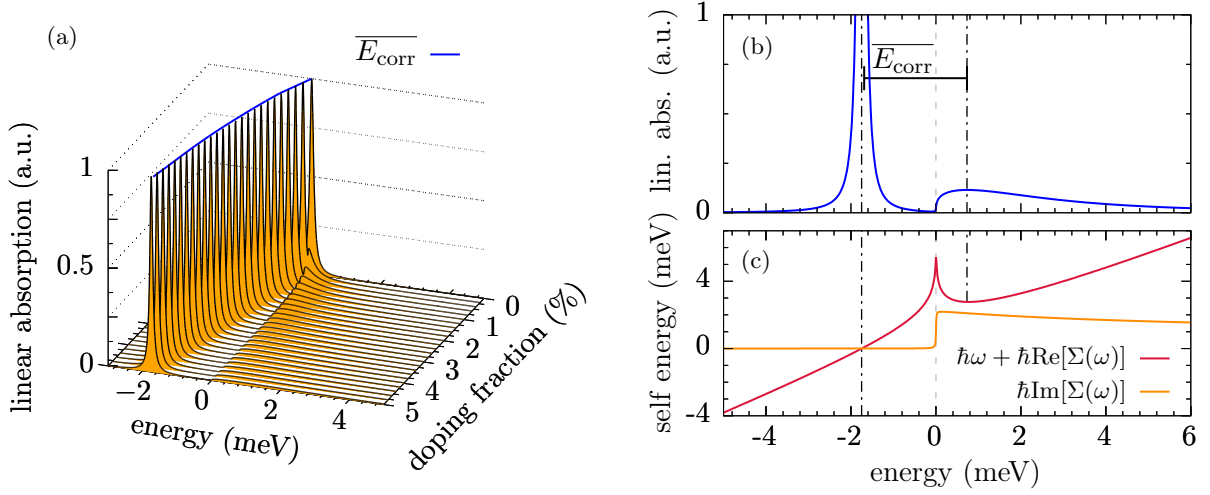
Figure 3.6: (a) Linear absorption spectra of a 15-nm-wide $Zn_{1-x}Mn_xSe$ QW for various doping fractions x. The origin of the energy scale coincides with the maximum of the $1s$ exciton resonance at $x = 0$ and the spectra are normalized with respect to each $1s$ absorption peak. The average correlation energy per exciton $\overline{E_{corr}}$ is indicated with respect to the maximum of each correlation-induced feature. To explain the absorption lineshape, (b) a zoom of the linear absorption for $x = 5\%$ is compared with (c) the real and imaginary parts of the self-energy $\hbar\Sigma(\omega)$.

the second feature and the maximum of the main exciton resonance with the computed average correlation energy per exciton reveals an excellent agreement. This shows that the correlation energy in DMSs can be directly extracted from a linear absorption spectrum for any given impurity content, provided that the exciton linewidth is narrow enough so the second feature is not completely covered by the main resonance. Although Fig. 3.6 is calculated only with an artificial broadening $\Gamma_0 = 0.1\,\text{ps}^{-1}$ without accounting for phonons, Pub. 3 shows that phonons only lead to a broadening and a shift of the resonance which are both on the order of a few µeV per K and can thus be neglected.

To gain insight into the lineshapes observed in Fig. 3.6(a), it is useful to express the linear absorption in terms of the self-energy $\hbar\Sigma(\omega)$, which yields

$$\alpha(\omega) \sim \frac{\Gamma_0 + \text{Im}[\Sigma(\omega)]}{\left(\omega + \text{Re}[\Sigma(\omega)]\right)^2 + \left(\Gamma_0 + \text{Im}[\Sigma(\omega)]\right)^2}. \tag{3.12}$$

An analytic expression for the self-energy can be found in the Supplemental Material of Pub. 3 along with an extended theory that also takes phonon broadening into account. The real and imaginary parts of the self-energy are plotted in Fig. 3.6(c) for $x = 5\%$ and, for comparison, a magnification of the corresponding absorption lineshape is depicted above in Fig. 3.6(b). A steplike behavior of $\hbar\text{Im}[\Sigma(\omega)]$ is found that reflects the density of states for a two-dimensional system, which is proportional to a step function that is constant for $\omega > 0$. Due to the scattering with localized impurities, the scattering potential is almost independent on the transferred wave vector, which implies that the corresponding scattering matrix element between excitonic states leads only to a slow decrease of $\hbar\text{Im}[\Sigma(\omega)]$ for larger energies due to the exciton form factor. The shape of

$\hbar\text{Re}[\Sigma(\omega)]$ follows from the Kramers-Kronig relation since the self-energy is a response function.

Figure 3.6(c) shows that the shift of the main exciton peak is determined by the condition $\hbar\omega + \hbar\text{Re}[\Sigma(\omega)] = 0$, whereas the second feature in the spectrum is a consequence of the sudden rise of $\hbar\text{Im}[\Sigma(\omega)]$ at $\omega > 0$. From Eq. (3.12), it follows that the width of the main exciton resonance is determined by Γ_0, whereas the second feature is smaller and broader due to the finite value of $\hbar\text{Im}[\Sigma(\omega)]$ and its maximum corresponds to a local minimum of $\hbar\omega + \hbar\text{Re}[\Sigma(\omega)]$ for $\omega > 0$. Again, one can see that the average correlation energy per exciton determines the separation of the two spectral features. For details regarding the computation of the correlation energy using the QKT, the reader is referred to the Supplemental Material of Pub. 3.

To summarize, compared with the case of quasi-free electrons investigated on a quantum kinetic level [117–119, 127], these results together with those regarding the spin dynamics in the previous sections not only show that the physics of excitons is significantly different but that excitons are much more affected by correlations beyond the mean-field level. While it has been shown that nonmagnetic scattering at impurities in fact strongly suppresses non-Markovian effects such as overshoots in the spin dynamics of quasi-free electrons [116], the exciton spin dynamics is significantly modified due to such correlations so that even spin-transfer rates are affected. Moreover, since excitons lead to a well-defined resonance in the linear absorption, as shown in Fig. 3.6(a), exciton-impurity correlations can leave a characteristic fingerprint in spectra of DMSs in the vicinity of the exciton resonance. This is in stark contrast to the quasi-free electron case, where a continuum of states is optically accessible above the semiconductor band gap and no spectrally isolated features occur.

3.2.4 Influence of excited states

Recalling the exciton energies calculated in Fig. 2.2(b), it is clear that the giant Zeeman splittings in DMSs are large enough to bring the spin-up exciton ground state into or close to resonance with an excited state of the opposite spin orientation. Taking four exciton states into account, namely the $1s$, $2s$, and the two energetically degenerate $2p$ states, corresponding simulations of the exciton occupation and the spin dynamics are the topic of Pub. 4. Although the giant Zeeman splittings for the DMSs with doping fractions of up to 1% at $2\,\text{K}$, which have been investigated in the previous section, only reach values of a few meV so that excited states can be neglected, a magnetic field of about $830\,\text{mT}$ is sufficient to overcome the energy separation between the $1s$ and the $2p$ state in a 20-nm-wide $\text{Zn}_{0.975}\text{Mn}_{0.025}\text{Se}$ QW at $1\,\text{K}$.

As shown in Pub. 4, however, the QKT predicts a sizable occupation of the $2p$ states already for magnetic fields well below this threshold. In fact, close to 40% of the excitons are transferred to the $2p$ states after $100\,\text{ps}$ at a magnetic field of $750\,\text{mT}$, almost $100\,\text{mT}$ before reaching the critical field. Using the MT for these parameters, all excitons remain in the ground state due to the strict conservation of independent-particle energies on the Markov level. In the QKT on the other hand, as pointed out in Sec. 3.2.1, the exciton-impurity exchange interaction leads to different energy eigenstates which can also contain admixtures of excited states. This means that excited states become accessible already for fields below the critical value required in a Markov approach. Alternatively, one can

also argue that the negative correlation energy in DMSs, which leads to an increase of the exciton kinetic energy, can be used to overcome the remaining energy difference between the exciton ground state and excited states.

Apart from influencing the occupations, populating higher exciton states also has consequences for the spin dynamics. In Pub. 4, this is revealed by a faster decay of the $1s$ exciton spin when four exciton states are accounted for compared with a calculation where only the ground state is present. Since the decay of the $1s$ exciton spin is accompanied by a polarization of $2p$ spins with the opposite sign, this mechanism also provides a means to store the spin information in an optically dark state that is protected against radiative decay.

3.3 Phonon influence in DMSs

For low temperatures, the phonon influence is expected to be minimal for optically generated excitons since phonon emission is impossible at the bottom of the exciton parabola and phonon absorption is virtually absent. This is why, up to this point, phonons have been disregarded in the exciton dynamics in DMSs. However, for nonequilibrium exciton distributions away from $K = 0$, phonon emission becomes possible and, in general, phonon absorption may also play a role at elevated temperatures. In this section, the necessary modifications to the QKT regarding the incorporation of carrier-phonon scattering are briefly discussed and the theory is applied to a distribution of hot excitons. Furthermore, the phonon impact on the long-time limit of the exciton spin dynamics in a finite magnetic field is investigated.

3.3.1 Dynamics of hot excitons

To account for carrier-phonon scattering in DMSs, the model presented in Sec. 3.1.1 is extended to account for longitudinal-acoustic (LA) phonons via deformation potential coupling. Restricting the investigations to temperatures below $80\,\mathrm{K}$, where LA phonons are known to dominate the exciton line widths in semiconductors [128], longitudinal-optical (LO) phonons can be neglected for the typical exciton energies encountered here since the emission of an LO phonon requires energies of at least $30\,\mathrm{meV}$ [129]. Due to the small carrier-phonon coupling compared with the carrier-impurity interaction, the phonon scattering is treated on the Markov level and cross terms between phonon- and impurity-assisted variables are dropped. This yields new contributions to the equations of motion in the QKT as well as the MT which are given in Pub. 5.

Including the carrier-phonon scattering in the description of resonantly excited excitons confirms that the exciton-impurity exchange interaction is indeed the dominant mechanism in DMSs. Although LA phonons visibly increase the kinetic energy per exciton at temperatures of a few $10\,\mathrm{K}$, their influence on the spin dynamics for vanishing magnetic field is negligible. In Pub. 5, this is shown by the temperature dependence of the spin-transfer rate, where phonons merely cause a change of 5% at $80\,\mathrm{K}$ in the MT and do not have any visible impact at all when the spin dynamics is treated on the quantum kinetic level. This observation holds even for small doping fractions below 1%.

Since phonon emission is blocked for resonantly excited excitons due to their proximity to the bottom of the exciton parabola, the question arises whether a more pronounced
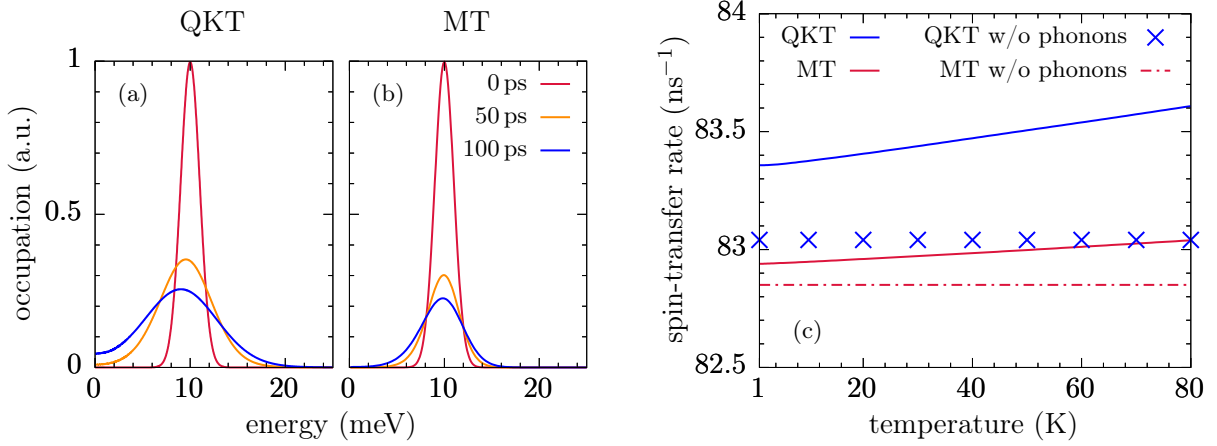
Figure 3.7: (a) Snapshots of the broadening of a hot exciton distribution calculated using the QKT and (b) the MT for three different times in a 15-nm-wide $\mathrm{Zn_{0.975}Mn_{0.025}Se}$ QW at 80 K. (a) Temperature dependence of the spin-transfer rate for hot excitons predicted by the QKT and the MT. Simulations with and without (w/o) phonons are compared.

phonon impact on the exciton dynamics exists for highly nonequilibrium exciton distributions away from $K = 0$. Such distributions are referred to as *hot excitons* and have been extensively studied in ZnSe nanostructures [130–132]. Experimentally, they can be generated via above band-gap optical excitation followed by LO-phonon assisted relaxation onto the $1s$ exciton parabola on a femtosecond timescale. Considering the timescale of the latter process, the corresponding simulations in Pub. 5 are carried out using an initial distribution of hot excitons modeled by a Gaussian centered at 10 meV with a standard deviation similar to experimental data. The main results are shown in Fig. 3.7.

At 80 K, where the LA-phonon influence is largest, one can see in Fig. 3.7(a) that a considerable broadening of the distribution takes place on a timescale of several 10 ps in the QKT. Most importantly, after 100 ps, some excitons reach the bottom of the exciton parabola at $E = 0$ and, thus, occupy optically bright states instead of the dark states for $E > 0$. A clear asymmetry of the exciton distribution is also visible, together with a slight shift of the maximum towards lower energies. Comparing these results to the simulations shown in Fig. 3.7(b), where the exciton-impurity scattering is treated on the Markov level, it becomes clear that the redistribution of excitons due to phonons alone does not account for the population of bright states on the timescale considered here. Rather, in the absence of the quantum kinetic redistribution, the exciton distribution remains much narrower even after 100 ps.

Turning to the spin-transfer rates in Fig. 3.7(c) and comparing them with the timescale discussed in the context of resonant excitation in Sec. 3.2, it becomes apparent that the dynamics is significantly slowed down to the nanosecond regime. This is caused by the exciton form factor in the rate given by Eq. (3.10), which is reduced by almost one order of magnitude compared to resonant excitation. For hot excitons, a phonon impact on the spin-transfer rates is indeed visible in both, the QKT and the MT, although it is rather small in both cases. More importantly, the predictions of the QKT and MT only show a difference of less than 1% even at high temperatures, which means that the spin dynamics effectively becomes Markovian for hot excitons far away from $K = 0$.

3.3.2 Phonon-induced quantum ratchet in a magnetic field

In the previous section, the phonon impact on the exciton spin dynamics has been considered without taking an external magnetic field into account. As discussed in Sec. 3.2.2, a finite magnetic field in the Faraday configuration leads to a giant Zeeman splitting of the exciton parabolas, which results in different kinetic energies of excitons before and after a spin-flip scattering event. In particular, this means that states with finite kinetic energies can be populated which are affected by phonon emission processes, the impact of which on the spin dynamics is analyzed in Pub. 6.

Figure 3.8(a) shows the exciton spin dynamics predicted by the MT on a nanosecond timescale for a typical $Zn_{0.99}Mn_{0.01}Se$ QW in an external magnetic field with a magnitude of $0.5\,T$. By comparing the figure to Fig. 3.8(b), where the phonon scattering is not accounted for, it becomes clear that LA phonons cause a nearly complete reversal of the spin polarization on a timescale of about $1\,ns$ for very low temperatures not exceeding a few Kelvin. At higher temperatures, a stationary value of the spin is not only reached much earlier but it is also much closer to the prediction without phonons. This points towards the imbalance between phonon emission and absorption processes as the origin of the observed effect since this imbalance is most pronounced in the limit $T \to 0$. It should be noted that, although phonon scattering is absent in Fig. 3.8(b), the stationary value of the exciton spin still depends on the temperature due the impurity subsystem. Since the average impurity spin and its second moments are calculated assuming a thermal impurity-spin density matrix, these values depend on the temperature of the system and, thus, the spin dynamics becomes temperature dependent as well. This also means that the giant Zeeman splitting $\hbar\omega_e$ decreases with rising temperature, as explained in Pub. 6.

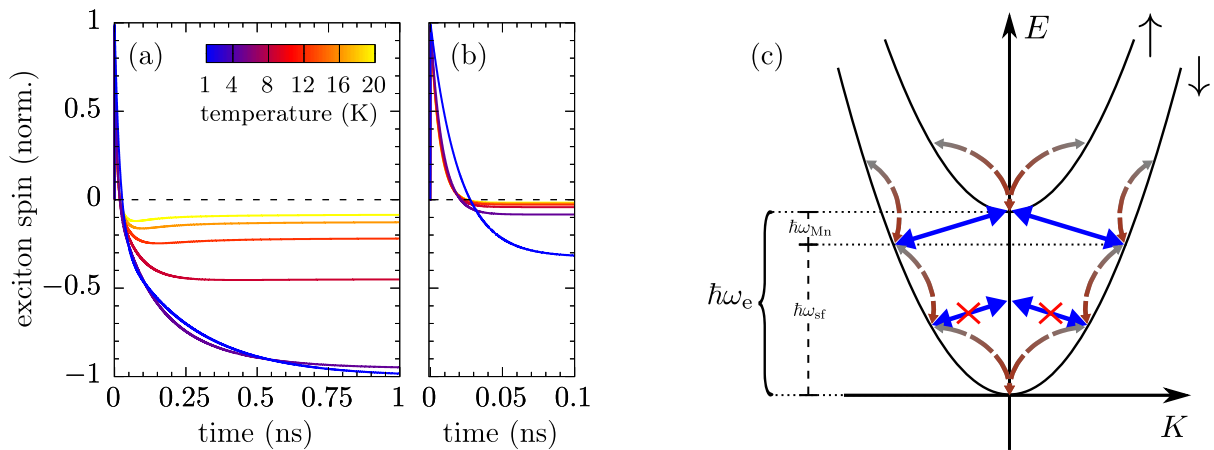The phonon impact on the exciton spin dynamics in a finite magnetic field can actually

Figure 3.8: [(c) taken from Pub. 6] (a) Long-time spin dynamics of resonantly excited excitons in the Markov approximation calculated with and (b) without phonons in a 15-nm-wide $Zn_{0.99}Mn_{0.01}Se$ QW at different temperatures in an external magnetic field $B = 0.5\,T$. (c) Sketch of the scattering processes between the Zeeman-split $1s$ exciton parabolas due to the sd exchange interaction. Spin-flip transitions are depicted by blue arrows and forbidden transitions are crossed out. LA phonon scattering on each parabola is included via curved arrows with a color gradient from grey to brown to illustrate the temperature-induced imbalance between absorption and emission processes.

be understood in terms of a quantum ratchet, which is typical for situations with a bias towards one specific scattering channel [133]. Here, the ratchet effect is perhaps best understood by visualizing the different scattering mechanisms, which is done in Fig. 3.8(c). Due to the optical excitation of spin-up excitons, the exciton population is initially confined to the bottom of the spin-up exciton parabola. In accordance with energy conservation, spin-flips induced by the magnetic exchange interaction take place from $\hbar\omega_e$ to $\hbar\omega_{sf}$ when measured with respect to the bottom of the spin-down parabola. Subsequently, exciton states with $E < \hbar\omega_{sf}$ become populated via LA-phonon emission, leading to a decrease of the exciton kinetic energy. However, again due to energy conservation, once an exciton has decreased its energy below $\hbar\omega_{sf}$ on the spin-down parabola, spin-flips become prohibited since there are no states on the spin-up parabola available with energies smaller than $\hbar\omega_e$. This means that, provided the temperature is low enough so phonon emission dominates, excitons effectively become trapped in states with $E < \hbar\omega_{sf}$ and spin down, thereby causing the complete sign reversal of the spin in Fig. 3.8(a).

Of course, the effect can also be studied on the quantum kinetic level, where it turns out that the sign reversal of the spin polarization is even slightly enhanced. However, as shown in Pub. 6, the main difference between the predictions of the MT and the QKT is that, while the ratchet effect is completely absent in the MT without phonon scattering, the QKT predicts a much larger spin-down population than the MT even when phonons are not accounted for. The reason for this behavior is the quantum kinetic redistribution, which causes a population of exciton states with $E < \hbar\omega_{sf}$ no matter if phonon scattering is present or not and which cannot be replicated on the Markov level. Nevertheless, it turns out that a feature previously discussed only in the context of the QKT can actually be replicated on the Markov level under appropriate conditions, as discussed in the next section.

3.4 On the origin of spin overshoots

Looking back at Sec. 3.2.1, where the impact of exciton-impurity correlations on the exciton spin dynamics and other observables is studied, one of the key features of the QKT is the prediction of a nonexponential time evolution characterized by an overshoot. Considering that overshoots of quantities are actually a common occurrence across different areas of physics [134–136], the question arises whether the appearance of an overshoot requires a quantum kinetic description or if a similar effect can also be obtained on a simpler level of theory. It turns out that, under appropriate conditions, the radiative decay of excitons combined with a spin-flip scattering is sufficient to cause an overshooting behavior of the spin, which is investigated in Pub. 7.

In the MT as well as the QKT, radiative decay can be rather straightforwardly included by introducing an additional rate which decreases the spin-up occupation but leaves the spin-down occupation unaffected. This reflects that the former are bright states while the latter are optically dark since the total electron and hh spin quantum number is given by $m = -2$. The situation has been previously discussed in Sec. 3.1.2 and a corresponding sketch can be found in Fig. 3.2. In Pub. 7, along with simulations using the QKT, a very simple model based on two coupled differential equations is presented which allows a straightforward understanding of the origin of spin overshoots due to a decay channel that mainly affects one out of two time-dependent variables, such as the spin-up and
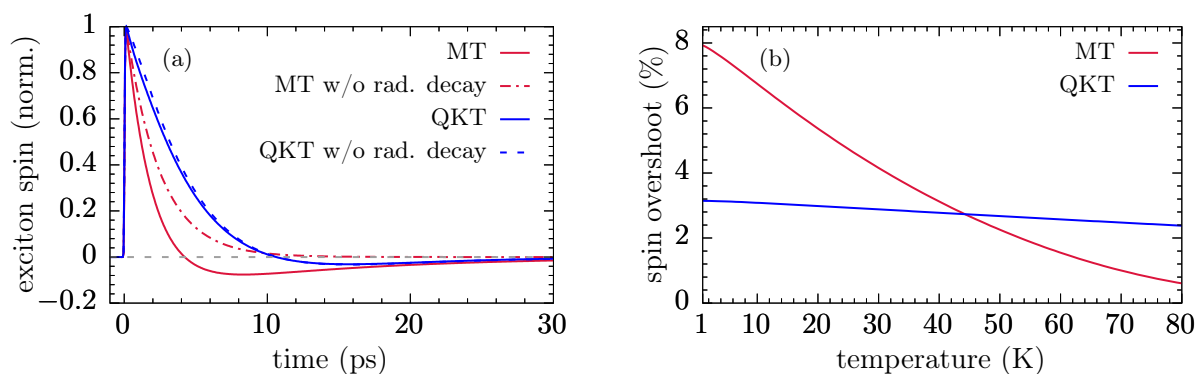
Figure 3.9: (a) Exciton spin dynamics in a 15-nm-wide $Zn_{0.975}Mn_{0.025}Se$ QW at 4 K with and without radiative decay in the MT and the QKT. (b) Maximum spin overshoot with respect to the spin polarization after the pulse predicted by the MT and the QKT as a function of temperature.

spin-down occupation.

Figure 3.9(a) shows the spin dynamics of resonantly excited $1s$ excitons in a typical $Zn_{0.975}Mn_{0.025}Se$ QW at 4 K including phonon scattering and radiative decay, where a rate of $0.1\,ps^{-1}$ is assumed for the latter. Turning first to the simulations using the MT, one can see that the inclusion of radiative decay indeed causes a spin overshoot a few picoseconds after the excitation. As discussed previously, the overshoot is completely absent when the radiative decay is switched off. In contrast, in the QKT, radiative decay only has a very limited impact on the spin dynamics that results in a slightly faster decay for short times. The position as well as the magnitude of the overshoot in particular are not at all affected by radiative decay. These observations already show that the overshoot in the MT and in the QKT must actually have a different physical origin.

With the help of the simple model developed in Pub. 7, the overshoot in the MT can be understood by decomposing the total spin shown in Fig. 3.9(a) into spin-up and spin-down contributions. As explained previously, radiative decay affects only spin-up excitons since only these couple to the light field. Although virtually all excitons are in the bright spin-up state directly after the pulse, the magnetic exchange interaction in DMSs enables spin flips between the bright and the dark states during the course of the dynamics. Even though the exchange interaction does not change the total number of excitons, this still means that the spin-up population decays faster as it is effectively prone to two decay rates simultaneously. When looking at the total exciton spin, which is the sum of the spin-up and spin-down components, one can thus find an overshoot whose position and magnitude depends on the ratio between the radiative decay and the spin-flip rate.

In the QKT, the overshoot has an entirely different origin and stems from the coherent dynamics beyond the Markov level as discussed in Sec. 3.2.1. Furthermore, the overall impact of radiative decay is negligible due to the pronounced quantum kinetic redistribution of excitons towards states with higher kinetic energies. Such states are optically dark not because of the spin but due to momentum conservation when a photon is emitted. From Fig. 3.9(a), one can also draw the conclusion that correlation effects dominate in DMSs and cause a suppression of radiative-decay induced overshoots.

Despite the different physical origins of the overshoot in the MT and the QKT, it will

be virtually impossible to experimentally determine whether a spin overshoot is caused by radiative decay or correlation effects just by looking at one time-resolved measurement. Thus, the question arises whether there is an efficient way to pin down the origin of spin overshoots in experiments. As shown in Fig. 3.9(b), this is possible by tracking the temperature dependence of the spin overshoot, i.e., how much the spin dips below zero with respect to the initial polarization after the pulse. Whereas the overshoot in the QKT is almost not affected by increasing the temperature up to 80 K, the overshoot purely due to radiative decay in the MT strongly decreases with rising temperature. The reason for the latter behavior is the phonon scattering, which enables the population of exciton states with $K > 0$ that becomes stronger at higher temperatures and thus decreases the number of excitons affected by radiative decay. Similarly, varying the doping fraction of the DMS, which is equivalent to tuning the strength of the spin-flip scattering, also yields different trends for the spin overshoot predicted by the QKT and the MT, as shown in Pub. 7.

An interesting aspect of the minimal model developed in Pub. 7 for the overshoot is that it is not limited to DMSs. Rather, the model can be applied to the spin dynamics in any semiconductor as long as one deals with a bright and a dark spin state coupled by any kind of spin-flip mechanism, such as electron-hole exchange in conjunction with momentum scattering or spin-orbit interaction. Concerning the conduction band, results of a preliminary study of the latter mechanism in DMSs are presented in the following section.

3.5 A first look into spin-orbit interaction in DMSs

In the context of nonmagnetic semiconductors, the SOI is typically one of the main contributions for spin relaxation or dephasing [96] and fundamentally appears as one of the terms in an expansion of the relativistic Dirac equation in $\left(\frac{v}{c}\right)^2$ [77]. Generally speaking, the SOI can always be written in terms of a wave-vector dependent effective magnetic field in which the carrier spins precess. In combination with momentum scattering, this leads to the well known Dyakonov-Perel mechanism with its characteristic inverse dependence of the spin-decay rate on the momentum-scattering rate [137], which is analogous to the motional narrowing in the context of nuclear magnetic resonance. In two dimensions, depending on the crystal symmetry, one often focuses on the Rashba SOI which arises in asymmetric QWs and can be further enhanced by applying a potential across the well [138]. Despite the commonly associated name, this type of interaction with its characteristic linear dependence on momentum was actually first studied by Ohkawa and Uemura already ten years prior to Rashba [139].

Here, a preliminary study of the impact of the Rashba SOI in the conduction band on the exciton spin dynamics in DMS QWs is presented. Although spin-orbit coupling certainly plays a major role also in the valence band, limiting the discussion to systems with a large hh-lh splitting and resulting pinned hh spins allows one to focus on the SOI in the conduction band. Pub. 8 provides details on how the Rashba SOI for electrons can be cast into the exciton basis so that it can be straightforwardly included into the previously developed framework. Due to the explicit dependence of the spin-orbit field on the wave vector, it is now necessary to resolve the full vector character of the exciton CoM motion so a quantum kinetic calculation is out of reach. However, one can make
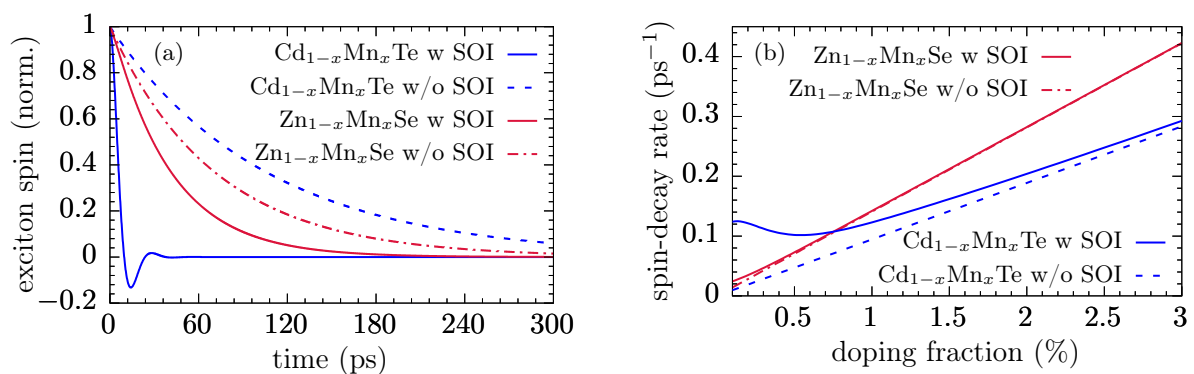
Figure 3.10: (a) Spin dynamics with and without the presence of Rashba SOI in 5-nm-wide $Cd_{1-x}Mn_xTe$ and $Zn_{1-x}Mn_xSe$ QWs with $x = 0.1\%$. (b) Spin-decay rate for the two DMSs as a function of the doping fraction, again with and without accounting for SOI. In contrast to Pub. 8, only half the potential drop across the QW ($V_{qw} = 50\,meV$) is used for the simulations.

use of the findings in Sec. 3.3.1 and consider the spin dynamics of hot excitons, which is found to be well described within a Markov approach. This is why only simulations using the MT are discussed in the following.

The impact of SOI on the spin dynamics in 5-nm-wide QWs is shown in Fig. 3.10(a) for the two most widely studied DMSs, namely $Cd_{1-x}Mn_xTe$ and $Zn_{1-x}Mn_xSe$. Since the Rashba coupling constant is typically much smaller than J_{sd}, the simulations are performed at rather small doping fractions $x = 0.1\%$ to see if a competition between the SOI and the exchange interaction can arise. Indeed, including the SOI causes a faster spin decay in both materials and even leads to a qualitative change in the form of a damped oscillation in the case of $Cd_{1-x}Mn_xTe$. The reason for this is the dependence of the Rashba constant on the ratio between the spin-orbit splitting and the band gap, which is much larger in this material compared with $Zn_{1-x}Mn_xSe$ [77]. The damped oscillations are a consequence of the precession of the exciton spin around the effective magnetic field provided by the SOI. Note that, while the simulations in Pub. 8 assume a potential drop of 100 meV across the QW, the simulations in Fig. 3.10 are carried out using only half this value to show that a significant impact of the SOI already takes place even for smaller Rashba constants.

As expected, increasing the doping fraction in the DMS causes the spin-decay rate obtained with SOI to converge to the rate without SOI since the magnetic exchange interaction quickly becomes the dominant spin-flip mechanism, as can be seen in Fig. 3.10(b). The results again show that the SOI in $Cd_{1-x}Mn_xTe$ is significantly stronger so that a pronounced increase of the spin-decay rate occurs for doping fractions below 1%. Instead of increasing the Mn content of the sample to reduce the influence of SOI, Pub. 8 also shows that the application of an external magnetic field in the Faraday configuration suppresses the SOI already for fields of a few 10 mT. This can be used as an effective way to mitigate potentially unwanted SOI effects on the spin dynamics.

At this point, the discussion of the SOI is certainly far from exhaustive. Already in the conduction band, there exists another type of SOI known as the Dresselhaus term that is also linear in momentum and acts similarly to the Rashba term, but with a prefactor that is solely determined by material parameters [140]. In conjunction with the Rashba-type

SOI, this term is known to cause a persistent spin helix in nonmagnetic semiconductors that forms when both interactions are of comparable strength [141].

4 Concluding remarks on magnetic systems

Despite the many findings that have resulted in Pub. 1-Pub. 8, the QKT developed over the course of this thesis provides a tool to study many other physical scenarios in DMSs. First of all, although the interaction between the excitons and the laser excitation is modeled explicitly, the question of coherent control of the exciton spin via the application of successive pulses has not been addressed so far. In this context, excitation protocols similar to Ref. [142] could be developed to control the exciton spin polarization instead of the impurity spins.

Alternatively, entirely different types of optical excitations can be investigated, such as using terahertz light sources to probe transitions between different exciton parabolas [143]. Regarding the optical excitation of higher exciton states with finite angular momentum, which cannot be excited by standard laser excitation, one can also think about completely different light sources. One such possibility is light with finite angular momentum, called twisted light [144], that has already been successfully used for the excitation of optically dark states in quantum dots [145].

Another way forward would be adapting the present theory to the description of the exciton-impurity interaction in magnetically-doped monolayers, such as the topical transition-metal dichalcogenides [90–92]. Apart from a necessary recalculation of the exciton states to account for the giant binding energies typical for these systems, the inherent valley degree of freedom can also be expected to become important [146, 147]. As proposed in a first-principles study, Mn-doped MoS_2 may be a suitable candidate for a two-dimensional DMS [148], although numerous other materials are also being discussed in this context in the literature [149, 150].

Finally, to extend the present description also to samples with a small hh-lh splitting, all four valence-band spin states would have to be accounted for in the simulations. Although the QKT in principle already supports all states in the valence band, performing the corresponding numerical calculations will be challenging and may well only be possible with additional approximations. Here, a possible way forward might be the inclusion of the long-range part of the Coulomb interaction, also known as exciton exchange interaction, which provides a means for a direct flip of the hh spin [125] without necessarily having to model the lh states explicitly.

Part II

Nonmagnetic systems – phonon influence on photonic properties of quantum dots

5 Quantum dots & real-time path integrals

In contrast to the magnetically-doped semiconductor QWs investigated in part I, the second part of this work is devoted to nonmagnetic semiconductor QDs embedded in optical resonators with a focus on the influence of phonons on photonic properties. This chapter briefly introduces QD-cavity systems regarding their experimental realization and theoretical description. To incorporate the phonon influence, the ultrafast dynamics in these systems is studied using a path-integral approach, which is explained subsequently.

5.1 Quantum dots in cavities

While QWs are two-dimensional systems with a confinement only in one direction perpendicular to the QW plane, QDs are characterized by a strong confinement of carriers in all spatial directions. Although growing such structures deterministically can be done in numerous ways [151], high-quality QDs can also be achieved via self-organized growth of nanometer-sized InAs islands on a GaAs substrate that form due to the lattice mismatch between the two materials [152]. Although the position of QDs grown in this manner cannot be precisely controlled, the structures are typically defect free and exhibit a strong electronic confinement. The latter causes electron and hole wave functions to be highly localized in space with well-separated energy levels, which can be further tuned by applying strain [153] or exploiting the DC Stark shift [154] and which can be selectively excited in accordance with the spin selection rules.

Regarding applications, this allows the focus on a subset of QD states and the dynamics between them, such as the exciton and the biexciton state characterized by one or two electron-hole pairs, respectively [155]. While the exciton is typically separated about $1\,\mathrm{eV}$ from the ground state, the energy of the biexciton is usually less than twice the exciton energy due to the Coulomb interaction. The difference between the two bare exciton energies and the biexciton energy is referred to as the biexciton binding energy with common values of a few meV [156]. To improve the light extraction efficiency, one can exploit the Purcell enhancement of the photon emission by embedding the QD in a microresonator or cavity [157]. Experimentally, such systems can be realized, e.g., in the form of micropillars [158] that can be highly optimized to allow for in-situ electrical tuning of the QD levels [64]. A schematic representation of a QD-cavity system can be found in Fig. 5.1.

In contrast to atoms in free space, QDs are influenced by their semiconductor environment via the carrier-phonon interaction. However, while energy-conserving inelastic phonon scattering dominates for extended nanostructures as investigated in part I, the large separation of the QD energy levels prohibits such processes and so-called pure dephasing dominates instead [159]. In particular, for the GaAs-based QDs investigated in
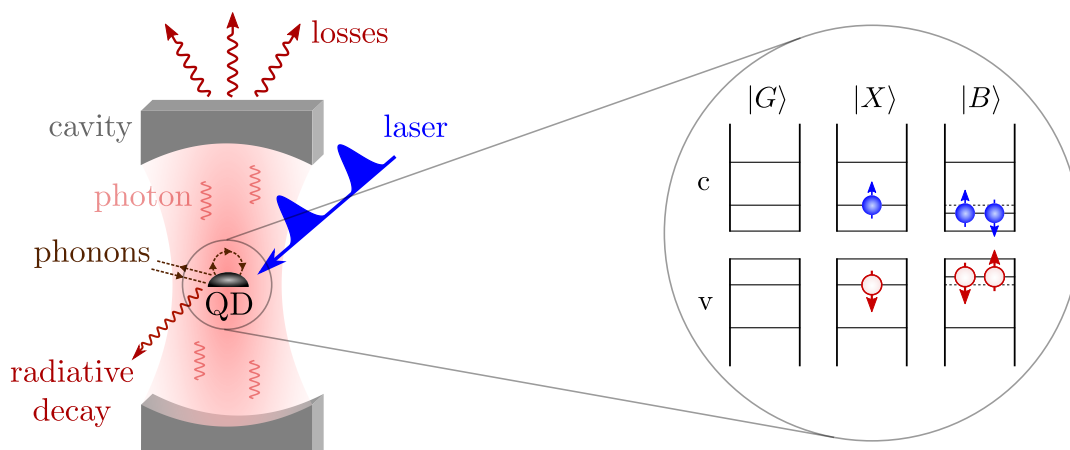
Figure 5.1: Schematic representation of a QD-cavity system under optical excitation. The zoom into the QD shows its electronic structure in electron-hole representation, where electrons in the conduction band (c) are depicted by filled blue circles and heavy holes in the valence band (v) are represented by red empty circles. The respective spin or angular momentum corresponds to the direction of the respective arrows. Indicated are the ground state $|G\rangle$, an exciton state $|X\rangle$, and the biexciton state $|B\rangle$ in the QD. Due to the two possible spin orientations for each carrier, two dark and two bright exciton states exist, but only one of the latter is shown here. In case of the biexciton, the Coulomb interaction slightly shifts the energy levels so that the biexciton is more strongly bound than two bare excitons.

this thesis, the pure dephasing is largely due to the deformation-potential coupling to LA phonons and can be written as

$$H_{\mathrm{ph}} = \hbar \sum_{\mathbf{q}} \omega_{\mathbf{q}} b_{\mathbf{q}}^{\dagger} b_{\mathbf{q}} + \hbar \sum_{\mathbf{q}\nu} n_{\nu}^{X} \left(\gamma_{\mathbf{q}}^{X} b_{\mathbf{q}}^{\dagger} + (\gamma_{\mathbf{q}}^{X})^{*} b_{\mathbf{q}} \right) |\nu\rangle\langle\nu| \tag{5.1}$$

with phonon creation and annihilation operators $b_{\mathbf{q}}^{\dagger}$ and $b_{\mathbf{q}}$, respectively, for a phonon mode with wave vector $\mathbf{q}$ and energy $\hbar\omega_{\mathbf{q}}$. The carrier-phonon coupling is assumed to scale with the number of excitons n_{ν}^{X} in the QD state $|\nu\rangle$ and $\gamma_{\mathbf{q}}^{X}$ denotes the coupling constant. In Fig. 5.1, the pure-dephasing action of phonons is depicted as a brown closed loop above the QD together with straight lines representing phonon emission or absorption. Similar to the carrier-impurity exchange interaction in DMSs, Eq. (5.1) describes a many-body interaction due to the sum over infinitely many phonon modes that can lead to pronounced non-Markovian behavior [67, 160]. In analogy to the QKT developed for DMSs, this manifests in the appearance of a finite memory when treated beyond the Markov approximation [74]. Although phonons are a major source of decoherence in QDs and are known to cause a damping of Rabi oscillations [67, 161], protocols for a robust phonon-assisted exciton or biexciton preparation can be devised [59] and phonons can be actively used to enable a nonresonant QD-cavity coupling [56].

Apart from the phonon influence, the QD is typically excited via an external laser pulse or is pumped continuously, which is usually modeled as an interaction with a classical field. Furthermore, the coupling to the quantized cavity mode leads to product states comprised of the dot state and the photon state of the cavity. In case of a two-level system, the QD-cavity coupling is described by the Jaynes-Cummings model [162]. In contrast to the

driven QD, which results in the population of laser-dressed states, resonantly coupling a QD to a cavity with the coupling strength g leads to the occupation of cavity-dressed states with a characteristic energy dependence $E_{n_{\text{ex}}} = g\sqrt{n_{\text{ex}}}$ on the number of excitations n_{ex}. Here, the number of excitations refers to the sum of the photon number in the cavity and the exciton occupation in the QD.

As sketched in Fig. 5.1, the system generally exhibits losses in the form of radiative decay in the QD into field modes outside the cavity. Furthermore, due to unavoidable imperfections in the cavity, there is also a finite probability for photons to leak out. In fact, the latter loss channel is typically the most important one for QDs [158]. From a theoretical point of view, such loss channels can often be sufficiently modeled in the Markov limit in the form of a non-Hamiltonian contribution to the dynamics. To still preserve important physical properties, such as positive definiteness, of the density matrix despite the non-Hamiltonian nature of these contributions, one may describe them using superoperators in the so-called Lindblad form [75, 163].

5.2 Real-time path-integral propagation

Many different methods are available to describe the coupling of the QD to its environment, particularly to phonons. As for DMSs, the simplest and most crude method is to use a more or less phenomenological pure-dephasing rate [164], which however is often insufficient to capture nonperturbative effects [68]. Thus, more sophisticated approaches in the form of a correlation expansion [155, 165] or Master equations in the polaron frame [69, 166] have been used to describe the QD dynamics with and without cavities. Nevertheless, all of these methods still rely on approximations, which cannot be expected to be valid for arbitrary system parameters.

A possible way to obtain a numerically complete treatment of the QD-phonon interaction is the use of path integrals for the time evolution of the reduced density matrix (RDM), i.e., the density matrix where the phonon bath is traced out [72, 73]. Albeit a PI approach formally requires the summation over all possible paths during the dynamics, it turns out that phonons lead to a finite memory with a sufficiently fast fall off so that system configurations further back in time than the typical memory length can be dropped [74]. Following Ref. [75], a recently extended formulation of the PI algorithm is presented here, which also allows for the inclusion of additional dissipative non-Hamiltonian contributions in the Lindblad form.

Starting from the Hamiltonian of a possibly time-dependent N-level system H_N coupled to a continuum of harmonic oscillators in the form of Eq. (5.1), the time evolution of the density matrix for the full system can be calculated according to

$$\frac{\partial}{\partial t}\rho = \underbrace{\frac{1}{i\hbar}[H_N, \rho] + \mathcal{L}_{\text{loss}}[\rho]}_{=\mathcal{L}_N[\rho]} + \underbrace{\frac{1}{i\hbar}[H_{\text{ph}}, \rho]}_{=\mathcal{L}_{\text{ph}}[\rho]} \tag{5.2}$$

with potential non-Hamiltonian losses $\mathcal{L}_{\text{loss}}[\rho]$ in the Lindblad form (cf. Ref. [75]). The time evolution can be conveniently split into the N-level part together with the losses on the one hand and the phonon coupling on the other hand by defining two corresponding Liouville propagators $\mathcal{L}$ as indicated in Eq. (5.2). Then, the propagation of the density

matrix by a sufficiently small time step Δt can be written as

$$\rho(t+\Delta t) = \underbrace{\mathcal{T} \exp\left(\int_t^{t+\Delta t} d\tau \left(\mathcal{L}_N + \mathcal{L}_{\mathrm{ph}}\right)\right)}_{=\mathcal{P}_{t \to t+\Delta t}} \rho(t) = \mathcal{U}\mathcal{M}_{t,t+\Delta t}\left[\rho(t)\right]\mathcal{U}^\dagger + \mathcal{O}(\Delta t^2), \quad (5.3)$$

which is achieved by separating the N-level dynamics represented by the superoperator

$$\mathcal{M}_{t,t+\Delta t}[\rho(t)] = \mathcal{T}\exp\left(\int_t^{t+\Delta t} d\tau \mathcal{L}_N\right)[\rho(t)] \quad (5.4)$$

from the Hamiltonian time evolution due to the phonons given by

$$\mathcal{U} = \exp\left(-\frac{i}{\hbar}H_{\mathrm{ph}}\Delta t\right). \quad (5.5)$$

Here, $\mathcal{T}$ is the time-ordering operator and Eq. (5.5) uses the fact that H_{ph} is constant in time. The superoperator $\mathcal{M}_{t,t+\Delta t}$ can be understood as mapping $\rho(t) \to \rho(t+\Delta t)$ when the system evolves only under the action of $\mathcal{L}_N$. Note that the last step in Eq. (5.3) is only accurate up to linear order in Δt.

Dividing the total propagation into equally-sized time slices so that $t_l = t_0 + l\Delta t$ with $l \in \mathbb{N}$, Eq. (5.3) can be used recursively to obtain the time evolution of the density matrix from t_0 to t_n. By additionally introducing identity operators $\sum_{\nu_l} |\nu_l\rangle\langle\nu_l|$ in terms of a basis of H_N at each time step t_l, the propagation effectively becomes a summation over all possible paths in the configuration space of the N-level system, albeit still containing the phonon modes. Thus, the elements of the density matrix $\rho_{\nu_n \mu_n} = \langle\nu_n|\rho(t_n)|\mu_n\rangle$ at the time t_n can be obtained via the relation

$$\rho_{\nu_n \mu_n} = \sum_{\substack{\nu_0...\nu_{n-1} \\ \mu_0...\mu_{n-1}}} \mathcal{U}_{\nu_n}\ldots\mathcal{U}_{\nu_1}\,\rho_{\nu_0\mu_0}\,\mathcal{U}^\dagger_{\mu_1}\ldots\mathcal{U}^\dagger_{\mu_n} \prod_{l=1}^n \mathcal{M}^{\nu_{l-1}\mu_{l-1}}_{\nu_l\mu_l}, \quad (5.6)$$

where $\mathcal{U}_{\nu_l} = \langle\nu_l|\mathcal{U}|\nu_l\rangle$ are the matrix elements of the time-evolution operator containing the pure-dephasing coupling to the phonons and are thus diagonal in the chosen basis. The phonon-free propagation is contained in the matrix elements

$$\mathcal{M}^{\nu_{l-1}\mu_{l-1}}_{\nu_l\mu_l} = \langle\nu_l|\mathcal{M}_{t_{l-1},t_l}\left[|\nu_{l-1}\rangle\langle\mu_{l-1}|\right]|\mu_l\rangle. \quad (5.7)$$

In practice, however, Eq. (5.6) is impractical since it still contains infinitely many phonon degrees of freedom at each point in time.

This is where the PI representation can be used to find an equation of motion for the RDM, where the phonon degrees of freedom are traced out so that only the desired information about the N-level system comprising the QD states and the cavity photons remains. To this end, one can again introduce identity operators at each discrete time step but, instead of using the states of the few-level system, now a basis of coherent states is considered, which enables an analytic evaluation of the appearing phonon matrix elements [74]. For the initial state of the dynamics, the system is assumed to be in a product state of the QD-cavity system and the phonon bath, where the latter is given by
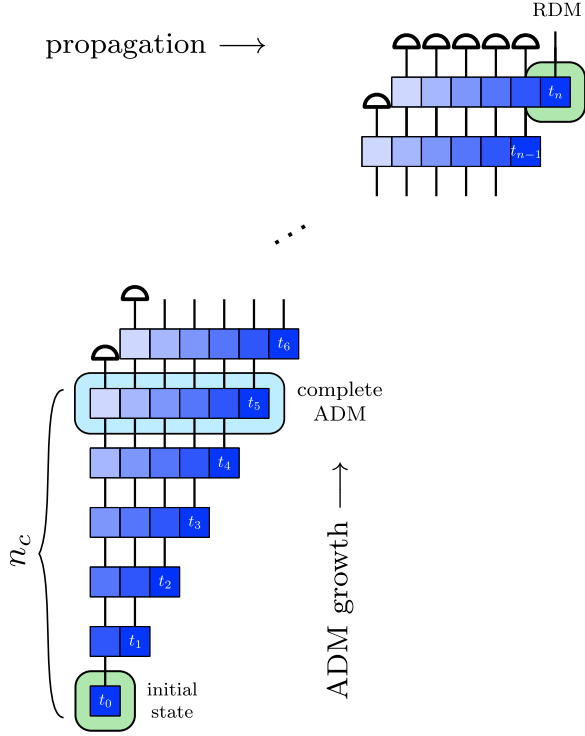
Figure 5.2: Schematic representation of the real-time PI algorithm. Each colored square represents a system configuration at one point in time, where configurations for past times are gradually desaturated. Outgoing straight lines symbolize N^2 entries corresponding to the weights of different system paths through the configuration space of the N-level system and the number m of outgoing lines from a given object determines the total entries of the ADM according to N^{2m}. The ADM grows by keeping the density matrix elements of past times until the memory depth n_c is reached. Thereafter, the leftmost paths corresponding to the maximum memory depth are traced out as indicated by the capped lines, such that the ADM no longer grows upon reaching a size of N^{2n_c}. At any time t_n, the RDM can be obtained by a summation over all elements in the ADM except the ones corresponding to the most recent time t_n.

a thermal distribution with a fixed temperature. Subsequently tracing out the phonon degrees of freedom, the elements of the RDM at the time t_n are given by

$$\overline{\rho}_{\nu_n \mu_n} = \mathrm{Tr}_{\mathrm{ph}}[\rho_{\nu_n \mu_n}] = \sum_{\substack{\nu_0 \ldots \nu_{n-1} \\ \mu_0 \ldots \mu_{n-1}}} \overline{\rho}_{\nu_0 \mu_0} \exp\left(\sum_{l=1}^{n} \sum_{k=1}^{l} S_{\nu_l \nu_k}^{\mu_l \mu_k} \right) \prod_{l=1}^{n} \mathcal{M}_{\nu_l \mu_l}^{\nu_{l-1} \mu_{l-1}} \tag{5.8}$$

with a phonon-influence functional $S_{\nu_l \nu_k}^{\mu_l \mu_k}$ containing the memory kernel, which is mainly determined by the phonon spectral density. An explicit expression for the influence functional is given in Ref. [74].

But even though Eq. (5.8) no longer contains a summation over phonon degrees of freedom, the numerical effort still grows exponentially with the number of time steps since the summations in Eq. (5.8) extend over all N states of the reduced system. Thus, a direct numerical calculation is only feasible for a small number of time steps even for a two-level system. As it turns out, however, the phonon-influence functional does not depend equally on past system configurations as the constituting memory kernels rapidly decay on a timescale of a few picoseconds [74]. Because the memory kernels only depend on the carrier-phonon coupling and material parameters, the corresponding memory depth is known in advance so that the influence functional can be truncated after the corresponding amount of time steps n_c. To maximally exploit this truncation, it is

advantageous to use an augmented density matrix (ADM) instead of the RDM [72, 73]. Effectively, the ADM can be understood as a tensor containing the weights of the different system configurations for the past n_c time steps. This $2n_c$-dimensional object obeys the recursion relation

$$\rho_{\nu_n...\nu_{n-n_c+1}}^{\mu_n...\mu_{n-n_c+1}} = \mathcal{M}_{\nu_n\mu_n}^{\nu_{n-1}\mu_{n-1}} \sum_{\substack{\nu_{n-n_c}\\\mu_{n-n_c}}} \exp\left(\sum_{l=n-n_c}^{n} S_{\nu_n\nu_l}^{\mu_n\mu_l}\right) \rho_{\nu_{n-1}...\nu_{n-n_c}}^{\mu_{n-1}...\mu_{n-n_c}} \tag{5.9}$$

and is connected to the RDM via

$$\overline{\rho}_{\nu_n\mu_n} = \sum_{\substack{\nu_{n-1}...\nu_{n-n_c+1}\\\mu_{n-1}...\mu_{n-n_c+1}}} \rho_{\nu_n...\nu_{n-n_c+1}}^{\mu_n...\mu_{n-n_c+1}}. \tag{5.10}$$

Given the rather technical nature of the PI algorithm, its main features are sketched in Fig. 5.2 to provide a schematic overview.

First, the initial state is propagated $n_c - 1$ times and the resulting path weights are added to the ADM. This is the growth phase of the ADM, where its size is multiplied by N^2 at every time step. Basically, each entry of the current $N \times N$ density matrix remains connected to the $N \times N$ density matrix for the previous time step as long as the memory depth is not exceeded, which is why the ADM grows exponentially in that phase. After the memory depth n_c is reached, however, the ADM no longer grows as the summation over the states $|\nu_{n-n_c}\rangle$ in Eq. (5.9) is applied to the last element of the ADM. In the figure, this is depicted by a capped line at the leftmost part of the ADM. Since the ADM thus remains constant in size, the numerical demand remains constant and scales with N^{2n_c} instead of N^{2n} for a propagation up to t_n. Finally, upon reaching t_n, all states except the most recent state $|\nu_n\rangle$ are traced out to obtain the desired RDM.

Provided that Δt is small enough and a sufficient memory depth is accounted for, the PI algorithm enables a numerically complete solution of Eq. (5.2) in the sense that no approximations to the model are required and only controllable numerical errors are introduced. Especially due to the possibility of including non-Hamiltonian decay rates, such as cavity losses, enabled by using a formulation in Liouville space, this algorithm presents a versatile tool to study phonon effects in QD-cavity systems. However, even though making use of the ADM significantly improves the numerical efficiency of the method, studies using the PI algorithm are still limited to systems with about four levels or less [59, 167–169]. Considering that QD-cavity systems consist of the QD states plus the photon states in the cavity, this again rather limits the applicability of the PI method to at least the low-driving limit. In this thesis, this problem is overcome by a reformulation of the PI method presented in Sec. 6.1. Along with extending the presented PI scheme to the calculation of multitime correlation functions, the algorithm is generally applied to QD-cavity systems with a focus on the phonon-influence on photonic properties. These studies have resulted in a number of publications, an introduction to which is provided in the following chapter 6.

6 Introduction to the publications on nonmagnetic systems

Nonmagnetic QD-cavity systems are the main topic of the last six publications listed in part III of this thesis. Starting with Pub. 9 in Sec. 6.1, where the previously presented PI algorithm is reformulated to handle systems with significantly more levels, the main results of these publications are summarized in this chapter. Section 6.2 first describes how multitime correlation functions can be evaluated within the PI scheme according to Pub. 10. Furthermore, using correlation functions, the single-photon purity for a QD-cavity system is calculated for off-resonant excitation scenarios, where phonons can be used to obtain high-quality single-photon sources, as shown in Pub. 11. Finally, Sec. 6.3 focuses on the biexciton cascade in QDs with the aim to generate a two-photon entangled state. To this end, the concurrence is introduced as a measure for entanglement and, based on results of Pub. 12, three different notions of concurrence used throughout the literature are compared with respect to their physical interpretation as well as their dependence on system parameters. Finally, the impact of different QD-cavity configurations on the concurrence in the presence of phonons studied in Pub. 13 is discussed. As shown in Pub. 14, it is even possible to find a regime where phonons enhance the entanglement, despite the fact that they are one of the main sources for decoherence in QDs. All simulations discussed in this chapter are performed for self-assembled InGaAs QDs with a radius of $3\,\mathrm{nm}$ in a GaAs matrix embedded in a cavity. The corresponding material parameters can be found in the Supplemental Material of Pub. 9.

6.1 Reformulation of the PI algorithm

According to Eq. (5.9), the full ADM of a four-level system with a memory depth of $n_c = 6$ already has almost $1.7 \cdot 10^7$ elements that need to be stored in memory at each point in time. Thus, it is clear that increasing the number of levels to, say, $N = 10$ and a resulting ADM with 10^{12} entries, a regime which is easily reached in strongly-driven strongly-coupled QD-cavity systems due to the occupation of states with more than one photon in the cavity, such systems can no longer be handled by the PI algorithm in its current form. Although there are approaches where a number of paths are artificially discarded [167, 168], these evidently entail uncontrolled approximations so a numerically complete time evolution is out of the question.

However, as explained in Pub. 9, the PI algorithm presented in Sec. 5.2 allows for a rather straightforward but very powerful reformulation regarding the phonon-influence functional introduced in Eq. (5.8). Since the exciton-phonon interaction in Eq. (5.1) is not affected by the photon number in the cavity as it only depends on the state of the QD itself, the total N states of the system can be split into N_g groups, where the states within each group consist of the same QD state but may contain arbitrarily many

photons. Considering, e.g., a QD with a ground state $|G\rangle$ and a single excited state $|X\rangle$, one thus arrives at only $N_{\mathrm{g}} = 2$. Denoting the states of any N-level system by $|\lambda, k\rangle$ with a group index $\lambda = \{1, 2, \dots N_{\mathrm{g}}\}$ and an index k for the states within a given group, the phonon-influence functional simplifies to

$$\sum_{l=n-n_c}^{n} S_{\nu_n \nu_l}^{\mu_n \mu_l} = \sum_{l=n-n_c}^{n} S_{(\lambda_n, k_n)(\lambda_l, k_l)}^{(\bar{\lambda}_n, \bar{k}_n)(\bar{\lambda}_l, \bar{k}_l)} = \sum_{l=n-n_c}^{n} S_{\lambda_n \lambda_l}^{\bar{\lambda}_n \bar{\lambda}_l}. \tag{6.1}$$

The fact that the functional only depends on the group index λ can then be used to define a partially-summed ADM (PSADM)

$$\rho_{(\lambda_n, k_n)\lambda_{n-1}\dots\lambda_{n-n_c+1}}^{(\bar{\lambda}_n, \bar{k}_n)\bar{\lambda}_{n-1}\dots\bar{\lambda}_{n-n_c+1}} = \sum_{\substack{k_{n-1}\dots k_{n-n_c+1} \\ \bar{k}_{n-1}\dots\bar{k}_{n-n_c+1}}} \rho_{(\lambda_n, k_n)(\lambda_{n-1}, k_{n-1})\dots(\lambda_{n-n_c+1}, k_{n-n_c+1})}^{(\bar{\lambda}_n, \bar{k}_n)(\bar{\lambda}_{n-1}, \bar{k}_{n-1})\dots(\bar{\lambda}_{n-n_c+1}, \bar{k}_{n-n_c+1})} \tag{6.2}$$

which obeys the recursion

$$\rho_{(\lambda_n, k_n)\lambda_{n-1}\dots\lambda_{n-n_c+1}}^{(\bar{\lambda}_n, \bar{k}_n)\bar{\lambda}_{n-1}\dots\bar{\lambda}_{n-n_c+1}} = \sum_{\substack{k_{n-1} \\ \bar{k}_{n-1}}} \mathcal{M}_{(\lambda_n, k_n)(\bar{\lambda}_n, \bar{k}_n)}^{(\lambda_{n-1}, k_{n-1})(\bar{\lambda}_{n-1}, \bar{k}_{n-1})} \sum_{\substack{\lambda_{n-n_c} \\ \bar{\lambda}_{n-n_c}}} \exp\left(\sum_{l=n-n_c}^{n} S_{\lambda_n \lambda_l}^{\bar{\lambda}_n \bar{\lambda}_l}\right)$$
$$\times \rho_{(\lambda_{n-1}, k_{n-1})\lambda_{n-2}\dots\lambda_{n-n_c}}^{(\bar{\lambda}_{n-1}, \bar{k}_{n-1})\bar{\lambda}_{n-2}\dots\bar{\lambda}_{n-n_c}}. \tag{6.3}$$

Iterating the PSADM instead of the ADM means that, rather than N^{2n_c} elements, only $N^2 N_{\mathrm{g}}^{2(n_c-1)}$ elements need to be calculated and stored in each time step after the memory depth is reached. To demonstrate the advantage of using Eq. (6.3), a 41-level system consisting of a two-level QD coupled to a cavity with up to 20 photons is studied in Pub. 9, where the above reformulation of the PI algorithm reduces the size of the full ADM by more than 15 orders of magnitude.

In the corresponding publication, mainly the phonon impact on the cavity feeding is investigated for a continuously-driven two-level QD resonantly coupled to a lossy cavity. For a situation with equally strong laser driving and QD-cavity coupling, significantly higher average photon numbers in the cavity are predicted when phonons are present compared with a phonon-free calculation. The reason for the increased photon occupation are phonon-assisted transitions between off-resonant states when the laser is detuned with respect to the QD transition. Here, the PI approach is particularly useful since one is dealing neither with the weak driving nor with the weak-coupling limit, where it can be expected that a description in terms of cavity dressed or laser-dressed states, respectively, is a suitable starting point for approximate models.

Apart from the mean photon number, the real-time PI approach also allows for the extraction of the photon distribution in the cavity at any given point in time. While the stationary distributions reached for long times for different detunings with and without the QD-phonon interaction are discussed in Pub. 9, here snapshots of the photon distribution are shown in Fig. 6.1. Specifically, a situation with equally strong driving and QD-cavity coupling of $0.1\,\mathrm{meV}$ is considered. Even though classically driving the cavity leads to a Poissonian photon statistics [170], it can be seen that the photon distribution in the cavity is strongly non-Poissonian in the case considered here and is closer to a
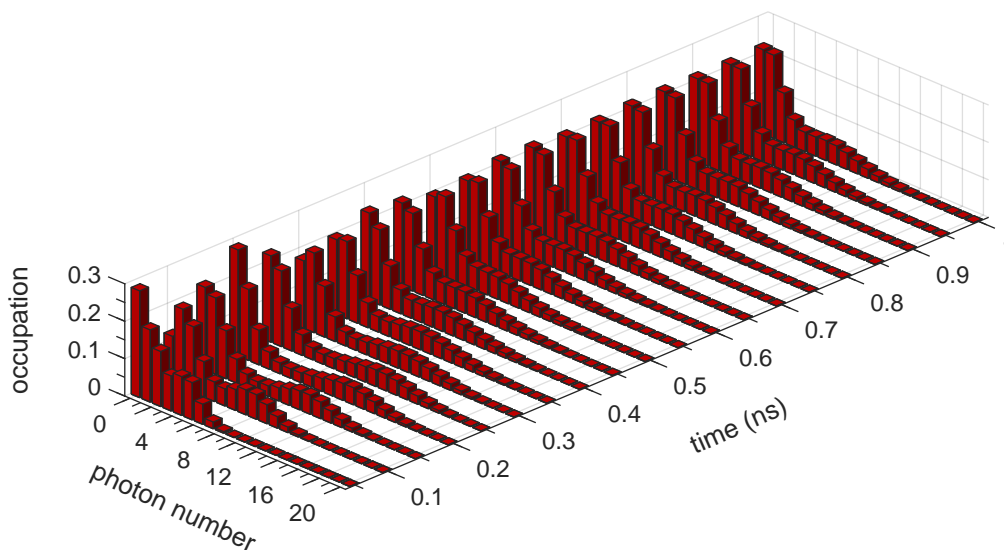
Figure 6.1: Photon occupation of a cavity in resonance with a QD at selected points in time with phonons initially at 3 K. The laser excitation is detuned by $-18\,\mu\text{eV}$ from the QD transition and the QD-cavity coupling and the driving are equally strong. Note that the photon distribution at $t = 0$ is not shown since, in the absence of laser driving, only the state with zero photons is occupied.

thermal distribution at long times. This is partly a result of indirectly driving the cavity via the dot but, as shown by the comparison to a phonon-free simulation in Pub. 9, the photon statistics at long times is strongly altered in the presence of phonons. Furthermore, phonon-free simulations using the driven Jaynes-Cummings model with a small negative detuning of the laser on the order of $-10\,\mu\text{eV}$ causes the appearance of a rather unconventional two-peaked structure in the photon distribution. Although phonons destroy this feature in the stationary limit, Fig. 6.1 reveals that it is still preserved on short timescales on the order of a few 100 ps after the pulse is switched on if the temperature is low enough.

Given that a structure with two peaks already appears in the Jaynes-Cummings model, it is clear that this is not a phonon-related effect. Rather, the appearance of a second peak and its dynamics may be a result of the energetic separation between energy eigenstates in the Jaynes-Cummings model, which crucially depends on the sign of the detuning [162]. In particular, negative detunings that are small compared with the QD-cavity coupling cause a large number of states with different photon numbers to be nearly identical in energy, so transitions between them become highly probable. At the time of writing, the physical origin of the two-peaked photon distribution is still not clearly understood. However, a nonlinear oscillator model developed for the description of the photon distribution at long times in the Jaynes-Cummings model with resonant driving may provide a suitable starting point for further investigation [171].

Apart from studying the phonon impact on systems with large photon numbers, another interesting question is the phonon influence on photonic correlation functions. However, since their calculation involves the evaluation of expectation values containing operators at different times, it is not immediately clear how this can be done using the PI method

presented here. The necessary modifications of the algorithm as well as its application to calculate the single-photon purity is the topic of the following section.

6.2 Multitime correlation functions with PIs and their application

This section briefly explains how multitime correlation functions, which are important for characterizing open quantum systems, can be evaluated using the PI scheme. Applying this scheme to the calculation of the single-photon purity of a QD-cavity system under pulsed excitation, it is shown how a high-quality single-photon source that is spectrally separated from the laser excitation can be realized with the help of phonons.

6.2.1 Evaluating multitime correlation functions with PIs

Multitime correlation functions play a key role in experimentally as well as theoretically accessing all kinds of information about open quantum systems. Starting from the Fourier transform of the first-order two-time correlation function to obtain the emission spectrum [172–174], where phonons cause characteristic non-Markovian signatures in the form of a broad sideband at low temperatures [175], correlation functions in general are the quantities of interest in coincidence measurements used for the characterization of the photon subsystem [176–179], even beyond two time arguments [180]. For open quantum systems, the theoretical evaluation of such correlation functions typically relies on the quantum regression theorem, which assumes a factorization of the density matrix into a system and environment part at all times [181], and the coupling to the environment is often treated in the Markov limit. Clearly, both of these assumption are not valid for QDs due to the non-Markovian character of the phonon coupling described in Sec. 5.2, which is why it is desirable to evaluate multitime correlation functions without these restrictions.

Instead of a recently proposed perturbative approach [175], Pub. 10 presents a recipe how nonequilibrium multitime correlation functions in the presence of non-Markovian environments can be obtained with PIs. Considering, for the sake of brevity, a two-time correlation function

$$G_{O_1 O_2 O_3 O_4}(t_1, t_2) = \langle O_1(t_1) O_2(t_2) O_3(t_2) O_4(t_1) \rangle \tag{6.4}$$

with operators O_l in the Hilbert space of the subsystem such as a QD, one first needs to trace out any Markovian environments. An example for the latter is a photonic bath giving rise to radiative decay. Changing to the Heisenberg picture with respect to O_l, rearranging the order of the operators under the trace, and explicitly performing the trace over the Markovian baths, Eq. (6.4) becomes

$$G_{O_1 O_2 O_3 O_4}(t_1, t_2) = \text{Tr}\Big[O_2 O_3 \mathcal{P}_{t_1 \to t_2} \big[O_4 [\mathcal{P}_{t_0 \to t_1} \tilde{\rho}(0)] O_1 \big] \Big]. \tag{6.5}$$

Here, $\mathcal{P}_{t_1 \to t_2}$ denotes the Liouville propagator introduced in Eq. (5.3) and $\tilde{\rho}(t)$ is the RDM containing the system of interest as well as the non-Markovian phonon bath.

Equation (6.5) can be adapted to the PI scheme presented in Sec. 5.2 by noting that, first of all, the time evolution of $\tilde{\rho}(t)$ until t_1 can be performed by using the ADM and

iterating it via Eq. (5.9) since the operators O_l do not enter up to this point. Upon reaching t_1, applying O_4 from the left and O_1 from the right can be done by replacing the phonon-free evolution $\mathcal{M}_{t_1,t_1+\Delta t}$ defined in Eq. (5.4) by $O_4 \mathcal{M}_{t_1,t_1+\Delta t} O_1$. Finally, at the time t_2, $G_{O_1 O_2 O_3 O_4}(t_1, t_2)$ is obtained by applying the product $O_2 O_3$ from the left to the ADM and subsequently calculating the RDM according to Eq. (5.10). The explicit expressions for the iteration of the thus modified ADM are provided in Pub. 10 and can be straightforwardly extended to correlation functions with more time arguments.

Note that the above procedure avoids using the quantum regression theorem for the non-Markovian phonon bath as the phonon-induced memory is explicitly kept in the form of the ADM at all times. The crucial point is, again, the separation of the propagation into a phonon free and a phonon-related part in terms of the phonon-influence functional. In other words, the calculation of multitime correlation functions can be understood similarly to the propagation of an N-level system whose Hamiltonian changes at t_1 and at t_2. To test the validity of the method, Pub. 10 also shows the emission spectrum of a two-level QD with the emergence of the characteristic Mollow triplet [182] as well as the phonon sidebands. Regarding correlation functions, the two-time photonic correlation function of a QD-cavity system is exemplarily calculated. Although the size of the ADM remains unchanged, the numerical demand nevertheless increases as separate simulations up to t_2 are required for each time pair (t_1, t_2).

6.2.2 Phonon-mediated high-quality single-photon sources

The previously presented algorithm for the calculation of multitime correlation functions enables an unbiased investigation of the phonon impact on photonic properties of QD-cavity systems. Regarding applications in quantum computing or quantum communication, on-demand high-quality single-photon sources are a major requirement of existing quantum protocols. Although semiconductor QDs, especially in combination with a cavity, are very suitable for this purpose [64, 183, 184], resonant excitation schemes inherently produce photons whose frequency is identical to that of the laser. Exciting the wetting layer rather than the QD itself [185] or using the two-photon resonance of the biexciton cascade [186] are promising options to overcome this problem, but they are prone to time jitter or require a precise control of excitation parameters, respectively.

As shown in Pub. 11, a viable alternative for the generation of single photons is provided by phonon-assisted off-resonant excitation of a QD embedded in a cavity. To characterize the fidelity of the obtained photon state regarding the single-photon character, one commonly uses the single-photon purity (SPP), which can be obtained via a Hanbury Brown and Twiss setup by measuring the conditional probability of detecting an additional photon if a first one is detected [176, 178, 187]. Therefore, the SPP theoretically follows from an integration of the two-time correlation function

$$G^{(2)}(t, \tau) = \langle a^\dagger(t) a^\dagger(t+\tau) a(t+\tau) a(t) \rangle \tag{6.6}$$

with photon creation and annihilation operators $a^\dagger$ and a, respectively. To this end, the method described in Sec. 6.2.1 can be employed to obtain $G^{(2)}(t, \tau)$ within the PI scheme, thus keeping the full phonon-induced memory. Another important figure of merit for single-photon sources is their brightness, which can be modeled as the photon number integrated over the duration of one pulse multiplied by the cavity loss rate. This effectively
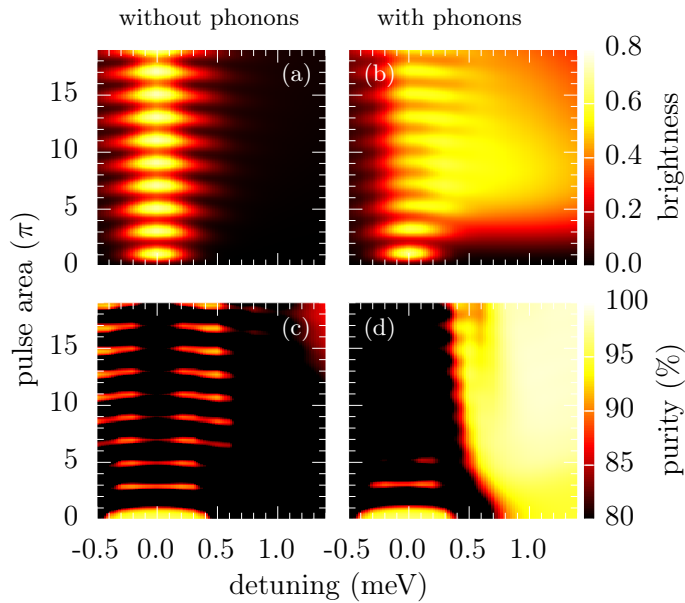
Figure 6.2: [data kindly provided by M. Cosacchi] Source brightness (a) with and (b) without phonons as a function of the laser-exciton detuning and the area of the excitation pulse at a temperature of 4.2 K. Also shown is the calculated single-photon purity (c) with and (d) without phonons for the same parameters.

captures the average photon emission of the cavity due to the losses. Further details regarding the calculation of the SPP and the brightness can be found in Pub. 11.

The system under consideration here consists of a QD-cavity system excited at the exciton resonance by a train of Gaussian pulses with a full width at half maximum of 7 ps. As sketched in Fig. 5.1, radiative decay and cavity losses are considered together with the QD-phonon interaction. The brightness as well as the SPP resulting from such a system as a function of the laser detuning with respect to the QD transition are shown in Fig. 6.2 for different pulse areas. The obtained brightness without phonons shown in Fig. 6.2(a) displays the characteristic pattern associated with the Rabi rotation of the exciton occupation as a function of the pulse area since the probability of emitting a photon is maximized when the system is driven to the exciton state at odd multiples of π. While the exciton preparation becomes less and less efficient with increasing detuning, LA phonons can bridge the energetic offset of the laser so a significant increase in brightness is found in Fig. 6.2(b). Note that this applies only to positive detunings due to the strong asymmetry between phonon emission and absorption at 4.2 K.

Although a similar behavior to the brightness is observed in Fig. 6.2(c) for the SPP without phonons, regions with high SPP actually shift to finite detunings for larger pulse areas. The reason for this is that a reexcitation of the QD significantly degrades the SPP since more than one photon is emitted per pulse, which is why resonant excitation schemes typically rely on π pulses with widths on the order of 3 ps [178, 184]. In contrast, a phonon-mediated excitation of the QD neither results in a significant loss of brightness nor a significantly lower SPP for a large area of positive detunings, as shown in Fig. 6.2(d). In fact, when choosing to simultaneously maximize the brightness and the SPP in terms of the sum of the squares of the two values, an SPP of 98.1% at a brightness of 0.53 is predicted at a detuning of about 1 meV for the system considered here. Compared with an SPP of 90.7% at a brightness of 0.67 in the resonantly-driven case for the parameters considered here, phonons thus even improve the SPP under off-resonant excitation.

The physical origin of this observation can be traced back to the phonon-mediated adiabatic undressing that takes place in the laser-dressed states, i.e., in the modified

energy eigenbasis of the QD states including the interaction with the laser [169]. In this modified basis, phonons mainly induce transitions to the lower dressed state for the low temperatures considered here, which, for positive detunings, corresponds to the exciton state when there is no laser pulse present [188]. Thus, adiabatically switching off the pulse results in a boost of the exciton occupation in the original eigenbasis of the QD due to the transformation of the lower dressed state back to the bare exciton state. Since this exciton boost occurs only at the end of the pulse, the time window for a reexcitation is reduced and, consequently, the SPP rises. The corresponding occupations of the system states can be found in Pub. 11 along with a more detailed explanation.

All in all, off-resonantly exciting the QD enables high-quality single-photon sources that are spectrally separated from the laser frequency by exploiting phonon-assisted processes. Furthermore, as demonstrated in Pub. 11, the scheme is robust with respect to a variation of system parameters such as the quality of the cavity and the pulse length. Apart from single photons, many quantum information protocols also rely on quantum entanglement between multiple quantum states [189–191]. In this context, QD-cavity systems also play a major role regarding the generation of entangled photon pairs via the biexciton cascade, which is the topic of the following section.

6.3 Phonon impact on two-photon entanglement in the biexciton cascade

After a reformulation of the PI algorithm and its application to the exciton resonance in QD-cavity systems, the generation of an entangled two-photon state via the biexciton resonance is investigated. To this end, the concurrence is introduced as a typical tool for quantifying the entanglement of a mixed bipartite state, with a focus on comparing the physical meaning of differently calculated concurrences in the literature. Restricting the considerations to photon pairs that are simultaneously emitted from the cavity, the dependence of the corresponding concurrence on different QD-cavity configurations in the presence of phonons is discussed. Finally, it is shown that phonons can even enhance the entanglement compared with the phonon-free expectation. For all following discussions, the QD is initially assumed to be in the biexciton state.

6.3.1 Concurrence as a measure for entanglement

Considering a pure state, the amount of entanglement of any subsystem with another is quantified by the individual von-Neumann entropies [192]. Performing a measurement on that subsystem causes its entropy to drop to zero, i.e., the previously missing information is recovered, and the entangled pure state collapses to a product state. In terms of the biexciton cascade in a QD-cavity system sketched in Fig. 6.3, the maximally-entangled pure state is given by $|\Psi^+\rangle = \frac{1}{\sqrt{2}}\big(|HH\rangle + |VV\rangle\big)$ in terms of horizontally and vertically polarized cavity photons emitted after the QD has decayed to the ground state. Measuring, e.g., the state $|H\rangle$ for one of the photons then necessarily yields the same state $|H\rangle$ also for the second one, making $|\Psi^+\rangle$ an ideal state for applications such as secure quantum communication protocols [53]. However, due to the coupling of the QD as well as the cavity to its environment via phonons and cavity losses, respectively, $|\Psi^+\rangle$ does not represent
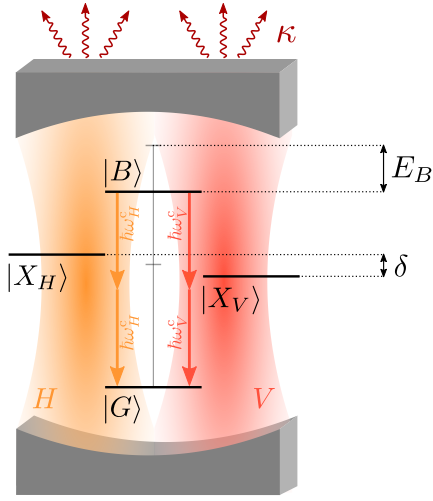
Figure 6.3: (a) Sketch of the biexciton cascade in a cavity with two orthogonally polarized modes H and V whose energies $\hbar\omega_H^{\mathrm{c}} = \hbar\omega_V^{\mathrm{c}}$ are chosen such that the two-photon transition between the biexciton and the ground state is matched. The biexciton state $|B\rangle$ can decay to the ground state $|G\rangle$ either by simultaneously emitting two photons or via one of the two exciton states $|X_H\rangle$ and $|X_V\rangle$ that are separated by the FSS δ. As already shown in Fig. 5.1, $|B\rangle$ is shifted by the biexciton binding energy E_B and photons can leave the cavity with a loss rate κ.

the system correctly and one has to use a mixed state instead. Furthermore, which-path information is introduced into the system via the fine-structure splitting (FSS) δ of the two exciton states, which is a consequence of the electron-hole exchange interaction and has typical values of several ten to a few hundred µeV [193, 194].

In contrast to a pure state, defining entanglement for a mixed system is rather ambiguous as missing information on a subsystem can arise not only due to its entanglement with other system parts but also as a consequence of ensemble averaging, which is why numerous proposals to quantify entanglement exist in that case [192]. Here, the entanglement of formation E_{f} is considered, which can be thought of as the minimum amount of pure-state entanglement in a given mixed state when it is decomposed into a sum of pure states. Since such a decomposition is not unique, E_{f} is formally obtained as an infimum over all possible decompositions [195]. Despite this rather impractical definition, the connection between E_{f} and the so-called concurrence C makes the entanglement of formation particularly advantageous for a two-qubit state as the concurrence can be calculated directly from the elements of the two-qubit density matrix [196]. Since there is a monotonic relation between E_{f} and C, the latter can be used as a measure for entanglement in its own right, albeit with a physical interpretation that is less clear. Most importantly, E_{f} and C both range between zero and unity and can be shown to agree at the boundaries, which means that a maximally entangled state as measured by the entanglement of formation is characterized by $C = 1$.

Coming back to the biexciton cascade sketched in Fig. 6.3, the two-photon subspace of interest is represented by a normalized density matrix with only four nonvanishing elements given by

$$\rho_{j,l}^N(t) = \frac{\left\langle a_j^\dagger(t) a_j^\dagger(t) a_l(t) a_l(t) \right\rangle}{\left\langle a_H^\dagger(t) a_H^\dagger(t) a_H(t) a_H(t) \right\rangle + \left\langle a_V^\dagger(t) a_V^\dagger(t) a_V(t) a_V(t) \right\rangle} \tag{6.7}$$

for the polarization directions $j, l \in \{H, V\}$. The reason why only four out of the sixteen elements of the two-photon density matrix are finite lies in the optical selection rules, which dictate that a decay of the biexciton results in one σ^- and one σ^+-polarized photon

(cf. Fig. 5.1). Switching from a circular to a rectangular polarization basis, the states $|HV\rangle$ and $|VH\rangle$ cancel out so that either two horizontally polarized or two vertically polarized photons can be emitted [190]. In that case, the concurrence is given by [196]

$$C(t) = 2|\rho_{H,V}^N(t)|, \tag{6.8}$$

thus effectively relating the concept of entanglement to the coherence in the two-photon subspace. Regarding the QD, the four relevant states correspond to the biexciton state $|B\rangle$, the two exciton states $|X_H\rangle$ and $|X_V\rangle$ separated by the FSS, and the ground state $|G\rangle$. Note that the concurrence in Eq. (6.8) is necessarily a time-dependent quantity since its constituting parts, namely the elements of the normalized density matrix, also depend on time even without any coupling to the environment.

Although the elements $\rho_{j,l}^N(t)$ are observable in principle, resolving their full time dependence is experimentally challenging due to the lack of an integration time to boost the signal-to-noise ratio. This is why experiments typically perform a quantum-state tomography based on polarization-dependent photon coincidence measurements [197]. While the delay time between two emitted photons can be resolved with this technique by extrapolating data obtained with different delay-time windows [198, 199], the actual emission time of the first photon of a pair with respect to the preparation of the biexciton is not resolved. In both cases, the result of such a measurement corresponds to an integrated two-time correlation function

$$\overline{\overline{G}}_{j,l}^{(2)}(\Delta t, \Delta \tau) = \frac{1}{\Delta t} \int_0^{\Delta t} dt \, \frac{1}{\Delta \tau} \int_0^{\Delta \tau} d\tau \, \langle a_j^\dagger(t) a_j^\dagger(t+\tau) a_l(t+\tau) a_l(t) \rangle. \tag{6.9}$$

In contrast to Eq. (6.7), the normalized reconstructed density matrix is given by

$$\rho_{j,l}^R(\Delta t, \Delta \tau) = \frac{\overline{\overline{G}}_{j,l}^{(2)}(\Delta t, \Delta \tau)}{\overline{\overline{G}}_{H,H}^{(2)}(\Delta t, \Delta \tau) + \overline{\overline{G}}_{V,V}^{(2)}(\Delta t, \Delta \tau)} \tag{6.10}$$

and formally depends on the time intervals used in the measurement.

As explained in detail in Pub. 12, rather than using the concurrence given by Eq. (6.8) that is associated with the density matrix at any given point in time, similar quantities based on the reconstructed density matrix are considered throughout the literature instead [164, 200–202]. Although such quantities by definition reflect properties of the reconstructed density matrix rather than the time-dependent one, they are also commonly referred to as concurrence. To distinguish them from the concurrence in Eq. (6.8), a naming scheme is proposed in Pub. 12 that reflects the number of time averages in a given quantity. First, the double-time integrated concurrence

$$\overline{\overline{C}} = \lim_{\substack{\Delta t \to \infty \\ \Delta \tau \to \infty}} 2|\rho_{H,V}^R(\Delta t, \Delta \tau)| \tag{6.11}$$

is obtained when neither the emission nor the delay time between the photons is resolved, resulting in an average over both time arguments in $\overline{\overline{G}}_{j,l}^{(2)}(\Delta t, \Delta \tau)$. Second, the single-time

integrated concurrence

$$\overline{C} = \lim_{\substack{\Delta t \to \infty \\ \Delta \tau \to 0}} 2|\rho_{H,V}^R(\Delta t, \Delta \tau)| \tag{6.12}$$

can be discussed, which is obtained by extrapolating data acquired for different delay-time windows $\Delta\tau$ towards zero delay time while still averaging over the emission time t. Whereas $\overline{\overline{C}}$ therefore explicitly contains sequential emission processes via the exciton states with a finite delay between successive emissions, $\overline{C}$ effectively selects only simultaneously-emitted photon pairs.

Since $\overline{\overline{C}}$ and $\overline{C}$ are based on measured correlation functions rather than the time-dependent density matrix, it is a priori not clear whether these quantities still reflect the entanglement of formation. In fact, following an argument put forth by Stevenson et al. [198], one can easily see that a time integration can mask the presence of entanglement already without any environmental couplings. Due to the FSS sketched in Fig. 6.3, any delay τ between the emission of the first and second photon results in a phase shift $\phi(\tau) = \frac{\tau\delta}{\hbar}$ in the desired state $|\Psi^+\rangle$. Any time integration of the resulting two-photon state $|\Psi(\tau)\rangle = \frac{1}{\sqrt{2}}\left(|HH\rangle + e^{i\phi(\tau)}|VV\rangle\right)$ then results in a cancellation of the phases, even though $|\Psi(\tau)\rangle$ is clearly maximally entangled for any given delay τ.

In Pub. 12, $\overline{\overline{C}}$ and $\overline{C}$ are compared with the time-dependent concurrence to find out whether the integrated quantities can still be used as a measure of entanglement. In the often encountered case of a large biexciton binding energy E_B compared with the QD-cavity coupling as well as δ and cavity modes in resonance with the two-photon transition, a Schrieffer-Wolff transformation [203] can be applied to eliminate the coupling between low and high-energy like states if the QD-phonon coupling is disregarded. This method allows a perturbative analytic calculation of the density matrix elements required to evaluate the time-dependent concurrence given by Eq. (6.8) and also yields an analytic expression for both, the single as well as the double-time integrated concurrence. While the expression for the latter is more involved, the approximate analytic result for C is actually constant in time so that

$$C_{\text{analytic}} = \overline{C}_{\text{analytic}} \approx \frac{E_B^2 - \delta^2}{E_B^2 + \delta^2}. \tag{6.13}$$

For details regarding the calculation and the explicit expression of $\overline{\overline{C}}_{\text{analytic}}$, the reader is referred to Pub. 12. However, it should be pointed out that the result in Eq. (6.13) is essentially a consequence of the mostly incoherent dynamics in the transformed system. There, the two exciton states act as a perturbation of the original biexciton and ground states, which causes the appearance of δ in the final equation. The QD-cavity coupling as well as the cavity losses do not influence the concurrence at all on this level of approximation.

Equation (6.13) shows that, at least up to second-order perturbation theory, C_{analytic} and $\overline{C}_{\text{analytic}}$ are identical since the former does not depend on time. This result is further supported by numerical calculations performed in Pub. 12, where $C(t)$ and $\overline{C}$ are compared with and without QD-phonon interaction, without relying on a perturbative approach. Apart from a decaying oscillatory behavior of $C(t)$ on a short timescale of a
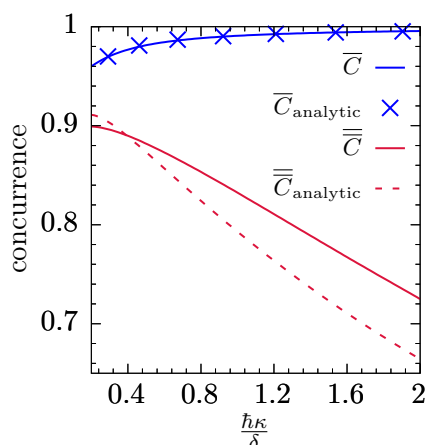
Figure 6.4: Single- ($\overline{C}$) and double-time integrated concurrence ($\overline{\overline{C}}$) as a function of the ratio between the cavity losses $\hbar\kappa$ and the FSS δ for fixed $\hbar\kappa\delta$ compared with the respective analytic expressions obtained via perturbation theory. The QD-phonon interaction is disregarded for the simulations.

few $10\,\text{ps}$ with a small amplitude, $C(t)$ is in good agreement with $\overline{C}$, which means that $\overline{C}$ can be considered a measure for the entanglement of formation. On a side note, one can immediately see from Eq. (6.9) that $\overline{C}$ is closely related to $C(t)$ since, apart from the time averaging, the two-time correlation function then reduces to the density matrix evaluated at the time t. Moreover, if the system is in a steady state so the density matrix elements no longer depend on time, the two quantities are even equivalent.

However, as shown in Fig. 6.4, the same cannot be said regarding $\overline{\overline{C}}$. Compared with $\overline{C}$, $\overline{\overline{C}}$ not only yields quantitatively different results but, more importantly, shows a different dependence on the ratio between cavity losses and the fine-structure splitting when their product is kept constant. The latter observation is crucial in this case since it determines whether $\overline{\overline{C}}$ measures the same physical information compared with $\overline{C}$, which is clearly not the case here. Since the results in Fig. 6.4 are obtained without taking the QD-phonon interaction into account, phonons can be excluded as a possible source for the disparity between the two quantities. A similar disagreement is also found when comparing $\overline{\overline{C}}$ and $\overline{C}$ as a function of δ, as shown in Pub. 12. While the former quantity abruptly drops when the splitting is finite, $\overline{C}$ retains much higher values over a wide range of δ.

All in all, the analysis in Pub. 12 suggests that $\overline{C}$ is an appropriate measure for the entanglement of formation that reflects the properties of simultaneously-emitted photon pairs, which is why only $\overline{C}$ is considered in the following. Although focusing on simultaneously emitted photons reduces the signal yield in experiments due to the extrapolation towards zero delay in Eq. (6.12), experiments [198, 199] as well as theoretical calculations [201] show that such photon pairs provide the highest degree of entanglement.

6.3.2 Impact of QD-cavity configurations on the concurrence

As immediately apparent from Eq. (6.13), it is desirable to have QDs with small or vanishing δ to avoid a degradation of the concurrence. Since naturally grown QDs generally have finite FSSs [193, 204], specifically engineered samples are required where δ can be tuned by electric fields [205], magnetic fields, [206] or strain [207]. Another approach to obtain high entanglement is to use QDs with large biexciton binding energies coupled to a cavity tuned to the two-photon resonance so that the exciton states are effectively bypassed and probing the FSS is avoided [164, 201]. However, none of these proposals can
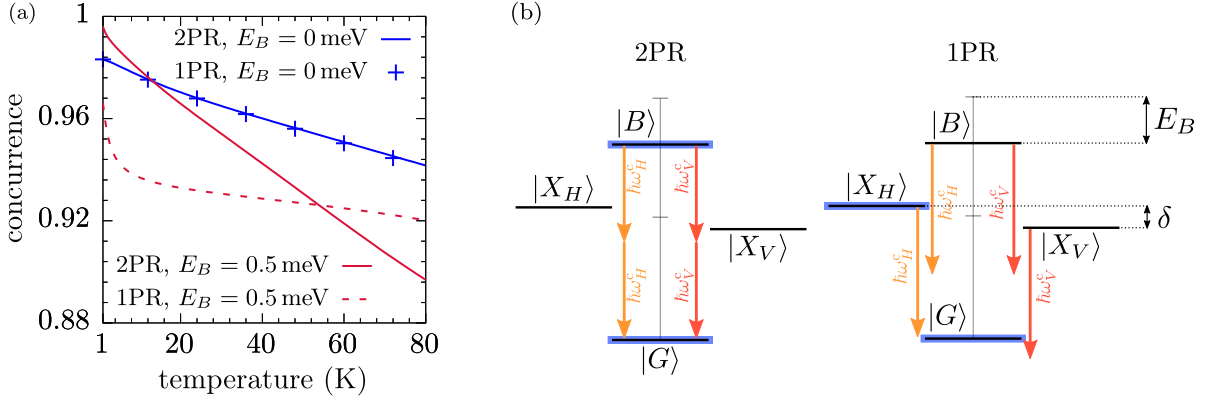
Figure 6.5: [data kindly provided by T. Seidelmann] (a) Temperature dependence of the concurrence for the four QD-cavity configurations studied in Pub. 13 assuming a FSS $\delta = 20\,\mu\text{eV}$. The two-photon resonant (2PR) and the one-photon resonant (1PR) configuration is studied with and without a finite biexciton binding energy. (b) Sketch of the 2PR and 1PR configuration, where levels connected by resonant transitions involving two photons or one photon, respectively, are highlighted in blue. If $E_B = 0$, the resonantly connected levels remain unchanged in the 2PR configuration, while $|B\rangle \leftrightarrow |X_V\rangle$ also becomes resonant in the 1PR case. The cavity modes are assumed to have the same frequency $\omega_H^c = \omega_V^c$.

eliminate the phonon influence, which is why a systematic study of different QD-cavity configurations using the PI algorithm is carried out in Pub. 13.

The temperature dependence of the concurrence is depicted in Fig. 6.5(a) for a strongly coupled QD-cavity system with a small FSS $\delta = 20\,\mu\text{eV}$. Four QD-cavity configurations are compared that differ with respect to the resonance setting of the cavity modes and whether the biexciton binding energy is finite or zero. Although the concurrence is rather large for all configurations due to the small FSS, clear variations between the configurations are found. While the two-photon resonant (2PR) configuration corresponds to the one depicted in Fig. 6.3, where the $|B\rangle \leftrightarrow |G\rangle$ transition can be resonantly bridged by two cavity photons, the one-photon resonant (1PR) configuration is chosen such that only the $|X_H\rangle \leftrightarrow |G\rangle$ transition is resonant with the corresponding cavity mode. For finite E_B, a sketch of the configurations is provided in Fig. 6.5(b).

As can be seen in Fig. 6.5(a), the concurrence for the 2PR as well as the 1PR configuration is virtually identical if $E_B = 0$. This is due to the fact that the configurations become identical in the limit $\delta \to 0$ in this case. For small but finite δ, a vanishing E_B in the 1PR configuration means that the $|B\rangle \leftrightarrow |X_V\rangle$ transition now also becomes resonant since the cavity modes are assumed to have equal frequencies for both polarizations and the two-photon resonance is only detuned on the order of δ. Therefore, it is not surprising that very similar values for the concurrence are predicted for the two configurations if the FSS is small and $E_B = 0$. However, as shown in Pub. 13, this changes drastically for larger FSSs, where the competition between direct two-photon and sequential single-photon processes is much more pronounced and governs the overall dependence of the concurrence on δ.

Turning to the results with finite E_B, the 2PR configuration mostly features a higher concurrence since, in the 1PR configuration, two-photon processes are then detuned by

$E_B \gg \delta$. However, considering the sequential emission pathway $|B\rangle \to |X_H\rangle \to |G\rangle$, the off-resonant $|B\rangle \to |X_H\rangle$ transition can be bridged by phonon absorption. Given that the subsequent $|X_H\rangle \to |G\rangle$ transition is resonant by definition, this means that this sequential transition is favored compared with the simultaneous two-photon transition as well as the vertically polarized sequential path, leading to a drop of the concurrence as soon as the temperature is high enough so that the required phonon absorption is possible. Once the temperature exceeds roughly 4 K, the concurrence effectively no longer depends on the temperature since the asymmetry between the horizontally and vertically polarized path remains the same. In contrast, the concurrence obtained for the 2PR configuration with finite E_B decreases monotonically with rising temperature, pointing to a rather pronounced phonon impact. Although this configuration shows the highest concurrence compared with the others for low temperatures up to about 10 K, it turns out that configurations with vanishing E_B actually become favorable at higher temperatures, as shown in Fig. 6.5(a). As explained in Pub. 13, the reason for the strong phonon influence is the energy dependence of the phonon spectral density, which is larger for detunings on the order of E_B compared with the detunings on the order of δ encountered in configurations with $E_B = 0$.

All in all, these results not only show that phonons have a significant impact on the concurrence in general, but that they can even be the decisive factor in a choice between different QD-cavity configurations. Specifically, the simulations reveal that the proposed 2PR configuration with large biexciton binding energy, which aims to avoid probing the which-path information introduced by the FSS [164, 201, 202], actually leads to a strongly temperature-dependent concurrence. For small to moderate δ on the order of a few 10 μeV, the concurrence in this configuration may even become smaller compared with a configuration with $E_B = 0$ already at temperatures on the order of 10 K.

6.3.3 Phonon-enhanced entanglement

As discussed in the previous section, phonons typically lead to a degradation of entanglement when the temperature is increased. This result is in line with the general expectation throughout the literature since phonons are known to largely contribute to the decoherence in QDs [67, 70, 161, 173, 208]. However, as shown in Pub. 14, the degrading phonon influence can in fact be overcompensated by another phonon-induced effect, namely the renormalization of the QD-cavity coupling, such that phonons actually lead to enhanced entanglement with rising temperature. This effect specifically occurs at close to vanishing biexciton-binding energies $E_B \lesssim \frac{\delta}{2}$ and QD-cavity couplings g not exceeding several 10 μeV.

For three different couplings, the calculated concurrence as a function of temperature is depicted in Fig. 6.6(a) assuming $E_B = 0$ and $\delta = 100$ μeV. While the concurrence monotonically decreases with rising temperature for the largest QD-cavity coupling considered here, it shows a nonmonotonic behavior for smaller couplings. In contrast to the common expectation that phonons will always degrade the concurrence, the data obtained for $g = 35$ μeV reveal that the concurrence including phonons is actually consistently higher than the phonon-free result over the whole temperature range considered here, with a maximum concurrence reached at approximately 70 K that is almost 12% higher compared with the phonon-free result. Consequently, the simulations predict a
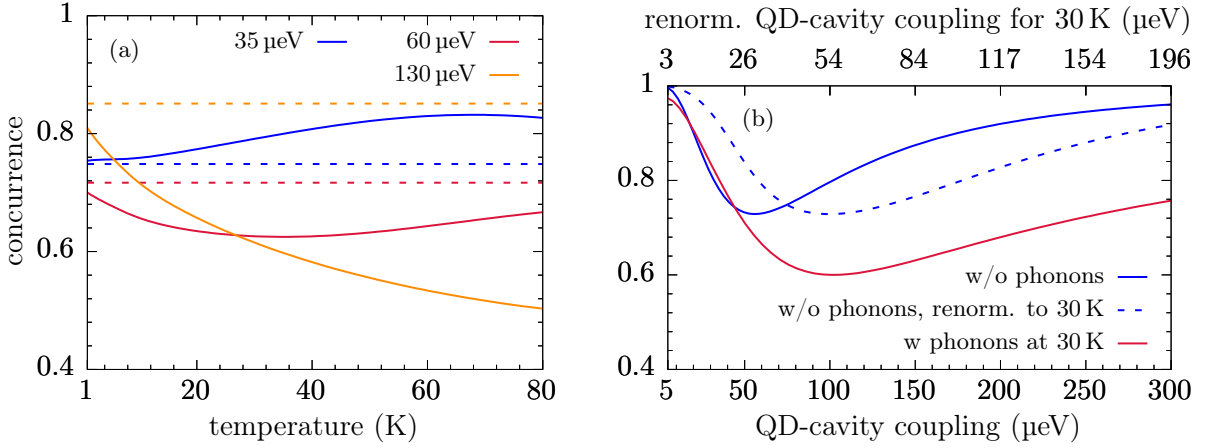
Figure 6.6: [data kindly provided by T. Seidelmann] (a) Concurrence as a function of temperature for three different QD-cavity couplings. The corresponding phonon-free values are indicated by dashed lines. (b) Concurrence as a function of the QD-cavity coupling without phonons compared with the PI result for 30 K. For the same temperature, the blue dashed line shows the concurrence as a function of the phonon-renormalized QD-cavity coupling indicated on the upper axis.

phonon-enhanced concurrence for these parameters.

The reason for this surprising effect can be traced back to the nonmonotonic dependence of the concurrence on the QD-cavity coupling, which is shown in Fig. 6.6(b). Without phonons, the concurrence exhibits a clear minimum at approximately $g \approx \frac{\delta}{2}$, the appearance of which can be understood by rescaling the system dynamics. When the equation of motion for the density matrix given by Eq. (5.2) is divided by g and the phonon influence is neglected, the system can be alternatively described using a rescaled time $t' = gt$, QD-cavity coupling $g' = g/g = 1$, FSS $\delta' = \delta/g$, and loss rate $\kappa' = \kappa/g$. Since the single-time averaged concurrence considered here is obtained in the limit of long averaging times as discussed in Sec. 6.3.1, rescaling the time does not affect the concurrence. However, taking the limit $g \to \infty$ causes δ' to approach zero. In combination with the vanishing biexciton binding energy considered here, a vanishing δ' implies an absence of which-path information and, consequently, a concurrence approaching unity. Looking at the opposite limit $g \to 0$, the only possible process is the direct two-photon transition $|B\rangle \leftrightarrow |G\rangle$ since δ' becomes increasingly large and the sequential single-photon transitions therefore become strongly detuned. The absence of which-path information in the direct two-photon transition then once again causes the concurrence to approach unity. In view of a lower concurrence expected at finite FSSs, the overall shape of the concurrence as a function of the QD-cavity coupling must have a minimum at a certain value of g, as is confirmed by Fig. 6.6(b).

Accounting for the QD-phonon interaction at 30 K not only reduces the concurrence overall but, more importantly, causes a shift of the minimum towards higher values of g compared with the phonon-free simulation. This shift is temperature dependent and originates from the phonon-induced renormalization of the light-matter coupling [209]. As explained in Pub. 14, the renormalized QD-cavity coupling $\tilde{g}$ can be approximately extracted from a fitting procedure to the PI calculations. Assuming that such a renor-

malization is the only phonon-induced effect, the corresponding concurrence would be obtained by shifting the phonon-free concurrence to the appropriately renormalized value $\tilde{g}$ at each g. The thus obtained concurrence $C(\tilde{g}(g))$ is also plotted in Fig. 6.6(b) and $\tilde{g}(g)$ is indicated on the upper axis, again for 30 K. Comparing $C(\tilde{g}(g))$ with $C(g)$ obtained using the PI algorithm, it is found that the shift of the minimum towards higher g is indeed well reproduced by $C(\tilde{g}(g))$, which confirms that this effect is due to the phonon-induced renormalization of the QD-cavity coupling.

Thus, the rising concurrence with increasing temperature observed in Fig. 6.6(a) is a consequence of shifting the minimum of $C(g)$ towards higher couplings. In regions where the phonon-free result for $C(g)$ decreases monotonically, phonons therefore lead to a larger concurrence. This also explains the existence of a maximal coupling strength beyond which a phonon-induced enhancement of the concurrence no longer occurs, namely for values of g beyond the minimum of the phonon-free result in Fig. 6.6(b).

7 Concluding remarks on nonmagnetic systems

As already mentioned in Sec. 6.1, the reformulation of the PI algorithm in terms of grouping states with equal phonon couplings opens up the possibility to investigate the phonon influence in hitherto out-of-reach systems with many levels in a numerically complete way. Specifically, an in-depth study of the photon statistics in the presence of phonons can be carried out regarding pulsed excitation scenarios of two level or lambda-like three-level systems [210]. Another interesting theoretical proposal regarding the generation of photon bundles with large photon numbers [180] would also benefit from the inclusion of the phonon influence, maybe even in terms of harnessing phonon-assisted processes. Finally, exotic quantum states such as Schrödinger cat states can be investigated using the PI algorithm. Although it is known that, in the Jaynes-Cummings model, the cavity photons can be found in a Schrödinger cat state under specific conditions [211], protocols that explicitly harness such states typically do not account for the phonon influence [212, 213]. Regarding the decoupling of the QD and the cavity upon reaching a desired photon state, a strongly off-resonant laser pulse may be used to limit the interaction time between the QD and the cavity via the optical Stark effect [214].

Of course, the results laid out in Sec. 6.2 regarding the evaluation of multitime correlation functions with PIs also only represent a first step towards an in-depth study of the phonon impact on quantities such as emission spectra [181], single-photon purity, or indistinguishability [185]. However, as already mentioned in this thesis, despite the improvements of the PI algorithm such calculations are still numerically very demanding, especially if high temporal resolutions in the femtosecond range are required. Integrating a recently-proposed scheme based on a singular-value decomposition for an on-the-fly compression of the ADM [215] into the algorithm presented here may therefore significantly extend the scope of the PI method.

Last but not least, the grouping of levels with the same phonon coupling in the PI algorithm is very advantageous when studying the field of solotronics, which aims to control the spin state of a single magnetic impurity in a QD [216, 217]. This topic also provides a direct link between the two parts of this thesis. Although optical protocols already exist for such systems [218], the presence of phonons may very well lead to significant changes or even open up alternative ways regarding the preparation of a desired impurity-spin state.

Bibliography

[1] J. Bardeen and W. H. Brattain, Phys. Rev. **74**, 230 (1948).

[2] D. Lindley, Phys. Rev. Focus **23**, 16 (2009).

[3] M. M. Waldrop, Nature **530**, 144 (2016).

[4] NobelPrize.org, The nobel prize in physics 1956 (accessed 27-05-2019).

[5] P. Ball, Nature **492**, 174 (2012).

[6] N. B. Brandt and V. V. Moshchalkov, Adv. Phys. **33**, 193 (1984).

[7] J. K. Furdyna, J. Appl. Phys. **64**, R29 (1988).

[8] H. Ohno, Science **281**, 951 (1998).

[9] K. Sato, L. Bergqvist, J. Kudrnovský, P. H. Dederichs, O. Eriksson, I. Turek, B. Sanyal, G. Bouzerar, H. Katayama-Yoshida, V. A. Dinh, T. Fukushima, H. Kizaki, and R. Zeller, Rev. Mod. Phys. **82**, 1633 (2010).

[10] T. Dietl and H. Ohno, Rev. Mod. Phys. **86**, 187 (2014).

[11] H. Ohno, A. Shen, F. Matsukura, A. Oiwa, A. Endo, S. Katsumoto, and Y. Iye, Appl. Phys. Lett. **69**, 363 (1996).

[12] K. W. Edmonds, K. Y. Wang, R. P. Campion, A. C. Neumann, C. T. Foxon, B. L. Gallagher, and P. C. Main, Appl. Phys. Lett. **81**, 3010 (2002).

[13] M. Wang, R. P. Campion, A. W. Rushforth, K. W. Edmonds, C. T. Foxon, and B. L. Gallagher, Appl. Phys. Lett. **93**, 132103 (2008).

[14] T. Dietl, A. Haury, and Y. Merle d'Aubigné, Phys. Rev. B **55**, R3347(R) (1997).

[15] T. Jungwirth, J. Sinova, J. Mašek, J. Kučera, and A. H. MacDonald, Rev. Mod. Phys. **78**, 809 (2006).

[16] C. Zener, Phys. Rev. **81**, 440 (1951).

[17] I. Di Marco, P. Thunström, M. I. Katsnelson, J. Sadowski, K. Karlsson, S. Lebègue, J. Kanski, and O. Eriksson, Nat. Commun. **4**, 2645 (2013).

[18] S. Nemsák, M. Gehlmann, C.-T. Kuo, S.-C. Lin, C. Schlueter, E. Mlynczak, T.-L. Lee, L. Plucinski, H. Ebert, I. Di Marco, J. Minár, C. M. Schneider, and C. S. Fadley, Nat. Commun. **9**, 3306 (2018).

[19] I. Žutić, J. Fabian, and S. Das Sarma, Rev. Mod. Phys. **76**, 323 (2004).

[20] D. D. Awschalom and M. E. Flatté, Nat. Phys. **3**, 153 (2007).

[21] H. Ohno, Nat. Mater. **9**, 952 (2010).

[22] T. Dietl, Nat. Mater. **9**, 965 (2010).

[23] V. K. Joshi, Eng. Sci. Technol. **19**, 1503 (2016).

[24] M. N. Baibich, J. M. Broto, A. Fert, F. N. Van Dau, F. Petroff, P. Etienne, G. Creuzet, A. Friederich, and J. Chazelas, Phys. Rev. Lett. **61**, 2472 (1988).

[25] G. Binasch, P. Grünberg, F. Saurenbach, and W. Zinn, Phys. Rev. B **39**, 4828(R) (1989).

[26] S. Datta and B. Das, Appl. Phys. Lett. **56**, 665 (1990).

[27] J. Wunderlich, B. Park, A. C. Irvine, L. P. Zârbo, E. Rozkotová, P. Nemec, V. Novák, J. Sinova, and T. Jungwirth, Science **330**, 1801 (2010).

[28] S. Cronenberger, D. Scalbert, D. Ferrand, H. Boukari, and J. Cibert, Nat. Commun. **6**, 8121 (2015).

[29] Z. Ben Cheikh, S. Cronenberger, M. Vladimirova, D. Scalbert, F. Perez, and T. Wojtowicz, Phys. Rev. B **88**, 201306(R) (2013).

[30] C. Thurn and V. M. Axt, Phys. Rev. B **85**, 165203 (2012).

[31] D. J. Wineland, C. Monroe, W. M. Itano, D. Leibfried, B. E. King, and D. M. Meekhof, J. Res. Natl. Inst. Stand. Tech. **103**, 259 (1998).

[32] D. Leibfried, R. Blatt, C. Monroe, and D. Wineland, Rev. Mod. Phys. **75**, 281 (2003).

[33] M. D. Barrett, J. Chiaverini, T. Schaetz, J. Britton, W. M. Itano, J. D. Jost, E. Knill, C. Langer, D. Leibfried, R. Ozeri, and D. J. Wineland, Nature **429**, 737 (2004).

[34] M. V. Gurudev Dutt, L. Childress, L. Jiang, E. Togan, J. Maze, F. Jelezko, A. S. Zibrov, P. R. Hemmer, and M. D. Lukin, Science **316**, 1312 (2007).

[35] J. R. Weber, W. F. Koehl, J. B. Varley, A. Janotti, B. B. Buckley, C. G. Van de Walle, and D. D. Awschalom, Proc. Natl. Acad. Sci. U.S.A. **107**, 8513 (2010).

[36] I. Aharonovich, A. D. Greentree, and S. Prawer, Nat. Photonics **5**, 397 (2011).

[37] P. C. Maurer, G. Kucsko, C. Latta, L. Jiang, N. Y. Yao, S. D. Bennett, F. Pastawski, D. Hunger, N. Chisholm, M. Markham, D. J. Twitchen, J. I. Cirac, and M. D. Lukin, Science **336**, 1283 (2012).

[38] L. Jacak, P. Hawrylak, and A. Wójs, *Quantum Dots* (Springer, Berlin, 1998).

[39] E. Biolatti, R. C. Iotti, P. Zanardi, and F. Rossi, Phys. Rev. Lett. **85**, 5647 (2000).

[40] X. Li, Y. Wu, D. Steel, D. Gammon, T. H. Stievater, D. S. Katzer, D. Park, C. Piermarocchi, and L. J. Sham, Science **301**, 809 (2003).

[41] B. Lounis and M. Orrit, Rep. Prog. Phys. **68**, 1129 (2005).

[42] B. Ruggiero, P. Delsing, C. Granata, Y. Pashkin, and P. Silvestrini, eds., *Quantum Computing in Solid State Systems* (Springer, New York, 2006).

[43] S. J. Boyle, A. J. Ramsay, F. Bello, H. Y. Liu, M. Hopkinson, A. M. Fox, and M. S. Skolnick, Phys. Rev. B **78**, 075301 (2008).

[44] F. Henneberger and O. Benson, eds., *Semiconductor Quantum Bits* (Pan Stanford Publishing Pte. Ltd., Singapore, 2009).

[45] R. P. Feynman, Int. J. Theor. Phys. **21**, 467 (1982).

[46] D. Deutsch and R. Penrose, Proc. Royal Soc. Lond. A. **400**, 97 (1985).

[47] P. W. Shor, An. S. Fdn. Co. **35**, 124 (1994).

[48] L. K. Grover, Phys. Rev. Lett. **79**, 325 (1997).

[49] D-Wave Systems Inc., The D-Wave 2000Q Quantum Computer Technology Overview (accessed 31-05-2019).

[50] M. I. Dyakonov, Solid State Electron. **155**, 4 (2019).

[51] J. I. Cirac, P. Zoller, H. J. Kimble, and H. Mabuchi, Phys. Rev. Lett. **78**, 3221 (1997).

[52] A. R. Dixon, Z. L. Yuan, J. F. Dynes, A. W. Sharpe, and A. J. Shields, Opt. Express **16**, 18790 (2008).

[53] S.-K. Liao, W.-Q. Cai, J. Handsteiner, B. Liu, J. Yin, L. Zhang, D. Rauch, M. Fink, J.-G. Ren, W.-Y. Liu, Y. Li, Q. Shen, Y. Cao, F.-Z. Li, J.-F. Wang, Y.-M. Huang, L. Deng, T. Xi, L. Ma, T. Hu, L. Li, N.-L. Liu, F. Koidl, P. Wang, Y.-A. Chen, X.-B. Wang, M. Steindorfer, G. Kirchner, C.-Y. Lu, R. Shu, R. Ursin, T. Scheidl, C.-Z. Peng, J.-Y. Wang, A. Zeilinger, and J.-W. Pan, Phys. Rev. Lett. **120**, 030501 (2018).

[54] B. D. Josephson, Phys. Lett. **1**, 251 (1962).

[55] P. Michler, ed., *Single Semiconductor Quantum Dots* (Springer, Berlin, 2009).

[56] S. Ates, S. M. Ulrich, A. Ulhaq, S. Reitzenstein, A. Löffler, S. Höfling, A. Forchel, and P. Michler, Nat. Photonics **3**, 724 (2009).

[57] P. Kaer, T. R. Nielsen, P. Lodahl, A.-P. Jauho, and J. Mørk, Phys. Rev. Lett. **104**, 157401 (2010).

[58] S. Hughes and H. J. Carmichael, New J. Phys. **15**, 053039 (2013).

[59] M. Glässl, A. M. Barth, and V. M. Axt, Phys. Rev. Lett. **110**, 147401 (2013).

[60] J. H. Quilter, A. J. Brash, F. Liu, M. Glässl, A. M. Barth, V. M. Axt, A. J. Ramsay, M. S. Skolnick, and A. M. Fox, Phys. Rev. Lett. **114**, 137401 (2015).

[61] D. G. Nahri, F. H. A. Mathkoor, and C. H. R. Ooi, J. Phys. Condens. Matter **29**, 055701 (2016).

[62] O. Gazzano, S. Michaelis de Vasconcellos, C. Arnold, A. Nowak, E. Galopin, I. Sagnes, L. Lanco, A. Lemaître, and P. Senellart, Nat. Commun. **4**, 1425 (2013).

[63] K. H. Madsen, S. Ates, J. Liu, A. Javadi, S. M. Albrecht, I. Yeo, S. Stobbe, and P. Lodahl, Phys. Rev. B **90**, 155303 (2014).

[64] N. Somaschi, V. Giesz, L. De Santis, J. C. Loredo, M. P. Almeida, G. Hornecker, S. L. Portalupi, T. Grange, C. Antón, J. Demory, C. Gómez, I. Sagnes, N. D. Lanzillotti-Kimura, A. Lemaítre, A. Auffeves, A. G. White, L. Lanco, and P. Senellart, Nat. Photonics **10**, 340 (2016).

[65] E. M. Purcell, H. C. Torrey, and R. V. Pound, Phys. Rev. **69**, 37 (1946).

[66] R. J. Coles, D. M. Price, J. E. Dixon, B. Royall, E. Clarke, P. Kok, M. S. Skolnick, A. M. Fox, and M. N. Makhonin, Nat. Commun. **7**, 11183 (2016).

[67] J. Förstner, C. Weber, J. Danckwerts, and A. Knorr, Phys. Rev. Lett. **91**, 127401 (2003).

[68] D. P. S. McCutcheon, N. S. Dattani, E. M. Gauger, B. W. Lovett, and A. Nazir, Phys. Rev. B **84**, 081305(R) (2011).

[69] A. Nazir and D. P. S. McCutcheon, J. Phys.: Condens. Matter **28**, 103002 (2016).

[70] D. E. Reiter, Phys. Rev. B **95**, 125308 (2017).

[71] R. P. Feynman, Phys. Rev. **76**, 769 (1949).

[72] N. Makri and D. E. Makarov, J. Chem. Phys. **102**, 4600 (1995).

[73] N. Makri and D. E. Makarov, J. Chem. Phys. **102**, 4611 (1995).

[74] A. Vagov, M. D. Croitoru, M. Glässl, V. M. Axt, and T. Kuhn, Phys. Rev. B **83**, 094303 (2011).

[75] A. M. Barth, A. Vagov, and V. M. Axt, Phys. Rev. B **94**, 125439 (2016).

[76] J. Kossut and J. A. Gaj, eds., *Introduction to the Physics of Diluted Magnetic Semiconductors* (Springer, Berlin, 2010).

[77] R. Winkler, *Spin-Orbit Coupling Effects in Two-Dimensional Electron and Hole Systems* (Springer, Berlin, 2003).

[78] G. Bastard, *Wave Mechanics Applied to Semiconductor Heterostructures* (Editions de Physique, Les Ulis, France, 1996).

[79] E. I. Rashba and M. D. Sturge, eds., *Excitons* (North-Holland, Amsterdam, 1982).

[80] J. Frenkel, Phys. Rev. **37**, 17 (1931).

[81] G. H. Wannier, Phys. Rev. **52**, 191 (1937).

[82] D. C. Reynolds and T. C. Collins, *Excitons - Their Properties and Uses* (Academic, New York, 1981).

[83] G. V. Astakhov, D. R. Yakovlev, V. P. Kochereshko, W. Ossau, W. Faschinger, J. Puls, F. Henneberger, S. A. Crooker, Q. McCulloch, D. Wolverson, N. A. Gippius, and A. Waag, Phys. Rev. B **65**, 165335 (2002).

[84] X. L. Yang, S. H. Guo, F. T. Chan, K. W. Wong, and W. Y. Ching, Phys. Rev. A **43**, 1186 (1991).

[85] G. Bastard, E. E. Mendez, L. L. Chang, and L. Esaki, Phys. Rev. B **26**, 1974 (1982).

[86] R. C. Iotti and L. C. Andreani, Semicond. Sci. Technol. **10**, 1561 (1995).

[87] R. Zimmermann, Phys. Status Solidi B **135**, 681 (1986).

[88] R. Winkler, Phys. Rev. B **51**, 14395 (1995).

[89] T. Kazimierczuk, D. Fröhlich, S. Scheel, H. Stolz, and M. Bayer, Nature **514**, 343 (2014).

[90] M. M. Ugeda, A. J. Bradley, S.-F. Shi, F. H. da Jornada, Y. Zhang, D. Y. Qiu, W. Ruan, S. Mo, Z. Hussain, Z. Shen, F. Wang, S. G. Louie, and M. F. Crommie, Nat. Mater. **13**, 1091 (2014).

[91] A. Chernikov, T. C. Berkelbach, H. M. Hill, A. Rigosi, Y. Li, O. B. Aslan, D. R. Reichman, M. S. Hybertsen, and T. F. Heinz, Phys. Rev. Lett. **113**, 076802 (2014).

[92] S. Brem, M. Selig, G. Berghaeuser, and E. Malic, Sci. Rep. **8**, 8238 (2018).

[93] J. K. Furdyna and J. Kossut, eds., *Semiconductors and Semimetals* (Academic, San Diego, 1988).

[94] J. Kossut, Phys. Status Solidi B **72**, 359 (1975).

[95] M. Nawrocki, R. Planel, G. Fishman, and R. Galazka, Phys. Rev. Lett. **46**, 735 (1981).

[96] M. W. Wu, J. H. Jiang, and M. Q. Weng, Phys. Rep. **493**, 61 (2010).

[97] J. J. Baumberg, D. D. Awschalom, N. Samarth, H. Luo, and J. K. Furdyna, Phys. Rev. Lett. **72**, 717 (1994).

[98] S. A. Crooker, J. J. Baumberg, F. Flack, N. Samarth, and D. D. Awschalom, Phys. Rev. Lett. **77**, 2814 (1996).

[99] S. A. Crooker, D. D. Awschalom, J. J. Baumberg, F. Flack, and N. Samarth, Phys. Rev. B **56**, 7574 (1997).

[100] C. Camilleri, F. Teppe, D. Scalbert, Y. G. Semenov, M. Nawrocki, M. Dyakonov, J. Cibert, S. Tatarenko, and T. Wojtowicz, Phys. Rev. B **64**, 085331 (2001).

[101] K. E. Rönnburg, E. Mohler, H. G. Roskos, K. Ortner, C. R. Becker, and L. W. Molenkamp, Phys. Rev. Lett. **96**, 117203 (2006).

[102] M. Vladimirova, S. Cronenberger, P. Barate, D. Scalbert, F. J. Teran, and A. P. Dmitriev, Phys. Rev. B **78**, 081305(R) (2008).

[103] S. Cronenberger, P. Barate, A. Brunetti, M. Vladimirova, D. Scalbert, F. J. Teran, G. Karzewski, and T. Wojtowicz, Superlattices Microstruct. **43**, 427 (2008).

[104] G. Bastard and R. Ferreira, Surf. Sci. **267**, 335 (1992).

[105] B. König, I. A. Merkulov, D. R. Yakovlev, W. Ossau, S. M. Ryabchenko, M. Kutrowski, T. Wojtowicz, G. Karczewski, and J. Kossut, Phys. Rev. B **61**, 16870 (2000).

[106] E. Tsitsishvili and H. Kalt, Phys. Rev. B **73**, 195402 (2006).

[107] Ł. Cywiński and L. J. Sham, Phys. Rev. B **76**, 045205 (2007).

[108] E. Tsitsishvili and H. Kalt, Phys. Rev. B **77**, 155305 (2008).

[109] O. Morandi, P. A. Hervieux, and G. Manfredi, Phys. Rev. B **81**, 155309 (2010).

[110] Y. G. Semenov, Phys. Rev. B **67**, 115319 (2003).

[111] J. H. Jiang, Y. Zhou, T. Korn, C. Schüller, and M. W. Wu, Phys. Rev. B **79**, 155201 (2009).

[112] R. Akimoto, K. Ando, F. Sasaki, S. Kobayashi, and T. Tani, J. Lumin. **72**, 309 (1997).

[113] C. J. P. Smits, S. C. A. van Driel, M. van Kampen, W. J. M. de Jonge, B. Koopmans, and G. Karczewski, Phys. Rev. B **70**, 115307 (2004).

[114] H. Sakurai, K. Seo, Z. H. Chen, K. Kayanuma, T. Tomita, A. Murayama, and Y. Oka, Phys. Status Solidi C **1**, 981 (2004).

[115] A. Murayama, K. Seo, K. Nishibayashi, I. Souma, and Y. Oka, Appl. Phys. Lett. **88**, 261105 (2006).

[116] M. Cygorek, F. Ungar, P. I. Tamborenea, and V. M. Axt, Phys. Rev. B **95**, 045204 (2017).

[117] C. Thurn, M. Cygorek, V. M. Axt, and T. Kuhn, Phys. Rev. B **87**, 205301 (2013).

[118] M. Cygorek, P. I. Tamborenea, and V. M. Axt, Phys. Rev. B **93**, 035206 (2016).

[119] M. Cygorek, P. I. Tamborenea, and V. M. Axt, Phys. Rev. B **93**, 205201 (2016).

[120] V. M. Axt and S. Mukamel, Rev. Mod. Phys. **70**, 145 (1998).

[121] F. Rossi and T. Kuhn, Rev. Mod. Phys. **74**, 895 (2002).

[122] V. M. Axt and A. Stahl, Z. Phys. B **93**, 195 (1994).

[123] T. Uenoyama and L. J. Sham, Phys. Rev. Lett. **64**, 3070 (1990).

[124] R. Ferreira and G. Bastard, Phys. Rev. B **43**, 9687 (1991).

[125] M. Z. Maialle, E. A. de Andrada e Silva, and L. J. Sham, Phys. Rev. B **47**, 15776 (1993).

[126] M. Z. Maialle and L. J. Sham, Surf. Sci. **305**, 256 (1994).

[127] M. Cygorek and V. M. Axt, J. Phys. Conf. Ser. **647**, 012042 (2015).

[128] S. Rudin and T. L. Reinecke, Phys. Rev. B **41**, 3017 (1990).

[129] E. Tsitsishvili, R. v. Baltz, and H. Kalt, Phys. Rev. B **71**, 155320 (2005).

[130] C. D. Poweleit, L. M. Smith, and B. T. Jonker, Phys. Rev. B **55**, 5062 (1997).

[131] M. Umlauff, J. Hoffmann, H. Kalt, W. Langbein, J. M. Hvam, M. Scholl, J. Söllner, M. Heuken, B. Jobst, and D. Hommel, Phys. Rev. B **57**, 1390 (1998).

[132] W. M. Chen, I. A. Buyanova, G. Y. Rudko, A. G. Mal'shukov, K. A. Chao, A. A. Toropov, Y. Terent'ev, S. V. Sorokin, A. V. Lebedev, S. V. Ivanov, and P. S. Kop'ev, Phys. Rev. B **67**, 125313 (2003).

[133] Y. S. Ang, Z. Ma, and C. Zhang, Sci. Rep. **5**, 7872 (2015).

[134] J. Mulet, S. Balle, J. Arias, V. Martín-Hériz, and I. Esquivias, Opt. Quantum Electron. **40**, 1199 (2008).

[135] J. Becker, A. Tsukamoto, A. Kirilyuk, J. C. Maan, T. Rasing, P. C. M. Christianen, and A. V. Kimel, Phys. Rev. B **92**, 180407(R) (2015).

[136] R. Fu, J. Li, J. Cui, and X. Peng, J. Magn. Reson. **268**, 107 (2016).

[137] M. I. Dyakonov and V. I. Perel, Zh. Eksp. Teor. Fiz. **60**, 1954 (1971), [Sov. Phys. JETP 33, 1053 (1971)].

[138] Y. A. Bychkov and E. I. Rashba, JETP Lett. **39**, 78 (1984).

[139] F. J. Ohkawa and Y. Uemura, J. Phys. Soc. Jpn. **37**, 1325 (1974).

[140] M. I. Dyakonov, ed., *Spin Physics in Semiconductors* (Springer, Berlin, 2008).

[141] F. Passmann, S. Anghel, T. Tischler, A. V. Poshakinskiy, S. A. Tarasenko, G. Karczewski, T. Wojtowicz, A. D. Bristow, and M. Betz, Phys. Rev. B **97**, 201413(R) (2018).

[142] E. Rozkotová, P. Němec, N. Tesařová, P. Malý, V. Novák, K. Olejník, M. Cukr, and T. Jungwirth, Appl. Phys. Lett. **93**, 232505 (2008).

[143] R. A. Kaindl, M. A. Carnahan, D. Hägele, R. Lövenich, and D. S. Chemla, Nature **423**, 734 (2003).

[144] G. F. Quinteiro, D. E. Reiter, and T. Kuhn, Phys. Rev. A **91**, 033808 (2015).

[145] T. Kuhn, D. E. Reiter, and G. F. Quinteiro, J. Phys. Conf. Ser. **647**, 012012 (2015).

[146] G. Plechinger, P. Nagler, A. Arora, R. Schmidt, A. Chernikov, J. Lupton, R. Bratschitsch, C. Schüller, and T. Korn, Phys. Status Solidi RRL **11**, 1700131 (2017).

[147] C. Schneider, M. M. Glazov, T. Korn, S. Höfling, and B. Urbaszek, Nature Commun. **9**, 2695 (2018).

[148] Y. C. Cheng, Z. Y. Zhu, W. B. Mi, Z. B. Guo, and U. Schwingenschlögl, Phys. Rev. B **87**, 100401 (2013).

[149] B. Li, T. Xing, M. Zhong, L. Huang, N. Lei, J. Zhang, J. Li, and Z. Wei, Nature Commun. **8**, 1958 (2017).

[150] Q. Zhao, Z. Xiong, L. Luo, Z. Sun, Z. Qin, L. Chen, and N. Wu, Appl. Surf. Sc. **396**, 480 (2017).

[151] D. Bimberg, M. Grundmann, and N. N. Ledentsov, *Quantum Dot Heterostructures* (Wiley, Chichester, 1999).

[152] J.-Y. Marzin, J.-M. Gérard, A. Izraël, D. Barrier, and G. Bastard, Phys. Rev. Lett. **73**, 716 (1994).

[153] F. Ding, R. Singh, J. D. Plumhof, T. Zander, V. Křápek, Y. H. Chen, M. Benyoucef, V. Zwiller, K. Dörr, G. Bester, A. Rastelli, and O. G. Schmidt, Phys. Rev. Lett. **104**, 067405 (2010).

[154] M. Kaniber, M. F. Huck, K. Müller, E. C. Clark, F. Troiani, M. Bichler, H. J. Krenner, and J. J. Finley, Nanotechnology **22**, 325202 (2011).

[155] D. E. Reiter, T. Kuhn, M. Glässl, and V. M. Axt, J. Phys. Cond. Matt. **26**, 423203 (2014).

[156] S. Bounouar, M. Müller, A. M. Barth, M. Glässl, V. M. Axt, and P. Michler, Phys. Rev. B **91**, 161302(R) (2015).

[157] J. M. Gérard, B. Sermage, B. Gayral, B. Legrand, E. Costard, and V. Thierry-Mieg, Phys. Rev. Lett. **81**, 1110 (1998).

[158] J. P. Reithmaier, G. Sek, A. Löffler, C. Hofmann, S. Kuhn, S. Reitzenstein, L. V. Keldysh, V. D. Kulakovskii, T. L. Reinecke, and A. Forchel, Nature **432**, 197 (2004).

[159] B. Krummheuer, V. M. Axt, and T. Kuhn, Phys. Rev. B **65**, 195313 (2002).

[160] A. Vagov, M. D. Croitoru, V. M. Axt, T. Kuhn, and F. M. Peeters, Phys. Rev. Lett. **98**, 227403 (2007).

[161] A. J. Ramsay, A. V. Gopal, E. M. Gauger, A. Nazir, B. W. Lovett, A. M. Fox, and M. S. Skolnick, Phys. Rev. Lett. **104**, 017402 (2010).

[162] C. C. Gerry and P. L. Knight, *Introductory Quantum Optics* (Cambridge University Press, Cambridge, 2005).

[163] H. P. Breuer and F. Petruccione, *The Theory of Open Quantum Systems* (Oxford University Press, Oxford, 2002).

[164] S. Schumacher, J. Förstner, A. Zrenner, M. Florian, C. Gies, P. Gartner, and F. Jahnke, Opt. Express **20**, 5335 (2012).

[165] M. Glässl, A. Vagov, S. Lüker, D. E. Reiter, M. D. Croitoru, P. Machnikowski, V. M. Axt, and T. Kuhn, Phys. Rev. B **84**, 195311 (2011).

[166] C. Roy and S. Hughes, Phys. Rev. X **1**, 021009 (2011).

[167] N. Makri, J. Chem. Phys. **141**, 134117 (2014).

[168] L. Magazzù, D. Valenti, A. Carollo, and B. Spagnolo, Entropy **17**, 2341 (2015).

[169] A. M. Barth, S. Lüker, A. Vagov, D. E. Reiter, T. Kuhn, and V. M. Axt, Phys. Rev. B **94**, 045306 (2016).

[170] R. J. Glauber, Phys. Rev. **131**, 2766 (1963).

[171] Y. T. Chough and H. J. Carmichael, Phys. Rev. A **54**, 1709 (1996).

[172] S. M. Ulrich, S. Ates, S. Reitzenstein, A. Löffler, A. Forchel, and P. Michler, Phys. Rev. Lett. **106**, 247402 (2011).

[173] C. Roy and S. Hughes, Phys. Rev. Lett. **106**, 247403 (2011).

[174] D. P. S. McCutcheon and A. Nazir, Phys. Rev. Lett. **110**, 217401 (2013).

[175] D. P. S. McCutcheon, Phys. Rev. A **93**, 022119 (2016).

[176] R. Hanbury Brown and R. Q. Twiss, Nature **177**, 27 (1956).

[177] C. K. Hong, Z. Y. Ou, and L. Mandel, Phys. Rev. Lett. **59**, 2044 (1987).

[178] X. Ding, Y. He, Z.-C. Duan, N. Gregersen, M.-C. Chen, S. Unsleber, S. Maier, C. Schneider, M. Kamp, S. Höfling, C.-Y. Lu, and J.-W. Pan, Phys. Rev. Lett. **116**, 020401 (2016).

[179] N. Prtljaga, C. Bentham, J. O'Hara, B. Royall, E. Clarke, L. R. Wilson, M. S. Skolnick, and A. M. Fox, Appl. Phys. Lett. **108**, 251101 (2016).

[180] C. S. Muñoz, E. del Valle, A. G. Tudela, K. Müller, S. Lichtmannecker, M. Kaniber, C. Tejedor, J. J. Finley, and F. P. Laussy, Nat. Photonics **8**, 550 (2014).

[181] H. Carmichael, *An Open Systems Approach to Quantum Optics* (Springer, Berlin, 1993).

[182] B. R. Mollow, Phys. Rev. **188**, 1969 (1969).

[183] C. Santori, D. Fattal, J. Vuckovic, G. S. Solomon, and Y. Yamamoto, Nature **419**, 594 (2002).

[184] Y.-M. He, Y. He, Y.-J. Wei, D. Wu, M. Atatüre, C. Schneider, S. Höfling, M. Kamp, C.-Y. Lu, and J.-W. Pan, Nat. Nanotech. **8**, 213 (2013).

[185] P. Senellart, G. Solomon, and A. White, Nat. Nanotechnol. **12**, 1026 (2017).

[186] L. Schweickert, K. D. Jöns, K. D. Zeuner, S. F. Covre da Silva, H. Huang, T. Lettner, M. Reindl, J. Zichi, R. Trotta, A. Rastelli, and V. Zwiller, Appl. Phys. Lett. **112**, 093106 (2018).

[187] C. Bentham, D. Hallett, N. Prtljaga, B. Royall, D. Vaitiekus, R. J. Coles, E. Clarke, A. M. Fox, M. S. Skolnick, I. E. Itskevich, and L. R. Wilson, Appl. Phys. Lett. **109**, 161101 (2016).

[188] S. Lüker, K. Gawarecki, D. E. Reiter, A. Grodecka-Grad, V. M. Axt, P. Machnikowski, and T. Kuhn, Phys. Rev. B **85**, 121302(R) (2012).

[189] N. Gisin, G. Ribordy, W. Tittel, and H. Zbinden, Rev. Mod. Phys. **74**, 145 (2002).

[190] A. Orieux, M. A. M. Versteegh, K. D. Jöns, and S. Ducci, Rep. Progr. Phys. **80**, 076001 (2017).

[191] A. Zeilinger, Phys. Scr. **92**, 072501 (2017).

[192] C. H. Bennett, D. P. DiVincenzo, J. A. Smolin, and W. K. Wootters, Phys. Rev. A **54**, 3824 (1996).

[193] M. Bayer, A. Kuther, A. Forchel, A. Gorbunov, V. B. Timofeev, F. Schäfer, J. P. Reithmaier, T. L. Reinecke, and S. N. Walck, Phys. Rev. Lett. **82**, 1748 (1999).

[194] J. D. Mar, J. J. Baumberg, X. L. Xu, A. C. Irvine, and D. A. Williams, Phys. Rev. B **93**, 045316 (2016).

[195] W. K. Wootters, Quantum Inf. Comput. **1**, 27 (2001).

[196] W. K. Wootters, Phys. Rev. Lett. **80**, 2245 (1998).

[197] D. F. V. James, P. G. Kwiat, W. J. Munro, and A. G. White, Phys. Rev. A **64**, 052312 (2001).

[198] R. M. Stevenson, A. J. Hudson, A. J. Bennett, R. J. Young, C. A. Nicoll, D. A. Ritchie, and A. J. Shields, Phys. Rev. Lett. **101**, 170501 (2008).

[199] S. Bounouar, C. de la Haye, M. Strauß, P. Schnauber, A. Thoma, M. Gschrey, J.-H. Schulze, A. Strittmatter, S. Rodt, and S. Reitzenstein, Appl. Phys. Lett. **112**, 153107 (2018).

[200] A. Carmele and A. Knorr, Phys. Rev. B **84**, 075328 (2011).

[201] E. del Valle, New J. Phys. **15**, 025019 (2013).

[202] D. Heinze, A. Zrenner, and S. Schumacher, Phys. Rev. B **95**, 245306 (2017).

[203] S. Bravyi, D. P. DiVincenzo, and D. Loss, Ann. Phys. **326**, 2793 (2011).

[204] D. Gammon, E. S. Snow, B. V. Shanabrook, D. S. Katzer, and D. Park, Phys. Rev. Lett. **76**, 3005 (1996).

[205] A. J. Bennett, M. A. Pooley, R. M. Stevenson, M. B. Ward, R. B. Patel, A. B. de la Giroday, N. Sköld, I. Farrer, C. A. Nicoll, D. A. Ritchie, and A. J. Shields, Nat. Phys. **6**, 947 (2010).

[206] R. M. Stevenson, R. J. Young, P. Atkinson, K. Cooper, D. A. Ritchie, and A. J. Shields, Nature **439**, 179 (2006).

[207] J. Zhang, J. S. Wildmann, F. Ding, R. Trotta, Y. Huo, E. Zallo, D. Huber, A. Rastelli, and O. G. Schmidt, Nat. Commun. **6**, 10067 (2015).

[208] P. Machnikowski, Phys. Rev. B **78**, 195320 (2008).

[209] A. J. Ramsay, T. M. Godden, S. J. Boyle, E. M. Gauger, A. Nazir, B. W. Lovett, A. M. Fox, and M. S. Skolnick, Phys. Rev. Lett. **105**, 177402 (2010).

[210] T. Close, E. M. Gauger, and B. W. Lovett, New J. Phys. **14**, 113004 (2012).

[211] B. W. Shore and P. L. Knight, J. Mod. Opt. **40**, 1195 (1993).

[212] J. Gea-Banacloche, Phys. Rev. Lett. **65**, 3385 (1990).

[213] J. Gea-Banacloche, Phys. Rev. A **44**, 5913 (1991).

[214] T. Unold, K. Mueller, C. Lienau, T. Elsaesser, and A. D. Wieck, Phys. Rev. Lett. **92**, 157401 (2004).

[215] A. Strathearn, P. Kirton, D. Kilda, J. Keeling, and B. W. Lovett, Nat. Commun. **9**, 3322 (2018).

[216] R. Hanson and D. D. Awschalom, Nature **453**, 1043 (2008).

[217] J. Kobak, T. Smolenski, M. Goryca, M. Papaj, K. Gietka, A. Bogucki, M. Koperski, J.-G. Rousset, J. Suffczynski, E. Janik, M. Nawrocki, A. Golnik, P. Kossacki, and W. Pacuski, Nature Communications **5**, 3191 (2014).

[218] D. E. Reiter, T. Kuhn, and V. M. Axt, Phys. Rev. Lett. **102**, 177403 (2009).

Acknowledgment

Eidesstattliche Versicherung

Hiermit versichere ich an Eides statt, dass ich die vorliegende Arbeit selbstständig verfasst und keine anderen als die von mir angegebenen Quellen und Hilfsmittel verwendet habe.

Weiterhin erkläre ich, dass ich die Hilfe von gewerblichen Promotionsberatern bzw. - vermittlern oder ähnlichen Dienstleistern weder bisher in Anspruch genommen habe, noch künftig in Anspruch nehmen werde.

Zusätzlich erkläre ich hiermit, dass ich keinerlei frühere Promotionsversuche unternommen habe.

Bayreuth, den 8. Januar 2020

_____

Florian Roland Ungar

Part III

Publications

List of publications as referred to in this thesis – magnetic systems

Pub. 1 F. Ungar, M. Cygorek, and V. M. Axt,
Quantum kinetic equations for the ultrafast spin dynamics of excitons in diluted magnetic semiconductor quantum wells after optical excitation,
Phys. Rev. B **95**, 245203 (2017)
& Erratum: Phys. Rev. B **96**, 239904 (2017).

Pub. 2 F. Ungar, M. Cygorek, and V. M. Axt,
Trend reversal in the magnetic-field dependence of exciton spin-transfer rates in diluted magnetic semiconductors due to non-Markovian dynamics,
Phys. Rev. B **97**, 045210 (2018).

Pub. 3 F. Ungar, M. Cygorek, and V. M. Axt,
Many-body correlations brought to light in absorption spectra of diluted magnetic semiconductors,
Phys. Rev. B **98**, 161201(R) (2018).

Pub. 4 F. Ungar, M. Cygorek, and V. M. Axt,
Role of excited states in the dynamics of excitons and their spins in diluted magnetic semiconductors,
Phys. Rev. B **99**, 195309 (2019).

Pub. 5 F. Ungar, M. Cygorek, and V. M. Axt,
Phonon impact on the dynamics of resonantly excited and hot excitons in diluted magnetic semiconductors,
Phys. Rev. B **99**, 115305 (2019).

Pub. 6 F. Ungar, M. Cygorek, and V. M. Axt,
Phonon-induced quantum ratchet in the exciton spin dynamics in diluted magnetic semiconductors in a magnetic field,
Phys. Rev. B **99**, 075301 (2019).

Pub. 7 F. Ungar, M. Cygorek, and V. M. Axt,
Origins of overshoots in the exciton spin dynamics in semiconductors,
Phys. Rev. B **99**, 165308 (2019)
& Erratum: Phys. Rev. B **100**, 049902 (2019).

Pub. 8 F. Ungar, P. I. Tamborenea, and V. M. Axt,
Spin dynamics of hot excitons in diluted magnetic semiconductors with spin-orbit interaction,
Phys. Rev. B **100**, 045306 (2019)
& Erratum: Phys. Rev. B **100**, 089901 (2019).

List of publications as referred to in this thesis – nonmagnetic systems

Pub. 9 M. Cygorek, A. M. Barth, F. Ungar, A. Vagov, and V. M. Axt,
Nonlinear cavity feeding and unconventional photon statistics in solid-state cavity QED revealed by many-level real-time path-integral calculations,
Phys. Rev. B **96**, 201201(R) (2017)
& Erratum: Phys. Rev. B **99**, 079906 (2019).

Pub. 10 M. Cosacchi, M. Cygorek, F. Ungar, A. M. Barth, A. Vagov, and V. M. Axt,
Path-integral approach for nonequilibrium multitime correlation functions of open quantum systems coupled to Markovian and non-Markovian environments,
Phys. Rev. B **98**, 125302 (2018), selected as *Editors' Suggestion.*

Pub. 11 M. Cosacchi, F. Ungar, M. Cygorek, A. Vagov, and V. M. Axt,
Emission-Frequency Separated High Quality Single-Photon Sources Enabled by Phonons,
Phys. Rev. Lett. **123**, 017403 (2019).

Pub. 12 M. Cygorek, F. Ungar, T. Seidelmann, A. M. Barth, A. Vagov, V. M. Axt, and T. Kuhn,
Comparison of different concurrences characterizing photon pairs generated in the biexciton cascade in quantum dots coupled to microcavities,
Phys. Rev. B **98**, 045303 (2018).

Pub. 13 T. Seidelmann, F. Ungar, M. Cygorek, A. Vagov, A. M. Barth, T. Kuhn, and V. M. Axt,
From strong to weak temperature dependence of the two-photon entanglement resulting from the biexciton cascade inside a cavity,
Phys. Rev. B **99**, 245301 (2019).

Pub. 14 T. Seidelmann, F. Ungar, A. Vagov, V. M. Axt, M. Cygorek, and T. Kuhn,
Phonon-Induced Enhancement of Photon Entanglement in Quantum Dot-Cavity Systems,
Phys. Rev. Lett. **123**, 137401 (2019).

Contributions to the publications

The author is responsible for most of the work in Pub. 1-Pub. 8. In particular, he has performed all analytic and numeric calculations, has designed all the figures, and has written the first draft for all of these papers. M. Cygorek has advised the author during parts of the analytic derivations for Pub. 1 and the author has used a Runge-Kutta framework written by M. Cygorek for the propagation of density matrices in time. Other programs, such as the Fourier transform to obtain the spectra in Pub. 3 as well as a solver for the exciton problem in real space have been written solely by the author. The original idea to develop a quantum kinetic description for the exciton spin dynamics, which resulted in Pub. 1, was put forth by M. Cygorek and V. M. Axt, while the concepts for Pub. 2-Pub. 8 were developed by the author. Regarding Pub. 3, V. M. Axt suggested the analytic calculation of the linear absorption, which was subsequently done by the author, and provided crucial details for the interpretation of the absorption lineshape. During the development of Pub. 8, P. I. Tamborenea hosted the author in Buenos Aires, contributed crucial ideas concerning the representation of spin-orbit coupling in the exciton basis, and pointed out relevant literature. The coauthors contributed to the discussion and interpretation of the results and assisted in the presentation of the content for the publications. Furthermore, they were involved in answering to comments of the referees before publication.

Concerning Pub. 9-Pub. 14, the author was mainly involved in discussing and interpreting the results, designing the figures as well as the overall presentation of the publications, and writing parts of the manuscripts. Specifically, the author contributed Fig. 3 in Pub. 9 and was responsible for pointing out the error in the implementation of the PMEs, which resulted in the subsequent erratum. The author advised M. Cosacchi regarding Pub. 10 and provided the code to calculate the spectra. For Pub. 11, the author assisted M. Cosacchi in the interpretation of the physical origin of the discussed effect and contributed to designing the figures. Although M. Cygorek wrote the original first draft for Pub. 12, V. M. Axt together with the author rewrote major parts of the paper after having received the referee reports. In addition, the author contributed Fig. 10 to the manuscript and performed the necessary calculations. Regarding Pub. 13, the author rewrote and shortened large parts of the manuscript provided by T. Seidelmann. Finally, the author suggested the inset in Fig. 1 of Pub. 14 during the revision process.

Conference and seminar contributions

Parts of this work were presented by the author at the following conferences in the form of poster presentations:

- OPON 2016, Wrocław, Poland (2016)

- NOEKS 13, Dortmund, Germany (2016)

- PLMCN 18, Würzburg, Germany (2017)

- OECS 2017, Bath, UK (2017)

- OPON 2018, Münster, Germany (2018)

- 50 Years of Optical Orientation in Semiconductors, Paris, France (2018)

- ICSNN 20, Madrid, Spain (2018)

- PASPS 10, Linz, Austria (2018)

- NOEKS 14, Berlin, Germany (2018)

Furthermore, the author was invited two times by Prof. P. Machnikowski to present his work in the form of seminary talks at the Wrocław University of Technology in Wrocław, Poland (December 2016 & June 2019). The author has also traveled to Buenos Aires, Argentina, for a research stay of two months (February & March 2019) to work with Prof. P. I. Tamborenea at the Universidad de Buenos Aires on the topic of twisted light and spin-orbit coupling (cf. Pub. 8).

Further publications contributed to by the author

F. Ungar, M. Cygorek, P. I. Tamborenea, and V. M. Axt,
Ultrafast spin dynamics in II-VI diluted magnetic semiconductors with spin-orbit interaction,
Phys. Rev. B **91**, 195201 (2015).

F. Ungar, M. Cygorek, P. I. Tamborenea, and V. M. Axt,
Relaxation and coherent oscillations in the spin dynamics of II-VI diluted magnetic quantum wells,
J Phys. Conf. Ser. **647** 012010 (2015).

M. Cygorek, F. Ungar, P. I. Tamborenea, and V. M. Axt,
Dependence of quantum kinetic effects in the spin dynamics of diluted magnetic semiconductors on the excitation conditions,
Proc. SPIE **9931**, 993147 (2016).

M. Cygorek, F. Ungar, P. I. Tamborenea, and V. M. Axt
Influence of nonmagnetic impurity scattering on spin dynamics in diluted magnetic semiconductors,
Phys. Rev. B **95**, 045204 (2017).

M. Cosacchi, M. Cygorek, F. Ungar, and V. M. Axt,
Nonexponential spin decay in a quantum kinetic description of the D'yakonov-Perel' mechanism mediated by impurity scattering,
Phys. Rev. B **95**, 195313 (2017).

Publication 1

Quantum kinetic equations for the ultrafast spin dynamics of excitons in diluted magnetic semiconductor quantum wells after optical excitation

F. Ungar, M. Cygorek, and V. M. Axt
Physical Review B **95**, 245203 (2017)

&

Erratum: Quantum kinetic equations for the ultrafast spin dynamics of excitons in diluted magnetic semiconductor quantum wells after optical excitation

F. Ungar, M. Cygorek, and V. M. Axt
Physical Review B **96**, 239904 (2017)

Quantum kinetic equations for the ultrafast spin dynamics of excitons in diluted magnetic semiconductor quantum wells after optical excitation

F. Ungar, M. Cygorek, and V. M. Axt

Theoretische Physik III, Universität Bayreuth, 95440 Bayreuth, Germany

(Received 14 March 2017; published 8 June 2017)

Quantum kinetic equations of motion for the description of the exciton spin dynamics in II-VI diluted magnetic semiconductor quantum wells with laser driving are derived. The model includes the magnetic as well as the nonmagnetic carrier-impurity interaction, the Coulomb interaction, Zeeman terms, and the light-matter coupling, allowing for an explicit treatment of arbitrary excitation pulses. Based on a dynamics-controlled truncation scheme, contributions to the equations of motion up to second order in the generating laser field are taken into account. The correlations between the carrier and the impurity subsystems are treated within the framework of a correlation expansion. For vanishing magnetic field, the Markov limit of the quantum kinetic equations formulated in the exciton basis agrees with existing theories based on Fermi's golden rule. For narrow quantum wells excited at the 1s exciton resonance, numerical quantum kinetic simulations reveal pronounced deviations from the Markovian behavior. In particular, the spin decays initially with approximately half the Markovian rate and a nonmonotonic decay in the form of an overshoot of up to 10% of the initial spin polarization is predicted.

I. INTRODUCTION

The idea behind the spintronics paradigm [1–4] is to combine state-of-the-art electronics based on carrier charge with the manipulation and control of the spin degree of freedom [5–7]. Diluted magnetic semiconductors (DMS) [8–10] present an interesting subclass of semiconductors in this context because they can be easily combined with current semiconductor technology while at the same time providing a wide range of spin and magnetization-related effects and applications [11–22]. In DMS, a small fraction of magnetic ions, usually manganese [23], is introduced into a semiconductor. While III-V compounds such as $Ga_{1-x}Mn_xAs$ are typically p-doped [8] and can thus exhibit carrier-mediated ferromagnetism [24], II-VI materials such as $Cd_{1-x}Mn_xTe$ are found to be intrinsic and paramagnetic due to the isoelectrical incorporation of the Mn impurities.

A lot of theoretical works on DMS has been devoted to the understanding of structural properties [25–30]. But in many experiments, also the spin dynamics studied via optical pump-probe experiments is of interest [17,18,31]. Theoretical descriptions of such experiments are less developed in the literature and are typically based on rate-equation models [12–14,17,31–35], coinciding with Fermi's golden rule for vanishing magnetic field. However, a number of experiments have provided strong evidence that these models fail to reproduce some of the pertinent characteristics of the spin dynamics in DMS. Most notably, experimentally observed spin-decay rates are found to be a factor of 5 larger than the Fermi's golden rule result for spin-flip scattering of conduction band electrons at magnetic impurities [31]. Camilleri *et al.* [17] have argued that their optical experiments probe excitons rather than separate electrons and holes. In this case, the effective mass entering the spin-flip rate has to be replaced by the exciton mass [12], offering a potential explanation for the discrepancy noted in Ref. [31].

On the rate-equation level, some groups have already investigated the exciton spin dynamics in DMS theoretically [36–41]. However, recent studies using a quantum kinetic theory for the spin relaxation of conduction band electrons

in DMS revealed that correlations between the carrier and impurity subsystems can induce a finite memory [42–45], which is not captured by rate equations. The resulting non-Markovian effects were found to be particularly pronounced for excitations close to the band edge ($\mathbf{k} \approx \mathbf{0}$) [46] and become more significant with increasing effective mass [47]. These tendencies suggest that non-Markovian features are particularly relevant for excitons since, first of all, the conservation of momentum implies a vanishing center of mass momentum ($\mathbf{K} \approx \mathbf{0}$) of optically generated excitons, and second, the exciton mass is much larger than the effective mass of conduction band electrons.

In this paper, we develop a microscopic quantum kinetic theory for the exciton spin dynamics in DMS that is also capable of describing non-Markovian effects by explicitly accounting for carrier-impurity correlations. In contrast to previous works [42] where independent electrons and holes were considered and where higher-order correlations were treated within a variant of Kubo's cumulant expansion [48], here a dynamics-controlled truncation (DCT) [49,50] is employed for the treatment of Coulomb correlations. This approach is especially advantageous for the description of optically driven systems since it ensures a correct description of the dynamics up to a given order in the generating field. The theory derived in this paper is applicable in a wide range of different scenarios as a number of interactions are accounted for, such as the magnetic and nonmagnetic interactions between impurities and electrons as well as holes, the Coulomb interaction responsible for the formation of excitons, Zeeman terms for electrons, holes, and impurities, as well as the light-matter coupling.

Moreover, we show that, in the Markov limit and for vanishing magnetic field, the quantum kinetic description coincides with the Fermi's golden rule result of Ref. [12]. Comparing numerical simulations using the quantum kinetic theory and Markovian rate equations reveals strong non-Markovian effects in the exciton spin dynamics. In particular, the quantum kinetic calculations predict that the exciton spin initially decays with approximately half the rate obtained from

Fermi's golden rule and exhibits a nonmonotonic behavior with an overshoot of up to 10% of the initial spin polarization. In contrast to the situation for conduction band electrons, where nonmagnetic impurity scattering typically strongly suppresses non-Markovian features [44], here we find that, for excitons, the presence of nonmagnetic impurity scattering enhances the characteristics of non-Markovian behavior.

The paper is structured as follows. First, we discuss the individual contributions to the Hamiltonian that determines the spin dynamics of optically generated excitons in DMS quantum wells. Next, quantum kinetic equations based on a DCT scheme are derived for reduced exciton and impurity density matrices as well as carrier-impurity correlations. We then derive the Markov limit of the quantum kinetic equations of motion. Finally, we present numerical calculations and discuss the results.

II. THEORY

In this section, we present the Hamiltonian that models the optical excitation and the subsequent spin evolution of excitons in II-VI DMS. We explain the derivation of the quantum kinetic equations and, for comparison, also give the Markov limit of the equations.

A. Hamiltonian

We consider an intrinsic II-VI DMS quantum well where initially no electrons are in the conduction band. The time evolution of the system can then be described by the Hamiltonian

$$H = H_0^e + H_0^h + H_{\text{conf}} + H_C + H_Z^e + H_Z^h + H_Z^{\text{Mn}} + H_{\text{lm}}$$
$$+ H_{sd} + H_{pd} + H_{\text{nm}}^e + H_{\text{nm}}^h, \tag{1}$$

where

$$H_0^e + H_0^h = \sum_{l\mathbf{k}} E_\mathbf{k}^l c_{l\mathbf{k}}^\dagger c_{l\mathbf{k}} + \sum_{v\mathbf{k}} E_\mathbf{k}^v d_{v\mathbf{k}}^\dagger d_{v\mathbf{k}} \tag{2}$$

is the crystal Hamiltonian for electrons and holes, respectively. Here, $c_{l\mathbf{k}}^\dagger$ ($c_{l\mathbf{k}}$) denotes the creation (annihilation) operator of an electron in the conduction band l with wave vector $\mathbf{k}$. Similarly, $d_{v\mathbf{k}}^\dagger$ ($d_{v\mathbf{k}}$) creates (annihilates) a hole in the valence band v. The confinement potentials for electrons and holes responsible for the formation of a quantum well is denoted by H_{conf}.

As usual for the description of near band-edge excitations of semiconductors, we consider the part of the Coulomb interaction conserving the number of electrons and holes, which corresponds to the typically dominant monopole-monopole part in a multipolar expansion [50–53]. The Coulomb interaction then reads

$$H_C = \frac{1}{2} \sum_{\mathbf{k}\mathbf{k}'\mathbf{q}} \left(V_\mathbf{q} \sum_{ll'} c_{l'\mathbf{k}'+\mathbf{q}}^\dagger c_{l\mathbf{k}-\mathbf{q}}^\dagger c_{l\mathbf{k}} c_{l'\mathbf{k}'} \right.$$
$$+ V_\mathbf{q} \sum_{vv'} d_{v'\mathbf{k}'+\mathbf{q}}^\dagger d_{v\mathbf{k}-\mathbf{q}}^\dagger d_{v\mathbf{k}} d_{v'\mathbf{k}'}$$
$$\left. - 2V_\mathbf{q} \sum_{lv} c_{l\mathbf{k}'+\mathbf{q}}^\dagger d_{v\mathbf{k}-\mathbf{q}}^\dagger d_{v\mathbf{k}} c_{l\mathbf{k}'} \right) \tag{3}$$

with the Fourier transform of the Coulomb potential given by $V_\mathbf{q} = \frac{e^2}{\epsilon\epsilon_0} \frac{1}{q^2}$, where e is the elementary charge and ϵ_0 is the vacuum permittivity. The dielectric constant $\epsilon \approx 10$ includes the contribution of the crystal lattice [54,55]. Thus H_C comprises all direct electron-electron, hole-hole, and electron-hole Coulomb interactions.

We account for the effects of a homogeneous external magnetic field $\mathbf{B}$ on the electrons, holes, and magnetic impurity atoms, respectively, via the Zeeman terms

$$H_Z^e = g_e \mu_B \sum_{ll'\mathbf{k}} \mathbf{B} \cdot \mathbf{s}_{ll'}^e c_{l\mathbf{k}}^\dagger c_{l'\mathbf{k}}, \tag{4a}$$

$$H_Z^h = -2\kappa \mu_B \sum_{vv'\mathbf{k}} \mathbf{B} \cdot \mathbf{J}_{vv'} d_{v\mathbf{k}}^\dagger d_{v'\mathbf{k}}, \tag{4b}$$

$$H_Z^{\text{Mn}} = g_{\text{Mn}} \mu_B \sum_{Inn'} \mathbf{B} \cdot \mathbf{S}_{nn'} \hat{P}_{nn'}^I. \tag{4c}$$

In the above formulas, g_e is the g factor of the electrons, κ is the isotropic valence-band g factor [56], g_{Mn} denotes the impurity g factor, and μ_B is the Bohr magneton. The vector of electron-spin matrices is given by $\mathbf{s}_{ll'}^e$, $\mathbf{J}_{vv'}$ is the vector of 4×4 angular momentum matrices when accounting for heavy hole (hh) and light hole (lh) bands with angular momentum $v,v' \in \{-\frac{3}{2}, -\frac{1}{2}, \frac{1}{2}, \frac{3}{2}\}$ and $\mathbf{S}_{nn'}$ denotes the vector of impurity spin matrices. In the case of manganese considered here, we have $n,n' \in \{-\frac{5}{2}, -\frac{3}{2}, \dots, \frac{5}{2}\}$. The impurity spin itself is described by the operator $\hat{P}_{nn'}^I = |I,n\rangle\langle I,n'|$ where the ket $|I,n\rangle$ denotes the spin state n of an impurity atom I.

Rather than assuming some initial carrier distribution, we explicitly account for the optical excitation and thus the light-matter coupling via the Hamiltonian

$$H_{\text{lm}} = -\sum_{lv\mathbf{k}} (\mathbf{E} \cdot \mathbf{M}_{lv} c_{l\mathbf{k}}^\dagger d_{v-\mathbf{k}}^\dagger + \mathbf{E} \cdot \mathbf{M}_{vl} d_{v-\mathbf{k}} c_{l\mathbf{k}}) \tag{5}$$

with an electric field $\mathbf{E}$ and the dipole moment $\mathbf{M}_{lv}$ for a transition from a state in the valence subband v to the conduction subband l. Here, the well-known dipole approximation [57] is used to consider only interband transitions with vanishing center of mass momentum.

The dominant spin depolarization mechanism in DMS is given by the sp-d exchange interaction which models the scattering of s-like conduction-band electrons and p-like valence-band holes, respectively, at the localized d-shell electrons of the Mn impurities. These interactions can be written as [8,9,43]

$$H_{sd} = \frac{J_{sd}}{V} \sum_{\substack{Inn' \\ ll'\mathbf{k}\mathbf{k}'}} \mathbf{S}_{nn'} \cdot \mathbf{s}_{ll'}^e c_{l\mathbf{k}}^\dagger c_{l'\mathbf{k}'} e^{i(\mathbf{k}'-\mathbf{k})\cdot\mathbf{R}_I} \hat{P}_{nn'}^I, \tag{6a}$$

$$H_{pd} = \frac{J_{pd}}{V} \sum_{\substack{Inn' \\ vv'\mathbf{k}\mathbf{k}'}} \mathbf{S}_{nn'} \cdot \mathbf{s}_{vv'}^h d_{v\mathbf{k}}^\dagger d_{v'\mathbf{k}'} e^{i(\mathbf{k}'-\mathbf{k})\cdot\mathbf{R}_I} \hat{P}_{nn'}^I \tag{6b}$$

with the hole spin matrices given by $\mathbf{s}_{vv'}^h = \frac{1}{3}\mathbf{J}_{vv'}$. Note that we employ the convention that the factor $\hbar$ which typically enters in the definition of the spin matrices is instead absorbed in the coupling constants J_{sd} and J_{pd} as well as μ_B in case of the Zeeman terms.

In a recently published paper, it was shown that the combined action of nonmagnetic impurity scattering and magnetic exchange interaction may have a significant impact on the spin dynamics of conduction band electrons [44]. Therefore we also include the nonmagnetic impurity scattering in the form

$$H_{\mathrm{nm}}^{\mathrm{e}} = \frac{J_0^{\mathrm{e}}}{V} \sum_{\substack{Il \\ \mathbf{k}\mathbf{k}'}} c_{l\mathbf{k}}^{\dagger} c_{l\mathbf{k}'} e^{i(\mathbf{k}'-\mathbf{k})\cdot\mathbf{R}_I}, \tag{7a}$$

$$H_{\mathrm{nm}}^{\mathrm{h}} = \frac{J_0^{\mathrm{h}}}{V} \sum_{\substack{Iv \\ \mathbf{k}\mathbf{k}'}} d_{v\mathbf{k}}^{\dagger} d_{v\mathbf{k}'} e^{i(\mathbf{k}'-\mathbf{k})\cdot\mathbf{R}_I} \tag{7b}$$

with scattering constants J_0^{e} and J_0^{h} for electrons and holes, respectively. Considering a DMS of the general form $\mathrm{A}_{1-x}\mathrm{Mn}_x\mathrm{B}$, these can be determined under the assumption that unit cells containing doping ions experience an energetic penalty due to being forced into the same structure as the surrounding semiconductor lattice AB. This allows for an estimation of the nonmagnetic coupling strength based on the change of the band gap of the pure AB material compared to the pure MnB material. Note that we only take into account the short-range part of the carrier-impurity interaction even though it stems largely from the Coulomb interaction between the impurity atoms and the quasifree carriers [44].

We do not include the influence of phonons on the carrier spin dynamics in our model since typical experiments [17,31,35] are performed at low temperatures of about 2 K where only phonon emission is relevant because there are no phonons available for absorption. But since we consider only direct laser-driven excitation of excitons with vanishing center of mass momenta, phonon emission processes are also strongly suppressed as there are no final exciton states lower in energy to scatter to. Additionally, phonons do not couple directly to the spin and thus represent a secondary relaxation process, which only becomes relevant in combination with other effects, such as spin-orbit coupling. Theoretical rate-equation models that include the scattering due to phonons also support that the *s*-*d* exchange interaction is the most important scattering mechanism at low temperatures [34]. Given that the recently reported [19] spin-lattice relaxation time of Mn^{2+} ions in typical DMS quantum wells is on the order of μs, the coupling of phonons to the Mn system can also be disregarded on the typical ps time scale of the carrier spin relaxation [31,44,58]. Furthermore, spin-orbit effects [58] as well as the hyperfine interaction [59] due to nuclear spins typically also only become relevant at much longer time scales.

In a quantum well, it is convenient to switch from a three-dimensional basis set to a description where only the in-plane part consists of plane waves and the z dependence is treated separately. One can then expand the single-particle basis functions Ξ in terms of a complete set of envelope functions, which yields

$$\Xi(\mathbf{r},z) = \frac{1}{\sqrt{A}} \sum_{n\mathbf{k}} a_{n\mathbf{k}} e^{i\mathbf{k}\cdot\mathbf{r}} u_n^{\mathrm{e/h}}(z) \tag{8}$$

with envelope functions $u_n^{\mathrm{e/h}}(z)$ of electrons and holes, respectively, and expansion coefficients $a_{n\mathbf{k}}$. Here and throughout the remainder of this paper, the appearing wave vectors $\mathbf{k}$ as well as the in-plane position $\mathbf{r}$ are two-dimensional quantities.

For narrow quantum wells, where the energetic separation between the individual confinement states is large, it is a good approximation to only consider the lowest confinement state [60] $u_0^{\mathrm{e/h}}(z)$, which corresponds to setting $a_{n\mathbf{k}} = 0$ for all $n \neq 0$. Thus we project the Hamiltonian given by Eq. (1) onto the corresponding subspace. For the carrier-impurity interactions in Eqs. (6) and (7), this amounts to substituting $\sum_{k_z k_z'} \to d|u_0^{\mathrm{e/h}}(Z_I)|^2$. In numerical calculations, we assume infinitely high potential barriers at $z = \pm\frac{d}{2}$, so that the envelope functions for electrons and holes become

$$u_0^{\mathrm{e/h}}(z) = \sqrt{\frac{2}{d}} \cos\left(\frac{\pi}{d}z\right). \tag{9}$$

B. Dynamical variables and truncation scheme

Our main target is the modeling of the electron or hole spin dynamics in a system where all particles are excited optically as electron-hole pairs. Within the DCT scheme this is most conveniently achieved by deriving quantum kinetic equations of motion for the four-point density matrices $\langle c_{l_1\mathbf{k}_1}^{\dagger} d_{v_1\mathbf{k}_2}^{\dagger} d_{v_2\mathbf{k}_3} c_{l_2\mathbf{k}_4}\rangle$ from which all relevant information can be deduced [50]. To provide an example, the electron density matrix is given by

$$\langle c_{l_1\mathbf{k}_1}^{\dagger} c_{l_2\mathbf{k}_2}\rangle = \sum_{v\mathbf{k}} \langle c_{l_1\mathbf{k}_1}^{\dagger} d_{v\mathbf{k}}^{\dagger} d_{v\mathbf{k}} c_{l_2\mathbf{k}_2}\rangle + \mathcal{O}(\mathbf{E}^4). \tag{10}$$

Starting from the Hamiltonian given by Eq. (1) and using the Heisenberg equation of motion, one ends up with an infinite hierarchy of equations that needs to be truncated in order to be solvable. In this paper, we employ a dynamics-controlled truncation [49] which classifies all appearing expectation values in terms of their order in the generating optical field. Using this procedure, we keep all contributions up to the order $\mathcal{O}(\mathbf{E}^2)$, which is sufficient in the low-density regime [61].

However, since we are dealing with a DMS, we also have to treat correlations between carriers and Mn atoms. This is done using a correlation expansion similarly to Ref. [42] where, due to the Mn atoms being far apart in a DMS, correlations that involve magnetic dopants at different sites are disregarded. Applications of correlation expansions in condensed matter physics are manifold and can be found explained numerous times in the literature [42,57,62–65].

Setting up the equations of motion for an on-average spatially homogeneous system, a closed set of equations of motion can be formulated for the following dynamical variables:

$$M_{n_1}^{n_2}(z) = \frac{d}{N_{\mathrm{Mn}}} \sum_I \delta(z - Z_I)\langle \hat{P}_{n_1 n_2}^I \rangle, \tag{11a}$$

$$Y_{\mathbf{k}_1}^{v_1 l_1} = \langle d_{v_1 - \mathbf{k}_1} c_{l_1 \mathbf{k}_1} \rangle, \tag{11b}$$

$$N_{\mathbf{k}_1 \mathbf{k}_2 \mathbf{k}_3 \mathbf{k}_4}^{l_1 v_1 v_2 l_2} = \langle c_{l_1 \mathbf{k}_1}^\dagger d_{v_1 - \mathbf{k}_2}^\dagger d_{v_2 - \mathbf{k}_3} c_{l_2 \mathbf{k}_4} \rangle \delta_{\mathbf{k}_1 - \mathbf{k}_2, \mathbf{k}_4 - \mathbf{k}_3}, \tag{11c}$$

$$Q_Y{}_{n_1 \mathbf{k}_1 \mathbf{k}_2}^{n_2 v_1 l_1}(z) = V \frac{d}{N_{\mathrm{Mn}}} \sum_I \delta(z - Z_I) \langle d_{v_1 - \mathbf{k}_1} c_{l_1 \mathbf{k}_2} e^{i(\mathbf{k}_2 - \mathbf{k}_1) \cdot \mathbf{R}_I} \hat{P}_{n_1 n_2}^I \rangle, \quad \text{for } \mathbf{k}_1 \neq \mathbf{k}_2, \tag{11d}$$

$$\bar{Y}_{\mathbf{k}_1 \mathbf{k}_2}^{v_1 l_1}(z) = V \frac{d}{N_{\mathrm{Mn}}} \sum_I \delta(z - Z_I) \langle d_{v_1 - \mathbf{k}_1} c_{l_1 \mathbf{k}_2} e^{i(\mathbf{k}_2 - \mathbf{k}_1) \cdot \mathbf{R}_I} \rangle, \quad \text{for } \mathbf{k}_1 \neq \mathbf{k}_2, \tag{11e}$$

$$Q_N{}_{n_1 \mathbf{k}_1 \mathbf{k}_2 \mathbf{k}_3 \mathbf{k}_4}^{n_2 l_1 v_1 v_2 l_2}(z) = V \frac{d}{N_{\mathrm{Mn}}} \sum_I \delta(z - Z_I) \langle c_{l_1 \mathbf{k}_1}^\dagger d_{v_1 - \mathbf{k}_2}^\dagger d_{v_2 - \mathbf{k}_3} c_{l_2 \mathbf{k}_4} e^{i(\mathbf{k}_2 - \mathbf{k}_1 + \mathbf{k}_4 - \mathbf{k}_3) \cdot \mathbf{R}_I} \hat{P}_{n_1 n_2}^I \rangle, \quad \text{for } \mathbf{k}_1 - \mathbf{k}_2 \neq \mathbf{k}_4 - \mathbf{k}_3, \tag{11f}$$

$$\bar{N}_{\mathbf{k}_1 \mathbf{k}_2 \mathbf{k}_3 \mathbf{k}_4}^{l_1 v_1 v_2 l_2} = V \frac{d}{N_{\mathrm{Mn}}} \sum_I \delta(z - Z_I) \langle c_{l_1 \mathbf{k}_1}^\dagger d_{v_1 - \mathbf{k}_2}^\dagger d_{v_2 - \mathbf{k}_3} c_{l_2 \mathbf{k}_4} e^{i(\mathbf{k}_2 - \mathbf{k}_1 + \mathbf{k}_4 - \mathbf{k}_3) \cdot \mathbf{R}_I} \rangle, \quad \text{for } \mathbf{k}_1 - \mathbf{k}_2 \neq \mathbf{k}_4 - \mathbf{k}_3. \tag{11g}$$

In the above equations, $M_{n_1}^{n_2}(z)$, $Y_{\mathbf{k}_1}^{v_1 l_1}$, and $N_{\mathbf{k}_1 \mathbf{k}_2 \mathbf{k}_3 \mathbf{k}_4}^{l_1 v_1 v_2 l_2}$ represent the Mn density matrices, the electron-hole coherences, and the exciton density matrices, respectively. The magnetic and nonmagnetic correlations between coherences and impurity atoms are given by $Q_Y{}_{n_1 \mathbf{k}_1 \mathbf{k}_2}^{n_2 v_1 l_1}(z)$ and $\bar{Y}_{\mathbf{k}_1 \mathbf{k}_2}^{v_1 l_1}(z)$, respectively, and in turn by $Q_N{}_{n_1 \mathbf{k}_1 \mathbf{k}_2 \mathbf{k}_3 \mathbf{k}_4}^{n_2 l_1 v_1 v_2 l_2}(z)$ and $\bar{N}_{\mathbf{k}_1 \mathbf{k}_2 \mathbf{k}_3 \mathbf{k}_4}^{l_1 v_1 v_2 l_2}$ between excitons and impurities. In addition to the usual quantum mechanical average of the operators, the brackets $\langle . \rangle$ in Eqs. (11) as well as throughout the rest of this paper also contain an average over the distribution of Mn positions in the sample. This distribution is assumed to be random but homogeneous on average, so that $\langle e^{i(\mathbf{k}_2 - \mathbf{k}_1) \cdot \mathbf{R}_I} \rangle = \delta_{\mathbf{k}_1, \mathbf{k}_2}$. The delta distribution in Eq. (11c) is a consequence of the spatial homogeneity of the system.

Using these variables, it is straightforward but lengthy to set up a hierarchy of equations of motion whilst retaining only terms up to $\mathcal{O}(\mathbf{E}^2)$ according to the DCT scheme. However, it turns out that the magnetic interactions H_{sd} and H_{pd} introduce additional source terms in the equations for the correlations that are not expressible using the variables from Eqs. (11) because they contain products of Mn operators as well as exponential functions containing the randomly distributed Mn positions $\mathbf{R}_I$ in the exponent. Following along the lines of Ref. [42], where a correlation expansion has been successfully employed to treat these terms, we sketch the general method of such an expansion when applied to the expressions derived in this paper. Our approach for dealing with random impurity positions can also be related to the treatment of interface roughness via random potentials as well as the influence of disorder in semiconductors [66–68].

Consider a general expectation value of the form

$$S_Q = \langle X e^{i \Delta \mathbf{k} \cdot \mathbf{R}_I} e^{i \Delta \mathbf{k}' \cdot \mathbf{R}_{I'}} \hat{P}_{n_1 n_2}^I \hat{P}_{n_1' n_2'}^{I'} \rangle, \tag{12}$$

where X contains up to four Fermi operators so that $\langle X \rangle$ is up to $\mathcal{O}(E^2)$ and $\Delta \mathbf{k} \neq \mathbf{0}$. Using the DCT scheme, it can be easily shown that assisted expectation values such as the quantity in Eq. (12) are of the same order in the generating electric field as the corresponding bare expectation values of the Fermi operators. We then treat the expression in Eq. (12) as follows.

(i) The situation $I = I'$ has to be considered separately since in this case we are dealing with Mn operators on the

same site, so that Eq. (12) reduces to

$$S_Q \overset{I = I'}{=} \langle X e^{i(\Delta \mathbf{k} + \Delta \mathbf{k}') \cdot \mathbf{R}_I} \hat{P}_{n_1 n_2'}^I \rangle \delta_{n_2, n_1'} \tag{13}$$

in accordance with the definition of the Mn operators $\hat{P}_{nn'}^I$. The remaining quantity can then be expressed in terms of the variables introduced in Eq. (11).

(ii) If $\Delta \mathbf{k}' = \mathbf{0}$, we get

$$S_Q \overset{\Delta \mathbf{k}' = \mathbf{0}}{=} \langle X e^{i \Delta \mathbf{k} \cdot \mathbf{R}_I} \hat{P}_{n_1 n_2}^I \hat{P}_{n_1' n_2'}^{I'} \rangle, \tag{14}$$

so that the number of operators effectively is reduced by one.

(iii) In the most general case, i.e., $I \neq I'$ and $\Delta \mathbf{k}' \neq 0$, we decompose Eq. (12) using a correlation expansion. This yields

$$S_Q = \delta \langle X e^{i \Delta \mathbf{k} \cdot \mathbf{R}_I} \hat{P}_{n_1 n_2}^I \rangle \langle e^{i \Delta \mathbf{k}' \cdot \mathbf{R}_{I'}} \rangle \langle \hat{P}_{n_1' n_2'}^{I'} \rangle$$
$$+ \delta \langle X e^{i \Delta \mathbf{k} \cdot \mathbf{R}_I} \rangle \langle \hat{P}_{n_1 n_2}^I \rangle \langle e^{i \Delta \mathbf{k}' \cdot \mathbf{R}_{I'}} \rangle \langle \hat{P}_{n_1' n_2'}^{I'} \rangle \tag{15}$$

with true correlations denoted by $\delta \langle \dots \rangle$. In the above equation, we have only written down the nonvanishing terms of the expansion by neglecting correlations evaluated either at different Mn sites or involving two or more impurity operators. Furthermore, it can be shown that correlations of the form $\delta \langle e^{i \Delta \mathbf{k} \cdot \mathbf{R}_I} \hat{P}_{n_1 n_2}^I \rangle$, which could be used to model impurity spin waves, are not driven during the dynamics if they are zero initially and thus need not be explicitly accounted for.

This approach enables the formulation of a closed set of equations of motion containing only reduced density matrices and the true correlations. However, instead of using the true correlations as dynamical variables, we switch back to the nonfactorized correlations [c.f. Eqs. (11)] because this allows for a much more condensed and convenient notation of the equations of motion.

C. Transformation to the exciton basis

Since the highest-order density matrices depend on four wave vectors, the resulting equations are numerically very demanding. Instead, when essentially only bound excitons are excited, it is much more convenient and efficient to use a two-particle basis [50,61,69–71], which in this case allows for a significant reduction of relevant basis states. We note in passing that one could also change to the exciton basis before deriving equations of motion. However, this way a classification of

contributions to the equations of motion in terms of powers of the electric field is not straightforward. Therefore we first derive the equations of motion in the single-particle basis and transform to the two-particle basis afterwards.

We consider the excitonic eigenvalue problem in the quantum well plane given by

$$\left(H_0^{\mathrm{e}} + H_0^{\mathrm{h}} + H_{\mathrm{C}}\right)\psi_{x\mathbf{K}}(\mathbf{r}^{\mathrm{e}},\mathbf{r}^{\mathrm{h}}) = E_{x\mathbf{K}}\,\psi_{x\mathbf{K}}(\mathbf{r}^{\mathrm{e}},\mathbf{r}^{\mathrm{h}}) \qquad (16)$$

with the exciton energy $E_{x\mathbf{K}}$ and the two-dimensional position vectors of the electron and the hole $\mathbf{r}^{\mathrm{e}}$ and $\mathbf{r}^{\mathrm{h}}$, respectively. Using the effective mass approximation as well as the strong confinement limit of the Coulomb interaction, the Hamiltonians read

$$H_0^{\mathrm{e}} = -\frac{\hbar^2}{2m_{\mathrm{e}}}\left(\partial_{x^{\mathrm{e}}}^2 + \partial_{y^{\mathrm{e}}}^2\right) + E_{\mathrm{g}}, \qquad (17a)$$

$$H_0^{\mathrm{h}} = -\frac{\hbar^2}{2m_{\mathrm{h}}}\left(\partial_{x^{\mathrm{h}}}^2 + \partial_{y^{\mathrm{h}}}^2\right), \qquad (17b)$$

$$H_{\mathrm{C}} = -\int dz \int dz' \frac{e^2\left|u_0^{\mathrm{e}}(z)\right|^2\left|u_0^{\mathrm{h}}(z')\right|^2}{4\pi\epsilon\epsilon_0\sqrt{(\mathbf{r}^{\mathrm{e}} - \mathbf{r}^{\mathrm{h}})^2 + (z - z')^2}} \qquad (17c)$$

with in-plane electron and heavy-hole effective masses m_{e} and m_{h}, respectively, as well as the band gap E_{g}. The exciton wave function can be decomposed into a center of mass and a relative part according to

$$\psi_{x\mathbf{K}}(\mathbf{r}^{\mathrm{e}},\mathbf{r}^{\mathrm{h}}) = \frac{1}{\sqrt{A}}e^{i\mathbf{K}\cdot\mathbf{R}}\phi_x(\mathbf{r}) \qquad (18)$$

with the exciton center of mass momentum $\mathbf{K}$ and the exciton quantum number x. The relative coordinate is given by $\mathbf{r} = \mathbf{r}^{\mathrm{e}} - \mathbf{r}^{\mathrm{h}}$ and $\mathbf{R} = \eta_{\mathrm{e}}\mathbf{r}^{\mathrm{e}} + \eta_{\mathrm{h}}\mathbf{r}^{\mathrm{h}}$ denotes the center of mass coordinate of the exciton with the mass ratios $\eta_{\mathrm{e}} := \frac{m_{\mathrm{e}}}{M}$ and $\eta_{\mathrm{h}} := \frac{m_{\mathrm{h}}}{M}$, where $M = m_{\mathrm{e}} + m_{\mathrm{h}}$ is the exciton mass.

Using polar coordinates, the relative part of the exciton wave function in two dimensions can be further decomposed into a radial part $R_n(r)$ with a principal quantum number $n \in \mathbb{N}$ and an angular part $e^{il\varphi}$ with angular momentum quantum number $|l| = 0, 1, \ldots, n - 1$ according to [72,73]

$$\phi_x(\mathbf{r}) = R_n(r)e^{il\varphi}, \qquad (19)$$

where the quantum numbers n and l are condensed into a single index x.

The creation operator of an exciton with an electron in the conduction band l and a hole in the valence band v can be written as

$$\hat{Y}_{lvx\mathbf{K}}^{\dagger} = \int d^2r^{\mathrm{e}} \int d^2r^{\mathrm{h}}\,\psi_{x\mathbf{K}}(\mathbf{r}^{\mathrm{e}},\mathbf{r}^{\mathrm{h}})\,\hat{\chi}_{l\mathbf{r}^{\mathrm{e}}}^{\dagger}\,\hat{\chi}_{v\mathbf{r}^{\mathrm{h}}} \qquad (20)$$

using the Wannier operators

$$\hat{\chi}_{l\mathbf{r}^{\mathrm{e}}}^{\dagger} = \frac{1}{\sqrt{A}}\sum_{\mathbf{k}^{\mathrm{e}}} e^{-i\mathbf{k}^{\mathrm{e}}\cdot\mathbf{r}^{\mathrm{e}}}c_{l\mathbf{k}^{\mathrm{e}}}^{\dagger}, \qquad (21a)$$

$$\hat{\chi}_{v\mathbf{r}^{\mathrm{h}}}^{\dagger} = \frac{1}{\sqrt{A}}\sum_{\mathbf{k}^{\mathrm{h}}} e^{-i\mathbf{k}^{\mathrm{h}}\cdot\mathbf{r}^{\mathrm{h}}}d_{v\mathbf{k}^{\mathrm{h}}}^{\dagger}. \qquad (21b)$$

Then, the relation between the exciton creation operator and the Fermi operators reads

$$\hat{Y}_{lvx\mathbf{K}}^{\dagger} = \sum_{\mathbf{k}^{\mathrm{e}}\mathbf{k}^{\mathrm{h}}} \psi_{x\mathbf{K}}^{\mathbf{k}^{\mathrm{e}},-\mathbf{k}^{\mathrm{h}}} c_{l\mathbf{k}^{\mathrm{e}}}^{\dagger}d_{v-\mathbf{k}^{\mathrm{h}}}^{\dagger}, \qquad (22a)$$

$$c_{l\mathbf{k}^{\mathrm{e}}}^{\dagger}d_{v-\mathbf{k}^{\mathrm{h}}}^{\dagger} = \sum_{x\mathbf{K}} \left(\psi_{x\mathbf{K}}^{\mathbf{k}^{\mathrm{e}},-\mathbf{k}^{\mathrm{h}}}\right)^{*}\hat{Y}_{lvx\mathbf{K}}^{\dagger} \qquad (22b)$$

with the matrix element

$$\psi_{x\mathbf{K}}^{\mathbf{k}^{\mathrm{e}}\mathbf{k}^{\mathrm{h}}} := \frac{1}{\sqrt{A}}\delta_{\mathbf{K},\mathbf{k}^{\mathrm{e}}+\mathbf{k}^{\mathrm{h}}}\int d^2r\,e^{-i\mathbf{r}\cdot(\eta_{\mathrm{h}}\mathbf{k}^{\mathrm{e}}-\eta_{\mathrm{e}}\mathbf{k}^{\mathrm{h}})}\phi_x(\mathbf{r}). \qquad (23)$$

Using the transformation in Eq. (22a), we switch from the quantities defined in Eqs. (11) to the new dynamical variables in the exciton basis:

$$Y_{x_1\mathbf{0}}^{v_1l_1} = \sum_{\mathbf{k}_1}\left(\psi_{x_1\mathbf{0}}^{\mathbf{k}_1,-\mathbf{k}_1}\right)^{*}Y_{\mathbf{k}_1}^{v_1l_1}, \qquad (24a)$$

$$N_{x_1\mathbf{K}_1}^{l_1v_1v_2l_2} = \sum_{\substack{\mathbf{k}_1\mathbf{k}_2 \\ \mathbf{k}_3\mathbf{k}_4}}\psi_{x_1\mathbf{K}_1}^{\mathbf{k}_1,-\mathbf{k}_2}\left(\psi_{x_1\mathbf{K}_1}^{\mathbf{k}_4,-\mathbf{k}_3}\right)^{*}N_{\mathbf{k}_1\mathbf{k}_2\mathbf{k}_3\mathbf{k}_4}^{l_1v_1v_2l_2}, \qquad (24b)$$

$$Q_{Y\,n_1x_1\mathbf{K}_1}^{n_2v_1l_1}(z) = \sum_{\mathbf{k}_1\mathbf{k}_2}\left(\psi_{x_1\mathbf{K}_1}^{\mathbf{k}_2,-\mathbf{k}_1}\right)^{*}Q_{Y\,n_1\mathbf{k}_1\mathbf{k}_2}^{n_2v_1l_1}(z), \qquad (24c)$$

$$\bar{Y}_{x_1\mathbf{K}_1}^{v_1l_1}(z) = \sum_{\mathbf{k}_1\mathbf{k}_2}\left(\psi_{x_1\mathbf{K}_1}^{\mathbf{k}_2,-\mathbf{k}_1}\right)^{*}\bar{Y}_{\mathbf{k}_1\mathbf{k}_2}^{v_1l_1}(z), \qquad (24d)$$

$$Q_{N\,n_1x_1\mathbf{K}_1x_2\mathbf{K}_2}^{n_2l_1v_1v_2l_2}(z) = \sum_{\substack{\mathbf{k}_1\mathbf{k}_2 \\ \mathbf{k}_3\mathbf{k}_4}}\psi_{x_1\mathbf{K}_1}^{\mathbf{k}_1,-\mathbf{k}_2}\left(\psi_{x_2\mathbf{K}_2}^{\mathbf{k}_4,-\mathbf{k}_3}\right)^{*}$$
$$\times\,Q_{N\,n_1\mathbf{k}_1\mathbf{k}_2\mathbf{k}_3\mathbf{k}_4}^{n_2l_1v_1v_2l_2}(z), \qquad (24e)$$

$$\bar{N}_{x_1\mathbf{K}_1x_2\mathbf{K}_2}^{l_1v_1v_2l_2}(z) = \sum_{\substack{\mathbf{k}_1\mathbf{k}_2 \\ \mathbf{k}_3\mathbf{k}_4}}\psi_{x_1\mathbf{K}_1}^{\mathbf{k}_1,-\mathbf{k}_2}\left(\psi_{x_2\mathbf{K}_2}^{\mathbf{k}_4,-\mathbf{k}_3}\right)^{*}\bar{N}_{\mathbf{k}_1\mathbf{k}_2\mathbf{k}_3\mathbf{k}_4}^{l_1v_1v_2l_2}(z). \qquad (24f)$$

D. Equations of motion

Applying the DCT scheme and the correlation expansion in the equations of motion in the electron-hole representation and subsequently using the transformation to the exciton basis

according to Eqs. (24) leads to the following equations of motion:

$$i\hbar \frac{\partial}{\partial t} M_{n_1}^{n_2}(z) = \sum_n \left(\mathbf{S}_{n_2 n} M_{n_1}^n(z) - \mathbf{S}_{n n_1} M_n^{n_2}(z)\right) \cdot \left(\hbar\boldsymbol{\omega}_{\mathrm{Mn}} + \frac{J_{sd}}{V} d |u_0^{\mathrm{e}}(z)|^2 \sum_{\substack{ll'v \\ x\mathbf{K}}} \mathbf{s}_{ll'}^{\mathrm{e}} N_{x\mathbf{K}}^{lvvl'} + \frac{J_{pd}}{V} d |u_0^{\mathrm{h}}(z)|^2 \sum_{\substack{vv'l \\ x\mathbf{K}}} \mathbf{s}_{vv'}^{\mathrm{h}} N_{x\mathbf{K}}^{lvv'l}\right)$$

$$+ \frac{J_{sd}}{V^2} d |u_0^{\mathrm{e}}(z)|^2 \sum_{\substack{ll'vn \\ x\mathbf{K}x'\mathbf{K}'}} \mathbf{s}_{ll'}^{\mathrm{e}} \cdot f_{-\eta_{\mathrm{h}}xx'}^{\mathbf{K}\mathbf{K}'} \left(\mathbf{S}_{n_2 n} Q_{N_{n_1 x\mathbf{K}x'\mathbf{K}'}}^{nlvvl'}(z) - \mathbf{S}_{n n_1} Q_{N_{n x\mathbf{K}x'\mathbf{K}'}}^{n_2 lvvl'}(z)\right)$$

$$+ \frac{J_{pd}}{V^2} d |u_0^{\mathrm{h}}(z)|^2 \sum_{\substack{vv'ln \\ x\mathbf{K}x'\mathbf{K}'}} \mathbf{s}_{vv'}^{\mathrm{h}} \cdot f_{\eta_{\mathrm{e}}xx'}^{\mathbf{K}\mathbf{K}'} \left(\mathbf{S}_{n_2 n} Q_{N_{n_1 x\mathbf{K}x'\mathbf{K}'}}^{nlvv'l}(z) - \mathbf{S}_{n n_1} Q_{N_{n x\mathbf{K}x'\mathbf{K}'}}^{n_2 lvv'l}(z)\right), \tag{25a}$$

$$i\hbar \frac{\partial}{\partial t} Y_{x_1 \mathbf{0}}^{v_1 l_1} = -\mathbf{E} \cdot \mathbf{M}_{l_1 v_1}^{x_1} + \left(E_{x_1 \mathbf{0}}^{v_1 l_1} + \frac{(J_0^{\mathrm{e}} + J_0^{\mathrm{h}}) N_{\mathrm{Mn}}}{V}\right) Y_{x_1 \mathbf{0}}^{v_1 l_1} + \sum_l \hbar\boldsymbol{\omega}_{\mathrm{e}} \cdot \mathbf{s}_{l_1 l}^{\mathrm{e}} Y_{x_1 \mathbf{0}}^{v_1 l} + \sum_v \hbar\boldsymbol{\omega}_{\mathrm{h}} \cdot \mathbf{s}_{v_1 v}^{\mathrm{h}} Y_{x_1 \mathbf{0}}^{vl_1}$$

$$+ \frac{N_{\mathrm{Mn}}}{V^2} \sum_{\substack{nn' \\ x\mathbf{K}}} \mathbf{S}_{nn'} \cdot \int dz \left(J_{sd} |u_0^{\mathrm{e}}(z)|^2 \sum_l \mathbf{s}_{l_1 l}^{\mathrm{e}} f_{-\eta_{\mathrm{h}}x_1 x}^{\mathbf{0}\mathbf{K}} Q_{Y_{nx\mathbf{K}}}^{n'v_1 l}(z) + J_{pd} |u_0^{\mathrm{h}}(z)|^2 \sum_v \mathbf{s}_{v_1 v}^{\mathrm{h}} f_{\eta_{\mathrm{e}}x_1 x}^{\mathbf{0}\mathbf{K}} Q_{Y_{nx\mathbf{K}}}^{n'vl_1}(z)\right)$$

$$+ \frac{N_{\mathrm{Mn}}}{V^2} \sum_{x\mathbf{K}} \int dz \left(J_0^{\mathrm{e}} |u_0^{\mathrm{e}}(z)|^2 f_{-\eta_{\mathrm{h}}x_1 x}^{\mathbf{0}\mathbf{K}} \bar{Y}_{x\mathbf{K}}^{v_1 l_1}(z) + J_0^{\mathrm{h}} |u_0^{\mathrm{h}}(z)|^2 f_{\eta_{\mathrm{e}}x_1 x}^{\mathbf{0}\mathbf{K}} \bar{Y}_{x\mathbf{K}}^{v_1 l_1}(z)\right), \tag{25b}$$

$$i\hbar \frac{\partial}{\partial t} N_{x_1 \mathbf{K}_1}^{l_1 v_1 v_2 l_2} = \mathbf{E} \cdot \left(\mathbf{M}_{v_1 l_1}^{x_1} Y_{x_1 \mathbf{0}}^{v_2 l_2} - \mathbf{M}_{l_2 v_2}^{x_1} \left(Y_{x_1 \mathbf{0}}^{v_1 l_1}\right)^*\right) \delta_{\mathbf{K}_1, \mathbf{0}} + \left(E_{x_1 \mathbf{K}_1}^{v_2 l_2} - E_{x_1 \mathbf{K}_1}^{v_1 l_1}\right) N_{x_1 \mathbf{K}_1}^{l_1 v_1 v_2 l_2}$$

$$+ \sum_l \hbar\boldsymbol{\omega}_{\mathrm{e}} \cdot \left(\mathbf{s}_{l_2 l}^{\mathrm{e}} N_{x_1 \mathbf{K}_1}^{l_1 v_1 v_2 l} - \mathbf{s}_{ll_1}^{\mathrm{e}} N_{x_1 \mathbf{K}_1}^{lv_1 v_2 l_2}\right) + \sum_v \hbar\boldsymbol{\omega}_{\mathrm{h}} \cdot \left(\mathbf{s}_{v_2 v}^{\mathrm{h}} N_{x_1 \mathbf{K}_1}^{l_1 v_1 v l_2} - \mathbf{s}_{v v_1}^{\mathrm{h}} N_{x_1 \mathbf{K}_1}^{l_1 v v_2 l_2}\right)$$

$$+ \frac{J_{sd} N_{\mathrm{Mn}}}{V^2} \int dz |u_0^{\mathrm{e}}(z)|^2 \sum_{\substack{lnn' \\ x\mathbf{K}}} \mathbf{S}_{nn'} \cdot \left(\mathbf{s}_{l_2 l}^{\mathrm{e}} f_{-\eta_{\mathrm{h}}x_1 x}^{\mathbf{K}_1 \mathbf{K}} Q_{N_{n x_1 \mathbf{K}_1 x\mathbf{K}}}^{n'l_1 v_1 v_2 l}(z) - \mathbf{s}_{ll_1}^{\mathrm{e}} f_{-\eta_{\mathrm{h}}xx_1}^{\mathbf{K}\mathbf{K}_1} Q_{N_{n x\mathbf{K}x_1 \mathbf{K}_1}}^{n'lv_1 v_2 l_2}(z)\right)$$

$$+ \frac{J_{pd} N_{\mathrm{Mn}}}{V^2} \int dz |u_0^{\mathrm{h}}(z)|^2 \sum_{\substack{vnn' \\ x\mathbf{K}}} \mathbf{S}_{nn'} \cdot \left(\mathbf{s}_{v_2 v}^{\mathrm{h}} f_{\eta_{\mathrm{e}}x_1 x}^{\mathbf{K}_1 \mathbf{K}} Q_{N_{n x_1 \mathbf{K}_1 x\mathbf{K}}}^{n'l_1 v_1 v l_2}(z) - \mathbf{s}_{v v_1}^{\mathrm{h}} f_{\eta_{\mathrm{e}}xx_1}^{\mathbf{K}\mathbf{K}_1} Q_{N_{n x\mathbf{K}x_1 \mathbf{K}_1}}^{n'l_1 v v_2 l_2}(z)\right)$$

$$+ \frac{J_0^{\mathrm{e}} N_{\mathrm{Mn}}}{V^2} \int dz |u_0^{\mathrm{e}}(z)|^2 \sum_{x\mathbf{K}} \left(f_{-\eta_{\mathrm{h}}x_1 x}^{\mathbf{K}_1 \mathbf{K}} \bar{N}_{x_1 \mathbf{K}_1 x\mathbf{K}}^{l_1 v_1 v_2 l_2}(z) - f_{-\eta_{\mathrm{h}}xx_1}^{\mathbf{K}\mathbf{K}_1} \bar{N}_{x\mathbf{K}x_1 \mathbf{K}_1}^{l_1 v_1 v_2 l_2}(z)\right)$$

$$+ \frac{J_0^{\mathrm{h}} N_{\mathrm{Mn}}}{V^2} \int dz |u_0^{\mathrm{h}}(z)|^2 \sum_{x\mathbf{K}} \left(f_{\eta_{\mathrm{e}}x_1 x}^{\mathbf{K}_1 \mathbf{K}} \bar{N}_{x_1 \mathbf{K}_1 x\mathbf{K}}^{l_1 v_1 v_2 l_2}(z) - f_{\eta_{\mathrm{e}}xx_1}^{\mathbf{K}\mathbf{K}_1} \bar{N}_{x\mathbf{K}x_1 \mathbf{K}_1}^{l_1 v_1 v_2 l_2}(z)\right), \tag{25c}$$

$$i\hbar \frac{\partial}{\partial t} Q_{Y_{n_1 x_1 \mathbf{K}_1}}^{n_2 v_1 l_1}(z) = \left(E_{x_1 \mathbf{K}_1}^{v_1 l_1} + \frac{(J_0^{\mathrm{e}} + J_0^{\mathrm{h}}) N_{\mathrm{Mn}}}{V}\right) Q_{Y_{n_1 x_1 \mathbf{K}_1}}^{n_2 v_1 l_1}(z) + \beta_{n_1 x_1 \mathbf{K}_1}^{n_2 v_1 l_1}(z)^I + \beta_{n_1 x_1 \mathbf{K}_1}^{n_2 v_1 l_1}(z)^{II} + \beta_{n_1 x_1 \mathbf{K}_1}^{n_2 v_1 l_1}(z)^{III}, \tag{25d}$$

$$i\hbar \frac{\partial}{\partial t} \bar{Y}_{x_1 \mathbf{K}_1}^{v_1 l_1}(z) = \left(E_{x_1 \mathbf{K}_1}^{v_1 l_1} + \frac{(J_0^{\mathrm{e}} + J_0^{\mathrm{h}}) N_{\mathrm{Mn}}}{V}\right) \bar{Y}_{x_1 \mathbf{K}_1}^{v_1 l_1}(z) + \bar{\beta}_{x_1 \mathbf{K}_1}^{v_1 l_1}(z)^I + \bar{\beta}_{x_1 \mathbf{K}_1}^{v_1 l_1}(z)^{II} + \bar{\beta}_{x_1 \mathbf{K}_1}^{v_1 l_1}(z)^{III}, \tag{25e}$$

$$i\hbar \frac{\partial}{\partial t} Q_{N_{n_1 x_1 \mathbf{K}_1 x_2 \mathbf{K}_2}}^{n_2 l_1 v_1 v_2 l_2}(z) = \mathbf{E} \cdot \left(\mathbf{M}_{v_1 l_1}^{x_1} Q_{Y_{n_1 x_1 \mathbf{K}_2}}^{n_2 v_2 l_2}(z) \delta_{\mathbf{K}_1, \mathbf{0}} - \mathbf{M}_{l_2 v_2}^{x_2} \left(Q_{Y_{n_1 x_1 \mathbf{K}_1}}^{n_2 v_1 l_1}(z)\right)^* \delta_{\mathbf{K}_2, \mathbf{0}}\right) + \left(E_{x_2 \mathbf{K}_2}^{v_2 l_2} - E_{x_1 \mathbf{K}_1}^{v_1 l_1}\right)$$

$$\times Q_{N_{n_1 x_1 \mathbf{K}_1 x_2 \mathbf{K}_2}}^{n_2 l_1 v_1 v_2 l_2}(z) + b_{n_1 x_1 \mathbf{K}_1 x_2 \mathbf{K}_2}^{n_2 l_1 v_1 v_2 l_2}(z)^I + b_{n_1 x_1 \mathbf{K}_1 x_2 \mathbf{K}_2}^{n_2 l_1 v_1 v_2 l_2}(z)^{II} + b_{n_1 x_1 \mathbf{K}_1 x_2 \mathbf{K}_2}^{n_2 l_1 v_1 v_2 l_2}(z)^{III}, \tag{25f}$$

$$i\hbar \frac{\partial}{\partial t} \bar{N}_{x_1 \mathbf{K}_1 x_2 \mathbf{K}_2}^{l_1 v_1 v_2 l_2}(z) = \mathbf{E} \cdot \left(\mathbf{M}_{v_1 l_1}^{x_1} \bar{Y}_{x_2 \mathbf{K}_2}^{v_2 l_2}(z) \delta_{\mathbf{K}_1, \mathbf{0}} - \mathbf{M}_{l_2 v_2}^{x_2} \left(\bar{Y}_{x_1 \mathbf{K}_1}^{v_1 l_1}(z)\right)^* \delta_{\mathbf{K}_2, \mathbf{0}}\right) + \left(E_{x_2 \mathbf{K}_2}^{v_2 l_2} - E_{x_1 \mathbf{K}_1}^{v_1 l_1}\right) \bar{N}_{x_1 \mathbf{K}_1 x_2 \mathbf{K}_2}^{l_1 v_1 v_2 l_2}(z)$$

$$+ \bar{b}_{x_1 \mathbf{K}_1 x_2 \mathbf{K}_2}^{l_1 v_1 v_2 l_2}(z)^I + \bar{b}_{x_1 \mathbf{K}_1 x_2 \mathbf{K}_2}^{l_1 v_1 v_2 l_2}(z)^{II} + \bar{b}_{x_1 \mathbf{K}_1 x_2 \mathbf{K}_2}^{l_1 v_1 v_2 l_2}(z)^{III}. \tag{25g}$$

The mean-field precession frequencies and directions of impurities, electrons, and holes, respectively, are given by

$$\boldsymbol{\omega}_{\mathrm{Mn}} = \frac{1}{\hbar} g_{\mathrm{Mn}} \mu_B \mathbf{B}, \tag{26a}$$

$$\boldsymbol{\omega}_{\mathrm{e}} = \frac{1}{\hbar} g_{\mathrm{e}} \mu_B \mathbf{B} + \frac{J_{sd} N_{\mathrm{Mn}}}{\hbar V} \int dz \left| u_0^{\mathrm{e}}(z) \right|^2 \langle \mathbf{S}(z) \rangle, \tag{26b}$$

$$\boldsymbol{\omega}_{\mathrm{h}} = -\frac{6}{\hbar} \kappa \mu_B \mathbf{B} + \frac{J_{pd} N_{\mathrm{Mn}}}{\hbar V} \int dz \left| u_0^{\mathrm{h}}(z) \right|^2 \langle \mathbf{S}(z) \rangle, \tag{26c}$$

where $\langle \mathbf{S}(z) \rangle = \sum_{nn'} \langle \mathbf{S}_{nn'} M_n^{n'}(z) \rangle$ is the mean impurity spin. In the exciton representation, the dipole matrix element becomes $\mathbf{M}_{lv}^x := \mathbf{M}_{lv} \phi_x(\mathbf{r} = 0)$. The wave-vector dependent form factors that arise in Eq. (25) are given by

$$\begin{aligned} f_{\eta x_1 x_2}^{\mathbf{K}_1 \mathbf{K}_2} &:= \int d^2 r \, e^{-i\eta(\mathbf{K}_1 - \mathbf{K}_2)\cdot\mathbf{r}} \phi_{x_1}^*(\mathbf{r}) \phi_{x_2}(\mathbf{r}) \\ &= 2\pi \int_0^\infty dr \, r \, R_{n_1}(r) R_{n_2}(r) i^{-\Delta l} e^{i\Delta l \psi_{12}} J_{\Delta l}(\eta K_{12} r) \end{aligned} \tag{27}$$

with $\eta \in \{-\eta_{\mathrm{h}}, \eta_{\mathrm{e}}\}$, $\Delta l = l_2 - l_1$, $K_{12} = |\mathbf{K}_1 - \mathbf{K}_2|$, and $J_{\Delta l}(x)$ denoting the cylindrical Bessel function of integer order Δl. Furthermore, ψ_{12} is the angle between the vector $(\mathbf{K}_1 - \mathbf{K}_2)$ and the x axis. To arrive at the above formula, the Jacobi-Anger expansion has been used. The source terms β, $\bar{\beta}$, b, and $\bar{b}$ for the correlations are listed in Eqs. (A1) in Appendix A.

In the equations of motion, one can identify terms with different physical interpretation. For instance, in Eq. (25b), the first term on the right-hand side represents the optical driving by the laser field, followed by a homogeneous term proportional to the quasiparticle energy of the exciton. Note that the nonmagnetic impurity interaction renormalizes the band gap and therefore the quasiparticle energy. The terms proportional to $\boldsymbol{\omega}_{\mathrm{e}}$ and $\boldsymbol{\omega}_{\mathrm{h}}$ describe the precession around the effective field due to the external magnetic field as well as the impurity magnetization. The influence of the magnetic carrier-impurity correlations is given by the terms proportional to the magnetic coupling constants J_{sd} and J_{pd}, while terms proportional to J_0^{e} and J_0^{h} describe the effects of the nonmagnetic correlations. Apart from the term proportional to $\boldsymbol{\omega}_{\mathrm{Mn}}$ in Eq. (25a), which describes the mean-field precession of the impurity spins around the external magnetic field, all other contributions in Eqs. (25a)–(25c) can be interpreted analogously.

A similar classification is possible for the source terms of the correlations in Eqs. (25d)–(25g): source terms with the upper index I contain inhomogeneous driving terms that only depend on the coherences $Y_{x_1 \mathbf{0}}^{v_1 l_1}$ and the exciton densities $N_{x_1 \mathbf{K}_1}^{l_1 v_1 v_2 l_2}$ and not on carrier-impurity correlations. The index II denotes homogeneous contributions that cause a precession-type motion of the correlations in the effective fields given by Eqs. (26). Finally, terms labeled by the index III describe an incoherent driving of the magnetic and nonmagnetic correlations by other carrier-impurity correlations with different wave vectors.

It is noteworthy that, in the absence of an electric field, Eqs. (25) conserve the number of particles as well as the total

energy comprised of mean-field and correlation contributions, which can be confirmed by a straightforward but lengthy analytical calculation. This provides an important consistency check of the equations and can be used as a convergence criterion for the numerical implementation.

E. Reduced equations for exciton-bound electron spins

An optical excitation with circularly polarized light generates excitons composed of electrons and holes with corresponding electron and hole spins in accordance with the selection rules. Here, we are dealing with a narrow semiconductor quantum well, where the hh and lh bands are split at the Γ point of the Brillouin zone due to the confinement as well as strain [56]. We consider the generation of heavy-hole excitons as they typically constitute the low-energy excitations. In this case, the hh spins are typically pinned because the precession of a hole spin involves an intermediary occupation of lh states which lie at higher energies. Furthermore, for direct transitions between the $-\frac{3}{2}$ and $\frac{3}{2}$ hh states, the corresponding matrix elements in the Hamiltonian given by Eq. (1) are zero. As a consequence, if the hh-lh splitting is large enough, hh spins do not take part in the spin dynamics and the initially prepared hole spin does not change. Therefore it is sufficient to concentrate only on the dynamics of the exciton-bound electron spins, which can be described by a reduced set of equations of motion.

In the following, we focus on an excitation with σ^- polarization, so that heavy-holes with $m_J = -\frac{3}{2}$ and electrons in the spin-up state $\uparrow$ are excited. Then, it is instructive to consider the dynamical variables

$$n_{x_1 K_1} = \frac{1}{2\pi} \int_0^{2\pi} d\psi_1 \sum_{\sigma} N_{x_1 \mathbf{K}_1}^{\sigma\sigma}, \tag{28a}$$

$$\mathbf{s}_{x_1 K_1} = \frac{1}{2\pi} \int_0^{2\pi} d\psi_1 \sum_{\sigma\sigma'} \mathbf{s}_{\sigma\sigma'} N_{x_1 \mathbf{K}_1}^{\sigma\sigma'}, \tag{28b}$$

$$y_{x_1}^{\uparrow/\downarrow} = \frac{1}{2\pi} \int_0^{2\pi} d\psi_1 \, Y_{x_1 \mathbf{0}}^{\uparrow/\downarrow}, \tag{28c}$$

$$\begin{aligned} q_{\eta l x_1 K_1}^{\uparrow/\downarrow x_2} &= \frac{1}{2\pi} \int_0^{2\pi} d\psi_1 \, f_{\eta x_2 x_1}^{\mathbf{0K}_1} \int dz |u_0(z)|^2 \sum_{nn'} S_{nn'}^l \\ &\quad \times Q_{Y n x_1 \mathbf{K}_1}^{n'\uparrow/\downarrow}(z), \end{aligned} \tag{28d}$$

$$z_{\eta x_1 K_1}^{\uparrow/\downarrow x_2} = \frac{1}{2\pi} \int_0^{2\pi} d\psi_1 \, f_{\eta x_2 x_1}^{\mathbf{0K}_1} \int dz |u_0(z)|^2 \bar{Y}_{x_1 \mathbf{K}_1}^{\uparrow/\downarrow}(z), \tag{28e}$$

$$\begin{aligned} Q_{\eta l x_1 K_1}^{\alpha x_2 K_2} &= \frac{1}{4\pi^2} \int_0^{2\pi} d\psi_1 \int_0^{2\pi} d\psi_2 \, f_{\eta x_1 x_2}^{\mathbf{K}_1 \mathbf{K}_2} \int dz |u_0(z)|^2 \\ &\quad \times \sum_{\substack{\sigma\sigma' \\ nn'}} S_{nn'}^l s_{\sigma\sigma'}^\alpha Q_{N n x_1 \mathbf{K}_1 x_2 \mathbf{K}_2}^{n'\sigma\sigma'}(z), \end{aligned} \tag{28f}$$

$$\begin{aligned} Z_{\eta \; x_1 K_1}^{\alpha x_2 K_2} &= \frac{1}{4\pi^2} \int_0^{2\pi} d\psi_1 \int_0^{2\pi} d\psi_2 \, f_{\eta x_1 x_2}^{\mathbf{K}_1 \mathbf{K}_2} \int dz |u_0(z)|^2 \\ &\quad \times \sum_{\sigma\sigma'} s_{\sigma\sigma'}^\alpha \bar{N}_{x_1 \mathbf{K}_1 x_2 \mathbf{K}_2}^{\sigma\sigma'}(z) \end{aligned} \tag{28g}$$

with $l \in \{1,2,3\}$ and $\alpha \in \{0,1,2,3\}$, where $s^0_{\sigma_1\sigma_2} = \delta_{\sigma_1,\sigma_2}$. We have introduced an average over polar angles ψ_i of the wave vectors $\mathbf{K}_i$, which does not introduce a further approximation in an isotropic system as defined by the Hamiltonian in Eq. (1) but significantly reduces the numerical demand. In Eqs. (28), $n_{x_1K_1}$ is the occupation density of the excitons with quantum number x_1 and modulus of the center of mass momentum K_1 and $s_{x_1K_1}$ describes the spin density of exciton-bound electrons. The interband coherences are described by y_{x_1} and the remaining variables are correlation functions modified by the form factors f_η defined in Eq. (27).

Note that, in order to obtain a closed set of equations for the dynamical variables defined in Eqs. (28) starting from Eqs. (25), the source terms β^{III}, $\bar{\beta}^{III}$, b^{III}, and $\bar{b}^{III}$ have to be neglected. However, since these terms contain only sums of correlations with different wave vectors, they can be expected to dephase very fast compared to the remaining source terms. In previous works on the spin dynamics of conduction band electrons [74], similar terms were shown to be irrelevant by numerical studies. Furthermore, the optically generated carrier density is typically much lower than the number of impurity atoms in the sample. This results in a negligible change of the impurity spin over time which is therefore disregarded.

With these assumptions, quantum kinetic equations of motion for the variables defined in Eqs. (28) can be derived. The results are given in Appendix B where we have introduced the angle-averaged products of form factors

$$
\begin{aligned}
F^{\eta_2 K_1 K_2}_{\eta_1 x_1 x_2} &:= \frac{1}{4\pi^2} \int_0^{2\pi} d\psi_1 \int_0^{2\pi} d\psi_2 f^{\mathbf{K}_1\mathbf{K}_2}_{\eta_1 x_1 x_2} \left(f^{\mathbf{K}_1\mathbf{K}_2}_{\eta_2 x_1 x_2} \right)^* \\
&= 2\pi \int_0^{2\pi} d\psi \int_0^\infty dr \int_0^\infty dr'\, rr' R_{n_1}(r) R_{n_2}(r) R_{n_1}(r') \\
&\quad \times R_{n_2}(r') J_{l-l_2}(\eta_1 K_{12}(\psi)r) J_{l_1-l_2}(\eta_2 K_{12}(\psi)r'),
\end{aligned}
$$

(29)

which contain the influence of the exciton wave function on the spin dynamics. In the second step, we have used the expansion in Eq. (27) together with the fact that $K_{12} = |\mathbf{K}_1 - \mathbf{K}_2|$ depends only on the angle ψ between $\mathbf{K}_1$ and $\mathbf{K}_2$. For infinite confinement potentials, the influence of the envelope functions defined in Eq. (9) enters the spin dynamics via the factor

$$
I = d \int_{-\frac{d}{2}}^{\frac{d}{2}} dz |u_0(z)|^4 = \frac{3}{2}.
$$

(30)

Note that Eqs. (B1) also contain second moments of the impurity spin given by $\langle S^i S^j \rangle = \sum_{n_1 n_2 n_3} S^i_{n_1 n_2} S^j_{n_2 n_3} M^{n_3}_{n_1}$. Instead of deriving equations of motion for these second moments, we once more exploit the fact that the carrier density is typically much lower than the impurity density, so that the impurity density matrix is well described by its initial thermal equilibrium value throughout the dynamics [74].

F. Markov limit

While the dynamics can in general contain memory effects mediated by carrier-impurity correlations, it is also instructive to consider the Markovian limit of the quantum kinetic theory, where an infinitesimal memory is assumed. On the one hand, this allows one to obtain analytical insights into the spin-flip processes described by the theory. On the other hand, a comparison between quantum kinetic and Markovian results facilitates the identification of true non-Markovian features and allows an estimation of the importance of correlations in the system.

To derive the Markov limit, we formally integrate Eqs. (B1f)–(B1i) for the correlations. Afterwards, the resulting integral expressions for the correlations are fed back into Eqs. (B1a) and (B1b) for the occupation densities n_{xK} and the spin densities $\mathbf{s}_{xK}$, respectively. This yields integro-differential equations for n_{xK} and $\mathbf{s}_{xK}$ alone. In the Markov limit, the memory integral in these equations is eliminated by assuming that the memory is short so that one can apply the Sokhotsky-Plemelj formula

$$
\int_0^t dt' e^{i\Delta\omega(t'-t)} \xrightarrow{t\to\infty} \pi\delta(\Delta\omega) - \frac{i}{\Delta\omega}.
$$

(31)

Note that, if a spin precession becomes important, such as in finite magnetic fields, the precession-type motion of carrier and impurity spins as well as of carrier-impurity correlations have to be treated as fast oscillating contributions that have to be split off in order to identify slowly varying terms that can be drawn out of the memory integral [74]. This procedure is similar to a rotating-wave description. The precession frequencies then lead to a modification of $\Delta\omega$ in Eq. (31), which, in the Markov limit, corresponds to additional energy shifts that ensure energy conservation during spin-flip processes [43].

In the following, we consider a situation where the impurity magnetization as well as the precession vectors are parallel or antiparallel to the external magnetic field. Then, we can write

$$
\boldsymbol{\omega}_e = \sigma^B_e \omega_e \mathbf{e}_B,
$$

(32a)

$$
\boldsymbol{\omega}_h = \sigma^B_h \omega_h \mathbf{e}_B,
$$

(32b)

$$
\boldsymbol{\omega}_{Mn} = \sigma^B_{Mn} \omega_{Mn} \mathbf{e}_B,
$$

(32c)

$$
\langle \mathbf{S} \rangle = \sigma^B_S \langle S^\parallel \rangle \mathbf{e}_B,
$$

(32d)

where the factors $\sigma^B_e, \sigma^B_h, \sigma^B_{Mn}, \sigma^B_S \in \{-1,1\}$ determine the direction of the corresponding vector with respect to the direction of the magnetic field $\mathbf{e}_B$. It is convenient to choose the variables

$$
n^{\uparrow/\downarrow}_{x_1 K_1} = \tfrac{1}{2} n_{x_1 K_1} \pm \mathbf{s}_{x_1 K_1} \cdot \mathbf{e}_B,
$$

(33a)

$$
\mathbf{s}^\perp_{x_1 K_1} = \mathbf{s}_{x_1 K_1} - \left(\mathbf{s}_{x_1 K_1} \cdot \mathbf{e}_B \right) \mathbf{e}_B,
$$

(33b)

which describe the spin-up and spin-down exciton density as well as the perpendicular exciton-bound electron spin density, respectively. For these variables, the Markovian equations of

motion are

$$\frac{\partial}{\partial t} n_{x_1 K_1}^{\uparrow/\downarrow} = \Gamma_{\mathbf{E}}^{\uparrow/\downarrow} + \frac{\pi I N_{\mathrm{Mn}}}{\hbar^2 V^2} \sum_{xK} \Big\{ \delta(\omega_{xK} - \omega_{x_1 K_1})(n_{xK}^{\uparrow/\downarrow} - n_{x_1 K_1}^{\uparrow/\downarrow}) \big[\big(J_{sd}^2 b^\parallel \pm 2 J_{sd} J_0^{\mathrm{e}} b^0 + 2 J_0^{\mathrm{e}2}\big) F_{\eta_{\mathrm{h}} x x_1}^{\eta_{\mathrm{h}} K K_1}$$

$$+ \big(J_{pd}^2 b^\parallel - 2 J_{pd} J_0^{\mathrm{h}} b^0 + 2 J_0^{\mathrm{h}2}\big) F_{\eta_{\mathrm{e}} x x_1}^{\eta_{\mathrm{e}} K K_1} + \big(4 J_0^{\mathrm{e}} J_0^{\mathrm{h}} - 2 J_{pd} J_0^{\mathrm{e}} b^0 \pm 2 J_{sd} J_0^{\mathrm{h}} b^0 \mp 2 J_{sd} J_{pd} b^\parallel\big) F_{-\eta_{\mathrm{h}} x x_1}^{\eta_{\mathrm{e}} K K_1} \big]$$

$$+ \delta\big(\omega_{xK} - \big(\omega_{x_1 K_1} \pm (\sigma_{\mathrm{e}}^B \omega_{\mathrm{e}} - \sigma_{\mathrm{Mn}}^B \omega_{\mathrm{Mn}})\big)\big) J_{sd}^2 F_{xx_1}^{K K_1} \big(b^\pm n_{xK}^{\downarrow/\uparrow} - b^\mp n_{x_1 K_1}^{\uparrow/\downarrow}\big) \Big\}, \tag{34a}$$

$$\frac{\partial}{\partial t} \mathbf{s}_{x_1 K_1}^\perp = \mathbf{\Gamma}_{\mathbf{E}}^\perp + \frac{\pi I N_{\mathrm{Mn}}}{\hbar^2 V^2} \sum_{xK} \Big\{ \delta(\omega_{xK} - \omega_{x_1 K_1})\big(\mathbf{s}_{xK}^\perp - \mathbf{s}_{x_1 K_1}^\perp\big) \big[\big(2 J_0^{\mathrm{e}2} - J_{sd}^2 b^\parallel\big) F_{\eta_{\mathrm{h}} x x_1}^{\eta_{\mathrm{h}} K K_1} + \big(J_{pd}^2 b^\parallel + 2 J_0^{\mathrm{h}2} - J_{pd} J_0^{\mathrm{h}} b^0\big)$$

$$\times F_{\eta_{\mathrm{e}} x x_1}^{\eta_{\mathrm{e}} K K_1} - \big(2 J_{pd} J_0^{\mathrm{e}} b^0 + J_{pd} J_0^{\mathrm{h}} b^0 - 2 J_0^{\mathrm{e}} J_0^{\mathrm{h}}\big) F_{-\eta_{\mathrm{h}} x x_1}^{\eta_{\mathrm{e}} K K_1} \big] - \Big[\frac{b^-}{2} \delta\big(\omega_{xK} - \big(\omega_{x_1 K_1} + (\sigma_{\mathrm{e}}^B \omega_{\mathrm{e}} - \sigma_{\mathrm{Mn}}^B \omega_{\mathrm{Mn}})\big)\big)$$

$$+ \frac{b^+}{2} \delta\big(\omega_{xK} - \big(\omega_{x_1 K_1} - (\sigma_{\mathrm{e}}^B \omega_{\mathrm{e}} - \sigma_{\mathrm{Mn}}^B \omega_{\mathrm{Mn}})\big)\big) + 2 b^\parallel \delta(\omega_{xK} - \omega_{x_1 K_1}) \Big] J_{sd}^2 F_{\eta_{\mathrm{h}} x x_1}^{\eta_{\mathrm{h}} K K_1} \mathbf{s}_{x_1 K_1}^\perp \Big\}$$

$$+ \big(\boldsymbol{\omega}_{\mathrm{e}} \times \mathbf{s}_{x_1 K_1}^\perp\big) \Big\{ 1 + \frac{1}{\omega_{\mathrm{e}}} \frac{I N_{\mathrm{Mn}}}{\hbar^2 V^2} \sum_{xK} \Big[\frac{J_{sd}}{\omega_{xK} - \omega_{x_1 K_1}} \Big(\big(2 J_{pd} b^\parallel - 2 J_0^{\mathrm{h}} b^0\big) F_{-\eta_{\mathrm{h}} x x_1}^{\eta_{\mathrm{e}} K K_1} - 2 J_0^{\mathrm{e}} b^0 F_{\eta_{\mathrm{h}} x x_1}^{\eta_{\mathrm{h}} K K_1}\Big)$$

$$+ \Big(\frac{b^+}{\omega_{xK} - \big(\omega_{x_1 K_1} - (\sigma_{\mathrm{e}}^B \omega_{\mathrm{e}} - \sigma_{\mathrm{Mn}}^B \omega_{\mathrm{Mn}})\big)} - \frac{b^-}{\omega_{xK} - \big(\omega_{x_1 K_1} + (\sigma_{\mathrm{e}}^B \omega_{\mathrm{e}} - \sigma_{\mathrm{Mn}}^B \omega_{\mathrm{Mn}})\big)} \Big) \frac{1}{2} J_{sd}^2 F_{\eta_{\mathrm{h}} x x_1}^{\eta_{\mathrm{h}} K K_1} \Big] \Big\}. \tag{34b}$$

In the above equations, the shorthand notation $b^\pm := \frac{1}{2}(\langle \mathbf{S}^2 - (\mathbf{S} \cdot \mathbf{e}_B)^2 \rangle \pm \sigma_S^B \langle S^\parallel \rangle)$, $b^\parallel := \frac{1}{2} \langle (\mathbf{S} \cdot \mathbf{e}_B)^2 \rangle$, and $b^0 := \sigma_S^B \langle S^\parallel \rangle$ has been used for the second moments of the Mn spin. Here, we model the optical excitation by the generation rates $\Gamma_{\mathbf{E}}^{\uparrow/\downarrow}$ and $\mathbf{\Gamma}_{\mathbf{E}}^\perp$ for the spin-up and spin-down occupations and the perpendicular spin component, respectively.

In Eq. (34a), the term proportional to $(n_{xK}^{\uparrow/\downarrow} - n_{x_1 K_1}^{\uparrow/\downarrow})$ describes processes conserving the exciton spin, whereas the term proportional to $(b^\pm n_{xK}^{\downarrow/\uparrow} - b^\mp n_{x_1 K_1}^{\uparrow/\downarrow})$ is responsible for the spin-flip scattering of excitons. The delta functions ensure conservation of energy. Similarly, the terms proportional to $(\mathbf{s}_{xK}^\perp - \mathbf{s}_{x_1 K_1}^\perp)$ in Eq. (34b) can be interpreted as exciton-spin conserving contributions, whereas the prefactors of $s_{x_1 K_1}^\perp$ are responsible for a decay of the perpendicular spin component. Finally, the cross product $\boldsymbol{\omega}_{\mathrm{e}} \times \mathbf{s}_{x_1 K_1}^\perp$ describes the mean-field precession around $\boldsymbol{\omega}_{\mathrm{e}}$ which is renormalized by terms resulting from the imaginary part of the memory integral given by Eq. (31).

The exciton spin-conserving parts of Eq. (34) lead to a redistribution within a given energy shell as well as to transitions between excitonic states with different quantum numbers, as can be seen from the argument of the corresponding delta functions. In situations where spin-orbit coupling and thus a D'yakonov-Perel'-type spin dephasing is important, these terms give rise to an additional momentum scattering and thereby indirectly influence the spin dynamics. However, spin-orbit coupling is typically of minor importance for the spin dynamics in DMS compared with the carrier-impurity interaction [58]. In an isotropic system as considered here, the exciton spin-conserving parts of Eqs. (34) do not influence the spin dynamics. Since the magnetic coupling constant J_{pd} for the valence band as well as the nonmagnetic coupling constants J_0^{e} and J_0^{h} only enter these terms, the nonmagnetic interactions and the pd interaction do not affect the spin dynamics on the Markovian level.

For spin-flip scattering processes, an exciton with a given spin an energy $\hbar \omega_{x_1 K_1}$ is scattered to a state with opposite spin and energy $\hbar \omega_{xK}$. The appearance of the energy shift $\pm \hbar(\sigma_{\mathrm{e}}^B \omega_{\mathrm{e}} - \sigma_{\mathrm{Mn}}^B \omega_{\mathrm{Mn}})$ in the corresponding delta function in Eq. (34a) can be understood as follows: a flip of the exciton-bound electron spin requires or releases a magnetic energy $\hbar \sigma_{\mathrm{e}}^B \omega_{\mathrm{e}}$. However, since a flip of a carrier spin also involves the flop of an impurity spin in the opposite direction, the corresponding change in magnetic energy of the impurity spin $\hbar \sigma_{\mathrm{Mn}}^B \omega_{\mathrm{Mn}}$ has to be accounted for to ensure conservation of energy.

An interesting limiting case can be worked out for zero external magnetic field, vanishing impurity magnetization, and optical excitation resonant with the $1s$ exciton state. Then, Eqs. (34) can be condensed into the simple rate equation

$$\frac{\partial}{\partial t} \mathbf{s}_{1sK_1} = -\tau_{1sK_1}^{-1} \mathbf{s}_{1sK_1}, \tag{35}$$

where the spin-decay rate is given by

$$\tau_{1sK_1}^{-1} = \frac{35}{12} \frac{N_{\mathrm{Mn}} I J_{sd}^2 M}{\hbar^3 dV} F_{\eta_{\mathrm{h}} 1s 1s}^{\eta_{\mathrm{h}} K_1 K_1} \tag{36}$$

and d denotes the width of the DMS quantum well. In contrast to the quasifree electron case, where the spin-decay rate is constant in a quantum well [11,59], the decay rate for excitons explicitly depends on K, which is consistent with previous findings in the literature [12].

III. RESULTS

We now apply our quantum kinetic theory to the exciton spin dynamics for vanishing external magnetic field and impurity magnetization after an ultrashort laser pulse resonant with the exciton ground state and compare the results with the corresponding Markovian calculations. In order to do so, it is

TABLE I. Selected material parameters of $Cd_{1-x}Mn_xTe$ and $Zn_{1-x}Mn_xSe$. The coupling constant is chosen such that it is consistent with the band offsets at a $CdTe/Cd_{1-x}Mn_xTe$ and $ZnSe/Zn_{1-x}Mn_xSe$ interface, respectively [44]. The cubic lattice constant is given by a and m_0 denotes the free electron mass.

Parameter	$Cd_{1-x}Mn_xTe$	$Zn_{1-x}Mn_xSe$
a (nm) [10]	0.648	0.567
m_e/m_0 [60,75]	0.1	0.15
m_{hh}/m_0 [60,75]	0.7	0.8
J_{sd} (meV nm^3) [10]	-15	-12
J_{pd} (meV nm^3) [10]	60	50
J_0^e (meV nm^3) [10]	110	22
J_0^h (meV nm^3) [10]	7	0
ϵ [55]	10	9

necessary to first calculate the exciton wave functions and the resulting form-factor products $F^{\eta_2 x_2 K_2}_{\eta_1 x_1 K_1}$.

A. Exciton form factors

In order to calculate the exciton form factors, we first decompose the exciton wave function according to Eq. (19) and then numerically solve the Coulomb eigenvalue problem given by Eq. (16) for the radial part using a finite-difference method, which yields the exciton energies as well as the wave functions. From the exciton wave functions, the form-factor products defined in Eq. (29) are calculated. The steps and cutoffs in the real-space discretization have been adjusted to ensure convergence.

The results for the form-factor product $F^{\eta_h K_1 K_2}_{\eta_h 1s1s}$ relevant for spin-slip scattering on the $1s$ exciton parabola can be found in Fig. 1(a) as a function of wave numbers K_1 and K_2 using the parameters for $Cd_{1-x}Mn_xTe$ listed in Table I. It can be seen that $F^{\eta_h K_1 K_2}_{\eta_h 1s1s}$ is symmetric with respect to the bisectrix and decreases continuously with increasing wave number. In Fig. 1(b), we present the spin-decay rate in the Markov limit according to Eq. (36), which follows the diagonal values $F^{\eta_h K_1 K_1}_{\eta_h 1s1s}$. To compare the resulting rate to the quasifree electron case, we also plot the spin-decay rate from Ref. [44] for electrons and normalize both results to the exciton spin-decay rate for $K = 0$. The spin-decay rate for excitons at $K = 0$ is about eight times faster than the electron spin-decay rate, which is due to the much larger exciton mass. Furthermore, the exciton spin-decay rate strongly depends on K and can even be smaller than the constant electron spin-decay rate for large wave numbers.

The fact that the spin-decay rate for excitons depends on K has already been pointed out in Ref. [12]. There, an exponential ansatz with a variational parameter for the radial part of the exciton wave function leads to the decay rate [12]

$$\frac{1}{\tau_{sf}}(K) = \frac{1}{\tau_{sf}}(0)\,\phi(\alpha^2 K^2), \qquad (37)$$

where the constant α contains the parameters of the model and the function ϕ is given by [12]

$$\phi(x) = \tfrac{1}{2}(1 + (1 + x))(1 + 2x)^{-\frac{5}{2}}. \qquad (38)$$

To compare this result to our calculations, we fit the constant α in Eq. (37) to our data obtained from Eq. (36) and plot the result in Fig. 1(b). It can be seen that the predictions of Ref. [12] agree with the Markovian limit of our quantum kinetic theory.

B. Spin dynamics

Having obtained the exciton form factors, we can now calculate the spin dynamics according to the quantum kinetic Eqs. (B1). To address the question of the importance of quantum kinetic effects in the exciton spin dynamics, we also present numerical solutions of the Markovian (34). Furthermore, we study the influence of nonmagnetic scattering as well as the magnetic pd coupling.

For the numerical implementation, we use a forth-order Runge-Kutta algorithm to solve the differential equations in the time domain and discretize the K space up to a cut-off energy of a few tens of meV. This is done in the quasicontinuous limit $\sum_K \rightarrow \int dK\, D^{2d}(K)$ using the two-dimensional density of states $D^{2d}(K) = \frac{A}{2\pi}K$ for a quantum well with area A. For all calculations, we have checked that the number of excitons in the system as well as the total energy remain constant after the pulse.

We limit our study to the exciton ground state and treat the optical excitation in a rotating-wave approximation. As discussed in Sec. II E, we focus on a situation where the hh spins are pinned and do not take part in the dynamics. Thus our main quantity of interest is the time evolution of the spin of the exciton-bound electron. In all cases, the optical excitation is modeled by a circularly polarized Gaussian laser beam with a width (FWHM) of 100 fs centered at $t = 0$ ps resonant to the exciton ground state and we consider a quantum well with width $d = 10$ nm. We calculate the time evolution of the exciton spin for two different materials, namely $Cd_{1-x}Mn_xTe$ [Fig. 2(a)] as well as $Zn_{1-x}Mn_xSe$ [Fig. 2(b)] with impurity concentration $x = 5\%$. The relevant parameters for these two materials, which are both of zinc blende crystal structure [10], are collected in Table I.

The mean-field results displayed in Fig. 2 show no spin decay because the time evolution of the exciton density matrix [cf. Eq. (B1b)] after the optical excitation in the absence of a magnetic field is governed by the magnetic and nonmagnetic correlations, which are neglected in the mean-field approximation. If the correlations are treated on a Markovian level, the spin decays exponentially with the spin-decay rate $\tau^{-1}_{1s K_1}$ defined in Eq. (36). The spin dynamics in $Cd_{0.95}Mn_{0.05}Te$ is slower than in $Zn_{0.95}Mn_{0.05}Se$, which is mainly due to the larger exciton mass in ZnSe.

However, the full quantum kinetic spin dynamics in both materials is clearly nonmonotonic and shows a pronounced overshoot after approximately 5 ps of about 10% of the spin polarization immediately after the pulse in the situation depicted in Fig. 2(a). Furthermore, for the first few picoseconds, the quantum kinetic result is actually closer to the results of a calculation using only half the Markovian spin-decay rate. The spin overshoot in Fig. 2 is absent if the nonmagnetic impurity scattering of electrons and holes in the DMS as well as the pd exchange interaction are neglected, as suggested by a calculation with $J_0^e = J_0^h = J_{pd} = 0$ (cf. black boxes in Fig. 2). Without these contributions, the time evolution of the
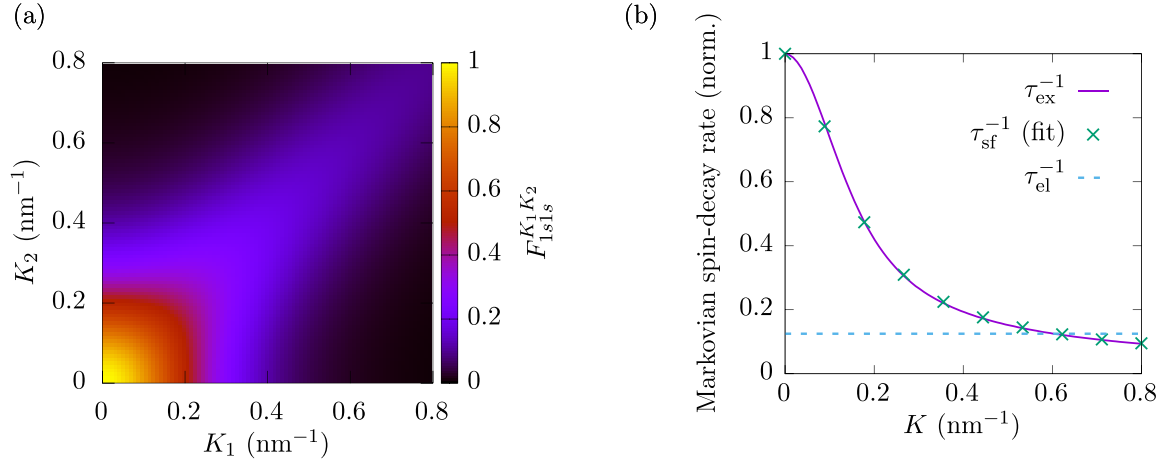
FIG. 1. (a) Angle-averaged form-factor product $F_{\eta_h 1s1s}^{\eta_h K_1 K_2}$ for the exciton ground state (1s) as a function of the center of mass momentum K. (b) K dependence of the Markovian spin-decay rate for excitons (τ_{ex}^{-1}), which follows the diagonal of plot (a), is compared to the constant rate found for quasifree electrons [43] (τ_{el}^{-1}). Both rates are normalized with respect to the exciton spin-decay rate for $K = 0$ and are calculated without external magnetic field. Additionally, Eq. (37) is used to fit τ_{sf}^{-1} to the exciton spin-decay rate of our model.

spin virtually coincides with an exponential decay with half the Markovian spin-decay rate. Note that the nonmagnetic scattering as well as the pd interaction do not influence the spin dynamics on the Markovian level, as follows from Eqs. (34).

Interestingly, the role of nonmagnetic impurity scattering is here opposite to what has been found for the electron spin dynamics in the band continuum [44]: while for excitonic excitations this scattering enhances the overshoot, for above

band-gap excitations it typically almost completely suppresses the nonmonotonic time dependence of the electron spin polarization.

The deviations from the Markovian limit can be traced back to the optical excitation at the bottom of the exciton parabola ($K \approx 0$): while the memory kernel in the Markovian limit given by Eq. (31) contracts to a delta function in energy space, for finite times the energy-time uncertainty relation leads to a
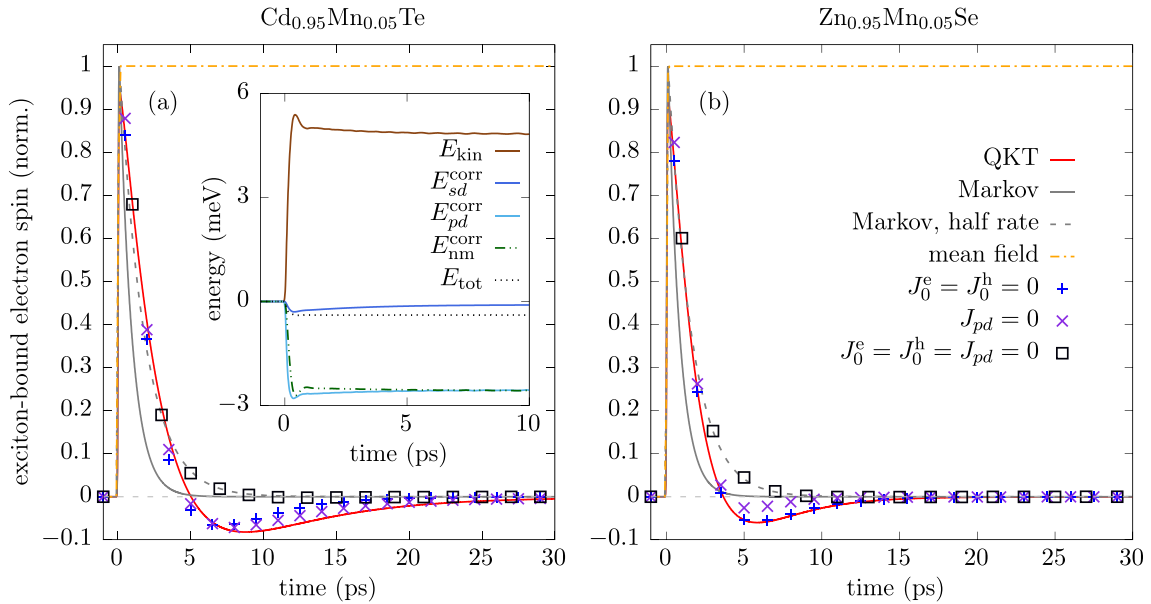

FIG. 2. Spin dynamics of the exciton-bound electron in a 10-nm quantum well using the parameters of (a) $Cd_{0.95}Mn_{0.05}Te$ and (b) $Zn_{0.95}Mn_{0.05}Se$ for vanishing external magnetic field after an optical excitation with a circularly polarized Gaussian laser beam resonant to the exciton ground state. The time axis is chosen such that the pulse maximum lies at $t = 0$ ps with a width (FWHM) of 100 fs. For each material, we show the quantum kinetic results based on Eqs. (B1) (QKT) as well as Markovian calculations using Eqs. (34) (Markov), a spin decay with half the Markovian rate (Markov, half rate), and the results of a calculation where all correlations are neglected (mean field). Additionally, we plot the spin dynamics in the artificial situation where different coupling constants J_0^e, J_0^h, and/or J_{pd} are set to zero. All results are normalized with respect to the mean-field spin polarization for long times. The inset in figure (a) shows the kinetic energy (E_{kin}), the magnetic sd/pd correlation energies ($E_{sd/pd}^{corr}$), the nonmagnetic correlation energy (E_{nm}^{corr}), and the total energy (E_{tot}) normalized with respect to the exciton density after the pulse.
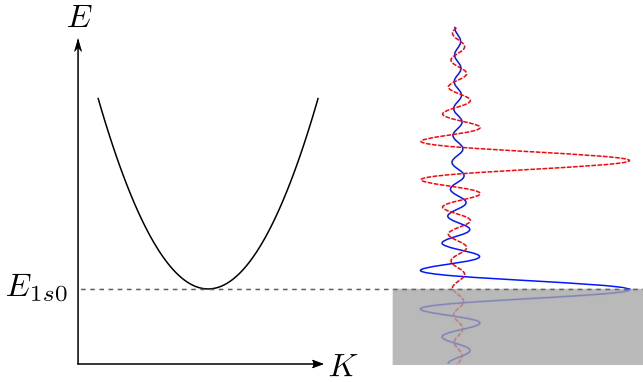
FIG. 3. Sketch of the $1s$ exciton parabola together with the real part of a typical memory kernel $\propto \frac{\sin[(E-E_1)t/\hbar]}{(E-E_1)/\hbar}$ [cf. the left-hand side of Eq. (31)] for a fixed time t with $E_1 = E_{1s0}$ (blue solid line) and $E_1 > E_{1s0}$ (red dashed line). For excitons optically generated at $K \approx 0$, the memory is effectively cut in half.

finite spectral width as sketched in Fig. 3. In a quantum well, the spectral density of states is constant but vanishes below the vertex of the exciton parabola, resulting in a cut-off of the memory kernel in energy space [46]. At $K = 0$, the integral over the memory kernel yields therefore only half the value predicted by the Markovian assumption of a deltalike memory. This translates into a reduction of the effective spin-decay rate by a factor of $\frac{1}{2}$.

The influence of nonmagnetic impurity scattering manifests itself in a redistribution of center of mass momenta on the $1s$ exciton parabola. As a result, states further away from $K = 0$ are populated. For these states, the cutoff of the memory integral due to the density of states is shifted correspondingly and oscillates with time, which causes the overshoots in the dynamics of the spin polarization in Fig. 2. It is noteworthy that, even if the heavy-hole spins are pinned throughout the dynamics, the magnetic pd exchange interaction can still influence the dynamics of the exciton-bound electron spin since it allows for spin-conserving scattering of exciton-bound holes at magnetic impurities. In this sense, the magnetic pd interaction has a similar effect as nonmagnetic scattering. This can be seen from the results depicted in Fig. 2 where either the nonmagnetic or the pd interactions are switched off. In the case of $Cd_{0.95}Mn_{0.05}Te$, where $J_{pd} \approx \frac{1}{2}J_0^e$, both interactions are of similar importance. However, for $Zn_{0.95}Mn_{0.05}Se$, where $J_{pd} \approx 2J_0^e$, the magnetic pd interaction dominates the spin dynamics and nonmagnetic impurity scattering is almost negligible.

The fact that the pd interaction and the nonmagnetic impurity scattering facilitate a redistribution of center of mass momenta can be seen from the inset of Fig. 2(a), which shows the time evolution of the kinetic energy as well as correlation energies. A significant increase in kinetic energy of about 5 meV per exciton is found, which is mainly provided by a build-up of correlation energies due to nonmagnetic scattering and due to the pd interaction. The inset in Fig. 2(a) also shows that the total exciton energy is indeed conserved after the pulse and obtains a small negative value with respect to the mean-field energy of a $1s$ exciton at $K = 0$. This is possible because carrier-impurity correlations are built up

already during the finite width of the pulse. In the case of $Cd_{0.95}Mn_{0.05}Te$, the magnetic pd interaction as well as the nonmagnetic impurity scattering lead to similar correlations energies, which is consistent with their comparable influence on the time evolution of the spin as depicted in the main panel of Fig. 2(a).

IV. CONCLUSION

We have derived quantum kinetic equations for density matrices in the exciton representation that describe the time evolution of the exciton spin in laser-driven DMS in the presence of an external magnetic field. Our theory takes into account contributions up to second order in the generating laser field and explicitly keeps correlations between the carrier and the impurity subsystem. The model not only includes the magnetic sp-d interaction between electrons, holes, and Mn atoms, but also accounts for elastic nonmagnetic scattering at the impurities. This makes our theory a widely applicable tool to study the ultrafast spin dynamics in DMS beyond the single-particle Born-Markov picture. Furthermore, we have shown how rate equations can be straightforwardly extracted from our quantum kinetic theory by using the Markov approximation to eliminate the correlations. This approach allows us to obtain spin-flip scattering rates for situations where the spin polarization is oriented parallel or perpendicular with respect to the external magnetic field. In contrast to the situation of quasifree conduction band electrons studied in Ref. [44], for excitons it is found that the Markovian spin-decay rate strongly depends on the wave vector via a form factor reflecting the shape of the exciton wave function.

A numerical solution of the quantum kinetic equations including exciton-impurity correlations in the absence of a magnetic field and for vanishing impurity magnetization reveals strong deviations from the Markovian predictions in the form of an overshoot of the spin polarization as well as a slower initial decay with about half of the Markovian rate. Accounting for nonmagnetic impurity interaction as well as the pd interaction in the valence band was found to have an essential impact on the spin polarization since the overshoot is only seen in calculations that include these interactions. In contrast, nonmonotonic behavior in the spin dynamics of conduction band electrons is strongly suppressed by nonmagnetic impurity scattering [44].

In Ref. [31], where results for spin-decay rates in DMS measured by different groups have been compared, it was found that the experimentally obtained rates for vanishing magnetic field are consistently about a factor of five larger than the value expected from Fermi's golden rule for conduction band electrons. A possible explanation for this deviation is that excitons instead of quasifree electrons have to be considered. Substituting the exciton mass for the electron mass in Fermi's golden rule leads to an approximately eight times larger spin-decay rate. However, in this article, we have found that non-Markovian effects lead to a spin decay on a time scale corresponding to about half the Markovian rate. Thus our theory predicts that the spin-decay rate measurable in ultrafast optical experiments is about four times larger than predicted by a Markovian model using quasifree carriers and is therefore close to the findings of experiments.

ACKNOWLEDGMENT

APPENDIX A: SOURCE TERMS FOR THE CORRELATIONS

The source terms for the correlations in Eq. (25) are

$$\beta^{n_2 v_1 l_1}_{n_1 x_1 \mathbf{K}_1}(z)^{I} = \sum_{nx} M_{n_1 n}(z) \mathbf{S}_{n_2 n} \cdot \left(J_{sd} d \left| u_0^{\mathrm{e}}(z) \right|^2 \sum_l \mathbf{s}^{\mathrm{e}}_{l_1 l} f_{-\eta_{\mathrm{h}} x_1 x}^{\mathbf{K}_1 \mathbf{0}} Y^{v_1 l}_{x\mathbf{0}} + J_{pd} d \left| u_0^{\mathrm{h}}(z) \right|^2 \sum_v \mathbf{s}^{\mathrm{h}}_{v_1 v} f_{\eta_{\mathrm{e}} x_1 x}^{\mathbf{K}_1 \mathbf{0}} Y^{v l_1}_{x\mathbf{0}} \right)$$

$$+ \sum_x M^{n_2}_{n_1}(z) \left(J_0^{\mathrm{e}} d \left| u_0^{\mathrm{e}}(z) \right|^2 f_{-\eta_{\mathrm{h}} x_1 x}^{\mathbf{K}_1 \mathbf{0}} + J_0^{\mathrm{h}} d \left| u_0^{\mathrm{h}}(z) \right|^2 f_{\eta_{\mathrm{e}} x_1 x}^{\mathbf{K}_1 \mathbf{0}} \right) Y^{v_1 l_1}_{x\mathbf{0}}, \tag{A1a}$$

$$\beta^{n_2 v_1 l_1}_{n_1 x_1 \mathbf{K}_1}(z)^{II} = \sum_l \hbar \boldsymbol{\omega}_{\mathrm{e}} \cdot \mathbf{s}^{\mathrm{e}}_{l_1 l} Q_{Y^{n_2 v_1 l}_{n_1 x_1 \mathbf{K}_1}}(z) + \sum_v \hbar \boldsymbol{\omega}_{\mathrm{h}} \cdot \mathbf{s}^{\mathrm{h}}_{v_1 v} Q_{Y^{n_2 v l_1}_{n_1 x_1 \mathbf{K}_1}}(z) + \sum_n \hbar \boldsymbol{\omega}_{\mathrm{Mn}} \cdot \left(\mathbf{S}_{n_2 n} Q_{Y^{n v_1 l_1}_{n_1 x_1 \mathbf{K}_1}}(z) - \mathbf{S}_{n n_1} Q_{Y^{n_2 v_1 l_1}_{n x_1 \mathbf{K}_1}}(z) \right), \tag{A1b}$$

$$\beta^{n_2 v_1 l_1}_{n_1 x_1 \mathbf{K}_1}(z)^{III} = \frac{1}{V} \sum_{nx\mathbf{K}} \mathbf{S}_{n_2 n} \cdot \left(J_{sd} d \left| u_0^{\mathrm{e}}(z) \right|^2 \sum_l \mathbf{s}^{\mathrm{e}}_{l_1 l} f_{-\eta_{\mathrm{h}} x_1 x}^{\mathbf{K}_1 \mathbf{K}} Q_{Y^{n v_1 l}_{n_1 x \mathbf{K}}}(z) + J_{pd} d \left| u_0^{\mathrm{h}}(z) \right|^2 \sum_v \mathbf{s}^{\mathrm{h}}_{v_1 v} f_{\eta_{\mathrm{e}} x_1 x}^{\mathbf{K}_1 \mathbf{K}} Q_{Y^{n v l_1}_{n_1 x \mathbf{K}}}(z) \right)$$

$$+ \frac{1}{V} \sum_{x\mathbf{K}} \left(J_0^{\mathrm{e}} d \left| u_0^{\mathrm{e}}(z) \right|^2 f_{-\eta_{\mathrm{h}} x_1 x}^{\mathbf{K}_1 \mathbf{K}} + J_0^{\mathrm{h}} d \left| u_0^{\mathrm{h}}(z) \right|^2 f_{\eta_{\mathrm{e}} x_1 x}^{\mathbf{K}_1 \mathbf{K}} \right) Q_{Y^{n_2 v_1 l_1}_{n_1 x \mathbf{K}}}(z), \tag{A1c}$$

$$\bar{\beta}^{v_1 l_1}_{x_1 \mathbf{K}_1}(z)^{I} = \sum_{nn'x} M^{n'}_{n}(z) \mathbf{S}_{nn'} \cdot \left(J_{sd} d \left| u_0^{\mathrm{e}}(z) \right|^2 \sum_l \mathbf{s}^{\mathrm{e}}_{l_1 l} f_{-\eta_{\mathrm{h}} x_1 x}^{\mathbf{K}_1 \mathbf{0}} Y^{v_1 l}_{x\mathbf{0}} + J_{pd} d \left| u_0^{\mathrm{h}}(z) \right|^2 \sum_v \mathbf{s}^{\mathrm{h}}_{v_1 v} f_{\eta_{\mathrm{e}} x_1 x}^{\mathbf{K}_1 \mathbf{0}} Y^{v l_1}_{x\mathbf{0}} \right)$$

$$+ \sum_x \left(J_0^{\mathrm{e}} d \left| u_0^{\mathrm{e}}(z) \right|^2 f_{-\eta_{\mathrm{h}} x_1 x}^{\mathbf{K}_1 \mathbf{0}} + J_0^{\mathrm{h}} d \left| u_0^{\mathrm{h}}(z) \right|^2 f_{\eta_{\mathrm{e}} x_1 x}^{\mathbf{K}_1 \mathbf{0}} \right) Y^{v_1 l_1}_{x\mathbf{0}}, \tag{A1d}$$

$$\bar{\beta}^{v_1 l_1}_{x_1 \mathbf{K}_1}(z)^{II} = \sum_l \hbar \boldsymbol{\omega}_{\mathrm{e}} \cdot \mathbf{s}^{\mathrm{e}}_{l_1 l} \bar{Y}^{v_1 l}_{x_1 \mathbf{K}_1}(z) + \sum_v \hbar \boldsymbol{\omega}_{\mathrm{h}} \cdot \mathbf{s}^{\mathrm{h}}_{v_1 v} \bar{Y}^{v l_1}_{x_1 \mathbf{K}_1}(z), \tag{A1e}$$

$$\bar{\beta}^{v_1 l_1}_{x_1 \mathbf{K}_1}(z)^{III} = \frac{1}{V} \sum_{\substack{nn' \\ x\mathbf{K}}} \mathbf{S}_{nn'} \cdot \left(J_{sd} d \left| u_0^{\mathrm{e}}(z) \right|^2 \sum_l \mathbf{s}^{\mathrm{e}}_{l_1 l} f_{-\eta_{\mathrm{h}} x_1 x}^{\mathbf{K}_1 \mathbf{K}} Q_{Y^{n' v_1 l}_{nx\mathbf{K}}}(z) + J_{pd} d \left| u_0^{\mathrm{h}}(z) \right|^2 \sum_v \mathbf{s}^{\mathrm{h}}_{v_1 v} f_{\eta_{\mathrm{e}} x_1 x}^{\mathbf{K}_1 \mathbf{K}} Q_{Y^{n' v l_1}_{nx\mathbf{K}}}(z) \right)$$

$$+ \frac{1}{V} \sum_{x\mathbf{K}} \left(J_0^{\mathrm{e}} d \left| u_0^{\mathrm{e}}(z) \right|^2 f_{-\eta_{\mathrm{h}} x_1 x}^{\mathbf{K}_1 \mathbf{K}} + J_0^{\mathrm{h}} d \left| u_0^{\mathrm{h}}(z) \right|^2 f_{\eta_{\mathrm{e}} x_1 x}^{\mathbf{K}_1 \mathbf{K}} \right) \bar{Y}^{v_1 l_1}_{x\mathbf{K}}(z), \tag{A1f}$$

$$b^{n_2 l_1 v_1 v_2 l_2}_{n_1 x_1 \mathbf{K}_1 x_2 \mathbf{K}_2}(z)^{I} = J_{sd} d \left| u_0^{\mathrm{e}}(z) \right|^2 \sum_{ln} f_{-\eta_{\mathrm{h}} x_2 x_1}^{\mathbf{K}_2 \mathbf{K}_1} \left(\mathbf{S}_{n_2 n} M^n_{n_1}(z) \cdot \mathbf{s}^{\mathrm{e}}_{l_2 l} N^{l_1 v_1 v_2 l}_{x_1 \mathbf{K}_1} - \mathbf{S}_{n n_1} M^{n_2}_{n}(z) \cdot \mathbf{s}^{\mathrm{e}}_{l l_1} N^{l v_1 v_2 l_2}_{x_2 \mathbf{K}_2} \right)$$

$$+ J_{pd} d \left| u_0^{\mathrm{h}}(z) \right|^2 \sum_{vn} f_{\eta_{\mathrm{e}} x_2 x_1}^{\mathbf{K}_2 \mathbf{K}_1} \left(\mathbf{S}_{n_2 n} M^n_{n_1}(z) \cdot \mathbf{s}^{\mathrm{h}}_{v_2 v} N^{l_1 v_1 v l_2}_{x_1 \mathbf{K}_1} - \mathbf{S}_{n n_1} M^{n_2}_{n}(z) \cdot \mathbf{s}^{\mathrm{h}}_{v v_1} N^{l_1 v v_2 l_2}_{x_2 \mathbf{K}_2} \right)$$

$$+ M^{n_2}_{n_1}(z) \left(J_0^{\mathrm{e}} d \left| u_0^{\mathrm{e}}(z) \right|^2 f_{-\eta_{\mathrm{h}} x_2 x_1}^{\mathbf{K}_2 \mathbf{K}_1} + J_0^{\mathrm{h}} d \left| u_0^{\mathrm{h}}(z) \right|^2 f_{\eta_{\mathrm{e}} x_2 x_1}^{\mathbf{K}_2 \mathbf{K}_1} \right) \left(N^{l_1 v_1 v_2 l_2}_{x_1 \mathbf{K}_1} - N^{l_1 v_1 v_2 l_2}_{x_2 \mathbf{K}_2} \right), \tag{A1g}$$

$$b^{n_2 l_1 v_1 v_2 l_2}_{n_1 x_1 \mathbf{K}_1 x_2 \mathbf{K}_2}(z)^{II} = \sum_l \hbar \boldsymbol{\omega}_{\mathrm{e}} \cdot \left(\mathbf{s}^{\mathrm{e}}_{l_2 l} Q_{N^{n_2 l_1 v_1 v_2 l}_{n_1 x_1 \mathbf{K}_1 x_2 \mathbf{K}_2}}(z) - \mathbf{s}^{\mathrm{e}}_{l l_1} Q_{N^{n_2 l v_1 v_2 l_2}_{n_1 x_1 \mathbf{K}_1 x_2 \mathbf{K}_2}}(z) \right)$$

$$+ \sum_v \hbar \boldsymbol{\omega}_{\mathrm{h}} \cdot \left(\mathbf{s}^{\mathrm{h}}_{v_2 v} Q_{N^{n_2 l_1 v_1 v l_2}_{n_1 x_1 \mathbf{K}_1 x_2 \mathbf{K}_2}}(z) - \mathbf{s}^{\mathrm{h}}_{v v_1} Q_{N^{n_2 l_1 v v_2 l_2}_{n_1 x_1 \mathbf{K}_1 x_2 \mathbf{K}_2}}(z) \right)$$

$$+ \sum_n \hbar \boldsymbol{\omega}_{\mathrm{Mn}} \cdot \left(\mathbf{S}_{n_2 n} Q_{N^{n l_1 v_1 v_2 l_2}_{n_1 x_1 \mathbf{K}_1 x_2 \mathbf{K}_2}}(z) - \mathbf{S}_{n n_1} Q_{N^{n_2 l_1 v_1 v_2 l_2}_{n x_1 \mathbf{K}_1 x_2 \mathbf{K}_2}}(z) \right), \tag{A1h}$$

$$b^{n_2 l_1 v_1 v_2 l_2}_{n_1 x_1 \mathbf{K}_1 x_2 \mathbf{K}_2}(z)^{III} = \frac{J_{sd}}{V} d \left| u_0^{\mathrm{e}}(z) \right|^2 \sum_{\substack{ln \\ x\mathbf{K}}} \left(\mathbf{S}_{n_2 n} \cdot \mathbf{s}^{\mathrm{e}}_{l_2 l} f_{-\eta_{\mathrm{h}} x_2 x}^{\mathbf{K}_2 \mathbf{K}} Q_{N^{n l_1 v_1 v_2 l}_{n_1 x_1 \mathbf{K}_1 x \mathbf{K}}}(z) - \mathbf{S}_{n n_1} \cdot \mathbf{s}^{\mathrm{e}}_{l l_1} f_{-\eta_{\mathrm{h}} x x_1}^{\mathbf{K} \mathbf{K}_1} Q_{N^{n_2 l v_1 v_2 l_2}_{n x \mathbf{K} x_2 \mathbf{K}_2}}(z) \right)$$

$$+ \frac{J_{pd}}{V} d \left| u_0^{\mathrm{h}}(z) \right|^2 \sum_{\substack{vn \\ x\mathbf{K}}} \left(\mathbf{S}_{n_2 n} \cdot \mathbf{s}^{\mathrm{h}}_{v_3 v} f_{\eta_{\mathrm{e}} x_2 x}^{(-\eta_{\mathrm{e}}) \mathbf{K}_2 \mathbf{K}} Q_{N^{n l_1 v_1 v l_2}_{n_1 x_1 \mathbf{K}_1 x \mathbf{K}}}(z) - \mathbf{S}_{n n_1} \cdot \mathbf{s}^{\mathrm{h}}_{v v_2} f_{\eta_{\mathrm{e}} x x_1}^{\mathbf{K} \mathbf{K}_1} Q_{N^{n_2 l_1 v v_2 l_2}_{n x \mathbf{K} x_2 \mathbf{K}_2}}(z) \right)$$

$$+ \frac{J_0^e}{V} \sum_{x\mathbf{K}} d|u_0^e(z)|^2 \big(f_{-\eta_h x_2 x}^{\mathbf{K}_2 \mathbf{K}} Q_{N_{n_1 x_1 \mathbf{K}_1 x\mathbf{K}}}^{n_2 l_1 v_1 v_2 l_2}(z) - f_{-\eta_h x x_1}^{\mathbf{K}\mathbf{K}_1} Q_{N_{n_1 x\mathbf{K} x_2 \mathbf{K}_2}}^{n_2 l_1 v_1 v_2 l_2}(z)\big)$$

$$+ \frac{J_0^h}{V} \sum_{x\mathbf{K}} d|u_0^h(z)|^2 \big(f_{\eta_e x_2 x}^{\mathbf{K}_2 \mathbf{K}} Q_{N_{n_1 x_1 \mathbf{K}_1 x\mathbf{K}}}^{n_2 l_1 v_1 v_2 l_2}(z) - f_{\eta_e x x_1}^{\mathbf{K}\mathbf{K}_1} Q_{N_{n_1 x\mathbf{K} x_2 \mathbf{K}_2}}^{n_2 l_1 v_1 v_2 l_2}(z)\big), \tag{A1i}$$

$$\bar{b}_{x_1 \mathbf{K}_1 x_2 \mathbf{K}_2}^{l_1 v_1 v_2 l_2}(z)^I = J_{sd} d|u_0^e(z)|^2 \sum_{lnn'} \mathbf{S}_{nn'} M_n^{n'}(z) \cdot f_{-\eta_h x_2 x_1}^{\mathbf{K}_2 \mathbf{K}_1} \big(\mathbf{s}_{l_2 l}^e N_{x_1 \mathbf{K}_1}^{l_1 v_1 v_2} - \mathbf{s}_{ll_1}^e N_{x_2 \mathbf{K}_2}^{l v_1 v_2 l_2}\big)$$

$$+ J_{pd} d|u_0^h(z)|^2 \sum_{vnn'} \mathbf{S}_{nn'} M_n^{n'}(z) \cdot f_{\eta_e x_2 x_1}^{\mathbf{K}_2 \mathbf{K}_1} \big(\mathbf{s}_{v_2 v}^h N_{x_1 \mathbf{K}_1}^{l_1 v_1 v l_2} - \mathbf{s}_{vv_1}^h N_{x_2 \mathbf{K}_2}^{l_1 v v_2 l_2}\big)$$

$$+ \big(J_0^e d|u_0^e(z)|^2 f_{-\eta_h x_2 x_1}^{\mathbf{K}_2 \mathbf{K}_1} + J_0^h d|u_0^h(z)|^2 f_{\eta_e x_2 x_1}^{\mathbf{K}_2 \mathbf{K}_1}\big)\big(N_{x_1 \mathbf{K}_1}^{l_1 v_1 v_2 l_2} - N_{x_2 \mathbf{K}_2}^{l_1 v_1 v_2 l_2}\big), \tag{A1j}$$

$$\bar{b}_{x_1 \mathbf{K}_1 x_2 \mathbf{K}_2}^{l_1 v_1 v_2 l_2}(z)^{II} = \sum_l \hbar \boldsymbol{\omega}_e \cdot \big(\mathbf{s}_{l_2 l}^e \bar{N}_{x_1 \mathbf{K}_1 x_2 \mathbf{K}_2}^{l_1 v_1 v_2 l}(z) - \mathbf{s}_{ll_1}^e \bar{N}_{x_1 \mathbf{K}_1 x_2 \mathbf{K}_2}^{l v_1 v_2 l_2}(z)\big)$$

$$+ \sum_v \hbar \boldsymbol{\omega}_h \cdot \big(\mathbf{s}_{v_2 v}^h \bar{N}_{x_1 \mathbf{K}_1 x_2 \mathbf{K}_2}^{l_1 v_1 v l_2}(z) - \mathbf{s}_{vv_1}^h \bar{N}_{x_1 \mathbf{K}_1 x_2 \mathbf{K}_2}^{l_1 v v_2 l_2}(z)\big), \tag{A1k}$$

$$\bar{b}_{x_1 \mathbf{K}_1 x_2 \mathbf{K}_2}^{l_1 v_1 v_2 l_2}(z)^{III} = \frac{J_{sd}}{V} d|u_0^e(z)|^2 \sum_{\substack{lnn'\\ x\mathbf{K}}} \mathbf{S}_{nn'} \cdot \big(\mathbf{s}_{l_2 l}^e f_{-\eta_h x_2 x}^{\mathbf{K}_2 \mathbf{K}} Q_{N_{n_1 x_1 \mathbf{K}_1 x\mathbf{K}}}^{n l_1 v_1 v_2 l}(z) - \mathbf{s}_{ll_1}^e f_{-\eta_h x x_1}^{\mathbf{K}\mathbf{K}_1} Q_{N_{nx\mathbf{K} x_2 \mathbf{K}_2}}^{n_2 l_1 v_1 v_2 l_2}(z)\big)$$

$$+ \frac{J_{pd}}{V} d|u_0^h(z)|^2 \sum_{\substack{vnn'\\ x\mathbf{K}}} \mathbf{S}_{nn'} \cdot \big(\mathbf{s}_{v_2 v}^h f_{\eta_e x_2 x}^{\mathbf{K}_2 \mathbf{K}} Q_{N_{n_1 x_1 \mathbf{K}_1 x\mathbf{K}}}^{n l_1 v_1 v l_2}(z) - \mathbf{s}_{vv_1}^h f_{\eta_e x x_1}^{\mathbf{K}\mathbf{K}_1} Q_{N_{nx\mathbf{K} x_2 \mathbf{K}_2}}^{n_2 l_1 v v_2 l_2}(z)\big)$$

$$+ \frac{J_0^e}{V} d|u_0^e(z)|^2 \sum_{x\mathbf{K}} \big(f_{-\eta_h x_2 x}^{\mathbf{K}_2 \mathbf{K}} \bar{N}_{x_1 \mathbf{K}_1 x\mathbf{K}}^{l_1 v_1 v_2 l_2}(z) - f_{-\eta_h x x_1}^{\mathbf{K}\mathbf{K}_1} \bar{N}_{x\mathbf{K} x_2 \mathbf{K}_2}^{l_1 v_1 v_2 l_2}(z)\big)$$

$$+ \frac{J_0^h}{V} d|u_0^h(z)|^2 \sum_{x\mathbf{K}} \big(f_{\eta_e x_2 x}^{\mathbf{K}_2 \mathbf{K}} \bar{N}_{x_1 \mathbf{K}_1 x\mathbf{K}}^{l_1 v_1 v_2 l_2}(z) - f_{\eta_e x x_1}^{\mathbf{K}\mathbf{K}_1} \bar{N}_{x\mathbf{K} x_2 \mathbf{K}_2}^{l_1 v_1 v_2 l_2}(z)\big). \tag{A1l}$$

APPENDIX B: QUANTUM KINETIC EQUATIONS OF MOTION WITH PINNED HOLE SPIN

In this section, we provide the equations of motion corresponding to the variables defined in Eq. (28) after performing an angle-averaging in $\mathbf{K}$ space. Using the Einstein summation convention, the equations read

$$\frac{\partial}{\partial t} n_{x_1 K_1} = \frac{1}{\hbar} \mathbf{E} \cdot \mathbf{M} 2\mathrm{Im}\big[y_{x_1}^\uparrow \phi_{x_1}\big]\delta_{K_1,0} - \frac{J_{sd} N_{\mathrm{Mn}}}{\hbar V^2} \sum_{xK} 2\mathrm{Im}\big[Q_{-\eta_h ixK}^{\ ix_1 K_1}\big] + \frac{J_{pd} N_{\mathrm{Mn}}}{\hbar V^2} \sum_{xK} \mathrm{Im}\big[Q_{\eta_e zxK}^{\ 0x_1 K_1}\big]$$

$$- \frac{J_0^e N_{\mathrm{Mn}}}{\hbar V^2} \sum_{xK} 2\mathrm{Im}\big[Z_{-\eta_h\ xK}^{\ 0x_1 K_1}\big] - \frac{J_0^h N_{\mathrm{Mn}}}{\hbar V^2} \sum_{xK} 2\mathrm{Im}\big[Z_{\eta_e\ xK}^{\ 0x_1 K_1}\big], \tag{B1a}$$

$$\frac{\partial}{\partial t} s_{x_1 K_1}^l = \frac{1}{\hbar} \mathbf{E} \cdot \mathbf{M}\big(\mathrm{Im}\big[y_{x_1}^\uparrow \phi_{x_1}\big]\delta_{K_1,0}\delta_{l,z} + \mathrm{Im}\big[y_{x_1}^\downarrow \phi_{x_1}\big]\delta_{K_1,0}\delta_{l,x} - \mathrm{Re}\big[y_{x_1}^\downarrow \phi_{x_1}\big]\delta_{K_1,0}\delta_{l,y}\big) + \epsilon_{ijl}\omega_e^i s_{x_1 K_1}^j$$

$$+ \frac{J_{sd} N_{\mathrm{Mn}}}{\hbar V^2} \sum_{xK} \big(\epsilon_{ijl}\mathrm{Re}\big[Q_{-\eta_h ixK}^{\ jx_1 K_1}\big] - \frac{1}{2}\mathrm{Im}\big[Q_{-\eta_h lxK}^{\ 0x_1 K_1}\big]\big) + \frac{J_{pd} N_{\mathrm{Mn}}}{\hbar V^2} \sum_{xK} \mathrm{Im}\big[Q_{\eta_e zxK}^{\ lx_1 K_1}\big]$$

$$- \frac{J_0^e N_{\mathrm{Mn}}}{\hbar V^2} \sum_{xK} 2\mathrm{Im}\big[Z_{-\eta_h\ xK}^{\ lx_1 K_1}\big] - \frac{J_0^h N_{\mathrm{Mn}}}{\hbar V^2} \sum_{xK} 2\mathrm{Im}\big[Z_{\eta_e\ xK}^{\ lx_1 K_1}\big], \tag{B1b}$$

$$\frac{\partial}{\partial t} y_{x_1}^{\uparrow/\downarrow} = \frac{i}{\hbar} \mathbf{E} \cdot \mathbf{M}\phi_{x_1}\delta_{\uparrow/\downarrow,\uparrow} - i\left(\omega_{0x_1} \pm \frac{1}{2}\omega_e^z - \frac{1}{2}\omega_h^z + \frac{(J_0^e + J_0^h)N_{\mathrm{Mn}}}{\hbar V}\right)y_{x_1}^{\uparrow/\downarrow} - i\frac{1}{2}\omega_e^\mp y_{x_1}^{\downarrow/\uparrow}$$

$$- i\frac{J_{sd} N_{\mathrm{Mn}}}{2\hbar V^2} \sum_{xK} \big(\pm q_{-\eta_h zxK}^{\uparrow/\downarrow x_1} + q_{-\eta_h \mp xK}^{\downarrow/\uparrow x_1}\big) + i\frac{J_{pd} N_{\mathrm{Mn}}}{2\hbar V^2} \sum_{xK} q_{\eta_e zxK}^{\uparrow/\downarrow x_1}$$

$$- i\frac{J_0^e N_{\mathrm{Mn}}}{\hbar V^2} \sum_{xK} z_{-\eta_h xK}^{\uparrow/\downarrow x_1} - i\frac{J_0^h N_{\mathrm{Mn}}}{\hbar V^2} \sum_{xK} z_{\eta_e xK}^{\uparrow/\downarrow x_1}, \tag{B1c}$$

$$\frac{\partial}{\partial t} q_{\eta l x_1 K_1}^{\uparrow/\downarrow x_2} = -i\left(\omega_{x_1 K_1} \pm \frac{1}{2}\omega_{\mathrm{e}}^z - \frac{1}{2}\omega_{\mathrm{h}}^z + \frac{I\left(J_0^{\mathrm{e}} + J_0^{\mathrm{h}}\right)N_{\mathrm{Mn}}}{\hbar V}\right) q_{\eta l x_1 K_1}^{\uparrow/\downarrow x_2} - i\frac{1}{2}\omega_{\mathrm{e}}^{\mp} q_{\eta l x_1 K_1}^{\downarrow/\uparrow x_2} + \epsilon_{ijl}\omega_{\mathrm{Mn}}^i q_{\eta j x_1 K_1}^{\uparrow/\downarrow x_2}$$

$$- i\frac{I J_{sd}}{2\hbar} F_{\eta\ x_2 x_1}^{-\eta_{\mathrm{h}} 0 K_1}\left(\pm \langle S^l S^z\rangle y_{x_2}^{\uparrow/\downarrow} + \langle S^l S^{\mp}\rangle y_{x_2}^{\downarrow/\uparrow}\right) + i\frac{I J_{pd}}{2\hbar} F_{\eta\ x_2 x_1}^{\eta_{\mathrm{e}} 0 K_1} y_{x_2}^{\uparrow/\downarrow}$$

$$- i\frac{I}{\hbar}\langle S^l\rangle\left(J_0^{\mathrm{e}} F_{\eta\ x_2 x_1}^{-\eta_{\mathrm{h}} 0 K_1} + J_0^{\mathrm{h}} F_{\eta\ x_2 x_1}^{\eta_{\mathrm{e}} 0 K_1}\right) y_{x_2}^{\uparrow/\downarrow}, \tag{B1d}$$

$$\frac{\partial}{\partial t} z_{\eta x_1 K_1}^{\uparrow/\downarrow x_2} = -i\left(\omega_{x_1 K_1} \pm \frac{1}{2}\omega_{\mathrm{e}}^z - \frac{1}{2}\omega_{\mathrm{h}}^z + \frac{I\left(J_0^{\mathrm{e}} + J_0^{\mathrm{h}}\right)N_{\mathrm{Mn}}}{\hbar V}\right) z_{\eta x_1 K_1}^{\uparrow/\downarrow x_2} - i\frac{1}{2}\omega_{\mathrm{e}}^{\mp} z_{\eta x_1 K_1}^{\downarrow/\uparrow x_2}$$

$$- i\frac{I J_{sd}}{2\hbar} F_{\eta\ x_2 x_1}^{-\eta_{\mathrm{h}} 0 K_1}\left(\pm \langle S^z\rangle y_{x_2}^{\uparrow/\downarrow} + \langle S^{\mp}\rangle y_{x_2}^{\downarrow/\uparrow}\right) + i\frac{I J_{pd}}{2\hbar} F_{\eta\ x_2 x_1}^{\eta_{\mathrm{e}} 0 K_1} y_{x_2}^{\uparrow/\downarrow}$$

$$- i\frac{I}{\hbar}\langle S^l\rangle\left(J_0^{\mathrm{e}} F_{\eta\ x_2 x_1}^{-\eta_{\mathrm{h}} 0 K_1} + J_0^{\mathrm{h}} F_{\eta\ x_2 x_1}^{\eta_{\mathrm{e}} 0 K_1}\right) y_{x_2}^{\uparrow/\downarrow}, \tag{B1e}$$

$$\frac{\partial}{\partial t} Q_{\eta l x_1 K_1}^{0 x_2 K_2} = -i\left(\omega_{x_2 K_2} - \omega_{x_1 K_1}\right) Q_{\eta l x_1 K_1}^{0 x_2 K_2} + \epsilon_{ijl}\omega_{\mathrm{Mn}}^i Q_{\eta j x_1 K_1}^{0 x_2 K_2} + \frac{i}{2\hbar}\mathbf{E}\cdot\mathbf{M}\left(\left(q_{\eta l x_1 K_1}^{\uparrow x_2}\phi_{x_2}\right)^* \delta_{K_2,0} - q_{\eta l x_2 K_2}^{\uparrow x_1}\phi_{x_1}\delta_{K_1,0}\right)$$

$$+ i\frac{I J_{sd}}{\hbar} F_{\eta\ x_1 x_2}^{-\eta_{\mathrm{h}} K_1 K_2}\left(\langle S^i S^l\rangle s_{x_2 K_2}^i - \langle S^l S^i\rangle s_{x_1 K_1}^i\right) - i\frac{I J_{pd}}{\hbar} F_{\eta\ x_1 x_2}^{\eta_{\mathrm{e}} K_1 K_2}\frac{1}{2}\left(\langle S^z S^l\rangle n_{x_2 K_2} - \langle S^l S^z\rangle n_{x_1 K_1}\right)$$

$$+ i\frac{I}{\hbar}\langle S^l\rangle\left(J_0^{\mathrm{e}} F_{\eta\ x_1 x_2}^{-\eta_{\mathrm{h}} K_1 K_2} + J_0^{\mathrm{h}} F_{\eta\ x_1 x_2}^{\eta_{\mathrm{e}} K_1 K_2}\right)\left(n_{x_2 K_2} - n_{x_1 K_1}\right), \tag{B1f}$$

$$\frac{\partial}{\partial t} Q_{\eta l x_1 K_1}^{m x_2 K_2} = -i\left(\omega_{x_2 K_2} - \omega_{x_1 K_1}\right) Q_{\eta l x_1 K_1}^{m x_2 K_2} + \epsilon_{ijm}\omega_{\mathrm{e}}^i Q_{\eta l x_1 K_1}^{j x_2 K_2} + \epsilon_{ijl}\omega_{\mathrm{Mn}}^i Q_{\eta j x_1 K_1}^{m x_2 K_2}$$

$$+ \frac{i}{2\hbar}\mathbf{E}\cdot\mathbf{M}\left[\left(\left(q_{\eta l x_1 K_1}^{\uparrow x_2}\phi_{x_2}\right)^* \delta_{K_2,0} - q_{\eta l x_2 K_2}^{\uparrow x_1}\phi_{x_1}\delta_{K_1,0}\right)\delta_{m,z} + \left(\left(q_{\eta l x_1 K_1}^{\downarrow x_2}\phi_{x_2}\right)^* \delta_{K_2,0} - q_{\eta l x_2 K_2}^{\downarrow x_1}\phi_{x_1}\delta_{K_1,0}\right)\delta_{m,x}\right.$$

$$\left.+ i\left(\left(q_{\eta l x_1 K_1}^{\downarrow x_2}\phi_{x_2}\right)^* \delta_{K_2,0} + q_{\eta l x_2 K_2}^{\downarrow x_1}\phi_{x_1}\delta_{K_1,0}\right)\delta_{m,y}\right] - i\frac{I J_{pd}}{\hbar} F_{\eta\ x_1 x_2}^{\eta_{\mathrm{e}} K_1 K_2}\frac{1}{2}\left(\langle S^z S^l\rangle s_{x_2 K_2}^m - \langle S^l S^z\rangle s_{x_1 K_1}^m\right)$$

$$+ i\frac{I J_{sd}}{2\hbar} F_{\eta\ x_1 x_2}^{-\eta_{\mathrm{h}} K_1 K_2}\left(\langle S^i S^l\rangle\left(\frac{1}{2}\delta_{i,m} n_{x_2 K_2} - i\epsilon_{ijm} s_{x_2 K_2}^j\right) - \langle S^l S^i\rangle\left(\frac{1}{2}\delta_{i,m} n_{x_1 K_1} + i\epsilon_{ijm} s_{x_1 K_1}^j\right)\right)$$

$$+ i\frac{I}{\hbar}\langle S^l\rangle\left(J_0^{\mathrm{e}} F_{\eta\ x_1 x_2}^{-\eta_{\mathrm{h}} K_1 K_2} + J_0^{\mathrm{h}} F_{\eta\ x_1 x_2}^{\eta_{\mathrm{e}} K_1 K_2}\right)\left(s_{x_2 K_2}^m - s_{x_1 K_1}^m\right), \tag{B1g}$$

$$\frac{\partial}{\partial t} Z_{\eta\ x_1 K_1}^{0 x_2 K_2} = -i\left(\omega_{x_2 K_2} - \omega_{x_1 K_1}\right) Z_{\eta\ x_1 K_1}^{0 x_2 K_2} + \frac{i}{2\hbar}\mathbf{E}\cdot\mathbf{M}\left(\left(z_{\eta x_1 K_1}^{\uparrow x_2}\phi_{x_2}\right)^* \delta_{K_2,0} - z_{\eta x_2 K_2}^{\uparrow x_1}\phi_{x_1}\delta_{K_1,0}\right)$$

$$+ i\frac{I J_{sd}}{\hbar} F_{\eta\ x_1 x_2}^{-\eta_{\mathrm{h}} K_1 K_2}\langle S^i\rangle\left(s_{x_2 K_2}^i - s_{x_1 K_1}^i\right) - i\frac{I J_{pd}}{\hbar} F_{\eta\ x_1 x_2}^{\eta_{\mathrm{e}} K_1 K_2}\frac{1}{2}\langle S^z\rangle\left(n_{x_2 K_2} - n_{x_1 K_1}\right)$$

$$+ i\frac{I}{\hbar}\left(J_0^{\mathrm{e}} F_{\eta\ x_1 x_2}^{-\eta_{\mathrm{h}} K_1 K_2} + J_0^{\mathrm{h}} F_{\eta\ x_1 x_2}^{\eta_{\mathrm{e}} K_1 K_2}\right)\left(n_{x_2 K_2} - n_{x_1 K_1}\right), \tag{B1h}$$

$$\frac{\partial}{\partial t} Z_{\eta\ x_1 K_1}^{l x_2 K_2} = -i\left(\omega_{x_2 K_2} - \omega_{x_1 K_1}\right) Z_{\eta\ x_1 K_1}^{l x_2 K_2} + \epsilon_{ijl}\omega_{\mathrm{e}}^i Z_{\eta\ x_1 K_1}^{j x_2 K_2} + \frac{i}{2\hbar}\mathbf{E}\cdot\mathbf{M}\left[\left(\left(z_{\eta x_1 K_1}^{\uparrow x_2}\phi_{x_2}\right)^* \delta_{K_2,0} - z_{\eta x_2 K_2}^{\uparrow x_1}\phi_{x_1}\delta_{K_1,0}\right)\delta_{l,z}\right.$$

$$\left.+ \left(\left(z_{\eta x_1 K_1}^{\downarrow x_2}\phi_{x_2}\right)^* \delta_{K_2,0} - z_{\eta x_2 K_2}^{\downarrow x_1}\phi_{x_1}\delta_{K_1,0}\right)\delta_{l,x} + i\left(\left(z_{\eta x_1 K_1}^{\downarrow x_2}\phi_{x_2}\right)^* \delta_{K_2,0} + z_{\eta x_2 K_2}^{\downarrow x_1}\phi_{x_1}\delta_{K_1,0}\right)\delta_{l,y}\right]$$

$$+ i\frac{I J_{sd}}{2\hbar} F_{\eta\ x_1 x_2}^{-\eta_{\mathrm{h}} K_1 K_2}\langle S^i\rangle\left(\left(\frac{1}{2}\delta_{i,l} n_{x_2 K_2} - i\epsilon_{ijl} s_{x_2 K_2}^j\right) - \left(\frac{1}{2}\delta_{i,l} n_{x_1 K_1} + i\epsilon_{ijl} s_{x_1 K_1}^j\right)\right)$$

$$- i\frac{I J_{pd}}{\hbar} F_{\eta\ x_1 x_2}^{\eta_{\mathrm{e}} K_1 K_2}\frac{1}{2}\langle S^z\rangle\left(s_{x_2 K_2}^l - s_{x_1 K_1}^l\right) + i\frac{I}{\hbar}\left(J_0^{\mathrm{e}} F_{\eta\ x_1 x_2}^{-\eta_{\mathrm{h}} K_1 K_2} + J_0^{\mathrm{h}} F_{\eta\ x_1 x_2}^{\eta_{\mathrm{e}} K_1 K_2}\right)\left(s_{x_2 K_2}^l - s_{x_1 K_1}^l\right). \tag{B1i}$$

[1] T. Dietl, Nat. Mater. **9**, 965 (2010).

[2] H. Ohno, Nat. Mater. **9**, 952 (2010).

[3] I. Žutić, J. Fabian, and S. Das Sarma, Rev. Mod. Phys. **76**, 323 (2004).

[4] D. Awschalom and M. Flatté, Nat. Phys. **3**, 153 (2007).

[5] D. D. Awschalom, L. C. Bassett, A. S. Dzurak, E. L. Hu, and J. R. Petta, Science **339**, 1174 (2013).

[6] J. Wunderlich, B. Park, A. C. Irvine, L. P. Zrbo, E. Rozkotov, P. Nemec, V. Novk, J. Sinova, and T. Jungwirth, Science **330**, 1801 (2010).

[7] C. Chappert, A. Fert, and F. N. Van Dau, Nat. Mater. **6**, 813 (2007).

[8] T. Dietl and H. Ohno, Rev. Mod. Phys. **86**, 187 (2014).

[9] *Introduction to the Physics of Diluted Magnetic Semiconductors*, edited by J. Kossut and J. A. Gaj (Springer, Berlin, 2010).

[10] J. K. Furdyna, J. Appl. Phys. **64**, R29 (1988).

[11] J. Kossut, Phys. Status Solidi B **72**, 359 (1975).

[12] G. Bastard and R. Ferreira, Surf. Sci. **267**, 335 (1992).

[13] Ł. Cywiński and L. J. Sham, Phys. Rev. B **76**, 045205 (2007).

[14] M. Nawrocki, R. Planel, G. Fishman, and R. Galazka, Phys. Rev. Lett. **46**, 735 (1981).

[15] M. D. Kapetanakis, J. Wang, and I. E. Perakis, J. Opt. Soc. Am. B **29**, A95 (2012).

[16] S. Das Sarma, E. H. Hwang, and A. Kaminski, Phys. Rev. B **67**, 155201 (2003).

[17] C. Camilleri, F. Teppe, D. Scalbert, Y. G. Semenov, M. Nawrocki, M. Dyakonov, J. Cibert, S. Tatarenko, and T. Wojtowicz, Phys. Rev. B **64**, 085331 (2001).

[18] H. Krenn, K. Kaltenegger, T. Dietl, J. Spałek, and G. Bauer, Phys. Rev. B **39**, 10918 (1989).

[19] J. Debus, V. Y. Ivanov, S. M. Ryabchenko, D. R. Yakovlev, A. A. Maksimov, Y. G. Semenov, D. Braukmann, J. Rautert, U. Löw, M. Godlewski, A. Waag, and M. Bayer, Phys. Rev. B **93**, 195307 (2016).

[20] D. Awschalom and N. Samarth, J. Magn. Magn. Mater. **200**, 130 (1999).

[21] S. A. Crooker, D. D. Awschalom, J. J. Baumberg, F. Flack, and N. Samarth, Phys. Rev. B **56**, 7574 (1997).

[22] J. J. Baumberg, D. D. Awschalom, N. Samarth, H. Luo, and J. K. Furdyna, Phys. Rev. Lett. **72**, 717 (1994).

[23] *Semiconductors and Semimetals*, edited by J. K. Furdyna and J. Kossut (Academic, San Diego, 1988).

[24] H. Ohno, A. Shen, F. Matsukura, A. Oiwa, A. Endo, S. Katsumoto, and Y. Iye, Appl. Phys. Lett. **69**, 363 (1996).

[25] T. Jungwirth, J. Sinova, J. Mašek, J. Kučera, and A. H. MacDonald, Rev. Mod. Phys. **78**, 809 (2006).

[26] T. Jungwirth, J. König, J. Sinova, J. Kučera, and A. H. MacDonald, Phys. Rev. B **66**, 012402 (2002).

[27] T. Jungwirth, K. Y. Wang, J. Mašek, K. W. Edmonds, J. König, J. Sinova, M. Polini, N. A. Goncharuk, A. H. MacDonald, M. Sawicki, A. W. Rushforth, R. P. Campion, L. X. Zhao, C. T. Foxon, and B. L. Gallagher, Phys. Rev. B **72**, 165204 (2005).

[28] T. Jungwirth, J. Mašek, K. Y. Wang, K. W. Edmonds, M. Sawicki, M. Polini, J. Sinova, A. H. MacDonald, R. P. Campion, L. X. Zhao, N. R. S. Farley, T. K. Johal, G. van der Laan, C. T. Foxon, and B. L. Gallagher, Phys. Rev. B **73**, 165205 (2006).

[29] T. Jungwirth, P. Horodyská, N. Tesařová, P. Němec, J. Šubrt, P. Malý, P. Kužel, C. Kadlec, J. Mašek, I. Němec, M. Orlita, V. Novák, K. Olejník, Z. Šobáň, P. Vašek, P. Svoboda, and J. Sinova, Phys. Rev. Lett. **105**, 227201 (2010).

[30] R. Bouzerar and G. Bouzerar, Europhys. Lett. **92**, 47006 (2010).

[31] Z. Ben Cheikh, S. Cronenberger, M. Vladimirova, D. Scalbert, F. Perez, and T. Wojtowicz, Phys. Rev. B **88**, 201306 (2013).

[32] Y. G. Semenov and F. V. Kirichenko, Semicond. Sci. Technol. **11**, 1268 (1996).

[33] Y. G. Semenov, Phys. Rev. B **67**, 115319 (2003).

[34] J. H. Jiang, Y. Zhou, T. Korn, C. Schüller, and M. W. Wu, Phys. Rev. B **79**, 155201 (2009).

[35] M. Vladimirova, S. Cronenberger, P. Barate, D. Scalbert, F. J. Teran, and A. P. Dmitriev, Phys. Rev. B **78**, 081305 (2008).

[36] E. Tsitsishvili and H. Kalt, Phys. Rev. B **73**, 195402 (2006).

[37] M. Z. Maialle, E. A. de Andrada e Silva, and L. J. Sham, Phys. Rev. B **47**, 15776 (1993).

[38] M. Maialle and L. Sham, Surf. Sci. **305**, 256 (1994).

[39] P. E. Selbmann, M. Gulia, F. Rossi, E. Molinari, and P. Lugli, Phys. Rev. B **54**, 4660 (1996).

[40] Y. Tang, W. Xie, K. C. Mandal, J. A. McGuire, and C. W. Lai, J. Appl. Phys. **118**, 113103 (2015).

[41] S. Adachi, T. Miyashita, S. Takeyama, Y. Takagi, and A. Tackeuchi, J. Lumin. **72**, 307 (1997).

[42] C. Thurn and V. M. Axt, Phys. Rev. B **85**, 165203 (2012).

[43] M. Cygorek, P. I. Tamborenea, and V. M. Axt, Phys. Rev. B **93**, 205201 (2016).

[44] M. Cygorek, F. Ungar, P. I. Tamborenea, and V. M. Axt, Phys. Rev. B **95**, 045204 (2017).

[45] M. Cygorek, F. Ungar, P. I. Tamborenea, and V. M. Axt, Proc. SPIE **9931**, 993147 (2016).

[46] M. Cygorek and V. M. Axt, J. Phys.: Conf. Ser. **647**, 012042 (2015).

[47] C. Thurn, M. Cygorek, V. M. Axt, and T. Kuhn, Phys. Rev. B **87**, 205301 (2013).

[48] R. Kubo, J. Phys. Soc. Jpn. **17**, 1100 (1962).

[49] V. M. Axt and A. Stahl, Z. Phys. B **93**, 195 (1994).

[50] V. M. Axt and S. Mukamel, Rev. Mod. Phys. **70**, 145 (1998).

[51] H. Haken, *Quantum Field Theory of Solids* (North-Holland, Amsterdam, 1976).

[52] A. Stahl, Z. Phys. B **72**, 371 (1988).

[53] W. Huhn and A. Stahl, Phys. Status Solidi B **124**, 167 (1984).

[54] *Excitons*, edited by E. I. Rashba and M. D. Sturge (North-Holland, Amsterdam, 1982).

[55] I. Strzalkowski, S. Joshi, and C. R. Crowell, Appl. Phys. Lett. **28**, 350 (1976).

[56] R. Winkler, *Spin-Orbit Coupling Effects in Two-Dimensional Electron and Hole Systems* (Springer, Berlin, 2003).

[57] F. Rossi and T. Kuhn, Rev. Mod. Phys. **74**, 895 (2002).

[58] F. Ungar, M. Cygorek, P. I. Tamborenea, and V. M. Axt, Phys. Rev. B **91**, 195201 (2015).

[59] M. W. Wu, J. H. Jiang, and M. Q. Weng, Phys. Rep. **493**, 61 (2010).

[60] G. V. Astakhov, D. R. Yakovlev, V. P. Kochereshko, W. Ossau, W. Faschinger, J. Puls, F. Henneberger, S. A. Crooker, Q. McCulloch, D. Wolverson, N. A. Gippius, and A. Waag, Phys. Rev. B **65**, 165335 (2002).

[61] K. Siantidis, V. M. Axt, and T. Kuhn, Phys. Rev. B **65**, 035303 (2001).

[62] R. Zimmermann and J. Wauer, J. Lumin. **58**, 271 (1994).

[63] M. Kira and S. W. Koch, Phys. Rev. A **78**, 022102 (2008).

[64] M. Kira and S. Koch, Prog. Quantum Electron. **30**, 155 (2006).

[65] T. Kuhn, *Theory of Transport Properties of Semiconductor Nanostructures* (Springer US, Boston, MA, 1998), Chap. Density matrix theory of coherent ultrafast dynamics, pp. 173–214.

[66] R. Zimmermann and E. Runge, J. Lumin. **60**, 320 (1994).

[67] R. Zimmermann, Phys. Status Solidi B **173**, 129 (1992).

[68] R. Zimmermann, Il Nuovo Cimento D **17**, 1801 (1995).

[69] G. Dresselhaus, J. Phys. Chem. Solids **1**, 14 (1956).

[70] R. C. Iotti and L. C. Andreani, Semicond. Sci. Technol. **10**, 1561 (1995).

[71] R. Winkler, Phys. Rev. B **51**, 14395 (1995).

[72] G. Bastard, *Wave Mechanics Applied to Semiconductor Heterostructures* (Les Éditions de Physique, France, 1996).

[73] X. L. Yang, S. H. Guo, F. T. Chan, K. W. Wong, and W. Y. Ching, Phys. Rev. A **43**, 1186 (1991).

[74] M. Cygorek and V. M. Axt, Phys. Rev. B **90**, 035206 (2014).

[75] *CdTe and Related Compounds; Physics, Defects, Hetero- and Nano-structures, Crystal Growth, Surfaces and Applications*, edited by R. Triboulet and P. Siffert, 1st ed., European Materials Research Society Series (Elsevier, Amsterdam, 2009).

Erratum: Quantum kinetic equations for the ultrafast spin dynamics of excitons in diluted magnetic semiconductor quantum wells after optical excitation [Phys. Rev. B 95, 245203 (2017)]

F. Ungar, M. Cygorek, and V. M. Axt

In Eq. (34b) there is a factor 2 missing in one of the terms proportional to $\delta(\omega_{xK} - \omega_{x_1 K_1})$. The correct equation should read

$$
\frac{\partial}{\partial t} \mathbf{s}_{x_1 K_1}^{\perp} = \mathbf{\Gamma}_{\mathbf{E}}^{\perp} + \frac{\pi I N_{\text{Mn}}}{\hbar^2 V^2} \sum_{xK} \Bigg\{ \delta\big(\omega_{xK} - \omega_{x_1 K_1}\big)\big(\mathbf{s}_{xK}^{\perp} - \mathbf{s}_{x_1 K_1}^{\perp}\big)\Big[\big(2J_0^{\text{e}2} - J_{sd}^2 b^{\parallel}\big) F_{\eta_{\text{h}} x x_1}^{\eta_{\text{h}} K K_1} + \big(J_{pd}^2 b^{\parallel} + 2J_0^{\text{h}2} - J_{pd} J_0^{\text{h}} b^0\big) F_{\eta_{\text{e}} x x_1}^{\eta_{\text{e}} K K_1}
$$
$$
- \big(2J_{pd} J_0^{\text{e}} b^0 + J_{pd} J_0^{\text{h}} b^0 - 4J_0^{\text{e}} J_0^{\text{h}}\big) F_{-\eta_{\text{h}} x x_1}^{\eta_{\text{e}} K K_1}\Big] - \Big[\frac{b^-}{2} \delta\big\{\omega_{xK} - \big[\omega_{x_1 K_1} + \big(\sigma_{\text{e}}^B \omega_{\text{e}} - \sigma_{\text{Mn}}^B \omega_{\text{Mn}}\big)\big]\big\}
$$
$$
+ \frac{b^+}{2} \delta\big\{\omega_{xK} - \big[\omega_{x_1 K_1} - \big(\sigma_{\text{e}}^B \omega_{\text{e}} - \sigma_{\text{Mn}}^B \omega_{\text{Mn}}\big)\big]\big\} + 2b^{\parallel} \delta\big(\omega_{xK} - \omega_{x_1 K_1}\big)\Big] J_{sd}^2 F_{\eta_{\text{h}} x x_1}^{\eta_{\text{h}} K K_1} \mathbf{s}_{x_1 K_1}^{\perp}\Big\}
$$
$$
+ \big(\boldsymbol{\omega}_{\text{e}} \times \mathbf{s}_{x_1 K_1}^{\perp}\big)\Bigg\{1 + \frac{1}{\omega_{\text{e}}} \frac{I N_{\text{Mn}}}{\hbar^2 V^2} \sum_{xK} \bigg[\frac{J_{sd}}{\omega_{xK} - \omega_{x_1 K_1}}\big[\big(2J_{pd} b^{\parallel} - 2J_0^{\text{h}} b^0\big) F_{-\eta_{\text{h}} x x_1}^{\eta_{\text{e}} K K_1} - 2J_0^{\text{e}} b^0 F_{\eta_{\text{h}} x x_1}^{\eta_{\text{h}} K K_1}\big]
$$
$$
+ \bigg(\frac{b^+}{\omega_{xK} - \big[\omega_{x_1 K_1} - \big(\sigma_{\text{e}}^B \omega_{\text{e}} - \sigma_{\text{Mn}}^B \omega_{\text{Mn}}\big)\big]} - \frac{b^-}{\omega_{xK} - \big[\omega_{x_1 K_1} + \big(\sigma_{\text{e}}^B \omega_{\text{e}} - \sigma_{\text{Mn}}^B \omega_{\text{Mn}}\big)\big]}\bigg) \frac{1}{2} J_{sd}^2 F_{\eta_{\text{h}} x x_1}^{\eta_{\text{h}} K K_1}\bigg]\Bigg\}. \tag{34b}
$$

Since only the parallel case is discussed in the paper and the equation for the perpendicular spin density was given merely for the sake of completeness, all results and discussions throughout the paper remain unaffected.

Furthermore, there are some typographical errors in Eqs. (B1) in Appendix B. The correct equations should read

$$
\frac{\partial}{\partial t} q_{\eta l x_1 K_1}^{\uparrow/\downarrow x_2} = -i\left(\omega_{x_1 K_1} \pm \frac{1}{2}\omega_{\text{e}}^z - \frac{1}{2}\omega_{\text{h}}^z + \frac{I\big(J_0^{\text{e}} + J_0^{\text{h}}\big) N_{\text{Mn}}}{\hbar V}\right) q_{\eta l x_1 K_1}^{\uparrow/\downarrow x_2} - i\frac{1}{2}\omega_{\text{e}}^{\mp} q_{\eta l x_1 K_1}^{\downarrow/\uparrow x_2} + \epsilon_{ijl}\omega_{\text{Mn}}^i q_{\eta j x_1 K_1}^{\uparrow/\downarrow x_2}
$$
$$
- i\frac{I J_{sd}}{2\hbar} F_{\eta\ x_2 x_1}^{-\eta_{\text{h}} 0 K_1}\big(\pm\langle S^l S^z\rangle y_{x_2}^{\uparrow/\downarrow} + \langle S^l S^{\mp}\rangle y_{x_2}^{\downarrow/\uparrow}\big) + i\frac{I J_{pd}}{2\hbar}\langle S^l S^z\rangle F_{\eta\ x_2 x_1}^{\eta_{\text{e}} 0 K_1} y_{x_2}^{\uparrow/\downarrow}
$$
$$
- i\frac{I}{\hbar}\langle S^l\rangle\big(J_0^{\text{e}} F_{\eta\ x_2 x_1}^{-\eta_{\text{h}} 0 K_1} + J_0^{\text{h}} F_{\eta\ x_2 x_1}^{\eta_{\text{e}} 0 K_1}\big) y_{x_2}^{\uparrow/\downarrow}, \tag{B1d}
$$
$$
\frac{\partial}{\partial t} z_{\eta x_1 K_1}^{\uparrow/\downarrow x_2} = -i\left(\omega_{x_1 K_1} \pm \frac{1}{2}\omega_{\text{e}}^z - \frac{1}{2}\omega_{\text{h}}^z + \frac{I\big(J_0^{\text{e}} + J_0^{\text{h}}\big) N_{\text{Mn}}}{\hbar V}\right) z_{\eta x_1 K_1}^{\uparrow/\downarrow x_2} - i\frac{1}{2}\omega_{\text{e}}^{\mp} z_{\eta x_1 K_1}^{\downarrow/\uparrow x_2}
$$
$$
- i\frac{I J_{sd}}{2\hbar} F_{\eta\ x_2 x_1}^{-\eta_{\text{h}} 0 K_1}\big(\pm\langle S^z\rangle y_{x_2}^{\uparrow/\downarrow} + \langle S^{\mp}\rangle y_{x_2}^{\downarrow/\uparrow}\big) + i\frac{I J_{pd}}{2\hbar}\langle S^z\rangle F_{\eta\ x_2 x_1}^{\eta_{\text{e}} 0 K_1} y_{x_2}^{\uparrow/\downarrow}
$$
$$
- i\frac{I}{\hbar}\big(J_0^{\text{e}} F_{\eta\ x_2 x_1}^{-\eta_{\text{h}} 0 K_1} + J_0^{\text{h}} F_{\eta\ x_2 x_1}^{\eta_{\text{e}} 0 K_1}\big) y_{x_2}^{\uparrow/\downarrow}. \tag{B1e}
$$

The errors in the two equations above only occurred during preparation of the paper and are not present in the numerical evaluation of the equations. Thus, all numerical results of the paper have been obtained using the correct equations and remain unchanged.

Publication 2

Trend reversal in the magnetic-field dependence of exciton spin-transfer rates in diluted magnetic semiconductors due to non-Markovian dynamics

F. Ungar, M. Cygorek, and V. M. Axt

Trend reversal in the magnetic-field dependence of exciton spin-transfer rates in diluted magnetic semiconductors due to non-Markovian dynamics

F. Ungar, M. Cygorek, and V. M. Axt

Theoretische Physik III, Universität Bayreuth, 95440 Bayreuth, Germany

We investigate theoretically the influence of an external magnetic field on the spin dynamics of excitons in diluted magnetic semiconductor quantum wells. To this end, we apply a quantum kinetic theory beyond the Markov approximation which reveals that non-Markovian effects can significantly influence the exciton spin dynamics. If the magnetic field is oriented parallel to the growth direction of the well, the Markovian spin-transfer rate decreases monotonically with increasing field as predicted by Fermi's golden rule. The quantum kinetic theory follows this result qualitatively but predicts pronounced quantitative differences in the spin-transfer rate as well as in the long-time spin polarization. However, for an in-plane magnetic field, where the Markovian spin-transfer rate first drops and then increases again, quantum kinetic effects become so pronounced that the Markovian trend is completely reversed. This is made evident by a distinct maximum of the rate followed by a monotonic decrease. The deviations can be traced back to a redistribution of carriers in energy space caused by correlations between excitons and magnetic dopants. The same effect leads to a finite electron-spin polarization at long times in longitudinal as well as transverse fields which is much larger than the corresponding Markovian prediction.

I. INTRODUCTION

Diluted magnetic semiconductors (DMS) [1–4] form a widely studied subclass of semiconductors that show promise for spintronics applications [5–8]. In these systems a small number of magnetic impurities such as manganese are introduced to create localized magnetic moments that interact with the carrier spin. We focus on the class of paramagnetic II-VI DMS where these ions are incorporated isoelectrically. The carrier spin dynamics in such systems is typically studied using optical pump-probe experiments while varying parameters such as doping concentration, temperature, well width, and magnetic field [9–17]. Regarding the dependence of dynamical spin relaxation on the magnetic field, a transverse field (Voigt geometry) is of particular interest since it allows not only a direct measurement of electron and hole g factors via their respective precession frequencies but also enables a straightforward separation of electron, hole, and manganese spin relaxation effects in experiments [9,10].

However, fundamental observations in the ultrafast spin dynamics in these systems remain not understood, as evident by the persistent underestimation of measured spin-transfer rates by calculations using Fermi's golden rule for quasifree electrons as well as an observed nonmonotonic dependence of the transverse spin relaxation on magnetic field [13,14]. It has been argued that some of the discrepancies between theory and experiment are the result of probing excitons rather than quasifree carriers since typical experiments are performed at the exciton resonance [10,12,14,15,18–21]. However, a simple replacement of the electron mass by the exciton mass in Fermi's golden rule strongly overestimates the spin decay. It has been shown only recently that theoretically and experimentally obtained spin-transfer rates for vanishing magnetic field can be reconciled if correlation effects are taken into account [22].

An analysis of the spin dynamics for quasifree carriers has revealed that non-Markovian effects become relevant for excitations in the vicinity of sharp structures in the electronic density of states [23]. In particular, this applies to the vicinity of the band edge where the density of states drops abruptly to zero. For electrons in a parabolic band structure, it has been shown [23] that the spin dynamics becomes Markovian provided that the kinetic energy $\hbar\omega$ of the carriers is large compared to $\hbar\tau^{-1}$ where τ^{-1} denotes the Markovian spin relaxation rate. For direct optical excitation of excitons this condition is never fulfilled since light couples only to excitons with vanishing center-of-mass motion. Thus, it can be expected that non-Markovian features will be pronounced in this case which will be corroborated in the present paper.

In this paper, we investigate theoretically the magnetic-field dependence of exciton spin-transfer rates in longitudinal as well as transverse fields. Although the spin dynamics of excitons has been investigated theoretically before, most theories do not go beyond Fermi's golden rule and therefore do not account for correlations between the carrier and the impurity subsystem [24–28], despite the fact that correlation effects have been shown to influence the spin dynamics even for quasifree carriers [29,30] and are necessary in order to obtain a quantitative agreement between theory and experiment for vanishing magnetic field. We perform numerical calculations using a recently developed quantum kinetic theory (QKT) for the spin dynamics of excitons [22] that accounts for genuine many-body correlations not captured by Fermi's golden rule. Apart from the usually considered $s-d$ exchange interaction in DMS [1,2] between electrons and magnetic impurities our theory also includes the nonmagnetic scattering of carriers at the localized impurities, which turns out to have a profound impact on the spin dynamics in finite magnetic fields despite

the fact that nonmagnetic scattering does not contribute to Markovian spin-transfer rates.

In Faraday geometry, it is found that the Markovian spin-transfer rate as a function of magnetic field decreases monotonically. A systematic comparison of theses results with numerically extracted exciton spin-transfer rates from a quantum kinetic calculation reveals quantitative differences but shows a similar overall trend. However, in Voigt configuration, where the Markovian rate increases after a short initial decrease, the QKT predicts a completely reversed dependency of the spin-transfer rate on the magnitude of the applied field. There, after a small initial rise of the rate with increasing magnetic field, a maximum followed by a virtually monotonic decrease appears. The origin of these deviations between quantum kinetic and Markovian calculations can be traced back to a redistribution of exciton center-of-mass momenta to regions which are inaccessible in the Markov limit. Such a redistribution of carrier momenta is made possible by a significant correlation energy which cannot be captured in a single-particle approach and is particularly caused by nonmagnetic scattering of carriers at impurities. Moreover, the spin polarization at long times predicted by the QKT is generally much larger than the corresponding Markovian value, an effect which is especially pronounced in Voigt geometry where a dephasing to zero is expected.

The paper is structured as follows: First, we discuss the different contributions to the Hamiltonian modeling the system and briefly recapitulate the derivation of the quantum kinetic equations from Ref. [22]. Second, the Markov limit of the quantum kinetic equations is established in order to obtain expressions for exciton spin-transfer rates in Faraday and Voigt configuration which can be compared with the predictions of the QKT. The Markovian expressions are also used to obtain analytical insights into correlation energies in the system. Turning to the numerics, we perform simulations of the exciton spin dynamics in a $Zn_{1-x}Mn_xSe$ quantum well in a longitudinal magnetic field and discuss the role of the correlation energy as well as the time-resolved redistribution of exciton kinetic energies. Finally, after discussing the spin dynamics in Voigt configuration, we numerically extract characteristic spin-transfer rates for both longitudinal and transverse magnetic fields from our simulations and compare them with the corresponding Markovian predictions.

II. MODEL AND EQUATIONS OF MOTION

In this section we briefly present the Hamiltonian along with the relevant dynamical quantities for the quantum kinetic description of the exciton spin.

A. Model

Our aim is to study the magnetic-field dependence of the spin transfer between excitons and the manganese subsystem in an intrinsic DMS quantum well excited at the $1s$ exciton resonance. To this end, we employ a recently developed quantum kinetic theory [22] accounting for correlation effects not captured by Fermi's golden rule. The model Hamiltonian comprises the following contributions [22]:

$$H = H_0^e + H_0^h + H_{conf} + H_C + H_Z^e + H_Z^h + H_Z^{Mn} + H_{lm}$$
$$+ H_{sd} + H_{pd} + H_{nm}^e + H_{nm}^h. \quad (1)$$

The crystal Hamiltonian for electrons and holes can be written as

$$H_0^e + H_0^h = \sum_{l\mathbf{k}} E_{\mathbf{k}}^l c_{l\mathbf{k}}^\dagger c_{l\mathbf{k}} + \sum_{v\mathbf{k}} E_{\mathbf{k}}^v d_{v\mathbf{k}}^\dagger d_{v\mathbf{k}}, \quad (2)$$

where $c_{l\mathbf{k}}^\dagger$ ($c_{l\mathbf{k}}$) denotes the electron creation (annihilation) operator in the conduction band l with wave vector $\mathbf{k}$ and $d_{v\mathbf{k}}^\dagger$ ($d_{v\mathbf{k}}$) is the respective creation (annihilation) operator for holes in the valence band v. Together with the confinement given by H_{conf} and the Coulomb interaction

$$H_C = \frac{1}{2} \sum_{\mathbf{kk'q}} \left(V_{\mathbf{q}} \sum_{ll'} c_{l'\mathbf{k'+q}}^\dagger c_{l\mathbf{k-q}}^\dagger c_{l\mathbf{k}} c_{l'\mathbf{k'}} \right.$$
$$+ V_{\mathbf{q}} \sum_{vv'} d_{v'\mathbf{k'+q}}^\dagger d_{v\mathbf{k-q}}^\dagger d_{v\mathbf{k}} d_{v'\mathbf{k'}}$$
$$\left. - 2V_{\mathbf{q}} \sum_{lv} c_{l\mathbf{k'+q}}^\dagger d_{v\mathbf{k-q}}^\dagger d_{v\mathbf{k}} c_{l\mathbf{k'}} \right), \quad (3)$$

a diagonalization of these four contributions in the single-pair subspace yields the exciton wave functions and energies. We consider a quantum well of width d with infinitely high barriers and project the wave function onto the lowest confinement state $u_0(z) = \sqrt{\frac{2}{d}} \cos\left(\frac{\pi}{d}z\right)$. The Fourier components of the bulk Coulomb potential before the projection onto the well states are $V_{\mathbf{q}} = \frac{e^2}{\epsilon\epsilon_0} \frac{1}{q^2}$, where e is the elementary charge, ϵ_0 denotes the vacuum permittivity, and ϵ is the static dielectric constant of the material.

A homogeneous external magnetic field $\mathbf{B}$ is incorporated via the Zeeman terms

$$H_Z^e = g_e \mu_B \sum_{ll'\mathbf{k}} \mathbf{B} \cdot \mathbf{s}_{ll'}^e c_{l\mathbf{k}}^\dagger c_{l'\mathbf{k}}, \quad (4a)$$

$$H_Z^h = -6\kappa \mu_B \sum_{vv'\mathbf{k}} \mathbf{B} \cdot \mathbf{s}_{vv'}^h d_{v\mathbf{k}}^\dagger d_{v'\mathbf{k}}, \quad (4b)$$

$$H_Z^{Mn} = g_{Mn} \mu_B \sum_{Inn'} \mathbf{B} \cdot \mathbf{S}_{nn'} \hat{P}_{nn'}^I, \quad (4c)$$

for electrons, holes, and Mn atoms, respectively. We denote the vector of electron spin matrices by $\mathbf{s}_{ll'}^e = \frac{1}{2}\boldsymbol{\sigma}_{ll'}$, where $\boldsymbol{\sigma}_{ll'}$ is the vector of Pauli matrices, and $\mathbf{s}_{vv'}^h = \frac{1}{3}\mathbf{J}_{vv'}$ describes the hole spin in terms of the vector of 4×4 angular momentum matrices $\mathbf{J}_{vv'}$ with $v, v' \in \{-\frac{3}{2}, -\frac{1}{2}, \frac{1}{2}, \frac{3}{2}\}$ [31]. Finally, $\mathbf{S}_{nn'}$ denotes the vector of impurity spin matrices with $n, n' \in \{-\frac{5}{2}, -\frac{3}{2}, ..., \frac{5}{2}\}$. To describe the impurity spin at a particular site in the DMS, we make use of the operator $\hat{P}_{nn'}^I = |I,n\rangle\langle I,n'|$ where the ket $|I,n\rangle$ denotes the spin state n of the Ith impurity atom. The constant g_e is the g factor of the electrons, κ is the isotropic valence-band g factor [32], g_{Mn} denotes the impurity g factor, and μ_B is the Bohr magneton. The light-matter coupling in the dipole approximation [33] is given by

$$H_{lm} = -\sum_{lv\mathbf{k}} (\mathbf{E} \cdot \mathbf{M}_{lv} c_{l\mathbf{k}}^\dagger d_{v-\mathbf{k}}^\dagger + \mathbf{E} \cdot \mathbf{M}_{vl} d_{v-\mathbf{k}} c_{l\mathbf{k}}) \quad (5)$$

with an electric field $\mathbf{E}$ and the dipole moment $\mathbf{M}_{lv}$ for a transition from a state in the valence subband v to the conduction subband l.

The exchange interaction between the s-like conduction-band electrons and the p-like valence-band holes with localized d-shell electrons of the Mn impurities typically dominates the spin dynamics in DMS and can be written as [1,2,22,34]

$$H_{sd} = \frac{J_{sd}}{V} \sum_{\substack{Inn' \\ ll'\mathbf{kk'}}} \mathbf{S}_{nn'} \cdot \mathbf{s}_{ll'}^{\mathrm{e}} c_{l\mathbf{k}}^{\dagger} c_{l'\mathbf{k'}} e^{i(\mathbf{k'}-\mathbf{k})\cdot\mathbf{R}_I} \hat{P}_{nn'}^{I}, \quad (6a)$$

$$H_{pd} = \frac{J_{pd}}{V} \sum_{\substack{Inn' \\ vv'\mathbf{kk'}}} \mathbf{S}_{nn'} \cdot \mathbf{s}_{vv'}^{\mathrm{h}} d_{v\mathbf{k}}^{\dagger} d_{v'\mathbf{k'}} e^{i(\mathbf{k'}-\mathbf{k})\cdot\mathbf{R}_I} \hat{P}_{nn'}^{I}. \quad (6b)$$

Throughout this paper, we absorb the factor $\hbar$ appearing in the spin matrices in the coupling constants J_{sd} and J_{pd} as well as the Bohr magneton μ_B.

Due to the band-gap mismatch that arises when doping atoms are incorporated into the host lattice, there is also a nonmagnetic scattering of carriers at impurities that we model via [29]

$$H_{\mathrm{nm}}^{\mathrm{e}} = \frac{J_0^{\mathrm{e}}}{V} \sum_{\substack{Il \\ \mathbf{kk'}}} c_{l\mathbf{k}}^{\dagger} c_{l\mathbf{k'}} e^{i(\mathbf{k'}-\mathbf{k})\cdot\mathbf{R}_I}, \quad (7a)$$

$$H_{\mathrm{nm}}^{\mathrm{h}} = \frac{J_0^{\mathrm{h}}}{V} \sum_{\substack{Iv \\ \mathbf{kk'}}} d_{v\mathbf{k}}^{\dagger} d_{v\mathbf{k'}} e^{i(\mathbf{k'}-\mathbf{k})\cdot\mathbf{R}_I}. \quad (7b)$$

An estimation for the scattering constants J_0^{e} and J_0^{h} for electrons and holes, respectively, in a DMS $A_{1-x}Mn_xB$ can be obtained by considering the change in the band gap of the host material AB compared to MnB [22]. It should be noted that we assume a short-range carrier-impurity interaction, which is a good approximation in isoelectrically doped II-VI DMS since the long-range contribution is already contained in the effective crystal Hamiltonian. There, the Coulomb interaction is screened by the valence-band electrons [29].

B. Quantum kinetic equations for the exciton spin

A quantum kinetic theory for the exciton spin dynamics in DMS quantum wells described by Eq. (1) has been derived in Ref. [22] in the two-particle exciton basis. This theory is based on a density-matrix formalism together with a correlation expansion and explicitly accounts for carrier-impurity correlations as dynamical variables. To obtain a tractable problem the resulting hierarchy of equations of motion is truncated by accounting only for terms up to second order in the external

laser field according to the dynamics-controlled truncation (DCT) [35].

Here, we consider excitations of heavy-hole excitons at the $1s$ resonance with circularly polarized (σ^-) light so that the hole spin is oriented antiparallel with respect to the growth direction ($m_J = -\frac{3}{2}$). We focus on narrow quantum wells with a large hh-lh splitting that arises, e.g., because of the confinement and strain [32]. Due to the conservation of angular momentum, the initial electron spin therefore points in the opposite direction ($\uparrow$). In principle there are various mechanisms which could change the spin orientation of the heavy hole. One such mechanism stems from the long-range exchange part of the Coulomb interaction [25,26,36] which allows for a transition from the $-\frac{3}{2}$ to the $\frac{3}{2}$ hh spin state accompanied by a simultaneous flip of the electron spin. However, for the quantum wells considered here, the corresponding interaction energy is on the order of 10 μeV. Comparing this value with the typical energy of the $s-d$ interaction $\sim$10 meV, we will neglect the exchange interaction in the following.

In DMS, another spin-flip mechanism for heavy holes arises from the $p-d$ exchange interaction given by Eq. (6b). If the band mixing between heavy and light holes is sufficiently small, H_{pd} provides no direct matrix element that could cause a hh spin flip to the state with $m_J = \frac{3}{2}$, so that a spin flip of the heavy hole induced by H_{pd} requires an intermediate occupation of light-hole states. However, such processes require an energy on the order of the hh-lh splitting and are suppressed for sufficiently large splittings [10,22,28,37,38]. The degree of band mixing as well as the magnitude of the hh-lh splitting depend on the width of the quantum well, the details of the barrier, as well as on the strain and are therefore strongly sample dependent. It is thus not surprising that measured hole spin relaxation times found in a particular sample can vary between a rapid decay of optically polarized hole spins [10,39] and extremely long hole spin lifetimes which may even exceed the radiative recombination time of excitons [12,37,40].

In the present paper we concentrate on samples where the heavy-hole spin lifetime is long such that on the time scale of interest the hh spins can be considered as being pinned along the growth direction of the quantum well. This allows us to focus only the exciton-bound electron spin dynamics.

Since Eq. (1) describes a system that is isotropic in the $x-y$ plane, one can average over the polar angles ψ_i of the two-dimensional center-of-mass wave vectors $\mathbf{K}_i$ by going over to the quasicontinuous limit, thereby reducing the numerical demand of the resulting equations of motion. Thus, we label the dynamical variables according to the absolute value K_i of the exciton center-of-mass momentum vector $\mathbf{K}_i$. Choosing the z axis along the growth direction of the quantum well, the dynamical variables are:

$$n_{K_1} = \int_0^{2\pi} \frac{d\psi_1}{2\pi} \sum_{\sigma} \langle \hat{Y}_{\sigma-\frac{3}{2}1s\mathbf{K}_1}^{\dagger} \hat{Y}_{\sigma-\frac{3}{2}1s\mathbf{K}_1} \rangle, \quad (8a)$$

$$\mathbf{s}_{K_1} = \int_0^{2\pi} \frac{d\psi_1}{2\pi} \sum_{\sigma\sigma'} \mathbf{s}_{\sigma\sigma'}^{\mathrm{e}} \langle \hat{Y}_{\sigma-\frac{3}{2}1s\mathbf{K}_1}^{\dagger} \hat{Y}_{\sigma'-\frac{3}{2}1s\mathbf{K}_1} \rangle, \quad (8b)$$

$$y^{\uparrow/\downarrow} = \langle \hat{Y}_{\uparrow/\downarrow-\frac{3}{2}1s0} \rangle, \quad (8c)$$

$$q_{\eta l K_1}^{\uparrow/\downarrow} = \frac{Vd}{N_{\mathrm{Mn}}} \int_0^{2\pi} \frac{d\psi_1}{2\pi} f_{\eta 1s1s}^{\mathbf{0}\mathbf{K}_1} \int dz |u_0(z)|^2 \sum_{nn'I} S_{nn'}^l \delta(z - Z_I) \langle \hat{Y}_{\uparrow/\downarrow - \frac{3}{2} 1s \mathbf{K}_1} e^{i\mathbf{K}_1 \cdot \mathbf{R}_I} \hat{P}_{nn'}^I \rangle, \tag{8d}$$

$$z_{\eta K_1}^{\uparrow/\downarrow} = \frac{Vd}{N_{\mathrm{Mn}}} \int_0^{2\pi} \frac{d\psi_1}{2\pi} f_{\eta 1s1s}^{\mathbf{0}\mathbf{K}_1} \int dz |u_0(z)|^2 \sum_{I} \delta(z - Z_I) \langle \hat{Y}_{\uparrow/\downarrow - \frac{3}{2} 1s \mathbf{K}_1} e^{i\mathbf{K}_1 \cdot \mathbf{R}_I} \rangle, \tag{8e}$$

$$Q_{\eta l K_1}^{\alpha K_2} = \frac{Vd}{N_{\mathrm{Mn}}} \int_0^{2\pi} \frac{d\psi_1}{2\pi} \int_0^{2\pi} \frac{d\psi_2}{2\pi} f_{\eta 1s1s}^{\mathbf{K}_1 \mathbf{K}_2} \int dz |u_0(z)|^2 \sum_{\substack{\sigma\sigma'I \\ nn'}} S_{nn'}^l s_{\sigma\sigma'}^{e,\alpha} \delta(z - Z_I) \langle \hat{Y}_{\sigma - \frac{3}{2} 1s \mathbf{K}_1}^\dagger \hat{Y}_{\sigma' - \frac{3}{2} 1s \mathbf{K}_2} e^{i(\mathbf{K}_2 - \mathbf{K}_1) \cdot \mathbf{R}_I} \hat{P}_{nn'}^I \rangle, \tag{8f}$$

$$Z_{\eta\ K_1}^{\ \alpha K_2} = \frac{Vd}{N_{\mathrm{Mn}}} \int_0^{2\pi} \frac{d\psi_1}{2\pi} \int_0^{2\pi} \frac{d\psi_2}{2\pi} f_{\eta 1s1s}^{\mathbf{K}_1 \mathbf{K}_2} \int dz |u_0(z)|^2 \sum_{\sigma\sigma'I} s_{\sigma\sigma'}^{e,\alpha} \delta(z - Z_I) \langle \hat{Y}_{\sigma - \frac{3}{2} 1s \mathbf{K}_1}^\dagger \hat{Y}_{\sigma' - \frac{3}{2} 1s \mathbf{K}_2} e^{i(\mathbf{K}_2 - \mathbf{K}_1) \cdot \mathbf{R}_I} \rangle \tag{8g}$$

with $l \in \{x,y,z\}$, $\alpha \in \{0,x,y,z\}$, and $s_{\sigma_1\sigma_2}^{e,0} = \delta_{\sigma_1,\sigma_2}$. The exciton creation (annihilation) operator $\hat{Y}_{\sigma-\frac{3}{2}1s\mathbf{K}_1}^\dagger$ ($\hat{Y}_{\sigma-\frac{3}{2}1s\mathbf{K}_1}$) refers to the $1s$ exciton ground state where the exciton-bound electron has spin $\sigma \in \{\uparrow,\downarrow\}$, the quantum number of the exciton-bound hole is $m_J = -\frac{3}{2}$, and the center-of-mass wave vector is given by $\mathbf{K}_1$.

In Eqs. (8), n_{K_1} represents the K-resolved occupation density of the excitons on the $1s$ parabola, $\mathbf{s}_{K_1}$ describes the spin density of $1s$ exciton-bound electrons, and $y^{\uparrow/\downarrow}$ are the interband coherences. We explicitly account for correlations between the exciton and the Mn subsystem which are described by the remaining quantities. The exciton wave function enters the dynamics via the form factors [22]

$$f_{\eta 1s1s}^{\mathbf{K}_1 \mathbf{K}_2} = 2\pi \int_0^\infty dr\, r R_{1s}^2(r) J_0(\eta |\mathbf{K}_1 - \mathbf{K}_2| r), \tag{9}$$

where $R_{1s}(r)$ is the radial part of the exciton wave function, $J_0(x)$ denotes the cylindrical Bessel function of order zero, and the constant η is either $\eta_e = \frac{m_e}{M}$ or $\eta_h = \frac{m_h}{M}$ with the electron mass m_e, the heavy-hole mass m_h, and the exciton mass $M = m_e + m_h$.

The complete equations of motion for the variables in Eqs. (8) can be found in Eqs. (A1) in Appendix A. Since the carrier density is typically much lower than the impurity density, it is a good approximation to describe the impurity spin density matrix by its initial thermal equilibrium value throughout the dynamics [41], which is why the impurity spin is not included as a dynamical variable. For all calculations in this paper we assume a thermal impurity-spin density matrix calculated with a temperature of 2 K.

III. MARKOV LIMIT

Most theoretical works on the spin dynamics in DMS are based on an application of Fermi's golden rule [9,12,14,28,42–45] where correlation effects are neglected. To be able to compare the predictions of our quantum kinetic theory to the existing literature, we perform the Markov limit of our equations, from which spin-transfer rates similar to Fermi's golden rule can be obtained. A comparison between the QKT and its Markov limit also makes it possible to pinpoint correlation effects in the spin dynamics that are not captured by Fermi's golden rule. In this section, we present the Markovian equations of motion derived from the QKT, extract

spin-transfer rates for Faraday and Voigt configuration, and provide an analytical expression for the correlation energy.

A. Derivation

If we choose the coordinate system such that the z axis is oriented along the magnetic field, the system is most conveniently described by the spin-up and spin-down exciton density as well as the perpendicular electron spin density with respect to the z axis given by

$$n_{\omega_1}^{\uparrow/\downarrow} = \tfrac{1}{2} n_{\omega_1} \pm s_{\omega_1}^z, \tag{10a}$$

$$\mathbf{s}_{\omega_1}^\perp = \mathbf{s}_{\omega_1} - s_{\omega_1}^z \mathbf{e}_z, \tag{10b}$$

respectively, where $\mathbf{e}_z$ is the unit vector along the z axis. Instead of the center-of-mass wave number K we label the variables by the angular frequency $\omega = \frac{\hbar K^2}{2M}$ which turns out to be advantageous for the numerical evaluation of energy-conserving delta functions. Thus, $\hbar\omega$ describes the kinetic energy of the center-of-mass motion of the $1s$-hh exciton. One can then make use of the quasicontinuous limit in order to convert the appearing sums over K into integrals over ω with a density of states $D(\omega) = \frac{VM}{2\pi\hbar d}$ for a quantum well with volume V and width d, with M denoting the mass of the hh exciton.

Treating the impurity spin system as a spin bath, the influence of the Mn spin can be subsumed in the constants $b^\pm = \frac{1}{2}(\langle \mathbf{S}^2 - (S^z)^2 \rangle \pm \langle S^z \rangle)$, $b^\parallel = \frac{1}{2}\langle (S^z)^2 \rangle$, and $b^0 = \langle S^z \rangle$. The mean-field precession frequencies of electrons and Mn impurities in the external magnetic field are given by

$$\boldsymbol{\omega}_e = \frac{1}{\hbar} g_e \mu_B \mathbf{B} + \frac{J_{sd} N_{\mathrm{Mn}} b^0}{\hbar V} \mathbf{e}_z, \tag{11a}$$

$$\boldsymbol{\omega}_{\mathrm{Mn}} = \frac{1}{\hbar} g_{\mathrm{Mn}} \mu_B \mathbf{B}, \tag{11b}$$

respectively.

Finally, let us define angle-averaged exciton form factors according to

$$F_{\eta_1 1s1s}^{\eta_2 \omega_1 \omega_2} = 2\pi \int_0^{2\pi} d\psi \int_0^\infty dr \int_0^\infty dr'\, rr' R_{1s}^2(r) R_{1s}^2(r')$$
$$\times J_0(\eta_1 K_{12}(\psi) r) J_0(\eta_2 K_{12}(\psi) r'), \tag{12}$$

where $K_{12} = |\mathbf{K}_1 - \mathbf{K}_2|$ and ψ denotes the angle between $\mathbf{K}_1$ and $\mathbf{K}_2$ and $K_i = \sqrt{\frac{2M\omega_i}{\hbar}}$. These form factors contain
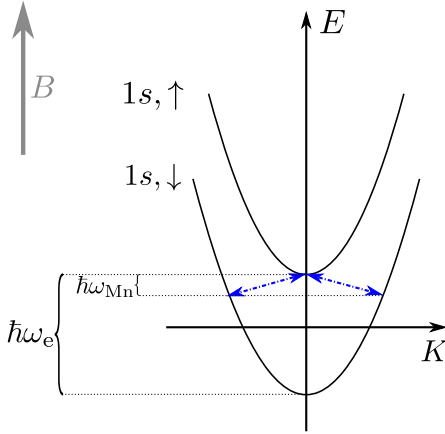
FIG. 1. Sketch of the exciton band structure with Markovian spin-flip processes in an external magnetic field B in the Faraday configuration. The figure shows the $1s$ exciton parabolas with the exciton-bound electron in the spin-up ($\uparrow$) and spin-down state ($\downarrow$), respectively. Transitions are sketched by blue arrows.

the influence of the exciton wave function on the dynamical quantities of interest.

B. Faraday configuration

If the magnetic field is oriented parallel to the growth direction of the quantum well (Faraday configuration), the equations for $n_{\omega_1}^{\uparrow/\downarrow}$ and $\mathbf{s}_{\omega_1}^{\perp}$ are completely decoupled since only spin-flip processes between the spin-up and the spin-down band occur. In this case, the z axis of the coordinate system coincides with the growth direction. Because the electron spins are initially prepared parallel to the growth direction, $\mathbf{s}_{\omega_1}^{\perp}$ is zero throughout the dynamics and the Markovian equations of motion read [22]:

$$\frac{\partial}{\partial t} n_{\omega_1}^{\uparrow/\downarrow} = \Gamma_{\mathbf{E}}^{\uparrow/\downarrow} + \frac{I N_{\mathrm{Mn}} M J_{sd}^2}{2\hbar^3 V d} \int_0^\infty d\omega \, \delta(\omega - (\omega_1 \pm \omega_{\mathrm{sf}}))$$
$$\times F_{\eta_{\mathrm{h}} 1s 1s}^{\eta_{\mathrm{h}} \omega \omega_1} \left(b^{\pm} n_{\omega}^{\downarrow/\uparrow} - b^{\mp} n_{\omega_1}^{\uparrow/\downarrow} \right). \quad (13)$$

Using a σ^- circularly polarized laser pulse, the optical generation rates are given by $\Gamma_{\mathbf{E}}^{\uparrow} = \Gamma_{\mathbf{E}}$ and $\Gamma_{\mathbf{E}}^{\downarrow} = 0$ for the spin-up and spin-down occupations, respectively. The rate $\Gamma_{\mathbf{E}}$ can be easily inferred by combining Eq. (A1c) for the coherence with Eq. (A1a) and is given explicitly in Eq. (B2). The constant I is an overlap integral involving the envelope functions due to the confinement along the growth direction and is given by Eq. (A2). The spin-flip scattering shift

$$\hbar \omega_{\mathrm{sf}} := \hbar \left(\omega_{\mathrm{e}}^z - \omega_{\mathrm{Mn}}^z \right) \quad (14)$$

appearing in the delta function in Eq. (13) ensures that the energy cost or release of spin flip-flop processes between the electron and the Mn system are correctly accounted for. Furthermore, only the magnetic coupling constant for the conduction band J_{sd} influences the spin transfer on the Markovian level since all contributions due to nonmagnetic scattering as well as the $p-d$ exchange interaction vanish. A sketch of the situation can be found in Fig. 1, which depicts

the Zeeman-shifted spin-up and spin-down bands as well as the spin-flip processes between them.

For an initial excitation of electrons in the spin-up state and no further driving, since excitons are optically generated with $K = 0$, i.e., $\omega = 0$, only the variables $n_0^{\uparrow}$ and $n_{\omega_{\mathrm{sf}}}^{\downarrow}$ retain finite values due to the conservation of energy enforced by the delta function. Thus, Eq. (13) reduces to the coupled equations

$$\frac{\partial}{\partial t} n_0^{\uparrow} = \frac{I N_{\mathrm{Mn}} M J_{sd}^2}{2\hbar^3 V d} F_{\eta_{\mathrm{h}} 1s 1s}^{\eta_{\mathrm{h}} \omega_{\mathrm{sf}} 0} \left(b^+ n_{\omega_{\mathrm{sf}}}^{\downarrow} - b^- n_0^{\uparrow} \right), \quad (15a)$$

$$\frac{\partial}{\partial t} n_{\omega_{\mathrm{sf}}}^{\downarrow} = \frac{I N_{\mathrm{Mn}} M J_{sd}^2}{2\hbar^3 V d} F_{\eta_{\mathrm{h}} 1s 1s}^{\eta_{\mathrm{h}} \omega_{\mathrm{sf}} 0} \left(b^- n_0^{\uparrow} - b^+ n_{\omega_{\mathrm{sf}}}^{\downarrow} \right). \quad (15b)$$

From Eqs. (15), we can infer that

$$\frac{\partial}{\partial t} \left(n_0^{\uparrow} + n_{\omega_{\mathrm{sf}}}^{\downarrow} \right) = \frac{\partial}{\partial t} n = 0 \quad (16)$$

with the total exciton density n being a conserved quantity.

We note in passing that the evaluation of Eq. (13) for the spin-down component for $\omega_1 = \omega_{\mathrm{sf}}$, which leads to Eq. (15b), is mathematically problematic since then the root of the argument of the delta function coincides with the lower boundary of the integration. In order to obtain physically meaningful results, we extend the integration over ω to the interval $(-\epsilon, \infty)$ with an arbitrarily small parameter ϵ so that the integration over the delta function can always be performed straightforwardly. Any other method for evaluating the contribution of this delta function would destroy the symmetry between Eq. (15a) and Eq. (15b) so that the conservation of the number of particles ensured by Eq. (16) would no longer hold.

Equation (16) can then be used to condense Eqs. (15) into a single differential equation for the spin-up occupation at $\omega = 0$:

$$\frac{\partial}{\partial t} n_0^{\uparrow} = - \frac{I N_{\mathrm{Mn}} M J_{sd}^2}{2\hbar^3 V d} F_{\eta_{\mathrm{h}} 1s 1s}^{\eta_{\mathrm{h}} \omega_{\mathrm{sf}} 0} (b^+ + b^-) n_0^{\uparrow}$$
$$+ \frac{I N_{\mathrm{Mn}} M J_{sd}^2}{2\hbar^3 V d} F_{\eta_{\mathrm{h}} 1s 1s}^{\eta_{\mathrm{h}} \omega_{\mathrm{sf}} 0} b^+ n. \quad (17)$$

This is solved by

$$n_0^{\uparrow}(t) = (n - \zeta) e^{-\tau_{\parallel}^{-1} t} + \zeta \quad (18)$$

with the parallel spin-transfer rate

$$\tau_{\parallel}^{-1} = \frac{I N_{\mathrm{Mn}} M J_{sd}^2}{2\hbar^3 V d} (b^+ + b^-) F_{\eta_{\mathrm{h}} 1s 1s}^{\eta_{\mathrm{h}} \omega_{\mathrm{sf}} 0} \quad (19)$$

and a parameter $\zeta = \frac{b^+}{b^+ + b^-} n$ related to the equilibrium value s_{eq}^z of the z component of the electron spin that is reached at $t \to \infty$ via

$$s_{\mathrm{eq}}^z = \zeta - \frac{1}{2} n = \frac{b^0}{2(b^+ + b^-)} n. \quad (20)$$

From Eq. (19) it becomes clear that the exciton form factor $F_{\eta_{\mathrm{h}} 1s 1s}^{\eta_{\mathrm{h}} \omega_{\mathrm{sf}} 0}$, which decreases when ω_{sf} becomes larger [22], significantly influences the Markovian rate depending on the value of ω_{sf}. Since ω_{sf} depends on the impurity content as well as the magnitude of the applied magnetic field, it is instructive to plot the form factor for various doping fractions as a function of magnetic field, which is done in Fig. 2.
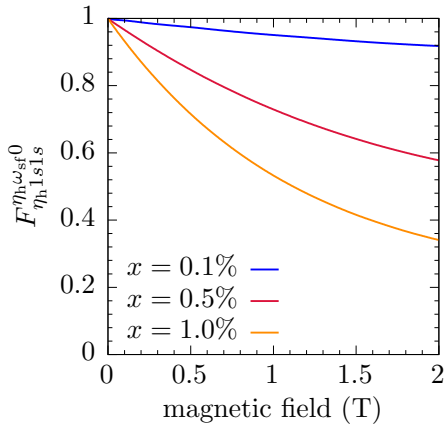
FIG. 2. Magnetic field dependence of the form factor $F_{\eta_h 1s1s}^{\eta_h \omega_{sf} 0}$ that enters the spin-transfer rate for three different Mn doping fractions x.

If the doping fraction is on the order of 0.1% or lower, the influence of the exciton form factor on the spin-transfer rate is less than 10%. However, for higher doping concentrations, the form factor causes a significant decrease of the rate that can be as large as 60%.

C. Voigt configuration

If an in-plane magnetic field is applied to the quantum well, the electron spins perform a precession dynamics. This precession is damped down by a characteristic rate which, in general, is different from the rate found in the Faraday configuration. For quasifree electrons, the precession axis is determined by the direction of the external magnetic field as well as the direction of the mean impurity magnetization and points along $\boldsymbol{\omega}_e$. Using the same convention as in the previous section, we choose the z axis parallel with respect to the magnetic field and rotate the coordinate system such that y labels the growth direction.

However, because the hole spins are pinned along the growth direction as described in Sec. II B, the combined field due to the impurity magnetization and the external magnetic field will experience a tilt out of the quantum-well plane. This tilt is caused by the correlations between the hh spins and the Mn ions which act back on the electron spins. Alternatively, one can also use a symmetry-based argument in order to understand why the precession axis changes: Since the hh spins always point along the growth direction, they effectively break the rotational symmetry of the system around the vector $\boldsymbol{\omega}_e$ so that the electron-spin precession is not damped down to zero but reaches a finite value instead. Therefore, in Voigt geometry, the expected dephasing of the electron spins due to the precession will be accompanied by a relaxation-type dynamics, resulting in a finite spin polarization at long times.

In the corresponding equations of motion, which can be found in Eqs. (B1) in Appendix B, the tilt of the overall field experienced by the electron spins manifests in a coupling between the variables $n_{\omega_1}^{\uparrow/\downarrow}$ and $\mathbf{s}_{\omega_1}^{\perp}$ which is proportional to the product $J_{sd} J_{pd}$. Since these coupling terms contain either b^+ or b^- as prefactors, which both depend on the Mn magnetization, it is clear that the magnitude of the long-time spin polarization

also depends on the magnitude of the applied magnetic field. However, some of these terms contain a divergence $\sim \frac{1}{\omega - \omega_0}$ at certain frequencies ω_0. These divergences are an artifact of the Markov limit, where one assumes for the memory integral [22]

$$\int_{-t}^{0} d\tau \, e^{-i(\omega - \omega_0)\tau} \overset{t \to \infty}{\approx} \pi \delta(\omega - \omega_0) - \mathcal{P}\frac{i}{\omega - \omega_0}. \quad (21)$$

Note that the above expression is only meaningful when integrated over ω and $\mathcal{P}$ denotes the Cauchy principle value. A divergence therefore appears in the imaginary part of the memory in the limit $t \to \infty$ as a consequence of the Markov limit.

Divergences of this kind also appear in the perpendicular spin component of quasifree electrons [46]. In contrast to the Faraday configuration, where contributions from the imaginary part of the memory cancel out [30,47], the imaginary part describes a renormalization of the spin precession frequency for electrons in the Voigt configuration. However, the broad initial carrier distributions of quasifree electrons (typically several meV) causes an averaging over many frequencies ω so that all observables remain finite [46]. For excitons, the spectrally sharp nature of the optically generated exciton distribution does not lead to such an averaging, so that divergences remain in the Markovian results. In order to obtain meaningful expressions, all terms stemming from the imaginary part of the memory integral are neglected in numerical calculations on the Markovian level throughout this paper.

If one is only interested in the spin-transfer rate for the perpendicular electron spin component without the influence of the hole spins, this amounts to neglecting all terms proportional to the magnetic coupling constant J_{pd} in Eqs. (B1). Disregarding the coupling to the hole spins is similar to what one would typically do when applying Fermi's golden rule since then only the electron-spin part is of interest. The resulting equation for the perpendicular spin component reads

$$\frac{\partial}{\partial t}\mathbf{s}_{\omega_1}^{\perp} = \boldsymbol{\Gamma}_{\mathbf{E}}^{\perp} + \boldsymbol{\omega}_e \times \mathbf{s}_{\omega_1}^{\perp} - \frac{I N_{\mathrm{Mn}} M J_{sd}^2}{4\hbar^3 V d}\int_0^{\infty} d\omega$$
$$\times [b^- \delta(\omega - (\omega_1 + \omega_{sf})) + b^+ \delta(\omega - (\omega_1 - \omega_{sf}))$$
$$+ 4b^{\parallel} \delta(\omega - \omega_1)] F_{\eta_h 1s1s}^{\eta_h \omega \omega_1} \mathbf{s}_{\omega_1}^{\perp}, \quad (22)$$

where the first term describes the optical excitation with rates $\Gamma_{\mathbf{E}}^x = 0$ and $\Gamma_{\mathbf{E}}^y = \Gamma_{\mathbf{E}}$ [cf. Eq. (B2)]. The vector product causes a precession of $\mathbf{s}_{\omega_1}^{\perp}$ around $\boldsymbol{\omega}_e$, which is damped down by the remaining term. Thus, when only accounting for the influence of J_{sd}, the equations for $n_{\omega_1}^{\uparrow/\downarrow}$ and $\mathbf{s}_{\omega_1}^{\perp}$ once more decouple so that a damped precession dynamics remains. From Eq. (22) we obtain a spin-transfer rate in the Voigt configuration given by

$$\tau_{\perp}^{-1} = \frac{I N_{\mathrm{Mn}} M J_{sd}^2}{4\hbar^3 V d}\left(F_{\eta_h 1s1s}^{\eta_h \omega_{sf} 0} b^- + 4b^{\parallel}\right) \quad (23)$$

for an exciton occupation at $\omega_1 = 0$. Note that the second delta function in Eq. (22), which is proportional to b^+, does not contribute to this result since $\omega_1 - \omega_{sf} < 0$ if $\omega_1 = 0$.

To summarize, in contrast to the Faraday case, the Markovian equations of motion for the Voigt geometry are complicated and display divergences at certain characteristic frequencies. This means that, for studying the time-resolved exciton spin dynamics, our quantum kinetic approach becomes

a necessity since it avoids the artificial divergences encountered in the Markov approximation. Nevertheless, when neglecting the influence of the hh spins, one can still derive analytical expressions for Faraday as well as Voigt geometry. In the Faraday configuration, the obtained expression corresponds to the typically considered Fermi-golden-rule result [28].

D. Correlation energy

One of the major changes when going beyond a Markovian description is that the correlation energy has to be taken into account in the energy balance, which is a consequence of the many-body nature of the problem that is not captured in a single-particle approach. In order to gain insight into the buildup and magnitude of the correlation energy in the system of interest here, it is instructive to derive an expression for the total energy as a functional of the exciton density n_{K_1} and the electron spin $\mathbf{s}_{K_1}$. To this end we split the total energy into parts corresponding to the individual contributions in Eq. (1) and treat them as functionals of the variables defined in Eqs. (8), which yields:

$$\langle H_0 \rangle = \sum_{K_1} \hbar \omega_{K_1} n_{K_1}, \tag{24a}$$

$$\left\langle H_Z^e \right\rangle = g_e \mu_B \mathbf{B} \cdot \sum_{K_1} \mathbf{s}_{K_1}, \tag{24b}$$

$$\left\langle H_Z^h \right\rangle = 3\kappa \mu_B B^z \sum_{K_1} n_{K_1}, \tag{24c}$$

$$\left\langle H_Z^{\mathrm{Mn}} \right\rangle = g_{\mathrm{Mn}} \mu_B \frac{N_{\mathrm{Mn}}}{d} \mathbf{B} \cdot \langle \mathbf{S} \rangle, \tag{24d}$$

$$\langle H_{sd} \rangle^{\mathrm{mf}} = \frac{J_{sd} N_{\mathrm{Mn}}}{V} \langle \mathbf{S} \rangle \cdot \sum_{K_1} \mathbf{s}_{K_1}, \tag{24e}$$

$$\langle H_{pd} \rangle^{\mathrm{mf}} = -\frac{J_{pd} N_{\mathrm{Mn}}}{2V} \langle S^z \rangle \sum_{K_1} n_{K_1}, \tag{24f}$$

$$\left\langle H_{\mathrm{nm}}^{\mathrm{e/h}} \right\rangle^{\mathrm{mf}} = \frac{J_0^{\mathrm{e/h}} N_{\mathrm{Mn}}}{V} \sum_{K_1} n_{K_1}, \tag{24g}$$

$$\langle H_{sd} \rangle^{\mathrm{c}} = \frac{J_{sd} N_{\mathrm{Mn}}}{V^2} \sum_{l K_1 K_2} Q_{-\eta_h l K_1}^{l K_2}, \tag{24h}$$

$$\langle H_{pd} \rangle^{\mathrm{c}} = -\frac{J_{pd} N_{\mathrm{Mn}}}{2V^2} \sum_{K_1 K_2} Q_{\eta_e z K_1}^{0 K_2}, \tag{24i}$$

$$\left\langle H_{\mathrm{nm}}^{\mathrm{e/h}} \right\rangle^{\mathrm{c}} = \frac{J_0^{\mathrm{e/h}} N_{\mathrm{Mn}}}{V^2} \sum_{K_1 K_2} Z_{-\eta_h / \eta_e \ K_1}^{0 K_2}, \tag{24j}$$

where $H_0 := H_0^{\mathrm{e}} + H_0^{\mathrm{h}} + H_{\mathrm{conf}}$. The expectation values are split into mean field (mf) and correlation (c) contributions. Note that, since the number of particles is a conserved quantity, the expectation values $\langle H_Z^h \rangle$, $\langle H_{pd} \rangle^{\mathrm{mf}}$, and $\langle H_{\mathrm{nm}}^{\mathrm{e/h}} \rangle^{\mathrm{mf}}$ are constant and only cause an energetic offset once the driving has ended.

In the Markov limit, the correlations $Q_{\eta l K_1}^{\alpha K_2}$ and $Z_{\eta \ K_1}^{\alpha K_2}$ can be written as functionals of n_{K_1} and $\mathbf{s}_{K_1}$, as explained in detail in Ref. [22]. Feeding these functionals back into Eqs. (24) one obtains the correlation energies

$$\langle H_{sd} \rangle^{\mathrm{c}} = -\frac{I N_{\mathrm{Mn}} J_{sd}}{\hbar V^2} \sum_{K_1 K_2} \left[J_{sd} F_{\eta_h 1s 1s}^{\eta_h K_1 K_2} \left(\frac{b^- \left(\frac{1}{2} n_{K_1} + s_{K_1}^z \right)}{\omega_{K_2} - \left(\omega_{K_1} + \omega_{\mathrm{sf}} \right)} + \frac{b^+ \left(\frac{1}{2} n_{K_1} - s_{K_1}^z \right)}{\omega_{K_2} - \left(\omega_{K_1} - \omega_{\mathrm{sf}} \right)} \right) \right.$$
$$\left. + \frac{1}{\omega_{K_2} - \omega_{K_1}} \left(F_{\eta_h 1s 1s}^{\eta_h K_1 K_2} \left(2 J_0^{\mathrm{e}} b^0 s_{K_1}^z + J_{sd} b^{\parallel} n_{K_1} \right) + 2 F_{-\eta_h 1s 1s}^{\eta_e K_1 K_2} \left(J_0^{\mathrm{h}} b^0 - J_{pd} b^{\parallel} \right) s_{K_1}^z \right) \right], \tag{25a}$$

$$\langle H_{pd} \rangle^{\mathrm{c}} = \frac{I N_{\mathrm{Mn}} J_{pd}}{\hbar V^2} \sum_{K_1 K_2} \frac{1}{\omega_{K_2} - \omega_{K_1}} \left(F_{\eta_e 1s 1s}^{\eta_e K_1 K_2} \left(J_0^{\mathrm{h}} b^0 - J_{pd} b^{\parallel} \right) n_{K_1} + F_{-\eta_h 1s 1s}^{\eta_e K_1 K_2} \left(J_0^{\mathrm{e}} b^0 n_{K_1} + 2 J_{sd} b^{\parallel} s_{K_1}^z \right) \right), \tag{25b}$$

$$\left\langle H_{\mathrm{nm}}^{\mathrm{e}} \right\rangle^{\mathrm{c}} = -\frac{I N_{\mathrm{Mn}} J_0^{\mathrm{e}}}{\hbar V^2} \sum_{K_1 K_2} \frac{1}{\omega_{K_2} - \omega_{K_1}} \left(2 F_{\eta_h 1s 1s}^{\eta_h K_1 K_2} \left(J_0^{\mathrm{e}} n_{K_1} + J_{sd} b^0 s_{K_1}^z \right) + F_{-\eta_h 1s 1s}^{\eta_e K_1 K_2} \left(2 J_0^{\mathrm{h}} - J_{pd} b^0 \right) n_{K_1} \right), \tag{25c}$$

$$\left\langle H_{\mathrm{nm}}^{\mathrm{h}} \right\rangle^{\mathrm{c}} = -\frac{I N_{\mathrm{Mn}} J_0^{\mathrm{h}}}{\hbar V^2} \sum_{K_1 K_2} \frac{1}{\omega_{K_2} - \omega_{K_1}} \left(F_{\eta_e 1s 1s}^{\eta_e K_1 K_2} \left(2 J_0^{\mathrm{h}} - J_{pd} b^0 \right) n_{K_1} + 2 F_{-\eta_h 1s 1s}^{\eta_e K_1 K_2} \left(J_0^{\mathrm{e}} n_{K_1} + J_{sd} b^0 s_{K_1}^z \right) \right). \tag{25d}$$

Here, the divergences appearing at the roots of the denominators are integrable, which can be easily verified in the quasicontinuous limit $\sum_K \rightarrow \int dK\, D(K)$ since the density of states $D(K)$ is linear in K for a quasi two-dimensional system.

IV. NUMERICAL RESULTS

In the following we present and discuss the exciton-bound electron spin dynamics in a finite external magnetic field in Faraday or Voigt configuration and focus in particular on the comparison between spin-transfer rates predicted by the

quantum kinetic theory and those in the Markov limit. For all calculations, we model a σ^--polarized excitation pulse with 100 fs FWHM resonant with the 1s-hh transition and consider a 20 nm wide $\mathrm{Zn}_{1-x}\mathrm{Mn}_x\mathrm{Se}$ quantum well for which we calculate an exciton binding energy of about 20 meV. The lattice constant [3] is 0.567 nm, $m_{\mathrm{e}}/m_0 = 0.1$ and $m_{\mathrm{hh}}/m_0 = 0.8$ are the effective electron and heavy-hole masses in terms of the free electron mass [48], and the coupling constants [3] are given by $J_{sd} = -12$ meV nm³, $J_{pd} = 50$ meV nm³, $J_0^{\mathrm{e}} = 22$ meV nm³, and $J_0^{\mathrm{h}} = 0$. For the dielectric constant [49] we use a value of $\epsilon = 9$.
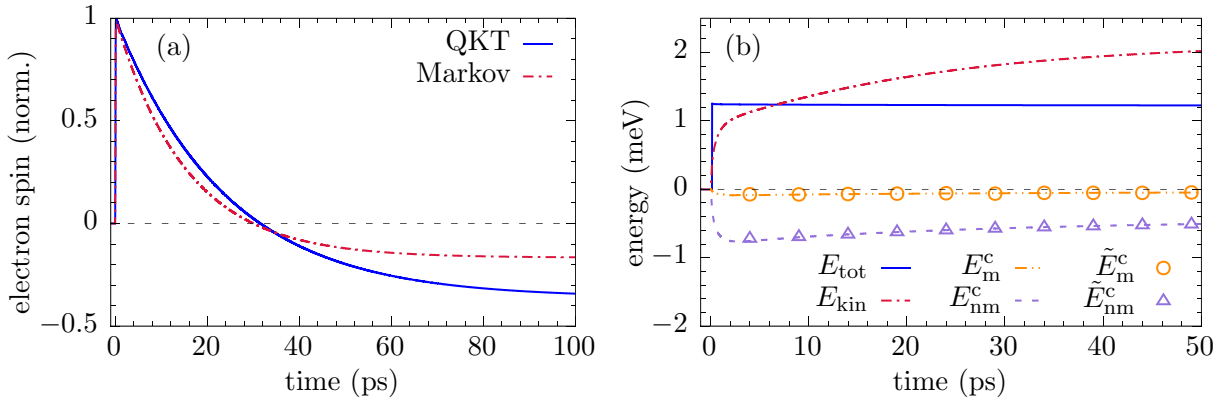
FIG. 3. (a) Time evolution of the exciton-bound electron spin in a $Zn_{0.99}Mn_{0.01}Se$ quantum well in a magnetic field $B = 0.5$ T in Faraday configuration according to the quantum kinetic theory (QKT) and the Markovian calculation (Markov) normalized to the maximum spin after the pulse. (b) Total energy (E_{tot}), kinetic energy (E_{kin}), magnetic correlation energy (E_m^c), and nonmagnetic correlation energy (E_{nm}^c) per exciton according to Eqs. (24). Also shown are the magnetic ($\tilde{E}_m^c$) and nonmagnetic ($\tilde{E}_{nm}^c$) correlation energies per exciton in the Markov limit according to Eqs. (25) evaluated using the occupations from the QKT.

A. Faraday configuration

In Faraday geometry, the magnetic field is oriented parallel to the spin polarization immediately after the excitation pulse. A typical example of the resulting electron spin dynamics in an external magnetic field with a magnitude of $B = 0.5$ T can be seen in Fig. 3(a). The results are normalized with respect to the maximum spin after the pulse.

When comparing the quantum kinetic (blue solid curve) with the Markovian result (red dashed-dotted curve) it becomes clear that, similar to the case without magnetic field [22], the quantum kinetic theory initially predicts a slower spin decay than the Markov theory. This stems from a cutoff of the memory kernel given by Eq. (21) due to the close proximity of excitons to the bottom of the exciton parabola. As discussed in detail in Ref. [22], the retraction of the memory integral to a delta function only happens in the limit $t \to \infty$. For finite times, however, the memory integral yields a sinclike behavior whose oscillations are cut off at the bottom of the exciton parabola, thus effectively lowering the observed spin decay rate.

Furthermore, due to the finite magnetic field, the spin no longer decays to zero but rather reaches a finite value for long times. In the Markov limit this can be attributed to the difference of the rates for the scattering from the spin-up to the spin-down band and vice versa. The resulting stationary value can be calculated analytically and is given by Eq. (20). Looking at Fig. 3(a) one can observe that the stationary value of the electron spin predicted by the quantum kinetic theory strongly deviates from the Markovian result. Similar deviations have previously been found for quasifree electrons and have been argued to arise due to strong carrier-impurity correlations [29].

The observed deviations clearly reveal effects that cannot be captured on a Markovian level. In order to obtain a quantitative understanding of the effects of correlations in the system, we plot various contributions to the total energy in Fig. 3(b). All energy expectation values are divided by the constant exciton density after the excitation pulse to obtain energies per exciton.

First of all, we see that the kinetic energy per exciton (red dashed-dotted curve) increases after the pulse, which is partly due to the scattering from the spin-up to the spin-down

exciton parabola (cf. Fig. 1). However, the kinetic energy becomes even larger than the total energy (blue solid curve) after the pulse, which is compensated by the buildup of a negative correlation energy of about -0.6 meV per exciton. A finite correlation energy is obtained due to the magnetic $s-d$ interaction (orange dashed curve) and, even more prominent, due to the nonmagnetic interactions given by E_{nm}^c which includes the $p-d$ interaction (purple dotted curve). Due to the pinned hole spins, the latter causes no spin flip of the electron and can therefore be regarded as a contribution to the nonmagnetic scattering [22]. The magnetic correlation energy is significantly smaller than the nonmagnetic one because both coupling constants associated with nonmagnetic scattering, namely J_{pd} and J_0^e, are about four or two times larger than the magnetic coupling constant J_{sd}, respectively.

It is also interesting to compare the analytical expressions for the correlation energies in the Markov limit with the predictions of the QKT. This is done by evaluating Eqs. (25) with the occupations and spins obtained from the quantum kinetic simulation at discrete time steps. In this way, the aforementioned increase in kinetic energy per exciton due to the correlations is also accounted for in the Markovian expressions for the energies. The results are given by the circles and triangles in Fig. 3(b) and are in good agreement with the full quantum kinetic calculation where the energies are calculated according to Eq. (24).

The occupation of states with higher kinetic energy can be seen most clearly in Fig. 4, which shows the time evolution of the energetically-resolved exciton occupation on the $1s$ parabola. Based on the discussion in Sec. III B, in the Markov limit one expects a scattering only between states with $E = 0$ and $E = \hbar\omega_{sf}$ (cf. dashed line in Fig. 4), so that no other energies would be occupied. However, the correlations cause a significant redistribution towards states with other center-of-mass momenta, so that excitons reach kinetic energies that are inaccessible in the Markov limit. The fact that states with kinetic energies other than $E = 0$ and $E = \hbar\omega_{sf}$ remain occupied even after tens of picoseconds underlines that the redistribution is not to be associated with energy-time uncertainty but is
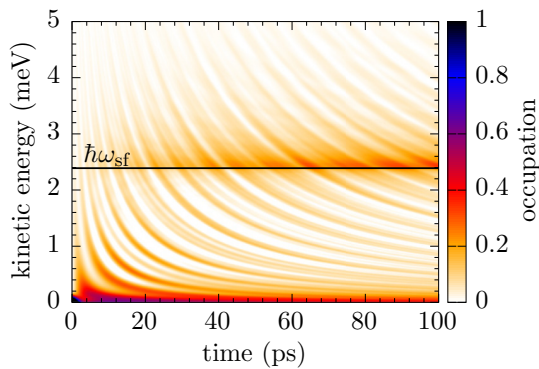
FIG. 4. Time evolution of the energetically-resolved exciton occupation using the same parameters as in Fig. 3. The dashed line corresponds to the spin-flip scattering shift $\hbar\omega_{sf} \approx 2.4$ meV.

rather caused by true many-body correlations in the system which remain finite even for long times. Experimentally, the time-resolved energetic redistribution of excitons on the $1s$ parabola can be observed, e.g., using LO-phonon-assisted photoluminescence which has been done for undoped ZnSe-based quantum wells by various groups in the past [50–53].

Figure 4 can also be used to understand the difference in the stationary value of the exciton-bound electron spin in Fig. 3(a) when comparing the quantum kinetic with the Markovian result. In the Markov approximation, finite occupations are only possible at a kinetic energy which corresponds exactly to the spin-flip scattering $\hbar\omega_{sf}$, which is represented in Fig. 4 by the dashed line. Due to the correlations it also becomes possible to occupy states below $\hbar\omega_{sf}$, which then cannot scatter back to $K = 0$ but remain in the opposite spin state. This causes the deviation of the stationary value of s_{eq}^z observed in Fig. 3(a).

B. Voigt configuration

If the magnetic field is oriented perpendicular with respect to the initial spin polarization, the Markovian Eqs. (B1) predict a damped oscillation of the spin, where the damping is typically associated with a T_2 time in experiments [24]. The time evolution of the electron spin in such a configuration is depicted in Fig. 5 and is normalized with respect to the maximum spin reached directly after the pulse.

The quantum kinetic calculation (blue solid curve) shows a damped precession that reaches an almost stationary value on a time scale of about 100 ps, whereas the Markovian simulation (black dashed-dotted curve) predicts a precession which decays to zero on approximately half that time scale. Surprisingly, the magnitude of the long-time spin polarization in the quantum kinetic result is even larger than 10% of the polarization directly after the pulse and is thus no marginal effect. Thus, instead of only quantitatively changing the damping of the spin precession, the quantum kinetics here also leads to a qualitatively different behavior of the electron spin.

A comparison of the precession frequencies in the quantum kinetic and the Markovian results reveals that the frequency predicted by the QKT is very close to the mean-field frequency ω_e for the first few oscillations but starts to become notably renormalized after approximately 30 ps. However, the Markovian result is nearly decayed by that time, whereas significant oscillations in the quantum kinetic result prevail.
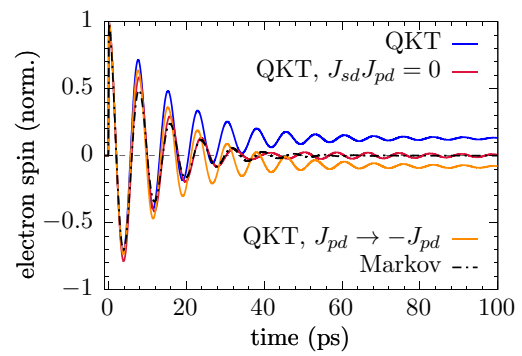

FIG. 5. Time evolution of the exciton-bound electron spin (z component) in an in-plane external magnetic field $B = 0.1$ T (x direction) using the quantum kinetic theory (QKT), data from a quantum kinetic simulation where the cross terms $J_{sd}J_{pd}$ have been artificially switched off (QKT, $J_{sd}J_{pd} = 0$), the quantum kinetic result with the opposite sign of J_{pd} (QKT, $J_{pd} \rightarrow -J_{pd}$), and a Markovian simulation (Markov). The results are normalized with respect to the maximum spin directly after the pulse and the Mn content of the quantum well is $x = 1\%$.

As discussed in Sec. III C, the finite value of the spin polarization at long times can be interpreted as a consequence of the symmetry breaking due to the hh spins which are pinned along the growth direction. Without the hole spins, only the initial value of the electron spin due to the optical excitation breaks the rotational symmetry around the axis of the magnetic field. But since one could, in principle, prepare the initial spin in any direction and the dynamics after the excitation remains the same, the information about the initial spin orientation is lost for long times so that the spin is expected to decay to zero. However, when taking the hole spins into account, there always exists a preferred direction (the growth direction) in the system which remains distinguished even for long times. In the Markovian Eqs. (B1), it was found that the coupling between the spin-up/spin-down occupations and the perpendicular spin components is mediated by terms proportional to the product of coupling constants $J_{sd}J_{pd}$, without which an exponentially damped oscillation of the spin around zero is predicted [cf. Eq. (22)]. Indeed, if we remove these cross terms in the quantum kinetic calculation and thus effectively eliminate the information about the direction of the hole spins we qualitatively recover this prediction (cf. red solid curve in Fig. 5). This finding corroborates that the hh spins cause a symmetry breaking and lead to a finite long-time electron spin polarization in the quantum kinetic result.

Based on the previous discussion, it is clear that the prefactor $J_{sd}J_{pd}$ not only determines the magnitude of the long-time spin polarization but also its sign. Thus, changing the sign of the coupling constant J_{pd} also causes the stationary value of the spin to change its sign, which is confirmed by the corresponding quantum kinetic calculation in Fig. 5 (orange solid curve). This provides a way to extract the sign of J_{pd} relative to J_{sd} in DMS.

C. Exciton spin-transfer rates

In order to quantify exciton spin-transfer rates as observed in the quantum kinetic simulations even for cases where the time
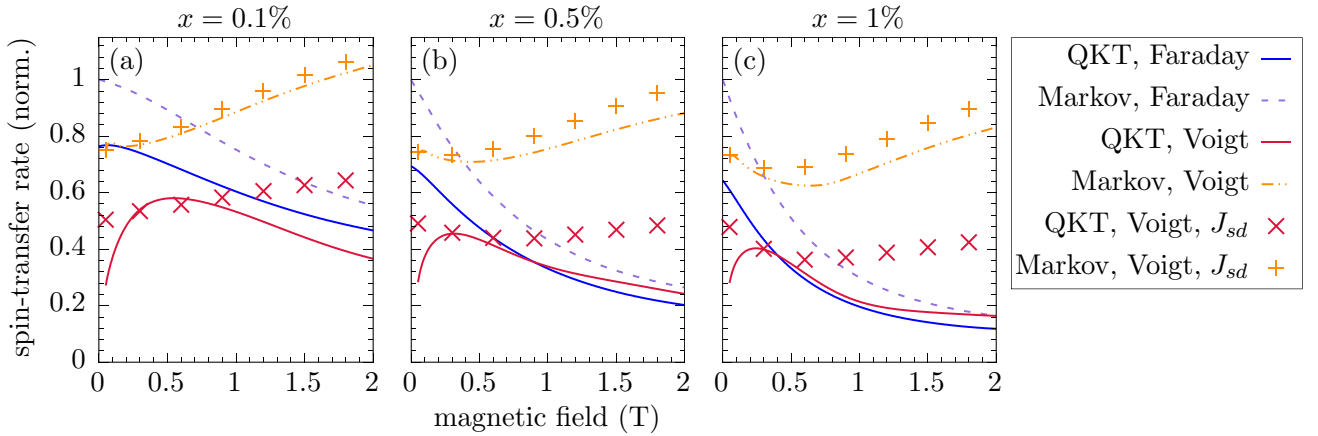
FIG. 6. Quantum kinetic prediction for the exciton spin-transfer rate as a function of magnetic field in Faraday (QKT, Faraday) and Voigt (QKT, Voigt) configuration, respectively, in a $Zn_{1-x}Mn_xSe$ quantum well with doping fraction (a) $x = 0.1\%$, (b) $x = 0.5\%$, and (c) $x = 1\%$. The rates are normalized with respect to the Fermi-golden-rule result for vanishing field and are compared with the Markovian predictions based on Eq. (19) (Markov, Faraday) and Eqs. (B1) (Markov, Voigt), respectively. Also shown are the quantum kinetic results for the Voigt configuration with only the magnetic coupling constant J_{sd} accounted for (QKT, Voigt, J_{sd}) as well as the corresponding Markovian predictions (Markov, Voigt, J_{sd}).

evolution of the spin is highly nonexponential, we numerically extract the time where the envelope of the spin component parallel to the growth direction has decayed to a value of $\frac{1}{e}$ times the difference between the maximum spin after the pulse and its stationary value reached at long times. This is done for simulations using three different Mn doping fractions with the magnetic field oriented along the growth direction (Faraday geometry) and perpendicular to it (Voigt geometry), respectively. The results obtained from the quantum kinetic calculations are compared with the corresponding Markovian predictions in Fig. 6. All results are normalized with respect to the Fermi-golden-rule value, which is 0.01 ps^{-1}, 0.07 ps^{-1}, and 0.13 ps^{-1} for a Mn content of $x = 0.1\%$, $x = 0.5\%$, and $x = 1\%$, respectively.

In Faraday geometry, the Markov approximation (purple dashed curve) predicts a decrease of the spin-transfer rate with increasing magnetic field. This is mainly due to evaluating the exciton form factor in Eq. (19) at larger values of ω_{sf} where the form factor has smaller values (cf. Fig. 2). Since the exciton form factor acts as a prefactor for the rate, a decrease in the form factor results in a smaller rate. For all Mn doping fractions depicted in Fig. 6, the quantum kinetic result (blue solid curve) also follows this trend, albeit quantitative differences of up to 30% are found for small magnetic fields in case of a 1% doping fraction. The quantitative deviations are most pronounced for vanishing magnetic field where the cutoff of the memory in the quantum kinetic equations due to the proximity to the bottom of the exciton parabola has the largest effect [22]. For higher fields, this cutoff becomes less and less important and the spin transfer is again dominated by the decay of the exciton form factor. This is also the reason why the quantum kinetic result approaches the Markov limit for high fields.

In contrast to Ref. [22], where it was found that the QKT predicts an exciton spin-transfer rate for vanishing magnetic field that is half as large as the Markovian one, here we find that the QKT rate for the Faraday configuration at $B = 0$ is approximately between 76% and 64% of the Markovian rate for

a Mn content of $x = 0.1\%$ and $x = 1\%$, respectively. The main reason for this discrepancy lies in the method which is used here to numerically extract the spin-transfer rate. Although the method can be used to obtain a quantitative description of the decay, it does not capture the highly nonexponential spin dynamics in this case which is characterized by a significant spin overshoot [22]. On the other hand, quantum kinetic features are generally more pronounced for higher doping concentrations, which means that for a Mn content on the order of 0.1% it is to be expected that such features are not as prominent as for doping fractions of about 5% as considered in Ref. [22].

Surprisingly, the behavior of the quantum kinetic spin-transfer rates obtained in Voigt geometry (red solid curve) differs from the Markovian result (orange dashed-dotted curve) not only quantitatively but also shows a completely reversed dependence on the magnetic field even for small doping fractions. For a very dilute quantum well with $x = 0.1\%$ in a transverse magnetic field, Fig. 6(a) shows that the Markovian result increases continuously with increasing magnetic field. Increasing the doping fraction of the quantum well causes the appearance of a minimum for small fields in the Markovian rates after which an almost linear increase of the rate is observed. This increase is a consequence of the term proportional to $b^{\parallel} F_{\eta_h 1s1s}^{\eta_h \omega \omega_1} \delta(\omega - \omega_1)$ that appears in the first line of Eq. (B1b) and Eq. (B1c). Since the majority of excitons remains at $\omega_1 \approx 0$ throughout the Markovian dynamics, the delta function causes the exciton form factor to be evaluated at $\omega = \omega_1 \approx 0$. However, for $\omega = 0$, Eq. (12) reduces to the normalization integral so that $F_{\eta_h 1s1s}^{\eta_h 00} = 1$ no longer depends on ω_1. Thus, only the dependence on the second moment $b^{\parallel}$ of the Mn spin system remains, which becomes larger for higher fields and is unaffected by the exciton form factor.

In contrast, in the quantum kinetic calculation, the described tendency is reversed: Instead of a minimum, one observes a distinct maximum in the magnetic-field dependence of the spin-transfer rates. The magnetic field corresponding to
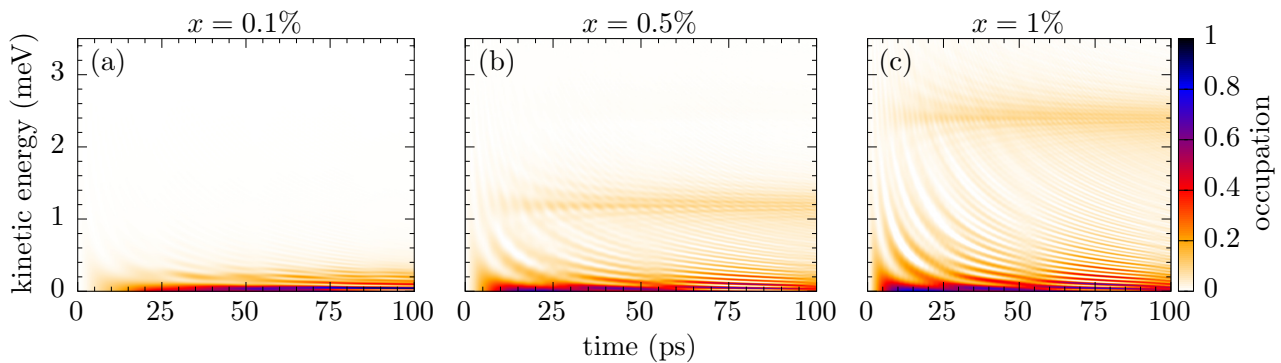
FIG. 7. Time evolution of the energetically-resolved exciton occupation in a transverse magnetic field $B = 0.5$ T in a $\text{Zn}_{1-x}\text{Mn}_x\text{Se}$ quantum well with doping fraction (a) $x = 0.1\%$, (b) $x = 0.5\%$, and (c) $x = 1\%$.

this maximum is $B_{max} \approx 0.5$ T for $x = 0.1\%$ and shifts to $B_{max} \approx 0.2$ T when increasing the impurity content by one order of magnitude to $x = 1\%$. For magnetic fields larger than B_{max}, the QKT then predicts a decrease of the rate with increasing magnetic field, a result which is completely opposite to the Markovian expectation. A similar nonmonotonic behavior of spin-transfer rates in transverse magnetic fields has been observed experimentally in this parameter regime for $\text{Cd}_{1-x}\text{Mn}_x\text{Te}$ quantum wells [13,14]. In order to understand the deviations between the quantum kinetic prediction and the Markovian result in the Voigt configuration, recall the explanation of the increasing Markovian rate given above. The crucial simplification there is the assumption that the excitons remain close to $\omega \approx 0$ throughout the dynamics. However, if correlations between excitons and impurities are taken into account there is a redistribution of excitons in K space even for the case of transverse magnetic fields. Thus, the delta functions appearing in Eqs. (B1) actually have to be evaluated using the quantum kinetic result for $\mathbf{s}_{\omega_1}^{\perp}$, which is broadened due to the redistribution and therefore has finite values also for $\omega_1 \neq 0$. This means that, overall, the spin decay will be damped down by an effective exciton form factor evaluated at ω values determined by the scattering, thereby explaining the observed decrease of the rate obtained by quantum kinetic calculations. The redistribution in K space for a transverse field $B = 0.5$ T for the three different doping concentrations discussed previously is shown in Fig. 7, revealing a visible redistribution even for a Mn content as low as $x = 0.1\%$. This underlines the fact that the deviations of the quantum kinetic transverse spin-transfer rates from the Markovian ones has to be indeed attributed to an energetic redistribution of the exciton center-of-mass momenta which grows stronger with increasing doping fraction.

Furthermore, if we artificially switch off the nonmagnetic scattering, the spin-transfer rates extracted from the corresponding quantum kinetic results (cf. red crosses in Fig. 6) qualitatively follow the Markovian prediction (cf. orange pluses in Fig. 6) for all doping concentrations considered here and only a quantitative difference is observed. In the equations of motion, neglecting the nonmagnetic scattering amounts to setting all coupling constants except J_{sd} to zero. The maxima in the exciton spin-transfer rates in Figs. 6(b) and 6(c), respectively, are qualitatively similar to experimentally

observed minima in the electron spin-transfer times [13,14]. In our model, this nonmonotonic behavior is a consequence of the formation of excitons and can be explained with an enhanced quantum kinetic redistribution due to the nonmagnetic scattering which is not captured on a Markovian level.

The fact that nonmagnetic scattering has a much more substantial impact in Voigt geometry compared with the Faraday configuration can also be understood on a more intuitive level. In Voigt geometry, the electron spin undergoes a precession-type dynamics, i.e., the overall spin decay is mainly due to ensemble averaging rather than a redistribution to different energy eigenstates. In this context, the observed decrease of the quantum kinetic spin-transfer rate compared with the Markovian prediction can be understood as a consequence of one or multiple scattering events which occur during one precession cycle of a particular spin. The scattering then acts similar to the well-known D'yakonov-Perel' mechanism [54,55] where the spin-decay rate is inversely proportional to the momentum scattering rate. Thus, if momentum scattering is important in the system (cf. Fig. 7), one would expect a reduction of the spin-transfer rate when compared to a situation where momentum scattering is not taken into account.

V. CONCLUSION

We have studied the exciton spin dynamics in a Mn-doped ZnSe quantum well after optical excitation using a recently developed quantum kinetic theory [22]. Besides the typically considered $s-d$ and $p-d$ exchange interactions between carriers and magnetic dopants we also account for nonmagnetic scattering at the impurities. Although it does not contribute to spin decay in a Markovian description, nonmagnetic scattering nevertheless gives rise to unexpected results when treated on a quantum kinetic level. Numerical studies of the time-resolved spin dynamics were carried out for Faraday and Voigt geometry in an external magnetic field of varying magnitude, revealing pronounced deviations from Markovian predictions which highlight the importance of correlations between excitons and Mn ions.

First of all, we find quantitative differences between predictions of the QKT and a Markovian theory in Faraday geometry, such as a much larger stationary spin polarization for long

times as well as significantly smaller spin-transfer rates. Our simulations also reveal a complete trend reversal in the exciton spin-transfer rates as a function of magnetic field in Voigt geometry even for an impurity content as low as 0.1%: Whereas the rate slightly decreases for small fields and then increases monotonically according to the Markovian results, the QKT predicts an increase of the rate for small fields followed by a rather monotonic decreasing behavior. This means that, in the QKT, a maximum in the spin-transfer rate for Voigt geometry emerges. Similar nonmonotonic features have also been observed in experiments performed on $Cd_{1-x}Mn_xTe$ in a transverse magnetic field [13,14].

Our calculations reveal that the discrepancy between quantum kinetic and Markovian results originates in correlations between the exciton and Mn subsystem which are particularly enhanced by nonmagnetic scattering of carriers at impurities. These correlations manifest in a time-dependent redistribution of exciton center-of-mass momenta on the $1s$ parabola to values that are prohibited in the Markov limit. This effect is experimentally accessible, e.g., via LO-phonon-assisted photoluminescence, a technique which has already been used successfully for nonmagnetic ZnSe quantum wells [50–53]. The redistribution is accompanied by a buildup of a significant

negative correlation energy, which is a consequence of the many-body nature of the system that is insufficiently described on the single-particle level.

Albeit there is a lengthy derivation involved, it is straightforward to derive Markovian equations from the QKT also for Voigt geometry, where the spin decay is no longer due to scattering between different energy eigenstates and Fermi's golden rule cannot be applied. For transverse magnetic fields, a quantum kinetic calculation furthermore reveals that one obtains an unexpected finite long-time spin polarization which is not observed in the Markov limit and which can be as large as 10% of the maximum spin polarization. We argue that this effect is due to the pinning of the hh spins along the growth direction which breaks the rotational symmetry around the axis of the applied magnetic field. In addition, we find that the sign of the polarization is determined by the sign of the magnetic coupling constant J_{pd} relative to J_{sd}.

APPENDIX A: QUANTUM KINETIC EQUATIONS

Using the notation $\sum_K = \int dK\, D(K)$ with the two-dimensional density of states $D(K) = \frac{V}{2\pi d} K$, the equations of motion corresponding to the variables defined in Eqs. (8) read [22]:

$$\frac{\partial}{\partial t} n_{K_1} = \frac{1}{\hbar}\mathbf{E}\cdot\mathbf{M} 2\mathrm{Im}[y^\uparrow \phi_{1s}]\delta_{K_1,0} - \frac{J_{sd}N_{\mathrm{Mn}}}{\hbar V^2}\sum_{lK} 2\mathrm{Im}[Q_{-\eta_{\mathrm{h}}lK}^{\ lK_1}] + \frac{J_{pd}N_{\mathrm{Mn}}}{\hbar V^2}\sum_K \mathrm{Im}[Q_{\eta_{\mathrm{e}}zK}^{\ 0K_1}]$$

$$- \frac{J_0^{\mathrm{e}}N_{\mathrm{Mn}}}{\hbar V^2}\sum_K 2\mathrm{Im}[Z_{-\eta_{\mathrm{h}}\ K}^{\ 0K_1}] - \frac{J_0^{\mathrm{h}}N_{\mathrm{Mn}}}{\hbar V^2}\sum_K 2\mathrm{Im}[Z_{\eta_{\mathrm{e}}\ K}^{\ 0K_1}], \tag{A1a}$$

$$\frac{\partial}{\partial t} s^l_{K_1} = \frac{1}{\hbar}\mathbf{E}\cdot\mathbf{M}\left(\mathrm{Im}[y^\uparrow\phi_{1s}]\delta_{K_1,0}\delta_{l,z} + \mathrm{Im}[y^\downarrow\phi_{1s}]\delta_{K_1,0}\delta_{l,x} - \mathrm{Re}[y^\downarrow\phi_{1s}]\delta_{K_1,0}\delta_{l,y}\right) + \sum_{jk}\epsilon_{jkl}\omega_{\mathrm{e}}^j s^k_{K_1}$$

$$+ \frac{J_{sd}N_{\mathrm{Mn}}}{\hbar V^2}\sum_K\left(\sum_{jk}\epsilon_{jkl}\mathrm{Re}[Q_{-\eta_{\mathrm{h}}jK}^{\ kK_1}] - \frac{1}{2}\mathrm{Im}[Q_{-\eta_{\mathrm{h}}lK}^{\ 0K_1}]\right) + \frac{J_{pd}N_{\mathrm{Mn}}}{\hbar V^2}\sum_K\mathrm{Im}[Q_{\eta_{\mathrm{e}}zK}^{\ lK_1}]$$

$$- \frac{J_0^{\mathrm{e}}N_{\mathrm{Mn}}}{\hbar V^2}\sum_K 2\mathrm{Im}[Z_{-\eta_{\mathrm{h}}\ K}^{\ lK_1}] - \frac{J_0^{\mathrm{h}}N_{\mathrm{Mn}}}{\hbar V^2}\sum_K 2\mathrm{Im}[Z_{\eta_{\mathrm{e}}\ K}^{\ lK_1}], \tag{A1b}$$

$$\frac{\partial}{\partial t} y^{\uparrow/\downarrow} = \frac{i}{\hbar}\mathbf{E}\cdot\mathbf{M}\phi_{1s}\delta_{\uparrow/\downarrow,\uparrow} - i\left(\omega_0 \pm \frac{1}{2}\omega_{\mathrm{e}}^z - \frac{1}{2}\omega_{\mathrm{h}}^z + \frac{(J_0^{\mathrm{e}}+J_0^{\mathrm{h}})N_{\mathrm{Mn}}}{\hbar V}\right)y^{\uparrow/\downarrow} - i\frac{1}{2}\omega_{\mathrm{e}}^\mp y^{\downarrow/\uparrow}$$

$$- i\frac{J_{sd}N_{\mathrm{Mn}}}{2\hbar V^2}\sum_K\left(\pm q_{-\eta_{\mathrm{h}}zK}^{\uparrow/\downarrow} + q_{-\eta_{\mathrm{h}}\mp K}^{\downarrow/\uparrow}\right) + i\frac{J_{pd}N_{\mathrm{Mn}}}{2\hbar V^2}\sum_K q_{\eta_{\mathrm{e}}zK}^{\uparrow/\downarrow}$$

$$- i\frac{J_0^{\mathrm{e}}N_{\mathrm{Mn}}}{\hbar V^2}\sum_K z_{-\eta_{\mathrm{h}}K}^{\uparrow/\downarrow} - i\frac{J_0^{\mathrm{h}}N_{\mathrm{Mn}}}{\hbar V^2}\sum_K z_{\eta_{\mathrm{e}}K}^{\uparrow/\downarrow}, \tag{A1c}$$

$$\frac{\partial}{\partial t} q_{\eta lK_1}^{\uparrow/\downarrow} = -i\left(\omega_{K_1} \pm \frac{1}{2}\omega_{\mathrm{e}}^z - \frac{1}{2}\omega_{\mathrm{h}}^z + \frac{I(J_0^{\mathrm{e}}+J_0^{\mathrm{h}})N_{\mathrm{Mn}}}{\hbar V}\right)q_{\eta lK_1}^{\uparrow/\downarrow} - i\frac{1}{2}\omega_{\mathrm{e}}^\mp q_{\eta lK_1}^{\downarrow/\uparrow} + \sum_{jk}\epsilon_{jkl}\omega_{\mathrm{Mn}}^j q_{\eta kK_1}^{\uparrow/\downarrow}$$

$$- i\frac{I J_{sd}}{2\hbar}F_{\eta\ 1s1s}^{-\eta_{\mathrm{h}}0K_1}(\pm\langle S^l S^z\rangle y^{\uparrow/\downarrow} + \langle S^l S^\mp\rangle y^{\downarrow/\uparrow}) + i\frac{I J_{pd}}{2\hbar}\langle S^l S^z\rangle F_{\eta\ 1s1s}^{\eta_{\mathrm{e}}0K_1} y^{\uparrow/\downarrow}$$

$$- i\frac{I}{\hbar}\langle S^l\rangle\left(J_0^{\mathrm{e}}F_{\eta\ 1s1s}^{-\eta_{\mathrm{h}}0K_1} + J_0^{\mathrm{h}}F_{\eta\ 1s1s}^{\eta_{\mathrm{e}}0K_1}\right)y^{\uparrow/\downarrow}, \tag{A1d}$$

$$\frac{\partial}{\partial t} z_{\eta K_1}^{\uparrow/\downarrow} = -i\left(\omega_{K_1} \pm \frac{1}{2}\omega_e^z - \frac{1}{2}\omega_h^z + \frac{I(J_0^e + J_0^h)N_{Mn}}{\hbar V}\right) z_{\eta K_1}^{\uparrow/\downarrow} - i\frac{1}{2}\omega_e^\mp z_{\eta K_1}^{\downarrow/\uparrow}$$

$$-i\frac{I J_{sd}}{2\hbar} F_{\eta\ 1s1s}^{-\eta_h 0 K_1}(\pm\langle S^z\rangle y^{\uparrow/\downarrow} + \langle S^\mp\rangle y^{\downarrow/\uparrow}) + i\frac{I J_{pd}}{2\hbar}\langle S^z\rangle F_{\eta\ 1s1s}^{\eta_e 0 K_1} y^{\uparrow/\downarrow}$$

$$-i\frac{I}{\hbar}\left(J_0^e F_{\eta\ 1s1s}^{-\eta_h 0 K_1} + J_0^h F_{\eta\ 1s1s}^{\eta_e 0 K_1}\right) y^{\uparrow/\downarrow}, \tag{A1e}$$

$$\frac{\partial}{\partial t} Q_{\eta l K_1}^{0 K_2} = -i(\omega_{K_2} - \omega_{K_1}) Q_{\eta l K_1}^{0 K_2} + \sum_{jk} \epsilon_{jkl}\omega_{Mn}^j Q_{\eta k K_1}^{0 K_2} + \frac{i}{2\hbar}\mathbf{E}\cdot\mathbf{M}\left((q_{\eta l K_1}^\uparrow \phi_{1s})^* \delta_{K_2,0} - q_{\eta l K_2}^\uparrow \phi_{1s}\delta_{K_1,0}\right)$$

$$+ i\frac{I J_{sd}}{\hbar} F_{\eta\ 1s1s}^{-\eta_h K_1 K_2} \sum_j \left(\langle S^j S^l\rangle s_{K_2}^j - \langle S^l S^j\rangle s_{K_1}^j\right) - i\frac{I J_{pd}}{\hbar} F_{\eta\ 1s1s}^{\eta_e K_1 K_2} \frac{1}{2}\left(\langle S^z S^l\rangle n_{K_2} - \langle S^l S^z\rangle n_{K_1}\right)$$

$$+ i\frac{I}{\hbar}\langle S^l\rangle\left(J_0^e F_{\eta\ 1s1s}^{-\eta_h K_1 K_2} + J_0^h F_{\eta\ 1s1s}^{\eta_e K_1 K_2}\right)\left(n_{K_2} - n_{K_1}\right), \tag{A1f}$$

$$\frac{\partial}{\partial t} Q_{\eta l K_1}^{m K_2} = -i(\omega_{K_2} - \omega_{K_1}) Q_{\eta l K_1}^{m K_2} + \sum_{jk} \epsilon_{jkm}\omega_e^j Q_{\eta l K_1}^{k K_2} + \sum_{jk} \epsilon_{jkl}\omega_{Mn}^j Q_{\eta k K_1}^{m K_2}$$

$$+ \frac{i}{2\hbar}\mathbf{E}\cdot\mathbf{M}\Big[\left((q_{\eta l K_1}^\uparrow \phi_{1s})^*\delta_{K_2,0} - q_{\eta l K_2}^\uparrow \phi_{1s}\delta_{K_1,0}\right)\delta_{m,z} + \left((q_{\eta l K_1}^\downarrow \phi_{1s})^*\delta_{K_2,0} - q_{\eta l K_2}^\downarrow \phi_{1s}\delta_{K_1,0}\right)\delta_{m,x}$$

$$+ i\left((q_{\eta l K_1}^\downarrow \phi_{1s})^*\delta_{K_2,0} + q_{\eta l K_2}^\downarrow \phi_{1s}\delta_{K_1,0}\right)\delta_{m,y}\Big] - i\frac{I J_{pd}}{\hbar} F_{\eta\ 1s1s}^{\eta_e K_1 K_2} \frac{1}{2}\left(\langle S^z S^l\rangle s_{K_2}^m - \langle S^l S^z\rangle s_{K_1}^m\right)$$

$$+ i\frac{I J_{sd}}{2\hbar} F_{\eta\ 1s1s}^{-\eta_h K_1 K_2} \sum_j \left(\langle S^j S^l\rangle\left(\frac{1}{2}\delta_{j,m}n_{K_2} - i\sum_k \epsilon_{jkm}s_{K_2}^k\right) - \langle S^l S^j\rangle\left(\frac{1}{2}\delta_{j,m}n_{K_1} + i\sum_k \epsilon_{jkm}s_{K_1}^k\right)\right)$$

$$+ i\frac{I}{\hbar}\langle S^l\rangle\left(J_0^e F_{\eta\ 1s1s}^{-\eta_h K_1 K_2} + J_0^h F_{\eta\ 1s1s}^{\eta_e K_1 K_2}\right)\left(s_{K_2}^m - s_{K_1}^m\right), \tag{A1g}$$

$$\frac{\partial}{\partial t} Z_{\eta\ K_1}^{0 K_2} = -i(\omega_{K_2} - \omega_{K_1}) Z_{\eta\ K_1}^{0 K_2} + \frac{i}{2\hbar}\mathbf{E}\cdot\mathbf{M}\left((z_{\eta K_1}^\uparrow \phi_{1s})^*\delta_{K_2,0} - z_{\eta K_2}^\uparrow \phi_{1s}\delta_{K_1,0}\right)$$

$$+ i\frac{I J_{sd}}{\hbar} F_{\eta\ 1s1s}^{-\eta_h K_1 K_2} \sum_j \langle S^j\rangle\left(s_{K_2}^j - s_{K_1}^j\right) - i\frac{I J_{pd}}{\hbar} F_{\eta\ 1s1s}^{\eta_e K_1 K_2} \frac{1}{2}\langle S^z\rangle\left(n_{K_2} - n_{K_1}\right)$$

$$+ i\frac{I}{\hbar}\left(J_0^e F_{\eta\ 1s1s}^{-\eta_h K_1 K_2} + J_0^h F_{\eta\ 1s1s}^{\eta_e K_1 K_2}\right)\left(n_{K_2} - n_{K_1}\right), \tag{A1h}$$

$$\frac{\partial}{\partial t} Z_{\eta\ K_1}^{l K_2} = -i(\omega_{K_2} - \omega_{K_1}) Z_{\eta\ K_1}^{l K_2} + \sum_{jk} \epsilon_{jkl}\omega_e^j Z_{\eta\ K_1}^{k K_2} + \frac{i}{2\hbar}\mathbf{E}\cdot\mathbf{M}\Big[\left((z_{\eta K_1}^\uparrow \phi_{1s})^*\delta_{K_2,0} - z_{\eta K_2}^\uparrow \phi_{1s}\delta_{K_1,0}\right)\delta_{l,z}$$

$$+ \left((z_{\eta K_1}^\downarrow \phi_{1s})^*\delta_{K_2,0} - z_{\eta K_2}^\downarrow \phi_{1s}\delta_{K_1,0}\right)\delta_{l,x} + i\left((z_{\eta K_1}^\downarrow \phi_{1s})^*\delta_{K_2,0} + z_{\eta K_2}^\downarrow \phi_{1s}\delta_{K_1,0}\right)\delta_{l,y}\Big]$$

$$+ i\frac{I J_{sd}}{2\hbar} F_{\eta\ 1s1s}^{-\eta_h K_1 K_2} \sum_j \langle S^j\rangle\left(\left(\frac{1}{2}\delta_{j,l}n_{K_2} - i\sum_k \epsilon_{jkl}s_{K_2}^k\right) - \left(\frac{1}{2}\delta_{j,l}n_{K_1} + i\sum_k \epsilon_{jkl}s_{K_1}^k\right)\right)$$

$$- i\frac{I J_{pd}}{\hbar} F_{\eta\ 1s1s}^{\eta_e K_1 K_2} \frac{1}{2}\langle S^z\rangle\left(s_{K_2}^l - s_{K_1}^l\right) + i\frac{I}{\hbar}\left(J_0^e F_{\eta\ 1s1s}^{-\eta_h K_1 K_2} + J_0^h F_{\eta\ 1s1s}^{\eta_e K_1 K_2}\right)\left(s_{K_2}^l - s_{K_1}^l\right), \tag{A1i}$$

where $\phi_{1s} := R_{1s}(r = 0)$ is the radial part of the $1s$ exciton wave function evaluated at $r = 0$ and quantities A with an index $\pm$ are defined as $A^\pm := A^x \pm i A^y$. The influence of the envelope function $u_0(z)$ due to the confinement is given by

$$I = d\int_{-\frac{d}{2}}^{\frac{d}{2}} dz |u_0(z)|^4 = \frac{3}{2}, \tag{A2}$$

where an infinitely deep quantum well is assumed in the last step.

APPENDIX B: MARKOVIAN EQUATIONS FOR VOIGT GEOMETRY

In Voigt geometry with the coordinate system oriented such that the external magnetic field points along z, the Markovian equations of motion become:

$$\frac{\partial}{\partial t} n^{\uparrow/\downarrow}_{\omega_1} = \Gamma_{\omega_1}(t) + \frac{I N_{\mathrm{Mn}} M}{4\hbar^3 V d} \int_0^\infty d\omega \Big[2 J_{sd}^2 F^{\eta_{\mathrm{h}}\omega\omega_1}_{\eta_{\mathrm{h}}1s1s} \delta(\omega - (\omega_1 \pm \omega_{\mathrm{sf}}))\big(b^\pm n^{\downarrow/\uparrow}_\omega - b^\mp n^{\uparrow/\downarrow}_{\omega_1}\big)$$

$$- J_{sd} J_{pd} F^{\eta_{\mathrm{e}}\omega\omega_1}_{-\eta_{\mathrm{h}}1s1s}\big(\delta(\omega - (\omega_1 \pm \omega_{\mathrm{sf}}))b^\pm s^y_\omega - \delta(\omega - (\omega_1 \mp \omega_{\mathrm{sf}}))b^\pm s^y_{\omega_1} + \delta\big(\omega - (\omega_1 \mp \omega^z_{\mathrm{Mn}})\big)\big(b^\pm s^y_\omega - b^\mp s^y_{\omega_1}\big)\big)$$

$$+ \frac{1}{2} J_{pd}^2 F^{\eta_{\mathrm{e}}\omega\omega_1}_{\eta_{\mathrm{e}}1s1s}\big(\delta\big(\omega - (\omega_1 + \omega^z_{\mathrm{Mn}})\big)\big(b^- n^{\uparrow/\downarrow}_\omega - b^+ n^{\uparrow/\downarrow}_{\omega_1}\big) + \delta\big(\omega - (\omega_1 - \omega^z_{\mathrm{Mn}})\big)\big(b^+ n^{\uparrow/\downarrow}_\omega - b^- n^{\uparrow/\downarrow}_{\omega_1}\big)\big)$$

$$\mp \frac{1}{\pi} J_{sd} J_{pd} F^{\eta_{\mathrm{e}}\omega\omega_1}_{-\eta_{\mathrm{h}}1s1s}\bigg(\frac{b^\pm s^x_\omega}{\omega - (\omega_1 \pm \omega_{\mathrm{sf}})} + \frac{b^\pm s^x_{\omega_1}}{\omega - (\omega_1 \mp \omega_{\mathrm{sf}})} - \frac{b^\pm s^x_\omega - b^\mp s^x_{\omega_1}}{\omega - \big(\omega_1 \mp \omega^z_{\mathrm{Mn}}\big)}\bigg)\Big], \tag{B1a}$$

$$\frac{\partial}{\partial t} s^x_{\omega_1} = -\frac{I N_{\mathrm{Mn}} M}{4\hbar^3 V d} \int_0^\infty d\omega \Big[J_{sd}^2 F^{\eta_{\mathrm{h}}\omega\omega_1}_{\eta_{\mathrm{h}}1s1s}\big(\delta(\omega - (\omega_1 + \omega_{\mathrm{sf}}))b^- + \delta(\omega - (\omega_1 - \omega_{\mathrm{sf}}))b^+ + 4\delta(\omega - \omega_1)b^\parallel\big)s^x_{\omega_1}$$

$$- \frac{1}{2} J_{pd}^2 F^{\eta_{\mathrm{e}}\omega\omega_1}_{\eta_{\mathrm{e}}1s1s}\big(\delta\big(\omega - (\omega_1 + \omega^z_{\mathrm{Mn}})\big)\big(b^- s^x_\omega - b^+ s^x_{\omega_1}\big) + \delta\big(\omega - (\omega_1 - \omega^z_{\mathrm{Mn}})\big)\big(b^+ s^x_\omega - b^- s^x_{\omega_1}\big)\big)$$

$$- \frac{1}{2\pi} J_{sd} J_{pd} F^{\eta_{\mathrm{e}}\omega\omega_1}_{-\eta_{\mathrm{h}}1s1s}\bigg(\frac{b^+ n^\downarrow_\omega - b^- n^\uparrow_{\omega_1}}{\omega - (\omega_1 + \omega_{\mathrm{sf}})} - \frac{b^- n^\uparrow_\omega - b^+ n^\downarrow_{\omega_1}}{\omega - (\omega_1 - \omega_{\mathrm{sf}})} + \frac{b^- n^\uparrow_\omega - b^+ n^\uparrow_{\omega_1}}{\omega - \big(\omega_1 + \omega^z_{\mathrm{Mn}}\big)} - \frac{b^+ n^\downarrow_\omega - b^- n^\downarrow_{\omega_1}}{\omega - \big(\omega_1 - \omega^z_{\mathrm{Mn}}\big)}\bigg)\Big]$$

$$- \bigg[\omega^z_{\mathrm{e}} - \frac{I N_{\mathrm{Mn}} M}{2\pi\hbar^3 d V} \int_0^\infty d\omega \bigg(\frac{2 J_{sd} J_0^{\mathrm{e}} F^{\eta_{\mathrm{h}}\omega\omega_1}_{\eta_{\mathrm{h}}1s1s} b^0 + 2 J_{sd} J_0^{\mathrm{h}} F^{\eta_{\mathrm{e}}\omega\omega_1}_{-\eta_{\mathrm{h}}1s1s} b^0}{\omega - \omega_1} + \frac{\frac{1}{2} J_{sd}^2 F^{\eta_{\mathrm{h}}\omega\omega_1}_{\eta_{\mathrm{h}}1s1s} b^-}{\omega - (\omega_1 + \omega_{\mathrm{sf}})} - \frac{\frac{1}{2} J_{sd}^2 F^{\eta_{\mathrm{h}}\omega\omega_1}_{\eta_{\mathrm{h}}1s1s} b^+}{\omega - (\omega_1 - \omega_{\mathrm{sf}})}\bigg)\bigg] s^y_{\omega_1}, \tag{B1b}$$

$$\frac{\partial}{\partial t} s^y_{\omega_1} = \Gamma_{\omega_1}(t) - \frac{I N_{\mathrm{Mn}} M}{4\hbar^3 V d} \int_0^\infty d\omega \Big[J_{sd}^2 F^{\eta_{\mathrm{h}}\omega\omega_1}_{\eta_{\mathrm{h}}1s1s}\big(\delta(\omega - (\omega_1 + \omega_{\mathrm{sf}}))b^- + \delta(\omega - (\omega_1 - \omega_{\mathrm{sf}}))b^+ + 4\delta(\omega - \omega_1)b^\parallel\big)s^y_{\omega_1}$$

$$- \frac{1}{2} J_{sd} J_{pd} F^{\eta_{\mathrm{e}}\omega\omega_1}_{-\eta_{\mathrm{h}}1s1s}\big(\delta(\omega - (\omega_1 + \omega_{\mathrm{sf}}))\big(b^+ n^\downarrow_\omega - b^- n^\uparrow_{\omega_1}\big) + \delta(\omega - (\omega_1 - \omega_{\mathrm{sf}}))\big(b^- n^\uparrow_\omega - b^+ n^\downarrow_{\omega_1}\big)\big)$$

$$- \frac{1}{2} J_{sd} J_{pd} F^{\eta_{\mathrm{e}}\omega\omega_1}_{-\eta_{\mathrm{h}}1s1s}\big(\delta\big(\omega - (\omega_1 + \omega^z_{\mathrm{Mn}})\big)\big(b^- n^\uparrow_\omega - b^+ n^\uparrow_{\omega_1}\big) + \delta\big(\omega - (\omega_1 - \omega^z_{\mathrm{Mn}})\big)\big(b^+ n^\downarrow_\omega - b^- n^\downarrow_{\omega_1}\big)\big)$$

$$- \frac{1}{2} J_{pd}^2 F^{\eta_{\mathrm{e}}\omega\omega_1}_{\eta_{\mathrm{e}}1s1s}\big(\delta\big(\omega - (\omega_1 + \omega^z_{\mathrm{Mn}})\big)\big(b^- s^y_\omega - b^+ s^y_{\omega_1}\big) + \delta\big(\omega - (\omega_1 - \omega^z_{\mathrm{Mn}})\big)\big(b^+ s^y_\omega - b^- s^y_{\omega_1}\big)\big)\Big]$$

$$+ \bigg[\omega^z_{\mathrm{e}} - \frac{I N_{\mathrm{Mn}} M}{2\pi\hbar^3 V d} \int_0^\infty d\omega \bigg(\frac{2 J_{sd} J_0^{\mathrm{e}} F^{\eta_{\mathrm{h}}\omega\omega_1}_{\eta_{\mathrm{h}}1s1s} b^0 + 2 J_{sd} J_0^{\mathrm{h}} F^{\eta_{\mathrm{e}}\omega\omega_1}_{-\eta_{\mathrm{h}}1s1s} b^0}{\omega - \omega_1} + \frac{\frac{1}{2} J_{sd}^2 F^{\eta_{\mathrm{h}}\omega\omega_1}_{\eta_{\mathrm{h}}1s1s} b^-}{\omega - (\omega_1 + \omega_{\mathrm{sf}})} - \frac{\frac{1}{2} J_{sd}^2 F^{\eta_{\mathrm{h}}\omega\omega_1}_{\eta_{\mathrm{h}}1s1s} b^+}{\omega - (\omega_1 - \omega_{\mathrm{sf}})}\bigg)\bigg] s^x_{\omega_1}. \tag{B1c}$$

Note that, for numerical calculations, terms of the form $\frac{1}{\omega - \omega_0}$, which stem from the imaginary part of the memory integral, are dropped since they contain nonintegrable divergences. Assuming a Gaussian laser pulse of the form $E(t) = E_0 \exp(-\frac{t^2}{2\sigma^2})$ and performing the Markov limit on the laser-induced carrier-generation term, we obtain for the generation rate

$$\Gamma_{\omega_1}(t) = \frac{1}{\hbar^2} E(t) E_0 |M|^2 \phi_{1s}^2 \int_{t_0}^t d\tau e^{-\frac{\tau^2}{2\sigma^2}} \delta_{\omega_1,0} \tag{B2}$$

with σ related to the time t_{FWHM} at full width at half maximum of the pulse via $\sigma = \frac{t_{\mathrm{FWHM}}}{2\sqrt{2\log 2}}$.

[1] T. Dietl and H. Ohno, Rev. Mod. Phys. **86**, 187 (2014).
[2] J. Kossut and J. A. Gaj, eds., *Introduction to the Physics of Diluted Magnetic Semiconductors* (Springer, Berlin, 2010).
[3] J. K. Furdyna, J. Appl. Phys. **64**, R29 (1988).
[4] J. K. Furdyna and J. Kossut, eds., *Semiconductors and Semimetals* (Academic Press, San Diego, 1988).
[5] T. Dietl, Nat. Mater. **9**, 965 (2010).
[6] H. Ohno, Nat. Mater. **9**, 952 (2010).
[7] I. Žutić, J. Fabian, and S. Das Sarma, Rev. Mod. Phys. **76**, 323 (2004).
[8] D. Awschalom and M. Flatté, Nat. Phys. **3**, 153 (2007).
[9] M. Vladimirova, S. Cronenberger, P. Barate, D. Scalbert, F. J. Teran, and A. P. Dmitriev, Phys. Rev. B **78**, 081305 (2008).
[10] S. A. Crooker, D. D. Awschalom, J. J. Baumberg, F. Flack, and N. Samarth, Phys. Rev. B **56**, 7574 (1997).

[11] S. A. Crooker, J. J. Baumberg, F. Flack, N. Samarth, and D. D. Awschalom, Phys. Rev. Lett. **77**, 2814 (1996).

[12] C. Camilleri, F. Teppe, D. Scalbert, Y. G. Semenov, M. Nawrocki, M. Dyakonov, J. Cibert, S. Tatarenko, and T. Wojtowicz, Phys. Rev. B **64**, 085331 (2001).

[13] S. Cronenberger, P. Barate, A. Brunetti, M. Vladimirova, D. Scalbert, F. Teran, G. Karzewski, and T. Wojtowicz, Superlattices Microstruct. **43**, 427 (2008), proceedings of the 7th International Conference on Physics of Light-Matter Coupling in Nanostructures.

[14] Z. Ben Cheikh, S. Cronenberger, M. Vladimirova, D. Scalbert, F. Perez, and T. Wojtowicz, Phys. Rev. B **88**, 201306 (2013).

[15] K. E. Rönnburg, E. Mohler, H. G. Roskos, K. Ortner, C. R. Becker, and L. W. Molenkamp, Phys. Rev. Lett. **96**, 117203 (2006).

[16] H. Krenn, K. Kaltenegger, T. Dietl, J. Spałek, and G. Bauer, Phys. Rev. B **39**, 10918 (1989).

[17] J. J. Baumberg, D. D. Awschalom, N. Samarth, H. Luo, and J. K. Furdyna, Phys. Rev. Lett. **72**, 717 (1994).

[18] R. Akimoto, K. Ando, F. Sasaki, S. Kobayashi, and T. Tani, J. Lumin. **72**, 309 (1997).

[19] A. Murayama, K. Seo, K. Nishibayashi, I. Souma, and Y. Oka, Appl. Phys. Lett. **88**, 261105 (2006).

[20] C. J. P. Smits, S. C. A. van Driel, M. van Kampen, W. J. M. de Jonge, B. Koopmans, and G. Karczewski, Phys. Rev. B **70**, 115307 (2004).

[21] H. Sakurai, K. Seo, Z. H. Chen, K. Kayanuma, T. Tomita, A. Murayama, and Y. Oka, Phys. Status Solidi C **1**, 981 (2004).

[22] F. Ungar, M. Cygorek, and V. M. Axt, Phys. Rev. B **95**, 245203 (2017).

[23] M. Cygorek and V. M. Axt, J. Phys.: Conf. Series **647**, 012042 (2015).

[24] E. Tsitsishvili and H. Kalt, Phys. Rev. B **73**, 195402 (2006).

[25] M. Z. Maialle, E. A. de Andrada e Silva, and L. J. Sham, Phys. Rev. B **47**, 15776 (1993).

[26] M. Maialle and L. Sham, Surf. Sci. **305**, 256 (1994).

[27] Y. Tang, W. Xie, K. C. Mandal, J. A. McGuire, and C. W. Lai, J. Appl. Phys. **118**, 113103 (2015).

[28] G. Bastard and R. Ferreira, Surf. Sci. **267**, 335 (1992).

[29] M. Cygorek, F. Ungar, P. I. Tamborenea, and V. M. Axt, Phys. Rev. B **95**, 045204 (2017).

[30] C. Thurn, M. Cygorek, V. M. Axt, and T. Kuhn, Phys. Rev. B **87**, 205301 (2013).

[31] M. W. Wu, J. H. Jiang, and M. Q. Weng, Phys. Rep. **493**, 61 (2010).

[32] R. Winkler, *Spin-Orbit Coupling Effects in Two-Dimensional Electron and Hole Systems* (Springer, Berlin, 2003).

[33] F. Rossi and T. Kuhn, Rev. Mod. Phys. **74**, 895 (2002).

[34] C. Thurn and V. M. Axt, Phys. Rev. B **85**, 165203 (2012).

[35] V. M. Axt and A. Stahl, Z. Phys. B **93**, 195 (1994).

[36] G. E. Pikus and G. L. Bir, Zh. Eksp. Teor. Fiz. **60**, 195 (1971) [Sov. Phys. JETP **33**, 108 (1971)].

[37] T. Uenoyama and L. J. Sham, Phys. Rev. Lett. **64**, 3070 (1990).

[38] R. Ferreira and G. Bastard, Phys. Rev. B **43**, 9687 (1991).

[39] R. Akimoto, K. Ando, F. Sasaki, S. Kobayashi, and T. Tani, Phys. Rev. B **56**, 9726 (1997).

[40] B. T. Jonker, L. P. Fu, W. Y. Yu, W. C. Chou, A. Petrou, and J. Warnock, J. Electron. Mater. **22**, 489 (1993).

[41] M. Cygorek and V. M. Axt, Phys. Rev. B **90**, 035206 (2014).

[42] Ł. Cywiński and L. J. Sham, Phys. Rev. B **76**, 045205 (2007).

[43] Y. G. Semenov and F. V. Kirichenko, Semicond. Sci. Technol. **11**, 1268 (1996).

[44] Y. G. Semenov, Phys. Rev. B **67**, 115319 (2003).

[45] J. H. Jiang, Y. Zhou, T. Korn, C. Schüller, and M. W. Wu, Phys. Rev. B **79**, 155201 (2009).

[46] M. Cygorek, P. I. Tamborenea, and V. M. Axt, Phys. Rev. B **93**, 035206 (2016).

[47] O. Morandi, P.-A. Hervieux, and G. Manfredi, New J. Phys. **11**, 073010 (2009).

[48] R. Triboulet and P. Siffert, eds., *CdTe and Related Compounds; Physics, Defects, Hetero- and Nano-structures, Crystal Growth, Surfaces and Applications*, 1st ed., European Materials Research Society Series (Elsevier, Amsterdam, 2009).

[49] I. Strzalkowski, S. Joshi, and C. R. Crowell, Appl. Phys. Lett. **28**, 350 (1976).

[50] H. Zhao, S. Moehl, and H. Kalt, Phys. Rev. Lett. **89**, 097401 (2002).

[51] H. Zhao, S. Moehl, and H. Kalt, Appl. Phys. Lett. **81**, 2794 (2002).

[52] M. Umlauff, J. Hoffmann, H. Kalt, W. Langbein, J. M. Hvam, M. Scholl, J. Söllner, M. Heuken, B. Jobst, and D. Hommel, Phys. Rev. B **57**, 1390 (1998).

[53] C. D. Poweleit, L. M. Smith, and B. T. Jonker, Phys. Rev. B **55**, 5062 (1997).

[54] M. I. D'yakonov and V. I. Perel', Zh. Eksp. Teor. Fiz. **60**, 1954 (1971) [Sov. Phys. JETP **33**, 1053 (1971)].

[55] M. Cosacchi, M. Cygorek, F. Ungar, and V. M. Axt, Phys. Rev. B **95**, 195313 (2017).

Publication 3

Many-body correlations brought to light in absorption spectra of diluted magnetic semiconductors

F. Ungar, M. Cygorek, and V. M. Axt

Many-body correlations brought to light in absorption spectra of diluted magnetic semiconductors

F. Ungar,[1] M. Cygorek,[2] and V. M. Axt[1]

[1]*Theoretische Physik III, Universität Bayreuth, 95440 Bayreuth, Germany*
[2]*Department of Physics, University of Ottawa, Ottawa, Ontario, Canada K1N 6N5*

Diluted magnetic semiconductors are materials well known to exhibit strong correlations which typically manifest in carrier-mediated magnetic ordering. In this Rapid Communication, we show that the interaction between excitons and magnetic impurities in these materials is even strong enough to cause a significant deviation from the bare exciton picture in linear absorption spectra of quantum well nanostructures. It is found that exciton-impurity correlations induce a characteristic fingerprint in the form of an additional feature close to the exciton resonance in combination with a shift of the main exciton line of up to a few meV. We trace back these features to the form of the self-energy and demonstrate that reliable values of the average correlation energy per exciton can be extracted directly from the spectra. Since the only requirement for our findings is sufficiently strong correlations, the results can be generalized to other strongly correlated systems.

Many-body correlations are an important and extensively studied phenomenon in many areas of physics [1–15], the impact of which is typically investigated using a nonlinear response such as four-wave mixing [16–21]. An interesting subclass of materials that are known for strong correlation effects are diluted magnetic semiconductors (DMSs), i.e., II-VI or III-V semiconductor alloys with a small percentage of magnetic dopants, typically manganese [22–26]. Most notably in these materials, correlations have been found to cause carrier-mediated ferromagnetic ordering [27], a topic which is still actively investigated [6]. DMSs are also known for possible applications in the field of spintronics [28–32], either as a spin aligner [33] or in terms of data storage applications [34].

The physics in DMSs is typically dominated by the strong exchange interaction between carriers and magnetic dopants which is usually modeled by a Kondo-type Hamiltonian for electrons and holes with well-established coupling constants [25]. Since typical experiments on DMS nanostructures are performed close to the exciton resonance [35–42], it is evident that effects due to the Coulomb interaction cannot be neglected. In addition, it was already pointed out in the literature that a mean-field treatment of the electron-impurity exchange interaction is often insufficient for an accurate description of ultrafast spin dynamics [43,44] as well as order parameters [6,45].

In this Rapid Communication we explore the impact of exciton-impurity correlations on linear absorption spectra of DMS nanostructures close to the exciton resonance. Considering that carrier-impurity correlations typically manifest themselves in the dynamical properties of DMSs such as spin overshoots on picosecond timescales [43,46] or modifications of spin-transfer rates [47], it is often challenging to pinpoint these features in experiments since they can be extremely dependent on the particular sample. This is, e.g., due to the variation of the degree of band mixing between light and heavy holes which may cause hole spin relaxation times to

vary between a few picoseconds [37] up to longer than the exciton lifetime [35], which makes it hard to accurately predict experimental observations. Furthermore, it is typically not possible to quantify the amount of correlation energy that has built up in the sample since correlations often merely manifest in band-gap renormalizations or influence spectral widths and are thus hard to isolate [48–52]. It is therefore of particular interest to be able to identify many-body correlation effects in an experimentally well accessible quantity such as the linear absorption spectrum. Indeed, we show that correlation effects are visible in the spectrum of DMSs and lead to an additional feature close to the main exciton peak accompanied by a shift of the bare exciton resonance. Our calculations reveal that the absorption spectrum provides direct access to the average correlation energy per exciton, which is otherwise hard to measure, and thus allows for an estimation of the importance of many-body effects without having to resort to high excitation powers.

We consider a narrow DMS quantum well that is excited close to the 1*s* exciton resonance below the band gap. Furthermore, we focus on the widely studied class of II-VI DMSs where the impurity ions are isoelectronic so that no excess charge carriers are present in the system. Accounting only for the energetically lowest confinement state with respect to the growth direction, which is justified for sufficiently narrow quantum wells below approximately 30 nm [53,54], we obtain the wave function and the binding energy of the exciton ground state by solving the corresponding Schrödinger equation for electrons and holes bound by the Coulomb interaction. The interactions that typically dominate the physics of DMSs are the *s-d* and *p-d* exchange mechanisms between *s*-type conduction band electrons or *p*-type valence band holes and the localized *d*-shell electrons of the impurity ions, respectively [23,25,26,45]. This interaction describes the scattering of electrons and holes accompanied by a simultaneous spin-flip event of the respective carriers and the magnetic dopants. We also account for a purely nonmagnetic type of

interaction between carriers and impurities that arises, e.g., due to the band-gap mismatch when doping atoms are incorporated into the host lattice. Finally, we fully take into account the optical excitation in the dipole approximation. The explicit expressions for all parts of the Hamiltonian can be found in the Supplemental Material [55].

Based on the model described above, a quantum kinetic theory for the exciton spin dynamics which explicitly includes the optical coherence has been developed in Ref. [46]. Using a formulation in terms of excitonic density matrices together with a correlation expansion to treat higher-order expectation values between exciton and impurity operators, exciton-impurity correlations can be kept explicitly as dynamical variables. A closed set of equations of motion is obtained by invoking the dynamics-controlled truncation (DCT) [56,57] so that variables up to second order in the laser field are taken into account. Here, we use this theory to calculate the linear absorption of a DMS nanostructure beyond the single-particle level.

Since optical spectra may also be affected by phonons, we extend the theory of Ref. [46] to also account for the influence of longitudinal acoustic phonons via deformation potential coupling, which typically dominates the linewidth in semiconductors for temperatures below 80 K [58]. We limit the description to bulk phonons which is justified because of the rather weak dependence of the lattice constant on the impurity content within the considered doping range [26]. To obtain the absorption, we set up the equation of motion for the excitonic interband coherence $y = \langle \hat{Y}_{1s} \rangle$, where $\hat{Y}_{1s}$ denotes the annihilation operator of an exciton in the $1s$ ground state with a vanishing center-of-mass wave vector. The appearing source terms are given by impurity- and phonon-assisted variables for which separate equations of motion have to be set up. A formal integration of the latter yields an integrodifferential equation which can be solved in Fourier space to obtain the susceptibility [57,59,60]. The details of the derivation as well as the resulting equations can be found in the Supplemental Material [55].

For the numerical simulations we focus on $Zn_{1-x}Mn_xSe$ quantum wells of varying widths and doping fractions x at a temperature of 30 K. Since typical exciton lifetimes vary between several 10 ps and 100 ps [61–64] we also include a radiative decay rate of 0.1 ps^{-1} which affects excitons close to the bottom of the exciton parabola [59,65]. Otherwise, standard parameters for a ZnSe-based semiconductor nanostructure and the necessary coupling constants are used [26,53,66,67].

Figure 1 shows the calculated linear absorption spectra of a 15-nm-wide quantum well for doping concentrations between 0% (pure nonmagnetic ZnSe) and 5%. As expected, in the case of undoped ZnSe, a single peak appears at the $1s$ exciton resonance which is broadened due to radiative decay and slightly asymmetric due to the phonon influence (cf. the inset of Fig. 1). Choosing the origin of the energy scale to coincide with the maximum of that peak, the exciton line becomes redshifted upon an increase of the doping fraction and lies at approximately −1.8 meV at an impurity content of 5%. In addition, a second feature appears in the spectrum that is completely absent for an undoped quantum well and splits off from the main exciton resonance with increasing
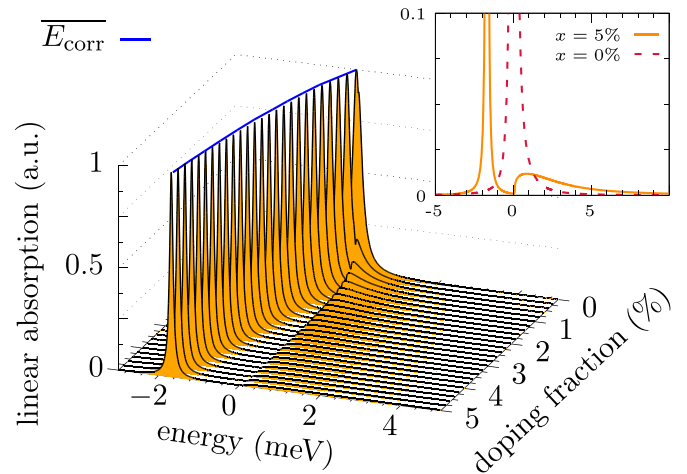

FIG. 1. Linear absorption spectra of a 15-nm-wide $Zn_{1-x}Mn_xSe$ quantum well at 30 K for various doping fractions x. The energy scale is chosen such that $E = 0$ coincides with the maximum of the $1s$ exciton resonance at $x = 0$ and the spectra are normalized with respect to each $1s$ absorption peak. The average correlation energy per exciton $\overline{E_{\mathrm{corr}}}$ obtained numerically from the full quantum kinetic model is indicated with respect to the maximum of each correlation-induced feature. The inset shows a magnified view of the absorption spectra without doping and with an impurity content $x = 5\%$.

doping fraction. It becomes gradually smeared out for larger doping fractions and shows an exponentially decaying tail on the high-energy side.

The average correlation energy per exciton can be defined as

$$\overline{E_{\mathrm{corr}}} = \frac{1}{T} \int_0^T dt \, \frac{\langle H \rangle(t) - \langle H \rangle^{\mathrm{mf}}(t)}{n_X(t)}, \tag{1}$$

where $n_X(t)$ denotes the number of excitons, $\langle H \rangle(t)$ is the expectation value of the complete Hamiltonian from which the mean-field contribution $\langle H \rangle^{\mathrm{mf}}(t)$ is subtracted, and T is the averaging time. As shown in the Supplemental Material, $\overline{E_{\mathrm{corr}}}$ becomes almost independent on T after a short initial period where the correlations build up after the pulsed excitation [55]. A comparison of $\overline{E_{\mathrm{corr}}}$ calculated using the full quantum kinetic model (cf. blue curve in Fig. 1) with the position of the exciton peak relative to the maximum of the second feature in the linear absorption spectra reveals an excellent agreement. This shows that the observed shift of the exciton line and the additional feature in the spectrum are indeed due to the influence of exciton-impurity correlations, an effect that cannot be obtained on the mean-field level. In accordance with energy conservation, the buildup of a negative correlation energy is accompanied by an increase in the average kinetic energy of excitons which manifests in a redistribution of exciton momenta away from the optically active state with $K \approx 0$. A more intuitive explanation of the correlation energy can be given in terms of energy eigenstates: Since the exchange interaction as well as the nonmagnetic impurity scattering couples the exciton and the impurity system, the bare exciton states are no longer the proper eigenstates of the many-body system, resulting in the observed modification of the linear absorption.
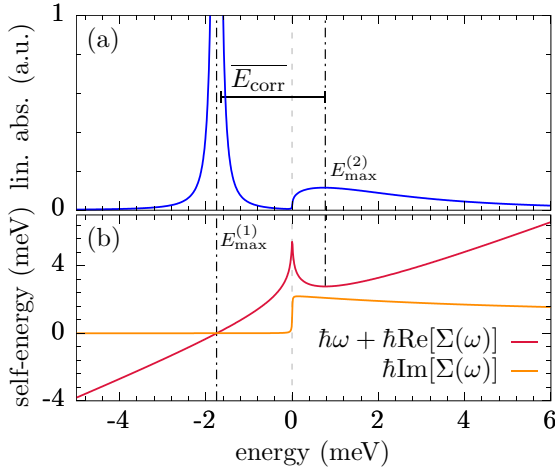
FIG. 2. Explanation of the absorption line shape. We compare (a) the linear absorption spectrum obtained from Eq. (2) with (b) the self-energy $\Sigma(\omega)$ for a 15-nm-wide $Zn_{0.95}Mn_{0.05}Se$ quantum well. The self-energy can be used to explain the position of the main exciton resonance ($E_{max}^{(1)}$) as well as the maximum of the additional feature in the spectrum ($E_{max}^{(2)}$). The average correlation energy per exciton $\overline{E_{corr}}$ calculated numerically from the full model is indicated by the length of the horizontal bar with respect to $E_{max}^{(2)}$.

Numerical calculations confirm that the additional feature in the spectrum remains visible even at liquid nitrogen temperatures of up to 77 K. This is due to the fact that the phonon-induced broadening of the exciton line is rather small for acoustic phonons, a result which is in line with experimental data as well as theoretical calculations where an increase in the half width at half maximum (HWHM) linewidth of only a few μeV per K has been found [68,69]. Thus, as long as temperatures below the longitudinal optic (LO)-phonon threshold are considered, phonons have a negligible influence on the exciton line regarding the phenomena discussed here. It should be noted that acoustic phonons cause the exciton line to become increasingly asymmetric with rising temperature since more and more states become accessible on the exciton parabola [68]. Phonons also provide a small contribution to the redshift of the exciton line on the order of 10 μeV at 30 K, which is clearly negligible compared with the shift due to impurity scattering.

In order to obtain a better understanding of the observed features in the linear absorption spectrum, it is thus justified to focus on a system without phonon influence. Then, the linear absorption is found to be

$$\alpha(\omega) \sim \frac{\Gamma_0 + \mathrm{Im}[\Sigma(\omega)]}{(\omega + \mathrm{Re}[\Sigma(\omega)])^2 + (\Gamma_0 + \mathrm{Im}[\Sigma(\omega)])^2}, \quad (2)$$

with a complex self-energy $\hbar\Sigma(\omega)$ and the radiative decay rate Γ_0 [50,68,70,71]. The explicit expression of the self-energy can be found in the Supplemental Material [55]. A comparison of $\alpha(\omega)$ with the shape of the self-energy in Fig. 2 indeed reveals that the physics behind the linear absorption spectra can be well understood by Eq. (2). Since $\mathrm{Im}[\Sigma(\omega)]$ is strictly positive, it follows that the strongest resonance is determined by the condition $\omega + \mathrm{Re}[\Sigma(\omega)] = 0$. Thus, the real part of the self-energy causes the shift of the exciton line whose

width is determined by the rate Γ_0 since $\mathrm{Im}[\Sigma(\omega)] = 0$ for $\omega < 0$ (cf. Fig. 2). In contrast, the additional feature in the spectrum is exclusively due to the imaginary part of the self-energy which becomes finite for $\omega \gtrsim 0$ and slowly decreases for larger energies. Figure 2 confirms that the onset of the additional feature indeed corresponds to the rise of $\mathrm{Im}[\Sigma(\omega)]$ and the maximum of the feature occurs at the minimum of $\omega + \mathrm{Re}[\Sigma(\omega)]$. For an explanation of the origin of the shape and the behavior of the self-energy, the reader is referred to the Supplemental Material [55]. Note that, if the spectra for finite doping fractions would consist of just a single discrete line shifted from its position at $x = 0\%$ by $\overline{E_{corr}}$, the interpretation of the spectral shift would remain valid but it would be challenging to extract the correlation energy per exciton since it would be necessary to compare spectra for different doping fractions in order to determine the shift. Such experiments can easily become inconclusive since it is hard to change the doping fraction without changing other sample characteristics such as, e.g., internal stress properties.

From a physical perspective, the elastic scattering at the impurity ions couples the optically dipole-allowed exciton states with vanishing wave vector to states on the exciton parabola with $K > 0$, resulting in the excitation of a many-body state that has both contributions. Such a mixing between $K = 0$ and $K \neq 0$ states due to disorder in the sample and its impact on the absorption spectrum has already been discussed in the literature in the context of semiconductor quantum wells with magnetic barriers on a mean-field level, i.e., without accounting for exciton-impurity correlations [72,73]. There, disorder has been found to lead to different shapes of the exciton line when comparing the σ^+ with the σ^- component of the exciton transition. A study of excitons in rough quantum wells based on random potentials [74] has also found a similar impact on the optical density, namely, a shift of the exciton peak towards lower energies combined with an asymmetry towards the high-energy side. However, the fluctuations of the random potential considered in that work were not strong enough to observe two distinct features. In contrast, the values for the exchange interaction in DMSs on the order of a few 10 meV are well established in the literature [23,25,26] and are sufficiently large to cause a drastically different spectrum.

Note that shifts of the optical band edge upon changing the doping fraction have been found in previous works but no relation between shifts and correlation energies has been established [75,76]. In contrast, here the shift of the exciton line occurs with respect to a new secondary spectral feature and directly reflects the correlation energy per exciton. Furthermore, the scattering with phonons can also be cast into a form similar to Eq. (2) so that a self-energy can be identified [68,71]. However, there are some fundamental differences compared with the exciton-impurity scattering: First, phonon scattering is an inelastic process, causing the phonon dispersion to appear in the self-energy. Second, phonons introduce two contributions that can be interpreted as phonon absorption and emission, respectively. The phonon self-energy leads primarily to an asymmetry of the exciton line at elevated temperatures and, as mentioned above, only causes a marginal shift of the exciton line due to the much smaller carrier-phonon coupling compared with the exchange interaction in DMSs. Thus, in a theory accounting only for phonons, the exciton peak as well
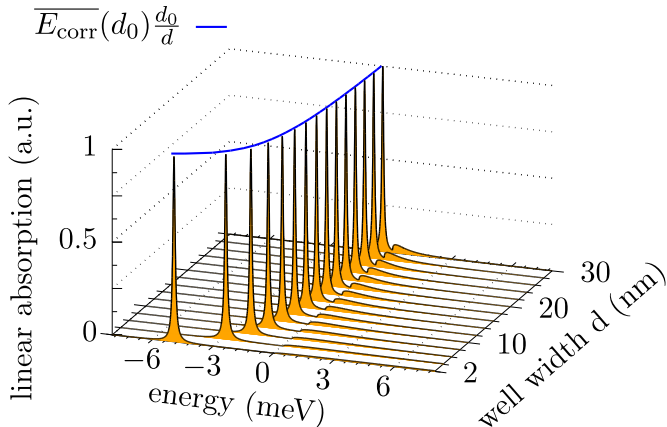
FIG. 3. Linear absorption spectra of a $Zn_{0.98}Mn_{0.02}Se$ quantum well at 30 K for various quantum well widths d. The energy scale is the same as in Fig. 1 and all spectra are normalized with respect to each 1s absorption peak. The blue line shows the inverse dependence of the correlation energy on the well width with respect to the reference point $d_0 = 15$ nm.

FIG. 4. Time evolution of the energy-resolved occupation of the 1s exciton parabola after optical excitation using a pulse with 0.1-ps full width at half maximum (FWHM) for a 10-nm-wide $Zn_{0.99}Mn_{0.01}Se$ quantum well. We compare (a) a calculation with phonons at a temperature of 80 K with (b) the phonon-free case.

as the onset of a finite imaginary part of the self-energy do not appear as separate features in the spectra.

A study of the dependence of the spectra on the width of the DMS nanostructure, as depicted in Fig. 3 for a $Zn_{0.98}Mn_{0.02}Se$ quantum well at 30 K, reveals that the correlation-induced feature becomes significantly broadened for smaller well widths and thus appears more pronounced and localized for moderate widths of about 10 nm and above. It is also found that the side feature starts to merge with the main exciton peak for larger well widths so that only a single line is to be expected in the bulk limit. The blueshift of the exciton line that occurs when the well width becomes larger corresponds to a decrease of the average correlation energy per exciton and shows an inverse dependence on the quantum well width, which suggests that correlations are enhanced in smaller nanostructures and become less significant in bulk. The scaling of the average correlation energy per exciton with $\frac{1}{d}$ follows directly from the prefactors of the complete expression for the correlation energy [55].

The fact that the formation of carrier-impurity correlations is accompanied by an occupation of states on the exciton parabola with a finite center-of-mass wave number K is confirmed by Fig. 4, where the time- and energy-resolved occupation of the exciton ground state is shown. Without phonons, the only mechanism that can change the exciton wave vector is the elastic scattering at the impurities. However, in the typically employed Markov approximation, this scattering is

energy conserving so that an initial exciton occupation at $K \approx 0$ would always remain at the bottom of the exciton parabola. Instead, Fig. 4(b) reveals that, even in the absence of phonons, a significant scattering towards higher center-of-mass energies takes place, which can be associated with many-body correlations between the excitons and impurities that remain finite even for long times and cause a deviation from an effective single-particle picture. Including phonons further enhances this redistribution, especially for higher temperatures [cf. Fig. 4(a)]. This effect should be observable in experiments by, e.g., LO-phonon-assisted photoluminescence, which has already been successfully demonstrated for undoped ZnSe nanostructures [77–79].

All in all, we expect that the fingerprint of exciton-impurity correlations in absorption spectra of DMSs can be experimentally resolved provided that the exciton linewidth stays below a few meV. We have shown that a correlation-induced feature appears in the spectrum on the high-energy side of the 1s exciton line which is particularly pronounced for quantum wells in the 10-nm range and impurity concentrations of a few percent. Furthermore, the shift of the exciton line with respect to this feature yields a reliable value for the average correlation energy per exciton from a single spectrum without having to compare different samples. Since the only requirement for our findings is sufficiently strong correlations, our results can be generalized to many other correlated systems.

[1] D. Karaiskaj, A. D. Bristow, L. Yang, X. Dai, R. P. Mirin, S. Mukamel, and S. T. Cundiff, Phys. Rev. Lett. **104**, 117401 (2010).

[2] D. N. Basov, R. D. Averitt, D. van der Marel, M. Dressel, and K. Haule, Rev. Mod. Phys. **83**, 471 (2011).

[3] D. S. Chemla and J. Shah, Nature (London) **411**, 549 (2001).

[4] J. Shumway, A. Franceschetti, and A. Zunger, Phys. Rev. B **63**, 155316 (2001).

[5] M. S. Hybertsen and S. G. Louie, Phys. Rev. B **34**, 5390 (1986).

[6] I. Di Marco, P. Thunström, M. I. Katsnelson, J. Sadowski, K. Karlsson, S. Lebègue, J. Kanski, and O. Eriksson, Nat. Commun. **4**, 2645 (2013).

[7] F. Görg, M. Messer, K. Sandholzer, G. Jotzu, R. Desbuquois, and T. Esslinger, Nature (London) **553**, 481 (2018).

[8] W.-L. Ma, G. Wolfowicz, N. Zhao, S.-S. Li, J. J. Morton, and R.-B. Liu, Nat. Commun. **5**, 4822 (2014).

[9] J. H. Mentink, K. Balzer, and M. Eckstein, Nat. Commun. **6**, 6708 (2015).

[10] V. Walther, R. Johne, and T. Pohl, Nat. Commun. **9**, 1309 (2018).

[11] S. M. Cronenwett, T. H. Oosterkamp, and L. P. Kouwenhoven, Science **281**, 540 (1998).

[12] O. V. Yazyev and M. I. Katsnelson, Phys. Rev. Lett. **100**, 047209 (2008).

[13] M. M. Qazilbash, J. J. Hamlin, R. E. Baumbach, L. Zhang, D. J. Singh, M. B. Maple, and D. N. Basov, Nat. Phys. **5**, 647 (2009).

[14] M. Ossiander, F. Siegrist, V. Shirvanyan, R. Pazourek, A. Sommer, T. Latka, A. Guggenmos, S. Nagele, J. Feist, J. Burgdörfer, R. Kienberger, and M. Schultze, Nat. Phys. **13**, 280 (2016).

[15] M. Bonitz, C. Henning, and D. Block, Rep. Prog. Phys. **73**, 066501 (2010).

[16] R. P. Smith, J. K. Wahlstrand, A. C. Funk, R. P. Mirin, S. T. Cundiff, J. T. Steiner, M. Schafer, M. Kira, and S. W. Koch, Phys. Rev. Lett. **104**, 247401 (2010).

[17] T. Östreich, K. Schönhammer, and L. J. Sham, Phys. Rev. Lett. **74**, 4698 (1995).

[18] P. Kner, W. Schäfer, R. Lövenich, and D. S. Chemla, Phys. Rev. Lett. **81**, 5386 (1998).

[19] V. M. Axt, G. Bartels, B. Haase, J. Meinertz, U. Neukirch, and J. Gutowski, Phys. Status Solidi B **221**, 205 (2000).

[20] S. R. Bolton, U. Neukirch, L. J. Sham, D. S. Chemla, and V. M. Axt, Phys. Rev. Lett. **85**, 2002 (2000).

[21] H. Tahara, Y. Ogawa, and F. Minami, Phys. Rev. Lett. **107**, 037402 (2011).

[22] R. Bouzerar and G. Bouzerar, Europhys. Lett. **92**, 47006 (2010).

[23] T. Dietl and H. Ohno, Rev. Mod. Phys. **86**, 187 (2014).

[24] H. Ohno, A. Shen, F. Matsukura, A. Oiwa, A. Endo, S. Katsumoto, and Y. Iye, Appl. Phys. Lett. **69**, 363 (1996).

[25] *Introduction to the Physics of Diluted Magnetic Semiconductors*, edited by J. Kossut and J. A. Gaj (Springer, Berlin, 2010).

[26] J. K. Furdyna, J. Appl. Phys. **64**, R29 (1988).

[27] H. Ohno, Science **281**, 951 (1998).

[28] D. Awschalom and M. Flatté, Nat. Phys. **3**, 153 (2007).

[29] T. Dietl, Nat. Mater. **9**, 965 (2010).

[30] H. Ohno, Nat. Mater. **9**, 952 (2010).

[31] I. Žutić, J. Fabian, and S. Das Sarma, Rev. Mod. Phys. **76**, 323 (2004).

[32] V. K. Joshi, Eng. Sci. Technol. **19**, 1503 (2016).

[33] R. Fiederling, M. Keim, G. Reuscher, W. Ossau, G. Schmidt, A. Waag, and L. W. Molenkamp, Nature (London) **402**, 787 (1999).

[34] C. Chappert, A. Fert, and F. N. Van Dau, Nat. Mater. **6**, 813 (2007).

[35] C. Camilleri, F. Teppe, D. Scalbert, Y. G. Semenov, M. Nawrocki, M. Dyakonov, J. Cibert, S. Tatarenko, and T. Wojtowicz, Phys. Rev. B **64**, 085331 (2001).

[36] K. E. Rönnburg, E. Mohler, H. G. Roskos, K. Ortner, C. R. Becker, and L. W. Molenkamp, Phys. Rev. Lett. **96**, 117203 (2006).

[37] S. A. Crooker, D. D. Awschalom, J. J. Baumberg, F. Flack, and N. Samarth, Phys. Rev. B **56**, 7574 (1997).

[38] Z. Ben Cheikh, S. Cronenberger, M. Vladimirova, D. Scalbert, F. Perez, and T. Wojtowicz, Phys. Rev. B **88**, 201306 (2013).

[39] R. Akimoto, K. Ando, F. Sasaki, S. Kobayashi, and T. Tani, J. Lumin. **72**, 309 (1997).

[40] A. Murayama, K. Seo, K. Nishibayashi, I. Souma, and Y. Oka, Appl. Phys. Lett. **88**, 261105 (2006).

[41] C. J. P. Smits, S. C. A. van Driel, M. van Kampen, W. J. M. de Jonge, B. Koopmans, and G. Karczewski, Phys. Rev. B **70**, 115307 (2004).

[42] H. Sakurai, K. Seo, Z. H. Chen, K. Kayanuma, T. Tomita, A. Murayama, and Y. Oka, Phys. Status Solidi C **1**, 981 (2004).

[43] C. Thurn, M. Cygorek, V. M. Axt, and T. Kuhn, Phys. Rev. B **87**, 205301 (2013).

[44] M. Cygorek, F. Ungar, P. I. Tamborenea, and V. M. Axt, Phys. Rev. B **95**, 045204 (2017).

[45] K. Sato, L. Bergqvist, J. Kudrnovský, P. H. Dederichs, O. Eriksson, I. Turek, B. Sanyal, G. Bouzerar, H. Katayama-Yoshida, V. A. Dinh, T. Fukushima, H. Kizaki, and R. Zeller, Rev. Mod. Phys. **82**, 1633 (2010).

[46] F. Ungar, M. Cygorek, and V. M. Axt, Phys. Rev. B **95**, 245203 (2017).

[47] F. Ungar, M. Cygorek, and V. M. Axt, Phys. Rev. B **97**, 045210 (2018).

[48] A. Hanbicki, M. Currie, G. Kioseoglou, A. Friedman, and B. Jonker, Solid State Commun. **203**, 16 (2015).

[49] M. M. Ugeda, A. J. Bradley, S.-F. Shi, F. H. da Jornada, Y. Zhang, D. Y. Qiu, W. Ruan, S.-K. Mo, Z. Hussain, Z.-X. Shen, F. Wang, S. G. Louie, and M. F. Crommie, Nat. Mater. **13**, 1091 (2014).

[50] N. H. Kwong, G. Rupper, and R. Binder, Phys. Rev. B **79**, 155205 (2009).

[51] C. Piermarocchi and F. Tassone, Phys. Rev. B **63**, 245308 (2001).

[52] F. Jahnke, M. Kira, W. Hoyer, and S. W. Koch, Phys. Status Solidi B **221**, 189 (2000).

[53] G. V. Astakhov, D. R. Yakovlev, V. P. Kochereshko, W. Ossau, W. Faschinger, J. Puls, F. Henneberger, S. A. Crooker, Q. McCulloch, D. Wolverson, N. A. Gippius, and A. Waag, Phys. Rev. B **65**, 165335 (2002).

[54] G. Bastard, *Wave Mechanics Applied to Semiconductor Heterostructures* (Les Éditions de Physique, Les Ulis Cedex, 1996).

[55] See Supplemental Material at http://link.aps.org/supplemental/10.1103/PhysRevB.98.161201 for a detailed description of the model, the derivation of the linear response, and details regarding the correlation energy.

[56] V. M. Axt and A. Stahl, Z. Phys. B: Condens. Matter **93**, 195 (1994).

[57] V. M. Axt and S. Mukamel, Rev. Mod. Phys. **70**, 145 (1998).

[58] S. Rudin and T. L. Reinecke, Phys. Rev. B **41**, 3017 (1990).

[59] A. Thränhardt, S. Kuckenberg, A. Knorr, T. Meier, and S. W. Koch, Phys. Rev. B **62**, 2706 (2000).

[60] M. Kira and S. Koch, Prog. Quantum Electron. **30**, 155 (2006).

[61] S. V. Poltavtsev, M. Reichelt, I. A. Akimov, G. Karczewski, M. Wiater, T. Wojtowicz, D. R. Yakovlev, T. Meier, and M. Bayer, Phys. Rev. B **96**, 075306 (2017).

[62] Z. Chen, H. Sakurai, K. Seo, K. Kayanuma, T. Tomita, A. Murayama, and Y. Oka, Physica B **340-342**, 890 (2003).

[63] E. Runge, A. Schülzgen, F. Henneberger, and R. Zimmermann, Phys. Status Solidi B **188**, 547 (1995).

[64] H. Kalt, J. Collet, S. D. Baranovskii, R. Saleh, P. Thomas, L. S. Dang, and J. Cibert, Phys. Rev. B **45**, 4253 (1992).

[65] K. Siantidis, V. M. Axt, and T. Kuhn, Phys. Rev. B **65**, 035303 (2001).

[66] M. Cardona and N. E. Christensen, Phys. Rev. B **35**, 6182 (1987).

[67] I. Strzalkowski, S. Joshi, and C. R. Crowell, Appl. Phys. Lett. **28**, 350 (1976).

[68] S. Rudin and T. L. Reinecke, Phys. Rev. B **66**, 085314 (2002).

[69] D. Gammon, S. Rudin, T. L. Reinecke, D. S. Katzer, and C. S. Kyono, Phys. Rev. B **51**, 16785 (1995).

[70] S. Wachter, M. Maute, H. Kalt, I. Galbraith, C. Sieh, T. Meier, and S. Koch, Physica B **314**, 309 (2002).

[71] G. Mannarini and R. Zimmermann, Phys. Rev. B **73**, 115325 (2006).

[72] V. I. Sugakov and G. V. Vertsimakha, J. Phys.: Condens. Matter **13**, 5635 (2001).

[73] A. V. Komarov, V. I. Sugakov, G. V. Vertsimakha, W. Zaleszczyk, G. Karczewski, and T. Wojtowicz, J. Phys.: Condens. Matter **18**, 7401 (2006).

[74] R. Zimmermann, Phys. Status Solidi B **173**, 129 (1992).

[75] M. Takahashi, Phys. Rev. B **70**, 035207 (2004).

[76] L. Gharaee and A. Saffarzadeh, Eur. Phys. J. B **85**, 289 (2012).

[77] H. Zhao, S. Moehl, and H. Kalt, Phys. Rev. Lett. **89**, 097401 (2002).

[78] H. Zhao, S. Moehl, and H. Kalt, Appl. Phys. Lett. **81**, 2794 (2002).

[79] M. Umlauff, J. Hoffmann, H. Kalt, W. Langbein, J. M. Hvam, M. Scholl, J. Söllner, M. Heuken, B. Jobst, and D. Hommel, Phys. Rev. B **57**, 1390 (1998).

Supplement: Extracting many-body correlation energies from absorption spectra of diluted magnetic semiconductors

F. Ungar,[1] M. Cygorek,[2] and V. M. Axt[1]

[1] *Theoretische Physik III, Universität Bayreuth, 95440 Bayreuth, Germany*
[2] *Department of Physics, University of Ottawa, Ottawa, Ontario, Canada K1N 6N5*

HAMILTONIAN

The Hamiltonian for the description of the excitation and the dynamics of a II-VI DMS quantum well in the electron-hole representation reads [1, 2]

$$H = H_0 + H_{\text{conf}} + H_{\text{C}} + H_{\text{lm}} + H_{\text{m}} + H_{\text{nm}} + H_{\text{ph}} + H_{\text{c-ph}}, \tag{1}$$

where H_0 contains the kinetic energies of electrons and holes in the effective mass approximation, H_{conf} describes the confinement in the growth direction, and H_{C} comprises the direct Coulomb interactions that can be subdivided into electron-hole, electron-electron, and hole-hole interactions. The light-matter coupling is given by H_{lm}, whereas H_{m} and H_{nm} refer to the magnetic and nonmagnetic carrier-impurity interaction, respectively. Here, we extend the previously developed model [1] to also account for phonons via H_{ph} and the carrier-phonon interaction $H_{\text{c-ph}}$. The individual contributions are given by

$$H_0 = \sum_{l\mathbf{k}} E_{\mathbf{k}}^l c_{l\mathbf{k}}^\dagger c_{l\mathbf{k}} + \sum_{v\mathbf{k}} E_{\mathbf{k}}^v d_{v\mathbf{k}}^\dagger d_{v\mathbf{k}}, \tag{2a}$$

$$H_{\text{C}} = \frac{1}{2} \sum_{\mathbf{k}\mathbf{k}'\mathbf{q}} \left(V_{\mathbf{q}} \sum_{ll'} c_{l'\mathbf{k}'+\mathbf{q}}^\dagger c_{l\mathbf{k}-\mathbf{q}}^\dagger c_{l\mathbf{k}} c_{l'\mathbf{k}'} + V_{\mathbf{q}} \sum_{vv'} d_{v'\mathbf{k}'+\mathbf{q}}^\dagger d_{v\mathbf{k}-\mathbf{q}}^\dagger d_{v\mathbf{k}} d_{v'\mathbf{k}'} - 2V_{\mathbf{q}} \sum_{lv} c_{l\mathbf{k}'+\mathbf{q}}^\dagger d_{v\mathbf{k}-\mathbf{q}}^\dagger d_{v\mathbf{k}} c_{l\mathbf{k}'} \right), \tag{2b}$$

$$H_{\text{lm}} = -\sum_{lv\mathbf{k}} \left(\mathbf{E} \cdot \mathbf{M}_{lv} c_{l\mathbf{k}}^\dagger d_{v-\mathbf{k}}^\dagger + \mathbf{E} \cdot \mathbf{M}_{vl} d_{v-\mathbf{k}} c_{l\mathbf{k}} \right), \tag{2c}$$

$$H_{\text{m}} = H_{sd} + H_{pd} = \frac{J_{sd}}{V} \sum_{\substack{Inn' \\ ll'\mathbf{k}\mathbf{k}'}} \mathbf{S}_{nn'} \cdot \mathbf{s}_{ll'}^{\text{e}} c_{l\mathbf{k}}^\dagger c_{l'\mathbf{k}'} e^{i(\mathbf{k}'-\mathbf{k})\cdot\mathbf{R}_I} \hat{P}_{nn'}^I + \frac{J_{pd}}{V} \sum_{\substack{Inn' \\ vv'\mathbf{k}\mathbf{k}'}} \mathbf{S}_{nn'} \cdot \mathbf{s}_{vv'}^{\text{h}} d_{v\mathbf{k}}^\dagger d_{v'\mathbf{k}'} e^{i(\mathbf{k}'-\mathbf{k})\cdot\mathbf{R}_I} \hat{P}_{nn'}^I, \tag{2d}$$

$$H_{\text{nm}} = H_{\text{nm}}^{\text{e}} + H_{\text{nm}}^{\text{h}} = \frac{J_0^{\text{e}}}{V} \sum_{\substack{Il \\ \mathbf{k}\mathbf{k}'}} c_{l\mathbf{k}}^\dagger c_{l\mathbf{k}'} e^{i(\mathbf{k}'-\mathbf{k})\cdot\mathbf{R}_I} + \frac{J_0^{\text{h}}}{V} \sum_{\substack{Iv \\ \mathbf{k}\mathbf{k}'}} d_{v\mathbf{k}}^\dagger d_{v\mathbf{k}'} e^{i(\mathbf{k}'-\mathbf{k})\cdot\mathbf{R}_I}, \tag{2e}$$

$$H_{\text{ph}} = \sum_{\mathbf{q}} \hbar \omega_{\mathbf{q}}^{\text{ph}} b_{\mathbf{q}}^\dagger b_{\mathbf{q}}, \tag{2f}$$

$$H_{\text{c-ph}} = \sum_{\mathbf{q}\mathbf{k}} \left(\gamma_{\mathbf{q}}^{\text{e}} c_{\mathbf{k}+\mathbf{q}}^\dagger c_{\mathbf{k}} b_{\mathbf{q}} + \gamma_{\mathbf{q}}^{\text{e}*} c_{\mathbf{k}}^\dagger c_{\mathbf{k}+\mathbf{q}} b_{\mathbf{q}}^\dagger + \gamma_{\mathbf{q}}^{\text{h}} d_{\mathbf{k}+\mathbf{q}}^\dagger d_{\mathbf{k}} b_{\mathbf{q}} + \gamma_{\mathbf{q}}^{\text{h}*} d_{\mathbf{k}}^\dagger d_{\mathbf{k}+\mathbf{q}} b_{\mathbf{q}}^\dagger \right). \tag{2g}$$

In the above equations, $c_{l\mathbf{k}}^\dagger$ ($c_{l\mathbf{k}}$) denotes the electron creation (annihilation) operator in the conduction band l with wave vector $\mathbf{k}$ and $d_{v\mathbf{k}}^\dagger$ ($d_{v\mathbf{k}}$) is the respective creation (annihilation) operator for holes in the valence band v. The Fourier components of the bulk Coulomb potential are given by $V_{\mathbf{q}} = \frac{e^2}{\epsilon\epsilon_0} \frac{1}{q^2}$ with the elementary charge e, the vacuum permittivity ϵ_0, and a static dielectric constant ϵ. In the light-matter interaction, $\mathbf{E}$ denotes the electric field and $\mathbf{M}_{lv}$ is the dipole moment for a transition from the valence subband v to the conduction subband l. We denote the vector of electron spin matrices by $\mathbf{s}_{ll'}^{\text{e}} = \frac{1}{2}\boldsymbol{\sigma}_{ll'}$, where $\boldsymbol{\sigma}_{ll'}$ is the vector of Pauli matrices, and $\mathbf{s}_{vv'}^{\text{h}} = \frac{1}{3}\mathbf{J}_{vv'}$ describes the hole spin in terms of the vector of 4×4 angular momentum matrices $\mathbf{J}_{vv'}$ with $v, v' \in \{-\frac{3}{2}, -\frac{1}{2}, \frac{1}{2}, \frac{3}{2}\}$. In the magnetic interaction, $\mathbf{S}_{nn'}$ denotes the vector of impurity spin matrices with $n, n' \in \{-\frac{5}{2}, -\frac{3}{2}, ..., \frac{5}{2}\}$. To describe the impurity spin at a particular site in the DMS, we make use of the operator $\hat{P}_{nn'}^I = |I, n\rangle\langle I, n'|$ where the ket $|I, n\rangle$ denotes the spin state n of the Ith impurity atom and $\mathbf{R}_I$ refers to its position. Throughout this paper, the factor $\hbar$ appearing in the spin matrices is absorbed in the coupling constants J_{sd} and J_{pd}. Finally, J_0^{e} and J_0^{h} are nonmagnetic scattering constants for electrons and holes that arise due to the band-gap mismatch of the doped material compared with the undoped barriers of the quantum well. The creation (annihilation) operators for acoustic phonons with wave vector $\mathbf{q}$ are denoted by $b_{\mathbf{q}}^\dagger$ ($b_{\mathbf{q}}$) with frequencies $\omega_{\mathbf{q}}^{\text{ph}} = vq$, where v is the sound velocity and a linear dispersion is assumed.

The deformation potential coupling for electrons and holes is given by $\gamma_{\mathbf{q}}^{\mathrm{e/h}} = \sqrt{\frac{\hbar q}{2\rho v V}} D^{\mathrm{e/h}}$ with the density ρ of the semiconductor and the deformation potentials $D^{\mathrm{e/h}}$.

EQUATIONS OF MOTION FOR THE COHERENCE AND ITS CORRELATIONS

In the exciton representation, the necessary variables to describe the linear absorption for an excitation with circularly polarized (σ^-) light in the absence of an external magnetic field are [1, 2]

$$y := \left\langle \hat{Y}_{\uparrow -\frac{3}{2} 1s0} \right\rangle, \tag{3a}$$

$$q_{\eta K} := \frac{Vd}{N_{\mathrm{Mn}}} \int_0^{2\pi} \frac{d\psi}{2\pi} f_{\eta 1s1s}^{\mathbf{0K}} \int_{-\frac{d}{2}}^{\frac{d}{2}} dz \, |u_0(z)|^2 \sum_{Inn'} S_{nn'}^z \left\langle \hat{Y}_{\uparrow -\frac{3}{2} 1s\mathbf{K}} e^{i\mathbf{K}\cdot\mathbf{R}_I} \hat{P}_{nn'}^I \delta(z - Z_I) \right\rangle, \tag{3b}$$

$$z_{\eta K} := \frac{Vd}{N_{\mathrm{Mn}}} \int_0^{2\pi} \frac{d\psi}{2\pi} f_{\eta 1s1s}^{\mathbf{0K}} \int_{-\frac{d}{2}}^{\frac{d}{2}} dz \, |u_0(z)|^2 \sum_{I} \left\langle \hat{Y}_{\uparrow -\frac{3}{2} 1s\mathbf{K}} e^{i\mathbf{K}\cdot\mathbf{R}_I} \delta(z - Z_I) \right\rangle, \tag{3c}$$

$$p_K^\kappa := \int_0^{2\pi} \frac{d\psi_1}{2\pi} f(\kappa)\big(\gamma_{\mathbf{K},\kappa}^{\mathrm{e}} f_{-\eta_{\mathrm{h}} 1s1s}^{\mathbf{K0}} + \gamma_{\mathbf{K},\kappa}^{\mathrm{h}} f_{\eta_{\mathrm{e}} 1s1s}^{\mathbf{K0}}\big) \langle \hat{Y}_{\uparrow -\frac{3}{2} 1s\mathbf{K}} b_{\mathbf{K},\kappa} \rangle, \tag{3d}$$

$$\tilde{p}_K^\kappa := \int_0^{2\pi} \frac{d\psi_1}{2\pi} f(\kappa)^* \big(\gamma_{\mathbf{K},\kappa}^{\mathrm{e}} f_{-\eta_{\mathrm{h}} 1s1s}^{\mathbf{K0}} + \gamma_{\mathbf{K},\kappa}^{\mathrm{h}} f_{\eta_{\mathrm{e}} 1s1s}^{\mathbf{K0}}\big)^* \langle \hat{Y}_{\uparrow -\frac{3}{2} 1s\mathbf{K}} b_{\mathbf{K},\kappa}^\dagger \rangle, \tag{3e}$$

which refer to the electron-hole coherence (y) and its correlations due to the magnetic ($q_{\eta K}$) as well as the nonmagnetic ($z_{\eta K}$) interaction with impurities, respectively. Additionally, we have introduced the phonon-assisted variables p_K^κ and $\tilde{p}_K^\kappa$. We consider a quantum well of volume V and width d with N_{Mn} being the number of impurities. The exciton annihilation operator is denoted by $\hat{Y}_{\uparrow -\frac{3}{2} 1s\mathbf{K}}$ for the $1s$ exciton ground state with the two dimensional center-of-mass wave vector $\mathbf{K}$ for an electron with spin up ($\uparrow$) and a heavy hole with quantum number $m_J = -\frac{3}{2}$. Note that the optical excitation only couples to the state with $K = 0$ in the dipole approximation. The z direction is chosen to coincide with the growth direction of the quantum well and $u_0(z)$ denotes the envelope function due to the confinement, for which we consider only the energetically lowest state since we are dealing with sufficiently narrow quantum wells. In addition, the expectation value $\langle . \rangle$ contains an average over the distribution of impurity positions, which are assumed to be random but spatially homogeneous on average in the sample. Finally, the variables are averaged over the angle ψ with respect to the center-of-mass wave vector $\mathbf{K}$ and the appearing form factors for the exciton ground state read [2]

$$f_{\eta 1s1s}^{\mathbf{K}_1\mathbf{K}_2} = 2\pi \int_0^\infty dr \, R_{1s}^2(r) J_0\big(\eta |\mathbf{K}_1 - \mathbf{K}_2| r\big), \tag{4}$$

where the constants $\eta_{\mathrm{e}} = m_{\mathrm{e}}/M$ as well as $\eta_{\mathrm{h}} = m_{\mathrm{h}}/M$ denote the ratio between the effective electron or heavy-hole mass and the exciton mass $M = m_{\mathrm{e}} + m_{\mathrm{h}}$, respectively. Furthermore, $\eta \in \{\eta_{\mathrm{e}}, \eta_{\mathrm{h}}\}$ and the function $J_0(x)$ is the cylindrical Bessel function of order zero. Regarding the phonon-assisted variables, the phonon wave vector is split into an in-plane component $\mathbf{K}$ and a one dimensional component κ so that the total phonon wave number which enters the carrier-phonon coupling is given by $\sqrt{K^2 + \kappa^2}$. Projecting the phonon dynamics onto the confinement ground state then yields the phonon form factor

$$f(\kappa) = \sum_z u_0^{\mathrm{e}}(z) u_0^{\mathrm{h}}(z) e^{i\kappa z} = \frac{\sin\left(\frac{\kappa d}{2}\right)}{\frac{\kappa d}{2}} \left[1 - \left(\frac{\kappa d}{2\pi}\right)^2\right]^{-1}.$$

Extending the equations of motion derived in Ref. [1] by also accounting for the phonon influence, the coupled equations for the coherence y and its correlation contributions $q_{\eta K}$ and $z_{\eta K}$ in the exciton representation become

$$\frac{\partial}{\partial t} y = \frac{i}{\hbar} \mathbf{E} \cdot \mathbf{M}\phi_{1s} - \Gamma_0(0)y - i\frac{N_{\mathrm{Mn}}}{2\hbar V^2} \int_0^{K_{\mathrm{c}}} dK \, D(K)\big(J_{sd} q_{-\eta_{\mathrm{h}} K} - J_{pd} q_{\eta_{\mathrm{e}} K} + 2J_0^{\mathrm{e}} z_{-\eta_{\mathrm{h}} K} + 2J_0^{\mathrm{h}} z_{\eta_{\mathrm{e}} K}\big)$$
$$- i\frac{d}{\pi\hbar} \int_0^{K_{\mathrm{c}}} dK \, D(K) \int_0^{K_{\mathrm{c}}} d\kappa \, \big(p_K^\kappa + \tilde{p}_K^\kappa\big), \tag{5a}$$

$$\frac{\partial}{\partial t} q_{\eta K} = -\big(i\omega_K + \Gamma_0(K)\big)q_{\eta K} - i\frac{35I}{24\hbar}\Big(J_{sd}F^{-\eta_{\mathrm{h}}0K}_{\eta\ 1s1s} - J_{pd}F^{\eta_{\mathrm{e}}0K}_{\eta\ 1s1s}\Big)y, \tag{5b}$$

$$\frac{\partial}{\partial t} z_{\eta K} = -\big(i\omega_K + \Gamma_0(K)\big)z_{\eta K} - i\frac{I}{\hbar}\Big(J^{\mathrm{e}}_0 F^{-\eta_{\mathrm{h}}0K}_{\eta\ 1s1s} + J^{\mathrm{h}}_0 F^{\eta_{\mathrm{e}}0K}_{\eta\ 1s1s}\Big)y, \tag{5c}$$

$$\frac{\partial}{\partial t} p^{\kappa}_K = -i\big(\omega_K + \omega^{\mathrm{ph}}_{K,\kappa} + \Gamma_0(K)\big)p^{\kappa}_K - i\frac{\sqrt{K^2+\kappa^2}}{2\rho vV}|f(\kappa)|^2\Big(D_{\mathrm{e}}^2 F^{\eta_{\mathrm{h}}0K}_{\eta_{\mathrm{h}}1s1s} + D_{\mathrm{h}}^2 F^{\eta_{\mathrm{e}}0K}_{\eta_{\mathrm{e}}1s1s} + 2D_{\mathrm{e}}D_{\mathrm{h}}F^{\ \eta_{\mathrm{e}}0K}_{-\eta_{\mathrm{h}}1s1s}\Big)(1+n^{\mathrm{ph}}_{K,\kappa})y, \tag{5d}$$

$$\frac{\partial}{\partial t} \tilde{p}^{\kappa}_K = -i\big(\omega_K - \omega^{\mathrm{ph}}_{K,\kappa} + \Gamma_0(K)\big)\tilde{p}^{\kappa}_K - i\frac{\sqrt{K^2+\kappa^2}}{2\rho vV}|f(\kappa)|^2\Big(D_{\mathrm{e}}^2 F^{\eta_{\mathrm{h}}0K}_{\eta_{\mathrm{h}}1s1s} + D_{\mathrm{h}}^2 F^{\eta_{\mathrm{e}}0K}_{\eta_{\mathrm{e}}1s1s} + 2D_{\mathrm{e}}D_{\mathrm{h}}F^{\ \eta_{\mathrm{e}}0K}_{-\eta_{\mathrm{h}}1s1s}\Big)n^{\mathrm{ph}}_{K,\kappa}y. \tag{5e}$$

The first term in Eq. (5a) describes the driving by the laser field where $\phi_{1s} = R_{1s}(r=0)$ is the radial part of the $1s$ exciton wave function evaluated at $r=0$. Radiative decay is included in the equations via the K dependent rate $\Gamma_0(K) = \Gamma_0\Theta(E_{1s} + \hbar\omega_K - \hbar cK)$ derived from the condition of energy conservation upon photon emission [3, 4]. In practice, this means that only excitons close to $K=0$ are affected by radiative decay. The third term captures the influence of magnetic and nonmagnetic exciton-impurity correlations and the double integral finally accounts for the phonon influence. The equations are formulated in the rotating frame with respect to the $1s$ exciton frequency and we have made use of the rotating-wave approximation so that $\mathbf{E}$ contains only the slowly varying envelope of the laser. In the effective-mass approximation, the exciton dispersion reads $\omega_K = \hbar K^2/2M$. Furthermore, we have used the continuum limit for the center-of-mass wave number K with the density of states given by $D(K) = AK/2\pi$. The cutoff value K_{c} appearing in the integral over the correlations is chosen such that it corresponds to an energy of $100\,\mathrm{meV}$. This should be compared with the exciton binding energy which, for a $10\,\mathrm{nm}$ wide ZnSe quantum well, is approximately $30\,\mathrm{meV}$. Thus, it is ensured that all oscillating terms encountered in Eqs. (5) are numerically well resolved. In the equations for the correlations, the factor $I = 3/2$ stems from the projection of all quantities onto the lowest confinement state in the growth direction, for which the approximation of an infinitely deep quantum well is employed. Finally, the angle-averaged exciton form factors are given by

$$F^{\eta_2 K_1 K_2}_{\eta_1 1s1s} = 2\pi\int_0^{2\pi} d\psi_{12} \int_0^{\infty} dr \int_0^{\infty} dr'\, rr' R^2_{1s}(r)R^2_{1s}(r') J_0\big(\eta_1 K_{12}(\psi_{12})r\big) J_0\big(\eta_2 K_{12}(\psi_{12})r'\big), \tag{6}$$

where $K_{12} = |\mathbf{K}_1 - \mathbf{K}_2|$ with ψ_{12} describing the angle between $\mathbf{K}_1$ and $\mathbf{K}_2$. It should be noted that, in order to arrive at Eq. (5d) and Eq. (5e), we have assumed the phonons to be in thermal equilibrium with an occupation given by $n^{\mathrm{ph}}_{K,\kappa} = 1/(\exp(\hbar v\sqrt{K^2+\kappa^2}/k_B T) - 1)$.

LINEAR RESPONSE

The linear response can be obtained from Eqs. (5) by formally integrating Eqs. (5b)–(5e) and feeding the results back into Eq. (5a), which yields an integro-differential equation for the coherence $y(t)$. Applying the Fourier transform in the time domain and making use of the convolution theorem then allows one to transform Eq. (5a) into an algebraic equation that can be solved for the coherence $y(\omega)$. The relation between the coherence and the polarization subsequently yields the complex susceptibility

$$\chi(\omega) \sim \frac{-1}{\omega + i\Gamma_0(0) + \int_0^{K_{\mathrm{c}}} dK\, \frac{D(K)\Gamma^2_{\mathrm{imp}}(K)}{\omega_K - \omega - i\Gamma_0(K)} + \int_0^{K_{\mathrm{c}}} dK \int_0^{K_{\mathrm{c}}} d\kappa\, \frac{D(K)\Gamma^2_{\mathrm{ph}}(K,\kappa)d}{\pi}\Big(\frac{1+n^{\mathrm{ph}}_{K,\kappa}}{\omega_K+\omega^{\mathrm{ph}}_{K,\kappa}-\omega-i\Gamma_0(K)} + \frac{n^{\mathrm{ph}}_{K,\kappa}}{\omega_K-\omega^{\mathrm{ph}}_{K,\kappa}-\omega-i\Gamma_0(K)}\Big)} \tag{7}$$

with

$$\Gamma^2_{\mathrm{imp}}(K) = \frac{IN_{\mathrm{Mn}}}{\hbar^2 V^2}\Big(\Big(\frac{35}{48}J^2_{sd} + J^{\mathrm{e}2}_0\Big)F^{\eta_{\mathrm{h}}0K}_{\eta_{\mathrm{h}}1s1s} + \Big(2J^{\mathrm{e}}_0 J^{\mathrm{h}}_0 - \frac{35}{24}J_{sd}J_{pd}\Big)F^{\ \eta_{\mathrm{e}}0K}_{-\eta_{\mathrm{h}}1s1s} + \Big(\frac{35}{48}J^2_{pd} + J^{\mathrm{h}2}_0\Big)F^{\eta_{\mathrm{e}}0K}_{\eta_{\mathrm{e}}1s1s}\Big), \tag{8}$$

$$\Gamma^2_{\mathrm{ph}}(K,\kappa) = \frac{\sqrt{K^2+\kappa^2}}{2\hbar\rho vV}|f(\kappa)|^2\Big(D_{\mathrm{e}}^2 F^{\eta_{\mathrm{h}}0K}_{\eta_{\mathrm{h}}1s1s} + D_{\mathrm{h}}^2 F^{\eta_{\mathrm{e}}0K}_{\eta_{\mathrm{e}}1s1s} + 2D_{\mathrm{e}}D_{\mathrm{h}}F^{\ \eta_{\mathrm{e}}0K}_{-\eta_{\mathrm{h}}1s1s}\Big). \tag{9}$$

The linear absorption is given by the imaginary part of χ.

Neglecting the phonon influence and separating χ into its real and imaginary part, one arrives at

$$\chi \sim -\frac{\omega + \mathrm{Re}[\Sigma(\omega)]}{\big(\omega + \mathrm{Re}[\Sigma(\omega)]\big)^2 + \big(\Gamma_0(K) + \mathrm{Im}[\Sigma(\omega)]\big)^2} + i\frac{\Gamma_0(K) + \mathrm{Im}[\Sigma(\omega)]}{\big(\omega + \mathrm{Re}[\Sigma(\omega)]\big)^2 + \big(\Gamma_0(K) + \mathrm{Im}[\Sigma(\omega)]\big)^2} \tag{10}$$

with a complex self energy resulting from the interaction between carriers and magnetic impurities given by

$$\hbar\Sigma(\omega) = \int_0^{K_c} dK\, D(K) \frac{\hbar(\omega_K - \omega)\Gamma_{\mathrm{imp}}^2(K)}{(\omega_K - \omega)^2 + \Gamma_0(K)^2} + i \int_0^{K_c} dK\, D(K) \frac{\hbar\Gamma_0(K)\Gamma_{\mathrm{imp}}^2(K)}{(\omega_K - \omega)^2 + \Gamma_0(K)^2}. \tag{11}$$

It is straightforward to show that $\mathrm{Im}[\Sigma(\omega)] \geq 0 \,\forall\, \omega$ and, as a consequence, $\mathrm{Im}[\chi] \geq 0 \,\forall\, \omega$. We model the radiative decay by

$$\Gamma_0(K) = (\Gamma_0 - \gamma) \exp\left(-\left(\frac{\hbar\omega_K}{2w}\right)^2 \right) + \gamma \tag{12}$$

which satisfies $\Gamma_0(0) = \Gamma_0$. The width of the Gaussian is chosen to be $w = 1\,\mu\mathrm{eV}$ so that only states in close proximity to $K = 0$ undergo radiative decay. Furthermore, we have introduced the constant $\gamma \ll \Gamma_0$ that enables a faster convergence of the numerical result. It has been carefully checked and verified that the numerical values for the linear absorption obtained from Eq. (7) coincide with the full solution of Eqs. (5) in the time domain and subsequent Fourier transform.

As can be seen in Fig. 2 in the main text, $\mathrm{Im}[\Sigma] = 0$ for $\omega < 0$, shows a finite step at $\omega = 0$, and slowly decreases for $\omega > 0$. This behavior can be understood as follows: Since excitons can only have energies larger than zero due to the cutoff at the edge of the exciton parabola, only states with $\omega > 0$ are available for the scattering processes so that $\mathrm{Im}[\Sigma] = 0$ otherwise. The steplike behavior of the imaginary part of the self energy reflects the density of states for a two-dimensional system, which is proportional to $\Theta(\omega)$ and does in particular no longer depend on ω for $\omega > 0$. Furthermore, we consider scattering with localized impurities and thus the scattering potential is almost independent on the transferred wave vector. This implies that the corresponding scattering matrix element between excitonic states leads only to a slow decrease of $\mathrm{Im}[\Sigma]$ for larger energies due to the exciton form factor, which also exhibits a decreasing behavior with increasing energies [1]. The shape of the real part of the self energy then follows from the Kramers-Kronig relation since the self energy is a response function.

Note also that, in the main text, correlations were found to cause a shift of the exciton peak as well as an additional side feature, whose impact becomes smaller with increasing doping fraction [cf. Fig. 1 in the main text]. The decreasing visibility of the correlation-induced side feature can also be understood with the help of the self energy: Since the magnitude of the real part of the self energy increases with increasing doping fraction due to the increasing correlation energy, the first term in the denominator of Eq. (10) becomes larger for $\omega > 0$ and, thus, the impact of the finite step of $\mathrm{Im}[\Sigma]$ is less pronounced, leading to an overall smaller side feature in the linear absorption spectrum.

AVERAGE CORRELATION ENERGY PER EXCITON

The correlation energy due to the magnetic and nonmagnetic exciton-impurity interactions is obtained by subtracting the mean-field contribution from the expectation value of the respective parts of the Hamiltonian given by Eq. (1). Following Ref. 2, the correlation energies can be written as

$$\langle H_{\mathrm{m}} \rangle^{\mathrm{c}} = \frac{N_{\mathrm{Mn}}}{V^2} \int_0^{K_c} dK \int_0^{K_c} dK'\, D(K)D(K') \Big(J_{sd} \sum_l Q_{-\eta_{\mathrm{h}} l K}^{l K'}(t) - \frac{J_{pd}}{2} Q_{\eta_{\mathrm{e}} z K}^{0 K'} \Big), \tag{13a}$$

$$\langle H_{\mathrm{nm}} \rangle^{\mathrm{c}} = \frac{N_{\mathrm{Mn}}}{V^2} \int_0^{K_c} dK \int_0^{K_c} dK'\, D(K)D(K') \Big(J_0^{\mathrm{e}} Z_{-\eta_{\mathrm{h}}\ K}^{0 K'}(t) + J_0^{\mathrm{h}} Z_{\eta_{\mathrm{e}}\ K}^{0 K'} \Big), \tag{13b}$$

with the correlations

$$Q_{\eta l K_1}^{\alpha K_2} = \frac{Vd}{N_{\mathrm{Mn}}} \int_0^{2\pi} \frac{d\psi_1}{2\pi} \int_0^{2\pi} \frac{d\psi_2}{2\pi} f_{\eta 1s1s}^{\mathbf{K}_1 \mathbf{K}_2} \int dz |u_0(z)|^2 \sum_{\substack{\sigma\sigma' I \\ nn'}} S_{nn'}^l s_{\sigma\sigma'}^{\mathrm{e},\alpha} \Big\langle \hat{Y}_{\sigma-\frac{3}{2}1s\mathbf{K}_1}^\dagger \hat{Y}_{\sigma'-\frac{3}{2}1s\mathbf{K}_2} e^{i(\mathbf{K}_2-\mathbf{K}_1)\cdot\mathbf{R}_I} \hat{P}_{nn'}^I \delta(z - Z_I) \Big\rangle, \tag{14a}$$

$$Z_{\eta\ K_1}^{\alpha K_2} = \frac{Vd}{N_{\mathrm{Mn}}} \int_0^{2\pi} \frac{d\psi_1}{2\pi} \int_0^{2\pi} \frac{d\psi_2}{2\pi} f_{\eta 1s1s}^{\mathbf{K}_1 \mathbf{K}_2} \int dz |u_0(z)|^2 \sum_{\sigma\sigma' I} s_{\sigma\sigma'}^{\mathrm{e},\alpha} \Big\langle \hat{Y}_{\sigma-\frac{3}{2}1s\mathbf{K}_1}^\dagger \hat{Y}_{\sigma'-\frac{3}{2}1s\mathbf{K}_2} e^{i(\mathbf{K}_2-\mathbf{K}_1)\cdot\mathbf{R}_I} \delta(z - Z_I) \Big\rangle. \tag{14b}$$

The correlation energy is obtained by solving the equations of motion for these correlations, which are given explicitly in Ref. 2. An analysis of the prefactors in Eqs. (13) and Eqs. (14) together with the scaling of the density of states
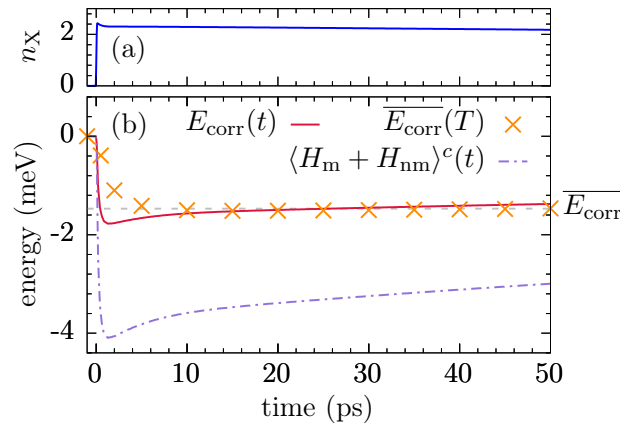
FIG. 1. Build up of the correlation energy in a 15 nm wide $Zn_{0.975}Mn_{0.025}Se$ quantum well at 30 K. We compare (a) the number of excitons n_X with (b) the correlation energy given by the expectation value $\langle H_m + H_{nm} \rangle^c(t)$. Also shown is the time-dependent quotient $E_{corr}(t)$ from Eq. (15) in relation to the time-averaged correlation energy per exciton $\overline{E_{corr}}(T)$ as a function of the averaging time. The final value for the average correlation energy per exciton is marked by $\overline{E_{corr}}$ and the grey dashed line. For the optical excitation, a 100 fs laser pulse is assumed.

yields an inverse dependence of the total correlation energy $\langle H_m + H_{nm} \rangle^c$ on the quantum well width. Since the so defined correlation energy depends on the strength of the optical excitation and thus on the number of excited excitons, it is preferable to instead consider the correlation energy per exciton as this quantity is independent on the optical driving strength in the low-intensity regime. However, due to the optical excitation as well as radiative decay, the correlation energy is a time-dependent quantity. A reliable value for the average correlation energy per exciton is then given by

$$\overline{E_{corr}} = \frac{1}{T} \int_0^T dt \, E_{corr}(t) = \frac{1}{T} \int_0^T dt \, \frac{\langle H_m + H_{nm} \rangle^c(t)}{n_X(t)}, \tag{15}$$

where $n_X(t)$ denotes the number of excitons at time t and T is a suitably long averaging time.

In order to provide an example for the time dependence of the correlation energy as well as the extraction of its corresponding average per exciton, Fig. 1 shows the correlation energy calculated using Eqs. (13) for a 15 nm wide $Zn_{0.975}Mn_{0.025}Se$ quantum well with acoustic phonon scattering at 30 K and a radiative decay rate of 0.1 ps^{-1}. Looking first at the number of excitons in Fig. 1(a) and the correlation energy in Fig. 1(b), the influence of radiative decay causes both quantities to decrease over time after the pulse is switched off. Note that this decrease occurs on large time scales compared to the radiative decay rate since only excitons close to $K = 0$ are allowed to recombine. Due to the pronounced scattering of excitons at the impurities as well as the scattering due to phonons, optically created excitons are scattered away from $K = 0$ and are thus no longer affected by radiative decay, which effectively slows down the decay.

Figure 1(b) also shows the time dependent correlation energy per exciton $E_{corr}(t)$ obtained from the quotient of the correlation energy and the number of excitons. Since both numerator and denominator in this quotient are decreasing as a function of time, the resulting quantity is much less affected by radiative decay and shows almost no time dependence after an initial overshoot that can be attributed to the energy-time uncertainty regarding the optical excitation. Fig. 1(b) confirms that $\overline{E_{corr}}(T)$ then indeed yields a reliable number for the correlation energy per exciton that remains virtually constant after an averaging time of about 10 ps. The final value of the average correlation energy per exciton used for the interpretation of the linear absorption spectra is marked by $\overline{E_{corr}}$.

[1] F. Ungar, M. Cygorek, and V. M. Axt, Phys. Rev. B **95**, 245203 (2017).
[2] F. Ungar, M. Cygorek, and V. M. Axt, Phys. Rev. B **97**, 045210 (2018).
[3] A. Thränhardt, S. Kuckenburg, A. Knorr, T. Meier, and S. W. Koch, Phys. Rev. B **62**, 2706 (2000).
[4] K. Siantidis, V. M. Axt, and T. Kuhn, Phys. Rev. B **65**, 035303 (2001).

Publication 4

Role of excited states in the dynamics of excitons and their spins in diluted magnetic semiconductors

F. Ungar, M. Cygorek, and V. M. Axt

Role of excited states in the dynamics of excitons and their spins in diluted magnetic semiconductors

F. Ungar,[1] M. Cygorek,[2] and V. M. Axt[1]

[1]*Theoretische Physik III, Universität Bayreuth, 95440 Bayreuth, Germany*
[2]*Department of Physics, University of Ottawa, Ottawa, Ontario, Canada K1N 6N5*

We theoretically investigate the impact of excited states on the dynamics of the exciton ground state in diluted magnetic semiconductor quantum wells. Exploiting the giant Zeeman shift in these materials, an external magnetic field is used to bring transitions between the exciton ground state and excited states close to resonance. It turns out that, when treating the exciton dynamics in terms of a quantum kinetic theory beyond the Markov approximation, higher exciton states are populated already well below the critical magnetic field required to bring the exciton ground state in resonance to an excited state. This behavior is explained by exciton-impurity correlations that can bridge energy differences on the order of a few meV and require a quantum kinetic description beyond the independent-particle picture. Of particular interest is the significant spin transfer toward states on the optically dark $2p$ exciton parabola which are protected against radiative decay.

I. INTRODUCTION

Ever since the seminal works by Frenkel [1] and Wannier [2], excitons in semiconductors have continued to attract attention and are nowadays routinely used in the optical characterization of materials [3]. Most notably, exciton states with very high principal quantum numbers have recently been experimentally observed in cuprous oxide [4], and exciton binding energies of several hundred meV have been found in transition-metal dichalcogenide (TMD) monolayers [5–7]. Although exciton binding energies are much smaller in standard bulk semiconductors, they can be significantly enhanced up to several tens of meV in semiconductor nanostructures such as quantum wells and wires [8]. Here, we theoretically study excitons in diluted magnetic semiconductors (DMSs), where a small number of impurity ions with a large magnetic moment such as manganese is incorporated in the crystal lattice [9–12]. To obtain sufficiently high binding energies, we consider $Zn_{1-x}Mn_xSe$ quantum wells. Being a II-VI semiconductor, ZnSe also allows for an isoelectronic incorporation of Mn impurities without the generation of excess carriers.

It is well known that correlations can play a decisive role in the magnitude of material properties such as band gaps and quasiparticle energies [5,13] or their optical properties [14–17]. DMSs are especially prominent materials in that regard since they are known to display strong correlation effects [12,18–20], which is in part due to the large coupling constants found in the carrier-impurity exchange interaction. This mechanism, which typically dominates the spin dynamics in DMSs [21,22], describes a spin-flip scattering of carriers at the localized impurities. Apart from its impact on the dynamics, the carrier-impurity exchange interaction also causes the giant Zeeman effect that significantly enhances the Zeeman splitting in an external magnetic field [12]. By applying a magnetic field, one can thus bring the exciton ground state with appropriate spin into or close to resonance with an excited exciton state so transitions between them can occur easily.

In this paper, we study the impact of excited states on the dynamics of the optically excited exciton ground state in terms of both its occupation and its spin. The simulations are performed for a system with a magnetic field that is tuned such that the $1s$ heavy-hole (hh) exciton is energetically close to one of the $2p$ states. Since correlations are important in DMSs, as mentioned previously, we describe the exciton dynamics in terms of a quantum kinetic theory (QKT) which explicitly captures exciton-impurity correlations beyond the mean-field level [23].

It turns out that correlations significantly impact the dynamics, causing a sizable population of optically dark $2p$ excitons already well below the magnetic field required for a resonance of the $2p$ state with the ground state. In contrast, a standard Markovian theory (MT), where all correlation effects are neglected such that excitons are effectively described as independent entities, yields only a finite occupation of the $2p$ state above this critical field. This makes clear that the large correlation energies found in DMS quantum wells [20] allow for a bridging of otherwise still off-resonant transitions to higher exciton states. It is worthwhile to note that the $2p$ excitons populated in this way cannot be directly addressed by optical excitation since they are dark. The mechanisms discussed in this paper thus allow a transfer to states where the carrier spins are protected against radiative decay even after a relaxation towards the subband minimum. Our analysis also reveals that the occupation of excited states is reflected in the spin dynamics of the exciton ground state, which becomes accelerated compared with a simulation where only the ground state is accounted for.

II. THEORY

First, we discuss the Hamiltonian used to model the exciton dynamics in DMSs and provide the equation of motion for the time-dependent occupation and spin of any given exciton state. We first focus on results obtained by a recently devel-

oped quantum kinetic description of exciton spins in DMSs quantum wells [23], which explicitly takes exciton-impurity correlations into account, and we discuss its Markov limit in the following section. In this limit, all correlations and thereby caused memory effects are disregarded to obtain a rate-type description.

A. Quantum kinetic model

We consider a II-VI DMS quantum well at a fixed temperature of 1 K which is optically excited with a short laser pulse. In its ground state, such a semiconductor compound has a completely filled valence band and an empty conduction band. If, additionally, an external magnetic field is applied along the growth direction, the Hamiltonian comprises the following parts [23]:

$$H = H_0^e + H_0^h + H_{\text{conf}} + H_C + H_Z^e + H_Z^h + H_Z^{\text{Mn}}$$
$$+ H_{\text{lm}} + H_{sd} + H_{pd} + H_{\text{nm}}^e + H_{\text{nm}}^h. \tag{1}$$

The kinetic energies of electrons and holes given by H_0^e and H_0^h, respectively, together with the confinement H_{conf} due to the quantum well and the Coulomb interaction given by H_C define the exciton problem. Its eigenfunctions are the exciton wave functions, labeled by their center-of-mass momentum K and a discrete exciton quantum number $x \in \{1s, 2s, 2p, \dots\}$ similar to that of the hydrogen problem in two dimensions, and its eigenvalues provide the corresponding energies.

The external magnetic field causes a Zeeman shift of electrons and holes given by H_Z^e and H_Z^h, respectively, but also similarly affects the magnetic impurities via H_Z^{Mn}. Furthermore, the interaction of the system with the laser pulse is contained in the light-matter interaction term H_{lm}, for which we use the usual dipole approximation [24].

The typically most important interaction in DMSs is the Kondo-type carrier-impurity exchange interaction [11,12,23,25] given by H_{sd} and H_{pd}. These terms describe the spin-flip scattering of s-like conduction band electrons and p-like valence band holes with the localized electrons in the d shell of an impurity ion, such as manganese. Apart from a spin-flip scattering, impurities in general also cause nonmagnetic scattering due to the local mismatch in the band

gap that arises when foreign atoms are incorporated into a host lattice. We model these nonmagnetic local potentials similarly to the exchange interaction but without the possibility to induce spin flips [26], which leads to the final contributions H_{nm}^e and H_{nm}^h in Eq. (1) for electrons and holes, respectively.

In principle one could also include the scattering with phonons in the model. However, recent investigations have shown that their effects either are negligible for resonantly excited excitons at low temperatures [27] or require long timescales on the order of nanoseconds when a magnetic field is applied [28]. Here, we are interested only in the low-temperature limit and timescales of up to 100 ps, so phonons can be disregarded. For explicit expressions as well as a more detailed discussion of each constituting part of the Hamiltonian given by Eq. (1), the reader is referred to Ref. [23].

In DMSs described by Eq. (1), the energetically lowest exciton state consists of an electron in the conduction band and a heavy hole in the topmost valence band [8,29]. Whereas the electrons are characterized by a spin quantum number $s_z = \pm\frac{1}{2}$, the hh spins consist of states with angular momentum quantum number $j_z = \pm\frac{3}{2}$. States with $j_z = \pm\frac{1}{2}$, the so-called light holes (lh), are located energetically below the hh states by the amount of the hh-lh splitting. This splitting is a direct result of the confinement in the quantum well but is also influenced by strain [29]. Focusing on systems where this splitting is large and using an excitation with σ^- polarization, the optically prepared hh spin with $j_z = -\frac{3}{2}$ remains effectively pinned along the growth direction of the quantum well in its initially prepared state [30–33]. Then, the description of the exciton spin dynamics can be limited to only two spin orientations for each exciton parabola, i.e., one where the exciton-bound electron spin is oriented parallel with respect to the growth direction and the exciton is bright ($s_z = \frac{1}{2}$) and another where it is flipped and thus optically dark ($s_z = -\frac{1}{2}$). Other than states that are not coupled to the light field because of their finite center-of-mass momenta, the latter states are dark due to spin selection rules. Denoting the two spin states by the symbols $\uparrow$ and $\downarrow$, respectively, the time evolution of the spin-dependent exciton density is given by

$$\frac{\partial}{\partial t} n_{x_1 K_1}^{\uparrow/\downarrow} = \frac{2}{\hbar} E(t) M_{\uparrow/\downarrow} \text{Im}\big[y_{x_1}^{\uparrow} \phi_{x_1}\big] \delta_{K_1,0} \pm \frac{J_{pd} n_{\text{Mn}}}{\hbar V} \sum_{x'K'} \big(\text{Im}\big[Q_{\eta_e 3x'K'}^{3x_1 K_1}\big] \pm \tfrac{1}{2} \text{Im}\big[Q_{\eta_e 3x'K'}^{0x_1 K_1}\big] \big)$$

$$\pm \frac{J_{sd} n_{\text{Mn}}}{\hbar V} \sum_{x'K'} \left(\sum_{ij} \epsilon_{ij3} \text{Re}\big[Q_{-\eta_h ix'K'}^{jx_1 K_1}\big] - \tfrac{1}{2} \text{Im}\big[Q_{-\eta_h 3x'K'}^{0x_1 K_1}\big] \mp \sum_i \text{Im}\big[Q_{-\eta_h ix'K'}^{ix_1 K_1}\big] \right)$$

$$\mp \frac{J_0^e n_{\text{Mn}}}{\hbar V} \sum_{x'K'} \big(2\text{Im}\big[Z_{-\eta_h \, x'K'}^{3x_1 K_1}\big] \pm \text{Im}\big[Z_{-\eta_h \, x'K'}^{0x_1 K_1}\big] \big) \mp \frac{J_0^h n_{\text{Mn}}}{\hbar V} \sum_{x'K'} \big(2\text{Im}\big[Z_{\eta_e \, x'K'}^{3x_1 K_1}\big] \pm \text{Im}\big[Z_{\eta_e \, x'K'}^{0x_1 K_1}\big] \big), \tag{2}$$

according to the QKT developed in Ref. [23]. Apart from the total exciton density $n_{x_1 K_1} = n_{x_1 K_1}^{\uparrow} + n_{x_1 K_1}^{\downarrow}$ in the state x_1 with center-of-mass wave number K_1, Eq. (2) also yields the corresponding z component of the exciton spin $s_{x_1 K_1}^z = \frac{1}{2}(n_{x_1 K_1}^{\uparrow} - n_{x_1 K_1}^{\downarrow})$. For an external magnetic field oriented along

the growth direction, the z component is the only one relevant as both in-plane components are not occupied during the dynamics. Note that our notation is such that each exciton state thus consists of two spin orientations, which are degenerate at zero magnetic field and show a Zeeman splitting otherwise.

In the above equation, $E(t)M_{\uparrow/\downarrow}$ denotes the product of the Gaussian laser pulse $E(t) = E_0 \exp(-\frac{t^2}{2\sigma^2})$ with amplitude E_0 and width σ, with the dipole matrix element $M_{\uparrow/\downarrow}$ containing the optical selection rules. The constant $\phi_{x_1} = R_{x_1}(r = 0)$ is the radial part of the x_1 exciton wave function evaluated at the origin, which, together with the factor $\delta_{K_1,0}$, is a consequence of the dipole approximation. The variable that directly describes the interband transition is the optical coherence $y_{x_1}^{\uparrow}$, where the spin index indicates that only the $\uparrow$ state is optically active. In the QKT, the dynamics is a consequence of exciton-impurity correlations Q and Z, for which separate equations of motion must be solved. The indices of the coupling constants J in front of these correlations indicate their respective origin in terms of the Hamiltonian given by Eq. (1). Additionally, n_{Mn} denotes the impurity density in the system with volume V, and the summation indices i, $j \in \{1, 2, 3\}$ reflect the spatial directions. We do not provide an explicit equation of motion for the impurity spin density matrix and instead assume that it is well approximated by its thermal equilibrium value, which is justified when the Mn concentration is much higher than the carrier density [34]. We thus also assume that the magnetic moments of the Mn impurities have had sufficient time to adjust their orientation in the applied external magnetic field before the laser pulse starts to excite any excitons.

Since the equations for the coherence as well as the various correlations are lengthy and not very transparent, we do not explicitly write them here but refer the interested reader to Ref. [23], where they were originally derived and discussed in detail. Here, it suffices to stress that any occupation of an exciton state with finite K should be viewed as a result of correlations in the system, as can be seen in Eq. (2). In contrast to a mean-field theory where the impurities are described as a homogeneous bath, the correlations in the QKT capture the breaking of the translational invariance due to the positional disorder of the impurities, which in turn is reflected by momentum nonconservation. Thus, in the QKT, the effective independent-particle exciton states are no longer the proper eigenstates of the system [20]. Rather, the proper

eigenstates are determined by the equations of motion for the correlations, which include the energy-time uncertainty as well as a possible violation of strict energy conservation on the independent-particle level.

B. Markov limit

To reveal the impact of quantum kinetic effects on the exciton dynamics, it is helpful to compare the results of the QKT to those of an effective independent-particle theory where all correlation effects are discarded. Such a Markovian description can be obtained by formally integrating the equations of motion for the correlations, which have the general form [23]

$$\frac{\partial}{\partial t} Q(t) = i\omega Q(t) + b(t) \tag{3}$$

with a frequency ω that, among other contributions, contains the exciton frequencies and a source term $b(t)$ that, in general, depends on the exciton density as well as the exciton spin. The solution to Eq. (3) is given by

$$Q(t) = \int_0^t d\tau\, e^{-i\omega(t-\tau)} b(\tau), \tag{4}$$

where an explicit memory appears. Assuming $b(\tau)$ does not vary strongly within the memory time so it can be replaced by $b(t)$ and thus drawn out of the integral, the remaining integration can be solved in the limit $t \to \infty$ using the Sokhotsky-Plemelj formula [23], so the time dependence of the integral vanishes. Physically, this also implies that one forces the system to occupy only independent-particle eigenstates (see also the Appendix in Ref. [35] for an extended discussion of the implications of the Markov limit). This is in contrast to Eq. (2), where the final energy eigenstates are determined by the correlations [20].

Applying this scheme to Eq. (2) and, for numerical reasons that become clear later on, switching to a representation in frequency space, the equations of motion in the Markov limit read [23]

$$
\begin{aligned}
\frac{\partial}{\partial t} n_{x_1,\omega_1}^{\uparrow/\downarrow} &= \Gamma_{x_1,\omega_1} + \frac{IMn_{\mathrm{Mn}}}{2\hbar^3 d} \sum_{x'\omega'} \Big\{ \delta(\omega'_{x'} - \omega_{1x_1})\big(n_{x'\omega'}^{\uparrow/\downarrow} - n_{x_1\omega_1}^{\uparrow/\downarrow}\big)\Big[\big(J_{sd}^2 b^{\parallel} \pm 2J_{sd}J_0^{\mathrm{e}} b^0 + 2J_0^{\mathrm{e}2}\big) F_{\eta_{\mathrm{h}} x'x_1}^{\eta_{\mathrm{h}}\omega'\omega_1} \\
&\quad + \big(J_{pd}^2 b^{\parallel} - 2J_{pd}J_0^{\mathrm{h}} b^0 + 2J_0^{\mathrm{h}2}\big) F_{\eta_{\mathrm{e}} x'x_1}^{\eta_{\mathrm{e}}\omega'\omega_1} + \big(4J_0^{\mathrm{e}}J_0^{\mathrm{h}} - 2J_{pd}J_0^{\mathrm{e}} b^0 \pm 2J_{sd}J_0^{\mathrm{h}} b^0 \mp 2J_{sd}J_{pd} b^{\parallel}\big) F_{-\eta_{\mathrm{h}} x'x_1}^{\eta_{\mathrm{e}}\omega'\omega_1}\Big] \\
&\quad + \delta\big[\omega'_{x'} - \big(\omega_{1x_1} \pm \omega_{\mathrm{sf}}\big)\big] J_{sd}^2 F_{x'x_1}^{\omega'\omega_1}\big(b^{\pm} n_{x'\omega'}^{\downarrow/\uparrow} - b^{\mp} n_{x_1\omega_1}^{\uparrow/\downarrow}\big)\Big\}.
\end{aligned}
\tag{5}
$$

Here, the optical excitation is subsumed in an optical generation rate of excitons given by

$$\Gamma_{x,\omega} = \frac{1}{\hbar^2} E(t)E_0 |M_{\uparrow/\downarrow}|^2 |\phi_x|^2 \int_{-\infty}^t d\tau\, e^{-\frac{\tau^2}{2\sigma^2}} \delta_{\omega,0}^b \delta_{x,1s}. \tag{6}$$

The function $\delta_{\omega,0}^b = \exp[-(\hbar\omega/2w_{\mathrm{b}})^2]$ with a small value of $w_{\mathrm{b}} = 1\,\mu\mathrm{eV}$ is used to achieve a numerically scalable and stable approximation of a δ function, reflecting the fact that the resonant optical excitation occurs only at the bottom of the spin-up exciton parabola ($\hbar\omega = 0$). Furthermore, the constant $I = \frac{3}{2}$ appears due to the envelope

functions of the quantum well in the approximation of infinitely high potential barriers, M is the exciton mass, and d denotes the width of the well. The Mn spin enters the equation via the spin moments $b^{\parallel}$, b^0, and $b^{\pm}$, which, together with the exciton form factors $F_{\eta_i x_1 x_2}^{\eta_j \omega_1 \omega_2}$, can be found in the Appendix.

The δ functions appearing in Eq. (5) are the reason for switching to the frequency domain since then their numerical evaluation is much more convenient. Apart from the indirect influence of the magnetic field via the moments of the impurity spin, the Zeeman energies directly appear in the energy-

conserving δ functions in terms of the spin-flip scattering shift

$$\hbar\omega_{\text{sf}} = \hbar\omega_{\text{e}}^z - \hbar\omega_{\text{Mn}}^z. \tag{7}$$

There, the Zeeman energy of the impurities $\hbar\omega_{\text{Mn}}^z = g_{\text{Mn}}\mu_B B^z$ is subtracted from the Zeeman energy of the excitons combined with the giant Zeeman shift due to the impurities $\hbar\omega_{\text{e}}^z = g_{\text{e}}\mu_B B^z + J_{sd}n_{\text{Mn}}\langle S^z \rangle$. In the energy balance together with the exciton kinetic energy $\hbar\omega_x$ in the state x, this term takes the energy cost of an exciton-impurity spin flip-flop process into account. Similar to the QKT, the energy of an x exciton is measured with respect to the $1s$ hh exciton ground state with $s_z = \frac{1}{2}$ and $j_z = -\frac{3}{2}$.

III. NUMERICAL SIMULATIONS

In this section, numerical simulations are performed for the QKT as well as the MT, and the respective results are compared to extract the fingerprint of quantum kinetic effects in the dynamics. For all simulations, a $\text{Zn}_{0.975}\text{Mn}_{0.025}\text{Se}$ quantum well with a width of 20 nm at a temperature of 1 K is considered. The optical excitation is always chosen to be resonant with the Zeeman-shifted $1s$ exciton ground state, which is excited using a Gaussian laser pulse with a full width at half maximum of 100 fs. In principle, Eqs. (2) and (5) are valid for an arbitrary number of states. However, here, we limit the description to the four energetically lowest exciton states, i.e., the $1s$, $2s$, $2p_x$, and $2p_y$ states. Numerically, this requires the discretization of the continuous center-of-mass momenta for each of the four states as well as their two possible spin orientations, as described in Sec. II A. The calculated exciton binding energies based on a diagonalization of the exciton problem in real space for standard ZnSe parameters (cf. Ref. [23]) can be found in Table I. The calculated values are in good agreement with experimental data [36–38].

From the exciton energies one can see that the two degenerate $2p$ states lie energetically below the $2s$ state, which is a consequence of the confinement due to the quantum well in combination with the finite angular momentum quantum number of the p states. This is similar to the case of monolayer TMDs, where the $2p$ excitons are also more strongly bound than the $2s$ excitons [7]. There are several possibilities to involve excited exciton states in the dynamics. Here, we choose the application of an external magnetic field and exploit the giant Zeeman shift of DMSs to bring the $1s$ state with a spin-up exciton-bound electron close to an excited state with a spin-down exciton-bound electron. The necessary values

TABLE I. Calculated energies of the first four exciton states in a 20-nm-wide $\text{Zn}_{0.975}\text{Mn}_{0.025}\text{Se}$ quantum well measured with respect to the band gap. The value of the magnetic field B_c indicates the threshold when the spin-flip scattering shift becomes large enough to enable a spin flip from the $1s$ state to the current state.

Exciton state	Energy (meV)	B_c (T)
$1s$	-20.37	0.00
$2p_x$	-7.14	0.83
$2p_y$	-7.14	0.83
$2s$	-5.35	1.31

of the magnetic field for such a transition are also given in Table I for the $2p$ and the $2s$ states. Considering, e.g., the energy difference $E_{1s-2p} = 13.23$ meV, a magnetic field of about 0.83 T is required to shift the two bands such that spin flips between them can be resonantly mediated by the exciton-impurity exchange interaction. Thus, in the MT with strict energy conservation, one can expect that higher exciton states will become occupied if the magnetic field exceeds this value but will remain completely unoccupied for magnetic fields with a smaller magnitude. Considering that excitons with higher principal quantum numbers are also energetically farther away from the $1s$ state, limiting the description to the four states shown in Table I is a good approximation as long as the magnetic field stays well below the threshold to the higher states.

The occupation of the energetically lowest four exciton states as a function of time is plotted in Figs. 1(a)–1(c). Note that the data are normalized with respect to the maximum occupation on the $1s$ exciton parabola reached due to the laser excitation. For three different magnitudes of the external magnetic field, namely, 0.75, 0.80, and 0.85 T, results of simulations using the QKT and the MT are shown. Since the two $2p$ states are degenerate, we plot only the sum of the result for the $2p_x$ and $2p_y$ states here and refer to them as the $2p$ state in the following. Based on the Markovian model given by Eq. (5) and the values in Table I, the $2p$ state should become populated only for the largest magnetic field, and the $2s$ state should remain empty for all considered magnetic fields. Surprisingly, when comparing the results of the QKT with those of the MT, we find that the QKT predicts a sizable occupation of the $2p$ state already for the smallest chosen magnetic field and even predicts a small but visible occupation of the $2s$ state. At 0.80 T, which is already close to but still below the magnetic field B_c required to enable a transition in the MT, the difference between the predictions of the QKT and the MT is almost as large as 50% at 100 ps after the pulse. Only when the $1s$-$2p$ transition is also allowed in the MT [see Fig. 1(c)] do the two theories predict similar occupations for the $1s$ and $2p$ states, but deviations are still visible, and the $2s$ state remains completely empty in the MT.

The reason for the pronounced deviations between the predictions of the QKT and the MT lies in the fact that correlations are captured only in the former theory, whereas the latter is an effective independent-particle theory for excitons. As pointed out in previous works on DMSs [34,39], carrier-impurity correlations can cause pronounced non-Markovian effects, especially in the exciton regime due to their large effective mass as well as the proximity of optically generated excitons to the bottom of the exciton parabola [20,23,40]. Indeed, exciton-impurity correlations are responsible for an occupation of higher exciton states when the Zeeman shift is not yet large enough to bring them into resonance with the exciton ground state. Qualitatively, this means that the exchange interaction between excitons and impurities causes the formation of stable connections between the independent-particle energy eigenstates obtained in the MT. These connections remain stable even at long times (see Fig. 1) and change the energetic structure of the problem. Since the correlation energy amounts to several meV for the parameters considered here [20,40], this energy can be used to overcome
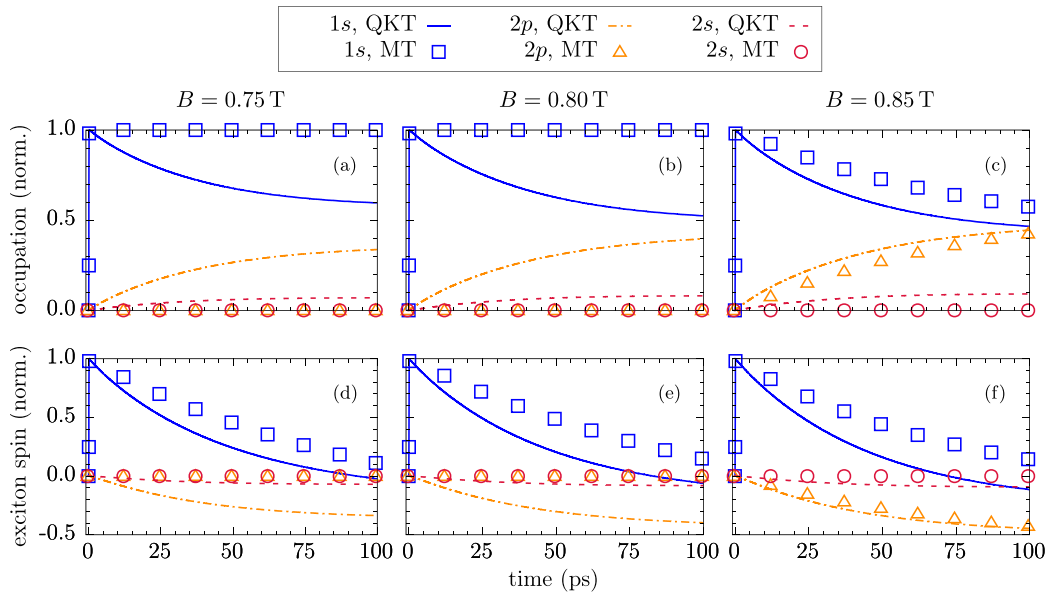
FIG. 1. Time evolution of (a)–(c) the occupation of the energetically lowest four exciton states and (d)–(f) their respective spin components in the z direction for three different choices of the external magnetic field B, as indicated. The occupation and the exciton spin are normalized with respect to their maximum value after the pulse, and the simulations are performed for a 20-nm-wide $Zn_{0.975}Mn_{0.025}Se$ quantum well excited at the $1s$ exciton resonance. We account for the $1s$, $2p_x$, $2p_y$, and $2s$ exciton state, where the label $2p$ denotes the sum of the degenerate $2p_x$ and $2p_y$ states. Results obtained by the quantum kinetic theory (QKT) are compared with those obtained by a standard Markovian theory (MT) without any memory.

the energy barrier between the exciton ground state and higher exciton states as the negative correlation energy increases the exciton kinetic energy [23]. The fact that the $2s$ state becomes occupied already at Zeeman shifts comparable to the energy difference between the $1s$ and $2p$ states means that the correlation energy is roughly on the order of the $2s$-$2p$ energy splitting here.

Looking at Figs. 1(a)–1(c), we see that the $2p$ occupation is significantly higher than that of the $2s$ state. In part, this is because the magnetic field is chosen such that the Zeeman shift is close to or larger than E_{1s-2p}; that is, the $2p$ state can also be occupied without the need for correlation energy as soon as the field is sufficiently large. More important, however, is the fact that, to reach the $2s$ state, excitons need to increase their kinetic energy by an additional amount of $E_{2p-2s} \approx 2$ meV. But since the scattering rate to higher energies is proportional to the exciton form factor, which quickly falls off for larger center-of-mass momenta [27], this process is significantly less likely.

Note that the energy-time uncertainty does not explain the observations in Fig. 1 as it affects only the dynamics on short timescales and thus cannot explain the occupation of excited states long after the pulse is switched off. In fact, Fig. 1 shows that the $1s$ occupation continuously decreases throughout the whole time interval considered. Conversely, the occupation of higher exciton states, especially the $2p$ state, continuously rises. Using this scheme thus allows one to achieve an efficient indirect preparation of the optically dark $2p$ state with an occupation close to 50% of the originally prepared $1s$ excitons on a timescale of 100 ps after the pulse.

Apart from their effect on the occupation of the exciton ground state, higher exciton states also affect the spin dynamics, as can be seen in Figs. 1(d)–1(f). As before, the

results are normalized with respect to the maximum spin of the $1s$ exciton reached due to the optical excitation. There, the occupation of higher exciton states manifests in a faster decay of the $1s$ exciton spin compared with the predictions of the MT. This can be straightforwardly understood by thinking about the higher exciton states in terms of the possibility to open up another channel to which the spin can be transferred. The availability of an additional channel thus causes a faster decay of the originally excited spin component. Furthermore, Figs. 1(d)–1(f) show that the spin polarization is almost completely transferred to the $2p$ excitons on the timescale investigated here and the $1s$ spin is essentially zero after 100 ps, even though the $1s$ state remains occupied by about 50% of the initial occupation [see Figs. 1(a)–1(c)]. Note the reversed sign of the $2p$ spin polarization compared with the optically prepared $1s$ spin, which is a consequence of the fact that $2p$ states can be reached only via a spin-flip process.

In contrast to the total exciton occupation, which remains constant after the pulse is switched off, the spin decays due to the exciton-impurity exchange interaction until it reaches a stationary value that is antiparallel with respect to the external magnetic field [40]. Just like for the occupations, the QKT predicts a pronounced influence of higher exciton states already below the critical magnetic field that is necessary to overcome the $1s$-$2p$ splitting on the mean-field level. To provide a better understanding of the influence of excited exciton states on the spin dynamics, Fig. 2 depicts the results of a simulation using the QKT with either only one or four exciton states accounted for at a magnetic field of 0.85 T.

Figure 2 confirms the previous observation that the presence of higher exciton states and thus additional decay channels causes the spin to decay faster. Looking at Fig. 1, this already occurs at magnetic fields that cause Zeeman shifts
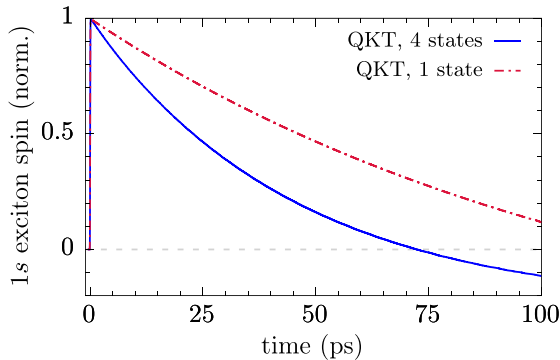
FIG. 2. Time evolution of the z component of the $1s$ exciton spin as obtained by the quantum kinetic theory (QKT) when the four energetically lowest exciton states (4 states) or only the exciton ground state (1 state) are accounted for. The simulations are performed for a 20-nm-wide $Zn_{0.975}Mn_{0.025}Se$ quantum well excited at the $1s$ exciton resonance in an external magnetic field $B = 0.85\,T$, and the results are normalized with respect to the maximum spin polarization after the pulse.

smaller than the separation between the exciton ground state and the lowest excited state. Furthermore, the faster decay is already visible on short timescales of a few picoseconds and causes the spin polarization to switch its sign much sooner. This analysis suggests that theoretical works should include transitions to higher exciton states even though they may not yet be fully resonant based on energy considerations on the independent-particle level.

Coming back to the correlation energy, its impact becomes most apparent when looking at the energy- and time-resolved exciton occupation. To this end, Fig. 3 displays the occupation of the exciton ground state predicted by the QKT as a function of time and kinetic energy with respect to the bottom of the $1s$ exciton parabola for a magnetic field of 0.85 T. The influence of excited exciton states becomes apparent when comparing Figs. 3(a) and 3(b) as the former takes only the exciton ground state into account, whereas the latter includes the four energetically lowest states in the calculation. To facilitate the comparison between the two situations, Fig. 3(c) displays the difference between the occupations in the two cases.
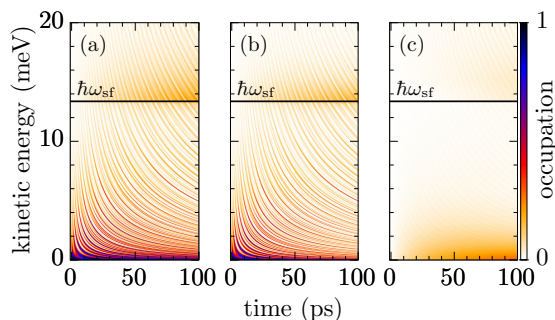
FIG. 3. Time- and energy-resolved occupation of the $1s$ exciton ground state as obtained by the quantum kinetic theory when (a) only the exciton ground state or (b) the four energetically lowest exciton states are accounted for. The simulations are performed for a 20-nm-wide $Zn_{0.975}Mn_{0.025}Se$ quantum well excited at the $1s$ exciton resonance in an external magnetic field $B = 0.85\,T$. The dashed line indicates the spin-flip scattering shift $\hbar\omega_{sf}$. (c) The difference between the occupations of (a) and (b).

Without any correlations and in the absence of redistribution mechanisms such as phonon scattering, Eq. (5) predicts a scattering between $\hbar\omega = 0$ and $\hbar\omega_{sf}$. In Fig. 3, these two points are represented by the bottom of the figure and the dashed line, respectively. Thus, in the MT, one would expect only a transfer of occupations between these two points. In contrast to that expectation, the exciton-impurity correlations captured by the QKT cause a significant occupation of states away from $\hbar\omega = 0$ that are not accessible in the MT. Although a large fraction of excitons is still located close to $\hbar\omega = 0$ and $\hbar\omega_{sf}$, as can be seen in Fig. 3, the occupation is strongly smeared out due to the correlations, which is the most prominent effect in the figure. Note also that the redistribution of excitons towards higher kinetic energies takes place on a timescale of only a few picoseconds after the pulse, which is why some excitons quickly gain enough kinetic energy to populate the $2s$ or $2p$ states, as found in Fig. 1.

When comparing Fig. 3(a) with Fig. 3(b), the effect of higher exciton states is small but most noticeable near $\hbar\omega = 0$ as well as above $\hbar\omega_{sf}$ [see also Fig. 3(c)]. There, the occupation is visibly smaller in the case when higher exciton states are accounted for since excitons are likely to get scattered to other states. This manifests in a slightly darker region above $\hbar\omega = 0$ and $\hbar\omega_{sf}$ in Fig. 3(c); that is, the exciton occupation is larger in these regions when only the exciton ground state is accounted for. The reason for this is that, while near $\hbar\omega = 0$ the scattering to the $2p$ state is likely to occur, states about 2 meV above $\hbar\omega_{sf}$ possess enough kinetic energy to populate the $2s$ state and are thus missing from the $1s$ parabola.

IV. CONCLUSION

We have investigated the role of excited states in the exciton dynamics in DMS quantum wells using a quantum kinetic theory that explicitly takes correlations between excitons and magnetic impurities into account. To enable spin-flip transitions between the exciton ground state and excited states, we have focused on systems with a sufficiently large magnetic field applied along the growth direction of the quantum well so the resulting Zeeman shift can be used to overcome the splitting between the states. DMSs are particularly well suited for this investigation since one can exploit the giant Zeeman shift found in these materials.

By means of a comparison with a corresponding Markovian theory that can be obtained from the QKT in the limit of vanishing memory, we find that the QKT predicts a significant occupation of higher exciton states already well below the critical magnetic field that is required to bring the exciton ground state in resonance with an excited state. The transitions can be traced back to exciton-impurity correlations that are large enough to overcome energy differences on the order of a few meV. Thus, a sizable occupation of the optically dark $2p$ states can be reached on timescales of tens of picoseconds.

The presence of higher exciton states also has consequences for the spin dynamics, causing a faster decay of the $1s$ exciton spin since more channels are available for a spin decay. All in all, our findings show that a faster spin decay will occur at sufficiently high magnetic fields compared to results obtained by a standard treatment using Fermi's golden rule. Furthermore, we show that there exists an efficient indirect mechanism to populate optically dark $2p$ excitons in

DMSs by applying a magnetic field and exciting the exciton ground state. This way, a spin transfer toward states which are protected against radiative decay can be achieved.

APPENDIX: IMPURITY SPIN MOMENTS AND EXCITON FORM FACTORS

The moments of the impurity spin $\mathbf{S}$ appearing in Eq. (5) are given by

$$b^{\pm} = \tfrac{1}{2}[\langle \mathbf{S}^2 - (S^z)^2 \rangle \pm \langle S^z \rangle], \tag{A1}$$

$$b^{\parallel} = \tfrac{1}{2}\langle (S^z)^2 \rangle, \tag{A2}$$

$$b^0 = \langle S^z \rangle. \tag{A3}$$

The exciton form factors read [23]

$$
\begin{aligned}
F_{\eta_1 x_1 x_2}^{\eta_2 \omega_1 \omega_2} = 2\pi \int_0^{2\pi} d\psi \int_0^\infty dr \int_0^\infty dr'\, rr' R_{n_1}(r) R_{n_2}(r) \\
\times R_{n_1}(r') R_{n_2}(r') J_{l_1-l_2}[\eta_1 K_{12}(\psi) r] \\
\times J_{l_1-l_2}[\eta_2 K_{12}(\psi) r'],
\end{aligned}
\tag{A4}
$$

with $K_{12} = |\mathbf{K}_1 - \mathbf{K}_2|$ and an average over the angle ψ between $\mathbf{K}_1$ and $\mathbf{K}_2$. The index n_i denotes the principle exciton quantum number, and l_i is the corresponding angular momentum quantum number of an exciton in the x_i state. Furthermore, $J_i(x)$ is the cylindrical Bessel function of order i, the constant $\eta_j = \frac{m_j}{M}$ with $j \in \{e, hh\}$ denotes the mass ratio between the carrier and exciton effective mass, and the exciton dispersion is given by $\omega = \frac{\hbar K^2}{2M}$.

[1] J. Frenkel, Phys. Rev. **37**, 17 (1931).

[2] G. H. Wannier, Phys. Rev. **52**, 191 (1937).

[3] S. W. Koch, M. Kira, G. Khitrova, and H. M. Gibbs, Nat. Mater. **5**, 523 (2006).

[4] T. Kazimierczuk, D. Fröhlich, S. Scheel, H. Stolz, and M. Bayer, Nature (London) **514**, 343 (2014).

[5] M. M. Ugeda, A. J. Bradley, S.-F. Shi, F. H. da Jornada, Y. Zhang, D. Y. Qiu, W. Ruan, S.-K. Mo, Z. Hussain, Z.-X. Shen, F. Wang, S. G. Louie, and M. F. Crommie, Nat. Mater. **13**, 1091 (2014).

[6] A. Chernikov, T. C. Berkelbach, H. M. Hill, A. Rigosi, Y. Li, O. B. Aslan, D. R. Reichman, M. S. Hybertsen, and T. F. Heinz, Phys. Rev. Lett. **113**, 076802 (2014).

[7] S. Brem, M. Selig, G. Berghaeuser, and E. Malic, Sci. Rep. **8**, 8238 (2018).

[8] G. Bastard, *Wave Mechanics Applied to Semiconductor Heterostructures* (Editions de Physique, Les Ulis, France, 1996).

[9] J. K. Furdyna, J. Appl. Phys. **64**, R29 (1988).

[10] *Semiconductors and Semimetals*, edited by J. K. Furdyna and J. Kossut (Academic, San Diego, 1988).

[11] *Introduction to the Physics of Diluted Magnetic Semiconductors*, edited by J. Kossut and J. A. Gaj (Springer, Berlin, 2010).

[12] T. Dietl and H. Ohno, Rev. Mod. Phys. **86**, 187 (2014).

[13] M. S. Hybertsen and S. G. Louie, Phys. Rev. B **34**, 5390 (1986).

[14] P. Kner, W. Schäfer, R. Lövenich, and D. S. Chemla, Phys. Rev. Lett. **81**, 5386 (1998).

[15] V. M. Axt, G. Bartels, B. Haase, J. Meinertz, U. Neukirch, and J. Gutowski, Phys. Status Solidi B **221**, 205 (2000).

[16] J. Shumway, A. Franceschetti, and A. Zunger, Phys. Rev. B **63**, 155316 (2001).

[17] D. S. Chemla and J. Shah, Nature (London) **411**, 549 (2001).

[18] H. Ohno, Science **281**, 951 (1998).

[19] I. Di Marco, P. Thunström, M. I. Katsnelson, J. Sadowski, K. Karlsson, S. Lebègue, J. Kanski, and O. Eriksson, Nat. Commun. **4**, 2645 (2013).

[20] F. Ungar, M. Cygorek, and V. M. Axt, Phys. Rev. B **98**, 161201(R) (2018).

[21] J. H. Jiang, Y. Zhou, T. Korn, C. Schüller, and M. W. Wu, Phys. Rev. B **79**, 155201 (2009).

[22] C. J. P. Smits, S. C. A. van Driel, M. van Kampen, W. J. M. de Jonge, B. Koopmans, and G. Karczewski, Phys. Rev. B **70**, 115307 (2004).

[23] F. Ungar, M. Cygorek, and V. M. Axt, Phys. Rev. B **95**, 245203 (2017).

[24] F. Rossi and T. Kuhn, Rev. Mod. Phys. **74**, 895 (2002).

[25] C. Thurn and V. M. Axt, Phys. Rev. B **85**, 165203 (2012).

[26] M. Cygorek, F. Ungar, P. I. Tamborenea, and V. M. Axt, Phys. Rev. B **95**, 045204 (2017).

[27] F. Ungar, M. Cygorek, and V. M. Axt, Phys. Rev. B **99**, 115305 (2019).

[28] F. Ungar, M. Cygorek, and V. M. Axt, Phys. Rev. B **99**, 075301 (2019).

[29] R. Winkler, *Spin-Orbit Coupling Effects in Two-Dimensional Electron and Hole Systems* (Springer, Berlin, 2003).

[30] T. Uenoyama and L. J. Sham, Phys. Rev. Lett. **64**, 3070 (1990).

[31] R. Ferreira and G. Bastard, Phys. Rev. B **43**, 9687 (1991).

[32] G. Bastard and R. Ferreira, Surf. Sci. **267**, 335 (1992).

[33] S. A. Crooker, D. D. Awschalom, J. J. Baumberg, F. Flack, and N. Samarth, Phys. Rev. B **56**, 7574 (1997).

[34] C. Thurn, M. Cygorek, V. M. Axt, and T. Kuhn, Phys. Rev. B **87**, 205301 (2013).

[35] K. Siantidis, V. M. Axt, and T. Kuhn, Phys. Rev. B **65**, 035303 (2001).

[36] R. Cingolani, M. Lomascolo, N. Lovergine, M. Dabbicco, M. Ferrara, and I. Suemune, Appl. Phys. Lett. **64**, 2439 (1994).

[37] G. V. Astakhov, D. R. Yakovlev, V. P. Kochereshko, W. Ossau, W. Faschinger, J. Puls, F. Henneberger, S. A. Crooker, Q. McCulloch, D. Wolverson, N. A. Gippius, and A. Waag, Phys. Rev. B **65**, 165335 (2002).

[38] H. Wagner, H.-P. Tranitz, W. Langbein, J. Hvam, G. Bacher, and A. Forchel, Phys. Status Solidi B **231**, 11 (2002).

[39] M. Cygorek and V. M. Axt, J. Phys.: Conf. Ser. **647**, 012042 (2015).

[40] F. Ungar, M. Cygorek, and V. M. Axt, Phys. Rev. B **97**, 045210 (2018).

Publication 5

Phonon impact on the dynamics of resonantly excited and hot excitons in diluted magnetic semiconductors

F. Ungar, M. Cygorek, and V. M. Axt

Phonon impact on the dynamics of resonantly excited and hot excitons in diluted magnetic semiconductors

F. Ungar,[1] M. Cygorek,[2] and V. M. Axt[1]

[1]*Theoretische Physik III, Universität Bayreuth, 95440 Bayreuth, Germany*
[2]*Department of Physics, University of Ottawa, Ottawa, Ontario, Canada K1N 6N5*

Phonons are well known to be the main mechanism for the coupling between bright and dark excitons in nonmagnetic semiconductors. Here, we investigate diluted magnetic semiconductors where this process is in direct competition with the scattering at localized magnetic impurities. To this end, a recently developed quantum kinetic description of the exciton spin dynamics in diluted magnetic semiconductor quantum wells is extended by the scattering with longitudinal acoustic phonons. A strong phonon impact is found in the redistribution of exciton momenta on the exciton parabola that becomes especially prominent for high temperatures and exciton distributions further away from the exciton resonance which are optically dark. Despite their impact on the energetic redistribution, acoustic phonons virtually do not affect the exciton spin dynamics as the exciton-impurity interaction always dominates. Furthermore, it turns out that the exciton spin lifetime increases by roughly one order of magnitude for nonequilibrium hot exciton distributions and, in addition, pronounced quantum kinetic signatures in the exciton spin dynamics appearing after resonant optical excitation are drastically reduced.

I. INTRODUCTION

Optical experiments on semiconductor nanostructures often use integrated or time-resolved photoluminsecence (PL) measurements to access physical quantities of interest. In such measurements, the exact position of excitons on the respective exciton parabola and, thus, their kinetic energies directly influences the measured signal since only excitons with nearly vanishing center-of-mass momenta are optically active. Redistribution mechanisms of excitons, i.e., processes that change the exciton kinetic energy, thus either indirectly affect the PL rise time or can be directly probed by monitoring the longitudinal-optical (LO) phonon-assisted PL [1]. In semiconductors, one of the most important redistribution mechanisms is the scattering with either longitudinal-acoustic (LA) or LO phonons [1–3] as it is nonelastic in nature so that a significant amount of kinetic energy can be exchanged between the phonon and the carrier system. However, it was also found that static disorder, e.g., due to impurities or surface roughness, can have an impact on the exciton distribution [4,5]. Furthermore, the redistribution of excitons to higher kinetic energies can also have consequences for the spin dynamics [6,7].

Although one usually tries to avoid any impurities in semiconductors to get as pure materials as possible, purposely doping semiconductors is a versatile technique to controllably alter intrinsic properties. In this context, the material class of diluted magnetic semiconductors (DMSs) [8–11], where impurity ions with large magnetic moments such as manganese are incorporated in a standard semiconductor lattice, displays rich physics in many different aspects. For example, such a material can act as a spin aligner for an electronic current in a light-emitting diode [12], excitonic transitions

in DMSs can be used for the purposes of spin-noise spectroscopy [13], and the material class is also promising for spintronics applications [14–17]. The doping with magnetic ions also introduces a carrier-impurity exchange scattering, which often plays the dominant role in the carrier spin dynamics [9].

In DMSs, the majority of studies regarding the ultrafast spin dynamics is conducted at very low temperatures [18–20], so phonon effects are often disregarded. However, when dealing with optical excitations above the band gap where carriers can show effective temperatures on the order of 10^4 K [21] or when considering hot excitons which are prepared by above band-gap excitation and subsequent femtosecond relaxation via the emission of LO phonons [1,22,23], phonon effects evidently become important. Since LO phonon relaxation typically occurs on much faster timescales than LA phonon relaxation, many theoretical works dealing with the spin dynamics in DMSs focus primarily on the former mechanism [24–27]. In contrast, in the case of resonantly excited excitons, LO phonon emission is strongly suppressed since excitons have nearly vanishing kinetic energies, thus making it impossible to emit an LO phonon which carries an energy of about 30 meV [27] since there are no states available with lower energies. Furthermore, at low enough temperatures below approximately 80 K, LO phonon absorption processes are also absent and LA phonons dominate [28].

In general, DMSs are known to exhibit pronounced many-body correlation effects [29–31] which, when treated beyond the usually employed Markov approximation, lead to a significant reduction of the exciton spin-transfer rate [6] as well as an unexpected trend reversal in their dependence on an external magnetic field [7]. However, these findings have been obtained only at nearly vanishing temperatures, completely

neglecting the phonon scattering. Apart from a derivation of the necessary equations in the exciton representation for quantum well systems, this paper provides the foundation to study the dynamics of excitons on a quantum kinetic level at elevated temperatures.

Here, we consider the subclass of II-VI DMS quantum well nanostructures where the impurity ions are isoelectronic, i.e., they do not lead to charge doping in the system. As a first application, we focus on DMSs without an external magnetic field and investigate the impact of finite temperatures on the exciton distribution as well as the temperature dependence of spin-transfer rates while varying parameters such as the impurity content. Since phonon emission processes are highly suppressed for the narrow optically generated exciton distributions, we also consider hot excitons where phonon emission especially is expected to be much more effective. In all cases, a particular focus is placed on the competition between the scattering of excitons at the localized impurities in DMSs compared with the phonon scattering. To gain insights into the importance and the signatures of non-Markovian effects, results of a standard Markovian treatment of the exciton-impurity scattering coinciding with Fermi's golden rule are presented together with the quantum kinetic approach, where correlations between excitons and impurities are explicitly taken into account.

We find a pronounced phonon influence on the time-resolved redistribution of the exciton momenta which can already be seen for optically generated excitons and is further enhanced for hot exciton distributions. Quantitatively, this influence most strikingly manifests in a pronounced increase of the kinetic energy per exciton when phonons are accounted for. However, despite the strong impact on the exciton occupation, the exciton spin dynamics shows little to no change with temperature, indicating a clear dominance of the magnetic exchange interaction. Our simulations also support the previously obtained finding that quantum kinetic effects in the spin dynamics are particularly pronounced for narrow carrier distributions close to sharp features in the density of states [32]. Here, this statement is corroborated by the observation that exciton spin-transfer rates for hot excitons are well described by a Markovian theory, which is in drastic contrast to resonantly excited excitons where the Markovian description strongly overestimates the decay. Nevertheless, quantum kinetic effects prevail in the time-resolved redistribution of exciton momenta for both excitation scenarios. It is also found that the hot excitons display significantly longer spin lifetimes than resonantly excited electron-hole pairs.

II. MODEL AND PHONON-INDUCED DYNAMICS

In this section, the Hamiltonian of our model is presented and discussed. Furthermore, we briefly discuss the derivation of quantum kinetic equations and explicitly extend them by phonon rate equations.

A. Hamiltonian

In electron-hole representation, the Hamiltonian for the description of the exciton spin dynamics in DMSs including the influence of phonons reads (cf. Ref. [6])

$$H_0 = \sum_{l\mathbf{k}} E_{\mathbf{k}}^l c_{l\mathbf{k}}^\dagger c_{l\mathbf{k}} + \sum_{v\mathbf{k}} E_{\mathbf{k}}^v d_{v\mathbf{k}}^\dagger d_{v\mathbf{k}}, \tag{1a}$$

$$H_{\mathrm{C}}^{\mathrm{eh}} = -\sum_{\mathbf{k}\mathbf{k}'\mathbf{q}} V_{\mathbf{q}} \sum_{lv} c_{l\mathbf{k}'+\mathbf{q}}^\dagger d_{v\mathbf{k}-\mathbf{q}}^\dagger d_{v\mathbf{k}} c_{l\mathbf{k}'}, \tag{1b}$$

$$H_{\mathrm{lm}} = -\sum_{lv\mathbf{k}} (\mathbf{E} \cdot \mathbf{M}_{lv} c_{l\mathbf{k}}^\dagger d_{v-\mathbf{k}}^\dagger + \mathbf{E} \cdot \mathbf{M}_{vl} d_{v-\mathbf{k}} c_{l\mathbf{k}}), \tag{1c}$$

$$H_{\mathrm{m}} = \frac{J_{sd}}{V} \sum_{\substack{Inn' \\ ll'\mathbf{k}\mathbf{k}'}} \mathbf{S}_{nn'} \cdot \mathbf{s}_{ll'}^{\mathrm{e}} c_{l\mathbf{k}}^\dagger c_{l'\mathbf{k}'} e^{i(\mathbf{k}'-\mathbf{k})\cdot\mathbf{R}_I} \hat{P}_{nn'}^I$$

$$+ \frac{J_{pd}}{V} \sum_{\substack{Inn' \\ vv'\mathbf{k}\mathbf{k}'}} \mathbf{S}_{nn'} \cdot \mathbf{s}_{vv'}^{\mathrm{h}} d_{v\mathbf{k}}^\dagger d_{v'\mathbf{k}'} e^{i(\mathbf{k}'-\mathbf{k})\cdot\mathbf{R}_I} \hat{P}_{nn'}^I, \tag{1d}$$

$$H_{\mathrm{nm}} = \frac{J_0^{\mathrm{e}}}{V} \sum_{\substack{Il \\ \mathbf{k}\mathbf{k}'}} c_{l\mathbf{k}}^\dagger c_{l\mathbf{k}'} e^{i(\mathbf{k}'-\mathbf{k})\cdot\mathbf{R}_I}$$

$$+ \frac{J_0^{\mathrm{h}}}{V} \sum_{\substack{Iv \\ \mathbf{k}\mathbf{k}'}} d_{v\mathbf{k}}^\dagger d_{v\mathbf{k}'} e^{i(\mathbf{k}'-\mathbf{k})\cdot\mathbf{R}_I}, \tag{1e}$$

$$H_{\mathrm{ph}} = \sum_{\mathbf{q}} \hbar\omega_{\mathbf{q}}^{\mathrm{ph}} b_{\mathbf{q}}^\dagger b_{\mathbf{q}}, \tag{1f}$$

$$H_{\mathrm{c-ph}} = \sum_{\mathbf{q}\mathbf{k}} \big(\gamma_{\mathbf{q}}^{\mathrm{e}} c_{\mathbf{k}+\mathbf{q}}^\dagger c_{\mathbf{k}} b_{\mathbf{q}} + \gamma_{\mathbf{q}}^{\mathrm{e}*} c_{\mathbf{k}}^\dagger c_{\mathbf{k}+\mathbf{q}} b_{\mathbf{q}}^\dagger$$

$$+ \gamma_{\mathbf{q}}^{\mathrm{h}} d_{\mathbf{k}+\mathbf{q}}^\dagger d_{\mathbf{k}} b_{\mathbf{q}} + \gamma_{\mathbf{q}}^{\mathrm{h}*} d_{\mathbf{k}}^\dagger d_{\mathbf{k}+\mathbf{q}} b_{\mathbf{q}}^\dagger\big). \tag{1g}$$

The first part H_0 contains the carrier kinetic energies where the operator $c_{l\mathbf{k}}^\dagger$ ($c_{l\mathbf{k}}$) creates (annihilates) an electron in the lth conduction band with wave vector $\mathbf{k}$, and $d_{v\mathbf{k}}^\dagger$ ($d_{v\mathbf{k}}$) is the analogous operator for holes in the vth valence band. The direct Coulomb interaction between electrons and holes is given by H_{C} with $V_q = \frac{e^2}{\epsilon_0 \epsilon q}$, where e is the elementary charge, ϵ_0 denotes the vacuum permittivity, and ϵ is the static dielectric constant. Note that the direct Coulomb interaction is actually comprised of three terms, namely the electron-electron, hole-hole, and electron-hole interaction. However, since it turns out that only the latter yields a finite contribution in the equations of motion up to third order in the driving field [33], we only write down the relevant electron-hole scattering here. The light-matter coupling is given by H_{lm}, where $\mathbf{E}$ denotes the electric field and $\mathbf{M}_{lv}$ is the transition dipole.

In DMSs, the dominant contribution to the spin dynamics is typically given by the magnetic s-d and p-d exchange interactions [9] for conduction band electrons and valence band holes, respectively, which are subsumed in H_{m}. There, J_{sd} and J_{pd} are the respective coupling constants and V is the volume of the semiconductor. The indices of the coupling constants refer to the interaction of s-like conduction-band electrons or p-like holes in the valence band with the bound electrons in the d shell of the magnetic impurities, respectively. The vector of electron (hole) spin matrices is given by $\mathbf{s}_{ll'}^{\mathrm{e}} = \boldsymbol{\sigma}_{ll'}$ ($\mathbf{s}_{vv'}^{\mathrm{h}} = \mathbf{J}_{vv'}$) with the vector of Pauli matrices $\boldsymbol{\sigma}_{ll'}$ and the vector of angular momentum matrices $\mathbf{J}_{vv'}$, where

$v, v' \in \{-3/2, -1/2, 1/2, 3/2\}$. Pauli matrices are used since they provide a convenient basis for the space spanned by the spin-up and spin-down states for the conduction band. Concerning the valence band, the angular momentum matrices are such that the quantum numbers $-3/2$ and $3/2$ correspond to the heavy-hole (hh) states, whereas the quantum numbers $-1/2$ and $1/2$ refer to the light-hole (lh) states. In typical semiconductor quantum wells, confinement and strain causes the hole states to split such that the lower-energy states are comprised of heavy holes [34]. The impurity spin is decomposed into the vector of spin matrices $\mathbf{S}_{nn'}$ with $n, n' \in \{-5/2, -3/2, \ldots, 5/2\}$ and the operator $\hat{P}_{nn'}^{I} = |I, n\rangle\langle I, n'|$, where $|I, n\rangle$ is the nth spin state of the Ith impurity atom and $\mathbf{R}_I$ refers to its position in the lattice. Using this representation allows us to straightforwardly discriminate between impurity operators evaluated at the same site and at different sites, which turns out to be crucial to obtain the correct scaling behavior of the carrier-impurity spin exchange [35]. Due to the local band-gap mismatch that is created upon doping, there also arises a nonmagnetic carrier-impurity interaction H_{nm}, which we model as a contactlike interaction similar to H_{m} with coupling constants J_0^{e} and J_0^{h} but without involving spin flips [36]. Note that the magnetic and nonmagnetic scattering contributions to the Hamiltonian given by Eqs. (1d) and (1e) do not conserve the carrier momentum, as should be the case for DMSs with few randomly oriented impurities.

To investigate the temperature dependence of the exciton spin relaxation, the model developed in Ref. [6] is extended to account for carrier-phonon scattering. The phonons are described by H_{ph} with creation (annihilation) operators $b_q^{\dagger}$ (b_q) for phonons with energy $\hbar\omega_{\mathbf{q}}^{\mathrm{ph}}$, where $\mathbf{q}$ contains the phonon momentum as well as the branch number. The interaction with electrons (holes) is modeled by $H_{\mathrm{c-ph}}$ with the coupling constant $\gamma_{\mathbf{q}}^{\mathrm{e}}$ ($\gamma_{\mathbf{q}}^{\mathrm{h}}$). We use bulk phonon modes due to the relatively small change of the lattice constant with impurity content for the small doping fractions typically found in DMSs [10] and limit the description to LA phonons, which have been found to dominate exciton line widths in semiconductors below 80 K [28]. Furthermore, when focusing on excitations below the band gap near the exciton ground state, the polar piezoelectric scattering is reduced since excitons are neutral quasiparticles and deformation potential coupling dominates [3]. The corresponding coupling constants thus read

$$\gamma_{\mathbf{q},q_z}^{\mathrm{e,h}} = \sqrt{\frac{q\hbar}{2\rho V v}} D_{\mathrm{e,h}} \tag{2}$$

for a semiconductor with density ρ, longitudinal sound velocity v, and deformation potential constants $D_{\mathrm{e,h}}$ for the

conduction and the valence band, respectively. Since we only consider excitons with small or even nearly vanishing center-of-mass momenta, a linear phonon dispersion $\omega_{\mathbf{q}}^{\mathrm{ph}} = vq$ is assumed.

B. Phonon rate equations

Quantum kinetic equations for the exciton spin dynamics based on the Hamiltonian given by Eqs. (1a)–(1e) have been derived in Ref. [6] in second order in the laser field within the dynamics-controlled truncation scheme [33]. Correlations between excitons and impurities are kept as explicit dynamical variables by applying a correlation expansion and the final equations are formulated in the exciton basis, which is convenient to model excitations below the band gap. Within this framework, the exciton variables directly related to observables such as the optical polarization or the exciton density are those not involving impurity or phonon operators. They are given by [6,7]

$$Y_{x_1 \mathbf{0}}^{\sigma_1} = \langle \hat{Y}_{\sigma-\frac{3}{2}x_1\mathbf{0}} \rangle, \tag{3a}$$

$$N_{x_1 \mathbf{K}_1}^{\sigma_1 \sigma_2} = \langle \hat{Y}_{\sigma_1-\frac{3}{2}x_1\mathbf{K}_1}^{\dagger} \hat{Y}_{\sigma_2-\frac{3}{2}x_1\mathbf{K}_1} \rangle, \tag{3b}$$

where $\hat{Y}_{\sigma-\frac{3}{2}x\mathbf{K}}^{\dagger}$ ($\hat{Y}_{\sigma-\frac{3}{2}x\mathbf{K}}$) denotes the creation (annihilation) operator for an exciton with quantum number x and two-dimensional center-of-mass wave vector $\mathbf{K}$. The spin state of the electron is given by σ and the angular momentum quantum number for the holes is $-3/2$, reflecting an optical excitation with σ^- polarization. We focus on semiconductors with a sufficiently large hh-lh splitting such that only the electron-spin part of the exciton needs to be considered. Neglecting the long-range electron-hole exchange because of its much smaller interaction energy compared with the magnetic scattering [7], one obtains a pinned hh spin state due to the energetic penalty of an intermediate occupation of a lh state involved in a hh spin flip [37–40]. All remaining impurity-assisted variables are discussed in Appendix A and may be found in Ref. [6].

Note that, apart from the bright excitons with vanishing center-of-mass momenta and electrons in the spin-up state, our theory also accounts for optically dark excitons: First, we refer to excitons with wave numbers $K > 0$ as dark excitons since they do not directly couple to light and can therefore not recombine to emit a photon. Thus, momentum scattering from $K \approx 0$ to $K > 0$ can convert bright excitons to dark excitons. Second, excitons that consist of an electron with spin down are optically dark even at $K = 0$ since their recombination is spin forbidden (as the hh angular momentum quantum number is fixed to $-3/2$).

Neglecting cross terms between phonon- and impurity-assisted variables, the phonon-induced contributions in the Markov approximation to the equations of motion can be written as

$$\frac{\partial}{\partial t}\bigg|_{\mathrm{ph}} Y_{x_1\mathbf{0}}^{\sigma_1} = -\sum_{\mathbf{K}} \Lambda_{x_1x_1}^{\mathbf{0K}} \Theta\big(\omega_{x_1\mathbf{K}} - \omega_{\mathbf{K}}^{\mathrm{ph}}\big) Y_{x_1\mathbf{0}}^{\sigma_1} n^{\mathrm{ph}}(\omega_{x_1\mathbf{K}}) = -\Gamma_{\mathrm{ph}} Y_{x_1\mathbf{0}}^{\sigma_1}, \tag{4a}$$

$$\frac{\partial}{\partial t}\bigg|_{\mathrm{ph}} N_{x_1\mathbf{K}_1}^{\sigma_1\sigma_2} = \sum_{x\mathbf{K}} \Lambda_{x_1x}^{\mathbf{K}_1\mathbf{K}} \big[\Theta\big(\omega_{x\mathbf{K}} - \omega_{x_1\mathbf{K}_1} - \omega_{\mathbf{K}-\mathbf{K}_1}^{\mathrm{ph}}\big)\big(N_{x\mathbf{K}}^{\sigma_1\sigma_2}\big(1 + n^{\mathrm{ph}}(\omega_{x\mathbf{K}} - \omega_{x_1\mathbf{K}_1})\big) - N_{x_1\mathbf{K}_1}^{\sigma_1\sigma_2} n^{\mathrm{ph}}(\omega_{x\mathbf{K}} - \omega_{x_1\mathbf{K}_1})\big)$$

$$+ \Theta\big(\omega_{x_1\mathbf{K}_1} - \omega_{x\mathbf{K}} - \omega_{\mathbf{K}_1-\mathbf{K}}^{\mathrm{ph}}\big)\big(N_{x\mathbf{K}}^{\sigma_1\sigma_2} n^{\mathrm{ph}}(\omega_{x_1\mathbf{K}_1} - \omega_{x\mathbf{K}}) - N_{x_1\mathbf{K}_1}^{\sigma_1\sigma_2}\big(1 + n^{\mathrm{ph}}(\omega_{x_1\mathbf{K}_1} - \omega_{x\mathbf{K}})\big)\big)\big]. \tag{4b}$$

Since the exciton coherences $Y_{x_1 \mathbf{0}}^{\sigma_1}$ are only driven at $\mathbf{K} = \mathbf{0}$, the sum in Eq. (4a) only needs to be performed once and yields an effective decay rate Γ_{ph} which no longer depends on $\mathbf{K}$. The terms in Eq. (4b) can be classified in terms of phonon emission and absorption processes depending on whether they are proportional to $1 + n^{ph}(\Delta\omega)$ or $n^{ph}(\Delta\omega)$, respectively, where n^{ph} denotes the thermal phonon occupation given by $1/(\exp(\hbar\Delta\omega/k_B T) - 1)$. Energy conservation is ensured by the Heaviside step function $\Theta(\Delta\omega)$ and $\omega_{x\mathbf{K}} = E_x + \hbar^2 K^2/2M$ with the exciton mass M is the exciton kinetic energy measured with respect to the exciton ground state, i.e., where the notation is such that $E_{1s} = 0$ and $E_x > 0$ for $x \neq 1s$. The confinement of the excitons to the quantum well plane is taken into account by projecting the coupling to the LA phonons down to the energetically lowest well states. Finally, the phonon matrix elements can be written as

$$\Lambda_{x_1 x_2}^{\mathbf{K}_1 \mathbf{K}_2} = \frac{P_{x_1 x_2}^{\mathbf{K}_1 \mathbf{K}_2} (\omega_{x_1 \mathbf{K}_1} - \omega_{x_2 \mathbf{K}_2})^2}{\sqrt{(\omega_{x_1 \mathbf{K}_1} - \omega_{x_2 \mathbf{K}_2})^2 - v^2 (\mathbf{K}_1 - \mathbf{K}_2)^2}}$$
$$\times \left| f\left(\frac{1}{v} \sqrt{(\omega_{x_1 \mathbf{K}_1} - \omega_{x_2 \mathbf{K}_2})^2 - v^2(\mathbf{K}_1 - \mathbf{K}_2)^2} \right) \right|^2 \quad (5)$$

with

$$P_{x_1 x_2}^{\mathbf{K}_1 \mathbf{K}_2} = \frac{2\pi}{\hbar \rho v^3 V} \left(D_e^2 F_{\eta_h x_1 x_2}^{\eta_h \mathbf{K}_1 \mathbf{K}_2} + D_h^2 F_{\eta_e x_1 x_2}^{\eta_e \mathbf{K}_1 \mathbf{K}_2} \right.$$
$$\left. + 2 D_e D_h F_{-\eta_h x_1 x_2}^{\eta_e \mathbf{K}_1 \mathbf{K}_2} \right). \quad (6)$$

Here, infinitely high quantum well barriers are assumed so the phonon form factor becomes

$$f(q_z) = \frac{\sin\left(\frac{qd}{2}\right)}{\frac{qd}{2}} \left[1 - \left(\frac{qd}{2\pi}\right)^2 \right]^{-1}. \quad (7)$$

An explicit expression for the exciton form factors $F_{\eta_1 x_1 x_2}^{\eta_2 \mathbf{K}_1 \mathbf{K}_2}$ can be found together with the full quantum kinetic equations of motion for the exciton ground state in Appendix A. Regarding the scattering with the magnetic ions we focus on the low carrier-density regime compared with the density of impurities, which allows us to describe the impurity spin density matrix by its thermal equilibrium value using the phonon temperature throughout the dynamics [41].

It should be noted that it is important to first transform the equations of motion due to the carrier-phonon coupling into the exciton basis before the Markov approximation is applied. This is because, in the Markov approximation, one actively selects the final states which are occupied in the long-time limit since the corresponding energies directly end up in the energy-conserving delta functions (cf. Appendix in Ref. [3]). Thus, when below band-gap excitations are considered so excitons rather than quasifree carriers are excited, a transformation to the exciton basis before introducing the Markov approximation ensures that the correct correlated pair energies appear in Eqs. (4).

Finally, to identify quantum kinetic signatures in the exciton dynamics, we also discuss the Markov limit of the exciton-impurity scattering [6]. In this approximation, all quantum kinetic effects are removed and only Markovian scattering processes without any memory remain. The corresponding equations can be found in Appendix B.

III. RESONANT EXCITATION

In the following, the phonon impact on the exciton dynamics is investigated numerically for $Zn_{1-x}Mn_x Se$ quantum wells. Special emphasis is put on a comparison of results where all scattering mechanisms are treated as Markovian processes without memory and calculations where the Markov approximation is only employed for the phonon scattering, but the exciton-impurity exchange interaction is accounted for on a quantum kinetic level so that many-body effects beyond a Markovian theory are captured. Although quantum kinetic effects have also been studied for the carrier-phonon interaction in semiconductor nanostructures, most studies have been performed for LO phonons and the resulting carrier dynamics is typically found to be close to the results of a rate-equation approach [24–26]. An indicator for the importance of quantum kinetic effects is the amount of correlation energy in the system, which is negligible for LA phonons compared with the exciton-impurity correlation energy [31]. Furthermore, while a treatment beyond the Markov limit is required to capture an energetic redistribution of excitons due to the exchange interaction, the scattering with phonons involves such a redistribution already on the Markov level. All in all, it follows that a quantum kinetic treatment is more important for the exciton-impurity interaction than for the exciton-phonon scattering, so a purely Markovian description of the latter can be expected to suffice.

A. Occupation of the exciton parabola

To find out to what extent phonons can be expected to impact the dynamics of excitons, we perform simulations for a 15-nm-wide $Zn_{1-x}Mn_x Se$ quantum well under resonant optical excitation of the 1s-hh exciton. Except for studies where the doping concentration is varied explicitly, we focus on samples with $x = 2.5\%$. To minimize the impact of the laser, the pulse length is chosen to be 100 fs and is thus short compared with typical timescales of the dynamics [6,7,19,35,42–44]. The remaining relevant parameters used for the numerical simulations are collected in Table I.

It is well-known that the redistribution of exciton kinetic energies due to phonon scattering leaves a fingerprint in

TABLE I. Selected material parameters of $Zn_{1-x}Mn_x Se$. The cubic lattice constant is denoted by a and m_0 is the free electron mass.

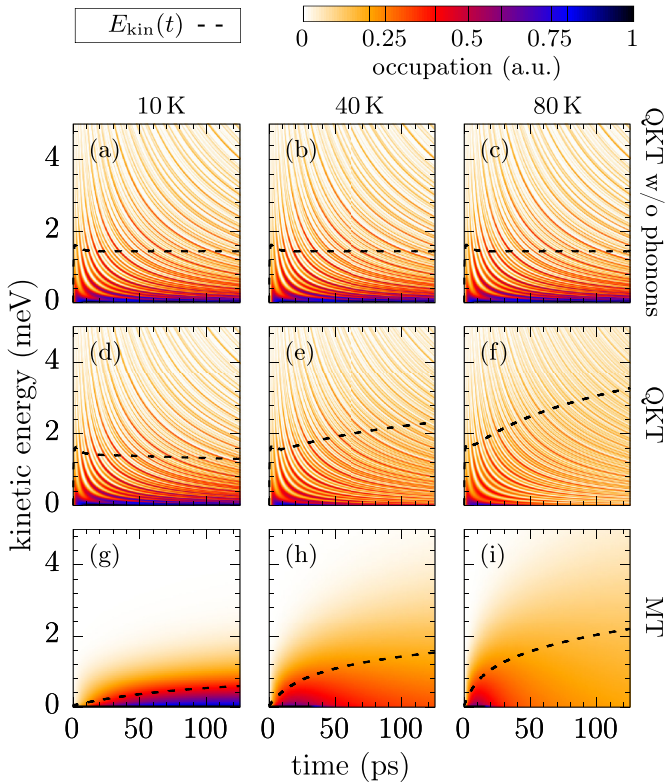| parameter	value for $Zn_{1-x}Mn_x Se$
a (nm)[10]	0.567
m_e/m_0[45,46]	0.15
m_{hh}/m_0[45,46]	0.8
J_{sd} (meV nm^3)[10]	−12
J_{pd} (meV nm^3)[10]	50
J_0^e (meV nm^3)[6]	22
J_0^h (meV nm^3)[6]	0
ϵ[47]	9
D_e (eV)[48]	−7.4
D_h (eV)[48]	−0.7
ρ (g cm^{-3})[49]	5.28
v (km s^{-1})[49]	4.21

FIG. 1. Time- and energy-resolved occupation of the $1s$ exciton parabola obtained by the quantum kinetic theory (QKT) without accounting for phonons [(a)–(c)], the quantum kinetic theory including LA phonon scattering [(d)–(f)], and the Markovian theory applied to all scattering processes [MT, (g)–(i)]. Apart from the occupation, we also show the time evolution of the kinetic energy per exciton E_{kin} for each case (dashed line). Results are shown for three different temperatures T as indicated in the figure.

time-resolved studies of the occupation on the $1s$ exciton parabola, which is also accessible in experiments [1,2,5]. To investigate this impact, Fig. 1 shows the time- and energy-resolved occupation of the exciton ground state obtained by the quantum kinetic calculation with and without phonons as well as its Markov limit.

Using the Markov approximation strictly enforces energy conservation where, however, interaction energies are completely disregarded. This implies that the exciton-impurity scattering in the Markov approximation is unable to change the kinetic energy of excitons since it is a completely elastic process. This can be directly seen in Eq. (B1), where the frequency of an exciton remains unchanged during the spin-flip process. Thus, any finite occupation of exciton kinetic energies in the Markovian theory seen in the bottom row of Fig. 1 is purely due to phonons. The phonon influence increases with increasing temperature because phonon emission is prohibited for optically generated excitons so that phonon absorption processes are required to affect the exciton occupation. Figure 1 also reveals that not only are higher kinetic energies reached at elevated temperatures, the scattering also becomes noticeably faster. While for 10 K only states below 2 meV are occupied after more than 100 ps, at 80 K exciton kinetic energies exceed 4 meV after approximately 50 ps.

Previous works have shown that, when treating the exciton-impurity scattering on a quantum kinetic level, one obtains a significant redistribution of exciton kinetic energies which is accompanied by a buildup of a many-body correlation energy [6,7,31,50]. In the top row of Fig. 1, where the interaction with phonons is completely switched off so only the exchange interaction remains, this manifests in an occupation of exciton states with high kinetic energies up to 4 meV and above. Note that the higher-energy states are not uniformly occupied; rather, a typical pattern appears which is caused by the memory kernel due to the exciton-impurity interaction. Since this memory kernel is proportional to $\frac{\sin(\omega t)}{\omega}$, it is large for short times and small energies and shows a damped oscillation for larger times [6]. This is a manifestation of the energy-time uncertainty which allows the violation of strict single-particle energy conservation rules on short timescales. Here, this effect is combined with a relaxation of the system to a new energy eigenstate that forms as a result of the interaction between excitons and impurities when correlations between them are accounted for. This is why elevated exciton kinetic energies remain occupied even in the long-time limit.

Comparing the top row in Fig. 1 with the bottom row, it becomes clear that the quantum kinetic redistribution is much stronger as well as faster than the phonon-induced scattering, which can be seen from the fact that after only a few picoseconds energies up to 4 meV and above are occupied even at a low temperature of 10 K. However, when comparing the quantum kinetic calculations for different temperatures, one can still clearly see the phonon influence by looking at excitons at very low energies. There, the occupation visibly decreases with time just like in the Markovian case, suggesting that phonons cause a smoothing out of the overall exciton occupation, which is still peaked near $E = 0$ in the quantum kinetic case at 10 K. All in all, phonons thus cause a more efficient coupling of excitons with vanishing center-of-mass motion toward the optically dark states away from $K = 0$, especially at elevated temperatures.

The phonon influence on the exciton occupation can also be studied on a more quantitative level by looking at the kinetic energy per exciton, which is indicated in Fig. 1 by a dashed line. As mentioned before, when the scattering of excitons with impurities is described on the Markovian level, there is no way for excitons to change their kinetic energy after the optical pulse except via the emission or absorption of phonons. Thus, the increase of the kinetic energy per exciton observed in Figs. 1(g)–1(i) is exclusively due to phonon scattering and consistently increases with rising temperature. To be specific, phonon absorption processes cause the excitons to reach energies in excess of 2 meV on the order of 100 ps at 80 K. The kinetic energy per exciton also directly reflects the many-body correlation energy per exciton that is built up after the optical excitation due to the non-Markovian nature of the exciton-impurity exchange interaction [6]. From Figs. 1(a)–1(c), a kinetic energy per exciton of about 1.5 meV can be determined for the parameters considered here, which is significantly larger than the phonon contribution for low temperatures and only becomes smaller than the phonon-induced kinetic energy at temperatures exceeding a few 10 K. As discussed previously in terms of the redistribution of excitons toward the optically dark states, the phonon impact
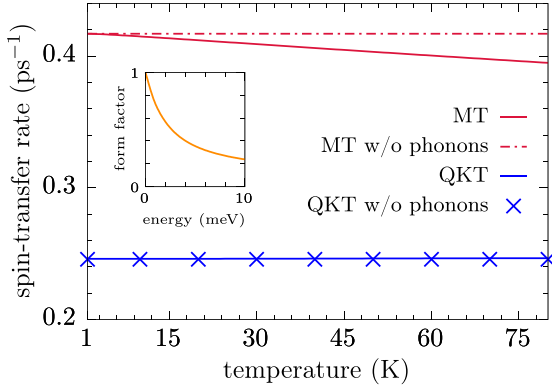
FIG. 2. Exciton spin-transfer rate as a function of temperature obtained by the Markovian theory (MT) and the quantum kinetic theory (QKT) after resonant excitation of the $1s$ exciton. We compare simulations with and without (w/o) phonons. The inset depicts the diagonal of the exciton form factor $F_{\eta_\text{h}1s1s}^{\eta_\text{h}\omega\omega}$ appearing in Fermi's golden rule as a function of energy $E = \hbar\omega$.

is also clearly visible in the increase of the kinetic energy per exciton in Figs. 1(d)–1(f). At a temperature of 80 K, the combined influence of the many-body correlations and the phonon scattering even cause energies in excess of 3 meV.

B. Exciton spin-transfer rates

Although phonons do not introduce spin-flip transitions, at least not without some type of spin-orbit coupling, they do cause a significant change in the kinetic energy of excitons by either phonon absorption or emission processes. Thus, it is an interesting question to ask whether these processes also affect the spin dynamics of excitons in DMSs, for which the magnetic exchange interaction is commonly regarded as the most important process [9]. As a measure for the spin dynamics, Fig. 2 shows the spin-transfer rate for the exciton-bound electron as a function of temperature. Since the spin dynamics is nonexponential in general [6,7], the rate is extracted as the inverse time that it takes the spin to decay to $\frac{1}{e}$ of its maximum value after the optical pulse.

Focusing first on the results when the exciton-impurity scattering is treated as a Markovian process, we find that phonons cause a slowdown of the spin-transfer rate, which becomes more significant with rising temperature. Whereas the phonon influence is completely negligible for temperatures below 4 K, at a temperature of 80 K phonons cause a change in the rate of approximately 5%. This behavior is directly connected to the redistribution of exciton momenta caused by the interaction with LA phonons. Remembering that we are considering optically created excitons with quasivanishing wave vector, it is clear that phonons have almost no impact on the spin dynamics for very low temperatures since, in this case, phonon absorption processes are highly suppressed. Such processes are, however, required to change the exciton kinetic energy, as phonon emission is prohibited for optically created excitons because there are no states available with lower energies to scatter to. As the temperature increases, phonon absorption processes become increasingly probable. Since the exciton-phonon interaction is spin conserving and

phonon emission is suppressed, the scattering of an exciton by a phonon thus increases its kinetic energy on average.

The observed slowdown of the spin-transfer rate with increasing temperature in Fig. 2 for the Markov approximation is directly related to the previously introduced exciton form factor $F_{\eta_\text{h}1s1s}^{\eta_\text{h}K_1K_2}$, whose diagonal is one for $K = 0$ and quickly decreases for larger center-of-mass momenta, i.e., larger kinetic energies [6,39]. Since the exciton form factor enters the rate obtained in Fermi's golden rule [cf. also Eq. (B1)] which, for an exciton with kinetic energy $\hbar\omega$, is given by [6]

$$\tau_\omega^{-1} = \frac{35}{12} \frac{N_\text{Mn} I J_{sd}^2 M}{\hbar^3 dV} F_{\eta_\text{h}1s1s}^{\eta_\text{h}\omega\omega}, \tag{8}$$

the rate becomes smaller when the form factor is evaluated at larger energies. In the above notation, the center-of-mass momentum of an exciton is connected with its frequency via the usual relation $\omega = \frac{\hbar K^2}{2M}$. The decrease of the diagonal elements of the exciton form factor are shown in the inset in Fig. 2. Thus, the increasing influence of phonons on the Markovian spin-transfer rate with rising temperature follows from the increase of the kinetic energy per exciton observed in Figs. 1(g)–1(i). On the other hand, when the quantum kinetic theory is used to calculate the rates, the phonon influence is more or less absent since there is already a significant kinetic energy per exciton even without phonons [cf. Figs. 1(a)–1(c)].

Turning to the quantum kinetic results in Fig. 2, one first notices a generally lower spin-transfer rate compared with the Markovian results, an effect which is due to the abrupt disappearance of the density of states at the onset of the exciton parabola, which effectively cuts off the memory kernel appearing in the quantum kinetic treatment of the exciton-impurity interaction [6,7]. Concerning the phonon influence, however, the spin-transfer rate is entirely dominated by the exchange interaction and remains constant over the whole temperature range considered here. Surprisingly, even though phonons increase the redistribution of excitons toward optically dark states, their effect on the spin dynamics is marginal. It should be noted here that this behavior is expected to change drastically when optical phonon scattering becomes important, which is either at higher temperatures or when looking at hot excitons with kinetic energies above the LO phonon threshold [1,3,22,23,51].

The observation that the exchange scattering dominates over the phonon scattering remains valid also for lower doping fractions, as can be seen in Fig. 3 where the spin-transfer rate in the Markov approximation and using the quantum kinetic theory is depicted as a function of the impurity concentration for two different temperatures. Again, when the exciton-impurity scattering is treated as a Markovian process, a slight phonon influence is visible when going from 2 K to 20 K. In contrast, the quantum kinetic result remains virtually unaffected by the increase in temperature.

IV. HOT EXCITONS

Having discussed the phonon impact on resonantly excited excitons, we now turn to an initially nonequilibrium exciton distribution, also referred to as *hot excitons*, that can be generated, e.g., by optical excitation above the band gap and subsequent formation of excitons on the $1s$ parabola via fast
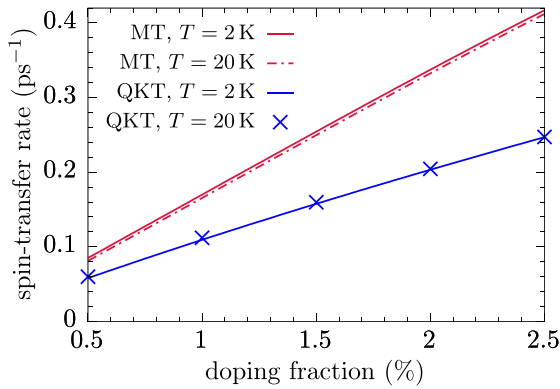
FIG. 3. Exciton spin-transfer rate as a function of Mn doping fraction obtained by the Markovian theory (MT) and the quantum kinetic theory (QKT) after resonant excitation of the $1s$ exciton. The simulations are performed for two different temperatures T.

LO phonon emission [1]. Apart from the resulting exciton spin-transfer rates, the dynamics of the exciton distribution is also investigated.

A. Time evolution of the exciton distribution

Since for the case of resonant optical excitation the phonon impact is most clearly visible in the time evolution of the exciton distribution, it is interesting to ask the question whether this is also true for hot excitons. As in the previous section, we focus on a 15-nm-wide $Zn_{1-x}Mn_xSe$ DMS quantum well at varying temperatures and consider a Mn content of $x = 2.5\%$ if the doping concentration is not varied explicitly. However, instead of modeling a resonant optical excitation of the $1s$ exciton, we instead consider an initially hot exciton distribution far away from $K = 0$ as created, e.g., by LO phonon emission after above band-gap excitation [1,22,23]. For the numerical simulations, we assume a Gaussian distribution on the $1s$ exciton parabola centered at an energy of 10 meV with a standard deviation of 1 meV, which translates to a distribution with a FWHM of roughly 2.5 meV similar to what has been observed in experiments [1]. The remaining parameters are the same as in Table I.

Figure 4 displays several snapshots of the exciton distribution for two different temperatures as calculated by either the quantum kinetic or the Markovian theory. Focusing first on the Markovian results in Figs. 4(c) and 4(d), the phonon influence clearly causes a broadening of the exciton distribution which becomes stronger at elevated temperatures. The asymmetry between phonon absorption and emission processes also affects the distributions since, for $T = 4$ K, only a broadening toward the low-energy side is observed while for 80 K there is also a significant broadening on the high-energy side. This is because, while phonon emission processes already occur even at very low temperatures, phonon absorption processes are proportional to the number of thermally excited phonons and therefore only become important at higher temperatures.

Turning to the quantum kinetic results in Figs. 4(a) and 4(b), it becomes clear that the redistribution is greatly enhanced due to the correlation energy already at very low temperatures, similar to what has been observed for resonantly ex-
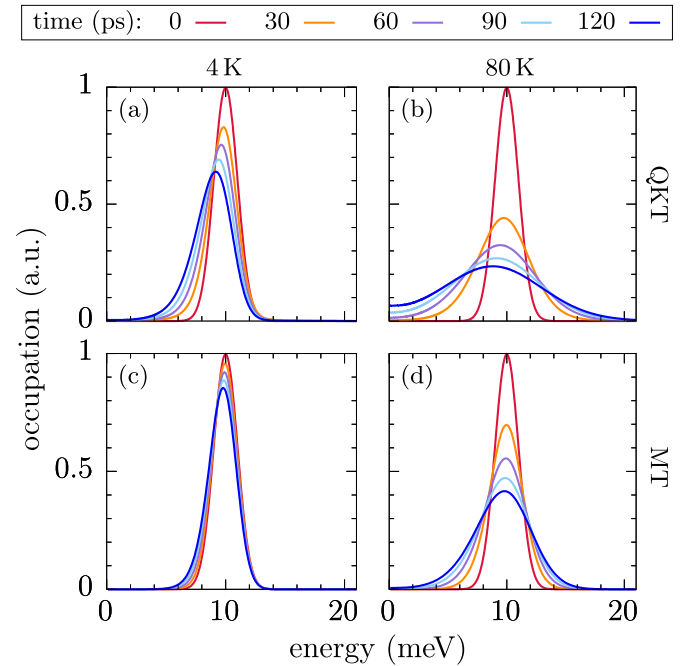
FIG. 4. Snapshots of the dynamics of the $1s$ exciton distribution of hot excitons. The simulations show results using (a) the quantum kinetic theory (QKT) with phonons at 4 K and (b) at 80 K as well as results obtained by the Markovian theory (MT) with phonons at 4 K and (d) at 80 K, respectively.

cited excitons. Furthermore, a slight shift of the maximum of the exciton distribution toward lower energies is found, which is almost completely absent in the Markovian simulations. Figure 4(b) also shows a sizable exciton occupation of bright states near $E = 0$ already before 100 ps in contrast to the simulation for low temperatures in Fig. 4(a). Comparing the two figures in question with the respective Markovian results, it becomes clear that a purely Markovian theory significantly underestimates the population of bright exciton states.

B. Exciton spin-transfer rates

Looking at the spin-transfer rate of hot excitons as a function of temperature depicted in Fig. 5, the most striking feature is that the spin relaxation is slowed down by an order of magnitude compared with the case of resonant optical excitation (cf. Fig. 2). As discussed already in Sec. IV B, this slowdown is directly related to the decrease of the exciton form factor for larger energies. Even though the hot exciton distribution is quite broad and thus covers a range of kinetic energies, the reduction of the form factor fits very well to the observed reduction of the rate. For the Markovian calculation without phonons, the rate after resonant optical excitation is approximately $\tau_{res}^{-1} \approx 0.417$ ps^{-1} whereas for hot excitons it is given by $\tau_{hot}^{-1} \approx 0.083$ ps^{-1}, which yields a ratio of about 0.2. For the parameters considered here, the exciton form factor is also reduced to approximately 0.2 when evaluated at an energy of 10 meV, thus quantitatively explaining the drastic reduction of the spin-transfer rate. Since shorter decay rates translate to longer spin lifetimes, this effect can potentially be
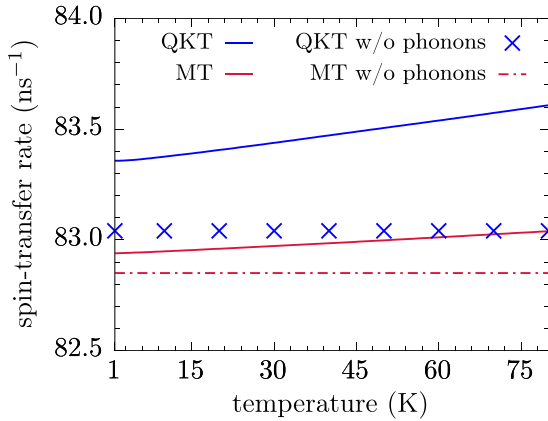
FIG. 5. Exciton spin-transfer rate as a function of temperature obtained by the Markovian theory (MT) and the quantum kinetic theory (QKT) assuming an initially hot exciton distribution. We compare simulations with and without (w/o) phonons.
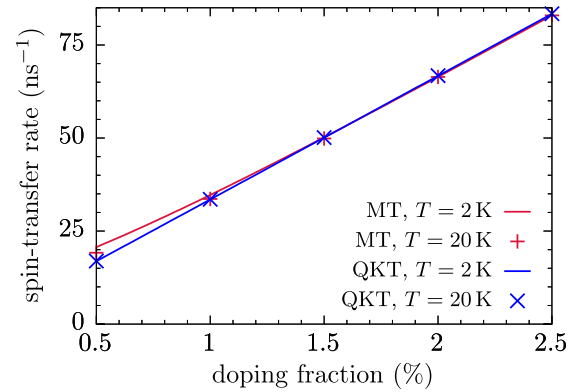

FIG. 6. Exciton spin-transfer rate as a function of Mn doping fraction obtained by the Markovian theory (MT) and the quantum kinetic theory (QKT), assuming an initially hot exciton distribution. The simulations are performed for two different temperatures T.

utilized to protect any information encoded in the exciton spin degree of freedom.

Apart from this striking quantitative difference with respect to the case of resonant optical excitation, the results from the quantum kinetic theory are much closer to those obtained by the Markovian theory for hot excitons. Note the change in units from picoseconds in Fig. 2 to nanoseconds in Fig. 5. This points to a drastic reduction of quantum kinetic effects on the spin dynamics for hot excitons, a finding which is expected since previous works have shown quantum kinetic effects to be particularly strong near sharp features in the density of states [6,32]. The broad distribution of the hot excitons, which is a few meV away from the center of the exciton parabola where the constant density of states is abruptly cut off, thus largely inhibits pronounced non-Markovian features in the spin dynamics so a Markovian approach yields very similar decay rates.

Turning finally to the phonon influence on the spin dynamics, Fig. 5 reveals a similar behavior as already found for resonant excitation in Fig. 2, namely that phonons only marginally influence the spin dynamics overall. Thus, even though the impact of phonons on the dynamics of the exciton occupation is even stronger for hot excitons, the spin dynamics is once more dominated by the exchange interaction. However, compared with Fig. 2, here phonons are found to slightly increase the spin-transfer rate in the quantum kinetic as well as the Markovian simulation. In addition, instead of a slowdown of the rate, even without phonons the quantum kinetic theory predicts a slightly larger spin-transfer rate compared with the Markovian results in the case of hot excitons. It can be argued that these two observations rely on a similar mechanism which, however, stems from completely different physical processes. Including phonons in the model evidently allows for a scattering of excitons toward lower energies which becomes stronger with higher temperatures. The resulting decrease of the kinetic energy of the scattered part of the exciton distribution then causes the spin-transfer rate to be evaluated at lower energies, where the exciton form factor is larger, which causes an increased spin-transfer rate. Since the quantum kinetic theory also predicts a

strong redistribution of carrier momenta due to the correlation energy (cf. Fig. 1), the quantum kinetic rate is expected to increase for the same reason. The strong phonon impact on the exciton distribution found for the quantum kinetic simulations in Fig. 4 directly translates to the more pronounced phonon impact in the quantum kinetic simulations in Fig. 5.

Regarding the dependence of the spin-transfer rate on the doping fraction as plotted in Fig. 6, we find only a small quantitative difference between the quantum kinetic and the Markovian theory for small doping fractions, which becomes smaller with increasing impurity content. Similar to the case of resonant excitation, the phonon influence is again almost completely negligible for hot excitons on the scale of the figure. However, comparing Fig. 6 to the the case of resonant optical excitation in Fig. 3 and noting the change in units, we find much slower rates in accordance with the exciton form factor.

V. CONCLUSION

We have investigated the phonon impact on the exciton dynamics in DMSs. To this end, we have extended a quantum kinetic description of the exciton spin dynamics in DMS quantum wells by accounting for the scattering with LA phonons on the Markov level. The derived equations open up the possibility to also study dynamical processes at elevated temperatures below the LO phonon threshold. Numerical calculations without an external magnetic field show a pronounced impact of LA phonons on the distribution of resonantly excited excitons on the $1s$ parabola, revealing that they introduce a significant occupation of states with higher kinetic energies in addition to the redistribution caused by quantum many-body effects due to the scattering of excitons with the localized impurities in DMSs. In contrast to the inelastic phonon scattering, which always induces transitions to states with different energies, the exciton-impurity exchange interaction is an elastic process and is therefore single-particle energy conserving when it is treated as a Markovian process. Although a phonon impact on the time- and energy-resolved exciton distribution can also be seen using the quantum kinetic theory, it is found that the quantum kinetic redistribution

enabled by a many-body correlation energy is the dominant process.

Considering a broad initial distribution of hot excitons as, e.g., generated by above band-gap excitation and subsequent LO phonon emission, reveals a more prominent role of LA phonon emission since states with lower energy become available. For these situations, the quantum kinetic redistribution is found to be greatly assisted by the phonon scattering, which leads to an increased broadening, especially on the low-energy side. Together, both scattering mechanisms provide an efficient pathway for the conversion of optically dark excitons to bright states.

Despite the clear influence of phonons on the exciton occupation, the phonon influence on exciton spin-transfer rates for the case of resonantly excited excitons is found to be completely negligible over a wide range of temperatures and doping fractions when the exchange interaction between excitons and impurities is treated on a quantum kinetic level. If the exchange interaction is treated as a purely Markovian process without any memory, LA phonons do, in fact, increasingly inhibit the spin transfer at elevated temperatures since they only cause spin conserving scattering and therefore provide a competition to spin-flip interactions.

Compared to a resonant excitation scheme, hot excitons show a significantly longer spin lifetime, making them promising for the protection of information stored in the spin degree of freedom. This long spin lifetime is related to the decrease of the exciton form factor with increasing exciton kinetic energy, thus causing significantly smaller spin-transfer rates. For these situations, quantum kinetic effects are strongly reduced so that a Markovian treatment of the spin transfer can be justified. Finally, phonons cause an increase of the spin-transfer rate for hot excitons in both considered theoretical models, albeit on a rather small scale.

APPENDIX A: QUANTUM KINETIC EQUATIONS OF MOTION FOR THE EXCITON GROUND STATE

In Ref. [7], a quantum kinetic description of the exciton spin dynamics without phonon scattering has been derived in the form of coupled equations for excitonic variables. Focusing on the exciton ground state and performing an average over angles in reciprocal space, the necessary variables are the exciton density n_{K_1}, the lth exciton spin component $s_{K_1}^l$, and the coherences $y^{\uparrow/\downarrow}$ for the different spin states. The correlations of excitons with magnetic impurities are explicitly taken into account via the variables $Q_{\eta l K_1}^{\alpha K_2}$, nonmagnetic correlations are given by $Z_\eta{}^{\alpha K_2}_{K_1}$. Similarly, correlations between the coherences and impurities are denoted by $q_{\eta l K_1}^{\uparrow/\downarrow}$ and $z_{\eta K_1}^{\uparrow/\downarrow}$ for the magnetic and nonmagnetic interactions, respectively. The notation is chosen such that $l \in \{1, 2, 3\}$, $\alpha \in \{0, 1, 2, 3\}$, and $\eta \in \{\eta_e, \eta_h\}$. Explicit expressions regarding the definition of all the above variables can be found in Ref. [6].

On a more technical level, we note that obtaining the equations of motion includes the assumption of a system which is homogeneous on average, so the positions of impurities no longer appear explicitly in the variables. Nevertheless, as discussed in detail in Ref. [35], our model still accounts for the transfer of occupations between states with different center-of-mass momenta. The reason for this is that, instead of performing the averaging procedure on the level of the Hamiltonian and thereby artificially enforcing momentum conservation, we only carry out the averaging over impurity positions on the level of the equations of motion. The fact that our theory does indeed allow a change of exciton momenta can be directly seen from Fig. 1, where the kinetic energy (and, thus, the momenta) of excitons remains finite even at long times. Regarding the variables of our model, momentum non-conservation during scattering processes with impurities is accounted for by the magnetic and nonmagnetic correlations.

If the coupling to LA phonons is treated on the Markovian level and cross terms between different interactions are disregarded, the quantum kinetic equations of motion become modified but no new dynamical variables have to be introduced. The modified equations including the phonon scattering read

$$
\frac{\partial}{\partial t} n_{K_1} = \frac{2}{\hbar} \mathbf{E} \cdot \mathbf{M} \text{Im}[y^\uparrow \phi_{1s}] \delta_{K_1,0} - \frac{J_{sd} N_{\text{Mn}}}{\hbar V^2} \sum_{lK} 2\text{Im}\big[Q_{-\eta_h lK}{}^{lK_1}\big] + \frac{J_{pd} N_{\text{Mn}}}{\hbar V^2} \sum_K \text{Im}\big[Q_{\eta_e zK}{}^{0K_1}\big]
$$

$$
- \frac{J_0^e N_{\text{Mn}}}{\hbar V^2} \sum_K 2\text{Im}\big[Z_{-\eta_h}{}^{0K_1}_K\big] - \frac{J_0^h N_{\text{Mn}}}{\hbar V^2} \sum_K 2\text{Im}\big[Z_{\eta_e}{}^{0K_1}_K\big]
$$

$$
+ \sum_K \Lambda_{1s1s}^{K_1 K}\big[\Theta\big(\omega_K - \omega_{K_1} - \omega_{K-K_1}^{\text{ph}}\big)\big(n_K\big(1 + n^{\text{ph}}\big(\omega_K - \omega_{K_1}\big)\big) - n_{K_1} n^{\text{ph}}\big(\omega_K - \omega_{K_1}\big)\big)
$$

$$
+ \Theta\big(\omega_{K_1} - \omega_K - \omega_{K_1-K}^{\text{ph}}\big)\big(n_K n^{\text{ph}}\big(\omega_{K_1} - \omega_K\big) - n_{K_1}\big(1 + n^{\text{ph}}\big(\omega_{K_1} - \omega_K\big)\big)\big)\big], \tag{A1a}
$$

$$
\frac{\partial}{\partial t} s_{K_1}^l = \frac{1}{\hbar} \mathbf{E} \cdot \mathbf{M}\big(\text{Im}[y^\uparrow \phi_{1s}] \delta_{K_1,0} \delta_{l,z} + \text{Im}[y^\downarrow \phi_{1s}] \delta_{K_1,0} \delta_{l,x} - \text{Re}[y^\downarrow \phi_{1s}] \delta_{K_1,0} \delta_{l,y}\big)
$$

$$
+ \frac{J_{sd} N_{\text{Mn}}}{\hbar V^2} \sum_K \bigg(\sum_{jk} \epsilon_{jkl} \text{Re}\big[Q_{-\eta_h jK}{}^{kK_1}\big] - \frac{1}{2}\text{Im}\big[Q_{-\eta_h lK}{}^{0K_1}\big]\bigg) + \frac{J_{pd} N_{\text{Mn}}}{\hbar V^2} \sum_K \text{Im}\big[Q_{\eta_e zK}{}^{lK_1}\big]
$$

$$
- \frac{J_0^e N_{Mn}}{\hbar V^2} \sum_K 2 \mathrm{Im}\big[Z_{-\eta_h \ K}^{\ lK_1}\big] - \frac{J_0^h N_{Mn}}{\hbar V^2} \sum_K 2 \mathrm{Im}\big[Z_{\eta_e \ K}^{\ lK_1}\big]
$$

$$
+ \sum_K \Lambda_{1s1s}^{K_1 K} \big[\Theta\big(\omega_K - \omega_{K_1} - \omega_{K-K_1}^{ph}\big)\big(s_K^l\big(1 + n^{ph}(\omega_K - \omega_{K_1})\big) - s_{K_1}^l n^{ph}(\omega_K - \omega_{K_1})\big)
$$

$$
+ \Theta\big(\omega_{K_1} - \omega_K - \omega_{K_1-K}^{ph}\big)\big(s_K^l n^{ph}(\omega_{K_1} - \omega_K) - s_{K_1}^l\big(1 + n^{ph}(\omega_{K_1} - \omega_K)\big)\big)\big], \tag{A1b}
$$

$$
\frac{\partial}{\partial t} y^{\uparrow/\downarrow} = \frac{i}{\hbar}\mathbf{E} \cdot \mathbf{M}\phi_{1s}\delta_{\uparrow/\downarrow,\uparrow} - i\bigg(\omega_0 + \frac{(J_0^e + J_0^h)N_{Mn}}{\hbar V}\bigg)y^{\uparrow/\downarrow} - i\frac{J_{sd}N_{Mn}}{2\hbar V^2}\sum_K \big(\pm q_{-\eta_h zK}^{\uparrow/\downarrow} + q_{-\eta_h \mp K}^{\downarrow/\uparrow}\big)
$$

$$
+ i\frac{J_{pd}N_{Mn}}{2\hbar V^2}\sum_K q_{\eta_e zK}^{\uparrow/\downarrow} - i\frac{J_0^e N_{Mn}}{\hbar V^2}\sum_K z_{-\eta_h K}^{\uparrow/\downarrow} - i\frac{J_0^h N_{Mn}}{\hbar V^2}\sum_K z_{\eta_e K}^{\uparrow/\downarrow}
$$

$$
- \sum_K \Lambda_{1s1s}^{0K}\Theta\big(\omega_K - \omega_K^{ph}\big)n^{ph}(\omega_K)y^{\uparrow/\downarrow}, \tag{A1c}
$$

$$
\frac{\partial}{\partial t} q_{\eta lK_1}^{\uparrow/\downarrow} = -i\bigg(\omega_{K_1} + \frac{I(J_0^e + J_0^h)N_{Mn}}{\hbar V}\bigg)q_{\eta lK_1}^{\uparrow/\downarrow} - i\frac{IJ_{sd}}{2\hbar}F_{\eta \ 1s1s}^{-\eta_h 0K_1}\big(\pm \langle S^l S^z\rangle y^{\uparrow/\downarrow} + \langle S^l S^\mp\rangle y^{\downarrow/\uparrow}\big)
$$

$$
+ i\frac{IJ_{pd}}{2\hbar}\langle S^l S^z\rangle F_{\eta \ 1s1s}^{\eta_e 0K_1}y^{\uparrow/\downarrow}, \tag{A1d}
$$

$$
\frac{\partial}{\partial t} z_{\eta K_1}^{\uparrow/\downarrow} = -i\bigg(\omega_{K_1} + \frac{I(J_0^e + J_0^h)N_{Mn}}{\hbar V}\bigg)z_{\eta K_1}^{\uparrow/\downarrow} - i\frac{I}{\hbar}\big(J_0^e F_{\eta \ 1s1s}^{-\eta_h 0K_1} + J_0^h F_{\eta \ 1s1s}^{\eta_e 0K_1}\big)y^{\uparrow/\downarrow}, \tag{A1e}
$$

$$
\frac{\partial}{\partial t} Q_{\eta lK_1}^{0K_2} = -i(\omega_{K_2} - \omega_{K_1})Q_{\eta lK_1}^{0K_2} + \sum_{jk}\epsilon_{jkl}\omega_{Mn}^j Q_{\eta kK_1}^{0K_2} + \frac{i}{2\hbar}\mathbf{E}\cdot\mathbf{M}\big((q_{\eta lK_1}^{\uparrow}\phi_{1s})^*\delta_{K_2,0} - q_{\eta lK_2}^{\uparrow}\phi_{1s}\delta_{K_1,0}\big)
$$

$$
+ i\frac{IJ_{sd}}{\hbar}F_{\eta \ 1s1s}^{-\eta_h K_1 K_2}\sum_j \big(\langle S^j S^l\rangle s_{K_2}^j - \langle S^l S^j\rangle s_{K_1}^j\big) - i\frac{IJ_{pd}}{\hbar}F_{\eta \ 1s1s}^{\eta_e K_1 K_2}\frac{1}{2}\big(\langle S^z S^l\rangle n_{K_2} - \langle S^l S^z\rangle n_{K_1}\big), \tag{A1f}
$$

$$
\frac{\partial}{\partial t} Q_{\eta lK_1}^{mK_2} = -i(\omega_{K_2} - \omega_{K_1})Q_{\eta lK_1}^{mK_2}
$$

$$
+ \frac{i}{2\hbar}\mathbf{E}\cdot\mathbf{M}\big[\big((q_{\eta lK_1}^{\uparrow}\phi_{1s})^*\delta_{K_2,0} - q_{\eta lK_2}^{\uparrow}\phi_{1s}\delta_{K_1,0}\big)\delta_{m,z} + \big((q_{\eta lK_1}^{\downarrow}\phi_{1s})^*\delta_{K_2,0} - q_{\eta lK_2}^{\downarrow}\phi_{1s}\delta_{K_1,0}\big)\delta_{m,x}
$$

$$
+ i\big((q_{\eta lK_1}^{\downarrow}\phi_{1s})^*\delta_{K_2,0} + q_{\eta lK_2}^{\downarrow}\phi_{1s}\delta_{K_1,0}\big)\delta_{m,y}\big] - i\frac{IJ_{pd}}{\hbar}F_{\eta \ 1s1s}^{\eta_e K_1 K_2}\frac{1}{2}\big(\langle S^z S^l\rangle s_{K_2}^m - \langle S^l S^z\rangle s_{K_1}^m\big)
$$

$$
+ i\frac{IJ_{sd}}{2\hbar}F_{\eta \ 1s1s}^{-\eta_h K_1 K_2}\sum_j \bigg(\langle S^j S^l\rangle\bigg(\frac{1}{2}\delta_{j,m}n_{K_2} - i\sum_k\epsilon_{jkm}s_{K_2}^k\bigg) - \langle S^l S^j\rangle\bigg(\frac{1}{2}\delta_{j,m}n_{K_1} + i\sum_k\epsilon_{jkm}s_{K_1}^k\bigg)\bigg), \tag{A1g}
$$

$$
\frac{\partial}{\partial t} Z_{\eta \ K_1}^{\ 0K_2} = -i(\omega_{K_2} - \omega_{K_1})Z_{\eta \ K_1}^{\ 0K_2} + \frac{i}{2\hbar}\mathbf{E}\cdot\mathbf{M}\big((z_{\eta K_1}^{\uparrow}\phi_{1s})^*\delta_{K_2,0} - z_{\eta K_2}^{\uparrow}\phi_{1s}\delta_{K_1,0}\big)
$$

$$
+ i\frac{I}{\hbar}\big(J_0^e F_{\eta \ 1s1s}^{-\eta_h K_1 K_2} + J_0^h F_{\eta \ 1s1s}^{\eta_e K_1 K_2}\big)(n_{K_2} - n_{K_1}), \tag{A1h}
$$

$$
\frac{\partial}{\partial t} Z_{\eta \ K_1}^{\ lK_2} = -i(\omega_{K_2} - \omega_{K_1})Z_{\eta \ K_1}^{\ lK_2} + \frac{i}{2\hbar}\mathbf{E}\cdot\mathbf{M}\big[\big((z_{\eta K_1}^{\uparrow}\phi_{1s})^*\delta_{K_2,0} - z_{\eta K_2}^{\uparrow}\phi_{1s}\delta_{K_1,0}\big)\delta_{l,z}
$$

$$
+ \big((z_{\eta K_1}^{\downarrow}\phi_{1s})^*\delta_{K_2,0} - z_{\eta K_2}^{\downarrow}\phi_{1s}\delta_{K_1,0}\big)\delta_{l,x} + i\big((z_{\eta K_1}^{\downarrow}\phi_{1s})^*\delta_{K_2,0} + z_{\eta K_2}^{\downarrow}\phi_{1s}\delta_{K_1,0}\big)\delta_{l,y}\big]
$$

$$
+ i\frac{I}{\hbar}\big(J_0^e F_{\eta \ 1s1s}^{-\eta_h K_1 K_2} + J_0^h F_{\eta \ 1s1s}^{\eta_e K_1 K_2}\big)\big(s_{K_2}^l - s_{K_1}^l\big), \tag{A1i}
$$

where $\phi_{1s} := R_{1s}(r=0)$ is the radial part of the $1s$ exciton wave function evaluated at $r = 0$. The factor $I = 3/2$ stems from the projection onto the quantum well and the exciton form factors are given by

$$
F_{\eta_1 1s1s}^{\eta_2\omega_1\omega_2} = 2\pi \int_0^{2\pi} d\psi \int_0^\infty dr \int_0^\infty dr'\, rr' R_{1s}^2(r)R_{1s}^2(r') J_0(\eta_1 K_{12}(\psi)r)J_0(\eta_2 K_{12}(\psi)r'), \tag{A2}
$$

with the cylindrical Bessel function of order zero $J_0(x)$ and $K_{12} = |\mathbf{K}_1 - \mathbf{K}_2|$ with angle between $\mathbf{K}_1$ and $\mathbf{K}_2$ given by ψ.

APPENDIX B: MARKOVIAN EQUATIONS OF MOTION FOR THE EXCITON GROUND STATE

When the magnetic and nonmagnetic scattering of excitons with impurities as well as the optical excitation are treated as a Markovian processes, one obtains the following equations of motion for the spin-up and spin-down exciton densities, respectively [6,7]:

$$
\begin{aligned}
\frac{\partial}{\partial t} n_{\omega_1}^{\uparrow/\downarrow} = \ & \Gamma_{\omega_1} + \frac{35 I N_{\mathrm{Mn}} M J_{sd}^2}{12\hbar^3 V d} F_{\eta_{\mathrm{h}} 1s1s}^{\eta_{\mathrm{h}} \omega_1 \omega_1} \big(n_{\omega_1}^{\downarrow/\uparrow} - n_{\omega_1}^{\uparrow/\downarrow} \big) \\
& + \int_0^\infty D(\omega) \Lambda_{1s1s}^{\omega_1 \omega} \Big[\Theta\big(\omega - \omega_1 - \omega_{\omega-\omega_1}^{\mathrm{ph}}\big) \big(n_\omega^{\uparrow/\downarrow}(1 + n^{\mathrm{ph}}(\omega - \omega_1)) - n_{\omega_1}^{\uparrow/\downarrow} n^{\mathrm{ph}}(\omega - \omega_1) \big) \\
& + \Theta\big(\omega_1 - \omega - \omega_{\omega_1-\omega}^{\mathrm{ph}}\big) \big(n_\omega^{\uparrow/\downarrow} n^{\mathrm{ph}}(\omega_1 - \omega) - n_{\omega_1}^{\uparrow/\downarrow}(1 + n^{\mathrm{ph}}(\omega_1 - \omega)) \big) \Big].
\end{aligned}
\tag{B1}
$$

The equations are formulated in frequency space with the constant density of states $D(\omega) = \frac{VM}{2\pi\hbar d}$ to achieve a better numerical evaluation of the delta functions. The frequency is connected to the exciton wave number via $\omega = \frac{\hbar K^2}{2M}$. Furthermore,

$$
\Gamma_{\omega_1}(t) = \frac{1}{\hbar^2} E(t) E_0 |M_{\uparrow/\downarrow}|^2 \phi_{1s}^2 \int_{-\infty}^t d\tau\, e^{-\frac{\tau^2}{2\sigma^2}} \, \delta_{\omega_1,0}
\tag{B2}
$$

is the optical generation rate of excitons with σ related to the time t_{FWHM} at full-width half-maximum of the pulse via $\sigma = \frac{t_{\mathrm{FWHM}}}{2\sqrt{2\log 2}}$. Note that $|M_{\uparrow/\downarrow}|^2$ still contains spin selection rules. From the spin-up and spin-down exciton density, the z component of the spin can be extracted via $s_\omega^z = \frac{1}{2}(n_\omega^\uparrow - n_\omega^\downarrow)$.

[1] M. Umlauff, J. Hoffmann, H. Kalt, W. Langbein, J. M. Hvam, M. Scholl, J. Söllner, M. Heuken, B. Jobst, and D. Hommel, Phys. Rev. B **57**, 1390 (1998).

[2] H. Zhao, S. Moehl, and H. Kalt, Appl. Phys. Lett. **81**, 2794 (2002).

[3] K. Siantidis, V. M. Axt, and T. Kuhn, Phys. Rev. B **65**, 035303 (2001).

[4] R. Zimmermann and E. Runge, Phys. Status Solidi A **164**, 511 (1997).

[5] H. Zhao, S. Moehl, and H. Kalt, Phys. Rev. Lett. **89**, 097401 (2002).

[6] F. Ungar, M. Cygorek, and V. M. Axt, Phys. Rev. B **95**, 245203 (2017).

[7] F. Ungar, M. Cygorek, and V. M. Axt, Phys. Rev. B **97**, 045210 (2018).

[8] T. Dietl and H. Ohno, Rev. Mod. Phys. **86**, 187 (2014).

[9] *Introduction to the Physics of Diluted Magnetic Semiconductors*, edited by J. Kossut and J. A. Gaj (Springer, Berlin, 2010).

[10] J. K. Furdyna, J. Appl. Phys. **64**, R29 (1988).

[11] *Semiconductors and Semimetals*, edited by J. K. Furdyna and J. Kossut (Academic Press, San Diego, 1988).

[12] R. Fiederling, M. Keim, G. Reuscher, W. Ossau, G. Schmidt, A. Waag, and L. W. Molenkamp, Nature **402**, 787 (1999).

[13] S. Cronenberger, D. Scalbert, D. Ferrand, H. Boukari, and J. Cibert, Nat. Commun. **6**, 8121 (2015).

[14] T. Dietl, Nat. Mater. **9**, 965 (2010).

[15] H. Ohno, Nat. Mater. **9**, 952 (2010).

[16] I. Žutić, J. Fabian, and S. Das Sarma, Rev. Mod. Phys. **76**, 323 (2004).

[17] D. Awschalom and M. Flatté, Nat. Phys. **3**, 153 (2007).

[18] C. Camilleri, F. Teppe, D. Scalbert, Y. G. Semenov, M. Nawrocki, M. Dyakonov, J. Cibert, S. Tatarenko, and T. Wojtowicz, Phys. Rev. B **64**, 085331 (2001).

[19] Z. Ben Cheikh, S. Cronenberger, M. Vladimirova, D. Scalbert, F. Perez, and T. Wojtowicz, Phys. Rev. B **88**, 201306 (2013).

[20] M. Vladimirova, S. Cronenberger, P. Barate, D. Scalbert, F. J. Teran, and A. P. Dmitriev, Phys. Rev. B **78**, 081305 (2008).

[21] Ł. Cywiński and L. J. Sham, Phys. Rev. B **76**, 045205 (2007).

[22] W. M. Chen, I. A. Buyanova, G. Yu. Rudko, A. G. Mal'shukov, K. A. Chao, A. A. Toropov, Y. Terent'ev, S. V. Sorokin, A. V. Lebedev, S. V. Ivanov, and P. S. Kop'ev, Phys. Rev. B **67**, 125313 (2003).

[23] C. D. Poweleit, L. M. Smith, and B. T. Jonker, Phys. Rev. B **55**, 5062 (1997).

[24] H. Haug, Phys. Status Solidi B **173**, 139 (1992).

[25] L. Bá;nyai, D. B. T. Thoai, C. Remling, and H. Haug, Phys. Status Solidi B **173**, 149 (1992).

[26] J. Schilp, T. Kuhn, and G. Mahler, Phys. Rev. B **50**, 5435 (1994).

[27] E. Tsitsishvili, R. v. Baltz, and H. Kalt, Phys. Rev. B **71**, 155320 (2005).

[28] S. Rudin and T. L. Reinecke, Phys. Rev. B **41**, 3017 (1990).

[29] H. Ohno, Science **281**, 951 (1998).

[30] I. Di Marco, P. Thunström, M. I. Katsnelson, J. Sadowski, K. Karlsson, S. Lebègue, J. Kanski, and O. Eriksson, Nat. Commun. **4**, 2645 (2013).

[31] F. Ungar, M. Cygorek, and V. M. Axt, Phys. Rev. B **98**, 161201(R) (2018).

[32] M. Cygorek and V. M. Axt, J. Phys.: Conf. Ser. **647**, 012042 (2015).

[33] V. M. Axt and A. Stahl, Z. Phys. B **93**, 195 (1994).

[34] R. Winkler, *Spin-Orbit Coupling Effects in Two-Dimensional Electron and Hole Systems* (Springer, Berlin, 2003).

[35] C. Thurn and V. M. Axt, Phys. Rev. B **85**, 165203 (2012).

[36] M. Cygorek, F. Ungar, P. I. Tamborenea, and V. M. Axt, Phys. Rev. B **95**, 045204 (2017).

[37] T. Uenoyama and L. J. Sham, Phys. Rev. Lett. **64**, 3070 (1990).

[38] R. Ferreira and G. Bastard, Phys. Rev. B **43**, 9687 (1991).

[39] G. Bastard and R. Ferreira, Surf. Sci. **267**, 335 (1992).

[40] S. A. Crooker, D. D. Awschalom, J. J. Baumberg, F. Flack, and N. Samarth, Phys. Rev. B **56**, 7574 (1997).

[41] M. Cygorek and V. M. Axt, Phys. Rev. B **90**, 035206 (2014).

[42] F. Ungar, M. Cygorek, P. I. Tamborenea, and V. M. Axt, Phys. Rev. B **91**, 195201 (2015).

[43] S. A. Crooker, J. J. Baumberg, F. Flack, N. Samarth, and D. D. Awschalom, Phys. Rev. Lett. **77**, 2814 (1996).

[44] D. Awschalom and N. Samarth, J. Magn. Magn. Mater. **200**, 130 (1999).

[45] G. V. Astakhov, D. R. Yakovlev, V. P. Kochereshko, W. Ossau, W. Faschinger, J. Puls, F. Henneberger, S. A. Crooker, Q. McCulloch, D. Wolverson, N. A. Gippius, and A. Waag, Phys. Rev. B **65**, 165335 (2002).

[46] R. Triboulet and P. Siffert (eds.), *CdTe and Related Compounds; Physics, Defects, Hetero- and Nano-structures, Crystal Growth, Surfaces and Applications*, 1st ed., European Mater. Res. Society Series (Elsevier, Amsterdam, 2009).

[47] I. Strzalkowski, S. Joshi, and C. R. Crowell, Appl. Phys. Lett. **28**, 350 (1976).

[48] M. Cardona and N. E. Christensen, Phys. Rev. B **35**, 6182 (1987).

[49] *Zinc Manganese Selenide—Zn(1-x)Mn(x)Se Physical Properties: Datasheet from Landolt-Börnstein - Group III Condensed Matter, Vol. 41B: II-VI and I-VII Compounds; Semimagnetic Compounds*, edited by O. Madelung, U. Rössler, and M. Schulz, (Springer, Berlin, 1999).

[50] C. Thurn, M. Cygorek, V. M. Axt, and T. Kuhn, Phys. Rev. B **87**, 205301 (2013).

[51] E. Tsitsishvili and H. Kalt, Phys. Rev. B **73**, 195402 (2006).

Publication 6

Phonon-induced quantum ratchet in the exciton spin dynamics in diluted magnetic semiconductors in a magnetic field

F. Ungar, M. Cygorek, and V. M. Axt

Phonon-induced quantum ratchet in the exciton spin dynamics in diluted magnetic semiconductors in a magnetic field

F. Ungar,[1] M. Cygorek,[2] and V. M. Axt[1]

[1]*Theoretische Physik III, Universität Bayreuth, 95440 Bayreuth, Germany*
[2]*Department of Physics, University of Ottawa, Ottawa, Ontario, Canada K1N 6N5*

Magnetically doped semiconductors are well known for their giant Zeeman splittings which can reach several meV even in relatively small external magnetic fields. After preparing a nonequilibrium exciton distribution via optical excitation, the spin dynamics in diluted magnetic semiconductor quantum wells is typically governed by spin-flip scattering processes due to the exciton-impurity exchange interaction. Our theoretical calculations show that the giant Zeeman splitting in these materials in combination with the influence of longitudinal acoustic phonons lead to a quantum ratchet-type dynamics, resulting in an almost complete reversal of the carrier spin polarization at very low temperatures. Furthermore, we find that the predictions of a much simpler rate-equation approach qualitatively agree with a more advanced and numerically demanding quantum-kinetic description of the spin dynamics for a wide range of temperatures, although quantitative differences are noticeable.

I. INTRODUCTION

In quantum mechanics, a ratchet-type dynamics can ensue whenever there is a bias in favor of a specific scatting channel such that, e.g., a driving by an unbiased force still causes a net current in the system [1,2]. An essential ingredient to the ratchet behavior is the breaking of time-reversal symmetry [3], which in solid state physics can be easily achieved by applying a magnetic field. Quantum ratchets have been experimentally realized and harnessed in a variety of systems, such as in atomic condensates [4], all-optical systems [5], or at the single-electron level using the spin degree of freedom [6]. The latter approach falls into the field of spintronics, which aims to augment traditional electronic devices based on the manipulation of charge currents by including the carrier spin [7–12].

A promising material class for bridging the gap between state-of-the-art semiconductor technology and spintronic devices are diluted magnetic semiconductors (DMSs) [13–16]. DMSs are doped with a small number of impurity ions that possess large magnetic moments, such as manganese, and which introduce a strong spin-dependent carrier-impurity exchange interaction. In this paper, we theoretically show how a quantum ratchet emerges in the exciton spin dynamics in DMS quantum wells in a finite magnetic field when, in addition to the exchange interaction, the carrier-phonon scattering is accounted for.

Focusing on the subclass of II-VI DMSs, where the doping does not cause excessive charges in the system due to the isoelectronic nature of the impurity ions, we consider the paramagnetic limit so that magnetic impurities at different sites in the crystal lattice can be considered to be independent. Furthermore, the exciton resonance represents a regime which is often chosen in experiments using optical excitation [17–21] due to its spectral isolation and rich physics. Since experiments are typically performed at very low temperatures

[18,21,22], phonon scattering is often not included in theoretical models and the focus instead lies on the description of spin-flip processes due to the carrier-impurity exchange interaction [23–29]. Here, we show that longitudinal acoustic (LA) phonons, despite their negligible influence on the spin dynamics on short timescales, in conjunction with the spin-flip scattering in a finite magnetic field in fact lead to a drastically different long time spin polarization which can be described in terms of a quantum ratchet. Specifically, we find that a spin-conserving scattering of excitons causes an almost complete reversal of the initial spin polarization created by the optical excitation at very low temperatures.

To describe the spin dynamics, a rate-equation model is used which captures the spin-dependent exciton-impurity exchange interaction as well as the scattering of excitons due to LA phonons. We also compare the results of this model with calculations based on a more advanced treatment of the exchange interaction on a quantum-kinetic level [30], which has recently been extended to account for LA phonon scattering [31]. That such a treatment of the exchange interaction beyond the mean-field level can be required for an accurate description of the physics in DMSs is supported by the pronounced correlation effects exhibited by the material [32–34]. In this study, our simulations reveal that both models yield qualitatively similar results provided that the phonon scattering is included. However, this agreement is lost as soon as the exciton-phonon interaction is disregarded in the rate-equation model.

II. THEORETICAL MODEL

In this section, we present the main interaction parts of the Hamiltonian used for the description of the exciton spin dynamics in DMSs. We also provide the resulting equations of motion in the Markov limit and discuss the energies

involved in the spin-flip scattering due to the exciton-impurity exchange interaction.

A. Interaction Hamiltonian

In DMSs, the dominant spin-flip mechanism is given by the sd (pd) exchange interaction between s-type electrons (p-type holes) and the localized d-shell electrons of the magnetic impurities [15]. It is described by [30]

$$
\begin{aligned}
H_\mathrm{m} = {} & \frac{J_{sd}}{V} \sum_{\substack{Inn' \\ ll'\mathbf{kk'}}} \mathbf{S}_{nn'} \cdot \mathbf{s}^\mathrm{e}_{ll'} c^\dagger_{l\mathbf{k}} c_{l'\mathbf{k'}} e^{i(\mathbf{k'}-\mathbf{k})\cdot\mathbf{R}_I} \hat{P}^I_{nn'} \\
& + \frac{J_{pd}}{V} \sum_{\substack{Inn' \\ vv'\mathbf{kk'}}} \mathbf{S}_{nn'} \cdot \mathbf{s}^\mathrm{h}_{vv'} d^\dagger_{v\mathbf{k}} d_{v'\mathbf{k'}} e^{i(\mathbf{k'}-\mathbf{k})\cdot\mathbf{R}_I} \hat{P}^I_{nn'}
\end{aligned} \tag{1}
$$

with the respective coupling constants J_{sd} and J_{pd} in a semiconductor with volume V. The operator $c^\dagger_{l\mathbf{k}}$ ($c_{l\mathbf{k}}$) creates (annihilates) an electron in the lth conduction band with wave vector $\mathbf{k}$. Analogously, $d^\dagger_{v\mathbf{k}}$ ($d_{v\mathbf{k}}$) refers to the respective hole operator in the valence band v. The vector of electron (hole) spin matrices is given by $\mathbf{s}^\mathrm{e}_{ll'} = \boldsymbol{\sigma}_{ll'}$ ($\mathbf{s}^\mathrm{h}_{vv'} = \mathbf{J}_{vv'}$) with the vector of Pauli matrices $\boldsymbol{\sigma}_{ll'}$ and the vector of angular momentum matrices $\mathbf{J}_{vv'}$, where $v, v' \in \{-3/2, -1/2, 1/2, 3/2\}$. The impurity spin is decomposed into the vector of spin matrices $\mathbf{S}_{nn'}$ with $n, n' \in \{-5/2, -3/2, \ldots, 5/2\}$ and the operator $\hat{P}^I_{nn'} = |I, n\rangle\langle I, n'|$, where $|I, n\rangle$ is the nth spin state of the Ith impurity atom and $\mathbf{R}_I$ denotes its position. This representation is advantageous for distinguishing impurity operators evaluated at the same and at different lattice sites, which in turn helps us to identify the predominant correlations [35].

Apart from the magnetic exchange interaction, we also take the scattering of carriers with LA phonons into account. As long as only optically excited low-energy excitons are considered, optical phonons can be disregarded for not too high temperatures since their energies are too high for an allowed phonon emission process. Furthermore, LA phonon scattering dominates the linewidth of optical spectra below temperatures of about 80 K [36]. The carrier-phonon interaction is given by

$$
\begin{aligned}
H_\mathrm{c\text{-}ph} = \sum_{\mathbf{qk}} \big(& \gamma^\mathrm{e}_\mathbf{q} c^\dagger_{\mathbf{k+q}} c_\mathbf{k} b_\mathbf{q} + \gamma^\mathrm{e*}_\mathbf{q} c^\dagger_\mathbf{k} c_{\mathbf{k+q}} b^\dagger_\mathbf{q} \\
& + \gamma^\mathrm{h}_\mathbf{q} d^\dagger_{\mathbf{k+q}} d_\mathbf{k} b_\mathbf{q} + \gamma^\mathrm{h*}_\mathbf{q} d^\dagger_\mathbf{k} d_{\mathbf{k+q}} b^\dagger_\mathbf{q} \big).
\end{aligned} \tag{2}
$$

Here, the creation (annihilation) operator for phonons with energy $\hbar\omega^\mathrm{ph}_\mathbf{q}$ is denoted by $b^\dagger_\mathbf{q}$ ($b_\mathbf{q}$), where $\mathbf{q}$ contains the phonon momentum as well as the branch number. We limit the description to bulk phonon modes and only consider deformation potential coupling [31]. Then, the coupling constants are given by

$$
\gamma^\mathrm{e,h}_{\mathbf{q},q_z} = \sqrt{\frac{q\hbar}{2\rho V v}} D_\mathrm{e,h} \tag{3}
$$

for a semiconductor with density ρ, longitudinal sound velocity v, and deformation potential constants $D_\mathrm{e,h}$ for the conduction and the valence band, respectively. For the phonon dispersion, a linear relation $\omega^\mathrm{ph}_\mathbf{q} = vq$ is assumed due to the small exciton center-of-mass momenta.

Apart from these interactions, we include the carrier kinetic energies, the Coulomb interaction responsible for the exciton binding, the light-matter coupling in the dipole approximation, as well as Zeeman terms for the carriers and the impurities that arise in an external magnetic field. Furthermore, we account for the local potential mismatch in the lattice due to the doping with impurities by adding a nonmagnetic scattering contribution to the Hamiltonian in a form similar to Eq. (1) but without the spin part [37]. Although this nonmagnetic impurity scattering does not affect the spin dynamics in a rate-equation model, it causes an enhancement of the correlation energy which can be captured by a quantum-kinetic approach [30]. For explicit expressions of these Hamiltonian contributions, we refer the reader to Ref. [38].

B. Rate-equation model

In the following, we restrict our considerations to systems with a sufficiently large energy splitting between heavy and light holes such that, using an optical excitation with σ^- polarization resonant with the $1s$ heavy-hole exciton, the electron-spin part plays the dominant role in the exciton spin dynamics and the hole-spin part remains pinned along the growth direction [17,23,39]. Thus, one can effectively assign two spin orientations to the excitons which follow directly from the electron spin.

If the z axis is chosen to coincide with the growth direction of the quantum well as well as the direction of the applied magnetic field $\mathbf{B}$, the mean-field precession frequencies of electrons and Mn impurities are given by [30]

$$
\boldsymbol{\omega}_\mathrm{e} = \frac{1}{\hbar} g_\mathrm{e} \mu_B \mathbf{B} + \frac{J_{sd} N_\mathrm{Mn} \langle S^z \rangle}{\hbar V} \mathbf{e}_z, \tag{4a}
$$

$$
\boldsymbol{\omega}_\mathrm{Mn} = \frac{1}{\hbar} g_\mathrm{Mn} \mu_B \mathbf{B}, \tag{4b}
$$

respectively. In the above equations, g_e (g_Mn) is the electron (Mn) g factor and μ_B denotes the Bohr magneton. The Zeeman contribution due to the impurities scales with the number of Mn atoms given by N_Mn and depends on the z component of the average impurity spin $\langle S^z \rangle$. Finally, $\mathbf{e}_z$ is the unit vector along the z axis. In this configuration, the z components of these quantities yield the energetic splitting of the different exciton spin states which emerges as a result of the applied magnetic field in combination with the successive alignment of the impurity spins.

To describe the spin dynamics, it is advantageous to use the spin-up ($n^\uparrow_{\omega_1}$) and spin-down exciton density ($n^\downarrow_{\omega_1}$) at a given frequency ω_1. From these variables, the z component of the spin can be extracted via $s^z_{\omega_1} = \frac{1}{2}(n^\uparrow_{\omega_1} - n^\downarrow_{\omega_1})$. Since the focus of this paper lies on the Faraday configuration, where the magnetic field is aligned with the growth direction, in-plane spin components will remain zero throughout the dynamics and can therefore be disregarded for typical optical excitation scenarios of spin-up excitons. Treating all couplings in the Markov limit so that a Markovian theory (MT) is obtained, one then ends up with the following equations of

motion [30,38]:

$$\frac{\partial}{\partial t} n_{\omega_1}^{\uparrow/\downarrow} = \Gamma_{\omega_1} + \frac{I N_{\mathrm{Mn}} M J_{sd}^2}{2\hbar^3 V d} \int_0^\infty d\omega\, \delta[\omega - (\omega_1 \pm \omega_{\mathrm{sf}})] F_{\eta_{\mathrm{h}}1s1s}^{\eta_{\mathrm{h}}\omega\omega_1} \left(b^\pm n_\omega^{\downarrow/\uparrow} - b^\mp n_{\omega_1}^{\uparrow/\downarrow} \right)$$

$$+ \int_0^\infty D(\omega) \Lambda_{1s1s}^{\omega_1\omega} \Big[\Theta\big(\omega - \omega_1 - \omega_{\omega-\omega_1}^{\mathrm{ph}}\big) \big(n_\omega^{\uparrow/\downarrow}[1 + n^{\mathrm{ph}}(\omega - \omega_1)] - n_{\omega_1}^{\uparrow/\downarrow} n^{\mathrm{ph}}(\omega - \omega_1) \big)$$

$$+ \Theta\big(\omega_1 - \omega - \omega_{\omega_1-\omega}^{\mathrm{ph}}\big) \big(n_\omega^{\uparrow/\downarrow} n^{\mathrm{ph}}(\omega_1 - \omega) - n_{\omega_1}^{\uparrow/\downarrow}[1 + n^{\mathrm{ph}}(\omega_1 - \omega)] \big) \Big]. \tag{5}$$

Here, the magnetic moments due to the Mn ions are subsumed in the constants $b^\pm = \frac{1}{2}[\langle \mathbf{S}^2 - (S^z)^2 \rangle \pm \langle S^z \rangle]$. The equations are formulated in frequency space with the constant density of states $D(\omega) = \frac{VM}{2\pi\hbar d}$ and $\omega = \frac{\hbar K^2}{2M}$. Furthermore, the optical generation rate of excitons is given by

$$\Gamma_{\omega_1}(t) = \frac{1}{\hbar^2} E(t) E_0 |M_{\uparrow/\downarrow}|^2 \phi_{1s}^2 \int_{-\infty}^t d\tau\, e^{-\frac{\tau^2}{2\sigma^2}} \, \delta_{\omega_1,0} \tag{6}$$

with $\sigma = \frac{t_{\mathrm{FWHM}}}{2\sqrt{2\log 2}}$, where t_{FWHM} is the time at the full-width at half-maximum (FWHM) of the pulse $E(t) = E_0 \exp(-\frac{t^2}{2\sigma^2})$. The optical spin selection rules are contained in the dipole matrix element $|M_{\uparrow/\downarrow}|^2$ and $\phi_{1s} = R_{1s}(r = 0)$ denotes the radial part of the $1s$ exciton wave function evaluated at the origin. Regarding the phonon influence, n^{ph} denotes a thermal phonon occupation given by $1/[\exp(\hbar\Delta\omega/k_B T) - 1]$ and $\Theta(x)$ is the Heaviside step function. Explicit expressions of the exciton form factor $F_{\eta_{\mathrm{h}}1s1s}^{\eta_{\mathrm{h}}\omega\omega_1}$ and the phonon matrix element $\Lambda_{1s1s}^{\omega_1\omega}$ can be found in the Appendix.

Finally, we have introduced the exciton spin-flip scattering shift

$$\hbar\omega_{\mathrm{sf}} := \hbar\big(\omega_{\mathrm{e}}^z - \omega_{\mathrm{Mn}}^z\big), \tag{7}$$

where ω_{e}^z and ω_{Mn}^z are the z components of the precession frequencies given by Eqs. (4). This quantity is a measure for the energy released or required during a spin-flip process of an exciton while simultaneously accounting for the resulting tilt of some Mn spins in accordance with total spin conservation. Instead of considering a time-dependent impurity spin density matrix, we focus on the limit of low exciton densities so that the Mn spin can be effectively treated as a spin bath with a fixed temperature [30].

Typically encountered spin-flip scattering shifts are plotted in Fig. 1 as a function of temperature for various impurity doping fractions. The results are obtained for a 15-nm-wide $\mathrm{Zn}_{1-x}\mathrm{Mn}_x\mathrm{Se}$ quantum well in an external magnetic field with a magnitude of 0.5 T. If the temperature is low enough so that the majority of Mn spins are more or less aligned along the same direction, energies exceeding 10 meV can be reached provided the doping fraction is high enough. The fact that these energies by far exceed the standard Zeeman shifts typically encountered in solid state physics is known as the giant Zeeman effect [13,15,16]. Since this effect relies on the overall magnitude of the average impurity spin [cf. Eq. (4a)], it strongly decreases with rising temperature since then the Mn spins become more and more randomly oriented such that the average impurity spin approaches zero.

III. NUMERICAL RESULTS

In the following, we present numerical calculations of the exciton spin dynamics in an external magnetic field with a focus on the influence of LA phonons. All calculations are performed for a 15-nm-wide $\mathrm{Zn}_{0.985}\mathrm{Mn}_{0.025}\mathrm{Se}$ quantum well in an external magnetic field with a magnitude of 0.5 T. The remaining material parameters are the same as in Ref. [31]. For the optical excitation, we model a Gaussian pulse with 100-fs FWHM resonant to the spin-up $1s$ exciton. First, the impact of phonon scattering on the longtime spin dynamics in DMSs is studied using the rate-equation model. Second, the results are compared with a more elaborate theoretical approach where the exciton-impurity interaction is treated beyond the Markov level.

A. Phonon impact on the long-time behavior of the exciton spin

Figure 2(a) shows the time evolution of the exciton spin for various temperatures under the influence of the magnetic exchange interaction as well as phonon scattering, which are both treated on the Markov level corresponding to Eq. (5). After the optical orientation of the exciton spins via a laser pulse which is resonant with the spin-up exciton ground state, a fast decay of the spin polarization occurs on a timescale of several picoseconds, followed by a slower decay until a stationary value is reached. Due to the external magnetic field in combination with the ensuing impurity spin polarization, the long-time value of the exciton spin is nonzero and instead shows a finite spin-down polarization which, below 10 K, can be even higher than 50% compared with the initial polarization. Since the value of this polarization depends on the magnitude of $\langle S^z \rangle$, i.e., the degree of polarization of impurity spins [38], it also depends on the temperature used to
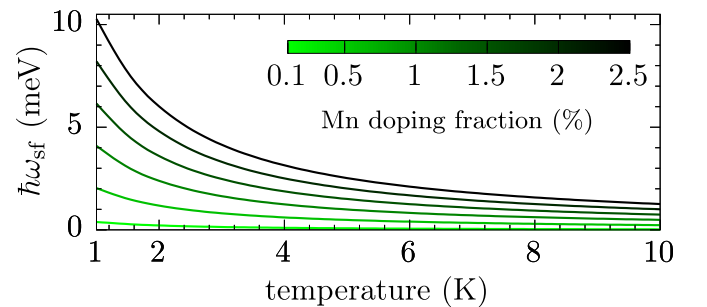

FIG. 1. Temperature dependence of the spin-flip scattering shift $\hbar\omega_{\mathrm{sf}}$ for various Mn doping fractions of a 15-nm-wide $\mathrm{Zn}_{1-x}\mathrm{Mn}_x\mathrm{Se}$ quantum well in an external magnetic field with a magnitude of 0.5 T.
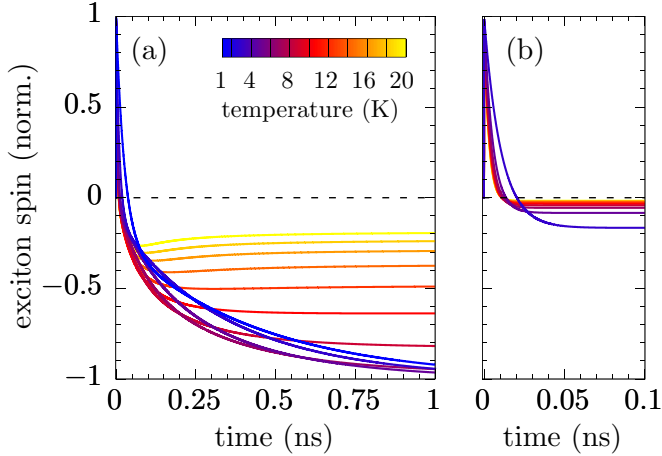
FIG. 2. Exciton spin dynamics after optical excitation for different temperatures (a) with LA phonon scattering and (b) without phonon scattering taken into account. All curves are normalized with respect to the maximum spin polarization.
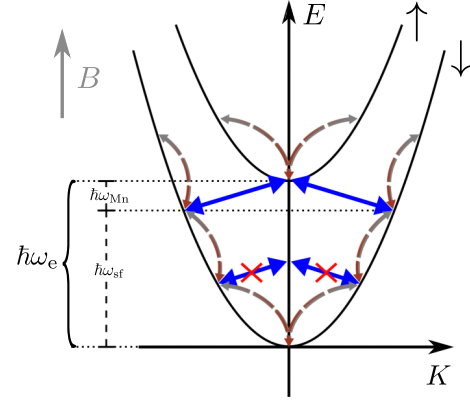

FIG. 3. Sketch of the scattering processes in an external magnetic field B between the spin-up ($\uparrow$) and spin-down ($\downarrow$) $1s$ exciton parabolas. The spin-flip scattering due to the sd exchange interaction is indicated by blue arrows while LA phonon scattering is sketched by arrows with a color gradient from gray to brown, which in turn indicates the imbalance between phonon emission and absorption at low temperatures. Forbidden spin-flip transitions are marked by red crosses and $\hbar\omega_{sf}$ denotes the spin-flip scattering shift given by $\hbar\omega_e - \hbar\omega_{Mn}$, where the Zeeman energy of excitons and impurities is denoted by $\hbar\omega_e$ and $\hbar\omega_{Mn}$, respectively.

calculate the impurity spin density matrix. In the limit of either zero magnetic field or infinite temperature, the Mn spins are randomly oriented such that $\langle S^z \rangle = 0$ and the long-time value of the exciton spin is zero. This explains the decrease of the absolute value of the long-time spin polarization with rising temperature observed in Fig. 2.

Interestingly, comparing Fig. 2(a) with Fig. 2(b) reveals that phonons completely alter the magnitude of the long-time spin polarization. In Fig. 2(b), where the phonon scattering is not included in the calculations, one observes a maximal negative polarization of only 20% for very low temperatures. However, turning to Fig. 2(a), it becomes clear that this polarization increases to more than 90% at very low temperatures when phonons are accounted for. Furthermore, the overall influence of the temperature on the spin dynamics is strongly reduced for calculations without phonon scattering, as becomes evident by comparing the wide spread of the longtime values in Fig. 2(a) with those observed in Fig. 2(b). This last observation already hints at the mechanism behind the strong phonon impact on the spin dynamics: Since phonon absorption and emission processes are not equally likely at low temperatures, an imbalance is created that is only overcome at elevated temperatures. However, one has to keep in mind that phonons do not directly couple to the spin in our model since some kind of spin-orbit interaction is required to mix momentum and spin scattering.

For a better understanding of the processes involved, the situation is sketched in Fig. 3, where two exemplary spin-flip transitions are indicated by blue arrows and the scattering with LA phonons is depicted by arrows with a color gradient, indicating the imbalance between phonon emission and absorption at the low temperatures studied here. The spin-up parabola is Zeeman shifted by $\hbar\omega_e$ with respect to the spin-down parabola and the laser excitation is chosen to be resonant with this state, such that practically only spin-up excitons are present shortly after the pump pulse. After a spin-flip scattering to the spin-down parabola, the energy of an exciton decreases to $\hbar\omega_{sf} = \hbar\omega_e - \hbar\omega_{Mn}$ in accordance with energy

conservation since an energy cost of $\hbar\omega_{Mn}$ is required for the corresponding flop of an impurity spin (cf. also Sec. II B). In the presence of phonons, excitons on the spin-down parabola can then further decrease their energy via phonon emission and effectively become captured in states with energies lower than $\hbar\omega_{sf}$ on the spin-down parabola. However, a backscattering to the spin-up parabola is prohibited for such states since the final states would be below $\hbar\omega_e$, where the density of states is zero for spin-up excitons. Such processes are exemplarily indicated by crossed-out blue arrows in Fig. 3. Therefore, excitons can in this case only scatter back to the opposite spin state after absorbing a phonon with high enough energy, which is why, especially in the low-temperature limit where virtually no phonon absorption occurs, the backscattering to the spin-up state will be largely suppressed.

Indeed, looking at Fig. 4 reveals that phonons have a decisive impact on the energetic occupation on the $1s$ exciton parabola. Considering first the simpler situation without phonons, the first line of Eq. (5) predicts a scattering of an initial occupation at $\hbar\omega_1$ to states with energy $\hbar\omega_1 + \hbar\omega_{sf}$ and vice versa. This means that, for optically generated excitons with nearly vanishing center-of-mass wave vector and, thus, negligible kinetic energy, a back-and-forth scattering between $E = 0$ and $\hbar\omega_{sf}$ is expected and no other states are involved. In Figs. 4(a) and 4(b), where results for $T = 4$ and 10 K are shown, respectively, the phonon-free results are indicated by dashed lines which show a separation of exactly $\hbar\omega_{sf}$. The decrease of the spin-flip scattering shift observed in the figure is due to the increased temperature in accordance with Fig. 1.

Turning to the phonon influence, one has to be aware that phonon emission is prohibited for states at $E = 0$ since there are no exciton states with lower energy to scatter to. Thus, phonon emission can only occur once a spin-flip scattering from the spin-up (red line) to the spin-down (blue line) state
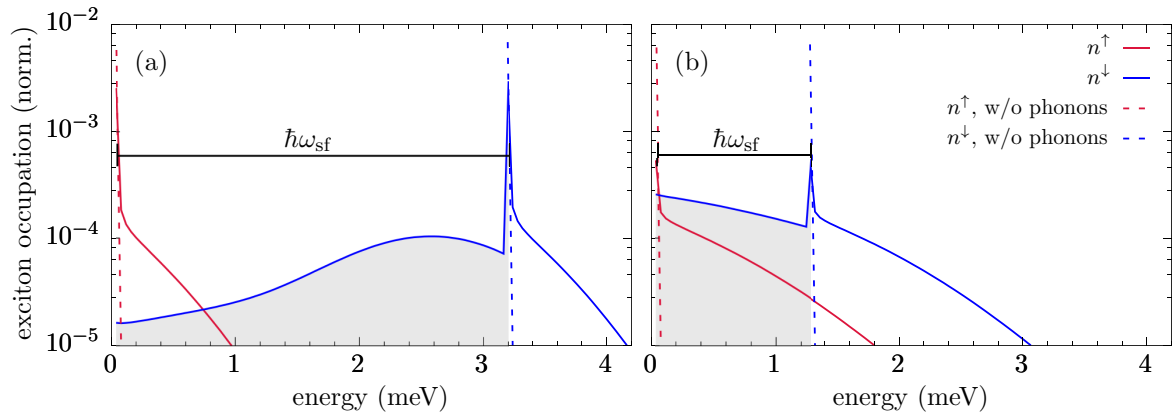
FIG. 4. Spin-up ($n^\uparrow$) and spin-down ($n^\downarrow$) occupation of the 1s exciton with and without scattering by LA phonons obtained 100 ps after the optical excitation at a temperature of (a) 4 K and (b) 10 K, respectively. For better visibility, the energy for each spin component is measured here from the bottom of the respective exciton parabola. In fact, the minimum of the spin-up exciton parabola is shifted by $\hbar\omega_e^z$ (cf. Fig. 3). Blocked spin-down states which cannot scatter back to the spin-up parabola are indicated by the grayed out area and $\hbar\omega_{sf}$ is the spin-flip scattering shift induced by the external magnetic field including the giant Zeeman shift. The occupation is normalized with respect to the exciton density after the pulse.

has taken place. However, since a spin flip of an exciton also implies a change of its kinetic energy by the spin-flip scattering shift, phonons start to decrease the kinetic energy of excitons via emission processes as soon as a spin flip occurs. But, because the energy of the exciton then inevitably falls below $\hbar\omega_{sf}$, there is suddenly no corresponding state with opposite spin available that can be reached via exchange interaction scattering as its energy would have to be below $E = 0$.

All in all, the resulting dynamics behaves like a quantum ratchet, i.e., there is an imbalance between different scattering processes such that spin-down states are strongly favored. For the curves in Fig. 4 where the phonon scattering is included, this means that the spin-down states with $E < \hbar\omega_{sf}$ are effectively blocked and cannot scatter back to a spin-up state (cf. the grayed-out areas in Fig. 4). This leads to a much larger spin-down occupation compared with the spin-up component already after 100 ps as depicted in the figure. Note that, after 100 ps, the exciton system has not yet reached its thermal equilibrium for the parameters studied here. In fact, a full thermalization of the exciton system due to the phonon influence only occurs on a nanosecond timescale. The observation that the ratchet effect is apparently diminished with rising temperature can be explained by the combination of two effects. First, the spin-flip scattering shift decreases with increasing temperature as shown in Fig. 1. Second, phonon absorption becomes increasingly likely so that the scattering towards higher energies becomes possible.

It should be noted that the sizable spin-flip scattering shift due to the giant Zeeman effect in DMSs is an important ingredient for the quantum ratchet discussed here. Since the typical Zeeman shifts in nonmagnetic semiconductors are rather small, the resulting energy gap between the spin-up and the spin-down parabola can be efficiently bridged by phonons already at very low temperatures. Thus, in DMSs, the large impact of phonons on the spin dynamics is a direct consequence of the magnitude of $\hbar\omega_{sf}$.

B. Markovian vs non-Markovian predictions

Up to this point, all scattering processes have been considered Markovian, i.e., on the single-particle level. However, a single exciton not only interacts with one isolated Mn atom, but rather with many impurities. Previous theoretical works have demonstrated that the many-body nature of the sp-d exchange interaction in fact manifests in non-Markovian features of the exciton spin dynamics [30,38] as well as distinct features in optical spectra [34], effects which require a treatment of the exciton-impurity interaction beyond the single-particle level.

Concerning the quantum-ratchet effect discussed in the previous section, the redistribution of exciton kinetic energies due to the scattering with LA phonons to values smaller than the spin-flip scattering shift is found to be of major importance. This leads to the question whether the exciton-phonon interaction is the only one causing such a redistribution. In fact, it turns out that a treatment of the carrier-impurity interaction beyond the mean-field level can also significantly change the energy of the carriers beyond what is expected if the sp-d exchange interaction is treated as a purely elastic process [30,38,40]. The reason why a change of the kinetic energy can occur is that a quantum-kinetic treatment accounts for the energy-time uncertainty and, thus, does not strictly enforce energy conservation on the single-particle level on short timescales. Moreover, due to the many-body character of the exciton-impurity interaction, the effective single-particle exciton states are no longer the correct energy eigenstates of the system. As it turns out, the latter effect is very important in DMS nanostructures and leads to the buildup of a negative many-body correlation energy that can reach values up to several meV per exciton [34,37,40]. Since this correlation energy persists even in the long-time limit, the carrier kinetic energy increases accordingly, leading to a pronounced broadening of the carrier distribution.

To investigate the impact of many-body effects due to the sp-d interaction on the ratchet-type dynamics discussed in the previous section, we look at the spin-down occupation
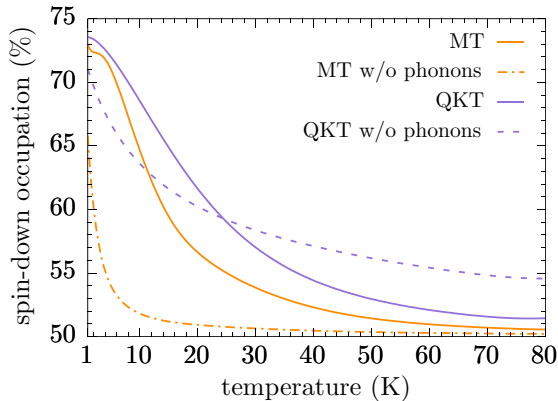
FIG. 5. Spin-down occupation after 100 ps with respect to the total exciton density calculated using the Markovian theory (MT) given by Eq. (5) and a quantum-kinetic theory (QKT), where the latter explicitly accounts for exciton-impurity correlations. Also included are simulations where the scattering with phonons is switched off (without phonons).

reached after 100 ps after the laser excitation as obtained by the purely Markovian theory described by Eq. (5) and compare the results to those of a calculation based on a quantum-kinetic theory (QKT) of the exciton-impurity scattering, which has been recently developed in Ref. [30] and explicitly takes correlations between excitons and impurities into account. For a finite magnetic field and limiting the discussion to the exciton ground state, the necessary equations of motion for the exciton density, the spin, and the exciton-impurity correlations can be found explicitly in the Appendix of Ref. [38]. In all cases, the exciton-phonon coupling is treated on the Markov level.

Figure 5 shows a comparison of the spin-down occupation at 100 ps normalized with respect to the total exciton density. The results are obtained by the MT and the QKT for the case with and without phonons as a function of the temperature. As has been already found in Fig. 2, phonons lead to large spin-down occupations especially at low temperatures when all interactions are treated on the Markov level. For higher temperatures, the spin-down occupation quickly decreases and approaches the phonon-free calculation. Note that a spin-down occupation of 50% implies a balanced distribution of exciton spins in both spin channels, as would be expected without an external magnetic field. Qualitatively, the QKT with phonon scattering shows a similar behavior compared with the MT, although the spin-down occupations as predicted by the QKT are consistently larger.

The influence of the many-body nature of the exciton-impurity interaction becomes most apparent when the phonon-free simulations are compared: There, we find a significantly higher occupation of the spin-down states for the QKT compared with the MT for all considered temperatures. The reason for this is that, while only a back-and-forth scattering between $E = 0$ and $\hbar\omega_{\text{sf}}$ can occur in the MT without phonons (cf. Fig. 4), the QKT captures a redistribution of excitons to other energies even without phonons in accordance with the buildup of a many-body correlation energy. This means that, similar to the scattering due to phonons, there

is now a finite possibility for spin-down excitons to occupy states below $E = \hbar\omega_{\text{sf}}$ such that they cannot directly scatter back to the spin-up state via the *sp-d* exchange interaction and, once again, a quantum-ratchet effect occurs. In fact, the scattering of excitons predicted by the QKT is rather significant for the impurity content considered here, which can be inferred from a comparison of the QKT results with and without phonons. Since the only change between the two results is the absence of phonon scattering in one case, the fact that the two curves lie close together compared to the respective results of the MT means that the quantum-kinetic scattering due to the exchange interaction provides the dominant contribution. The reason why in the MT phonons seem to have a larger impact is the strict single-particle energy conservation which makes the ratchet effect impossible when only the spin-flip exchange scattering on the Markov level is accounted for.

IV. CONCLUSION

We have investigated the phonon impact on the long-time value of the exciton spin polarization in DMS quantum wells after optical excitation resonant with the exciton ground state. The scattering of excitons to states with lower energies, which is the dominant phonon process at low temperatures, in combination with the much faster spin-flip scattering due to the exciton-impurity interaction in DMSs leads to a ratchet-type spin dynamics that highly favors the energetically lower spin polarization. For temperatures on the order of 5 K or below and a complete spin-up polarization after the excitation pulse, this effect is so strong that spin-down polarizations in excess of 90% can be reached on a nanosecond timescale.

A rate-equation model, where all interactions are treated equally on the Markov level, allowed us to identify the quantum-ratchet effect in terms of spin-flip processes that become energetically blocked after phonon emission has occurred. The fingerprint of the significant spin-down polarization is also visible in the exciton distribution as a function of energy. A comparison of the spin-down occupation reached at 100 ps predicted by the MT with the results of a more advanced quantum-kinetic description of the exciton spin dynamics reveals an overall qualitative agreement, provided that the exciton-phonon scattering is included in both approaches. However, quantitative differences are not negligible.

Without phonons, the quantum ratchet completely disappears in the MT while it is still present when the exciton-impurity scattering is treated on a quantum-kinetic level. The reason for this behavior is the redistribution of exciton kinetic energies due to a finite correlation energy, a many-body effect which is automatically included in the QKT but is not captured in the MT since it is beyond the single-particle level. As this effect does not depend on the phonon scattering and is independent of the temperature, the quantum-ratchet effect is retained by the QKT even in the absence of phonon scattering.

APPENDIX: EXCITON AND PHONON FORM FACTORS

The form factor stemming from the projection onto the exciton basis reads [30]

$$
F_{\eta_1 1s1s}^{\eta_2 \omega_1 \omega_2} = 2\pi \int_0^{2\pi} d\psi \int_0^\infty dr \int_0^\infty dr'\, rr' R_{1s}^2(r) R_{1s}^2(r')
$$
$$
\times J_0(\eta_1 K_{12}(\psi) r) J_0(\eta_2 K_{12}(\psi) r'), \quad \text{(A1)}
$$

where $K_{12} = |\mathbf{K}_1 - \mathbf{K}_2|$, ψ denotes the angle between $\mathbf{K}_1$ and $\mathbf{K}_2$, and $K_i = \sqrt{\frac{2M\omega_i}{\hbar}}$. In addition, $J_0(x)$ is the cylindrical Bessel function of order zero and $\eta_i = \frac{m_i}{M}$ with $i \in \{e, h\}$ is the ratio between either the electron mass m_e or the heavy-hole mass m_h and the exciton mass M, respectively. Projected down to the energetically lowest quantum well confinement state,

the coupling to the LA phonons can be subsumed in [31]

$$
\Lambda_{1s1s}^{\omega_1 \omega_2} = \frac{P_{1s1s}^{\omega_1 \omega_2} |\omega_1 - \omega_2|}{\sqrt{1 - \frac{2Mv^2}{\hbar}}} \left| f\left(\frac{|\omega_1 - \omega_2|}{v} \sqrt{1 - \frac{2Mv^2}{\hbar}} \right) \right|^2
$$
$$
\text{(A2)}
$$

with

$$
P_{1s1s}^{\omega_1 \omega_2} = \frac{2\pi}{\hbar \rho v^3 V} \left(D_e^2 F_{\eta_h 1s1s}^{\eta_h \omega_1 \omega_2} + D_h^2 F_{\eta_e 1s1s}^{\eta_e \omega_1 \omega_2} \right.
$$
$$
\left. + 2 D_e D_h F_{-\eta_h 1s1s}^{\eta_e \omega_1 \omega_2} \right). \quad \text{(A3)}
$$

We assume infinitely high quantum well barriers so that

$$
f(q_z) = \frac{\sin\left(\frac{qd}{2}\right)}{\frac{qd}{2}} \left[1 - \left(\frac{qd}{2\pi} \right)^2 \right]^{-1}. \quad \text{(A4)}
$$

[1] P. Reimann, M. Grifoni, and P. Hänggi, Phys. Rev. Lett. **79**, 10 (1997).

[2] Y. S. Ang, Z. Ma, and C. Zhang, Sci. Rep. **5**, 7872 (2015).

[3] M. O. Magnasco, Phys. Rev. Lett. **71**, 1477 (1993).

[4] T. Salger, S. Kling, T. Hecking, C. Geckeler, L. Morales-Molina, and M. Weitz, Science **326**, 1241 (2009).

[5] C. Zhang, C.-F. Li, and G.-C. Guo, Sci. Bull. **60**, 249 (2015).

[6] M. V. Costache and S. O. Valenzuela, Science **330**, 1645 (2010).

[7] I. Žutić, J. Fabian, and S. Das Sarma, Rev. Mod. Phys. **76**, 323 (2004).

[8] D. Awschalom and M. Flatté, Nat. Phys. **3**, 153 (2007).

[9] T. Dietl, Nat. Mater. **9**, 965 (2010).

[10] H. Ohno, Nat. Mater. **9**, 952 (2010).

[11] D. D. Awschalom, L. C. Bassett, A. S. Dzurak, E. L. Hu, and J. R. Petta, Science **339**, 1174 (2013).

[12] V. K. Joshi, Eng. Sci. Technol., Int. J. (Wash.) **19**, 1503 (2016).

[13] J. K. Furdyna, J. Appl. Phys. **64**, R29 (1988).

[14] *Semiconductors and Semimetals*, edited by J. K. Furdyna and J. Kossut (Academic, San Diego, 1988).

[15] *Introduction to the Physics of Diluted Magnetic Semiconductors*, edited by J. Kossut and J. A. Gaj (Springer, Berlin, 2010).

[16] T. Dietl and H. Ohno, Rev. Mod. Phys. **86**, 187 (2014).

[17] S. A. Crooker, D. D. Awschalom, J. J. Baumberg, F. Flack, and N. Samarth, Phys. Rev. B **56**, 7574 (1997).

[18] C. Camilleri, F. Teppe, D. Scalbert, Y. G. Semenov, M. Nawrocki, M. Dyakonov, J. Cibert, S. Tatarenko, and T. Wojtowicz, Phys. Rev. B **64**, 085331 (2001).

[19] C. J. P. Smits, S. C. A. van Driel, M. van Kampen, W. J. M. de Jonge, B. Koopmans, and G. Karczewski, Phys. Rev. B **70**, 115307 (2004).

[20] A. Murayama, K. Seo, K. Nishibayashi, I. Souma, and Y. Oka, Appl. Phys. Lett. **88**, 261105 (2006).

[21] Z. Ben Cheikh, S. Cronenberger, M. Vladimirova, D. Scalbert, F. Perez, and T. Wojtowicz, Phys. Rev. B **88**, 201306 (2013).

[22] M. Vladimirova, S. Cronenberger, P. Barate, D. Scalbert, F. J. Teran, and A. P. Dmitriev, Phys. Rev. B **78**, 081305 (2008).

[23] G. Bastard and R. Ferreira, Surf. Sci. **267**, 335 (1992).

[24] Y. G. Semenov, Phys. Rev. B **67**, 115319 (2003).

[25] S. Das Sarma, E. H. Hwang, and A. Kaminski, Phys. Rev. B **67**, 155201 (2003).

[26] Ł. Cywiński and L. J. Sham, Phys. Rev. B **76**, 045205 (2007).

[27] J. H. Jiang, Y. Zhou, T. Korn, C. Schüller, and M. W. Wu, Phys. Rev. B **79**, 155201 (2009).

[28] M. Z. Maialle, E. A. de Andrada e Silva, and L. J. Sham, Phys. Rev. B **47**, 15776 (1993).

[29] E. Tsitsishvili and H. Kalt, Phys. Rev. B **73**, 195402 (2006).

[30] F. Ungar, M. Cygorek, and V. M. Axt, Phys. Rev. B **95**, 245203 (2017).

[31] F. Ungar, M. Cygorek, and V. M. Axt, arXiv:1810.11241.

[32] H. Ohno, Science **281**, 951 (1998).

[33] I. Di Marco, P. Thunström, M. I. Katsnelson, J. Sadowski, K. Karlsson, S. Lebègue, J. Kanski, and O. Eriksson, Nat. Commun. **4**, 2645 (2013).

[34] F. Ungar, M. Cygorek, and V. M. Axt, Phys. Rev. B **98**, 161201(R) (2018).

[35] C. Thurn and V. M. Axt, Phys. Rev. B **85**, 165203 (2012).

[36] S. Rudin and T. L. Reinecke, Phys. Rev. B **41**, 3017 (1990).

[37] M. Cygorek, F. Ungar, P. I. Tamborenea, and V. M. Axt, Phys. Rev. B **95**, 045204 (2017).

[38] F. Ungar, M. Cygorek, and V. M. Axt, Phys. Rev. B **97**, 045210 (2018).

[39] T. Uenoyama and L. J. Sham, Phys. Rev. Lett. **64**, 3070 (1990).

[40] C. Thurn, M. Cygorek, V. M. Axt, and T. Kuhn, Phys. Rev. B **87**, 205301 (2013).

Publication 7

Origins of overshoots in the exciton spin dynamics in semiconductors

F. Ungar, M. Cygorek, and V. M. Axt

&

Erratum: Origins of overshoots in the exciton spin dynamics in semiconductors

F. Ungar, M. Cygorek, and V. M. Axt

Origins of overshoots in the exciton spin dynamics in semiconductors

F. Ungar,[1] M. Cygorek,[2] and V. M. Axt[1]

[1]*Theoretische Physik III, Universität Bayreuth, 95440 Bayreuth, Germany*
[2]*Department of Physics, University of Ottawa, Ottawa, Ontario, Canada K1N 6N5*

We investigate the origin of overshoots in the exciton spin dynamics after resonant optical excitation. As a material system, we focus on diluted magnetic semiconductor quantum wells as they provide a strong spin-flip scattering for the carriers. Our study shows that overshoots can appear as a consequence of radiative decay even on the single-particle level in a theory without any memory. The magnitude of the overshoots in this case depends strongly on the temperature as well as the doping fraction of the material. If many-body effects beyond the single-particle level become important so that a quantum-kinetic description is required, a spin overshoot appears already without radiative decay and is much more robust against variations of system parameters. We show that the origin of the spin overshoot can be determined either via its temperature dependence or via its behavior for different doping fractions. The results can be expected to apply to a wide range of semiconductors as long as radiative decay and a spin-flip mechanism are present.

I. INTRODUCTION

It is well known that, whereas the dynamics of isolated few-level quantum systems is oscillatory with frequencies corresponding to its eigenenergies, quantum systems weakly coupled to a Markovian environment exhibit an exponentially decaying dynamics. If, however, the coupling to the bath is not weak or the bath is non-Markovian, the decay is, in general, not exponential. Instead, traces of the underlying coherent oscillatory behavior can remain visible in the dynamics in the form of overshoots. Thus signal overshoots are a quite fundamental property of many physical systems. In the literature, overshoots are encountered in a wide variety of material systems and have recently been discussed and observed, e.g., in vertical-cavity surface-emitting lasers [1], the ultrafast dynamics of amorphous magnets [2], or in the spin-lattice relaxation measured via nuclear magnetic resonance [3].

Here, we focus on the latter area of spin physics and provide a theoretical description of spin overshoots in diluted magnetic semiconductors (DMSs), a material class where standard semiconductors are doped with a small number of magnetic impurities such as manganese [4–7]. Besides their importance for possible spintronics applications [8–13], these materials exhibit rich many-body physics [14–16] due to pronounced correlation effects between the carrier and the impurity subsystem.

In II-VI DMSs, where the doping with Mn ions does not lead to additional charges, the impurities provide a strong spin-flip mechanism for the carriers via the exchange interaction which typically dominates the spin dynamics [6,7]. Recent theoretical work shows that an adequate description of the spin dynamics in these systems actually requires a treatment of the exchange interaction beyond the single-particle level in order to account for carrier-impurity correlations [17–20]. Using such a quantum kinetic approach, the finite memory induced by the correlations was found to lead to

overshoots in the spin dynamics both for quasifree carriers [17] as well as for electron-hole pairs bound by the Coulomb interaction [19]. Furthermore, it has been shown that for excitons such non-Markovian effects can even explain the quantitative deviation between spin-transfer rates obtained by Fermi's golden rule and the experimental data obtained by several independent groups [19,21].

In general, spin overshoots represent a very attractive qualitative signature of non-Markovian effects since they are easy to distinguish from a monoexponential decay as predicted by Fermi's golden rule. However, it turns out that overshoots can also be caused by another, much simpler mechanism: the combination of radiative decay with optical spin selection rules. To see this, one can envision a system with two spin channels where only one couples to the light field and the other is dark. Then the occupation in the bright channel will decay while spins in the dark channel are not affected until a spin flip occurs. Thus, when looking at the total spin given by the sum of the populations of the two channels, an overshoot can occur. This appears very naturally already on the Markov level where no correlations are accounted for since the only requirements for such a dynamics are the existence of a bright and a dark spin channel as well as a suitably strong spin-flip mechanism.

It is therefore an important task to discern overshoots in the spin dynamics in DMSs caused by radiative decay from those caused by genuine non-Markovian effects, which is the main goal of this paper. To this end, simulations are performed for manganese-doped ZnSe quantum well nanostructures which are optically excited at the $1s$ exciton resonance. On the Markov level, the origin of the spin overshoot can also be made quite transparent by going over to a minimal model, retaining only a decay of each spin population as well as a spin-transfer rate between them. It is found that overshoots in this model caused by radiative decay are most pronounced at low temperatures where phonon absorption is negligible

and that phonons significantly inhibit overshoots at elevated temperatures. However, a quantum kinetic treatment of the exciton-impurity exchange interaction yields an overshoot which is much more robust against variations of the temperature and does not rely on a finite radiative decay rate.

In order to provide suggestions as to how the origin of spin overshoots can be determined in experiments for a particular sample, we provide a comparison of the results of the Markovian theory (MT) as well as the quantum kinetic theory (QKT) that reveals drastically different trends and dependences of the overshoot on parameters such as the temperature and the doping fraction. These results can be expected to hold also for a larger class of materials since they in principle only rely on radiative decay and the presence of a spin-flip mechanism. Thus our investigation allows one to determine whether an overshoot encountered in the spin dynamics is dominated by radiative decay or many-body effects in a particular sample.

II. THEORETICAL BACKGROUND

First, the constituting parts of the Hamiltonian which is used for the description of the spin dynamics in DMSs are briefly discussed and an intuitive explanation of the relevant spin-flip processes is given. Furthermore, we provide the equation of motion for the spin-up and spin-down exciton density in the Markov approximation from which the spin dynamics can be calculated. Finally, the general structure of this equation is discussed using a minimal model which also allows us to analyze the preconditions for the appearance of spin overshoots.

A. Exciton-spin dynamics in diluted magnetic semiconductors

Concerning the spin dynamics in DMSs, the dominant interaction is given by the *sd* (*pd*) exchange interaction that induces spin flips between *s*-type electrons (*p*-type holes) and the localized *d*-shell electrons of the magnetic impurities [6]. Apart from the magnetic exchange interaction, we also take the scattering of carriers with longitudinal acoustic (LA) phonons into account [22,23]. Longitudinal optical (LO) phonon scattering can be disregarded here since it is negligible below temperatures of about 80 K and the kinetic energies encountered here are well below the LO-phonon threshold [24]. We also assume a linear phonon dispersion $\omega_{\mathbf{q}}^{\mathrm{ph}} = vq$ because of the small exciton center-of-mass momenta involved in the dynamical processes after an optical excitation resonant with the exciton ground state. Additional contributions to the Hamiltonian include the carrier kinetic energies, the Coulomb interaction responsible for the exciton binding, and the light-matter coupling in the dipole approximation. Furthermore, the local potential mismatch in the lattice due to the doping with impurities is captured by adding a non-magnetic scattering contribution that does not depend on the carrier spin [25]. The model is further extended to include the radiative decay of excitons quantified by a fixed rate Γ_0 [16]. Instead of providing the lengthy explicit expressions for all contributions to the Hamiltonian, here we merely present a comprehensive sketch of the relevant processes and refer the reader to Ref. [22] for the formal details.
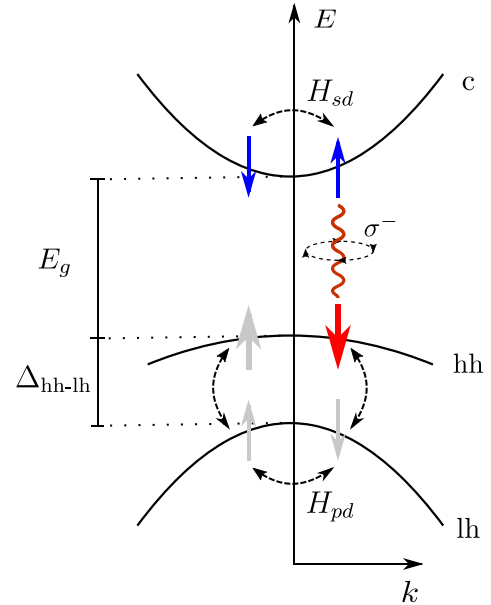
FIG. 1. Sketch of the spin system under consideration. Illustrated are the dispersions of the conduction (c), and the heavy-hole (hh), as well as the light-hole (lh) band in the parabolic effective-mass approximation. The former two are separated by the band gap E_g, whereas the latter two are split by the hh-lh splitting Δ. Small arrows denote either spins in the conduction band with quantum number $s_z = \pm\frac{1}{2}$ or spins in the valence band with angular momentum quantum number $j_z = \pm\frac{1}{2}$, whereas the larger arrows correspond to hh spins characterized by $j_z = \pm\frac{3}{2}$. The *sd* exchange interaction (H_{sd}) mediates spin flips in the conduction band and the *pd* exchange interaction (H_{pd}) causes transitions between hh and lh spins. Photons with σ^- polarization (squiggly line) either create an electron-hh pair in the right spin channel or are emitted upon its recombination. Grayed-out arrows indicate spin states which are not accessible after excitation of a hh with $j_z = -\frac{3}{2}$ due to energetic separation.

When discussing excitons in quantum wells, it is typically sufficient to account for the lowest *s*-like conduction band as well as the topmost *p*-like valence band, which are separated by the band gap E_g [26]. However, due to the confinement along the growth direction as well as strain in the semiconductor structure, the valence band splits in a heavy (hh) and a light hole (lh) branch separated by the hh-lh splitting Δ, as sketched in Fig. 1. There, small arrows denote electrons with spin quantum number $s_z = \pm\frac{1}{2}$ as well as lh states with total angular momentum quantum number $j_z = \pm\frac{1}{2}$. Heavy holes with $j_z = \pm\frac{3}{2}$ are represented by thick arrows. An optical excitation with σ^--polarized light creates an electron-hole pair with $s_z = \frac{1}{2}$ and $j_z = -\frac{3}{2}$ in accordance with angular momentum conservation. In Fig. 1, this process as well as the reverse process, where an electron-hole pair recombines and emits a photon, is represented on the right side of the figure by the squiggly line.

The previously mentioned carrier-impurity exchange interaction mediates spin-flips in this model, such that H_{sd} couples spin-up and spin-down electrons in the conduction band and H_{pd} couples lh spins in the valence band. However, in the absence of mixing between heavy and light holes, H_{pd} does

not provide a direct coupling between the different hh spin states. Thus, in order to flip its spin, the hh must pass through the lh states. If the hh-lh splitting is large enough, this process is off resonant on the order of Δ such that the hh spin is effectively pinned [27–30]. Although there are mechanisms causing a hh-lh mixing such as the long-range part of the Coulomb interaction [31,32], the corresponding interaction energy is several orders of magnitude smaller than the typical energy of the carrier-impurity exchange interaction in DMSs [20], which is why we neglect the hh-lh mixing here. In that case, the description of the spin dynamics can be effectively limited to only two exciton parabolas, namely that of an electron with spin up or down combined with a hh with $j_z = -\frac{3}{2}$. These states are then conveniently labeled by the spin state of the electron since the hh spin does not change throughout the dynamics, as well as the corresponding center-of-mass wave number (or kinetic energy) of the exciton.

Treating the scattering of excitons with impurities and the optical excitation, as well as the exciton-phonon scattering as Markov processes, the equations of motion for the spin-up and spin-down exciton density $n_{\omega_1}^{\uparrow/\downarrow}$ at a fixed frequency ω_1 can be written as [22]

$$
\begin{aligned}
\frac{\partial}{\partial t} n_{\omega_1}^{\uparrow/\downarrow} = {} & \Gamma_E(\omega_1, t) - \Gamma_{\text{rad}}^{\uparrow/\downarrow}(\omega_1)\, n_{\omega_1}^{\uparrow/\downarrow} + \Gamma_{\text{sf}}(\omega_1)\big(n_{\omega_1}^{\downarrow/\uparrow} - n_{\omega_1}^{\uparrow/\downarrow}\big) \\
& + \int_0^\infty d\omega\, D(\omega) \Lambda_{1s1s}^{\omega_1\omega}\big[\Theta\big(\omega - \omega_1 - \omega_{\omega-\omega_1}^{\text{ph}}\big)(n_\omega^{\uparrow/\downarrow}[1 + n^{\text{ph}}(\omega - \omega_1)] - n_{\omega_1}^{\uparrow/\downarrow} n^{\text{ph}}(\omega - \omega_1)) \\
& + \Theta\big(\omega_1 - \omega - \omega_{\omega_1-\omega}^{\text{ph}}\big)(n_\omega^{\uparrow/\downarrow} n^{\text{ph}}(\omega_1 - \omega) - n_{\omega_1}^{\uparrow/\downarrow}[1 + n^{\text{ph}}(\omega_1 - \omega)])\big].
\end{aligned}
\tag{1}
$$

Considering a Gaussian pulse shape $E(t) = E_0 \exp(-\frac{t^2}{2\sigma^2})$ with amplitude E_0, the optical generation of excitons is given by the rate

$$
\Gamma_E(\omega, t) = \frac{1}{\hbar^2} E(t) E_0 |M_{\uparrow/\downarrow}|^2 \phi_{1s}^2 \int_{-\infty}^t d\tau\, e^{-\frac{\tau^2}{2\sigma^2}}\, \delta_{\omega,0}^b, \tag{2}
$$

with the matrix element $|M_{\uparrow/\downarrow}|^2$ containing the spin selection rules and $\phi_{1s} = R_{1s}(r = 0)$ denoting the radial part of the 1s exciton wave function evaluated at the origin. The delta function $\delta_{\omega,0}^b$ reflects the fact that resonant optical excitation occurs only at the bottom of the exciton parabola, which is chosen as the origin of the energy scale here as indicated by the second subscript of the delta function. To ensure a scalable as well as stable numerical evaluation of the delta function, we approximate it by a narrow Gaussian according to $\delta_{\omega,0}^b = \frac{1}{\sqrt{\pi} w_b} \exp[-(\hbar\omega/2w_b)^2]$ that is normalized with respect to an integration over all positive frequencies. Thus we obtain an effectively broadened delta function as indicated by the superscript b. The width of the Gaussian $w_b = 1$ eV is chosen such that only states in close proximity of the exciton resonance at $\hbar\omega = 0$ couple to the light field. We focus on excitation scenarios where few excitons compared to the number of impurities are excited such that the average impurity spin remains essentially constant during the dynamics. Radiative decay is modeled via the spin-dependent rates $\Gamma_{\text{rad}}^\uparrow(\omega) = \Gamma_0 \delta_{\omega,0}^b$ and $\Gamma_{\text{rad}}^\downarrow(\omega) = 0$, where the latter reflects the optically dark nature of the spin-down exciton state. As for the optical excitation, the slightly broadened delta function $\delta_{\omega,0}^b$ ensures that only states in the vicinity of the bottom of the exciton parabola can undergo radiative decay.

Without an external magnetic field, the spin-flip rate due to the scattering of excitons with the magnetic impurities in the crystal does not distinguish any spin orientation and only depends on the exciton frequency ω. It is given by [19]

$$
\Gamma_{\text{sf}}(\omega) = \frac{35 I N_{\text{Mn}} M J_{sd}^2}{12 \hbar^3 V d} F_{\eta_{\text{h}} 1s1s}^{\eta_{\text{h}}\omega\omega} \tag{3}
$$

with a factor $I = 3/2$ from the projection of the wave function onto the quantum well whose thickness is given by d. The number of Mn impurities in the sample is given by N_{Mn} and M is the exciton mass. Furthermore, $F_{\eta_{\text{h}} 1s1s}^{\eta_{\text{h}}\omega\omega}$ denotes the frequency-dependent exciton form factor which appears due to the projection of the dynamics onto the exciton basis and which contains the exciton wave function [19]. An explicit expression of the form factor can be found in the Appendix of Ref. [23].

The integral that appears in Eq. (1) contains expressions stemming from the exciton-phonon scattering. There, $D(\omega) = \frac{VM}{2\pi\hbar d}$ is the constant density of states for a two dimensional system and $\Theta(\omega)$ is the Heaviside step function and the phonon density is assumed to follow a thermal occupation according to $n^{\text{ph}}(\omega) = 1/[\exp(\hbar\omega/k_B T) - 1]$. Finally, $\Lambda_{1s1s}^{\omega_1\omega}$ is the exciton-phonon matrix element which contains the influence of the exciton wave function and the exciton-phonon coupling. For an explicit expression of this matrix element, the reader is referred to the Appendix of Ref. [23]. Note that the z component of the spin can be extracted from the spin-up and spin-down exciton density via $s_\omega^z = \frac{1}{2}(n_\omega^\uparrow - n_\omega^\downarrow)$.

However, as shown in previous theoretical works for excitons [16,19,20,22] as well as quasifree conduction-band electrons [17,18,33], a Markovian treatment of the typically dominant carrier-impurity exchange interaction such as given by Eq. (1) is often insufficient since it cannot capture correlation effects beyond the single-particle picture. Furthermore, typical theoretical descriptions of the spin dynamics in DMSs based on Fermi's golden rule [29,34–37] artificially enforce momentum as well as energy conservation on the single-particle level, where the former assumption is violated for systems with few randomly localized scatterers such as DMSs [25] and the latter neglects the energy-time uncertainty. To account for these effects we have developed a full quantum kinetic theory which explicitly keeps exciton-impurity correlations as dynamical variables, which also allows us to straightforwardly describe scattering processes that do not conserve momentum [19,38]. The QKT has also just recently been extended to account for phonon scattering on the Markov

level in Ref. [22], where also the complete equations of motion can be found. In the present article, we will make use of this advanced theory to compare it with the more intuitive Markovian theory presented above. For this purpose, radiative decay is also included in the QKT in a similar manner to Eq. (1) (cf. also the Supplemental Material of Ref. [16]).

B. Minimal model for overshooting behavior

To analyze the requirements of observing an overshooting behavior in some physical quantity, we consider the following system of coupled differential equations for the time-dependent quantities a and b:

$$\frac{\partial}{\partial t}a = -\kappa_a a + \lambda(b - a),\tag{4a}$$

$$\frac{\partial}{\partial t}b = -\kappa_b b + \lambda(a - b).\tag{4b}$$

The model includes decay rates κ_a and κ_b for a and b, respectively, and allows for a transfer between the two quantities via the rate λ. Since the time scales of this model are solely determined by the value of the rates, we rescale the time such that it becomes dimensionless. The signs in Eqs. (4) are chosen such that, for typically encountered physical systems, $\kappa_{a/b} \geqslant 0$ and $\lambda \geqslant 0$. Although the transfer rate in general may be different for a transfer from a to b compared with one in the opposite direction, we limit the discussion to equal transfer rates since this is also the case for the spin-flip scattering in Eq. (1), where the scattering rate is given by Eq. (3) and does not depend on the scattering direction. The main difference with respect to the full model given by Eq. (1) is that the phonon scattering is completely left out. In terms of Eqs. (4), such a contribution would cause the quantities a and b to become a continuum of values which are all coupled to one another. However, in order to understand to origin of the overshooting behavior, the phonon contribution can be neglected, especially at low temperatures where phonon absorption is limited and phonon emission cannot occur for optically generated excitons with vanishing center-of-mass momentum.

Coming back to the minimal model at hand and using the initial conditions $a(0) = 1$ and $b(0) = 0$, Eqs. (4) can be solved exactly and a and b are both strictly between zero and one. However, instead of solving for the dynamics of a and b separately, we are interested in a third variable which is represented by a linear combination of the two. Supposing that, e.g., a and b are spin channels corresponding to spin up and spin down, respectively, the total spin in the system is $s \sim a - b$. Depending on the constants of the model, such a variable may then display the overshooting behavior we are looking for since the analytic solution will in general contain a biexponential decay.

Instead of discussing the analytic solution, which is lengthy and does not clearly display the physical insights we seek, we plot the resulting dynamics for $a - b$ for two representative choices of parameters in Fig. 2(a). Indeed, choosing $\kappa_a = 0.1$ and $\kappa_b = 0$, an overshoot appears which results from the faster decay of a compared with b, such that $a - b$ takes on negative values after a certain point in the dynamics. Reversing the situation by choosing $\kappa_a = 0$ and $\kappa_b = 0.1$ then leads to no
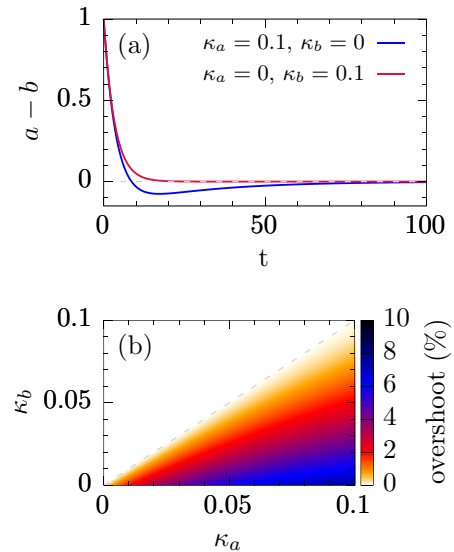
FIG. 2. Dynamics of the minimal model given by Eqs. (4) with $\lambda = 0.1$. We show (a) the dynamics of $a - b$ for two representative choices of κ_a and κ_b as well as (b) a color-coded map of the parameter space where an overshoot occurs. The percentage value of the overshoot refers to how much $a - b$ maximally dips below zero with respect to its initial value.

overshooting behavior since $b < a$ throughout the dynamics. Furthermore, due to the transitions between a and b, as soon as either κ_a or κ_b are finite both variables eventually decay to zero, which thus also holds for $a - b$ as can be seen in the figure.

To obtain an overview of the parameter space where an overshoot occurs and how large it can actually be, we plot the overshoot versus both decay rates, κ_a and κ_b, in Fig. 2(b). Any given value for the overshoot reflects the percentage of how much $a - b$ maximally dips below zero compared with its initial value of $(a - b)|_{t=0} = 1$, i.e., we define the overshoot as the distance from the global minimum of the curve with respect to its long-time value, which is zero in this case (also indicated by the gray dashed line in Fig. 2). As motivated above, the figure confirms that an overshoot can only occur in the region where $\kappa_b < \kappa_a$ below the gray dashed line and is most pronounced when $\kappa_b = 0$. The maximum overshoot obtained in the latter case is slightly below 10%. Although this model is strongly simplified, it nevertheless allows for an intuitive understanding of the physical processes encountered in the exciton spin dynamics.

Concerning DMSs, the minimal model can be applied as follows. Taking a look at Fig. 1, it is apparent that an optical pump pulse promotes an electron from the valence band to the conduction band. However, due to the optical selection rules, this creates an exciton consisting of a hh with $j_z = -\frac{3}{2}$ and an electron with $s_z = \frac{1}{2}$. Since directly after the pulse only this state is occupied, it corresponds to channel a in the minimal model, which has a finite occupation at $t = 0$. If the hh-lh splitting is large enough, only spin flips in the conduction band are likely to occur since the hh-lh splitting acts as an energy barrier which prevents a spin flip of the hh, effectively pinning it along its initial orientation. After the spin flip of
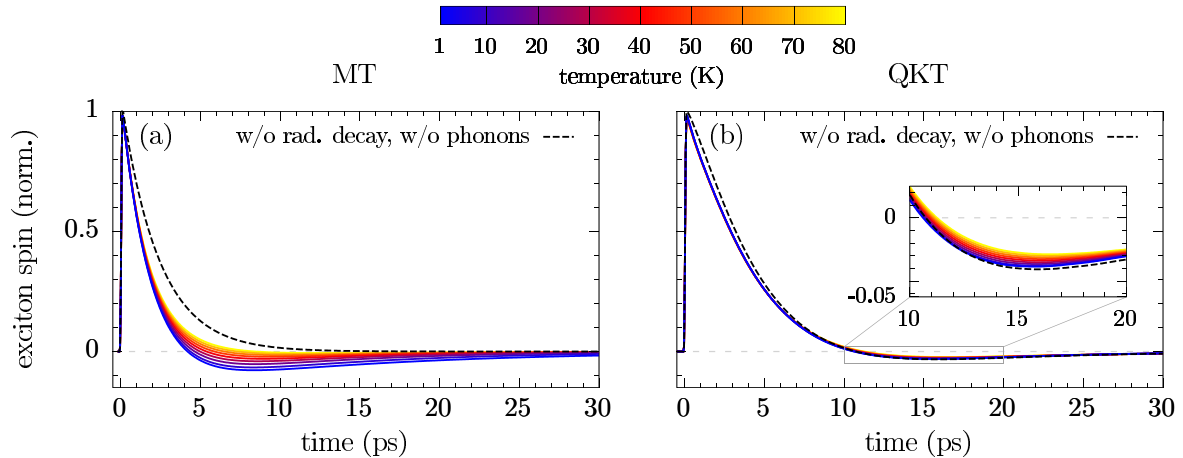
FIG. 3. Exciton-spin dynamics normalized to the maximum value after the optical excitation pulse for different temperatures for a $Zn_{0.975}Mn_{0.025}Se$ quantum well. We compare (a) results using a completely Markovian theory (MT) with (b) simulations obtained by a quantum kinetic treatment (QKT) of the exciton-impurity scattering. In addition, simulation results without radiative decay and without phonon scattering are provided for both theoretical approaches. The inset in panel (b) shows a magnified view of the area indicated by the gray rectangle.

an electron mediated by H_{sd}, one ends up with an exciton consisting again of a hh with $j_z = -\frac{3}{2}$ and an electron with $s_z = -\frac{1}{2}$, which then corresponds to channel b in the minimal model. In general, any excitation can leave the system only via radiative decay, corresponding to κ_a and κ_b for excitations involving a spin-up and a spin-down electron, respectively. Since the optical selection rules also apply in the case of radiative decay, only the population of channel a can decay since channel b is optically dark. For the minimal model, this means that one is in the regime where only κ_a has a finite value. As long as only excitons with vanishing center-of-mass momentum are present in the system, which is true in the absence of phonon scattering, the transfer rate λ between the two channels a and b can be exactly identified with $\Gamma_{sf}(0)$ as given by Eq. (3).

III. SIMULATIONS OF EXCITON-SPIN OVERSHOOTS

In this section, simulations of the exciton spin dynamics in DMSs under the influence of exciton impurity as well exciton-phonon scattering are performed while also accounting for radiative decay. Special emphasis is put on the observation of spin overshoots as well as a comparison of two different theoretical approaches, namely the MT and the more advanced QKT. First, the appearance of overshoots is investigated using both theories and the impact of higher temperatures and, thus, stronger phonon scattering is discussed. Second, we suggest specific parameter studies which would allow for an experimental determination of the origin of the spin overshoot in a given sample. For all calculations, we model a 15 nm wide $Zn_{1-x}Mn_xSe$ quantum well with doping fraction x and suppose a resonant excitation of the $1s$-hh exciton with a 100 fs long pulse. For the radiative decay we assume a rate of 0.1 ps^{-1}, such that the resulting lifetime is in line with typical experiments [39–42]. The values for the coupling constants as well as all other material parameters are the same as in Ref. [22].

A. Phonon influence on spin overshoots

Without an external magnetic field, optically oriented exciton spins are expected to decay to a vanishing net spin polarization after a characteristic time given by the inverse of the rate in Eq. (3). The typically resulting dynamics for the first 30 ps is shown in Fig. 3(a), where the data calculated using the MT given by Eq. (1) is normalized with respect to the maximum spin polarization after the pulse. Without radiative decay and the phonon influence, Eq. (1) reduces to just the optical excitation and the spin-decay rate given by Eq. (3) so that a monoexponential decay to zero occurs after the optical orientation (cf. black dashed line). With radiative decay and phonon scattering, however, this behavior changes drastically: the MT now predicts an overshoot of the exciton spin that becomes less pronounced with increasing temperature. For very low temperatures on the order of 1 K the overshoot is almost 10%, whereas it vanishes almost completely for 80 K.

To explain this behavior we turn to the minimal model introduced in Sec. II B in Eqs. (4). There, the overshoot was traced back to a slower decay of the b component compared with the a component in a signal given by $a - b$. Consequently, $a - b$ then follows a biexponential decay and is thus able to dip below zero before it completely decays, thus causing an overshoot of the signal. As already motivated in this discussion, identifying a with the spin-up and b with the spin-down exciton density allows us to straightforwardly explain the curves in Fig. 3(a) by comparing them to the results shown in Fig. 2. In the present case, the decay rate of the spin-up channel is given by 0.1 ps^{-1}, whereas the spin-down channel is unaffected by the decay since it represents a dark exciton. For comparison, the spin-decay rate (which corresponds to the transfer rate λ in the minimal model) is roughly 0.44 ps^{-1} for the parameters in Fig. 3. Since we also find an overshoot of about 10% in Fig. 2 for the appropriate parameters, we can conclude that the overshoot observed in Fig. 3(a) for very low temperatures is entirely due to radiative decay.

To understand the influence of phonons on the overshooting behavior one has to be aware that phonon absorption and emission processes are not equally likely for low temperatures and only become similar in probability when the temperature is high enough. Since phonon absorption obviously requires the presence of phonons in the system and is proportional to n^{ph} in Eq. (1), only phonon emission proportional to $1 + n^{ph}$ can occur in the low-temperature limit. However, keeping in mind that excitons are optically created with nearly vanishing center-of-mass momenta, there are simply no states with lower kinetic energies for excitons available to scatter to such that a phonon could be emitted. This explains why for temperatures on the order of a few K the dynamics is virtually unaffected by phonons since neither absorption nor emission are likely to occur. Figure 3(a) also shows that the magnitude of the overshoot decreases for elevated temperatures, which can be explained by the fact that the now more probable phonon absorption increases the exciton kinetic energy and, thus, shifts the center-of-mass momenta away from zero. But as light only couples to excitons with nearly vanishing momenta, excitons with larger momenta are optically dark and, thus, are no longer affected by radiative decay.

Turning now to Fig. 3(b), where simulations for the same parameters are shown using the QKT, we see a strikingly different behavior. There, even a calculation without radiative decay and no phonon scattering leads to an overshoot, albeit with a smaller magnitude compared with the corresponding predictions of the MT. As pointed out in a previous publication [19], the overshoot in the QKT without radiative decay is an effect that cannot be reproduced on the Markov level [cf. black dashed line in Fig. 3(a)] since it requires exciton-impurity correlations that are not captured in an effective single-particle theory. In fact, the overshoot is related to the behavior of the memory kernel which is given by a sinclike function that shows decaying oscillations [18]. Since the frequency of these oscillations depends on the energy of the carriers, the oscillations typically become averaged out when a distribution of carriers is considered so that only an overshoot remains. In general, this quantum kinetic effect becomes more pronounced in nanostructures compared with bulk systems [17]. Note also the slower decay of the exciton spin when using the QKT compared with the MT which can be traced back to a cutoff of the memory kernel at the bottom of the exciton parabola [19]. Since the MT assumes a vanishing memory, it is unable to account for either of these effects. Apart from the fact that the QKT predicts an overshoot even without radiative decay, Fig. 3(b) also reveals that phonons have basically no impact on the spin dynamics for resonantly excited excitons up to the maximum temperature of 80 K considered here [22]. This means that, for typical DMSs, correlation effects dominate and suppress overshoots due to radiative decay.

It is important to emphasize that the Markovian results shown in Fig. 3(a) become valid in non-DMS systems that are not dominated by strong correlations due to the exciton-impurity interaction. In nonmagnetic semiconductors, provided there is a suitably strong spin-flip mechanism such as, e.g., the Dyakonov-Perel' mechanism due to spin-orbit coupling [43–45], one should therefore indeed expect overshoots because of radiative decay. For the quantum kinetic results
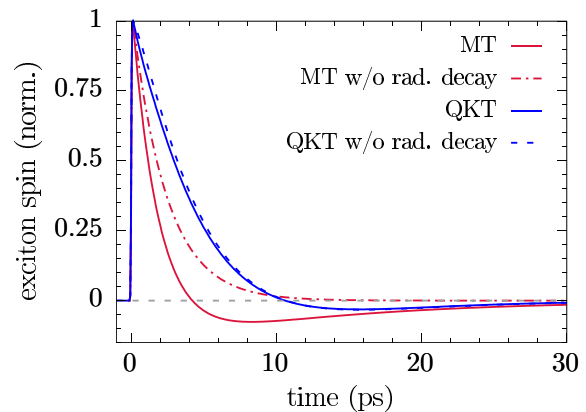

FIG. 4. Direct comparison of the overshoot predicted by the Markovian theory (MT) and the quantum kinetic theory (QKT) with and without radiative decay. The simulations are performed for a $Zn_{0.975}Mn_{0.025}Se$ quantum well at 4 K including phonon scattering.

shown in Fig. 3(b), however, exciton-impurity correlations are the crucial ingredient for the overshooting behavior. Indeed, this is typical for DMSs since the many-body interaction is strongly boosted by the magnitude of the coupling constants J_{sd} and J_{pd} in these systems [16]. From this point of view, the results obtained by the MT may be interpreted as corresponding to materials where radiative decay dominates. The range of validity of the QKT of course includes that of the MT. Thus deviations between these two levels of theory, as found for DMSs, indicate a dominance of many-body physics.

A more direct comparison between the results of the two theories regarding the influence of radiative decay is presented in Fig. 4 for a $Zn_{0.975}Mn_{0.025}Se$ quantum well at 4 K. First of all, not only does the overshoot in the MT appear sooner, but it is also more pronounced compared with the QKT result. However, as soon as radiative decay is switched off, the MT reverts to a monoexponential decay in the manner of Fermi's golden rule and no longer displays an overshooting behavior. In contrast, the influence of radiative decay on the QKT simulations is very limited. Although it does cause a slightly faster decay for the first few picoseconds, after approximately 10 ps its effect is completely negligible. This again shows that the spin dynamics in DMSs is dominated by correlations induced by the exciton-impurity exchange interaction.

B. Markovian vs quantum kinetic predictions

Regarding experiments, it is an important question to ask how the origin of a spin overshoot can be determined, i.e., how one can decide whether it is dominated by radiative decay or many-body correlations. To answer this question, we compare results of the MT with those of the QKT while varying either the temperature or the doping fraction of the DMS quantum well.

As can already be seen from Fig. 3, the influence of phonons and, thus, changing the temperature is quite different for the MT compared with the QKT. To make this different behavior more apparent, Fig. 5 displays the spin overshoot discussed in the previous section as a function
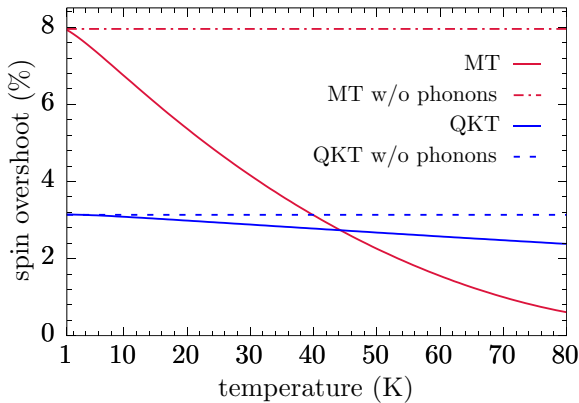
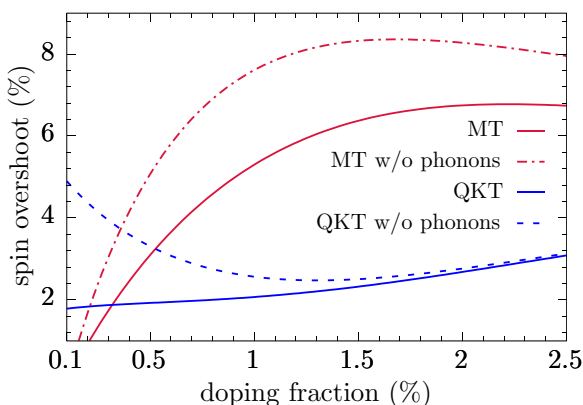FIG. 5. Overshoot of the exciton spin polarization with respect to the maximum polarization reached after optical excitation as a function of the temperature for a $Zn_{0.975}Mn_{0.025}Se$ quantum well. We compare simulations using the Markovian theory (MT) with results obtained by the quantum-kinetic approach (QKT). Results without carrier-phonon interaction (w/o phonons) are also shown.

of the temperature for the two theoretical approaches with and without phonons, respectively. In the MT, increasing the temperature causes a steep drop of the spin overshoot from 8% to almost zero when phonons are accounted for. In contrast, while a phonon influence is visible in the QKT, it does not significantly affect the spin overshoot and only causes it to decrease from about 3% at 0 K to 2.5% at 80 K. The figure also shows that the spin overshoot at low temperatures is generally smaller in the QKT compared with the MT.

Similarly, the theories predict a different dependence of the spin overshoot on the doping fraction of the quantum well, as shown in Fig. 6. In the MT, the doping fraction basically scales the spin-decay rate given by Eq. (3) since it appears as a prefactor there. This means that for fewer Mn ions the spin-decay rate becomes significantly smaller than the constant radiative decay rate, which in turn causes

FIG. 6. Overshoot of the exciton spin polarization with respect to the maximum polarization reached after optical excitation as a function of the doping fraction for a $Zn_{1-x}Mn_xSe$ quantum well at a temperature of 10 K. We compare simulations using the Markovian theory (MT) with results obtained by the quantum-kinetic approach (QKT). Results without carrier-phonon interaction (w/o phonons) are also shown.

a much faster decrease of the spin-up population compared with the scattering to the spin-down state. Thus the majority of excitons have already decayed before a significant spin-down population can be reached and only a small overshoot occurs. Increasing the doping fraction increases the spin-flip scattering and thus allows for a more pronounced overshoot that begins to slightly decrease again for doping fraction of about 2% and larger. In that case, the spin-flip scattering rate given by Eq. (3) is at least four times larger than the radiative decay rate, thus making spin flips very efficient so that the imbalance due to radiative decay becomes less pronounced. As seen before, phonons generally decrease the spin overshoot in this model.

Turning to the results of the QKT, we find an overall smaller overshoot which is, however, enhanced compared with the MT at low doping, where also the phonon influence is most noticeable. Without phonons, the spin overshoot continuously increases with increasing impurity content because of the similarly increasing correlation energy, which is roughly proportional to the doping fraction [16]. The decreasing impact of phonons on the spin overshoot with rising impurity content is explained by the quantum kinetic redistribution of excitons in K space which is not captured on the Markov level. This redistribution is made possible by the finite exciton-impurity correlations that cause the proper many-body eigenstates of the system to be a combination of states with different center-of-mass momenta, thus effectively smearing out the exciton population. This additional scattering towards higher momenta can be substantially larger than the phonon scattering, especially at high doping fractions and on short time scales [22]. All in all, it becomes clear that an overshoot stemming from carrier-impurity correlations is much more robust against variations of the temperature as well as a change of the doping fraction compared with the effect of radiative decay.

IV. CONCLUSION

We have investigated the origin of overshoots appearing in the spin dynamics of resonantly excited excitons in DMS quantum wells. On the Markov level, overshoots can appear as a consequence of radiative decay combined with strong spin-flip scattering mechanisms, such as the carrier-impurity exchange interaction in DMSs. Using a minimal model where only radiative decay and a spin-flip rate between two spin populations are present even allowed for a straightforward estimation of the parameter space where overshoots can occur.

Modeling realistic samples, we have investigated the temperature influence on spin overshoots by accounting for LA phonon scattering within a Markovian description that is expected to be valid for situations where no strong many-body correlations are built up (e.g., in nonmagnetic semiconductors with spin flips resulting from spin-orbit coupling). Phonons reduce the spin overshoot and can even cause it to nearly vanish close to liquid nitrogen temperatures. The reason for this is the enhanced scattering of excitons away from the region near $K = 0$ towards higher center-of-mass momenta and, thus, optically dark states. If the temperature is low enough, however, overshoots of up to 10% are predicted by our model.

To the best of our knowledge, such a nonmonotonic spin decay has so far only been found using a more advanced quantum kinetic theory [18,19].

Having found spin overshoots on the Markov level caused by radiative decay obviously raises the question as to how one can determine the origin of an overshooting behavior observed in experiments. We provide an answer to this question by directly comparing parameter dependences of the spin overshoot as obtained by the MT as well as the QKT. When the exciton-impurity interaction is treated quantum kinetically, a spin overshoot appears as a consequence of the many-body nature of the system even without radiative decay and correlations beyond the Markov level are required to obtain this behavior. Comparing results of the MT and the QKT reveals that the overshoot in the QKT is much more stable against the phonon influence; albeit it is not as pronounced as in the MT at low temperatures. Furthermore, the two theories predict a different dependence of the magnitude of the spin overshoot on the doping fraction. All in all, our theoretical investigations reveal that radiative decay has in fact little to no impact on the exciton spin dynamics in DMSs. Instead, the

dynamics is completely dominated by correlations caused by the exciton-impurity exchange interaction.

Although we focus on the spin dynamics in DMSs, the results of our paper are not restricted to this specific material system. Instead, they can be used to analyze the exciton spin dynamics also in standard nonmagnetic semiconductors where radiative decay combined with a spin-flip mechanism plays a role. Since non-DMS samples can be expected to be much less affected by the carrier-impurity correlations appearing in DMSs, we expect the results of the Markov approximation to be relevant in this case. In this sense, our study provides a means to trace back the origin of an observed spin overshoot since it allows one to discriminate between overshoots dominantly caused by either radiative decay or non-Markovian effects.

ACKNOWLEDGMENT

[1] J. Mulet, S. Balle, J. Arias, V. Martín-Hériz, and I. Esquivias, Opt. Quantum Electron. **40**, 1199 (2008).

[2] J. Becker, A. Tsukamoto, A. Kirilyuk, J. C. Maan, T. Rasing, P. C. M. Christianen, and A. V. Kimel, Phys. Rev. B **92**, 180407(R) (2015).

[3] R. Fu, J. Li, J. Cui, and X. Peng, J. Magn. Reson. **268**, 107 (2016).

[4] J. K. Furdyna, J. Appl. Phys. **64**, R29 (1988).

[5] *Semiconductors and Semimetals*, edited by J. K. Furdyna and J. Kossut (Academic Press, San Diego, 1988).

[6] *Introduction to the Physics of Diluted Magnetic Semiconductors*, edited by J. Kossut and J. A. Gaj (Springer, Berlin, 2010).

[7] T. Dietl and H. Ohno, Rev. Mod. Phys. **86**, 187 (2014).

[8] I. Žutić, J. Fabian, and S. Das Sarma, Rev. Mod. Phys. **76**, 323 (2004).

[9] D. Awschalom and M. Flatté, Nat. Phys. **3**, 153 (2007).

[10] D. D. Awschalom, L. C. Bassett, A. S. Dzurak, E. L. Hu, and J. R. Petta, Science **339**, 1174 (2013).

[11] T. Dietl, Nat. Mater. **9**, 965 (2010).

[12] H. Ohno, Nat. Mater. **9**, 952 (2010).

[13] V. K. Joshi, Eng. Sci. Technol., InterNatl. J. (Wash.) **19**, 1503 (2016).

[14] H. Ohno, Science **281**, 951 (1998).

[15] I. Di Marco, P. Thunström, M. I. Katsnelson, J. Sadowski, K. Karlsson, S. Lebègue, J. Kanski, and O. Eriksson, Nat. Commun. **4**, 2645 (2013).

[16] F. Ungar, M. Cygorek, and V. M. Axt, Phys. Rev. B **98**, 161201(R) (2018).

[17] C. Thurn, M. Cygorek, V. M. Axt, and T. Kuhn, Phys. Rev. B **87**, 205301 (2013).

[18] M. Cygorek and V. M. Axt, J. Phys. Conf. Ser. **647**, 012042 (2015).

[19] F. Ungar, M. Cygorek, and V. M. Axt, Phys. Rev. B **95**, 245203 (2017).

[20] F. Ungar, M. Cygorek, and V. M. Axt, Phys. Rev. B **97**, 045210 (2018).

[21] Z. Ben Cheikh, S. Cronenberger, M. Vladimirova, D. Scalbert, F. Perez, and T. Wojtowicz, Phys. Rev. B **88**, 201306(R) (2013).

[22] F. Ungar, M. Cygorek, and V. M. Axt, Phys. Rev. B **99**, 115305 (2019).

[23] F. Ungar, M. Cygorek, and V. M. Axt, Phys. Rev. B **99**, 075301 (2019).

[24] S. Rudin and T. L. Reinecke, Phys. Rev. B **41**, 3017 (1990).

[25] M. Cygorek, F. Ungar, P. I. Tamborenea, and V. M. Axt, Phys. Rev. B **95**, 045204 (2017).

[26] R. Winkler, *Spin-Orbit Coupling Effects in Two-Dimensional Electron and Hole Systems* (Springer, Berlin, 2003).

[27] T. Uenoyama and L. J. Sham, Phys. Rev. Lett. **64**, 3070 (1990).

[28] R. Ferreira and G. Bastard, Phys. Rev. B **43**, 9687 (1991).

[29] G. Bastard and R. Ferreira, Surf. Sci. **267**, 335 (1992).

[30] S. A. Crooker, D. D. Awschalom, J. J. Baumberg, F. Flack, and N. Samarth, Phys. Rev. B **56**, 7574 (1997).

[31] M. Z. Maialle, E. A. de Andrada e Silva, and L. J. Sham, Phys. Rev. B **47**, 15776 (1993).

[32] M. Maialle and L. Sham, Surf. Sci. **305**, 256 (1994).

[33] M. Cygorek, P. I. Tamborenea, and V. M. Axt, Phys. Rev. B **93**, 035206 (2016).

[34] M. Nawrocki, R. Planel, G. Fishman, and R. Galazka, Phys. Rev. Lett. **46**, 735 (1981).

[35] C. Camilleri, F. Teppe, D. Scalbert, Y. G. Semenov, M. Nawrocki, M. Dyakonov, J. Cibert, S. Tatarenko, and T. Wojtowicz, Phys. Rev. B **64**, 085331 (2001).

[36] Ł. Cywiński and L. J. Sham, Phys. Rev. B **76**, 045205 (2007).

[37] E. Tsitsishvili and H. Kalt, Phys. Rev. B **73**, 195402 (2006).

[38] C. Thurn and V. M. Axt, Phys. Rev. B **85**, 165203 (2012).

[39] H. Kalt, J. Collet, S. D. Baranovskii, R. Saleh, P. Thomas, L. S. Dang, and J. Cibert, Phys. Rev. B **45**, 4253 (1992).

[40] E. Runge, A. Schülzgen, F. Henneberger, and R. Zimmermann, Phys. Status Solidi B **188**, 547 (1995).

[41] Z. Chen, H. Sakurai, K. Seo, K. Kayanuma, T. Tomita, A. Murayama, and Y. Oka, *Proceedings of the 22nd International Conference on Defects in Semiconductors* [Physica B **340-342**, 890 (2003)] .

[42] S. V. Poltavtsev, M. Reichelt, I. A. Akimov, G. Karczewski, M. Wiater, T. Wojtowicz, D. R. Yakovlev, T. Meier, and M. Bayer, Phys. Rev. B **96**, 075306 (2017).

[43] M. W. Wu, J. H. Jiang, and M. Q. Weng, Phys. Rep. **493**, 61 (2010).

[44] F. Ungar, M. Cygorek, P. I. Tamborenea, and V. M. Axt, Phys. Rev. B **91**, 195201 (2015).

[45] M. Cosacchi, M. Cygorek, F. Ungar, and V. M. Axt, Phys. Rev. B **95**, 195313 (2017).

Erratum: Origins of overshoots in the exciton spin dynamics in semiconductors [Phys. Rev. B 99, 165308 (2019)]

F. Ungar, M. Cygorek, and V. M. Axt

The width of the broadened δ-function $\delta_{\omega,0}^{b} = \frac{1}{\sqrt{\pi}w_{b}} \exp[-(\hbar\omega/2w_{b})^2]$ in Eq. (2) should read $w_{b} = 1\ \mu\text{eV}$.

Publication 8

Spin dynamics of hot excitons in diluted magnetic semiconductors with spin-orbit interaction

F. Ungar, P. I. Tamborenea, and V. M. Axt

&

Erratum: Spin dynamics of hot excitons in diluted magnetic semiconductors with spin-orbit interaction

F. Ungar, P. I. Tamborenea, and V. M. Axt

Spin dynamics of hot excitons in diluted magnetic semiconductors with spin-orbit interaction

F. Ungar,[1] P. I. Tamborenea,[2] and V. M. Axt[1]

[1]*Theoretische Physik III, Universität Bayreuth, 95440 Bayreuth, Germany*
[2]*Departamento de Física and IFIBA, FCEN, Universidad de Buenos Aires, Ciudad Universitaria,*
Pabellón I, C1428EHA Buenos Aires, Argentina

We explore the impact of a Rashba-type spin-orbit interaction in the conduction band on the spin dynamics of hot excitons in diluted magnetic semiconductor quantum wells. In materials with strong spin-orbit coupling, we identify parameter regimes where spin-orbit effects greatly accelerate the spin decay and even change the dynamics qualitatively in the form of damped oscillations. Furthermore, we show that the application of a small external magnetic field can be used to either mitigate the influence of spin-orbit coupling or entirely remove its effects for fields above a material-dependent threshold.

I. INTRODUCTION

Diluted magnetic semiconductors (DMSs) are well known for the strong exchange interaction between the localized magnetic dopants and the quasifree carriers in the material [1–4], an effect which famously can give rise to complete ferromagnetic ordering at sufficiently large doping concentrations in III-V compounds [5]. In contrast, typical II-VI DMSs are paramagnetic [4] and can be used as a spin aligner [6] or to perform spin-noise spectroscopy [7]. Here, we focus on the latter material class which has the advantage that the doping atoms, typically manganese, can be incorporated isoelectronically into the host lattice so that no excess charge carriers are introduced.

Since the carrier-impurity exchange coupling is so strong, its effects typically dominate the carrier spin dynamics in DMSs for a vast range of parameters [3]. This is why, in contrast to nonmagnetic semiconductors, other spin relaxation mechanisms such as phonon or spin-orbit effects are often not considered in theoretical models [8–13]. However, it has already been shown that, for suitable materials under appropriate parameters, a nonequilibrium distribution of quasifree electron spins can be significantly affected by spin-orbit interaction (SOI) in bulk as well as nanostructures [14]. But instead of exciting quasifree electron spins, many experimental works choose to focus on the exciton resonance [9,11,15,16], which opens up the question of whether a regime of a true competition between the exchange interaction and the SOI in DMSs can be reached also in the spin dynamics of electron-hole pairs.

To answer this question, we consider a nonequilibrium distribution of so-called hot excitons under the influence of SOI. In contrast to resonantly excited excitons, which are characterized by vanishing center-of-mass momenta due to momentum conservation, hot excitons are formed, e.g., by above band-gap excitation and subsequent relaxation onto the exciton parabola via the emission of longitudinal optical (LO) phonons [17–19]. This makes hot excitons ideal candidates to investigate the interplay between exchange interaction and SOI since their distribution is strongly out of equilibrium and

they are created with sizable center-of-mass kinetic energies, which is favorable for SOI since it becomes stronger with larger wave numbers.

Although many articles have pointed out the importance of correlations in DMSs [5,13,20–23], it has been recently shown that the spin dynamics of hot excitons is in fact well described by a Markovian model along the lines of Fermi's golden rule [24]. This is because, in DMSs, correlation effects requiring a full quantum kinetic description are most pronounced near the band edge [25] and the center of a hot exciton distribution is typically a few meV away from the corresponding bottom of the exciton parabola [18], where the density of states abruptly drops to zero. Regarding the SOI, we focus on Rashba-type spin-orbit coupling in quasi two-dimensional quantum wells in the conduction band and neglect the corresponding valence band terms. Since the latter are inversely proportional to the splitting between heavy holes (hh) and light holes (lh) [26], they can be expected to be less relevant in samples with a sufficiently large hh-lh splitting such as in narrow quantum wells or in the presence of strain [27].

Our findings suggest that there is indeed a regime where the SOI is comparable or even exceeds the carrier-impurity exchange interaction, provided that the doping fraction is sufficiently low and the Rashba coupling constant is large enough. In our numerical simulations, the latter dependence is revealed by comparing the results for two different materials with drastically different band gaps and, consequently, different coupling constants, namely $Zn_{1-x}Mn_xSe$ and $Cd_{1-x}Mn_xTe$. It is also found that SOI effects are particularly pronounced for narrow quantum wells. Finally, we show that the influence of SOI can be drastically reduced and even be completely switched off by applying an external magnetic field, a finding which is particularly important for potential applications.

II. THEORY

In this section, the individual contributions to the Hamiltonian of a DMS quantum well with SOI in the conduction

band are discussed. We also provide the equations of motion to describe the exciton spin dynamics in the Markov limit without SOI. To add the influence of the latter, the Rashba Hamiltonian is projected onto the exciton basis, where it is found to take the form of an effective magnetic field in terms of the exciton center-of-mass momentum that can be added to the equations of motion.

A. Spin dynamics of excitons in DMSs

We model the spin dynamics of hot excitons on the 1s exciton parabola in a II-VI DMS quantum well. As a distribution of hot excitons typically forms on a femtosecond timescale via LO-phonon emission after above band-gap excitation [17–19], we do not explicitly model the exciton formation process here since it is orders of magnitude faster than the typical spin dynamics in DMSs [3,11,15,28–31]. Rather, we perform initial-value calculations using an exciton distribution that is close to what is reported in experiments. Note that the distribution of excitons on the 1s parabola is experimentally accessible via LO-phonon assisted photoluminescence measurements [18,32,33]. Restricting our model to 1s excitons is possible due to the energy separation between the exciton ground state and the excited states, which is 10 meV or larger for the systems studied here. In combination with the finite LO-phonon energy of about 30 meV [18], this means that excited exciton states can be effectively eliminated by appropriately tuning the excess excitation energy above the band gap.

The exciton spin dynamics including the Rashba spin-orbit interaction can then be modeled by the Hamiltonian [22,24]

$$H = H_X + H_Z + H_m + H_{nm} + H_R. \tag{1}$$

Here, H_X comprises the kinetic energies of electrons and holes as well as the confinement due to the quantum well and the Coulomb interaction between the carriers. A diagonalization of H_X yields the exciton wave functions and the corresponding energies. We also account for an external magnetic field via Zeeman terms for electrons, holes, and magnetic impurities via H_Z.

The interaction which typically dominates the spin dynamics in DMSs is the magnetic carrier-impurity exchange interaction [2,3,13,22] denoted by H_m. It comprises the spin-flip scattering of s-like conduction band electrons and p-like valence band holes with the localized electrons in the d shell of an impurity ion. Despite being typically only investigated in transport studies [34], recent theoretical investigations have shown that nonmagnetic scattering can also significantly affect the spin dynamics [21,22,35], which is why we include nonmagnetic scattering via H_{nm}. A more detailed description of these parts of the Hamiltonian is given in Ref. [22].

Finally, we extend the model by accounting for a Rashba-type SOI in the conduction band, the Hamiltonian of which

is denoted by H_R and will be discussed in more detail in the following section. Although the scattering with longitudinal acoustic (LA) phonons leads to the eventual thermalization of hot excitons, we do not include LA phonons in our model since it has been recently shown that they have a negligible influence on the ultrafast spin dynamics of hot excitons and mainly affect the shape of the distribution [24]. Another mechanism which is commonly discussed in the context of exciton spin relaxation in nonmagnetic systems is the long-range exchange coupling induced by the Coulomb interaction [28]. For the resonant excitation of excitons with quasivanishing center-of-mass momenta, the typical energy associated with this interaction has been estimated previously and was found to be in the 10 μeV range, much smaller than the meV energy scale of the sd exchange interaction [35]. Considering a distribution of hot excitons in a typical 5-nm-wide quantum well and using the expression from Ref. [28], we estimate an energy of about 0.03 meV for the long-range exchange interaction. This corresponds to a timescale of about 140 ps, which is longer than the typical timescales of the magnetic exchange interaction and the SOI for the parameters considered in Sec. III so the long-range exchange part is neglected here.

Even though our model is specifically adapted to describe the exciton spin dynamics in DMS nanostructures, it can also be straightforwardly applied to nonmagnetic systems if the magnetic exchange interaction is switched off. In that case, also the effect of a long-range exchange interaction may become more important and should be incorporated. Furthermore, the model could be extended to the topical material class of transition-metal dichalcogenide monolayers [36]. There, the exciton states would need to be recalculated to account for the large binding energies observed in these systems and also the valley degree of freedom can be expected to play a role [37,38].

We assume a distribution of hot excitons that is spin polarized such that electrons are in the state with $s_z = \frac{1}{2}$ and heavy holes have an angular momentum quantum number of $j_z = -\frac{3}{2}$, corresponding to the energetically lowest optically active exciton state in typical semiconductors [27,39]. Light-hole states with $j_z = \pm\frac{1}{2}$ are energetically separated from the hh states by the hh-lh splitting due to the confinement in the quantum well and strain [27]. In the following, we consider the limit of a sufficiently large hh-lh splitting so that the hh spins remain pinned in the state $j_z = -\frac{3}{2}$ [15,40–42]. Then, it is sufficient to describe the exciton spin dynamics with two states, i.e., one where the exciton-bound electron spin is oriented parallel with respect to the growth direction and another where it points in the opposite direction. Assigning the symbol ↑ to the former state ($s_z = \frac{1}{2}$), the latter is denoted by ↓ ($s_z = -\frac{1}{2}$).

Without SOI, the equation of motion for the spin-up and spin-down exciton density as well as for the spin components in the quantum well plane due to the exciton-impurity interaction are given by [22]

$$\frac{\partial}{\partial t} n_{\mathbf{K}_1}^{\uparrow/\downarrow} = \frac{\pi I N_{Mn}}{\hbar^2 V^2} \sum_{\mathbf{K}} \Big[\delta(\omega_{\mathbf{K}} - \omega_{\mathbf{K}_1})(n_{\mathbf{K}}^{\uparrow/\downarrow} - n_{\mathbf{K}_1}^{\uparrow/\downarrow}) \big((J_{sd}^2 b^{\parallel} \pm 2 J_{sd} J_0^e b^0 + 2 J_0^{e\,2}) F_{\eta_h 1s1s}^{\eta_h \mathbf{K}\mathbf{K}_1} + (J_{pd}^2 b^{\parallel} - 2 J_{pd} J_0^h b^0 + 2 J_0^{h\,2}) F_{\eta_e 1s1s}^{\eta_e \mathbf{K}\mathbf{K}_1} $$
$$+ (4 J_0^e J_0^h - 2 J_{pd} J_0^e b^0 \pm 2 J_{sd} J_0^h b^0 \mp 2 J_{sd} J_{pd} b^{\parallel}) F_{-\eta_h 1s1s}^{\eta_e \mathbf{K}\mathbf{K}_1} \big) + \delta(\omega_{\mathbf{K}} - (\omega_{\mathbf{K}_1} \pm \omega_{sf})) J_{sd}^2 F_{\eta_h 1s1s}^{\eta_h \mathbf{K}\mathbf{K}_1} (b^{\pm} n_{\mathbf{K}}^{\downarrow/\uparrow} - b^{\mp} n_{\mathbf{K}_1}^{\uparrow/\downarrow}) \Big], \tag{2a}$$

$$\frac{\partial}{\partial t}\mathbf{s}_{\mathbf{K}_1}^{\perp} = \frac{\pi I N_{\mathrm{Mn}}}{\hbar^2 V^2}\sum_{\mathbf{K}}\left[\delta(\omega_{\mathbf{K}}-\omega_{\mathbf{K}_1})(\mathbf{s}_{\mathbf{K}}^{\perp}-\mathbf{s}_{\mathbf{K}_1}^{\perp})\left((2J_0^{\mathrm{e}2}-J_{sd}^2 b^{\parallel})F_{\eta_{\mathrm{h}}1s1s}^{\eta_{\mathrm{h}}\mathbf{K}\mathbf{K}_1}+\left(J_{pd}^2 b^{\parallel}+2J_0^{\mathrm{h}2}-J_{pd}J_0^{\mathrm{h}}b^0\right)F_{\eta_{\mathrm{e}}1s1s}^{\eta_{\mathrm{e}}\mathbf{K}\mathbf{K}_1}\right.\right.$$
$$-\left(2J_{pd}J_0^{\mathrm{e}}b^0+J_{pd}J_0^{\mathrm{h}}b^0-2J_0^{\mathrm{e}}J_0^{\mathrm{h}}\right)F_{-\eta_{\mathrm{h}}1s1s}^{\eta_{\mathrm{e}}\mathbf{K}\mathbf{K}_1}\Big)-\left(\frac{b^-}{2}\delta(\omega_{\mathbf{K}}-(\omega_{\mathbf{K}_1}+\omega_{\mathrm{sf}}))+\frac{b^+}{2}\delta(\omega_{\mathbf{K}}-(\omega_{\mathbf{K}_1}-\omega_{\mathrm{sf}}))\right.$$
$$\left.\left.+2b^{\parallel}\delta(\omega_{\mathbf{K}}-\omega_{\mathbf{K}_1})\right)J_{sd}^2 F_{\eta_{\mathrm{h}}1s1s}^{\eta_{\mathrm{h}}\mathbf{K}\mathbf{K}_1}\mathbf{s}_{\mathbf{K}_1}^{\perp}\right]+\boldsymbol{\omega}_{\mathrm{e}}\times\mathbf{s}_{\mathbf{K}_1}^{\perp}. \tag{2b}$$

The overall prefactor in front of the sum contains the factor $I = 1.5$, which stems from the influence of the lowest confinement state in the quantum well under the assumption of infinitely high barriers and the number of Mn ions N_{Mn} in the system with volume V. The coupling constants J are labeled according to the respective interaction: J_{sd} (J_{pd}) denotes the coupling for the sd (pd) exchange interaction and J_0^{e} (J_0^{h}) stems from the nonmagnetic scattering at impurities in the conduction (valence) band. We assume a magnetic field oriented along the growth direction (z axis), which enters via $\boldsymbol{\omega}_{\mathrm{e}} = \frac{g_{\mathrm{e}}\mu_B}{\hbar}\mathbf{B} + \frac{J_{sd}N_{\mathrm{Mn}}b^0}{\hbar V}\mathbf{e}_z$ and $\boldsymbol{\omega}_{\mathrm{Mn}} = \frac{g_{\mathrm{Mn}}\mu_B}{\hbar}\mathbf{B}$ for the carriers and the impurity ions, respectively. Regarding the impurity magnetization $\mathbf{S}$ we consider the regime of small exciton densities so the impurity spin density matrix can be described by its thermal equilibrium value. Then, the influence of $\mathbf{S}$ is contained in the constants $b^{\pm} = \frac{1}{2}(\langle\mathbf{S}^2-(S^z)^2\rangle \pm \langle S^z\rangle)$, $b^{\parallel} = \frac{1}{2}\langle(S^z)^2\rangle$, and $b^0 = \langle S^z\rangle$. The spin-flip scattering shift appearing in Eqs. (2) is given by $\hbar\omega_{\mathrm{sf}} = \hbar\omega_{\mathrm{e}}^z - \hbar\omega_{\mathrm{Mn}}^z$. Finally, an analytic expression for the exciton form factors $F_{\eta_1 1s1s}^{\eta_2 \mathbf{K}_1\mathbf{K}_2}$ is provided in the Appendix. Note that the z component of the exciton spin can be obtained via $s_{\mathbf{K}}^z = \frac{1}{2}(n_{\mathbf{K}}^{\uparrow}-n_{\mathbf{K}}^{\downarrow})$.

Instead of using the full quantum kinetic description of the exciton spin dynamics developed in Ref. [22], here we only consider its Markov limit. As a recent theoretical study suggests [24], this is justified as long as hot excitons are considered since they are far away from the bottom of the exciton parabola where quantum kinetic effects are most pronounced [25]. Note that all appearing wave vectors $\mathbf{K}$ are two-dimensional variables. Since the SOI introduces an effective magnetic field that explicitly depends on the wave vector [26], performing an average over angles in $\mathbf{K}$ space to reduce the numerical demand would not capture any spin-orbit physics. This means that even terms proportional to $\delta(\omega_{\mathbf{K}}-\omega_{\mathbf{K}_1})$ give a finite contribution to the dynamics as they only limit the sum over the absolute value K but still allow for a scattering to an arbitrary angle.

B. Rashba SOI in the exciton basis

In an asymmetric quantum well, the Rashba SOI for a single electron can be written as [26,43,44]

$$H_{\mathrm{R}} = \alpha_{\mathrm{R}}(k_y\sigma_x - k_x\sigma_y) \tag{3}$$

with a coupling constant α_{R} and Pauli matrices σ_x and σ_y that couple the electron spin with the components of the wave vector $\mathbf{k}$. For the coupling constant, we use the expression [14,45,46]

$$\alpha_{\mathrm{R}} = \frac{\hbar^2}{2m_{\mathrm{e}}}\frac{\Delta}{E_{\mathrm{g}}}\frac{2E_{\mathrm{g}}+\Delta}{(E_{\mathrm{g}}+\Delta)(3E_{\mathrm{g}}+2\Delta)}\frac{V_{\mathrm{qw}}}{d} \tag{4}$$

with the electron effective mass m_{e}, the spin-orbit splitting Δ in the valence band, the band gap E_{g}, and a potential drop V_{qw} across a quantum well of width d.

In order to incorporate the SOI in our existing description of the exciton spin dynamics, we project Eq. (3) onto the exciton basis characterized by the states $|\sigma x\mathbf{K}\rangle$ with a spin index σ, the exciton quantum number x, and the center-of-mass wave vector $\mathbf{K}$. We restrict our considerations to the exciton ground state ($x = 1s$) for which the exciton wave function in the quantum well plane can be written as [39]

$$\Psi_{1s\mathbf{K}}(\mathbf{r},\mathbf{R}) = e^{-i\mathbf{K}\cdot\mathbf{R}}\Phi_{1s}(\mathbf{r}). \tag{5}$$

Using polar coordinates for the center-of-mass position $\mathbf{R} = \mathbf{R}(R,\phi)$ and the relative coordinate $\mathbf{r} = \mathbf{r}(r,\varphi)$, respectively, the wave function for the relative motion $\Phi_{1s}(\mathbf{r}) = \Phi_{1s}(r)$ of the exciton ground state does not depend on the angle φ since an s state is characterized by vanishing angular momentum. To shorten the notation, we shall drop the index $1s$ in the following.

To express the Rashba Hamiltonian in Eq. (3) in terms of the exciton ground state, it is convenient to first write it in terms of center-of-mass and relative coordinates as well. This yields

$$H_{\mathrm{R}} = \alpha_{\mathrm{R}}(s^+(\partial_{\mathbf{R}}^- + \partial_{\mathbf{r}}^-) - s^-(\partial_{\mathbf{R}}^+ + \partial_{\mathbf{r}}^+)) \tag{6}$$

with the partial derivatives

$$\partial_{\mathbf{R}}^{\pm} = e^{\pm i\phi}\left(\frac{\partial}{\partial R} \pm i\frac{1}{R}\frac{\partial}{\partial\phi}\right), \tag{7a}$$

$$\partial_{\mathbf{r}}^{\pm} = e^{\pm i\varphi}\left(\frac{\partial}{\partial r} \pm i\frac{1}{r}\frac{\partial}{\partial\varphi}\right) \tag{7b}$$

and spin raising and lowering operators $s^{\pm}$, respectively. In second quantization with respect to the states $|\sigma\mathbf{K}\rangle$, one then has to compute the corresponding matrix elements of Eq. (6). It turns out that matrix elements containing a derivative with respect to the relative motion vanish for the exciton ground state, i.e.,

$$\langle\sigma_1\mathbf{K}_1|\partial_{\mathbf{r}}^{\pm}|\sigma_2\mathbf{K}_2\rangle = 0. \tag{8}$$

To see this, the two terms in Eq. (7b) can be considered separately. First, the second part of Eq. (7b) containing the derivative with respect to φ vanishes since the exciton wave function does not depend on φ. Second, the matrix element contains an integral over φ, which vanishes due to the φ-dependent phase in Eq. (7b) no matter what the result of the derivative with respect to r is. For the remaining matrix element of the center-of-mass motion, it is advantageous to

switch back to Cartesian coordinates, where

$$\partial_{\mathbf{R}}^{\pm} = \frac{\partial}{\partial X} \pm i \frac{\partial}{\partial Y}. \tag{9}$$

The resulting matrix element can then be straightforwardly evaluated to be

$$\langle \sigma_1 \mathbf{K}_1 | \partial_{\mathbf{R}}^{\pm} | \sigma_2 \mathbf{K}_2 \rangle = \alpha_{\mathrm{R}} (-iK_{1,X} \pm K_{1,Y}) \delta_{\mathbf{K}_1,\mathbf{K}_2} \tag{10}$$

under the condition that $\Phi_{1s}(\mathbf{r})$ is normalized with respect to the quantum well area.

Combining Eqs. (8) and (10) with the spin selection rules enforced by $s^{\pm}$, the conduction-band SOI in the exciton basis becomes

$$H_{\mathrm{R}} = \alpha_{\mathrm{R}} \sum_{\mathbf{K}} ((-iK_X - K_Y) Y_{\uparrow\mathbf{K}}^{\dagger} Y_{\downarrow\mathbf{K}} + (iK_X - K_Y) Y_{\downarrow\mathbf{K}}^{\dagger} Y_{\uparrow\mathbf{K}}) \tag{11}$$

in terms of the creation (annihilation) operator $Y_{\sigma\mathbf{K}}^{\dagger}$ ($Y_{\sigma\mathbf{K}}$) of a $1s$ exciton with spin σ and center-of-mass wave vector $\mathbf{K}$. Using the Heisenberg equation of motion, Eq. (11) leads to the typical precession-type dynamics in an effective spin-orbit magnetic field that depends on the wave vector [14,26,44,47,48]. For the exciton spin $\mathbf{s}_{\mathbf{K}}$, this amounts to an additional contribution to the equation of motion of the form

$$\frac{\partial}{\partial t}\bigg|_{\mathrm{SOI}} \mathbf{s}_{\mathbf{K}} = \mathbf{\Omega}_{\mathbf{K}} \times \mathbf{s}_{\mathbf{K}} \tag{12}$$

with an effective magnetic field in the quantum well plane given by

$$\mathbf{\Omega}_{\mathbf{K}} = \frac{\alpha_{\mathrm{R}}}{\hbar} \begin{pmatrix} -K_Y \\ K_X \\ 0 \end{pmatrix}. \tag{13}$$

This means that the SOI induces a $\mathbf{K}$-dependent precession of exciton spins which, provided it is strong enough, can be expected to lead to a faster spin decay due to dephasing.

Note that, in bulk semiconductors, one typically discusses the Dresselhaus SOI in combination with momentum scattering for the spin relaxation, which is known as the Dyakonov-Perel mechanism [49]. However, in two-dimensional systems such as quantum wells, the strong confinement in the z direction reduces the characteristic cubic dependence of the Dresselhaus spin-orbit field on $\mathbf{k}$ to a linear dependence, just like in Eq. (3) but with a different coupling constant and proportional to $k_x \sigma_x - k_y \sigma_y$. In contrast to the Rashba interaction, where α_{R} is tunable via an electric field, the Dresselhaus coupling constant is fixed and depends only on the specific semiconductor [27]. As discussed in the previous section, momentum scattering is present in our model due to the scattering of excitons at the impurities in the DMS. Thus, provided that the coupling constants are comparable, a similar spin decay is expected due to the Rashba and the Dresselhaus SOI independently. Although including a Dresselhaus term in our model is straightforward, studying this mechanism is beyond the scope of this paper.

III. NUMERICAL SIMULATIONS

To analyze how SOI in the conduction band can impact the exciton spin dynamics of hot excitons in DMS quantum
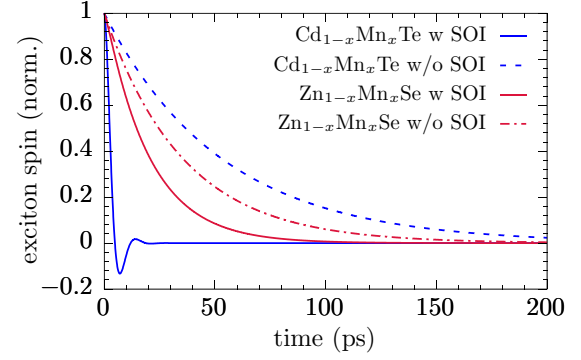

FIG. 1. Spin dynamics in 5-nm-wide DMS quantum wells with a doping fraction $x = 0.2\%$. Results are shown for two different compounds with and without spin-orbit interaction (SOI) taken into account.

wells, we perform numerical simulations for two different materials, namely $\mathrm{Zn}_{1-x}\mathrm{Mn}_x\mathrm{Se}$ and $\mathrm{Cd}_{1-x}\mathrm{Mn}_x\mathrm{Te}$, for varying doping fractions x and different quantum well widths. Furthermore, we explore the impact of an external magnetic field. We assume an initial distribution of hot excitons on the $1s$ parabola that is spin polarized in the $\uparrow$ state. The distribution is modeled as a Gaussian with a standard deviation of 1 meV centered at 10 meV above the bottom of the $1s$ exciton parabola, which is similar to what has been observed in experiments for ZnSe [18]. The spin moments of the impurity ions are calculated using a fixed temperature of 2 K.

The microscopic parameters used for the simulations are the same as in Ref. [22]. To calculate the SOI prefactor given by Eq. (4), we use a spin-orbit splitting $\Delta = 403$ meV and a band gap $E_{\mathrm{g}} = 2.820$ eV for $\mathrm{Zn}_{1-x}\mathrm{Mn}_x\mathrm{Se}$, while $\Delta = 949$ meV and $E_{\mathrm{g}} = 1.606$ eV are used for $\mathrm{Cd}_{1-x}\mathrm{Mn}_x\mathrm{Te}$ [27]. Apart from the coupling constants J_0^{e} and J_0^{h}, which are obtained by considering the change of the band gap when going over from a completely undoped semiconductor to a compound where all group II atoms have been replaced by Mn [21], all other microscopic parameters are taken directly from experiments. Since we study DMSs with a relatively small concentration of doping atoms, the change of the band gap with increasing doping fraction is disregarded here. In all simulations, a potential drop $V_{\mathrm{qw}} = 100$ meV across the quantum well is assumed. Considering, e.g., a 10-nm-wide DMS quantum well, we obtain $\alpha_{\mathrm{R}} \approx 0.07$ meV nm for $\mathrm{Zn}_{1-x}\mathrm{Mn}_x\mathrm{Se}$ and $\alpha_{\mathrm{R}} \approx 0.36$ meV nm for $\mathrm{Cd}_{1-x}\mathrm{Mn}_x\mathrm{Te}$, respectively. These values are realistic compared to what has been reported in the literature [50,51]. Note that the Rashba coefficient is recalculated for simulations where the quantum well width is varied using the constant value for the potential drop across the well given above.

Since the SOI has to compete with the rather strong carrier-impurity exchange interaction in DMSs, effects of the former can be expected to become particularly relevant for small impurity content where the exchange interaction is less significant [14]. Indeed, Fig. 1 shows that the SOI can have a substantial impact on the spin dynamics of hot excitons in 5-nm-wide DMS quantum wells with 0.2% Mn doping. In the case of $\mathrm{Cd}_{1-x}\mathrm{Mn}_x\mathrm{Te}$, the calculation including the SOI reveals a substantially faster spin decay accompanied by an

oscillatory behavior on short time scales compared to the calculation without SOI, which shows a standard exponential decay. For $Zn_{1-x}Mn_xSe$, the SOI also accelerates the decay but does not lead to any oscillations. Compared to the previous compound, its impact is much less pronounced.

Since a Markovian description of the carrier-impurity exchange interaction results in a rate-type dynamics [52], a monoexponential spin decay is expected on that level of theory [26]. Figure 1 reveals that this behavior can change dramatically when the SOI becomes significant, leading to a spin decay which is no longer exponential and may even show oscillations. In fact, a nonexponential decay is a characteristic feature of the presence of SOI [14,47,48]. As noted before, the impact of the SOI on the spin dynamics is much stronger for $Cd_{1-x}Mn_xTe$ than for $Zn_{1-x}Mn_xSe$ for a given doping fraction and nanostructure. The reason for this is the larger Rashba coupling constant in the former compound due to its significantly smaller band gap. A typical time scale for the SOI can be roughly obtained by $\tau_{SOI} \approx \frac{\hbar\bar{K}}{\alpha_R}$, where $\bar{K}$ is the average exciton wave number. This definition is such that τ_{SOI} corresponds to the precession time in the effective magnetic field due to the SOI at the fixed wave number $\bar{K}$. Using the parameters of Fig. 1 with a value of $\bar{K}$ corresponding to the center of the exciton distribution, we find $\tau_{SOI} \approx 2.5$ ps and $\tau_{SOI} \approx 13.8$ ps for $Cd_{1-x}Mn_xTe$ and $Zn_{1-x}Mn_xSe$, respectively, which fits well to the behavior of the curves with SOI taken into account and also confirms that the SOI in $Cd_{1-x}Mn_xTe$ is about five times stronger than in $Zn_{1-x}Mn_xSe$.

The reason for the accelerated decay of the z component of the exciton spin in the presence of SOI is the **K**-dependent magnetic field, which causes a precession whose frequency depends not only on the absolute value of the wave vector but also on its angle. This causes individual spins in an ensemble to dephase and, when looking at the average spin in the system, leads to a decay [26]. As shown in Fig. 1, SOI effects are particularly pronounced for hot excitons since their distributions span a wide range of **K** vectors with sizable absolute values. This is in stark contrast to optically excited excitons which are generated with quasivanishing wave vectors close to the exciton resonance, where SOI effects are thus expected to be much less significant.

Without an external magnetic field and SOI, a simple K-dependent expression for the spin-decay rate due to the sd exchange interaction can be derived [22]. For the parameters of Fig. 1, one then obtains a corresponding spin relaxation time $\tau_{sd} \approx 41.0$ ps and $\tau_{sd} \approx 26.0$ ps for $Cd_{1-x}Mn_xTe$ and $Zn_{1-x}Mn_xSe$, respectively, when the expression is evaluated with the value $\bar{K}$ used previously for the SOI. These numbers provide the correct time scales seen in the spin decay in Fig. 1 without SOI, although one has to be aware that, since the distribution of hot excitons extends over a wide K range, the correct spin relaxation time would have to be obtained by averaging the K dependence of the rate weighted according to the exciton distribution. In any case, comparing the timescales of the SOI with those of the exchange interaction nicely shows that we are in a regime where spin-orbit coupling competes with or even dominates the magnetic scattering.

To find out if such a regime can also be reached in larger nanostructures, we plot the spin-decay rate as a function of the
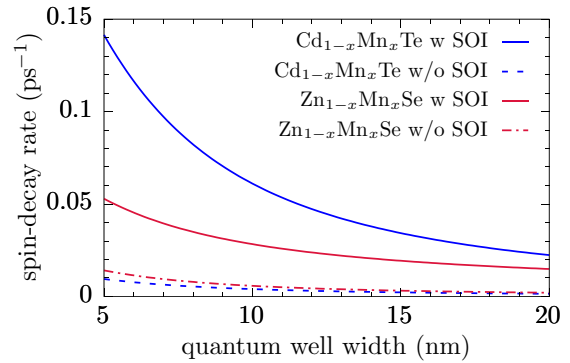

FIG. 2. Spin-decay rate in DMS quantum wells with a doping fraction $x = 0.1\%$ as a function of the well width. Results are shown for two different compounds with and without spin-orbit interaction (SOI) taken into account.

quantum well width in Fig. 2 for DMSs with a doping fraction $x = 0.1\%$. The spin-decay rate is obtained numerically as the inverse time where the spin has decayed to $\frac{1}{e}$ with respect to its initial value. If oscillations appear in the spin dynamics, the envelope of a decaying cosine is used for the extraction of the spin relaxation time so as not to capture the oscillations themselves in the spin-decay rate. The same procedure is used whenever a spin-decay rate is determined in the following.

It turns out that the SOI accelerates the spin decay even for relatively large quantum wells with a width of 20 nm. As found before, this increase is stronger for $Cd_{1-x}Mn_xTe$ compared with $Zn_{1-x}Mn_xSe$ and can be larger than an order of magnitude for very small quantum wells in the former compound. We find an inverse dependence of the rate on the quantum well width for the results with and without SOI, which is the common tendency in DMSs [28,42,53]. The inverse dependence on the width can be directly inferred from the Rashba prefactor given by Eq. (4) as well as the spin-decay rate in the absence of SOI [22].

However, in contrast to the SOI, the timescale of the exchange interaction is strongly controlled by the amount of impurities in the sample [3,35], suggesting that a dominance of SOI effects should disappear for larger doping fractions [14]. Indeed, as shown in Fig. 3, the impact of the
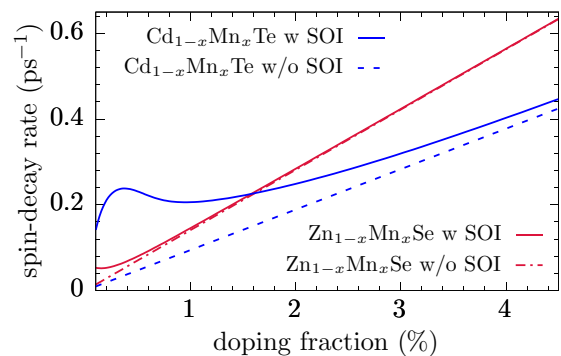

FIG. 3. Spin-decay rate in 5-nm-wide DMS quantum wells as a function of the doping fraction x. Results are shown for two different compounds with and without spin-orbit interaction (SOI) taken into account.
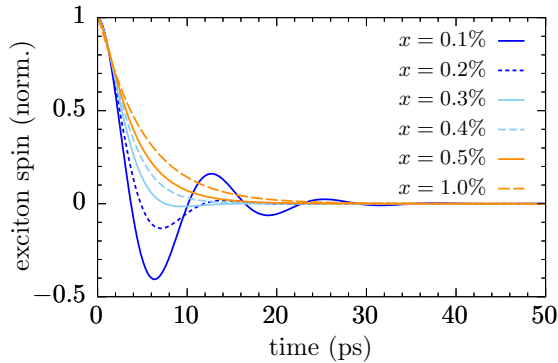
FIG. 4. Spin dynamics in a 5-nm-wide $Cd_{1-x}Mn_xTe$ quantum well for varying doping fractions x under the influence of SOI.
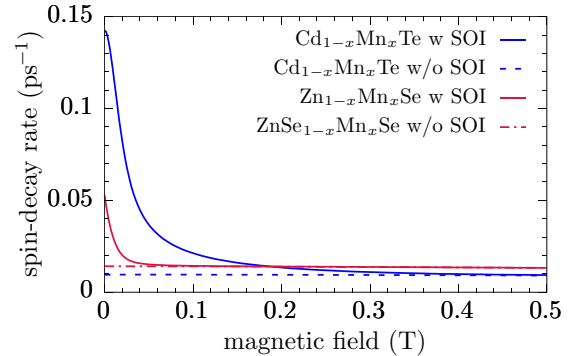

FIG. 5. Spin-decay rate in 5-nm-wide DMS quantum wells with a doping fraction $x = 0.1\%$ as a function of the applied external magnetic field. Results are shown for two different compounds with and without spin-orbit interaction (SOI) taken into account.

SOI on the spin-decay rate decreases with increasing impurity content. For $Zn_{1-x}Mn_xSe$, where Rashba spin-orbit coupling is rather weak, we find that the exchange interaction clearly dominates the exciton spin decay for doping fractions above 0.5%. A similar behavior was found for the spin dynamics of quasifree electrons in the same material [14]. However, the spin dynamics in $Cd_{1-x}Mn_xTe$ remains visibly affected by the SOI even at doping fractions of a few percent, suggesting that SOI effects may contribute to the experimentally determined significant spread of spin relaxation rates for different samples collected in Ref. [11].

While the results for $Zn_{1-x}Mn_xSe$ with SOI go smoothly over to those without SOI, there is a visible local maximum in the spin-decay rate for small doping fractions below 1% in $Cd_{1-x}Mn_xTe$. There, the rate obtained when the SOI is included first rises with increasing Mn content, then decreases and finally increases once more. The second increase starting at about 1% doping stems from the exchange interaction, which is directly proportional to the number of Mn ions in the sample [cf. Eqs. (2)] as can be seen from the behavior of the curve without SOI. In contrast, the initial rise, maximum, and following decrease of the rate is indicative of a qualitative change in the dynamics. For very small doping fractions where the SOI completely dominates, the z component of the spin exhibits a decaying oscillatory behavior (cf. Fig. 1). This is eliminated with increasing strength of the exchange interaction as the latter always leads to an exponential decay without any oscillations. In that sense, the local maximum observed in Fig. 3 is related to a change from the oscillatory to the nonoscillatory regime that takes place for small doping fractions.

To corroborate this interpretation, we show the exciton spin dynamics in a 5-nm-wide $Cd_{1-x}Mn_xTe$ quantum well under the influence of SOI for small doping fractions in Fig. 4. While below doping fractions of about 0.3% pronounced oscillations can be observed, they disappear entirely above that threshold and the dynamics becomes exponential. As stated before, the appearance of oscillations in the spin dynamics is a telltale sign of spin-orbit effects, so that we find indeed that the spin dynamics is dominated by SOI at very small doping fractions and a regime change occurs when the doping increases. The value of the threshold deduced from Fig. 4 also nicely fits to the position of the local maximum in Fig. 3. In contrast, the

spin dynamics in $Zn_{1-x}Mn_xSe$ never reaches the point where it is dominated by SOI so that oscillations appear, not even at the smallest doping fractions considered here (cf. Fig. 1).

Since our results reveal a strong impact of SOI on the spin dynamics for a range of parameters, the question arises if its effects can be mitigated or even entirely removed. It turns out that this can be achieved by applying an external magnetic field, as shown in Fig. 5. Choosing parameters where spin-orbit coupling was found to be most pronounced, i.e., small well widths and small doping fractions, the increased spin-decay rate due to the SOI quickly drops to the rate without SOI when an external magnetic field is applied. When the field reaches approximately 50 mT in the case of $Zn_{1-x}Mn_xSe$ and 300 mT in the case of $Cd_{1-x}Mn_xTe$, any increase due to the SOI has almost entirely disappeared. Thus, unwanted SOI effects can be easily suppressed by applying a relatively moderate magnetic field.

The reason why small external magnetic fields are already sufficient to inhibit the SOI is the giant Zeeman splitting in DMSs [2–4], which enhances the local magnetic field experienced by the carriers. Since the giant Zeeman splitting is so large in these structures, it quickly becomes the dominant contribution with increasing magnitude of the applied field so that, in comparison, the effective magnetic field due to the SOI becomes less and less significant. This is also the reason why the impact of SOI on the spin dynamics of hot excitons has, to the best of our knowledge, not been observed in experiments so far as most of the experimental data available for the spin dynamics of hot excitons in DMS nanostructures has been obtained in finite magnetic fields [19,54,55]. On the other hand, studies performed without magnetic field have been focused so far typically on the exciton thermalization dynamics and did not probe the spin [17,18,32].

IV. CONCLUSION

We have derived and implemented Rashba spin-orbit coupling for excitons in DMS quantum wells to investigate its impact on the spin dynamics of hot excitons in these materials. The hot excitons are modeled using an initial distribution of excitons on the $1s$ parabola that is chosen according to measurements performed in ZnSe quantum wells after optical excitation above the band gap and subsequent LO-phonon

relaxation [18]. Numerical simulations have been performed for two compounds, namely $Zn_{1-x}Mn_xSe$ and $Cd_{1-x}Mn_xTe$, for which spin-decay rates were extracted and compared.

It is found that the SOI is particularly pronounced for small doping fractions and narrow quantum wells, where it leads to a sizable increase of the spin-decay rate compared with simulations not accounting for spin-orbit coupling. The faster spin decay observed in the simulations is a consequence of dephasing in the wave-vector dependent effective magnetic field provided by the SOI. In $Cd_{1-x}Mn_xTe$ quantum wells, where the SOI is especially strong due to the relatively small band gap and high spin-orbit splitting, SOI effects even cause visible oscillations in the spin dynamics for small doping fractions which disappear when the impurity content increases. The appearance of a local maximum in the spin-decay rate as a function of the doping fraction is indicative of this qualitative change from a decaying oscillatory to an exponentially decaying dynamics. In the bulk limit as well as for samples with higher impurity content, our results suggest that SOI effects are either completely suppressed or at least strongly reduced, which is in line with previous works [14].

Finally, we have shown that the influence of SOI on the spin dynamics in DMSs can be overcome by applying a moderate external magnetic field. Due to the strength of the giant Zeeman effect in these materials, the exchange interaction quickly becomes the dominant spin-decay mechanism as soon as the magnetic field passed a threshold determined by the specific material. Experimentally, applying a small magnetic field may thus be used to mitigate unwanted spin-orbit contributions.

APPENDIX: ANALYTICAL SOLUTION FOR THE EXCITON FORM FACTORS

The wave-vector dependent exciton form factors can be calculated via the relation [22]

$$F_{\eta_1 1s1s}^{\eta_2 \mathbf{K}_1 \mathbf{K}_2} = f_{\eta_1 1s1s}^{\mathbf{K}_1 \mathbf{K}_2} \left(f_{\eta_2 1s1s}^{\mathbf{K}_1 \mathbf{K}_2} \right)^* \qquad (A1)$$

with

$$f_{\eta 1s1s}^{\mathbf{K}_1 \mathbf{K}_2} = 2\pi \int_0^\infty dr\, r \phi_{1s}^2(r) J_0(\eta r |\mathbf{K}_1 - \mathbf{K}_2|), \qquad (A2)$$

where η is either the ratio between the hh or the electron mass and the exciton mass. A common ansatz for a trial exciton wave function is given by [39,42]

$$\phi_{1s}(r) = \frac{\beta_{1s}}{\sqrt{2\pi}} e^{-\frac{1}{2}\beta_{1s}r} \qquad (A3)$$

with a free parameter β_{1s} that is typically determined using a variational approach. Here, we use β_{1s} as a fitting parameter which is chosen such that an optimal fit to the numerical solution of the exciton problem is obtained, whereas the exciton problem itself is solved in real space using a finite-difference method. Substituting Eq. (A3) into Eq. (A2) allows one to evaluate the appearing integral analytically, which yields

$$f_{\eta 1s1s}^{\mathbf{K}_1 \mathbf{K}_2} = \frac{1}{\left(1 + \left(\frac{\eta |\mathbf{K}_1 - \mathbf{K}_2|}{\beta_{1s}}\right)^2\right)^{\frac{3}{2}}}. \qquad (A4)$$

Finally, inserting this into Eq. (A1), we obtain a closed expression for the exciton form factor that only depends on β_{1s}.

[1] R. Bouzerar and G. Bouzerar, Europhys. Lett. **92**, 47006 (2010).

[2] T. Dietl and H. Ohno, Rev. Mod. Phys. **86**, 187 (2014).

[3] J. Kossut and J. A. Gaj (Eds.), *Introduction to the Physics of Diluted Magnetic Semiconductors* (Springer, Berlin, 2010).

[4] J. K. Furdyna, J. Appl. Phys. **64**, R29 (1988).

[5] H. Ohno, Science **281**, 951 (1998).

[6] R. Fiederling, M. Keim, G. Reuscher, W. Ossau, G. Schmidt, A. Waag, and L. W. Molenkamp, Nature (London) **402**, 787 (1999).

[7] S. Cronenberger, D. Scalbert, D. Ferrand, H. Boukari, and J. Cibert, Nat. Commun. **6**, 8121 (2015).

[8] Y. G. Semenov, Phys. Rev. B **67**, 115319 (2003).

[9] C. Camilleri, F. Teppe, D. Scalbert, Y. G. Semenov, M. Nawrocki, M. Dyakonov, J. Cibert, S. Tatarenko, and T. Wojtowicz, Phys. Rev. B **64**, 085331 (2001).

[10] O. Morandi, P.-A. Hervieux, and G. Manfredi, New J. Phys. **11**, 073010 (2009).

[11] Z. Ben Cheikh, S. Cronenberger, M. Vladimirova, D. Scalbert, F. Perez, and T. Wojtowicz, Phys. Rev. B **88**, 201306(R) (2013).

[12] M. Vladimirova, S. Cronenberger, P. Barate, D. Scalbert, F. J. Teran, and A. P. Dmitriev, Phys. Rev. B **78**, 081305(R) (2008).

[13] C. Thurn and V. M. Axt, Phys. Rev. B **85**, 165203 (2012).

[14] F. Ungar, M. Cygorek, P. I. Tamborenea, and V. M. Axt, Phys. Rev. B **91**, 195201 (2015).

[15] S. A. Crooker, D. D. Awschalom, J. J. Baumberg, F. Flack, and N. Samarth, Phys. Rev. B **56**, 7574 (1997).

[16] K. E. Rönnburg, E. Mohler, H. G. Roskos, K. Ortner, C. R. Becker, and L. W. Molenkamp, Phys. Rev. Lett. **96**, 117203 (2006).

[17] C. D. Poweleit, L. M. Smith, and B. T. Jonker, Phys. Rev. B **55**, 5062 (1997).

[18] M. Umlauff, J. Hoffmann, H. Kalt, W. Langbein, J. M. Hvam, M. Scholl, J. Söllner, M. Heuken, B. Jobst, and D. Hommel, Phys. Rev. B **57**, 1390 (1998).

[19] W. M. Chen, I. A. Buyanova, G. Yu. Rudko, A. G. Mal'shukov, K. A. Chao, A. A. Toropov, Y. Terent'ev, S. V. Sorokin, A. V. Lebedev, S. V. Ivanov, and P. S. Kop'ev, Phys. Rev. B **67**, 125313 (2003).

[20] I. Di Marco, P. Thunström, M. I. Katsnelson, J. Sadowski, K. Karlsson, S. Lebègue, J. Kanski, and O. Eriksson, Nat. Commun. **4**, 2645 (2013).

[21] M. Cygorek, F. Ungar, P. I. Tamborenea, and V. M. Axt, Phys. Rev. B **95**, 045204 (2017).

[22] F. Ungar, M. Cygorek, and V. M. Axt, Phys. Rev. B **95**, 245203 (2017).

[23] F. Ungar, M. Cygorek, and V. M. Axt, Phys. Rev. B **98**, 161201(R) (2018).

[24] F. Ungar, M. Cygorek, and V. M. Axt, Phys. Rev. B **99**, 115305 (2019).

[25] M. Cygorek and V. M. Axt, J. Phys. Conf. Ser. **647**, 012042 (2015).

[26] M. W. Wu, J. H. Jiang, and M. Q. Weng, Phys. Rep. **493**, 61 (2010).

[27] R. Winkler, *Spin-Orbit Coupling Effects in Two-Dimensional Electron and Hole Systems* (Springer, Berlin, 2003).

[28] M. Z. Maialle, E. A. de Andrada e Silva, and L. J. Sham, Phys. Rev. B **47**, 15776 (1993).

[29] M. Z. Maialle and L. J. Sham, Surf. Sci. **305**, 256 (1994).

[30] R. Akimoto, K. Ando, F. Sasaki, S. Kobayashi, and T. Tani, J. Lumin. **72**, 309 (1997).

[31] S. Kamimura, A. Date, M. Nakajima, G. Karczewski, T. Wojtowicz, J. Kossut, T. Tsuchiya, and H. Mino, J. Phys. Soc. Jpn. **84**, 104704 (2015).

[32] H. Zhao, S. Moehl, and H. Kalt, Appl. Phys. Lett. **81**, 2794 (2002).

[33] H. Zhao, S. Moehl, and H. Kalt, Phys. Rev. Lett. **89**, 097401 (2002).

[34] J. Kossut, Phys. Status Solidi (b) **72**, 359 (1975).

[35] F. Ungar, M. Cygorek, and V. M. Axt, Phys. Rev. B **97**, 045210 (2018).

[36] S. Brem, M. Selig, G. Berghaeuser, and E. Malic, Sci. Rep. **8**, 8238 (2018).

[37] M. M. Ugeda, A. J. Bradley, S.-F. Shi, F. H. da Jornada, Y. Zhang, D. Y. Qiu, W. Ruan, S. Mo, Z. Hussain, Z. Shen, F. Wang, S. G. Louie, and M. F. Crommie, Nat. Mater. **13**, 1091 (2014).

[38] A. Chernikov, T. C. Berkelbach, H. M. Hill, A. Rigosi, Y. Li, O. B. Aslan, D. R. Reichman, M. S.

[39] G. Bastard, *Wave Mechanics Applied to Semiconductor Heterostructures* (Editions de Physique, Les Ulis, France, 1996).

[40] T. Uenoyama and L. J. Sham, Phys. Rev. Lett. **64**, 3070 (1990).

[41] R. Ferreira and G. Bastard, Phys. Rev. B **43**, 9687 (1991).

[42] G. Bastard and R. Ferreira, Surf. Sci. **267**, 335 (1992).

[43] Y. A. Bychkov and E. I. Rashba, Pis'ma Zh. Eksp. Teor. Fiz. **39**, 66 (1984) [JETP Lett. **39**, 78 (1984)].

[44] M. M. Glazov, E. Y. Sherman, and V. K. Dugaev, Phys. E **42**, 2157 (2010).

[45] E. A. de Andrada e Silva, G. C. La Rocca, and F. Bassani, Phys. Rev. B **55**, 16293 (1997).

[46] K. Gnanasekar and K. Navaneethakrishnan, Phys. E **35**, 103 (2006).

[47] M. M. Glazov and E. Y. Sherman, Phys. Rev. B **71**, 241312(R) (2005).

[48] M. Cosacchi, M. Cygorek, F. Ungar, and V. M. Axt, Phys. Rev. B **95**, 195313 (2017).

[49] M. I. Dyakonov (Ed.), *Spin Physics in Semiconductors* (Springer, Berlin, 2008).

[50] J. Schliemann, J. C. Egues, and D. Loss, Phys. Rev. Lett. **90**, 146801 (2003).

[51] J. R. Bindel, M. Pezzotta, J. Ulrich, M. Liebmann, E. Y. Sherman, and M. Morgenstern, Nat. Phys. **12**, 920 (2016).

[52] F. Rossi and T. Kuhn, Rev. Mod. Phys. **74**, 895 (2002).

[53] R. Akimoto, K. Ando, F. Sasaki, S. Kobayashi, and T. Tani, Phys. Rev. B **56**, 9726 (1997).

[54] I. A. Buyanova, G. Y. Rudko, W. M. Chen, A. A. Toropov, S. V. Sorokin, S. V. Ivanov, and P. S. Kop'ev, J. Appl. Phys. **93**, 7352 (2003).

[55] I. A. Buyanova, G. Y. Rudko, W. M. Chen, K. Kayanuma, A. Murayama, Y. Oka, A. A. Toropov, S. V. Sorokin, and S. V. Ivanov, Phys. Rev. B **71**, 165203 (2005).

Erratum: Spin dynamics of hot excitons in diluted magnetic semiconductors with spin-orbit interaction [Phys. Rev. B 100, 045306 (2019)]

F. Ungar, P. I. Tamborenea, and V. M. Axt

In contrast to the expression in the original paper, the typical timescale of the spin-orbit interaction (SOI) should read $\tau_{\mathrm{SOI}} = h(\alpha_{\mathrm{R}}\bar{K})^{-1}$. Using the parameters of Fig. 1, we then find $\tau_{\mathrm{SOI}} \approx 12.4$ and $\tau_{\mathrm{SOI}} \approx 56.4$ ps for $\mathrm{Cd}_{1-x}\mathrm{Mn}_x\mathrm{Te}$ and $\mathrm{Zn}_{1-x}\mathrm{Mn}_x\mathrm{Se}$, respectively, which are a bit longer compared with the previously reported values. Apart from the change in estimated dephasing times, no results in the paper are affected.

Publication 9

Nonlinear cavity feeding and unconventional photon statistics in solid-state cavity QED revealed by many-level real-time path-integral calculations

M. Cygorek, A. M. Barth, F. Ungar, A. Vagov, and V. M. Axt

&

Erratum: Nonlinear cavity feeding and unconventional photon statistics in solid-state cavity QED revealed by many-level real-time path-integral calculations

M. Cygorek, A. M. Barth, F. Ungar, A. Vagov, and V. M. Axt

Nonlinear cavity feeding and unconventional photon statistics in solid-state cavity QED revealed by many-level real-time path-integral calculations

M. Cygorek, A. M. Barth, F. Ungar, A. Vagov, and V. M. Axt

Theoretische Physik III, Universität Bayreuth, 95440 Bayreuth, Germany

The generation of photons in a microcavity coupled to a laser-driven quantum dot interacting with longitudinal acoustic (LA) phonons is studied in the regime of simultaneously strong driving and strong dot-cavity coupling. The stationary cavity photon number is found to depend in a nontrivial way on the detuning between the laser and the exciton transition in the dot. In particular, the maximal efficiency of the cavity feeding is obtained for detunings corresponding to transition energies between cavity-dressed states with excitation numbers larger than one. Phonons significantly enhance the cavity feeding at large detunings. In the strong-driving, strong-coupling limit, the photon statistics is highly non-Poissonian. While without phonons a double-peaked structure in the photon distribution is predicted, phonons make the photon statistics thermal-like with very high effective temperatures $\sim 10^5$ K, even for low phonon temperatures ~ 4 K. These results were obtained by numerical calculations where the driving, the dot-cavity coupling, and the dot-phonon interactions are taken into account without approximations. This is achieved by a reformulation of an exact iterative path-integral scheme which is applicable to a large class of quantum-dissipative systems and which in our case reduces the numerical demands by 15 orders of magnitude.

Solid-state quantum dots (QDs) have attracted much attention in recent years since they promise applications in photonic devices and quantum information technology, e.g., as qubits [1] and sources of single [2–4] or entangled photons [5–7]. Embedding QDs in microcavities increases the light extraction efficiency via the Purcell effect [2] and allows one to study cavity QED in solid-state systems [8–16]. Cavities may be used as buses mediating a selective coupling of two qubits stored in two QDs within the same cavity [17–19]. Investigating cavity QED in a solid is a rich field, also because the interaction with longitudinal acoustic (LA) phonons may have a profound impact on the physics [20–22], e.g., enabling phonon-mediated inversion of the QD [23] or providing a nonresonant coupling between the QD and the cavity [24].

Recently, experiments [25] on solid-state cavity QED systems have advanced into the largely unexplored regime of strong dot-cavity coupling combined with strong laser driving. While strongly driven dots can be described in terms of laser-dressed states and the physics of strongly coupled dot-cavity systems is best discussed in the basis of the cavity-dressed states, developing a physical intuition is more difficult when driving and coupling are equally strong. A further challenge is the coupling of the QD to phonons, in particular, since phonon influences on the QD dynamics are typically not well described by Born-Markov rate equations [26]. Thus, more sophisticated approaches are required, such as the correlation expansion [27–29] or polaron master equations [14,22,30–32].

For possible applications of strongly coupled dot-cavity systems, e.g., as building blocks of photonic devices, it is of fundamental interest how efficiently photons can be generated in the microcavity by driving the QD with an external laser field. In this Rapid Communication, we address this question for cases where QD-cavity and QD-laser couplings are simultaneously strong while also accounting for the QD-phonon interaction. Intuition suggests that the cavity feeding is enhanced when the laser is tuned to the resonances in the linear absorption of the dot-cavity system, i.e., when the dot-laser detuning matches the vacuum-Rabi-split peaks corresponding

to the transitions between the ground state and the first excited cavity-dressed states. We demonstrate that this expectation is only confirmed at low driving strength where the average cavity photon number is much smaller than one due to the photon blockade [33]. At strong driving, we find the maximum feeding efficiency at much smaller detunings, while there is no enhancement at the resonances of the linear absorption.

Phonons are a major reason why solid-state cavity QED differs from atomic cavity QED. In most cases phonons limit the performance of device relevant processes by introducing decoherence. However, in this Rapid Communication, we demonstrate that, already for small detunings compared to the vacuum Rabi splitting, phonons lead to a strongly enhanced generation of cavity photons that becomes almost independent of the detuning and all traces of the photon blockade are eliminated.

While in weak-coupling or weak-driving situations only cavity states with one or two photons can be significantly occupied, strong-driving+strong-coupling conditions lead to the excitation of states with larger photon numbers. This makes the shape of the photon distribution a meaningful target for investigations. In contrast to the case of classical (direct) driving of a cavity, which leads to a Poissonian photon distribution [34], we find strongly non-Poissonian distributions when the cavity is driven indirectly via the dot. Here, phonons not only lead to drastic quantitative effects but change the photon statistics qualitatively by transforming the photon distribution into a nearly thermal one.

We study a QD-cavity system interacting with LA phonons considering a single ground-to-exciton transition of the QD coupled to a single cavity mode and driven by an external laser field as sketched in Fig. 1. The Hamiltonian for the dot-cavity system in the interaction picture with respect to the laser energy $\hbar\omega_L$ is given by

$$
\begin{aligned}
H_N = {} & \hbar\Delta\omega_{XL}|X\rangle\langle X| - \hbar f(|G\rangle\langle X| + |X\rangle\langle G|) \\
& + \hbar\Delta\omega_{cL}\hat{a}^\dagger\hat{a} + \hbar g(\hat{a}^\dagger|G\rangle\langle X| + \hat{a}|X\rangle\langle G|), \quad (1)
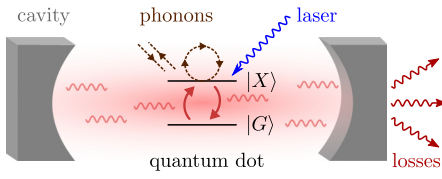\end{aligned}
$$

FIG. 1. Laser-driven quantum dot inside a microcavity and coupled to longitudinal acoustic phonons.

where $|G\rangle$ ($|X\rangle$) denotes the ground (excited) state of the QD and $\hat{a}^\dagger$ ($\hat{a}$) is the creation (annihilation) operator of a cavity photon. $\hbar\Delta\omega_{XL} = \hbar(\omega_X - \omega_L)$ and $\hbar\omega_X$ is the exciton transition energy while $\hbar\Delta\omega_{cL} = \hbar\omega_c - \hbar\omega_L$ is the detuning of the cavity with respect to the external driving. g is the strength of the dot-cavity coupling and f denotes the strength of the external cw laser driving.

LA phonons are included by the Hamiltonian [35,36]

$$\hat{H}_{\mathrm{ph}} = \hbar \sum_{\mathbf{q}} \omega_{\mathbf{q}} \hat{b}_{\mathbf{q}}^\dagger \hat{b}_{\mathbf{q}} + \hbar \sum_{\mathbf{q}} \left(\gamma_{\mathbf{q}}^X \hat{b}_{\mathbf{q}}^\dagger + \gamma_{\mathbf{q}}^{X*} \hat{b}_{\mathbf{q}} \right) |X\rangle\langle X|, \quad (2)$$

where $\hat{b}_{\mathbf{q}}^\dagger$ and $\hat{b}_{\mathbf{q}}$ are creation and annihilation operators for phonons with energy $\hbar\omega_{\mathbf{q}}$. $\gamma_{\mathbf{q}}^X$ are the exciton-phonon-coupling matrix elements [37,38] given explicitly in the Supplemental Material [39]. Finally, cavity losses are taken into account via the Lindblad term [40] $\mathcal{L}_{\mathrm{loss}}[\hat{\rho}] = \kappa[\hat{a}\hat{\rho}\hat{a}^\dagger - \frac{1}{2}\{\hat{\rho}, \hat{a}^\dagger\hat{a}\}_+]$ with loss rate κ.

The number of cavity photons generated by driving via the dot is limited by the losses. However, when the driving ($f \gg \kappa$) and the QD-cavity coupling ($g \gg \kappa$) are strong, describing the dynamics requires accounting for a large number of states of the QD-cavity system. Here, we consider all dot-cavity product states with up to $n_x \leqslant 20$ excitations, where the excitation number n_x is the photon number n plus the exciton occupation. Since there is one pair of states ($|G,n_x\rangle, |X,n_x - 1\rangle$) per excitation $n_x > 0$ and only one state $|G,0\rangle$ with $n_x = 0$, this amounts to a system with $N = 41$ levels.

It is important to note that strongly driven, strongly coupled solid-state cavity QED systems are simultaneously highly nonlinear with respect to the driving, the dot-cavity coupling, and the dot-phonon coupling, so that there is no obvious small parameter in the system. As a consequence, it is *a priori* unclear whether conclusive results can be obtained from established approximate methods, such as master equation or correlation expansion approaches. In principle, the time evolution of the reduced density matrix of an N-level system coupled to a continuum of phonons can be calculated using numerically exact path-integral (PI) methods [20,41–44]. Unfortunately, the numerical effort required in such calculations rises exponentially with the number of levels N, so that complete PI simulations have been performed only for rather small systems [20,45–50]. In particular, when the phonon-induced memory time is as long as a few picoseconds (which is typical for LA phonons coupled to a QD), numerically complete simulations are usually restricted to $N \leqslant 4$, while larger systems may be treated by heuristically discarding a large number of paths with numerically small contributions [51–53]. For solid-state cavity QED systems with $N \sim 40$ levels, complete PI simulations have, so far, been performed only for lossless cavities without

external driving [54], where the quantum dynamics of the system mixes only pairs of states with fixed excitation numbers n_x. However, external driving or cavity losses introduce transitions between states with different excitation numbers, so that the fully coupled system has to be considered, which increases the computation time dramatically.

We have overcome this problem by reformulating a standard iterative algorithm [41] to perform the sum over the paths, which in our case reduces the number of entities that have to be iterated by more than 15 orders of magnitude without introducing approximations. Full details of the reformulated path-integral method and its derivation are given in the Supplemental Material [39]. Here, we only note that the reformulation can be applied generally to any N-level system coupled to an oscillator continuum, provided the N states can be subdivided into N_g groups with identical oscillator couplings within each group. In our case, the interaction with phonons does not distinguish between states that differ only in the number of cavity photons. Thus, we have $N_g = 2$ where one group comprises the states $|G,n_x\rangle$ while a second group contains the states $|X,n_x - 1\rangle$.

It is worthwhile to note that, apart from the specific case treated in this Rapid Communication, there is a wealth of other systems of topical interest where the algorithm can be applied. An example of such systems are QDs with embedded magnetic dopants, e.g., Mn ions, which are highly attractive for spintronic applications [55–57]. Here, the phonon coupling does not distinguish between different spin configurations of the dot-dopant system. Another possible application is the description of phonon effects on the biexciton cascade in a QD, proposed as a source of entangled photon pairs [5–7]. As in our system, the phonon coupling does not distinguish between states differing only by photon numbers such that for the biexciton cascade $N_g = 3$ groups have to be considered (ground state, excitons, and biexciton). Cavity QED has also been studied in systems where superconducting charge qubits are strongly coupled to a microwave cavity [58]. There, the dephasing is determined by charge fluctuations that can be represented by a bath of harmonic oscillators [59], so that our PI method can be applied to these systems as well.

For the present study of cavity feeding in QD-based solid-state cavity QED systems, we assume a cavity in resonance with the polaron-shifted QD-exciton transition and a laser coupled to the QD transition detuned by an energy δ from the cavity mode. Before the laser is switched on at time $t = 0$ the electronic system is in the ground state $|G,0\rangle$ while the phonons are initially in thermal equilibrium at temperature T. The dot-cavity coupling and the driving are chosen to be of equal strength $\hbar g = \hbar f = 0.1$ meV, if not stated otherwise. The cavity loss rate is taken to be $\kappa = 0.01$ ps^{-1}, which corresponds to a quality factor $Q \approx 10^5$. For the phonon environment and dot-phonon coupling we assume parameters of a self-assembled InGaAs QD with radius $a_e = 3$ nm embedded in a GaAs matrix (cf. the Supplemental Material [39]).

Figures 2(a) and 2(b) depict the time evolution of the average cavity photon number $\langle n \rangle$ and the exciton occupation for a detuning $\delta = 20\ \mu$eV. Both quantities show an oscillatory transient behavior in the first ~ 1 ns and eventually reach stationary values. We find that phonons have little impact on the exciton occupations but can change the average photon number
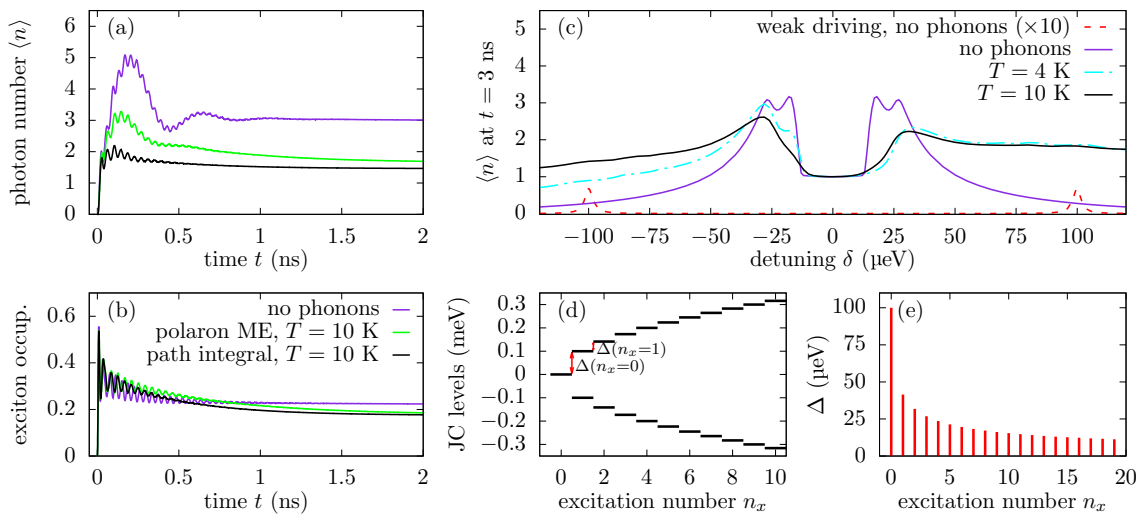
FIG. 2. Time evolution of the average photon number (a) and of the exciton occupation (b) for a detuning $\delta = 20\ \mu$eV at $T = 10$ K calculated using the path-integral theory (black), Markovian polaron master equations (green), and without phonons (violet). (c) Average photon number $\langle n \rangle$ in the cavity at $t = 3$ ns as a function of the detuning δ. (d) Energy of the Jaynes-Cummings levels in the rotating frame. (e) Transition energies $\Delta(n_x)$ between neighboring Jaynes-Cummings levels [as indicated in (d)].

significantly. For comparison, we present results obtained using polaron master equations (PMEs, cf. the Supplemental Material [39]), a well-established method for the treatment of the dot-phonon interaction [14,30,32,60]. These results demonstrate that, while exciton occupations are reasonably well described by the PMEs, photon-related quantities are much more affected by the approximations used to derive the PMEs. In particular, the PMEs predict significantly larger (e.g., more than 60% at $t = 150$ ps) photon numbers than the PI method, revealing that the PMEs are insufficient for an accurate description of the situation studied here. We note that this inaccuracy of the PMEs can be explained by the fact that the dot-cavity system possesses a number of different energy gaps on scales $\sim$10–1000 μeV [cf. Fig. 2(d)], which can be bridged by phonon-assisted transitions. These are, however, only strictly treated up to second order in the dot-phonon interaction within the PME approach.

Phonon effects on the cavity feeding are illustrated in Fig. 2(c), showing the average photon number at long times ($t = 3$ ns) as a function of δ with and without a dot-phonon interaction. In the weak-driving limit ($\hbar f = 1\ \mu$eV, red line), the driving of the cavity via the dot is most effective if one excites at the resonances of the linear absorption, manifested in the appearance of two peaks at $\delta = \pm\hbar g = \pm 100\ \mu$eV separated by the vacuum Rabi splitting. Surprisingly, for strong driving the maximum number of photons in the cavity is obtained neither at $\delta = \pm\hbar g$ nor when the driving is in resonance with the ground-to-exciton transition ($\delta = 0$, i.e., where the linear absorption has a resonance for vanishing dot-cavity coupling), but in a region with small detunings of $\sim$20–40 μeV. This is explained by the fact that with strong driving the cavity is partially filled with photons and thus transitions between states with higher photon numbers become important. When the dot and the cavity are in resonance, the energy eigenvalues of the cavity-dressed states are $E_{n_x} = \pm\sqrt{n_x}\hbar g$ [cf. Fig. 2(d)] and transitions between neighboring states can occur at energies $\Delta(n_x) = (\sqrt{n_x + 1} - \sqrt{n_x})\hbar g$

depicted in Fig. 2(e). For the chosen parameters, the efficiency of the cavity feeding increases drastically when δ becomes similar to $\Delta(n_x)$ for $n_x \approx 5$, which corresponds to the typical photon number of states that are significantly occupied. When the driving strength increases further and states with higher photon numbers are occupied, the maxima in Fig. 2(c) will eventually shift to zero and merge into the central peak of a Mollow triplet [61].

Figure 2(c) also reveals an asymmetry of the average photon number with respect to a sign change of the detuning. This asymmetry diminishes at higher temperatures, indicating that it originates from the asymmetry between phonon absorption and emission. Compared with phonon-free calculations, the interaction with phonons results in a reduced efficiency at the maxima because it suppresses the coherent driving. However, at larger detunings, phonon-assisted processes facilitate otherwise prohibited transitions between off-resonant states, which enables a much more efficient generation of cavity photons. Interestingly, the phonon-induced feeding efficiency in this regime is almost independent of the detuning in a wide parameter range.

More detailed information than the mean number of photons is provided by examining how the photons are distributed across different photonic states. It is well known that direct (classical) driving of a cavity leads to a Poissonian statistics [34]. Here, however, we find that driving the cavity via the dot creates highly non-Poissonian distributions, as depicted in Fig. 3. Figure 3(a) illustrates the case where the dot-phonon interaction is neglected. There, large detunings lead to a shift of the peak in the photon distribution to higher photon numbers with a rapidly decaying tail, as expected for a Poisson distribution. For values of the detuning at which the resonance condition with neighboring cavity-dressed energy eigenstates is met, a double-peaked structure appears in the photon statistics. This two-peak structure is a rather unconventional feature, which is possible only due to the resonance in the nonlinear driving regime.
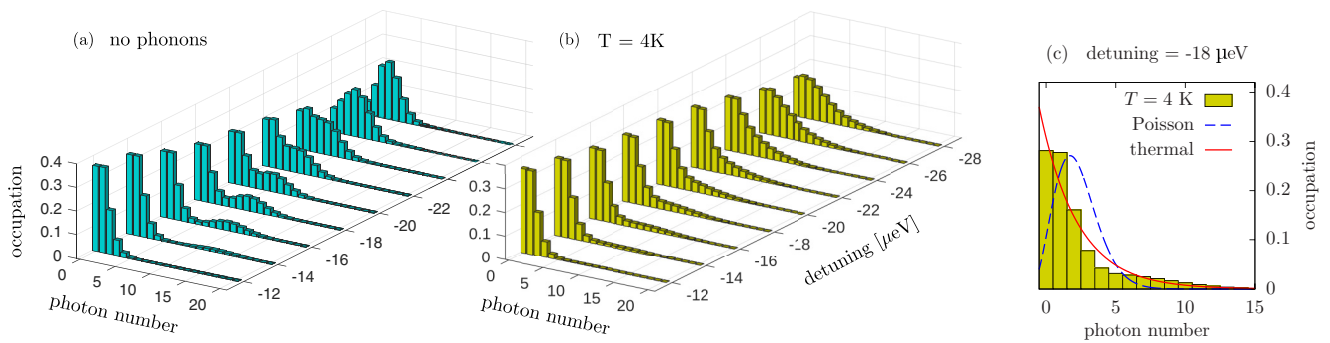
FIG. 3. Cavity photon distribution at $t = 3$ ns for different detunings δ and $\hbar g = \hbar f = 0.1$ meV without dot-phonon interaction (a) and with phonons at temperature $T = 4$ K (b). (c) Photon distribution at detuning $\delta = -18$ μeV with phonons at $T = 4$ K compared with Poissonian and thermal distributions.

When the dot-phonon interaction is accounted for [cf. Fig. 3(b)], significant changes in the photon distributions are observed. Most prominently, the double-peaked structure predicted by the phonon-free calculation disappears. Furthermore, for large photon numbers, the photon distribution has a maximum closer to $n = 0$ and possesses a significantly longer tail than expected for a Poissonian distribution. In Fig. 3(c), we compare the photon statistics for $\delta = -18$ μeV, where the maximal efficiency of cavity feeding was reached, with a Poissonian as well as with a thermal distribution [$P_{\text{th}}(n) = (1 - e^{-\epsilon})e^{-\epsilon n}$] with the same average photon number $\langle n \rangle \approx 2.25$ as obtained in the numerical simulations for $T = 4$ K. It can be seen that the obtained photon statistics in the presence of phonons is much closer to the thermal distribution than to the Poissonian. For a cavity mode with energy $\hbar\omega_c \approx 1.5$ eV, one can extract an effective temperature $T = \hbar\omega_c/(k_B\epsilon) \approx 47\,000$ K. It is worth noting that, although the qualitative change of the photon statistics toward a thermal distribution is caused by the dot-phonon interaction, the value of the photon temperature is four orders of magnitude larger than the phonon temperature and is rather determined by the average photon number, which can be tuned by changing the driving strength.

To summarize, we have investigated the generation of photons in a QD-cavity system coupled to LA phonons in the regime of strong driving and simultaneously strong coupling. Conclusive results have been obtained using a variant of the numerically exact real-time path-integral approach, which for a large class of systems of topical interest speeds up the numerics by many orders of magnitude. Our simulations show that, when a dot is in resonance with a microcavity, the feeding efficiency depends nontrivially on the dot-laser detuning. In the strong-driving limit, the maximal feeding is observed for much smaller detunings than expected from the linear absorption. The dot-phonon interaction is found to suppress the feeding efficiency at resonances. However, for larger detunings, it opens up the possibility of a highly efficient phonon-mediated feeding which is robust against variations of the detuning. Furthermore, the dot-phonon interaction modifies the photon statistics qualitatively, so that a double-peaked distribution for the phonon-free case is transformed to a nearly thermal occupation of photon states with a huge effective temperature.

[1] P. Chen, C. Piermarocchi, and L. J. Sham, Phys. Rev. Lett. **87**, 067401 (2001).

[2] N. Somaschi, V. Giesz, L. De Santis, J. Loredo, M. P. Almeida, G. Hornecker, S. L. Portalupi, T. Grange, C. Antón, J. Demory, C. Gómez, I. Sagnes, N. D. Lanzillotti-Kimura, A. Lemaître, A. Auffeves, A. G. White, L. Lanco, and P. Senellart, Nat. Photonics **10**, 340 (2016).

[3] P. Michler, A. Kiraz, C. Becher, W. V. Schoenfeld, P. M. Petroff, L. Zhang, E. Hu, and A. Imamoglu, Science **290**, 2282 (2000).

[4] Y.-M. He, Y. He, Y.-J. Wei, D. Wu, M. Atatüre, C. Schneider, S. Höfling, M. Kamp, C.-Y. Lu, and J.-W. Pan, Nat. Nanotechnol. **8**, 213 (2013).

[5] M. A. M. Versteegh, M. E. Reimer, K. D. Jöns, D. Dalacu, P. J. Poole, A. Gulinatti, A. Guidice, and V. Zwiller, Nat. Commun. **5**, 5298 (2014).

[6] M. Müller, S. Bounouar, K. D. Jöns, M. Glässl, and P. Michler, Nat. Photonics **8**, 224 (2014).

[7] N. Akopian, N. H. Lindner, E. Poem, Y. Berlatzky, J. Avron, D. Gershoni, B. D. Gerardot, and P. M. Petroff, Phys. Rev. Lett. **96**, 130501 (2006).

[8] D. Englund, A. Faraon, I. Fushman, N. Stoltz, P. Petroff, and J. Vučković, Nat. Lett. **450**, 857 (2007).

[9] K. Hennessy, A. Badolato, M. Winger, D. Gerace, M. Atatüre, S. Gulde, S. Fält, E. L. Hu, and A. Imamoğlu, Nature (London) **445**, 896 (2007).

[10] J. P. Reithmaier, Semicond. Sci. Technol. **23**, 123001 (2008).

[11] J. Kasprzak, S. Reitzenstein, E. A. Muljarov, C. Kistner, C. Schneider, M. Strauss, S. Höfling, A. Forchel, and W. Langbein, Nat. Mater. **9**, 304 (2010).

[12] S. Reitzenstein, IEEE J. Sel. Top. Quantum Electron. **18**, 1733 (2012).

[13] J. Kasprzak, K. Sivalertporn, F. Albert, C. Schneider, S. Höfling, M. Kamp, A. Forchel, S. Reitzenstein, E. A. Muljarov, and W. Langbein, New J. Phys. **15**, 045013 (2013).

[14] C. Roy and S. Hughes, Phys. Rev. X **1**, 021009 (2011).
[15] C. Roy and S. Hughes, Phys. Rev. Lett. **106**, 247403 (2011).
[16] S. M. Ulrich, S. Ates, S. Reitzenstein, A. Löffler, A. Forchel, and P. Michler, Phys. Rev. Lett. **106**, 247402 (2011).
[17] M. Feng, I. D'Amico, P. Zanardi, and F. Rossi, Phys. Rev. A **67**, 014306 (2003).
[18] A. Imamoglu, D. D. Awschalom, G. Burkard, D. P. DiVincenzo, D. Loss, M. Sherwin, and A. Small, Phys. Rev. Lett. **83**, 4204 (1999).
[19] M. S. Sherwin, A. Imamoglu, and T. Montroy, Phys. Rev. A **60**, 3508 (1999).
[20] D. G. Nahri, F. H. A. Mathkoor, and C. H. R. Ooi, J. Phys.: Condens. Matter **29**, 055701 (2017).
[21] P. Kaer, T. R. Nielsen, P. Lodahl, A.-P. Jauho, and J. Mørk, Phys. Rev. Lett. **104**, 157401 (2010).
[22] P. Kaer, T. R. Nielsen, P. Lodahl, A.-P. Jauho, and J. Mørk, Phys. Rev. B **86**, 085302 (2012).
[23] S. Hughes and H. J. Carmichael, New J. Phys. **15**, 053039 (2013).
[24] S. Ates, S. M. Ulrich, A. Ulhaq, S. Reitzenstein, A. Löffler, S. Höfling, A. Forchel, and P. Michler, Nat. Photonics **3**, 724 (2009).
[25] C. Hopfmann, A. Carmele, A. Musiał, C. Schneider, M. Kamp, S. Höfling, A. Knorr, and S. Reitzenstein, Phys. Rev. B **95**, 035302 (2017).
[26] D. P. S. McCutcheon, N. S. Dattani, E. M. Gauger, B. W. Lovett, and A. Nazir, Phys. Rev. B **84**, 081305 (2011).
[27] J. Förstner, C. Weber, J. Danckwerts, and A. Knorr, Phys. Rev. Lett. **91**, 127401 (2003).
[28] M. Glässl, A. Vagov, S. Lüker, D. E. Reiter, M. D. Croitoru, P. Machnikowski, V. M. Axt, and T. Kuhn, Phys. Rev. B **84**, 195311 (2011).
[29] D. E. Reiter, Phys. Rev. B **95**, 125308 (2017).
[30] A. Nazir and D. P. S. McCutcheon, J. Phys.: Condens. Matter **28**, 103002 (2016).
[31] P. Karwat and P. Machnikowski, Phys. Rev. B **91**, 125428 (2015).
[32] J. Iles-Smith and A. Nazir, Optica **3**, 207 (2016).
[33] A. Faraon, I. Fushman, D. Englund, N. Stoltz, P. Petroff, and J. Vučković, Nat. Phys. **4**, 859 (2008).
[34] R. J. Glauber, Phys. Rev. **131**, 2766 (1963).
[35] L. Besombes, K. Kheng, L. Marsal, and H. Mariette, Phys. Rev. B **63**, 155307 (2001).
[36] P. Machnikowski and L. Jacak, Phys. Rev. B **69**, 193302 (2004).
[37] B. Krummheuer, V. M. Axt, and T. Kuhn, Phys. Rev. B **65**, 195313 (2002).

[38] B. Krummheuer, V. M. Axt, T. Kuhn, I. D'Amico, and F. Rossi, Phys. Rev. B **71**, 235329 (2005).
[39] See Supplemental Material at http://link.aps.org/supplemental/10.1103/PhysRevB.96.201201 for a detailed description of the reformulated iterative real-time path-integral method, the dot-phonon couplings, as well as the polaron master equations.
[40] H. P. Breuer and F. Petruccione, *The Theory of Open Quantum Systems*, 1st ed. (Oxford University Press, Oxford, U.K., 2002).
[41] N. Makri and D. E. Makarov, J. Chem. Phys. **102**, 4600 (1995).
[42] N. Makri and D. E. Makarov, J. Chem. Phys. **102**, 4611 (1995).
[43] A. Vagov, M. D. Croitoru, M. Glässl, V. M. Axt, and T. Kuhn, Phys. Rev. B **83**, 094303 (2011).
[44] A. M. Barth, A. Vagov, and V. M. Axt, Phys. Rev. B **94**, 125439 (2016).
[45] A. J. Leggett, S. Chakravarty, A. T. Dorsey, M. P. A. Fisher, A. Garg, and W. Zwerger, Rev. Mod. Phys. **59**, 1 (1987).
[46] E. Sim and N. Makri, J. Phys. Chem. B **101**, 5446 (1997).
[47] P. Nalbach and M. Thorwart, Phys. Rev. Lett. **103**, 220401 (2009).
[48] A. M. Barth, S. Lüker, A. Vagov, D. E. Reiter, T. Kuhn, and V. M. Axt, Phys. Rev. B **94**, 045306 (2016).
[49] M. Glässl, A. M. Barth, and V. M. Axt, Phys. Rev. Lett. **110**, 147401 (2013).
[50] M. Glässl and V. M. Axt, Phys. Rev. B **86**, 245306 (2012).
[51] E. Sim, J. Chem. Phys. **115**, 4450 (2001).
[52] N. Makri, J. Chem. Phys. **141**, 134117 (2014).
[53] L. Magazzù, D. Valenti, A. Carollo, and B. Spagnolo, Entropy **17**, 2341 (2015).
[54] M. Glässl, L. Sörgel, A. Vagov, M. D. Croitoru, T. Kuhn, and V. M. Axt, Phys. Rev. B **86**, 035319 (2012).
[55] L. Besombes, Y. Léger, L. Maingault, D. Ferrand, H. Mariette, and J. Cibert, Phys. Rev. Lett. **93**, 207403 (2004).
[56] A. Kudelski, A. Lemaître, A. Miard, P. Voisin, T. C. M. Graham, R. J. Warburton, and O. Krebs, Phys. Rev. Lett. **99**, 247209 (2007).
[57] D. E. Reiter, T. Kuhn, and V. M. Axt, Phys. Rev. Lett. **102**, 177403 (2009).
[58] A. Blais, R.-S. Huang, A. Wallraff, S. M. Girvin, and R. J. Schoelkopf, Phys. Rev. A **69**, 062320 (2004).
[59] Y. Makhlin, G. Schön, and A. Shnirman, Rev. Mod. Phys. **73**, 357 (2001).
[60] D. P. S. McCutcheon and A. Nazir, New J. Phys. **12**, 113042 (2010).
[61] B. R. Mollow, Phys. Rev. **188**, 1969 (1969).

Supplement: Nonlinear cavity feeding and unconventional photon statistics in solid-state cavity QED revealed by many-level real-time path-integral calculations

M. Cygorek,[1] A. M. Barth,[1] F. Ungar,[1] A. Vagov,[1] and V. M. Axt[1]

[1]*Theoretische Physik III, Universität Bayreuth, 95440 Bayreuth, Germany*

REFORMULATON OF THE ITERATIVE REAL-TIME PATH-INTEGRAL ALGORITHM

In this section, we describe in detail the iterative real-time path-integral algorithm used in the main text for the description of solid-state cavity QED systems. Our starting point is a well established iteration scheme for the so called *augmented density matrix* that has been introduced and implemented before [1–4] to perform the sum over paths needed to obtain the reduced density matrix. First, in the next subsection we shall summarize the main results of this scheme in order to have a basis for the reformulation of the algorithm as an iteration scheme for a partially summed augmented density matrix. This reformulation is the key for the huge reduction of the numerical effort which enabled us to perform a numerically complete study for a system with 41 fully coupled levels interacting with a continuum of acoustic phonons. As this reformulation is not restricted to the specific system considered in the main text, we shall formulate the algorithm for a general N-level system that can be subdivided into N_g groups with identical pure-dephasing-type couplings to a continuum of bosons within each group and explain alongside how the general scheme reduces to the special case treated in the main text.

Augmented density matrix iteration for simulating the system dynamics

The time evolution of the full many-body statistical operator $\hat{\rho}$ for a system with N levels coupled to a continuum of independent boson oscillators is given by:

$$\frac{\partial}{\partial t}\hat{\rho} = \mathcal{L}_N[\hat{\rho}] + \mathcal{L}_{\text{osc}}[\hat{\rho}], \tag{1}$$

where $\mathcal{L}_N$ is the Liouville operator for the evolution of the N-level system in the absence of the boson oscillators. It can usually be decomposed according to:

$$\mathcal{L}_N[\hat{\rho}] = \frac{1}{i\hbar}\{\hat{H}_N, \hat{\rho}\}_- + \mathcal{L}_{\text{loss}}[\hat{\rho}], \tag{2}$$

where $\{,\}_-$ is the commutator and $\hat{H}_N$ stands for an N-level Hamiltonian, which besides defining couplings between the N levels may contain a time dependent driving. Let $\{|\mu\rangle\}$ be a basis of ket states for the N-level system and $\{\langle\nu|\}$ the corresponding bra states. Then, $\hat{H}_N$ can be written as:

$$\hat{H}_N = \sum_{\mu\nu} H_{\mu\nu}^N(t)\,|\mu\rangle\langle\nu|. \tag{3}$$

In the specific case studied in the main text, the basis $|\nu\rangle$ comprises the states $|G, n_x\rangle$, $|X, n_x - 1\rangle$ with $1 \leq n_x \leq 20$ as well as $|G, 0\rangle$ and $H_{\mu\nu}^N(t)$ is obtained by taking the corresponding matrix elements of Eq. (1) in the main text, i.e. $\hat{H}_N$ comprises here the Jaynes-Cummings-type couplings between the basis states as well as the dipole coupling of the dot to an external laser field.

$\mathcal{L}_{\text{loss}}$ describes non-Hamiltonian contributions to the dynamics which arise in open quantum systems primarily by losses due to the coupling with the surrounding environment. Often such contributions can be represented by Liouville operators in the so called Lindblad form: [5]

$$\mathcal{L}_{\text{loss}} = \sum_p \kappa_p\big[\hat{A}_p\hat{\rho}\hat{A}_p^\dagger - \frac{1}{2}\{\hat{\rho}, \hat{A}_p^\dagger\hat{A}_p\}_+\big], \tag{4}$$

where $\{,\}_+$ denotes the anti-commutator, $\hat{A}_p$ are system operators characterizing the process to be modeled and κ_p are the corresponding rates. This form applies in particular to the cavity losses considered in the main text. Finally

$$\mathcal{L}_{\text{osc}}[\hat{\rho}] = \frac{1}{i\hbar}\{\hat{H}_{\text{osc}}, \hat{\rho}\}_-, \quad \text{with} \quad \hat{H}_{\text{osc}} = \hbar\sum_{\mathbf{q}} \omega_{\mathbf{q}}\hat{b}_{\mathbf{q}}^\dagger\hat{b}_{\mathbf{q}} + \hbar\sum_{\nu\mathbf{q}}\big(\gamma_{\mathbf{q}}^\nu\hat{b}_{\mathbf{q}}^\dagger + \gamma_{\mathbf{q}}^{\nu*}\hat{b}_{\mathbf{q}}\big)|\nu\rangle\langle\nu| \tag{5}$$

is the Liouville operator accounting for a pure-dephasing type interaction with bosonic oscillators. $\hat{b}_{\mathbf{q}}^{\dagger}$ and $\hat{b}_{\mathbf{q}}$ are, respectively, the creation and annihilation operators of bosons in mode $\mathbf{q}$ with energy $\hbar\omega_{\mathbf{q}}$ while $\gamma_{\mathbf{q}}^{\nu}$ defines the coupling strength between the mode $\mathbf{q}$ and the state $|\nu\rangle$.

We are interested in the dynamics of the reduced density matrix $\bar{\rho}$ which is obtained from the statistical operator of the total system by tracing over the oscillator degrees of freedom and taking matrix elements in the basis of the N-level system: $\bar{\rho}_{\nu\mu} = \langle\nu|\text{Tr}_{\text{osc}}(\hat{\rho})|\mu\rangle$. It is known for a long time that $\bar{\rho}_{\nu\mu}$ can be represented as a sum over paths when the system dynamics is Hamiltonian [1]. Recently, it has been shown that this still holds when in addition to Hamiltonian contributions the Liouville operator for the N-level system of interest also contains non-Hamiltonian parts [4]. As in the latter paper, we consider an equally spaced discretization of time $t_\ell = \Delta t\,\ell$ with time steps of width Δt and integer ℓ and label the states of the N-level system at time t_ℓ by ν_ℓ or μ_ℓ. Furthermore, we assume that at time t_0 the system is in its ground state $|0\rangle$ while the oscillators are in a thermal distribution at temperature T. Then the sum-over-paths representation of the reduced density matrix is given by [4]:

$$\bar{\rho}_{\nu_n\mu_n} = \sum_{\substack{\nu_0\ldots\nu_{n-1}\\\mu_0\ldots\mu_{n-1}}} R_{\nu_n\ldots\nu_0}^{\mu_n\ldots\mu_0}, \qquad \text{with} \qquad R_{\nu_n\ldots\nu_0}^{\mu_n\ldots\mu_0} := \bar{\rho}_{\nu_0\mu_0}\prod_{\ell=1}^{n}\mathcal{M}_{\nu_\ell\mu_\ell}^{\nu_{\ell-1}\mu_{\ell-1}}\exp\Big(\sum_{\ell=1}^{n}\sum_{\ell'=1}^{\ell}S_{\nu_\ell\mu_\ell}^{\nu_{\ell'}\mu_{\ell'}}\Big). \tag{6}$$

Here, a path is any possible sequence $\nu_0\ldots\nu_{n-1}$ of states that the system may run through while stepping forward in time from t_0 to t_{n-1}. Equation (6) involves two summations over all paths since for obtaining the reduced density matrix the ket- $|\mu\rangle$ as well as the bra-states $\langle\nu|$ have to be propagated. Thus, for an N-level system the sum runs over N^{2n} terms. Each term contains three factors: the initial reduced density matrix $\bar{\rho}_{\nu_0\mu_0}$ at time t_0, a factor $\prod_{\ell=1}^{n}\mathcal{M}_{\nu_\ell\mu_\ell}^{\nu_{\ell-1}\mu_{\ell-1}}$ accounting for the dynamics induced by $\mathcal{L}_N$ and a factor $\exp\big(\sum_{\ell=1}^{n}\sum_{\ell'=1}^{\ell}S_{\nu_\ell\mu_\ell}^{\nu_{\ell'}\mu_{\ell'}}\big)$ capturing the influences of the oscillators.

$\bar{\rho}_{\nu_0\mu_0}$ is determined by the initial conditions to be the reduced density matrix of the system ground state. The factor $\prod_{\ell=1}^{n}\mathcal{M}_{\nu_\ell\mu_\ell}^{\nu_{\ell-1}\mu_{\ell-1}}$ is most easily defined by introducing the time evolution operator $\mathcal{M}_{t,t'}$ for the propagation of the N-level system without oscillator coupling from time t to t':

$$\mathcal{M}_{t,t'}[\,\cdot\,] = \mathcal{T}\exp\Big(\int_t^{t'}\mathcal{L}_N dt'\Big)[\,\cdot\,], \tag{7}$$

i.e., $\mathcal{M}_{t,t'}$ maps the reduced density matrix at time t to its values reached at time t' when the system evolves under the action of the Liouville operator $\mathcal{L}_N$. For time-independent $\mathcal{L}_N$, $\mathcal{M}_{t,t'}$ can be conveniently constructed using standard methods for taking the exponential of a finite size matrix. Alternatively, one can solve numerically the equation of motion for the reduced density matrix in the oscillator-free case (i.e., solving an ordinary differential equation for a $N\times N$ matrix). The factors $\mathcal{M}_{\nu_\ell\mu_\ell}^{\nu_{\ell-1}\mu_{\ell-1}}$ are then obtained by acting with $\mathcal{M}_{t_{\ell-1},t_\ell}$ on the basis projectors $|\nu_{\ell-1}\rangle\langle\mu_{\ell-1}|$ and taking the matrix elements between states $|\nu_\ell\rangle$ and $|\mu_\ell\rangle$ of the result:

$$\mathcal{M}_{\nu_\ell\mu_\ell}^{\nu_{\ell-1}\mu_{\ell-1}} = \langle\nu_\ell|\,\mathcal{M}_{t_{\ell-1},t_\ell}\big[\,|\nu_{\ell-1}\rangle\langle\mu_{\ell-1}|\,\big]\,|\mu_\ell\rangle. \tag{8}$$

Finally, the oscillator influence is encoded in the functions $S_{\nu_\ell\mu_\ell}^{\nu_{\ell'}\mu_{\ell'}}$ which represent a phonon-induced memory with a memory depth $t_\ell - t_{\ell'}$. The explicit expression for $S_{\nu_\ell\mu_\ell}^{\nu_{\ell'}\mu_{\ell'}}$ used for the simulations in the main text are given below. For the discussion of the numerical algorithm only two properties are important: (i) $S_{\nu_\ell\mu_\ell}^{\nu_{\ell'}\mu_{\ell'}}$ depends on the indices $\nu_\ell,\mu_\ell,\nu_{\ell'},\mu_{\ell'}$ only via its dependence on the corresponding couplings $\gamma_q^{\nu_\ell},\gamma_q^{\mu_\ell},\gamma_q^{\nu_{\ell'}},\gamma_q^{\mu_{\ell'}}$ and (ii) for a continuum of oscillators, $S_{\nu_\ell\mu_\ell}^{\nu_{\ell'}\mu_{\ell'}}$ is negligibly small when $t_\ell - t_{\ell'}$ exceeds a certain finite memory time $t_m = n_m\Delta t$.

From the definition of the terms $R_{\nu_n\ldots\nu_0}^{\mu_n\ldots\mu_0}$ one obtains immediately the recurrence:

$$R_{\nu_n\ldots\nu_0}^{\mu_n\ldots\mu_0} = \mathcal{M}_{\nu_n\mu_n}^{\nu_{n-1}\mu_{n-1}}\exp\Big(\sum_{\ell=1}^{n}S_{\nu_n\mu_n}^{\nu_\ell\mu_\ell}\Big)R_{\nu_{n-1}\ldots\nu_0}^{\mu_{n-1}\ldots\mu_0}, \quad n\geq 1 \tag{9}$$

with the initial condition $R_{\nu_0}^{\mu_0} = \bar{\rho}_{\nu_0\mu_0}$. For obtaining an efficient numerical algorithm, in the pioneering work of Makri et al. [1, 2] the *augmented density matrix* (ADM) is introduced for $n > n_m$ as $\rho_{\nu_n\ldots\nu_{n-n_m+1}}^{\mu_n\ldots\mu_{n-n_m+1}} := \sum_{\substack{\nu_{n-n_m}\ldots\nu_0\\\mu_{n-n_m}\ldots\mu_0}}R_{\nu_n\ldots\nu_0}^{\mu_n\ldots\mu_0}$. Exploiting the finite depth of the phonon-induced memory [property (ii)] it was shown in Ref. 1 that the ADM obeys the recursion:

$$\rho_{\nu_n\ldots\nu_{n-n_m+1}}^{\mu_n\ldots\mu_{n-n_m+1}} = \mathcal{M}_{\nu_n\mu_n}^{\nu_{n-1}\mu_{n-1}}\sum_{\substack{\nu_{n-n_m}\\\mu_{n-n_m}}}\exp\Big(\sum_{\ell=n-n_m}^{n}S_{\nu_n\mu_n}^{\nu_\ell\mu_\ell}\Big)\rho_{\nu_{n-1}\ldots\nu_{n-n_m}}^{\mu_{n-1}\ldots\mu_{n-n_m}}. \tag{10}$$

From the ADM, the reduced N-level density matrix can be obtained by:

$$\bar{\rho}_{\nu_n \mu_n}(t_n) = \sum_{\substack{\nu_{n-1}\dots\nu_{n-n_m+1} \\ \mu_{n-1}\dots\mu_{n-n_m+1}}} \rho_{\nu_n\dots\nu_{n-n_m+1}}^{\mu_n\dots\mu_{n-n_m+1}}. \tag{11}$$

The main advantage of using the above recurrence for the ADM is that after reaching the memory time t_m the effort for a further propagation step does no longer increase as the number of elements of the ADM stays at $N_{ADM} = N^{2n_m}$. In this way, the iterative scheme allows one to calculate the dynamics up to arbitrary final times t_n.

Decomposition into groups and recurrence for a partially summed augmented density matrix

The central methodological improvement presented in this article is based on the observation that in many situations, some states ν and μ of the N-level system couple identically to the bath of bosons, i.e. $\gamma_q^\mu = \gamma_q^\nu$. In this case, the numerical complexity of the real-time path-integral method can be drastically decreased as follows:

Decompose the N levels into N_g groups where the states within a single group have the same coupling to the boson modes. Relabel the states $|\nu\rangle \rightarrow |\lambda, k\rangle$ and $|\mu\rangle \rightarrow |\bar{\lambda}, \bar{k}\rangle$, where $\lambda = \{1, 2, \dots, N_g\}$ denotes the group and k distinguishes the different states within the respective group. As a result, the coupling can be described by the group index $\gamma_q^\lambda := \gamma_q^{(\lambda,k)}$, $\forall k$. Since the phonon-memory functions $S_{\nu_\ell \mu_\ell}^{\nu_{\ell'} \mu_{\ell'}}$ depend on the state indices only via their dependence on the phonon couplings [property (i)], the influence functional in Eq. (10) can be written as:

$$\sum_{\ell=n-n_m}^{n} S_{\nu_n \mu_n}^{\nu_\ell \mu_\ell} = \sum_{\ell=n-n_m}^{n} S_{(\lambda_n, k_n)(\bar{\lambda}_n, \bar{k}_n)}^{(\lambda_\ell, k_\ell)(\bar{\lambda}_\ell, \bar{k}_\ell)} = \sum_{\ell=n-n_m}^{n} S_{\lambda_n \bar{\lambda}_n}^{\lambda_\ell \bar{\lambda}_\ell} =: S_{\lambda_n \dots \lambda_{n-n_m}}^{\bar{\lambda}_n \dots \bar{\lambda}_{n-n_m}}. \tag{12}$$

Because the influence functional no longer depends on the index k of levels within a group, it is possible to obtain the reduced N-level density matrix $\bar{\rho}_{\nu_n \mu_n}(t_n)$ from a partially summed ADM defined as:

$$\rho_{(\lambda_n, k_n)\lambda_{n-1}\dots\lambda_{n-n_m+1}}^{(\bar{\lambda}_n, \bar{k}_n)\bar{\lambda}_{n-1}\dots\bar{\lambda}_{n-n_m+1}} := \sum_{\substack{k_{n-1}\dots k_{n-n_m+1} \\ \bar{k}_{n-1}\dots\bar{k}_{n-n_m+1}}} \rho_{(\lambda_n, k_n)(\lambda_{n-1}, k_{n-1})\dots(\lambda_{n-n_m+1}, k_{n-n_m+1})}^{(\bar{\lambda}_n, \bar{k}_n)(\bar{\lambda}_{n-1}, \bar{k}_{n-1})\dots(\bar{\lambda}_{n-n_m+1}, \bar{k}_{n-n_m+1})}. \tag{13}$$

From Eq. (10), one obtains the recursion relation for the partially summed ADM:

$$\rho_{(\lambda_n, k_n)\lambda_{n-1}\dots\lambda_{n-n_m+1}}^{(\bar{\lambda}_n, \bar{k}_n)\bar{\lambda}_{n-1}\dots\bar{\lambda}_{n-n_m+1}} = \sum_{\substack{k_{n-1} \\ \bar{k}_{n-1}}} \mathcal{M}_{(\lambda_n, k_n)(\bar{\lambda}_n, \bar{k}_n)}^{(\lambda_{n-1}, k_{n-1})(\bar{\lambda}_{n-1}, \bar{k}_{n-1})} \sum_{\substack{\lambda_{n-n_m} \\ \lambda'_{n-n_m}}} \exp\left(S_{\lambda_n \dots \lambda_{n-n_m}}^{\bar{\lambda}_n \dots \bar{\lambda}_{n-n_m}}\right) \rho_{(\lambda_{n-1}, k_{n-1})\lambda_{n-2}\dots\lambda_{n-n_m}}^{(\bar{\lambda}_{n-1}, \bar{k}_{n-1})\bar{\lambda}_{n-2}\dots\bar{\lambda}_{n-n_m}}. \tag{14}$$

Equation (14) is the central methodological result of this article as it allows the reduction of the number of terms to be iterated from $N_{ADM} = N^{2n_m}$ for the full ADM to $N_{PSADM} = N^2 \cdot N_g^{2(n_m-1)}$ for the partially summed ADM without introducing any approximation.

The above described algorithm has two sources of numerical errors: a discretization error introduced by using a finite time step Δt and an error due to the truncation of the memory to t_m. We call a simulation *numerically complete* if neither a further reduction of Δt nor a further increase of t_m leads to noticeable changes of the resulting reduced density matrix. The required memory time t_m can be easily determined before starting the iteration since the memory functions $S_{\nu_\ell \mu_\ell}^{\nu_{\ell'} \mu_{\ell'}}$ can be evaluated beforehand (see next subsection). For the memory induced by LA phonons t_m is of the order of a few pico seconds. For the system studied in the main text we obtained numerically complete results for $\Delta t = 0.5$ ps and $n_m = 7$. Calculations iterating the full ADM with $n_m = 7$ have been performed for 4-level systems [6, 7] where $N_{ADM} \simeq 2.7 \cdot 10^8$, which is large but manageable. A 5-level system would require $N_{ADM} \simeq 6.1 \cdot 10^9$ which is already ambitious. A system with $N = 41$ and $N_{ADM} \simeq 3.7 \cdot 10^{22}$ is definitely intractable by iterating the full ADM. The number of terms to be iterated using the partially summer ADM in our case with $n_m = 7$, $N = 41$, and $N_g = 2$ is $N_{PSADM} = 6.8 \cdot 10^6$, i.e., more than 15 orders of magnitude less than for the full ADM.

LA PHONON COUPLINGS TO DOT-CAVITY SYSTEMS

For GaAs-based systems as studied in the main text, the coupling between electrons (holes) confined in a quantum dot with LA phonons is typically dominated by the deformation potential interaction [8], which can be described by:

$$\gamma_{\mathbf{q}}^{e(h)} = \mathcal{F}_{\mathbf{q}}^{e(h)} \frac{|\mathbf{q}| D_{e(h)}}{\sqrt{2V \rho \hbar \omega_{\mathbf{q}}}}, \tag{15}$$

where the form factor $\mathcal{F}_{\mathbf{q}}^{e(h)}$ is the Fourier transform of the absolute square of the electron (hole) wave function, $D_{e(h)}$ is the electron (hole) deformation potential constant, V is the sample volume, and ρ is the mass density of the bulk material. Thus, the phonon coupling to states $|\nu\rangle = |X, n\rangle$ which are product states of the exciton $|X\rangle$ and cavity-photon number states is given by: $\gamma_{\mathbf{q}}^{X} = \gamma_{\mathbf{q}}^{e} - \gamma_{\mathbf{q}}^{h}$. States $|\nu\rangle = |G, n\rangle$ involving the ground state $|G\rangle$ are not dynamically coupled to phonons since the phonons primarily couple to electrons and holes which are both absent in the ground state and thus $\gamma_{\mathbf{q}}^{\nu} = 0$ in this case. Assuming a harmonic confinement, the wave functions are Gaussians resulting in real Gaussian form factors and therefore real $\gamma_{\mathbf{q}}^{X}$. A general expression relating the memory functions $S_{\nu_{\ell}\mu_{\ell}}^{\nu_{\ell'}\mu_{\ell'}}$ to the couplings $\gamma_{\mathbf{q}}^{\nu}$ is given in Ref. 3. For real couplings it simplifies to:

$$S_{\nu_{\ell}\mu_{\ell}}^{\nu_{\ell'}\mu_{\ell'}} = - K_{\nu_{\ell'}\nu_{\ell}}(t_{\ell} - t_{\ell'}) - K_{\mu_{\ell}\mu_{\ell'}}^{*}(t_{\ell} - t_{\ell'}) + K_{\nu_{\ell}\mu_{\ell'}}^{*}(t_{\ell} - t_{\ell'}) + K_{\nu_{\ell'}\mu_{\ell}}(t_{\ell} - t_{\ell'}) \tag{16}$$

with the memory kernel:

$$K_{\nu_{\ell}\mu_{\ell'}}(\tau) = 2 \int_{0}^{\infty} d\omega \frac{J_{\nu_{\ell}\mu_{\ell'}}(\omega)}{\omega^2} \left[1 - \cos(\omega\Delta t)\right] \left[\coth\left(\frac{\hbar\omega}{2k_B T}\right) \cos(\omega\tau) - i\sin(\omega\tau)\right], \qquad \tau > 0 \tag{17a}$$

$$K_{\nu_{\ell}\mu_{\ell}}(0) = \int_{0}^{\infty} d\omega \frac{J_{\nu_{\ell}\mu_{\ell}}(\omega)}{\omega^2} \left[\coth\left(\frac{\hbar\omega}{2k_B T}\right) (1 - \cos(\omega\Delta t)) + i\sin(\omega\Delta t) - i\omega\Delta t\right], \tag{17b}$$

where $J_{\nu\mu}(\omega)$ is the spectral density given by:

$$J_{\nu\mu}(\omega) = \sum_{j} \gamma_{j}^{\nu} \gamma_{j}^{\mu*} \delta(\omega - \omega_j). \tag{18}$$

As can be seen from these explicit expressions, the dynamics of the N-level system depends on the bosons only via the spectral density $J_{\nu\mu}(\omega)$, which therefore captures all relevant information of the boson bath. For a linear dispersion $\omega_{\mathbf{q}} = c_s|\mathbf{q}|$ with sound velocity c_s and Gaussian wave functions for electrons and holes with radii a_e and a_h, respectively, one obtains the phonon spectral density:

$$J_{\nu\mu}(\omega) = \frac{\omega^3}{4\pi^2 \rho \hbar c_s^5} \left(D_e e^{-\omega^2 a_e^2/(4c_s^2)} - D_h e^{-\omega^2 a_h^2/(4c_s^2)}\right)^2 \tag{19}$$

when $\nu, \mu = |X, n\rangle$ and $J_{\nu\mu}(\omega) = 0$ if $\nu = |G, n\rangle$ or $\mu = |G, n\rangle$.

For the calculations in the main article, we use typical values for GaAs-based self-assembled quantum dots [9]: $D_e = 7.0$ eV, $D_h = -3.5$ eV, $\rho = 5370$ kg/m^3, $c_s = 5110$ m/s, $a_e/a_h = 1.15$, and $a_e = 3.0$ nm.

POLARON MASTER EQUATION

In this section we briefly summarize the polaron master equations (PME), the results of which are compared in the main text with the numerically complete path-integral calculations. The PME are a widely used [10–12] approximate approach for the calculation of the dynamics of quantum dots coupled to LA phonons. For more details on this method we refer the reader to the review by Nazir and McCutcheon in Ref. 10.

A standard tool for studying the dynamnics in open quantum systems, i.e., systems of interest coupled to an environment, is the perturbative description using master equations [10] based on the Born-Markov approximation. In second order in the system-environment interaction, one typically ends up with Lindblad-type rate equations describing, e.g., the damping of certain processes in the system due to the interaction with the environment. However, in the case of quantum dots coupled to LA phonons, it has been found [13] that the weak-coupling master equations obtained in this way are only valid for a very limited set of parameters, because they do not account for multi-phonon effects and they do not correctly describe the phonon-induced renormalization of the driving or of the dot-cavity coupling. This problem can be partially circumvented by formulating master equations in the polaron frame[13]. In this approach, a unitary transformation is employed that diagonalizes the dot+phonon Hamiltonian in the absence of driving and coupling to a cavity, i.e., it removes the dot-phonon interaction term. Physically, the transformed states can be interpreted as polarons consisting of dot states and a cloud of phonons that follow the evolution of the dot state instantaneously. This picture breaks down when the system is exposed to driving that is strong enough such that the phonons can no longer follow the dynamics of the dot states. Thus, the polaron frame is suitable for many

experimentally realizable situations with weak driving, but can reach its limits for strong driving. Indeed, we have verified that when the PME are applied to the system in the main text in the weak driving limit (not shown) that the results perfectly agree with the path-integral simulations. A further comparison between path-integrals and the PME for driven two-level systems can be found in Ref. 14.

The polaron transformation is established by:

$$H'_N = e^S H_N e^{-S}, \qquad \text{with} \qquad S = |X\rangle\langle X| \sum_{\mathbf{k}} \big(\alpha_{\mathbf{k}} \hat{b}^\dagger_{\mathbf{k}} - \alpha^*_{\mathbf{k}} \hat{b}_{\mathbf{k}}\big), \tag{20}$$

with $\alpha_{\mathbf{k}} = \gamma^X_{\mathbf{k}}/\omega_{\mathbf{k}}$. The Hamiltonian of the dot-cavity system in the polaron frame reads: [12]

$$\hat{H}'_N = \hat{H}'_{\text{sys}} + \hat{H}'_{\text{bath}} + \hat{H}'_{\text{int}}, \tag{21a}$$

$$\text{with} \quad \hat{H}'_{\text{sys}} = \hbar\Delta\omega_{XL}|X'\rangle\langle X'| + \hbar\Delta\omega_{cL}\hat{a}^\dagger\hat{a} + \langle B\rangle\hat{X}_g, \qquad \hat{H}'_{\text{bath}} = \hbar \sum_{\mathbf{k}} \omega_{\mathbf{k}}\hat{b}^\dagger_{\mathbf{k}}\hat{b}_{\mathbf{k}}, \qquad \hat{H}'_{\text{int}} = \hat{X}_g\hat{\zeta}_g + \hat{X}_u\hat{\zeta}_u, \tag{21b}$$

$$\text{and} \qquad \hat{B}_\pm = \exp\Big[\pm\sum_{\mathbf{q}}\big(\alpha^*_{\mathbf{q}}\hat{b}_{\mathbf{q}} - \alpha_{\mathbf{q}}\hat{b}^\dagger\big)\Big], \qquad \langle B\rangle = \exp\Big[-\frac{1}{2}\int_0^\infty d\omega\frac{J(\omega)}{\omega^2}\coth\big(\hbar\omega/(2k_BT)\big)\Big], \tag{21c}$$

$$\hat{X}_g = \hbar g\big(\hat{a}^\dagger|0\rangle\langle X'| + |X'\rangle\langle 0|\hat{a}\big) - \hbar f\big(|0\rangle\langle X'| + |X'\rangle\langle 0|\big), \qquad \hat{\zeta}_g = \frac{1}{2}\big(\hat{B}_+ + \hat{B}_- - 2\langle B\rangle\big), \tag{21d}$$

$$\hat{X}_u = -i\hbar g\big(\hat{a}^\dagger|0\rangle\langle X'| - |X'\rangle\langle 0|\hat{a}\big) + i\hbar f\big(|0\rangle\langle X'| - |X'\rangle\langle 0|\big), \qquad \hat{\zeta}_u = \frac{1}{2i}\big(\hat{B}_+ - \hat{B}_-\big). \tag{21e}$$

The Markovian polaron master equations (PME) are established by applying the Born-Markov approximation to the polaron-transformed system coupled to the phonon environment via $\hat{H}'_{\text{int}}$. The resulting equation of motion for the reduced density matrix in the polaron frame $\hat{\rho}'$ reads: [11, 12]:

$$\frac{\partial}{\partial t}\hat{\rho}' = -\frac{i}{\hbar}\big[\hat{H}'_{\text{sys}}, \hat{\rho}'\big] + \kappa\big[\hat{a}\hat{\rho}'\hat{a}^\dagger - \frac{1}{2}\{\hat{\rho}', \hat{a}^\dagger\hat{a}\}_+\big] + \mathcal{K}[\hat{\rho}'], \tag{22}$$

$$\text{with} \qquad \mathcal{K}[\hat{\rho}'] = -\frac{1}{\hbar^2}\big([\hat{X}_g, \hat{\Phi}_g\hat{\rho}'] + [\hat{X}_u, \hat{\Phi}_u\hat{\rho}'] + \text{H.c.}\big), \tag{23a}$$

where "H.c." denotes the Hermitian conjugate and

$$\hat{\Phi}_g = \langle B\rangle^2\int_0^\infty d\tau\frac{1}{2}\big(e^{\phi(\tau)} + e^{-\phi(\tau)} - 2\big)e^{-\frac{i}{\hbar}\hat{H}'_{\text{sys}}\tau}\hat{X}_g e^{\frac{i}{\hbar}\hat{H}'_{\text{sys}}\tau}, \quad \hat{\Phi}_u = \langle B\rangle^2\int_0^\infty d\tau\frac{1}{2}\big(e^{\phi(\tau)} - e^{-\phi(\tau)}\big)e^{-\frac{i}{\hbar}\hat{H}'_{\text{sys}}\tau}\hat{X}_u e^{\frac{i}{\hbar}\hat{H}'_{\text{sys}}\tau},$$
$$\tag{23b}$$

with the phonon correlation function:

$$\phi(t) = \int_0^\infty d\omega\frac{J(\omega)}{\omega^2}\big[\coth\big(\hbar\omega/(2k_BT)\big)\cos(\omega t) - i\sin(\omega t)\big]. \tag{23c}$$

[1] N. Makri and D. E. Makarov, The Journal of Chemical Physics **102**, 4600 (1995).
[2] N. Makri and D. E. Makarov, The Journal of Chemical Physics **102**, 4611 (1995).
[3] A. Vagov, M. D. Croitoru, M. Glässl, V. M. Axt, and T. Kuhn, Phys. Rev. B **83**, 094303 (2011).
[4] A. M. Barth, A. Vagov, and V. M. Axt, Phys. Rev. B **94**, 125439 (2016).
[5] H. P. Breuer and F. Petruccione, *The Theory of Open Quantum Systems*, 1st ed. (Oxford University Press, Oxford, 2002).
[6] M. Glässl and V. M. Axt, Phys. Rev. B **86**, 245306 (2012).
[7] A. M. Barth, S. Lüker, A. Vagov, D. E. Reiter, T. Kuhn, and V. M. Axt, Phys. Rev. B **94**, 045306 (2016).
[8] B. Krummheuer, V. M. Axt, and T. Kuhn, Phys. Rev. B **65**, 195313 (2002).
[9] B. Krummheuer, V. M. Axt, T. Kuhn, I. D'Amico, and F. Rossi, Phys. Rev. B **71**, 235329 (2005).
[10] A. Nazir and D. P. S. McCutcheon, Journal of Physics: Condensed Matter **28**, 103002 (2016).
[11] J. Iles-Smith and A. Nazir, Optica **3**, 207 (2016).
[12] C. Roy and S. Hughes, Phys. Rev. X **1**, 021009 (2011).
[13] D. P. S. McCutcheon and A. Nazir, New Journal of Physics **12**, 113042 (2010).
[14] D. P. S. McCutcheon, N. S. Dattani, E. M. Gauger, B. W. Lovett, and A. Nazir, Phys. Rev. B **84**, 081305 (2011).

Erratum: Nonlinear cavity feeding and unconventional photon statistics in solid-state cavity QED revealed by many-level real-time path-integral calculations [Phys. Rev. B 96, 201201(R) (2017)]

M. Cygorek, A. M. Barth, F. Ungar, A. Vagov, and V. M. Axt

In our article, we have studied phonon effects on the cavity feeding in a quantum-dot (QD) microcavity system. To this end, we have formulated a numerically exact real-time path-integral (PI) method that is able to efficiently treat a large class of multilevel systems. As a side aspect, we have compared the results obtained from the PI calculations with the results of polaron master equations (PMEs). Upon closer inspection of the numerical results obtained by solving the PMEs, we have found an error in our numerical implementation of these equations. The error occurs in a subroutine which is only called during the numerical evaluation of the PMEs and is thus neither present in the phonon free nor in the PI simulations. We have checked our corrected implementation of the PMEs against results obtained by an independent Runge-Kutta approach and find a perfect agreement between the two results.

Since the resulting changes only affect calculations using the PMEs, we limit the updated calculations to the results presented in Figs. 2(a) and 2(b) of the original paper.

In contrast to the previously published results where a difference of up to 60% between the PME results and the PI results for the average photon number was claimed, we now find a perfect agreement of the two theoretical approaches for the parameters chosen in the original paper (cf. Fig. 1). Thus, we have to conclude that the 41-level system with simultaneously strong driving and strong coupling is equally well described by the PMEs and a PI approach for these specific parameters. Apart from the discussed changes regarding the implementation of the PMEs, all other results in the paper are not affected and do not change.

It should be pointed out that the agreement between the PI simulations and the PMEs does not hold for arbitrary system parameters. As an example, doubling the radius of
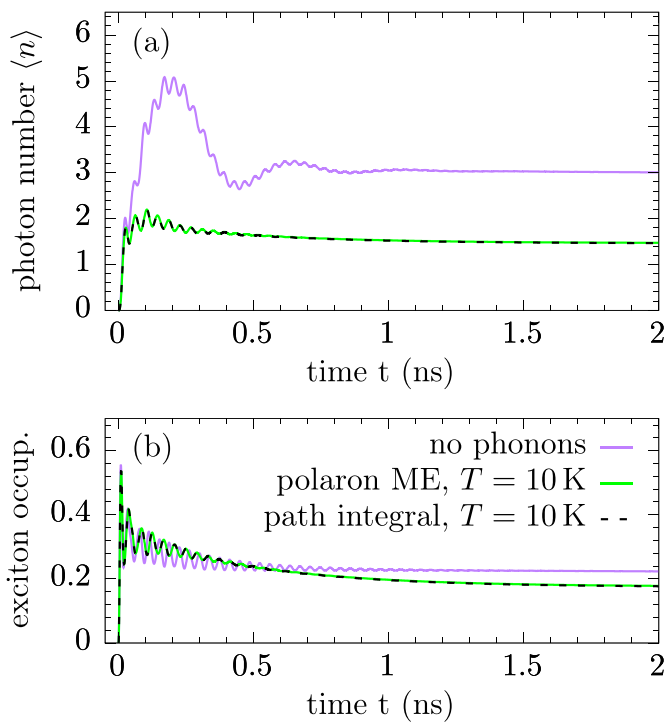

FIG. 1. Time evolution (a) of the average photon number and (b) of the exciton occupation for a detuning $\delta = 20\,\mu$eV at $T = 10$ K calculated using the path-integral theory (black dashed curve), Markovian polaron master equations (green), and without phonons (violet) for a QD with a radius of 3 nm.
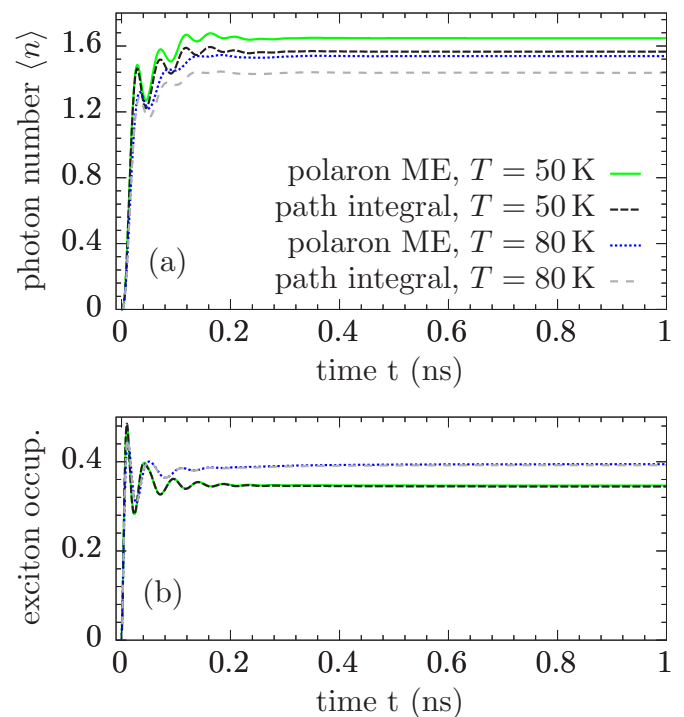

FIG. 2. Same as Fig. 1 but with an increased QD radius of 6 nm and higher temperatures of 50 and 80 K, respectively.

the InGaAs QD from 3 to 6 nm, which is still typical for self-assembled QDs, and increasing the temperature results in an underestimation of the phonon influence by the PME approach as can be seen in Fig. 2. Note that the difference between the PI and the PME calculations is larger for the average photon number compared with the exciton occupation. Since the phonon-free calculation does not change as it does not depend on the size of the dot, it is omitted in the figure. In the long-time limit, we find differences of about 5% and 7% between the prediction for the average photon number by the PI and the PME simulations for temperatures of 50 and 80 K, respectively.

Publication 10

Path-integral approach for nonequilibrium multitime correlation functions of open quantum systems coupled to Markovian and non-Markovian environments

M. Cosacchi, M. Cygorek, F. Ungar, A. M. Barth, A. Vagov, and V. M. Axt

Physical Review B **98**, 125302 (2018)

Path-integral approach for nonequilibrium multitime correlation functions of open quantum systems coupled to Markovian and non-Markovian environments

M. Cosacchi,[1] M. Cygorek,[2] F. Ungar,[1] A. M. Barth,[1] A. Vagov,[1,3] and V. M. Axt[1]

[1]*Theoretische Physik III, Universität Bayreuth, 95440 Bayreuth, Germany*
[2]*Department of Physics, University of Ottawa, Ottawa, Ontario, Canada K1N 6N5*
[3]*ITMO University, 49 Kronverksky Pr., St. Petersburg, 197101, Russia*

Using a real-time path integral approach we develop an algorithm to calculate multitime correlation functions of open few-level quantum systems that is applicable to highly nonequilibrium dynamics. The calculational scheme fully keeps the non-Markovian memory introduced by the pure-dephasing type coupling to a continuum of oscillators. Furthermore, we discuss how to deal consistently with the simultaneous presence of non-Markovian and Markovian system reservoir interactions. We apply the method to a crucial test case, namely the evaluation of emission spectra of a laser-driven two-level quantum dot coupled to a continuum of longitudinal acoustic phonons, which give rise to non-Markovian dynamics. Here, we also account for the coupling to a photonic environment, which models radiative decay and can be treated as a Markovian bath. The phonon side bands are found on the correct side of the zero phonon line in our calculation, in contrast to known results where the quantum regression theorem is applied naively to non-Markovian dynamics. Combining our algorithm with a recently improved iteration scheme for performing the required sum over paths we demonstrate the numerical feasibility of our approach to systems with more than two levels. Results are shown for the second-order photonic two-time correlation function of a quantum dot-cavity system with seven states on the Jaynes-Cummings ladder taken into account.

DOI: 10.1103/PhysRevB.98.125302

I. INTRODUCTION

To understand the dynamics of quantum few-level systems influenced by a huge number of degrees of freedom that one commonly refers to as a bath is of major importance in many areas of physics. Often, matters are further complicated by the fact that baths of many types couple simultaneously to the subsystem of interest. For example, solid state quantum emitters can couple to photonic reservoirs, i.e., free electromagnetic field modes as well as to phonons that are always present in a solid state environment. While the former can usually be approximated in a Markovian fashion to a reasonable extent, the latter is known to show pronounced non-Markovian behavior [1–6]. In the case of strongly confined quantum dots that have been proposed as candidates for numerous technological applications in quantum communications, quantum computing, and quantum cryptography as sources of single photons [7–9] and entangled photon pairs [10–14], the coupling of longitudinal acoustic phonons to the system is usually modeled as being of the pure-dephasing type [5,15–17]. The non-Markovian nature of this interaction manifests itself in a finite but not necessarily short memory for the reduced system density matrix.

Multitime correlation functions contain a huge amount of important information about open quantum systems. They constitute the interface between theory and a large class of measurements. Emission spectra that can easily be obtained in experiment are represented by the Fourier transform of the first-order two-time photon correlation function [15,18–25]. In the stationary emission spectrum of a quantum dot

for example, it can clearly be seen that the inclusion of the non-Markovian phonon dynamics is essential since it manifests itself in distinct features like an energetically broad phonon sideband at low temperatures [25]. Multitime correlation functions with two or more time arguments can be recorded in coincidence measurements [26,27]. Such experiments shed light on photonic properties of the system like, e.g., (anti)bunching, photon purities, or indistinguishabilities [28–33]. Although the most commonly considered case is the two-time correlation function, multitime correlation functions with more than two time arguments can also be a valuable tool, e.g., for the characterization of the statistics of photon bundles [34].

The theoretical analysis of multitime correlations is a challenging task, especially in systems with extended memory. The most widely used approximate approach is based on the quantum regression theorem (QRT). In the derivation of the QRT it is assumed that the statistical operator factorizes at all times into a system and an environment part [35]. In addition, the environment-induced dynamics is assumed to be Markovian. With these assumptions the two-time correlation function is calculated in two steps: (i) one obtains the dependence of the reduced density matrix on the first time argument t by solving the master equation within the Markov approximation and (ii) then the result of the t propagation is used to construct suitable initial values for the subsequent propagation in the second argument τ, which relies on the same dynamical equation. It is tempting to extend this QRT-based approach to treat a system with a non-Markovian environment simply by replacing the Markovian propagator for

the t and τ evolution with the non-Markovian one. Such a naive extension, however, completely neglects the influence of the memory built up during the t propagation on the subsequent τ evolution since this memory is discarded by starting the τ propagation as an initial value problem. Indeed, it has been recently demonstrated [25] that this approach may lead to unphysical results. In particular, it predicts phonon sidebands in the emission spectra on the wrong side of the Mollow triplet. In Ref. [25] this problem has been overcome by accounting perturbatively for corrections to the QRT.

Furthermore, the system may couple to Markovian baths simultaneously to the above described interaction with a non-Markovian environment. When a bath is known to influence a system only in Markovian ways, it is unnecessary and typically also impractical to account for the system-bath coupling by formulating the Hamiltonian time evolution for the total system. One usually approximates these bath influences by inserting Lindblad-type superoperators into the equation of motion for the system's reduced density matrix. Therefore, the reduced Markovian dynamics becomes non-Hamiltonian and thus nonunitary. However, the definition of multitime correlation functions makes use of the Heisenberg picture in order to assign the time arguments to the operators of interest, i.e., it relies on the existence of a unitary time evolution operator. If all baths are Markovian, one can use the QRT and ends up with Lindblad-type contributions for both the t and the τ propagation. So the question arises what to do when the QRT cannot be used because of the memory induced by a non-Markovian environment.

In the present paper we present a practical scheme for evaluating multitime correlation functions based on path integral (PI) methods [36–39]. Most importantly, the scheme fully accounts for the non-Markovian memory induced in the system by the pure-dephasing type coupling to a continuum of harmonic oscillators. This allows the inclusion of the memory built up during the t propagation and start the τ propagation without assuming an initial value problem, contrary to the QRT approach. In addition, it is shown how to consistently include the impact of non-Hamiltonian Markovian contributions to the dynamics, while keeping the accuracy with respect to the non-Markovian environment. Our approach is a considerable extension of earlier PI-based calculations [40] which addressed equilibrium two-time correlation functions that depend only on the time difference τ and which did not consider additional Markovian baths. It also extends PI descriptions where simultaneously Hamiltonian and non-Hamiltonian contributions have been treated for the evaluation of single-time expectation values [41] to the case of multitime functions. Finally, our algorithm can be combined with a recently developed improved iteration scheme for performing the required sum of paths [42] which greatly enhances the numerical efficiency such that quantum systems with much more than two levels can be explored. Moreover, we would like to note that recently an article has been brought to our attention in which the path integral algorithm was optimized even further by employing tensor-network techniques [43]. Combining this approach with the algorithm presented here may be used to greatly extend the range of applicability of PI methods.

We also would like to mention that a first application of our algorithm beyond the proof of principle calculations shown in

the present paper can be found in Ref. [44], where the second-order two-time correlation function $G^{(2)}(t, \tau)$ has been evaluated for an exciton-biexciton QD system coupled to two cavity modes. Reference [44] gave only the final results without any description of the used formalism. Here we fill the gap by presenting details of the method in a general formulation that allows one to calculate arbitrary multitime correlations. As illustrative examples we present results for the two-time correlation function in the photon antibunching regime and for emission spectra demonstrating that our algorithm yields phonon sidebands energetically on the correct side.

II. MODEL

To demonstrate the derivation of our algorithm, we choose the probably simplest prototype of an open quantum dissipative system coupled simultaneously to a non-Markovian and a Markovian environment exhibiting a nonstationary driven dynamics, which is provided by an externally driven two-level system with pure-dephasing coupling to an oscillator continuum and an additional reservoir. Since all formal developments of the present paper can be discussed within this showcase model we shall present all derivations explicitly for this case, also to keep the notation simple. Generalizations, e.g., to systems with more levels or further bath couplings are straightforward.

To be specific, we study a strongly confined self-assembled two-level quantum dot (QD) driven by an external laser field and coupled to a continuum of longitudinal acoustic (LA) phonons as well as to a photonic reservoir. The phonon coupling is commonly assumed to be of pure-dephasing type and is known to give rise to non-Markovian features in many cases [1–6]. The interaction with a broad photonic reservoir is the origin of radiative decay which is typically to a good approximation represented as a Markovian process.

The Hamiltonian for this system is given by

$$H(t) = H_1(t) + H_{\text{Rad}} + H_{\text{QD-Rad}}, \tag{1a}$$

$$H_1(t) = H_0(t) + H_{\text{Ph}} + H_{\text{QD-Ph}}, \tag{1b}$$

$$H_0(t) = H_{\text{QD}} + H_{\text{driv}}(t), \tag{1c}$$

where $H_0(t)$ represents the laser driven QD without reservoir coupling which is actually the subsystem of interest. $H_1(t)$ in addition comprises the interaction with the phonons and, finally $H(t)$ is the total Hamiltonian where also the coupling to the photonic reservoir is accounted for. In the common dipole and rotating wave approximation in a frame co-rotating with the laser frequency, the two-level and the driving parts of the Hamiltonian are given by

$$H_{\text{QD}} = \hbar \Delta\omega_{\text{XL}} |X\rangle\langle X| \tag{2}$$

and $\quad H_{\text{driv}}(t) = -\dfrac{\hbar}{2}\big(f(t)|X\rangle\langle G| + f^*(t)|G\rangle\langle X|\big), \tag{3}$

respectively, where $|G\rangle$ denotes the ground and $|X\rangle$ the excited state of the dot. $f(t)$ comprises the envelope of the driving laser field that is detuned by $\Delta\omega_{\text{XL}}$ from the ground to excited state transition frequency of the dot as well as the dipole matrix element for the transition. Note that $H_{\text{driv}}(t)$

introduces an explicit time dependence and puts the system out of equilibrium. The free evolution of the phonon subsystem is described by

$$H_{\text{Ph}} = \hbar \sum_{\mathbf{q}} \omega_{\mathbf{q}} b_{\mathbf{q}}^{\dagger} b_{\mathbf{q}} , \qquad (4a)$$

while the dot-phonon coupling reads [15,45]

$$H_{\text{QD-Ph}} = \hbar \sum_{\mathbf{q}} \left(\gamma_{\mathbf{q}}^{\text{X}} b_{\mathbf{q}}^{\dagger} + \gamma_{\mathbf{q}}^{\text{X*}} b_{\mathbf{q}} \right) |X\rangle\langle X| . \qquad (4b)$$

Here, the bosonic operator $b_{\mathbf{q}}^{\dagger}$ ($b_{\mathbf{q}}$) creates (destroys) phonons with the frequency $\omega_{\mathbf{q}}$. $\gamma_{\mathbf{q}}^{\text{X}}$ denotes the deformation-potential-type coupling constant between the exciton state and the $\mathbf{q}$th bosonic mode. Finally, the Hamiltonian for the photonic reservoir is given by

$$H_{\text{Rad}} = \hbar \sum_{j} \omega_{j} d_{j}^{\dagger} d_{j} , \qquad (5a)$$

and the dot is radiatively coupled to the photons via

$$H_{\text{QD-Rad}} = \hbar \sum_{j} (\Gamma_{j} d_{j}^{\dagger} |G\rangle\langle X| + \Gamma_{j}^{*} d_{j} |X\rangle\langle G|) . \qquad (5b)$$

$d_{j}^{\dagger}$ (d_{j}) creates (destroys) a photon with energy $\hbar\omega_{j}$, where the coupling constant is Γ_{j}.

Since the characteristic super-Ohmic coupling of the phonons leads to pronounced non-Markovian behavior [1–6], a simple Born-Markov approximation for the phononic environment is typically insufficient. In contrast, the photonic memory is negligible compared to all time scales of the subsystem of interest. Therefore, it is a good approximation to treat the photonic reservoir as being Markovian. The central result of this paper is to derive a practical algorithm to calculate multitime correlation functions using PI methods, which is capable of keeping all memory effects induced by the non-Markovian environment (here represented by LA phonons). Apart from discretization errors the scheme does neither introduce approximations with respect to the dot-laser interaction nor to the dot-phonon coupling. Furthermore, we show how additional couplings to Markovian baths (in our example the radiative coupling) can be accounted for consistently with the non-Markovian parts of the dynamics by using a reduced description that eliminates the degrees of freedom corresponding to the Markovian baths.

It is important to note that even when the Markovian interactions are included all memory effects related to the non-Markovian environment are still retained. Furthermore, even though the photon and the phonon coupling are evaluated in the bare state basis of the QD, mutual photonic and phononic renormalizations are nevertheless fully contained in the model. These renormalizations build up during the propagation since dot-phonon and dot-photon interactions do not commute, a property which still holds also for the Lindblad operators that are derived from the dot-photon coupling Hamiltonian.

III. EVALUATION OF MULTITIME CORRELATION FUNCTIONS

A general multitime correlation function can be defined as

$$G_{O_{1}...O_{2N}}(t_{1}, ..., t_{N}) = \langle O_{1}(t_{1}) O_{2}(t_{2})...O_{N}(t_{N}) O_{N+1}(t_{N})... \\ \times\ O_{2N-1}(t_{2}) O_{2N}(t_{1}) \rangle, \qquad (6)$$

where $O_{1}...O_{2N}$ are Hilbert space operators of the subsystem of interest (here the QD system) in the Heisenberg picture and the times are ordered as $t_{1} \leqslant t_{2} \leqslant ... \leqslant t_{N}$. Note that this definition covers the common case where operator pairs with the same time argument appear as, e.g., in the second-order two-time polarization correlation function

$$G^{(2)}(t, \tau) := G_{\sigma^{+}\sigma^{+}\sigma^{-}\sigma^{-}}(t, t + \tau) \\ = \langle \sigma^{+}(t)\sigma^{+}(t + \tau)\sigma^{-}(t + \tau)\sigma^{-}(t) \rangle \qquad (7)$$

with the polarization operators $\sigma^{+} = |X\rangle\langle G|$ and $\sigma^{-} = |G\rangle\langle X|$. Also multitime functions are covered by this definition, where a given time argument is assigned to only one operator, as applies for the first-order two-time correlation function $G^{(1)}(t, \tau) := \langle \sigma^{+}(t + \tau)\sigma^{-}(t) \rangle$. The latter can be obtained from the general expression Eq. (6) for $N = 2$ by setting two of the four appearing operators to the identity operator. Note also that by definition the time dependence of the operators $O_{j}(t_{\ell})$ refers to the Heisenberg picture and thus presumes the existence of a unitary time evolution operator.

In the following we consider $N = 2$ to keep the notation concise and since the major step from one- to multitime functions is already captured in that case. The generalization to arbitrary N is straightforward and will be explained at the end of the section.

A. Tracing out the Markovian bath

The first step in order to obtain a reduced description of multitime correlation functions is to eliminate the degrees of freedom corresponding to the Markovian bath (here the photonic bath). This reduction is most simple when single-time expectation values of operators not acting on the photonic reservoir are considered, since all such expectation values can be evaluated using the reduced density matrix

$$\bar{\rho}(t) = \text{Tr}_{\text{Rad}}[\rho(t)], \qquad (8)$$

where $\text{Tr}_{\text{Rad}}[\cdot]$ denotes the partial trace over the photonic subspace giving rise to radiative decay. Consider now the following four requirements: (i) the continuum described by $H_{\text{Rad}} + H_{\text{QD-Rad}}$ can be treated within the Markov approximation, (ii) system and environment subspaces factorize initially, i.e., $\rho(0) = \bar{\rho}(0) \otimes \rho_{\text{Rad}}$, where ρ_{Rad} is a thermal distribution, (iii) $H_{1}(t)$ does not depend on $d_{j}^{\dagger}$ and d_{j}, and (iv) the frequency renormalization (Lamb shift) induced by the mode continuum can be neglected as well as the finite temperature of the Markovian bath. As discussed in textbooks [35,46], if these requirements are fulfilled, the reduced density matrix obeys the dynamical equation

$$\frac{\partial}{\partial t} \bar{\rho}(t) = \mathcal{L}\bar{\rho}(t) \qquad (9)$$

with $\quad \mathcal{L} = \mathcal{L}_{1} + \mathcal{L}_{\sigma^{-},\gamma} , \qquad (10)$

where $\mathcal{L}_1$ is defined by

$$\mathcal{L}_1\bar{\rho} = -\frac{i}{\hbar}[H_1(t), \bar{\rho}] \tag{11}$$

and describes the Hamiltonian dynamics induced by $H_1(t)$. The second term accounts for the interaction with the Markovian bath by the Lindblad superoperator $\mathcal{L}_{\sigma^-,\gamma}$ which is constructed following the well known scheme for Lindblad operators:

$$\mathcal{L}_{O,\gamma}\rho = \frac{\gamma}{2}(2O\rho O^\dagger - O^\dagger O\rho - \rho O^\dagger O) \tag{12}$$

with a loss rate γ and a system operator O. Provided that $\mathcal{L}_{\sigma^-,\gamma}$ is nonzero, Eq. (9) represents a nonunitary time evolution in Liouville space. The simultaneous treatment of such non-Hamiltonian and Hamiltonian dynamics within a PI approach for single-time functions is discussed in Ref. [41], where the phonon subspace is traced out keeping its full memory structure. Note that due to condition (iii) the phononic subspace is not affected by tracing out the Markovian bath, i.e., it is still formulated as a Hamiltonian contribution to the dynamics. Introducing the Liouvillian propagator

$$\mathcal{P}_{t' \to t} = \mathcal{T}e^{\int_{t'}^{t} \mathcal{L}(t'')dt''} \tag{13}$$

with the time ordering operator $\mathcal{T}$, the formal solution of Eq. (9) is $\bar{\rho}(t) = \mathcal{P}_{0\to t}\bar{\rho}(0)$.

For the evaluation of two-time functions we start with the definition in Eq. (6) for the case $N = 2$ where the time evolution of the operators follows from the total Hamiltonian $H(t)$. Using the cyclic property of the trace, which is taken over the entire space considered, we can rearrange this expression to yield

$$G_{O_1 O_2 O_3 O_4}(t_1, t_2) = \text{Tr}_{\text{QD,Ph,Rad}}[O_2(t_2)O_3(t_2) \\ \times O_4(t_1)\rho(0)O_1(t_1)], \tag{14}$$

where the indices QD, Ph, Rad indicate the decomposition of the total trace into parts referring to the QD, the phonon, and the photon degrees of freedom, respectively. Changing the dynamical picture with the help of the unitary time evolution operator $\mathcal{U}_{t' \to t} = \mathcal{T}e^{-\frac{i}{\hbar}\int_{t'}^{t} H(t'')dt''}$ leads to

$$G_{O_1 O_2 O_3 O_4}(t_1, t_2) = \text{Tr}_{\text{QD,Ph}}[O_2(0)O_3(0) \\ \times \text{Tr}_{\text{Rad}}[\mathcal{U}_{t_1 \to t_2}O_4(0)\rho(t_1)O_1(0)\mathcal{U}_{t_1 \to t_2}^\dagger]]. \tag{15}$$

Equation (15) is the starting point for the standard elimination of the Markovian bath, where the central assumption is made that the total density matrix $\rho(t_1)$ factorizes not only at some initial time t_0 but at every single point in time t_1 into system and reservoir parts. Furthermore, the reservoir is taken to be static, i.e., it is described by the thermal distribution ρ_{Rad} for all times. When these conditions are fulfilled to a good approximation, the two-time correlation function can be written as [35,46]

$$G_{O_1 O_2 O_3 O_4}(t_1, t_2) = \text{Tr}_{\text{QD,Ph}}[O_2(0)O_3(0) \\ \times \mathcal{P}_{t_1 \to t_2}[O_4(0)[\mathcal{P}_{0 \to t_1}\bar{\rho}(0)]O_1(0)]], \tag{16}$$

where $\mathcal{P}_{t' \to t}$ is the Liouville space propagator that has been introduced in Eq. (13). The advantage of using Eq. (16) instead

of Eq. (15) is that $\mathcal{P}_{t' \to t}$ acts in the reduced space, where the operators of the Markovian bath have been eliminated, while the unitary time evolution operators $\mathcal{U}_{t' \to t}$ act in the unreduced total space.

We stress that, up to this point, the phononic environment is treated completely Hamiltonian. In the absence of a non-Markovian environment, Eq. (16) would constitute the desired reduced description, which in that case reduces to the QRT.

B. Path integral treatment of the non-Markovian reservoir

Equation (16) is a formal representation of the sought two-time correlation function. The main target of the present paper is to provide a practical algorithm that enables a complete numerical evaluation of $G_{O_1 O_2 O_3 O_4}(t_1, t_2)$. For single-time functions this goal has been reached before with the use of PI methods [36–39,41]. The extension to two-time functions is most easily understood after first recalling how the PI approach works for single-time functions. The task to evaluate single-time expectation values of system operators O_j (QD operators in our example) can be split in first obtaining the reduced density matrix $\bar{\rho}$ for the QD subsystem and then taking the trace over $O_j\bar{\rho}$. As usual, the reduced density matrix of the QD subsystem is defined as:

$$\bar{\rho}(t) = \text{Tr}_{\text{Ph}}[\bar{\rho}(t)], \tag{17}$$

where the trace is taken over the phonon degrees of freedom. In fact, the evaluation of the matrix elements $\bar{\rho}_{\nu\mu}$ is a special case of Eq. (16), where $t_1 = t_2 = t$, $O_2 = O_3 = O_4 = \text{Id}$ with Id being the identity operator and $O_1 = |\mu\rangle\langle\nu|$, such that

$$\bar{\rho}_{\nu\mu}(t) = \text{Tr}_{\text{QD,Ph}}[[\mathcal{P}_{0\to t}\bar{\rho}(0)]|\mu\rangle\langle\nu|]. \tag{18}$$

The expression in Eq. (18) can be cast into a PI representation by decomposing the Liouvillian propagator according to

$$\mathcal{P}_{0\to t} = \text{Id}^{(n)}\mathcal{P}_{(n-1)\Delta t \to n\Delta t}\text{Id}^{(n-1)} \cdots \\ \cdots \text{Id}^{(2)}\mathcal{P}_{\Delta t \to 2\Delta t}\text{Id}^{(1)}\mathcal{P}_{0\to\Delta t}\text{Id}^{(0)}. \tag{19}$$

Here we have subdivided the time interval $[0, t]$ into n equidistant time steps Δt, such that $n\Delta t = t$. Furthermore, the operators $\text{Id}^{(j)}$ that are inserted after the jth time step are identity operators that according to the completeness relation may be written as

$$\text{Id}^{(j)} = \sum_{\xi_j} |\xi_j\rangle\langle\xi_j|, \tag{20}$$

where $\{|\xi_j\rangle\}$ is a complete set of states in the QD and phonon subspace. Inserting the identity operators in this form replaces the operators $\mathcal{P}_{(j-1)\Delta t \to j\Delta t}$ by their matrix elements and thus the reduced density matrix in Eq. (18) appears as a sum over paths in configuration space of QD and phonons. It is well known that all parts of these summations involving phonons can be performed analytically for the pure-dephasing coupling model [36,37,41], such that in the numerical treatment only summations over paths in the QD configuration space have to be carried out. Note that the classification of the coupling as being of pure-dephasing type refers to the bare state basis of the QD, where this coupling is diagonal. Working in a QD basis, where the coupling to phonons is diagonal, simplifies

greatly the task of analytically performing the required integrations over the phonon degrees of freedom, which eventually leads to the phonon memory kernels. However, even for a two-level system the direct summation over all paths is feasible only for few time steps, since the number of contributions grows exponentially with the number of time steps.

A highly efficient algorithm for performing the sum over paths has been introduced by Makri and Makarov [36,37], which makes use of the fact that after integrating out the phonon degrees of freedom, their influence is captured by phonon induced memory kernels that for a continuum of phonons decay on a finite time scale (for LA phonon coupling to a QD typically on the order of a few picoseconds). Note that the phonon induced memory kernels can be evaluated from the knowledge of the phonon coupling constants $\gamma_{\mathbf{q}}^X$ and thus the memory depth is known before starting any path summations. Using the finite memory depth the summation over paths can be carried out by an iterative scheme for the so-called augmented density matrix (ADM). The ADM is a $2n_c$ dimensional tensor of weights assigned to each path where n_c is the number of time steps needed to cover the full memory depth. In the case where the Liouville propagator contains simultaneously Hamiltonian and non-Hamiltonian contributions, the calculation of the ADM proceeds according to the following recursion [41]:

$$\bar{\bar{\rho}}_{\nu_n...\nu_{n-n_c+1}}^{\mu_n...\mu_{n-n_c+1}}$$

$$= \mathcal{M}_{\nu_n\mu_n}^{\nu_{n-1}\mu_{n-1}} \sum_{\substack{\nu_{n-n_c} \\ \mu_{n-n_c}}} \exp\left(\sum_{l=n-n_c}^{n} S_{\nu_n\nu_l\mu_n\mu_l}\right) \bar{\bar{\rho}}_{\nu_{n-1}...\nu_{n-n_c}}^{\mu_{n-1}...\mu_{n-n_c}}, \quad (21)$$

where $S_{\nu_n\nu_l\mu_n\mu_l}$ is the phonon influence functional that describes the time-delayed back action of the phononic environment, in short, the phonon-induced memory of the system. $\mathcal{M}_{\nu_n\mu_n}^{\nu_{n-1}\mu_{n-1}}$ is the matrix element of the Liouville propagator $\mathcal{M}_t$ representing the combined time evolution induced in the QD subsystem [41,42] by $H_0(t)$ and $\mathcal{L}_{\sigma^-,\gamma}$ from time step $n-1$ to n. For the sake of a self-contained presentation, we repeat the explicitly known expressions for $S_{\nu_n\nu_l\mu_n\mu_l}$ and $\mathcal{M}_{\nu_n\mu_n}^{\nu_{n-1}\mu_{n-1}}$ in the Appendix. The iteration is started by calculating the ADM for the first n_c time steps by directly performing the corresponding summations [39,42].

To obtain the reduced density matrix $\bar{\rho}_{\nu\mu}$ from the ADM one has to trace out all indices except those referring to the most recent time step, i.e.,

$$\bar{\bar{\rho}}_{\nu_n\mu_n} = \sum_{\substack{\nu_{n-1}...\nu_{n-n_c+1} \\ \mu_{n-1}...\mu_{n-n_c+1}}} \bar{\bar{\rho}}_{\nu_n...\nu_{n-n_c+1}}^{\mu_n...\mu_{n-n_c+1}}. \quad (22)$$

In order to develop a PI-based algorithm for the evaluation of the two-time function in Eq. (16) we proceed along the same lines as done for the evaluation of the single-time reduced density matrix, i.e., in a first step we decompose in Eq. (16) both $\mathcal{P}_{0\to t_1}$ as well as $\mathcal{P}_{t_1\to t_2}$ according to Eq. (19). As for the single-time functions the insertion of identity operators resolved by the completeness relation Eq. (20) casts the expression Eq. (16) into a sum over paths in configuration space. It should be noted that the operators O_j in Eq. (16) act only within the QD subspace and not on the phonon degrees

of freedom. Therefore, all integrals over phonon variables that show up after inserting the completeness relation Eq. (20) for the identity operators are identical to those appearing in the corresponding expressions for single-time functions. In particular, all related integrations can be carried out analytically such that the phonon influence again ends up in memory kernels that can be evaluated beforehand and thus the memory depth is known. For efficiently performing the summations over paths an iterative scheme analogous to Eq. (21) may be set up. To this end we assume a time discretization such that n equidistant time steps of length Δt are needed to cover the interval $[0, t_1]$ while another m time steps of the same length connect t_1 with t_2, i.e., $t_1 = n\Delta t$ and $\tau_1 := t_2 - t_1 = m\Delta t$. From Eq. (16) it can be seen that in order to reach t_1 starting from $t = 0$ the ADM can be iterated in the same way as for single-time functions, i.e., according to Eq. (21). Applying the operator O_4 from the left and O_1 from the right to the operator $\mathcal{P}_{0\to t_1}\bar{\rho}(0)$ is formally equivalent to replacing the operator $\mathcal{M}_t$, which describes the time evolution of the QD subsystem without phonon coupling from t_1 to $t_1 + \Delta t_1$, in the nth time step by $O_4(0)\mathcal{M}_{t_1}O_1(0)$. We can therefore define a modified ADM which for the first n time steps coincides with the original ADM. At the nth time step the modified ADM is defined as:

$$\bar{\bar{\rho}}_{O_4O_1\nu_n...\nu_{n-n_c+1}}^{\mu_n...\mu_{n-n_c+1}} = \sum_{\nu_n'\mu_n'} (O_4)_{\nu_n\nu_n'} \mathcal{M}_{\nu_n'\mu_n'}^{\nu_{n-1}\mu_{n-1}} (O_1)_{\mu_n'\mu_n}$$

$$\times \sum_{\substack{\nu_{n-n_c} \\ \mu_{n-n_c}}} \exp\left(\sum_{l=n-n_c}^{n} S_{\nu_n\nu_l\mu_n\mu_l}\right) \bar{\bar{\rho}}_{\nu_{n-1}...\nu_{n-n_c}}^{\mu_{n-1}...\mu_{n-n_c}}, \quad (23)$$

where $(O_1)_{\nu\mu}$ and $(O_4)_{\nu\mu}$ are the representations of the system operators in the QD basis $\{|\nu\rangle\}$ obtained by inserting the completeness relation with respect to this basis between O_1 (O_4) and $\mathcal{M}_t$. From Eq. (16) it is evident that after applying the operators O_1 and O_4 at time t_1 there is no further modification compared with the single-time case during the propagation from time t_1 to $t_2 = t_1 + \tau_1$ and thus the modified ADM $\bar{\bar{\rho}}_{O_4O_1}$ obeys the same recursion as the ADM, i.e., Eq. (21), for the subsequent m time steps covering the interval $[t_1, t_2]$.

Finally, the calculation of the two-time function $G_{O_1O_2O_3O_4}(t_1, t_2)$ is completed by applying $O_2(0)O_3(0)$ from the left and then taking the trace over the QD degrees of freedom, i.e.,

$$G_{O_1O_2O_3O_4}(t_1, t_2)$$

$$= \sum_{\substack{\nu_{n+m}...\nu_{n+m-n_c+1} \\ \mu_{n+m}...\mu_{n+m-n_c+1}}} [O_2(0)O_3(0)]_{\mu_{n+m}\nu_{n+m}} \bar{\bar{\rho}}_{O_4O_1\nu_{n+m}...\nu_{n+m-n_c+1}}^{\mu_{n+m}...\mu_{n+m-n_c+1}}, \quad (24)$$

where $[O_2(0)O_3(0)]_{\mu\nu}$ is the matrix element of the operator product $O_2(0)O_3(0)$ in the QD basis. It is important to note that for evaluating the two-time function $G_{O_1O_2O_3O_4}(t_1, t_2)$ for finite delays $\tau_1 = t_2 - t_1 > 0$ it is not sufficient to know the reduced density matrix at time t_1. This is the crucial difference compared with the QRT where the two-time function is

propagated with respect to the delay τ_1 by solving an initial value problem where the initial values are determined from the reduced density matrix at t_1. The physical meaning of this difference is that iterating the modified ADM keeps the complete phonon induced memory before and after the time t_1.

Altogether, the above described iteration scheme for performing a PI-based calculation of the two-time function $G_{O_1 O_2 O_3 O_4}(t_1, t_2)$ requires $n + m$ iterations, the effort of which is the same as needed for the iteration of the ADM in the single-time case. Thus, the evaluation of $G_{O_1 O_2 O_3 O_4}(t_1, t_2)$ for a given pair t_1, t_2 can be done with the same numerical effort as needed for tracing a single-time function over a time interval $[0, t_1 + \tau_1]$. Of course, this implies that mapping out the dependence on both t_1 and τ_1 is much more demanding than following a single-time function over an extended time interval since the calculation has to be performed anew for each pair t_1, τ_1.

Finally, we would like to note that the generalization to an arbitrary multitime function as defined in Eq. (6) can easily be done by repeating the derivations of Secs. III A and III B for every time argument t_j with $2 < j \leqslant N$ for the subsequent dynamics in τ_j. This amounts to (i) reordering the operators in Eq. (6) such that operators with equal times appear on either side of the density matrix as in Eq. (14), (ii) then, if present, tracing out Markovian baths which converts the unitary time evolution into a Liouville space propagation described by operators $\mathcal{P}_{t_j \to t_{j+1}}$, (iii) decomposing these operators according to Eq. (19), (iv) obtaining a representation of the multitime function as a sum over paths in configuration space by resolving the identity operators introduced in the decomposition using the completeness relation Eq. (20), (v) representing the phonon induced memory in terms of memory kernels by performing the integrations over phonon degrees of freedom, (vi) performing the remaining sum over paths in the QD subspace by iterating a modified ADM which at every intermediate time argument t_j of the N-time function picks up operators O_j and O_{2N-j+1}, (vii) finally, after the last time step applying operators O_N and O_{N+1} to the modified ADM and taking the sum over all system

indices of the modified ADM. Again for a given ordered tuple $(t_1, \cdots, t_N)$ the numerical demand is identical to the effort of following a single-time function from time $t = 0$ to the final time $t = t_N$. This is due to the fact that—as a simple recipe—the derivation amounts to modifying the Liouvillian propagator $\mathcal{M}_t$ that describes the combined Hamiltonian and non-Hamiltonian evolution of the subsystem of interest, at times $t \in \{t_1, ..., t_{N-1}\}$ in complete analogy to Eq. (23).

IV. NUMERICAL EXAMPLES

In order to illustrate the applicability of our algorithm we first consider a laser driven two-level system coupled to LA phonons and accounting for radiative decay by a Lindblad operator derived from a Markovian photonic bath as described in Sec. II. For the explicit calculation we take a GaAs-based self-assembled dot with a diameter of 6 nm and standard material parameters [47]. The laser is tuned in resonance to the two-level transition and, after being switched on at $t = 0$, has a constant amplitude corresponding to $\hbar f(t)/2 = 39$ μeV. The radiative decay rate is taken to be $\hbar \gamma = 6.6$ μeV. The phonons are assumed to be initially in thermal equilibrium at a temperature of $T = 10$ K.

Before we discuss two-time correlation functions of this system, we would like to demonstrate that this system indeed exhibits pronounced non-Markovian dynamics for the chosen parameter set. To this end, we show the time derivative of the trace distance $\frac{d}{dt} D(\rho_+, \rho_-)$, as defined in Refs. [25,48], in Fig. 1(a), which can be interpreted as a measure of non-Markovianity [25,48]. According to Ref. [48] the Markovianity of a system implies that $\frac{d}{dt} D(\rho_+, \rho_-)$ be less than zero. In other words, a value larger than zero for this quantity indicates non-Markovian environment influences. There is an intuitive interpretation to this criterion: When the distance, i.e., the distinguishability between two states, increases with time ($\frac{d}{dt} D(\rho_+, \rho_-) > 0$) there has to be a flow of information from the environment to the subsystem of interest. Thus, the system dynamics cannot be Markovian. For the application of this criterion it is sufficient to find a pair of states ρ_+
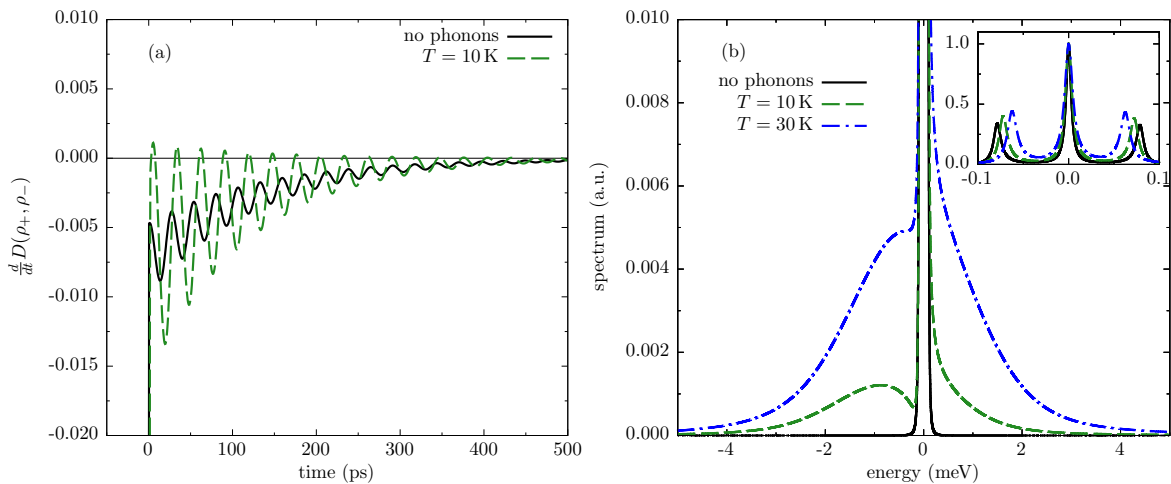

FIG. 1. (a) Derivative of the trace distance and (b) incoherent resonance fluorescence, i.e., emission spectrum including phonons initially at $T = 10$ K, $T = 30$ K, and without phonons for comparison for a 6 nm GaAs QD with cw excitation. The inset shows the same data on a scale, where the Mollow triplet is visible. The spectra are normalized to the height of the central peak.

and ρ_- for whom this statement holds. Here, we choose the same states as defined in Ref. [25]. Clearly, non-Markovian behavior is established in Fig. 1(a). The origin of the non-Markovian dynamics is the phononic environment as can be seen by switching off the dot-phonon coupling which results in values of $\frac{d}{dt}D(\rho_+, \rho_-)$ strictly lower than zero [cf. the black solid line in Fig. 1(a)].

A. Emission spectrum of a two-level QD

Next we turn to the calculation of the emission spectrum $S(\omega)$ of our driven two-level system [49] which we evaluate from the two-time correlation function $G^{(1)}(t, \tau) = \langle \sigma^+(t + \tau)\sigma^-(t) \rangle$ by considering times t long enough such that a stationary nonequilibrium state has been reached. Then the Fourier transform is taken with respect to τ after subtracting the limiting value $\lim_{t\to\infty} \lim_{\tau\to\infty} G^{(1)}(t, \tau)$ which in Ref. [35] is referred to as the *coherent part* of the emission, i.e.,

$$S(\omega) = \lim_{t\to\infty} \mathrm{Re}\left[\int_{-\infty}^{\infty} d\tau (G^{(1)}(t, \tau) - \lim_{\tau\to\infty} G^{(1)}(t, \tau))e^{-i\omega\tau} \right].$$
(25)

The determination of the emission spectrum can be considered to be a crucial test of our method since in Ref. [25] it has been demonstrated that a naive application of the QRT yields the phonon side band energetically on the wrong side. Our result is shown in Fig. 1(b), where spectra calculated for phonons initially at $T = 10$ K and $T = 30$ K as well as for the phonon-free case are shown. Clearly, a broad phonon side band is found below the zero phonon line (ZPL) corresponding to transitions involving phonon emission, whereas above the ZPL a tail is found originating from transitions where phonons are absorbed [50,51]. As expected, the tail is reduced with decreasing temperature while the broad phonon side band remains. Furthermore, the same data plotted on a different scale [cf. inset in Fig. 1(b)] shows the well known Mollow triplet [52]. The Rabi splitting is due to the strong driving of $\hbar f = 78$ μeV compared with the radiative decay rate. Also clearly visible is the phonon-induced renormalization and damping of the Rabi oscillations that manifest themselves in the shift of the two side peaks towards the central peak of the Mollow triplet and their broadening, respectively [1,4,45,53–56]. Altogether, this demonstrates that our method reliably accounts for the phonon induced memory which is reflected by the phonon-induced features in the spectra that appear on the energetically correct side of the ZPL.

B. Two-time photonic correlation function of a QD-cavity system

Usually two-level systems are used to showcase the application of PI methods because the rapid increase of the number of elements of the ADM with rising number of levels of the system of interest imposes severe limitations to the size of systems that can be dealt with numerically. For QD systems, which exhibit typically a rather long memory of the order of a few picoseconds, already for single-time functions corresponding calculations have been mostly restricted to two-, three- or four-level systems [3,4,57–59]. Recently, it has

been demonstrated in Ref. [42] that for an important class of systems, where the levels of the system of interest can be subdivided into groups with identical phonon coupling within each group, the iterative summation over paths can be speeded up enormously by iterating instead of the full ADM a quantity where the partial sum over states within each group has already been performed. Indeed, in Ref. [42] a QD-cavity system with 41 states of the Jaynes-Cummings ladder coupled to LA phonons and accounting for cavity losses has been treated. This has become possible because in this case the reformulation reduced the numerical effort by more than 15 orders of magnitude without introducing approximations. It is easily seen that the idea of iterating a partially summed ADM can be combined with our algorithm for obtaining multitime correlation functions without conflict.

To show the feasibility of such an enhanced scheme which paves the way toward numerically complete calculations of multitime correlation functions for systems beyond the very few level limit, we have considered a laser driven two-level QD with a Jaynes-Cummings type coupling to a cavity mode with photon rising (lowering) operator $a^\dagger$ (a) and deformation potential coupling to LA phonons. This amounts to considering an additional Hamiltonian contribution to the previously defined H_0 in the form of

$$H_{\mathrm{Cav}} = \hbar\Delta\omega_{CL}a^\dagger a + \hbar g(a^\dagger|G\rangle\langle X| + a|X\rangle\langle G|),$$
(26)

where $\Delta\omega_{CL}$ is the detuning between the cavity mode and the central laser frequency. In addition we account for cavity losses by a Lindblad term $\mathcal{L}_{a,\kappa}$ with a cavity loss rate κ. Our system of interest consists of the states of the Jaynes-Cummings ladder. We show results where the system is driven by a pulse train $f(t)$ where every $T_{\mathrm{Pulse}} = 2.5$ ns a laser pulse with Gaussian envelope $e(t) = \Theta/(\sqrt{2\pi}\sigma)\exp(-t^2/(2\sigma^2))$ hits the QD, i.e.,

$$f(t) = \sum_{n=0}^{\infty} e(t + nT_{\mathrm{Pulse}}).$$
(27)

The pulse area Θ is set to π and the full width at half maximum to 1 ps. The laser is in resonance with the phonon-shifted two-level transition as well as the cavity mode. The dot-cavity coupling is set to $\hbar g = 100$ μeV and the cavity loss rate is chosen to be $\hbar\kappa = 6.6$ μeV while the temperature is taken to be $T = 4.2$ K. The radiative decay rate is $\hbar\gamma = 6.6$ μeV as before. For these parameters converged results are obtained by keeping states with up to three excitations on the Jaynes-Cummings ladder, which is a system with seven levels, namely three pairs of states $|G, n_X\rangle$, $|X, n_X - 1\rangle$ for excitation numbers n_X in the range $1 \leqslant n_X \leqslant 3$ and one state $|G, 0\rangle$ for $n_X = 0$. Here, $|G, n\rangle$ and $|X, n\rangle$ denote product states where the dot is in one of its two energy eigenstates ($|G\rangle$ or $|X\rangle$) and n photons are excited. The excitation number n_X refers to the sum of excited photons and excitons. In the Jaynes-Cummings model (i.e., a system without phonons, cavity or radiative losses and without laser driving) n_X is preserved.

The pulse driven QD-cavity systems under discussion are of particular interest concerning applications as single-photon emitters. It is possible to determine the quality of the emitted photons with respect to this goal by examining the nonclassical antibunching behavior of the photonic subsystem. To
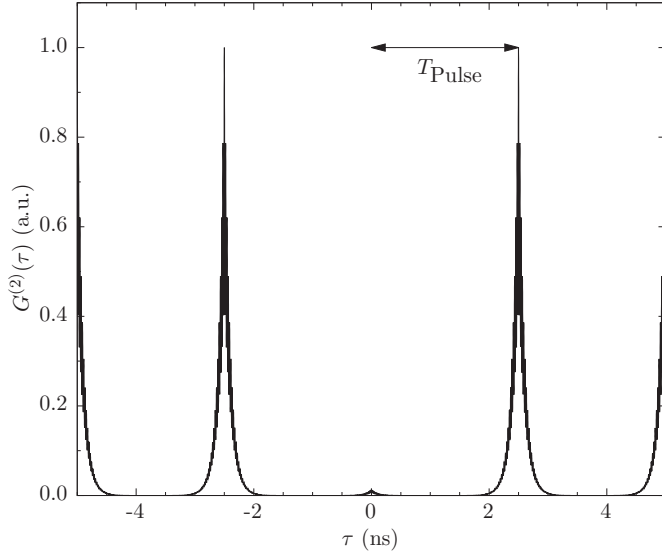
FIG. 2. Averaged two-time photon correlation function at $T = 4.2$ K for a 6 nm GaAs QD embedded in a single-mode microcavity with pulsed excitation accounting for seven states on the Jaynes-Cummings ladder.

this end, the second-order two-time correlation function of the cavity photons is often considered both in experiment and in theoretical modeling. It is defined as

$$G^{(2)}(t, \tau) := \langle a^\dagger(t) a^\dagger(t + \tau) a(t + \tau) a(t) \rangle, \quad (28)$$

i.e., we set $N = 2$ in Eq. (6) as well as $O_1 = O_2 = a^\dagger$, $O_3 = O_4 = a$, $t_1 = t$, and $t_2 = t + \tau$. $G^{(2)}(t, \tau)$ averaged over the first time argument is shown in Fig. 2. As expected, the dot-cavity system displays pronounced antibunching behavior. The small amplitude modulations on top of the pronounced peak structure occur because we are in the strong coupling limit where the QD-cavity coupling induces Rabi-type oscillations. Overall, our results confirm the feasibility of reliable numerically complete PI calculations for systems noticeably larger than two-level systems.

V. CONCLUSION

We have presented a path-integral based algorithm for evaluating nonequilibrium multitime correlation functions of a few-level subsystem that has a pure-dephasing type coupling to a continuum of oscillators which may induce non-Markovian dynamics. The algorithm is formulated in a way that allows us to account for non-Hamiltonian contributions to the dynamics resulting from further couplings to Markovian baths in addition to the Hamiltonian coupling to the oscillators. In contrast to calculations of multitime correlation functions based on the quantum regression theorem, which is valid only for systems with Markovian dynamics, our approach keeps the full memory structure induced by the oscillator continuum. The algorithm can be applied to situations with explicit time dependence, e.g., due to external laser driving, as well as to initial value problems. Apart from limitations arising from the assumptions made in the formulation of the model and, if applicable, apart from making use of a Markovian description for some of the bath interactions, no

approximations are made in our treatment except for discretization errors. In particular, all interactions are treated completely and nonperturbatively. For example, for a quantum dot coupled to phonons all multiphonon processes are included as well as the laser driving to all orders in the driving field. We have demonstrated that our method passes the crucial test case of determining the emission spectrum of a two-level quantum dot coupled to LA phonons by showing that the phonon side band appears on the correct side of the zero phonon line in contrast to results obtained from the naive application of the quantum regression theorem. In addition we have shown that the algorithm can be combined with a recent improvement of the iteration scheme for performing the sum over paths which opens up new opportunities by making numerically complete calculations of multitime correlation functions feasible for systems where the number of relevant levels is considerably larger than two. As an example for the latter situation we have shown converged results for the second-order photonic correlation function evaluated for a seven-level system.

APPENDIX: EXPLICIT EXPRESSIONS FOR THE INFLUENCE FUNCTIONAL AND LIOUVILLIAN PROPAGATOR MATRICES

The following definitions are a repetition of those in Ref. [41] for the sake of a self-contained presentation of the present paper. In the special case where the dot-phonon coupling constants are all either purely real or purely imaginary (which applies to the deformation potential coupling to LA phonons), the phonon influence functional reads

$$S_{\nu_l \nu_{l'} \mu_l \mu_{l'}} = - K_{\nu_{l'} \nu_l}(t_l - t_{l'}) - K^*_{\mu_l \mu_{l'}}(t_l - t_{l'})$$
$$+ K^*_{\nu_l \mu_{l'}}(t_l - t_{l'}) + K_{\nu_{l'} \mu_l}(t_l - t_{l'}) \quad (A1)$$

with the memory kernels

$$K_{\nu_l \mu_{l'}}(\tau) = 2 \int_0^\infty d\omega \frac{J_{\nu_l \mu_{l'}}(\omega)}{\omega^2} (1 - \cos(\omega \Delta t))$$
$$\times \left[\coth\left(\frac{\hbar \omega}{2 k_B T} \right) \cos(\omega \tau) - i \sin(\omega \tau) \right] \quad (A2)$$

and

$$K_{\nu_l \mu_l}(0) = \int_0^\infty d\omega \frac{J_{\nu_l \mu_l}(\omega)}{\omega^2}$$
$$\times \left[\coth\left(\frac{\hbar \omega}{2 k_B T} \right) (1 - \cos(\omega \Delta t)) \right.$$
$$\left. + i \sin(\omega \Delta t) - i \omega \Delta t \right]. \quad (A3)$$

Here, the phonon spectral density

$$J_{\nu \mu}(\omega) = \sum_{\mathbf{q}} \gamma_{\mathbf{q}}^\nu \gamma_{\mathbf{q}}^{\mu*} \delta(\omega - \omega_{\mathbf{q}}) \quad (A4)$$

has been introduced. Although in our case the spectral density is of the super-Ohmic type (cf. Ref. [39]), we would like to mention that various spectral densities describing vastly different systems may lead to pronounced non-Markovian behavior, e.g., nonanalyticities of the spectral function can induce power law tails in multitime observables [60].

Defining the combined Hamiltonian and non-Hamiltonian Liouvillian for the subsystem of interest

$$\mathcal{L}_{\mathrm{S}} \bullet = -\frac{i}{\hbar}[H_0(t), \bullet] + \mathcal{L}_{\sigma^-, \gamma} \bullet \qquad (A5)$$

the propagator

$$\mathcal{M}_t \bullet = \mathcal{T} \exp\left(\int_t^{t+\Delta t} \mathcal{L}_{\mathrm{S}} \, dt'\right) \bullet \qquad (A6)$$

is introduced. The matrix elements

$$\mathcal{M}_{\nu_l \mu_l}^{\nu_{l-1} \mu_{l-1}} = \langle \nu_l | \mathcal{M}_t [|\nu_{l-1}\rangle \langle \mu_{l-1}|] | \mu_l \rangle \qquad (A7)$$

are defined as the elements of the operator that is obtained by applying the propagator $\mathcal{M}_t$ to the canonical basis operator $|\nu_{l-1}\rangle \langle \mu_{l-1}|$.

[1] J. Förstner, C. Weber, J. Danckwerts, and A. Knorr, Phys. Rev. Lett. **91**, 127401 (2003).

[2] A. Vagov, V. M. Axt, T. Kuhn, W. Langbein, P. Borri, and U. Woggon, Phys. Rev. B **70**, 201305 (2004).

[3] M. Thorwart, J. Eckel, and E. R. Mucciolo, Phys. Rev. B **72**, 235320 (2005).

[4] A. Vagov, M. D. Croitoru, V. M. Axt, T. Kuhn, and F. M. Peeters, Phys. Rev. Lett. **98**, 227403 (2007).

[5] A. J. Ramsay, A. V. Gopal, E. M. Gauger, A. Nazir, B. W. Lovett, A. M. Fox, and M. S. Skolnick, Phys. Rev. Lett. **104**, 017402 (2010).

[6] P. Kaer, T. R. Nielsen, P. Lodahl, A.-P. Jauho, and J. Mørk, Phys. Rev. Lett. **104**, 157401 (2010).

[7] P. Michler, A. Kiraz, C. Becher, W. V. Schoenfeld, P. M. Petroff, L. Zhang, E. Hu, and A. Imamoglu, Science **290**, 2282 (2000).

[8] Y.-M. He, Y. He, Y.-J. Wei, D. Wu, M. Atatüre, C. Schneider, S. Höfling, M. Kamp, C.-Y. Lu, and J.-W. Pan, Nat. Nanotech. **8**, 213 (2013).

[9] N. Somaschi, V. Giesz, L. De Santis, J. C. Loredo, M. P. Almeida, G. Hornecker, S. L. Portalupi, T. Grange, C. Antón, J. Demory, C. Gómez, I. Sagnes, N. D. Lanzillotti-Kimura, A. Lemaítre, A. Auffeves, A. G. White, L. Lanco, and P. Senellart, Nat. Photonics **10**, 340 (2016).

[10] R. M. Stevenson, R. J. Young, P. Atkinson, K. Cooper, D. A. Ritchie, and A. J. Shields, Nature (London) **439**, 179 (2006).

[11] N. Akopian, N. H. Lindner, E. Poem, Y. Berlatzky, J. Avron, D. Gershoni, B. D. Gerardot, and P. M. Petroff, Phys. Rev. Lett. **96**, 130501 (2006).

[12] R. Hafenbrak, S. M. Ulrich, P. Michler, L. Wang, A. Rastelli, and O. G. Schmidt, New J. Phys. **9**, 315 (2007).

[13] A. Dousse, J. Suffczynski, A. Beveratos, O. Krebs, A. Lemaître, I. Sagnes, J. Bloch, P. Voisin, and P. Senellart, Nature (London) **466**, 217 (2010).

[14] M. Müller, S. Bounouar, K. D. Jöns, M. Glässl, and P. Michler, Nat. Photonics **8**, 224 (2014).

[15] L. Besombes, K. Kheng, L. Marsal, and H. Mariette, Phys. Rev. B **63**, 155307 (2001).

[16] P. Borri, W. Langbein, S. Schneider, U. Woggon, R. L. Sellin, D. Ouyang, and D. Bimberg, Phys. Rev. Lett. **87**, 157401 (2001).

[17] B. Krummheuer, V. M. Axt, and T. Kuhn, Phys. Rev. B **65**, 195313 (2002).

[18] S. M. Ulrich, S. Ates, S. Reitzenstein, A. Löffler, A. Forchel, and P. Michler, Phys. Rev. Lett. **106**, 247402 (2011).

[19] C. Roy and S. Hughes, Phys. Rev. Lett. **106**, 247403 (2011).

[20] C. Roy and S. Hughes, Phys. Rev. X **1**, 021009 (2011).

[21] Z. Harsij, M. Bagheri Harouni, R. Roknizadeh, and M. H. Naderi, Phys. Rev. A **86**, 063803 (2012).

[22] C. Roy and S. Hughes, Phys. Rev. B **85**, 115309 (2012).

[23] D. P. S. McCutcheon and A. Nazir, Phys. Rev. Lett. **110**, 217401 (2013).

[24] K. Roy-Choudhury and S. Hughes, Phys. Rev. B **92**, 205406 (2015).

[25] D. P. S. McCutcheon, Phys. Rev. A **93**, 022119 (2016).

[26] R. Hanbury Brown and R. Q. Twiss, Nature (London) **178**, 1046 (1956).

[27] R. J. Glauber, *Quantum Theory of Optical Coherence: Selected Papers and Lectures* (Wiley, Weinheim, 2007).

[28] C. Santori, D. Fattal, J. Vuckovic, G. S. Solomon, and Y. Yamamoto, Nature (London) **419**, 594 (2002).

[29] C. Bentham, D. Hallett, N. Prtljaga, B. Royall, D. Vaitiekus, R. J. Coles, E. Clarke, A. M. Fox, M. S. Skolnick, I. E. Itskevich, and L. R. Wilson, Appl. Phys. Lett. **109**, 161101 (2016).

[30] N. Prtljaga, C. Bentham, J. O'Hara, B. Royall, E. Clarke, L. R. Wilson, M. S. Skolnick, and A. M. Fox, Appl. Phys. Lett. **108**, 251101 (2016).

[31] M. Weiß, S. Kapfinger, T. Reichert, J. J. Finley, A. Wixforth, M. Kaniber, and H. J. Krenner, Appl. Phys. Lett. **109**, 033105 (2016).

[32] X. Ding, Y. He, Z.-C. Duan, N. Gregersen, M.-C. Chen, S. Unsleber, S. Maier, C. Schneider, M. Kamp, S. Höfling, C.-Y. Lu, and J.-W. Pan, Phys. Rev. Lett. **116**, 020401 (2016).

[33] L. Schweickert, K. D. Jöns, K. D. Zeuner, S. F. C. da Silva, H. Huang, T. Lettner, M. Reindl, J. Zichi, R. Trotta, A. Rastelli, and V. Zwiller, Appl. Phys. Lett. **112**, 093106 (2018).

[34] C. S. Muñoz, E. del Valle, A. G. Tudela, K. Müller, S. Lichtmannecker, M. Kaniber, C. Tejedor, J. J. Finley, and F. P. Laussy, Nat. Photonics **8**, 550 (2014).

[35] H. Carmichael, *An Open Systems Approach to Quantum Optics* (Springer, Berlin, 1993).

[36] N. Makri and D. E. Makarov, J. Chem. Phys. **102**, 4600 (1995).

[37] N. Makri and D. E. Makarov, J. Chem. Phys. **102**, 4611 (1995).

[38] M. Thorwart, P. Reimann, and P. Hänggi, Phys. Rev. E **62**, 5808 (2000).

[39] A. Vagov, M. D. Croitoru, M. Glässl, V. M. Axt, and T. Kuhn, Phys. Rev. B **83**, 094303 (2011).

[40] J. Shao and N. Makri, J. Chem. Phys. **116**, 507 (2002).

[41] A. M. Barth, A. Vagov, and V. M. Axt, Phys. Rev. B **94**, 125439 (2016).

[42] M. Cygorek, A. M. Barth, F. Ungar, A. Vagov, and V. M. Axt, Phys. Rev. B **96**, 201201 (2017).

[43] A. Strathearn, P. Kirton, D. Kilda, J. Keeling, and B. W. Lovett, Nat. Commun. **9**, 3322 (2018).

[44] M. Cygorek, F. Ungar, T. Seidelmann, A. M. Barth, A. Vagov, V. M. Axt, and T. Kuhn, Phys. Rev. B **98**, 045303 (2018).

[45] P. Machnikowski and L. Jacak, Phys. Rev. B **69**, 193302 (2004).

[46] W. H. Louisell, *Quantum Statistical Properties of Radiation* (Wiley, New York, 1973).

[47] B. Krummheuer, V. M. Axt, T. Kuhn, I. D'Amico, and F. Rossi, Phys. Rev. B **71**, 235329 (2005).

[48] H.-P. Breuer, E.-M. Laine, and J. Piilo, Phys. Rev. Lett. **103**, 210401 (2009).

[49] D. E. Reiter, Phys. Rev. B **95**, 125308 (2017).

[50] J. Iles-Smith, D. P. S. McCutcheon, J. Mørk, and A. Nazir, Phys. Rev. B **95**, 201305 (2017).

[51] J. Iles-Smith, D. P. S. McCutcheon, A. Nazir, and J. Mørk, Nat. Photonics **11**, 521 (2017).

[52] B. R. Mollow, Phys. Rev. **188**, 1969 (1969).

[53] A. Krügel, V. Axt, T. Kuhn, P. Machnikowski, and A. Vagov, Appl. Phys. B **81**, 897 (2005).

[54] A. Nazir, Phys. Rev. B **78**, 153309 (2008).

[55] A. J. Ramsay, T. M. Godden, S. J. Boyle, E. M. Gauger, A. Nazir, B. W. Lovett, A. M. Fox, and M. S. Skolnick, Phys. Rev. Lett. **105**, 177402 (2010).

[56] Y.-J. Wei, Y. He, Y.-M. He, C.-Y. Lu, J.-W. Pan, C. Schneider, M. Kamp, S. Höfling, D. P. S. McCutcheon, and A. Nazir, Phys. Rev. Lett. **113**, 097401 (2014).

[57] M. Glässl and V. M. Axt, Phys. Rev. B **86**, 245306 (2012).

[58] A. M. Barth, S. Lüker, A. Vagov, D. E. Reiter, T. Kuhn, and V. M. Axt, Phys. Rev. B **94**, 045306 (2016).

[59] D. G. Nahri, F. H. A. Mathkoor, and C. H. R. Ooi, J. Phys.: Condens. Matter **29**, 055701 (2017).

[60] A. Chakraborty and R. Sensarma, Phys. Rev. B **97**, 104306 (2018).

Publication 11

Emission-Frequency Separated High Quality Single-Photon Sources Enabled by Phonons

M. Cosacchi, F. Ungar, M. Cygorek, A. Vagov, and V. M. Axt

Emission-Frequency Separated High Quality Single-Photon Sources Enabled by Phonons

M. Cosacchi,[1] F. Ungar,[1] M. Cygorek,[2] A. Vagov,[1,3] and V. M. Axt[1]

[1]*Theoretische Physik III, Universität Bayreuth, 95440 Bayreuth, Germany*
[2]*Department of Physics, University of Ottawa, Ottawa, Ontario, Canada K1N 6N5*
[3]*ITMO University, St. Petersburg, 197101, Russia*

We demonstrate theoretically that the single-photon purity of photons emitted from a quantum dot exciton prepared by phonon-assisted off-resonant excitation can be significantly higher in a wide range of parameters than that obtained by resonant preparation for otherwise identical conditions. Despite the off-resonant excitation, the brightness stays on a high level. These surprising findings exploit the fact that the phonon-assisted preparation is a two-step process where phonons first lead to a relaxation between laser-dressed states while high exciton occupations are reached only with a delay to the laser pulse maximum by adiabatically undressing the dot states. Due to this delay, possible subsequent processes, in particular multiphoton excitations, appear at a time when the laser pulse is almost gone. The resulting suppression of reexcitation processes increases the single-photon purity. Due to the spectral separation of the signal photons from the laser frequencies this enables the emission of high quality single photons not disturbed by a laser background while taking advantage of the robustness of the phonon assisted scheme.

On-demand single-photon sources continue to gain attention as key building blocks in quantum technological applications, ranging from novel metrology over quantum communication to quantum computing. Semiconductor quantum dots (QDs) have proven to be suitable single-photon emitters [1–8] that, due to their high compatibility with existing semiconductor technology, are promising candidates for device applications. In contrast to atomic systems, these nanoscale structures are prone to the influence of the surrounding solid state crystal matrix. Longitudinal acoustic (LA) phonons are the main source of decoherence of excitons in semiconductor QDs even at cryogenic temperatures of a few kelvin [9–13]. Nevertheless, phonon-assisted off-resonant QD excitations have been shown to provide a robust alternative to resonant exciton preparation schemes [14–18]. In this Letter, we demonstrate theoretically that, quite unexpectedly, the coupling to LA phonons combined with off-resonant driving can be extremely beneficial for a single-photon source based on a QD-cavity system, allowing for the generation of high-quality single-photons that are easily detectable due to their spectral separation from the laser pulses used for the excitation of the QD.

Placing a QD in a cavity strongly enhances the photon emission by enlarging the effective dot-cavity coupling and by setting a preferable emission axis. When exciting the QD exciton resonantly, the frequencies of the excitation and the signal are identical—separating the two is a formidable experimental challenge. In fact, spectral separability is achievable, e.g., by wetting layer excitation or by exciting the biexciton via the two-photon resonance and subsequently

exploiting the biexciton-exciton cascade [8,19]. But while the former introduces a time jitter that reduces the on-demand character of the photon source, the latter is sensitive to small fluctuations of excitation parameters such as the laser energy and the pulse area. Both problems are overcome by an off-resonant excitation of the quantum dot, which is thus extremely advantageous. Indeed, it has recently been shown that the robustness of off-resonant excitation schemes paves the way to excite two spatially separated QDs with different transition energies simultaneously with the same laser pulse, which is a milestone towards the scalability of complex quantum networks [20].

The quality of a QD-cavity system as an on-demand single-photon source is typically quantified by several key figures of merit, such as the single-photon purity $\mathcal{P}$ and the brightness $\mathcal{B}$. While the former measures whether indeed a single photon is emitted by the source, the latter characterizes its total photon yield [5]. When $\mathcal{P} = \mathcal{B} = 1$, the source emits a single photon with a probability of unity at every excitation pulse via the cavity. The single-photon purity (SPP) can be extracted from a Hanbury Brown–Twiss coincidence experiment [3,7,8,21–24], which gives a conditional probability to detect a second photon when a first one has already been detected. Suppressing this probability is possible, e.g., by parametric down-conversion, which enhances the SPP, albeit at the cost of a severely reduced brightness of the photon source [25]. Maximizing both SPP and brightness is of utmost importance to create efficient single-photon emitters.

Simultaneously large $\mathcal{P}$ and $\mathcal{B}$ in a QD-cavity system can be achieved by exciting the dot resonantly by ultrashort
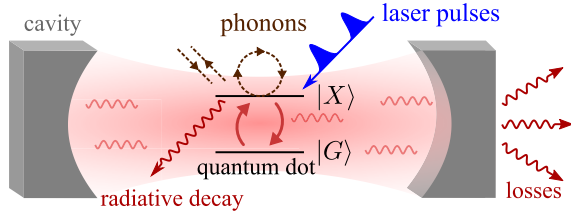
FIG. 1. Sketch of the system under consideration. A two-level QD with a ground state $|G\rangle$ and an exciton state $|X\rangle$ is coupled to a lossy single-mode microcavity. The $|G\rangle \rightarrow |X\rangle$ transition is driven by external laser pulses and the exciton state is coupled to LA phonons in a pure-dephasing manner. Finally, the dot can decay radiatively.

laser pulses [3,4,7]. However, shortening the pulse duration is equivalent to widening it spectrally. The detrimental influence of exciting higher-lying states, especially the biexciton state of the QD by short pulses is discussed in Ref. [26]. In view of the various advantages of phonon-assisted off-resonant excitations listed above, the question arises how photonic characteristics such as SPP and brightness perform under off-resonant schemes. In short, we want to explore whether all of the advantages of phonon-assisted off-resonant schemes come at the cost of severely reduced photonic properties.

It is expected that driving a QD off-resonantly is much less efficient. For longer and stronger pulses the resulting quantum state of a QD-cavity system contains an admixture of multiphoton states, which reduces the SPP. Phonon-induced dephasing is expected to degrade the quantum state even further. But paradoxically quite the opposite can take place: a combination of off-resonant driving with the phonon-induced relaxation between laser-dressed QD states leads eventually to high exciton occupations in a subsequent adiabatic undressing process [27]. In this Letter, we demonstrate that the delay of the exciton creation caused by the undressing suppresses the probability for multiphoton generation. Therefore, comparing off-resonant and resonant excitation with otherwise same conditions may, quite unexpectedly, yield enhanced SPPs in the off-resonant case. The best values predicted in this Letter are even comparable to the best values obtained so far within resonant schemes addressing the exciton.

We model the QD-cavity system as a laser-driven two-level system with a ground state $|G\rangle$ and an excited state $|X\rangle$, $H_{\mathrm{DL}} = -\hbar\Delta\omega_{\mathrm{LX}}|X\rangle\langle X| - (\hbar/2)f(t)(|X\rangle\langle G| + |G\rangle\langle X|)$, coupled to a single-mode microcavity (cf., Fig. 1), $H_{\mathrm{C}} = \hbar\Delta\omega_{\mathrm{CL}}a^\dagger a + \hbar g(a^\dagger|G\rangle\langle X| + a|X\rangle\langle G|)$, which is on resonance with the QD exciton. Here, $\Delta\omega_{\mathrm{LX}}$ and $\Delta\omega_{\mathrm{CL}}$ are the laser-exciton and cavity-laser detuning, respectively, and a is the photon annihilation operator in the cavity, which is coupled to the dot by the coupling constant g. A train of Gaussian pulses is assumed represented by the laser envelope function $f(t)$. The excitation can leave the system either via radiative decay or cavity losses modeled by Lindblad rates γ

and κ, respectively. Finally, the exciton is coupled to a continuum of LA phonons in a pure-dephasing manner [28], $H_{\mathrm{Ph}} = \hbar\sum_{\mathbf{q}}\omega_{\mathbf{q}}b_{\mathbf{q}}^\dagger b_{\mathbf{q}} + \hbar\sum_{\mathbf{q}}(\gamma_{\mathbf{q}}^{\mathrm{X}}b_{\mathbf{q}}^\dagger + \gamma_{\mathbf{q}}^{\mathrm{X}*}b_{\mathbf{q}})|X\rangle\langle X|$. $b_{\mathbf{q}}$ annihilates a phonon in the mode $\mathbf{q}$ coupled to the dot by the coupling constant $\gamma_{\mathbf{q}}^{\mathrm{X}}$. Full details of the model and of our numerical approach are given in the Supplemental Material [29]. It is worthwhile to note that we use path-integral methods for our simulations that allow us to perform all simulations without approximation to the model [29,36–38].

For the calculations, standard GaAs parameters are used [39] for a QD of 6 nm diameter (for details on the phonon coupling consider the Supplemental Material [29]). If not stated otherwise, the excitation pulse full width at half maximum is set to 7 ps, the cavity mode is resonant with the QD transition, the dot-cavity coupling is $\hbar g = 50~\mu\mathrm{eV}$, the radiative decay rate is $\hbar\gamma = 20~\mu\mathrm{eV}$, and the cavity loss rate is $\hbar\kappa = 50~\mu\mathrm{eV}$. This corresponds to a Purcell factor of $F_{\mathrm{P}} = g^2/(\gamma\kappa) = 2.5$. The initial phonon distribution is assumed to be thermal with a temperature of $T = 4.2$ K.

The main target quantities of interest in this Letter, the SPP $\mathcal{P}$ and the brightness $\mathcal{B}$, are obtained from path-integral simulations of the two-time photonic correlation function $G^{(2)}(t,\tau) = \langle a^\dagger(t)a^\dagger(t+\tau)a(t+\tau)a(t)\rangle$ and the time dependent photon occupation $\langle a^\dagger a\rangle(t)$, respectively. In order to express the SPP in terms of $G^{(2)}(t,\tau)$ one first needs to take the average over the first time argument t, i.e., $G^{(2)}(\tau) = \int_{-\infty}^{\infty} dt\, G^{(2)}(t,\tau)$, which yields a function with the delay time τ of the coincidence measurement as its single argument. The probability p of detecting a second photon during the same excitation pulse after a first one has already been emitted thus can be obtained by

$$p = \frac{\int_{-T_{\mathrm{Pulse}}/2}^{T_{\mathrm{Pulse}}/2} d\tau\, G^{(2)}(\tau)}{\int_{T_{\mathrm{Pulse}}/2}^{3T_{\mathrm{Pulse}}/2} d\tau\, G^{(2)}(\tau)}, \qquad (1)$$

where T_{Pulse} is the separation of the pulses in the pulse train. The SPP is then defined as $\mathcal{P} = 1 - p$. Note that $-\infty < \mathcal{P} \leq 1$, where the lack of a lower bound is due to the possibility of bunching instead of antibunching.

In this Letter, the brightness of the source is modeled as the integrated leakage of the average photon number during the duration of one pulse, i.e., $\mathcal{B} = \kappa \int_{-T_{\mathrm{Pulse}}/2}^{T_{\mathrm{Pulse}}/2} dt\langle a^\dagger a\rangle(t)$. Due to the definition, this quantity formally ranges in $0 \leq \mathcal{B} < \infty$ without an upper bound since in principal infinitely many photons can exist in a single electromagnetic field mode.

In Fig. 2(a) the brightness simulated without phonons is shown as a function of the detuning $\Delta\omega_{\mathrm{LX}}$ between the central laser frequency and the transition frequency connecting the ground and the exciton state of the QD as well as the pulse area Θ. An oscillatory behavior as a function of the pulse area with maxima at odd multiples of π is observed [cf., Fig. 2(a)]. This is a consequence of the well-known Rabi rotation of the exciton occupation since
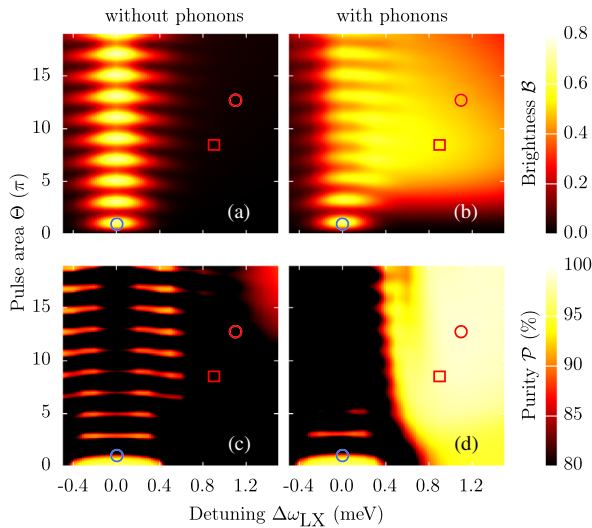
FIG. 2. Brightness $\mathcal{B}$ [panels (a) and (b)] and SPP $\mathcal{P}$ [panels (c) and (d)] as a function of the laser-exciton detuning $\Delta\omega_{LX}$ and the excitation pulse area Θ of a pulse in the pulse train. The left column (a), (c) is the result of a phonon-free calculation, the right column (b), (d) includes the coupling to a continuum of LA phonons. Blue circle: resonant π-pulse excitation. Red circle: maximal SPP (with phonons). Red square: optimal SPP and brightness for off-resonant excitation (with phonons).

the exciton feeds the cavity photons, which in turn are measured by the brightness. As a function of the detuning, the regions of high brightness are confined to a fairly small range around resonance. The inclusion of phonons drastically changes this picture [cf., Fig. 2(b)]. Through off-resonant excitation with detunings that can be bridged by the emission of LA phonons, a nonvaninshing brightness can be obtained in a previously dark region. Note that the asymmetry with respect to the sign of the detuning is due to the low temperature of $T = 4.2$ K considered here where phonon absorption is largely suppressed.

The SPP in the phonon-free case [cf., Fig. 2(c)] also displays Rabi rotational behavior but decreases with rising pulse area close to resonance, which is due to a reexcitation of the QD during the same laser pulse. This leads to the emission of more than one photon per pulse, thus diminishing the SPP. Although a SPP can always be calculated, one should be aware that it constitutes a physically meaningful quantity only for finite brightness. Therefore, the area of increased SPP in the upper right corner of Fig. 2(c) is of no physical relevance.

It is intuitively expected that the continuum of LA phonons reduces the quantum correlations of the system and thus the SPP by inducing a manifold of transitions between its quantum states. However, contrary to these expectations Fig. 2(d) reveals a huge systematic increase in $\mathcal{P}$ at $\Delta\omega_{LX} \gtrsim 0.5$ meV. Moreover, the maximum $\mathcal{P}_{max} = 98.8\%$ (red circle) is even larger than 90.7% obtained for the resonantly driven system (blue circle). Combined with

an appreciably large $\mathcal{B}$, this indicates a possibility to have a good quality single-photon source in the off-resonant excitation regime. Note that $\mathcal{B} = 0.46$ observed at the point of $\mathcal{P}_{max}$ [cf., red circle in Fig. 2(b)] is not much smaller than the maximal value of 0.67 achieved in the resonantly driven case [cf., blue circle in Fig. 2(b)]. It is also noteworthy that it is possible to obtain a significantly larger brightness at the cost of a slight decrease in the SSP. For example, if we choose a trade-off by maximizing the sum of the squares of the two figures of merit in the off-resonant regime, we obtain $\mathcal{B} = 0.53$ and $\mathcal{P} = 98.1\%$ (red square). This value for $\mathcal{P}$ is close to typical experimental values obtained for resonant excitation of the quantum dot exciton (98.8% [4], 99.1% [7]) even though the pulse lengths in Refs. [4,7] have been slightly shorter [40].

To explain the mechanism behind this observation, one needs to consider the dynamics of the QD-cavity states. In Fig. 3, the time dependent occupations in the resonant and the off-resonant case (cf., the blue and red circles in Fig. 2, respectively) are compared. The considered states are product states between the QD states and a photon state with photon number n. After resonant π-pulse excitation [cf., Fig. 3(a)], the exciton state $|X, 0\rangle$ without photons is occupied (blue curve). The cavity coupling rotates the dot back to its ground state and produces one photon in the cavity (orange curve). Because the driving is still nonzero at this point, the dot is reexcited to produce an occupation of the state $|X, 1\rangle$ (green curve), which is shown in the inset of Fig. 3(a). Finally, the cavity coupling leads to an occupation of the ground state with two photons $|G, 2\rangle$ (red curve), such that the SPP is diminished.

In contrast to the π-pulse induced rotation of the Bloch vector, the off-resonant excitation scheme exploits an effect called adiabatic undressing [27]. Switching on the laser transforms the dot states to a new energy eigenbasis commonly known as laser-dressed states, the gap between which can be bridged by LA phonons with typical energies of a few meV. At low temperatures, the lower dressed state becomes occupied via phonon emission. However, the phonon-induced relaxation is only efficient when both dressed states have roughly equal exciton components. Thus, the exciton state exhibits typically occupations of the order of 50% after the relaxation is completed [27]. When the laser is turned off adiabatically, the lower dressed state is subsequently transformed to the exciton state in the original basis provided the detuning is positive (otherwise the ground state is reached [27]). This adiabatic undressing of the dot states therefore boosts the exciton occupation only at the end of the pulse [cf., the blue curve in Fig. 3(b)]. This in turn means that during the phase of phonon relaxation no photon can be put into the cavity efficiently [cf., the orange curve in Fig. 3(b)]. When finally the adiabatic undressing-induced exciton boost occurs, the occupation of $|G, 1\rangle$ follows [cf., Fig. 3(b)]. Since the excitation pulse is basically gone by then, the reexcitation of the QD is strongly
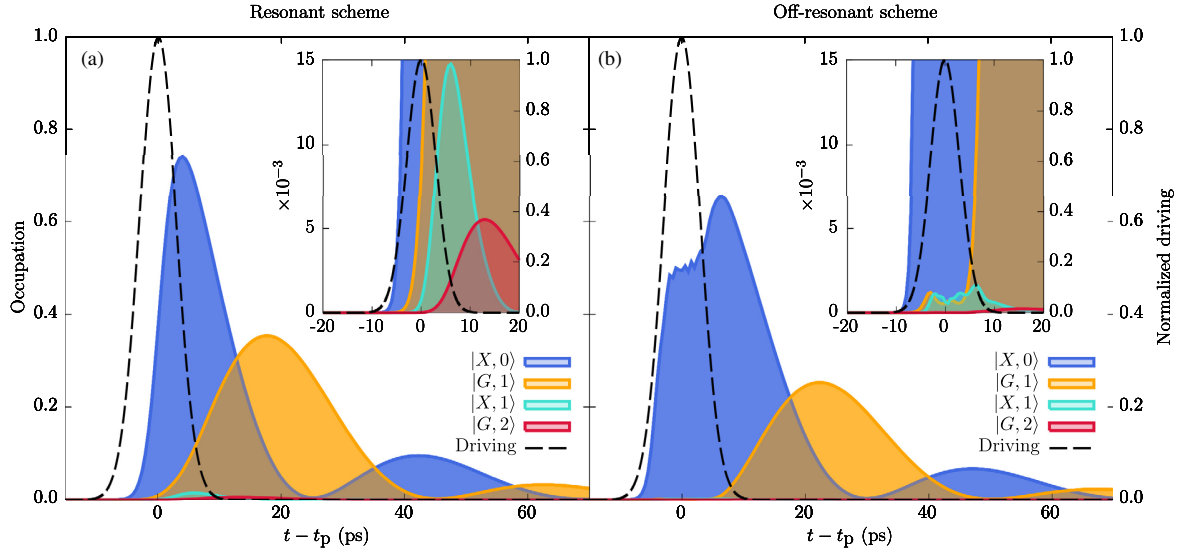
FIG. 3. Time-dependent occupations: (a) after resonant π-pulse excitation (cf., blue circle in Fig. 2) and (b) in the off-resonant phonon-assisted case (cf., red circle in Fig. 2). The occupations of the states $|X,0\rangle$, $|G,1\rangle$, $|X,1\rangle$, and $|G,2\rangle$ are shown as colored filled curves. The Gaussian envelope of the laser driving pulse normalized to its maximum value centered at t_p is shown as a black dashed line. The insets show the same curves, respectively, on an enlarged scale for the occupations.

suppressed (green curve), such that effectively no second photon can be put into the cavity (red curve). This implies a far higher SPP than in the resonant counterpart, as is observed in Fig. 2(d). In summary, the delay of the exciton occupation caused by the two-step procedure of first relaxing to a dressed state via phonon emission and then reaching the exciton by adiabatic undressing is responsible for the enhancement of the SPP.

To quantify the robustness of the phonon-induced SPP enhancement against variations of other system parameters,
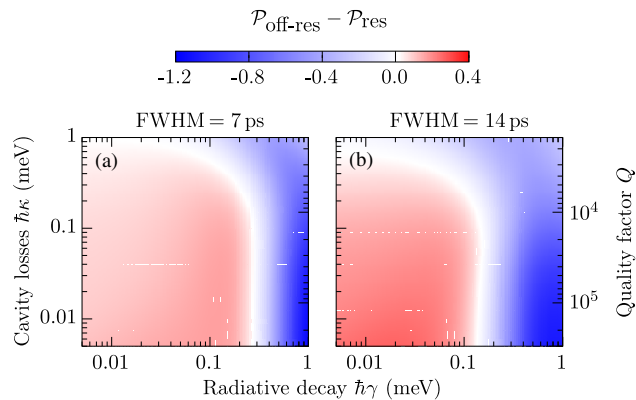

FIG. 4. The difference between the SPP after off-resonant phonon-assisted excitation $\mathcal{P}_{\text{off-res}}$ and after resonant π-pulse rotation $\mathcal{P}_{\text{res}}$ is shown for two different pulse lengths (FWHM), namely: (a) 7 ps and (b) 14 ps, as a function of radiative decay $\hbar\gamma$ and cavity losses $\hbar\kappa$. The cavity quality factor $Q = \omega_c/\kappa$ is obtained via the cavity losses assuming a cavity single-mode energy of $\hbar\omega_c = 1.5$ eV. The pulse area is set to 12.75π and $\Delta\omega_{\text{LX}} = 1.1$ meV.

the difference between the SPP after off-resonant excitation and after the resonant one is shown as a function of the radiative decay γ and the cavity loss rate κ in Fig. 4. A positive value (reddish shade) indicates a set of parameters where the SPP is enhanced for off-resonant excitation. We find such an enhancement for a wide parameter regime in κ and γ that is experimentally well accessible. Also, changing the pulse length from 7 ps in Fig. 4(a) to 14 ps in Fig. 4(b) does not change the phonon-induced SPP enhancement qualitatively. The reason why the SPP for off-resonant excitation falls below the resonant one in the bad cavity limit and/or in the limit of high radiative losses is that relaxation processes limit the time available for the adiabatic undressing which eventually becomes incomplete.

In conclusion, we have presented a seemingly paradoxical scheme for the phonon-assisted operation of a QD-cavity system as a single-photon source, where the excitation is spectrally separated from the generated photons. Two factors that would separately lead to a quality degradation—off-resonant driving and dot-phonon coupling—in combination result in a huge boost in critical characteristics of a single-photon source. We have demonstrated that the achievable single-photon purity can be noticeably higher than for resonant excitation while the brightness is still at an acceptable level. The physical mechanism of this enhancement—the adiabatic undressing—is realized in a wide interval of physically accessible parameters.

————————

[1] P. Michler, A. Kiraz, C. Becher, W. V. Schoenfeld, P. M. Petroff, L. Zhang, E. Hu, and A. Imamoglu, Science **290**, 2282 (2000).

[2] C. Santori, M. Pelton, G. Solomon, Y. Dale, and Y. Yamamoto, Phys. Rev. Lett. **86**, 1502 (2001).

[3] C. Santori, D. Fattal, J. Vuckovic, G. S. Solomon, and Y. Yamamoto, Nature (London) **419**, 594 (2002).

[4] Y.-M. He, Y. He, Y.-J. Wei, D. Wu, M. Atatüre, C. Schneider, S. Höfling, M. Kamp, C.-Y. Lu, and J.-W. Pan, Nat. Nanotechnol. **8**, 213 (2013).

[5] N. Somaschi, V. Giesz, L. De Santis, J. C. Loredo, M. P. Almeida, G. Hornecker, S. L. Portalupi, T. Grange, C. Antón, J. Demory, C. Gómez, I. Sagnes, N. D. Lanzillotti-Kimura, A. Lemaître, A. Auffeves, A. G. White, L. Lanco, and P. Senellart, Nat. Photonics **10**, 340 (2016).

[6] Y.-J. Wei, Y.-M. He, M.-C. Chen, Y.-N. Hu, Y. He, D. Wu, C. Schneider, M. Kamp, S. Höfling, C.-Y. Lu, and J.-W. Pan, Nano Lett. **14**, 6515 (2014).

[7] X. Ding, Y. He, Z.-C. Duan, N. Gregersen, M.-C. Chen, S. Unsleber, S. Maier, C. Schneider, M. Kamp, S. Höfling, C.-Y. Lu, and J.-W. Pan, Phys. Rev. Lett. **116**, 020401 (2016).

[8] L. Schweickert, K. D. Jöns, K. D. Zeuner, S. F. Covre da Silva, H. Huang, T. Lettner, M. Reindl, J. Zichi, R. Trotta, A. Rastelli, and V. Zwiller, Appl. Phys. Lett. **112**, 093106 (2018).

[9] J. Förstner, C. Weber, J. Danckwerts, and A. Knorr, Phys. Rev. Lett. **91**, 127401 (2003).

[10] A. Vagov, M. D. Croitoru, V. M. Axt, T. Kuhn, and F. M. Peeters, Phys. Rev. Lett. **98**, 227403 (2007).

[11] A. J. Ramsay, A. V. Gopal, E. M. Gauger, A. Nazir, B. W. Lovett, A. M. Fox, and M. S. Skolnick, Phys. Rev. Lett. **104**, 017402 (2010).

[12] P. Kaer, T. R. Nielsen, P. Lodahl, A.-P. Jauho, and J. Mørk, Phys. Rev. Lett. **104**, 157401 (2010).

[13] D. E. Reiter, Phys. Rev. B **95**, 125308 (2017).

[14] M. Glässl, A. M. Barth, and V. M. Axt, Phys. Rev. Lett. **110**, 147401 (2013).

[15] P.-L. Ardelt, L. Hanschke, K. A. Fischer, K. Müller, A. Kleinkauf, M. Koller, A. Bechtold, T. Simmet, J. Wierzbowski, H. Riedl, G. Abstreiter, and J. J. Finley, Phys. Rev. B **90**, 241404 (2014).

[16] D. E. Reiter, T. Kuhn, M. Glässl, and V. M. Axt, J. Phys. Condens. Matter **26**, 423203 (2014).

[17] S. Bounouar, M. Müller, A. M. Barth, M. Glässl, V. M. Axt, and P. Michler, Phys. Rev. B **91**, 161302 (2015).

[18] J. H. Quilter, A. J. Brash, F. Liu, M. Glässl, A. M. Barth, V. M. Axt, A. J. Ramsay, M. S. Skolnick, and A. M. Fox, Phys. Rev. Lett. **114**, 137401 (2015).

[19] L. Hanschke, K. A. Fischer, S. Appel, D. Lukin, J. Wierzbowski, S. Sun, R. Trivedi, J. Vučković, J. J. Finley, and K. Müller, npj Quantum Inf. **4**, 43 (2018).

[20] M. Reindl, K. D. Jns, D. Huber, C. Schimpf, Y. Huo, V. Zwiller, A. Rastelli, and R. Trotta, Nano Lett. **17**, 4090 (2017).

[21] R. Hanbury Brown and R. Q. Twiss, Nature (London) **178**, 1046 (1956).

[22] C. Bentham, D. Hallett, N. Prtljaga, B. Royall, D. Vaitiekus, R. J. Coles, E. Clarke, A. M. Fox, M. S. Skolnick, I. E. Itskevich, and L. R. Wilson, Appl. Phys. Lett. **109**, 161101 (2016).

[23] N. Prtljaga, C. Bentham, J. O'Hara, B. Royall, E. Clarke, L. R. Wilson, M. S. Skolnick, and A. M. Fox, Appl. Phys. Lett. **108**, 251101 (2016).

[24] M. Weiß, S. Kapfinger, T. Reichert, J. J. Finley, A. Wixforth, M. Kaniber, and H. J. Krenner, Appl. Phys. Lett. **109**, 033105 (2016).

[25] J.-W. Pan, Z.-B. Chen, C.-Y. Lu, H. Weinfurter, A. Zeilinger, and M. Żukowski, Rev. Mod. Phys. **84**, 777 (2012).

[26] C. Gustin and S. Hughes, Phys. Rev. B **98**, 045309 (2018).

[27] A. M. Barth, S. Lüker, A. Vagov, D. E. Reiter, T. Kuhn, and V. M. Axt, Phys. Rev. B **94**, 045306 (2016).

[28] B. Krummheuer, V. M. Axt, and T. Kuhn, Phys. Rev. B **65**, 195313 (2002).

[29] See Supplemental Material at http://link.aps.org/supplemental/10.1103/PhysRevLett.123.017403 for a complete definition of our model, in particular the phonon coupling, and the numerical procedure used. It includes Refs. [30–35] in addition to other references already cited in the main text.

[30] L. Besombes, K. Kheng, L. Marsal, and H. Mariette, Phys. Rev. B **63**, 155307 (2001).

[31] P. Borri, W. Langbein, S. Schneider, U. Woggon, R. L. Sellin, D. Ouyang, and D. Bimberg, Phys. Rev. Lett. **87**, 157401 (2001).

[32] A. Vagov, M. D. Croitoru, M. Glässl, V. M. Axt, and T. Kuhn, Phys. Rev. B **83**, 094303 (2011).

[33] N. Makri and D. E. Makarov, J. Chem. Phys. **102**, 4600 (1995).

[34] N. Makri and D. E. Makarov, J. Chem. Phys. **102**, 4611 (1995).

[35] D. P. S. McCutcheon, Phys. Rev. A **93**, 022119 (2016).

[36] A. M. Barth, A. Vagov, and V. M. Axt, Phys. Rev. B **94**, 125439 (2016).

[37] M. Cygorek, A. M. Barth, F. Ungar, A. Vagov, and V. M. Axt, Phys. Rev. B **96**, 201201(R) (2017).

[38] M. Cosacchi, M. Cygorek, F. Ungar, A. M. Barth, A. Vagov, and V. M. Axt, Phys. Rev. B **98**, 125302 (2018).

[39] B. Krummheuer, V. M. Axt, T. Kuhn, I. D'Amico, and F. Rossi, Phys. Rev. B **71**, 235329 (2005).

[40] Note that other system parameters in these experiments are also different from the ones used here, e.g., the Purcell factor reported in Ref. [7] is 6.3 compared with 2.5 in our case.

Supplement: Emission-frequency separated high quality single-photon sources enabled by phonons

M. Cosacchi,[1] F. Ungar,[1] M. Cygorek,[2] A. Vagov,[1,3] and V. M. Axt[1]

[1]*Theoretische Physik III, Universität Bayreuth, 95440 Bayreuth, Germany*
[2]*Department of Physics, University of Ottawa, Ottawa, Ontario, Canada K1N 6N5*
[3]*ITMO University, St. Petersburg, 197101, Russia*

MODEL AND NUMERICAL METHOD

In this supplement we specify in detail the model used in the main paper and outline the numerical procedure used for our simulations. We represent the quantum dot (QD)-cavity system by a Hamiltonian comprising three parts:

$$H = H_{\mathrm{DL}} + H_C + H_{\mathrm{Ph}}, \tag{1}$$

where H_{DL} describes the QD driven by an external laser, H_C accounts for the coupling of the QD to a quantized cavity mode, while H_{Ph} represent the interaction with a continuum of longitudinal acoustic (LA) phonons.

Within the usual dipole and rotating wave approximations, the dot-laser Hamiltonian takes the form

$$H_{\mathrm{DL}} = -\hbar \Delta \omega_{\mathrm{LX}} |X\rangle\langle X| - \frac{\hbar}{2} f(t) \left(|X\rangle\langle G| + |G\rangle\langle X| \right) \tag{2}$$

in a frame co-rotating with the laser frequency ω_{L}. Here, $|G\rangle$ denotes the QD ground state and $|X\rangle$ is the exciton state and a detuning between the laser and exciton frequency $\Delta\omega_{\mathrm{LX}} := \omega_{\mathrm{L}} - \omega_{\mathrm{X}}$ is introduced. $\mathbf{d}$ is the transition dipole and $\mathbf{E}(t)$ the laser field, such that $-\mathbf{d} \cdot \mathbf{E}(t) = -\hbar f(t)/2 \exp(-i\omega_{\mathrm{L}}t)$, where $f(t)$ denotes the real envelope function of the exciting laser. $f(t)$ is taken to be a pulse train consisting of Gaussian functions, where each Gaussian has an area Θ and a pulse length measured by the full-width-at-half-maximum (FWHM). Every T_{Pulse} the maximum of a Gaussian hits the QD. The dot is coupled to a single-mode microcavity via

$$H_{\mathrm{C}} = \hbar \Delta \omega_{\mathrm{CL}} a^\dagger a + \hbar g \left(a^\dagger |G\rangle\langle X| + a|X\rangle\langle G| \right) . \tag{3}$$

The single-mode photons of the cavity are created (annihilated) by the bosonic operator $a^\dagger$ (a) and are detuned by $\Delta\omega_{\mathrm{CL}} := \omega_{\mathrm{C}} - \omega_{\mathrm{L}}$ with respect to the laser frequency. The coupling strength between the QD and the microcavity is denoted by $\hbar g$. Furthermore, the pure dephasing-type coupling [1–3] between the QD and a continuum of longitudinal acoustic (LA) phonons is modeled as

$$H_{\mathrm{Ph}} = \hbar \sum_{\mathbf{q}} \omega_{\mathbf{q}} b_{\mathbf{q}}^\dagger b_{\mathbf{q}} + \hbar \sum_{\mathbf{q}} \left(\gamma_{\mathbf{q}}^{\mathrm{X}} b_{\mathbf{q}}^\dagger + \gamma_{\mathbf{q}}^{\mathrm{X}*} b_{\mathbf{q}} \right) |X\rangle\langle X|, \tag{4}$$

where the bosonic operator $b_{\mathbf{q}}^\dagger$ ($b_{\mathbf{q}}$) creates (destroys) phonons with frequency $\omega_{\mathbf{q}}$. $\gamma_{\mathbf{q}}^{\mathrm{X}}$ denotes the deformation-potential-type coupling constant between the exciton state and the $\mathbf{q}$-th bosonic mode, which is obtained as the difference between the electron-phonon and hole-phonon constants, $\gamma_{\mathbf{q}}^{\mathrm{X}} = \gamma_{\mathbf{q}}^{\mathrm{e}} - \gamma_{\mathbf{q}}^{\mathrm{h}}$. We consider bulk-phonon modes with linear dispersion, $\omega_{\mathbf{q}} = v_s|\mathbf{q}|$, with the sound velocity v_s. With these assumptions the coupling constants take on the form

$$\gamma_{\mathbf{q}}^{\mathrm{e(h)}} = \Psi^{\mathrm{e(h)}}(\mathbf{q}) \frac{|\mathbf{q}|D_{\mathrm{e(h)}}}{\sqrt{2V\rho\hbar\omega_{\mathbf{q}}}} , \tag{5}$$

where ρ is the density of the material, V the sample volume, $D_{\mathrm{e(h)}}$ the deformation potential constant, and $\Psi^{\mathrm{e(h)}}(\mathbf{q})$ the form factor that is obtained as the Fourier transform of the absolute square of the confined carrier wave functions. The coupling constant enters the phonon spectral density

$$J(\omega) = \sum_{\mathbf{q}} \left| \gamma_{\mathbf{q}}^{\mathrm{X}} \right|^2 \delta(\omega - \omega_{\mathbf{q}}), \tag{6}$$

which in turn determines the depth of the phonon-induced memory [4]. Assuming a spherical dot with harmonic confinement yields

$$J(\omega) = \frac{\omega^3}{4\pi^2\rho\hbar v_s^5} \left\{ D_{\mathrm{e}} \exp\left(-\frac{\omega^2 a_{\mathrm{e}}^2}{4v_s^2} \right) - D_{\mathrm{h}} \exp\left(-\frac{\omega^2 a_{\mathrm{h}}^2}{4v_s^2} \right) \right\}^2 , \tag{7}$$

where $a_{e(h)}$ denotes the electron (hole) confinement length.

For the calculations in the main text, we use values that are typical for GaAs self-assembled QDs [5]: $D_e = 7.0\,\text{eV}$, $D_h = -3.5\,\text{eV}$, $\rho = 5370\,\text{kg/m}^3$, $v_s = 5110\,\text{m/s}$, $a_e/a_h = 1.15$. This leaves only the dot diameter as a free parameter in the shape of the electron confinement length, i.e., $6\,\text{nm} = 2a_e$, as quoted in the main text.

Finally, radiative decay of the QD exciton as well as cavity losses are included via Lindblad-type superoperators $\mathcal{L}_{|G\rangle\langle X|,\gamma}\bullet$ and $\mathcal{L}_{a,\kappa}\bullet$, respectively, with

$$\mathcal{L}_{O,\Gamma}\bullet = \Gamma\left(O\bullet O^\dagger - \frac{1}{2}\left\{\bullet, O^\dagger O\right\}_+\right).\tag{8}$$

Here, $\{\cdot,\cdot\}_+$ denotes the anti-commutator, O is a system operator, and Γ the decay rate of the associated loss process.

We solve the Liouville-von Neumann equation

$$\dot{\rho} = -\frac{i}{\hbar}\{H,\rho\}_- + \mathcal{L}\rho\tag{9}$$

with $H = H_{\text{DL}} + H_C + H_{\text{Ph}}$ and $\mathcal{L}\bullet = \mathcal{L}_{|G\rangle\langle X|,\gamma}\bullet + \mathcal{L}_{a,\kappa}\bullet$, where $\{\cdot,\cdot\}_-$ is the commutator. The density matrix ρ is assumed to initially factorize into a subsystem part corresponding to the dot-cavity system (DL+C) and a phonon part (Ph). The phonon part is initially taken to be a thermal distribution. We employ an iterative real-time path integral method [6, 7] to obtain the time-dependent reduced density matrix $\bar{\rho} = \text{Tr}_{\text{Ph}}[\rho]$. To the best of our knowledge this method is so far the only one where accounting for the influence of the infinitely many LA phonon modes has been realized in a numerically complete way, i.e., without any further approximations to the model described above, since all phonon contributions can be integrated out analytically. Furthermore, recent developments within this formalism allow for the consistent and natural inclusion of Lindblad-type losses [8] and the consideration of more subsystem levels beyond the few-level limit due to an exact reformulation of the iterative scheme [9]. In fact, the reformulation presented in the supplement of Ref. [9] reduces the numerical demand in our present application by many orders of magnitude without which the simulations presented in the main text would have been impossible. Finally, the two-time photonic correlation function $G^{(2)}(t,\tau) = \langle a^\dagger(t)a^\dagger(t+\tau)a(t+\tau)a(t)\rangle$ necessary for the calculation of the single-photon purity is obtained following a numerically complete algorithm that has been proposed recently [10]. In particular, this algorithm avoids the quantum regression theorem, which is valid only when all bath interactions are Markovian [11]. Indeed, it is known that the coupling to LA phonons induces a memory of several picoseconds [4] and thus a Markovian treatment of the QD-phonon interaction would not be adequate.

---

[1] L. Besombes, K. Kheng, L. Marsal, and H. Mariette, Phys. Rev. B **63**, 155307 (2001).

[2] P. Borri, W. Langbein, S. Schneider, U. Woggon, R. L. Sellin, D. Ouyang, and D. Bimberg, Phys. Rev. Lett. **87**, 157401 (2001).

[3] B. Krummheuer, V. M. Axt, and T. Kuhn, Phys. Rev. B **65**, 195313 (2002).

[4] A. Vagov, M. D. Croitoru, M. Glässl, V. M. Axt, and T. Kuhn, Phys. Rev. B **83**, 094303 (2011).

[5] B. Krummheuer, V. M. Axt, T. Kuhn, I. D'Amico, and F. Rossi, Phys. Rev. B **71**, 235329 (2005).

[6] N. Makri and D. E. Makarov, The J. Chem. Phys. **102**, 4600 (1995).

[7] N. Makri and D. E. Makarov, The J. Chem. Phys. **102**, 4611 (1995).

[8] A. M. Barth, A. Vagov, and V. M. Axt, Phys. Rev. B **94**, 125439 (2016).

[9] M. Cygorek, A. M. Barth, F. Ungar, A. Vagov, and V. M. Axt, Phys. Rev. B **96**, 201201(R) (2017).

[10] M. Cosacchi, M. Cygorek, F. Ungar, A. M. Barth, A. Vagov, and V. M. Axt, Phys. Rev. B **98**, 125302 (2018).

[11] D. P. S. McCutcheon, Phys. Rev. A **93**, 022119 (2016).

Publication 12

Comparison of different concurrences characterizing photon pairs generated in the biexciton cascade in quantum dots coupled to microcavities

M. Cygorek, F. Ungar, T. Seidelmann, A. M. Barth, A. Vagov, V. M. Axt, and T. Kuhn

Comparison of different concurrences characterizing photon pairs generated in the biexciton cascade in quantum dots coupled to microcavities

M. Cygorek

Department of Physics, University of Ottawa, ON K1N 6N5 Ottawa, Canada

F. Ungar, T. Seidelmann, A. M. Barth, A. Vagov, and V. M. Axt

Lehrstuhl für Theoretische Physik III, Universität Bayreuth, 95440 Bayreuth, Germany

T. Kuhn

Institut für Festkörpertheorie, Universität Münster, 48149 Münster, Germany

We compare three different notions of concurrence to measure the polarization entanglement of two-photon states generated by the biexciton cascade in a quantum dot embedded in a microcavity. The focus of the paper lies on the often-discussed situation of a dot with finite biexciton binding energy in a cavity tuned to the two-photon resonance. Apart from the time-dependent concurrence, which can be assigned to the two-photon density matrix at any point in time, we study single- and double-time integrated concurrences commonly used in the literature that are based on different quantum state reconstruction schemes. In terms of the photons detected in coincidence measurements, we argue that the single-time integrated concurrence can be thought of as the concurrence of photons simultaneously emitted from the cavity without resolving the common emission time, while the more widely studied double-time integrated concurrence refers to photons that are neither filtered with respect to the emission time of the first photon nor with respect to the delay time between the two emitted photons. Analytic and numerical calculations reveal that the single-time integrated concurrence indeed agrees well with the typical value of the time-dependent concurrence at long times, even when the interaction between the quantum dot and longitudinal acoustic phonons is accounted for. Thus the more easily measurable single-time integrated concurrence gives access to the physical information represented by the time-dependent concurrence. However, the double-time integrated concurrence shows a different behavior with respect to changes in the exciton fine structure splitting and even displays a completely different trend when the ratio between the cavity loss rate and the fine structure splitting is varied while keeping their product constant. This implies the nonequivalence of the physical information contained in the time-dependent and single-time integrated concurrence on the one hand and the double-time integrated concurrence on the other hand.

I. INTRODUCTION

Many applications in quantum communication require the generation of entangled photon pairs [1–6]. One particularly promising way of producing such pairs consists of using the biexciton cascade in quantum dots [3,7–14], which can be sketched roughly as follows. An initially prepared biexciton state of a quantum dot decays to one of two possible single exciton states while emitting a photon. A second photon can be emitted while the quantum dot relaxes to its ground state. Because of the optical selection rules, the two different paths lead to an emission of either two horizontally or two vertically polarized photons. As the biexciton decay is a quantum mechanical process, the system will, in general, be in a superposition of states from both paths. If both paths are completely symmetric, one expects that there is a high probability to find the system in the fully entangled state $|\psi^+\rangle = \frac{1}{\sqrt{2}}(|HH\rangle + |VV\rangle)$, where $|HH\rangle$ ($|VV\rangle$) denotes the state where the quantum dot is in its ground state and two horizontally (vertically) polarized photons have been emitted.

However, the situation in real quantum dots often deviates from the ideal picture described above. First of all, the exchange interaction typically introduces an energetic splitting between the two excitonic states on the order of several tens to hundreds of μeV [7,15,16]. Thus the two paths become asymmetric, leading to a deviation from the usually desired state $|\psi^+\rangle$. Besides effects related to the fine structure splitting another source for deviations from the ideal situation are environment couplings, in particular to phonons. These couplings lead to decoherence and relaxation and are the reason why the system has to be represented by a mixed rather than a pure state. These detrimental effects can be suppressed by engineering the quantum dot devices accordingly. For example, the fine structure splitting between the excitonic states can be reduced by applying electrical [15,16] or strain fields [17] or by growing quantum dots within highly symmetric structures such as nanowires [18]. Here, we consider another approach to obtain more symmetric paths, which is achieved by embedding the quantum dot in a microcavity. Then, the coupling between the electronic states in the dot and the cavity modes leads to an overall faster dynamics, which reduces the time available for

dephasing processes. Furthermore, tuning the cavity modes
to the two-photon resonance between the ground and the
biexciton state of the dot enhances two-photon processes that
are much less affected by the splitting of the excitonic states
than successive single-photon processes [19,20].

The wide interest in entanglement is twofold: on the
one hand the occurrence of entanglement is one of the key
differences between classical and quantum physics and on the
other hand it has practical implications as it provides new ways
of control as needed, e.g., for establishing secure quantum
communication protocols [21]. The essence of the control
aspect is that by performing a measurement on one part of
the system one determines the outcome of measurements on
another part of the system which otherwise would have been
undetermined. If, e.g., the system is in the maximally entangled
(nonfactorizable) state $|\psi^+\rangle$ and one detects the polarization
of one of the photons to be H, the state collapses into the
factorized state $|HH\rangle$ and a polarization measurement on the
second photon will necessarily yield H.

In order to compare two arbitrary states with respect to the
amount of control obtainable by performing measurements as
described above, one needs a measure of entanglement. For
a pure state $|\Psi\rangle$ in a bipartite system with density matrix ρ
and parts A and B with reduced density matrices $\rho_A = \mathrm{Tr}_B \rho$
and $\rho_B = \mathrm{Tr}_A \rho$, respectively, it is common to define the
entanglement $E(|\Psi\rangle)$ using the von-Neumann entropies of the
subsystems [22]:

$$E(|\Psi\rangle) = -\mathrm{Tr}_A(\rho_A \log_2 \rho_A) = -\mathrm{Tr}_B(\rho_B \log_2 \rho_B), \quad (1)$$

where the second equality in Eq. (1) follows from the Schmidt
decomposition [23]. This entropy represents the missing in-
formation about a subsystem because of its entanglement with
the other. Performing a measurement on one of the subsystems
that collapses the system state into a factorizable state causes
the subsystem entropy to drop to zero such that the previously
missing information $E(|\Psi\rangle)$ is recovered. Therefore $E(|\Psi\rangle)$
can also be considered to be a measure of the possible amount
of control over subsystem A by performing measurements
on B.

For a mixed state, missing information on a subsystem
can arise due to its entanglement with the remaining part of
the system as well as because of the ensemble averaging.
There are a number of proposals to identify the corresponding
contribution resulting from entanglement [22,24]. Probably the
most common proposal is the entanglement of formation. For
a decomposition

$$\rho = \sum_j p_j |\Psi_j\rangle\langle\Psi_j| \quad (2)$$

of a density matrix ρ with probabilities p_j and not necessarily
orthogonal states $|\Psi_j\rangle$, one assigns the entanglement

$$E(\rho, \{p_j, |\Psi_j\rangle\}) = \sum_j p_j E(|\Psi_j\rangle). \quad (3)$$

Then the entanglement of formation is defined as

$$E_f(\rho) = \inf E(\rho, \{p_j, |\Psi_j\rangle\}), \quad (4)$$

where the infimum is taken over all possible decompositions
in the form of Eq. (2). Thus $E_f(\rho)$ represents the amount

of pure-state entanglement that is at least present in a mixed
state described by a given density matrix ρ. The entanglement
of formation is particularly attractive because, unlike most
other proposed measures of entanglement, it can be evaluated
directly from the elements of the density matrix. To this end,
usually, the concurrence C is introduced which is related to the
entanglement of formation by

$$E_f(\rho) = \mathcal{E}(C(\rho)), \quad (5)$$

where $\mathcal{E}$ is monotonically increasing for $0 \leqslant C \leqslant 1$ (cf.
Ref. [24] for an explicit expression for $\mathcal{E}$). Due to the mono-
tonicity of $\mathcal{E}$ the concurrence is a measure of the entanglement
of formation in its own right. Although the concurrence is less
intuitive than the entanglement of formation and its physical
interpretation derives only from its relation to $E_f(\rho)$, it is
particularly attractive for practical applications because, as
shown by Wootters [25], it can be easily calculated from the
elements of ρ without having to perform a search for the
infimum over all possible decompositions of ρ.

In the case of the biexciton cascade where no direct transi-
tions between the two exciton states occur, the (unnormalized)
density matrix in the two-photon subspace

$$\rho_{ij,kl}(t) = \langle a_i^\dagger(t) a_j^\dagger(t) a_k(t) a_l(t) \rangle, \quad (6)$$

with $a_i^\dagger(t)$ and $a_l(t)$ being the cavity photon creation and
annihilation operators with polarization directions $i, j, k, l \in \{H, V\}$ in the Heisenberg picture, has only four nonvanish-
ing elements, namely $\rho_{HH,HH}, \rho_{VV,VV}, \rho_{HH,VV}$, and $\rho_{VV,HH}$.
Since we are dealing with a system where the photon number
is not conserved, $\rho_{ij,kl}(t)$ has not a unit trace for all times. The
nonvanishing elements of the normalized density matrix can
be represented accordingly by

$$\rho_{j,l}^N(t) = \frac{\rho_{jj,ll}(t)}{\rho_{HH,HH}(t) + \rho_{VV,VV}(t)}. \quad (7)$$

The general expression for the concurrence [25] then reduces to
the normalized coherences between the states $|HH\rangle$ and $|VV\rangle$,
which correspond to horizontal H or vertical V polarization
of the emitted photons, i.e.,

$$C(t) = 2|\rho_{H,V}^N(t)|. \quad (8)$$

Thereby, the concurrence relates two conceptually distinct
properties of quantum systems: entanglement, which specifies
how much the measurement of one qubit influences the
measurement outcome of the second qubit, and coherence,
which determines, e.g., the visibility of interference effects.
A theoretical study where the time-dependent concurrence,
which is assigned to the density matrix in the two-photon
subspace at a given time, has been used as a figure of merit for
entanglement has been performed, e.g., in Ref. [26]. However,
in contrast to the investigation here, in Ref. [26], the coupling
of the dot to a continuum of half-space photon modes has been
considered.

Although the elements of the density matrix are in prin-
ciple all observable, it is often difficult to resolve their full
time dependence experimentally and thereby determine the
time-dependent concurrence given by Eq. (8). To reconstruct
the two-photon density matrix from experimental data, one
usually uses quantum state tomography, a technique based

on polarization-dependent photon coincidence measurements [27,28]. Because these coincidence measurements typically give only information about the polarization degree of freedom and the time delay τ between the two measured photons, but do not resolve the time t of the first photon count with respect to the preparation of the biexciton state ($t = 0$), in such experiments one only has access to quantities integrated over the time t. Therefore studies of the photon pairs generated via the biexciton cascade often define figures of merit, which are then also called concurrence, but replace the density matrix in Eq. (8) by the respective expressions obtained from the quantum state reconstruction. The latter involve in general averages over t and τ. Most often discussed is the limiting case of long averaging intervals for both times [13,20,29]. However, also the case where the averaging window for t is infinite, while for τ the limit of a vanishing averaging interval is approached, is experimentally accessible [11,12] and has been studied theoretically [30,31].

That these figures of merit may indeed differ substantially because of the differences in time averaging can be readily seen from the following argument due to Stevenson *et al.* [11]. Consider a biexciton cascade where an initially prepared biexciton decays to an exciton while emitting a single photon. A second photon is emitted after a delay time τ, during which the different exciton states aquire a phase difference $\phi = \tau \delta / \hbar$ due to the fine structure splitting δ. Disregarding environment influences which lead to a mixed photon state and concentrating only on the free time evolution the resulting two-photon state is $|\Psi\rangle = \frac{1}{\sqrt{2}}(|HH\rangle + e^{i\tau\delta/\hbar}|VV\rangle)$. Obviously, $|\Psi\rangle$ is a maximally entangled state at each point in time for any given delay. If, however, measurements are performed that do not discriminate between different delay times τ of the emission, the effective time-integration leads to significant cancellations of the phases $e^{i\tau\delta/\hbar}$. Stevenson *et al.* [11] have performed experiments where the probability for finding the maximally entangled state $|\Psi\rangle = \frac{1}{\sqrt{2}}(|HH\rangle + |VV\rangle)$ in the two-photon state generated via the biexciton cascade has been determined as a function of the integration window for the delay time τ. Indeed, it was found that this probability significantly drops the longer the τ sampling interval is taken. Thus, filtering photon pairs with nearly equal emission times reveals a high degree of entanglement while measurements involving long τ sampling times indicate a much lower entanglement. A similar experimental analysis has been recently performed by Bounouar *et al.* [12] where it was concluded that the main limit of entanglement fidelity is the time resolution in the experiment.

The goal of this article is to compare the definitions of concurrences commonly used in the literature involving either single- or double-time averages with the time-dependent concurrence given by Eq. (8). To be specific, we study the case of the biexciton cascade in a quantum dot inside a microcavity. Concentrating at first on a model without phonons, we derive analytic expressions for the different concurrences for a quantum dot with finite biexciton binding energy in a cavity tuned to the two-photon resonance, a configuration which was already found to be favorable for a high degree of polarization entanglement [20]. The analytic results are valid also beyond the weak-coupling limit and agree qualitatively with numerical calculations. We find that the concurrence

based on a single-time integrated two-photon density matrix yields very similar results as the time-dependent concurrence in Eq. (8). It is therefore possible to access the information represented by the time-dependent concurrence, i.e., the entanglement of formation contained in the so prepared state of the cavity photons, by recording the more easily measurable single-time integrated concurrence. This remains true even when the interaction between the quantum dot states and longitudinal acoustic phonons is taken into account in numerical calculations. However, this information cannot be accessed by measuring two-time integrated correlation functions since it turns out that the latter exhibit quantitatively and qualitatively different dependencies on parameters like the fine structure splitting. It is most striking that when comparing single- and double-time integrated concurrences even trends reverse, such as the dependence on the cavity loss rate in the presence of phonons. Furthermore, already without phonons, these two quantities show a completely reversed trend when the ratio between the cavity loss rate and the fine structure splitting is varied while their product is kept constant. This leads to the conclusion that the single-time integrated and the double-time integrated concurrence are measures for different types of entanglement.

II. SYSTEM

A. Hamiltonian

We consider a quantum dot in a microcavity as depicted in Fig. 1. We assume that the quantum dot is initialized at time $t = 0$ in the biexciton state with an empty cavity, e.g., by incoherent excitation from the wetting layer or direct laser excitation. The biexciton is coupled to two quantum states with an exciton in the quantum dot and a photon in the cavity. The two excitons are labeled by X_H and X_V corresponding to the polarization of the cavity mode, horizontal (H) or vertical (V), to which the respective transition is coupled. The excitonic states are also coupled to the ground state of the dot with one more photon in the cavity. At the same time, the cavity is subject to losses and the excitons in the dot interact with longitudinal acoustic (LA) phonons. Radiative decay is assumed to be negligible compared with cavity losses, which is a typical case [32].

The dot-cavity Hamiltonian is given by [29]

$$
\begin{aligned}
H_{dc} = {} & \left(\hbar\bar{\omega}_X + \frac{\delta}{2}\right)|X_H\rangle\langle X_H| + \left(\hbar\bar{\omega}_X - \frac{\delta}{2}\right)|X_V\rangle\langle X_V| \\
& + (2\hbar\bar{\omega}_X - E_B)|B\rangle\langle B| + \hbar\omega_H a_H^\dagger a_H + \hbar\omega_V a_V^\dagger a_V \\
& + \hbar g[(|G\rangle\langle X_H| + |X_H\rangle\langle B|)a_H^\dagger \\
& + (|G\rangle\langle X_V| - |X_V\rangle\langle B|)a_V^\dagger \\
& + (|X_H\rangle\langle G| + |B\rangle\langle X_H|)a_H \\
& + (|X_V\rangle\langle G| - |B\rangle\langle X_V|)a_V],
\end{aligned}
\tag{9}
$$

where $\hbar\bar{\omega}_X$ is the average exciton energy, δ is the fine structure splitting and E_B is the biexciton binding energy. The energies of the cavity modes are $\hbar\omega_H$ and $\hbar\omega_V$, respectively, and g is the dot-cavity coupling constant. Here, we assume that the cavity modes are in resonance with the two-photon transition between the ground and the biexciton state $\hbar\omega_H = \hbar\omega_V = \frac{2\hbar\bar{\omega}_X - E_B}{2}$. $|G\rangle$ denotes the ground state of the dot, $|X_H\rangle$ and $|X_V\rangle$ are the
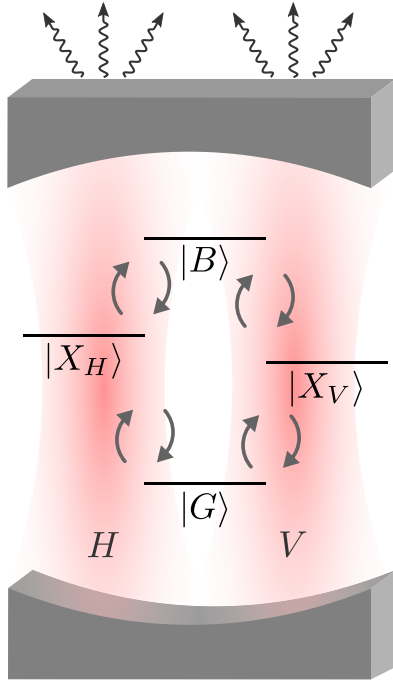
FIG. 1. Sketch of the quantum dot states involved in the biexciton cascade inside a microcavity. The quantum dot is coupled to a microcavity with two orthogonally polarized cavity modes (H: horizontal, V: vertical). Due to optical selection rules, the biexciton state ($|B\rangle$) can be deexcited to one of two exciton states ($|X_H\rangle$ and $|X_V\rangle$) under the emission of a H or V polarized cavity photon. The exciton states can be further deexcited to the ground state ($|G\rangle$) of the dot by emitting a second photon. The reverse processes are also possible. The red circular arrows indicate the dot-cavity coupling compatible with the optical selection rules. Wavy arrows symbolize the photon losses due to the imperfect cavity.

exciton states, and $|B\rangle$ is the biexciton state. Finally, $a_i^\dagger$ (a_i) is the creation (annihilation) operator for a photon in the cavity mode $i = \{H, V\}$.

Cavity losses are taken into account via the Lindblad term

$$\mathcal{L}_{\text{cavity}}[\rho] = \frac{\kappa}{2} \sum_{i=H,V} (2a_i \rho a_i^\dagger - a_i^\dagger a_i \rho - \rho a_i^\dagger a_i), \quad (10)$$

where κ is the cavity loss rate. The interaction between the dot and the LA phonons is described by the Hamiltonian

$$\hat{H}_{ph} = \hbar \sum_{\mathbf{q}} \omega_{\mathbf{q}} b_{\mathbf{q}}^\dagger b_{\mathbf{q}}$$
$$+ \hbar \sum_{\mathbf{q}} \sum_{\nu} n_\nu^X (\gamma_{\mathbf{q}}^X b_{\mathbf{q}}^\dagger + \gamma_{\mathbf{q}}^{X*} b_{\mathbf{q}}) |\nu\rangle\langle\nu|, \quad (11)$$

where $b_{\mathbf{q}}^\dagger$ and $b_{\mathbf{q}}$ are the creation and annihilation operators for phonons with wave vectors $\mathbf{q}$ and energies $\hbar\omega_{\mathbf{q}}$. $n_\nu^X = \{0, 1, 1, 2\}$ is the number of excitons in the dot state $\nu = \{G, X_H, X_V, B\}$ and $\gamma_{\mathbf{q}}^X$ is the exciton-phonon coupling constant.

B. Concurrences

The time-dependent concurrence, which has been shown by Wootters [25] to be a measure for the entanglement of formation, is, for the two-photon state created in the biexciton cascade, given by Eq. (8). Since the density matrix in this equation is evaluated with cavity operators [cf. Eq. (6)], it immediately follows that $C(t)$ contains information about the entanglement of formation of the two-photon state inside the cavity at any given time t. Experimentally, the reduced two-photon density matrix is typically reconstructed via quantum state tomography, where polarization-resolved two-photon coincidence rates are measured which are proportional to the two-time correlation functions

$$G_{ij,kl}^{(2)}(t,\tau) = \langle a_i^\dagger(t) a_j^\dagger(t+\tau) a_k(t+\tau) a_l(t)\rangle. \quad (12)$$

Here, t is the time of the first click at a detector, τ is the delay time until the second photon is detected and $i, j, k, l \in \{H, V\}$. Since in experiments one measures photons that have left the cavity, the cavity operators in Eq. (12) should in fact be replaced by operators for the field modes outside the cavity. However, considering the outcoupling of light out of the cavity to be a Markovian process, the quantities measured outside the cavity are proportional to the ones inside [33]. Therefore a measurement of $G_{ij,kl}^{(2)}(t,\tau)$ outside the cavity can indeed be described by Eq. (12). Finally, we note that in the present analysis we have assumed the radiative decay to be negligible compared with the cavity losses and, consequently, we only consider the case that photons are emitted via the cavity. For a direct emission of photons into modes outside, the cavity by radiative decay, two-time correlation functions involving polarization operators instead of photon operators would have to be considered [28].

Typically, corresponding experiments record data points over extended time intervals $t_0 \leqslant t \leqslant t_0 + \Delta t$ and $\tau_0 \leqslant \tau \leqslant \tau_0 + \Delta\tau$. For the reconstruction of the unnormalized density matrix defined in Eq. (6), the delay line between the two detectors measuring the coincidence is adjusted such that the two intervals where the detectors are sensitive start simultaneously, i.e., $\tau_0 = 0$. Setting $t_0 = 0$, the measured signals are then proportional to

$$\overline{\overline{G}}_{ij,kl}^{(2)}(\Delta t, \Delta\tau) = \frac{1}{\Delta t \, \Delta\tau} \int_0^{\Delta t} dt \int_0^{\Delta\tau} d\tau$$
$$\times \langle a_i^\dagger(t) a_j^\dagger(t+\tau) a_k(t+\tau) a_l(t)\rangle. \quad (13)$$

Thus, the result of an experimental reconstruction of the normalized two-photon density matrix is [28]

$$\rho_{j,l}^R(\Delta t, \Delta\tau) = \frac{\overline{\overline{G}}_{jj,ll}^{(2)}(\Delta t, \Delta\tau)}{\overline{\overline{G}}_{HH,HH}^{(2)}(\Delta t, \Delta\tau) + \overline{\overline{G}}_{VV,VV}^{(2)}(\Delta t, \Delta\tau)}. \quad (14)$$

Associated with the reconstructed density matrix is the concurrence

$$C^R(\Delta t, \Delta\tau) = 2|\rho_{H,V}^R(\Delta t, \Delta\tau)|. \quad (15)$$

As low counting rates limit the experimental accuracy, common measurements are performed using rather long intervals for the data collection. These experiments often approach the limiting case $\Delta t \to \infty$ and $\Delta\tau \to \infty$ such that in theory the corresponding concurrence becomes [20,29]

$$\overline{\overline{C}} = \lim_{\substack{\Delta t \to \infty \\ \Delta\tau \to \infty}} C^R(\Delta t, \Delta\tau). \quad (16)$$

Due to the double-time averaging, the information about the time evolution of the system is completely lost such that, in contrast to the time dependent concurrence $C(t)$, the double-time integrated concurrence $\overline{\overline{C}}$ does not reflect properties of the cavity photons at any given time but rather describes the properties of the reconstructed density matrix in experiments.

While the case of extended measuring intervals for both t and τ is probably the most often discussed situation, in the literature also another limiting case has been considered [30,31], where the concurrence is defined as

$$\overline{C} = \lim_{\substack{\Delta t \to \infty \\ \Delta \tau \to 0}} C^R(\Delta t, \Delta \tau). \tag{17}$$

Experimentally, the limit $\Delta \tau \to 0$ can be performed using time-windowing techniques [11] which record signals over different delay-time windows $\Delta \tau$ and extrapolate to $\Delta \tau = 0$. More recently, it has been shown experimentally that using time bins with a width of 4 ps is sufficient to resolve the full τ dependence of the signal if the exciton fine-structure splitting is on a scale of a few tens of μeV [12]. Henceforth, we refer to the concurrence $\overline{C}$ defined in Eq. (17) as the single-time integrated concurrence. If the photon pairs are emitted from a dot-cavity system in the steady state, $\overline{C}$ is equivalent to $C(t)$ since the two-photon density matrix no longer depends on time in such a case. However, when considering dynamical systems that are, e.g., driven by laser pulses, this equivalence in general no longer holds.

It should be noted that, as for the time-dependent concurrence $C(t)$, also for the single-time integrated concurrence $\overline{C}$ it is not necessary to evaluate the two-time correlation function defined in Eq. (12) since in the limit $\Delta \tau \to 0$ only the unnormalized density matrix given by Eq. (6) enters the expression in Eq. (17). However, one should be aware that $\overline{C}$ is not the time average of the time-dependent concurrence $C(t)$. Instead, the time average of the concurrence is given by

$$\langle C \rangle_T := \frac{1}{T} \int_0^T dt \, C(t)$$
$$= \frac{1}{T} \int_0^T dt \, \frac{2|\rho_{HH,VV}(t)|}{\rho_{HH,HH}(t) + \rho_{VV,VV}(t)}, \tag{18}$$

where T corresponds to the averaging time.

In the following, we shall compare the time-dependent concurrence $C(t)$, which measures the entanglement of formation of the two-photon system inside the cavity at a given point in time, with the double- and single-time integrated concurrences $\overline{\overline{C}}$ and $\overline{C}$, respectively, obtained as a result of different quantum state reconstruction strategies that involve data collection over extended time intervals. Due to the one-to-one correspondence between two-time correlation functions of photon operators inside and outside the cavity shown in Ref. [33], the comparison between $C(t)$, $\overline{C}$, and $\overline{\overline{C}}$ can also be interpreted in terms of the photons recorded in the two detectors used in coincidence measurement. Since the photons outside the cavity propagate with the speed of light they can be recorded at a given time in one of the detectors only when they have been emitted from the cavity at a retarded time that matches the flight time between cavity and detector.

Thus, recording the correlation function $G_{ij,kl}^{(2)}(t,\tau)$ for given values of t and τ selects photons according to their emission time from the cavity. Note that for the photons inside the cavity there is no obvious relation between their emission times from the dot since standing wave modes localized in the cavity are excited and thus these excitations contribute to the two-time correlation functions as long as the photons stay in the cavity.

The above analysis suggests that a density matrix constructed from the two-time correlation function for given values of t and τ, i.e., $\rho_{j,l}(t,\tau) = \frac{G_{jj,ll}^{(2)}(t,\tau)}{G_{HH,HH}^{(2)}(t,\tau) + G_{VV,VV}^{(2)}(t,\tau)}$, represents a measurement of photons in two detectors where the photons are selected according to their respective emission times from the cavity. Then, $C(t,\tau) = 2|\rho_{H,V}(t,\tau)|$ can be interpreted as a measure for the entanglement of formation of the so selected photons. The question now arises how to interpret the quantity $C^R(\Delta t, \Delta \tau)$ defined in Eq. (15), which is obtained by first taking a coherent superposition of signal contributions associated with different emission times and then constructing the concurrence by taking twice the absolute value of the off-diagonal element of the normalized superposition. At this point, it is helpful to discuss in more detail the emission process from the cavity. If we were dealing with an ensemble of randomly distributed emission events where each emission has a sharply defined emission time t_e and where the uncertainty concerning the emission time is described by a classical probability distribution for t_e, then the concurrence of this ensemble would be obtained by first evaluating the concurrence separately for each ensemble member, which would be $C(t,\tau) = 2|\rho_{H,V}(t,\tau)|$, and then averaging over the emission times, i.e., t and τ. The result would be an average concurrence similar to $\langle C \rangle_T$ except that here the average would be taken over t and τ. However, in a full quantum description, the uncertainty concerning the emission times is not represented by a classical ensemble of events with sharp emission times. Instead, states where a photon has been emitted are typically in a coherent superposition with states where no photon has been emitted. Thus the emission is not pointlike in time but is a process of finite duration, so that $\overline{\overline{G}}_{ij,kl}^{(2)}(\Delta t, \Delta \tau)$ can be thought of as filtering out the coherent superposition corresponding to those contributions where the emission times are restricted to t and τ intervals of lengths Δt and $\Delta \tau$, respectively. This means that $C^R(\Delta t, \Delta \tau)$ represents the concurrence associated with a reconstructed two-photon density matrix which is filtered with respect to emission times within finite intervals. From this point of view, $C(t)$ represents the concurrence of photons recorded in two detectors that are simultaneously (i.e. $\tau = \Delta \tau = 0$) emitted from the cavity at a given time t, while $\overline{C}$ also describes the concurrence of simultaneously emitted photons but without resolving their common emission time. Finally, $\overline{\overline{C}}$ is the concurrence associated with a two-photon density matrix where one neither resolves the emission time of the first recorded photon nor the delay time τ between the photons.

III. TIME-DEPENDENT CONCURRENCE

In the following, we first present an approximate analytic expression for the time-dependent concurrence of the two-

photon state generated by the biexciton cascade in a dot-cavity system in the absence of dot-phonon interaction. Subsequently, we compare the anayltic results with numerical calculations of the time-dependent concurrence as well as the single-time integrated concurrence with and without dot-phonon interaction.

A. Analytic results

In order to discuss how the time-dependent concurrence $C(t)$ depends on the parameters of the system, it is instructive to look for an approximate analytic solution of the dynamics in the absence dot-phonon interaction.

First, note that only few states contribute to the biexciton cascade: the general states of the system can be described by $|\nu, n_H, n_V\rangle$, where $\nu \in \{G, X_H, X_V, B\}$ denotes the dot state and n_H and n_V are the numbers of horizontally and vertically polarized cavity photons, respectively. Without losses and under the assumption that the system is initially prepared in the biexciton state $|B, 0, 0\rangle$ and not driven externally, the number of total excitations (number of excitons plus number of photons) in the system is fixed to two for all times. When accounting for losses via the Lindblad operator defined in Eq. (10), also states with excitation numbers smaller than two become occupied. However, these states need not be considered for the subsequent dynamics since first, they do not contribute to the two-photon density matrix $\rho_{ij,kl}(t)$ defined in Eq. (6) and second, states with lower excitation numbers do not couple back to states with higher excitation numbers. Since there are no direct transitions between the different excitons X_H and X_V or between horizontally and vertically polarized photons, only five remaining states contribute, which we denote by

$$|G_H\rangle := |G, 2, 0\rangle, \tag{19a}$$

$$|G_V\rangle := |G, 0, 2\rangle, \tag{19b}$$

$$|X_H\rangle := |X_H, 1, 0\rangle, \tag{19c}$$

$$|X_V\rangle := |X_V, 0, 1\rangle, \tag{19d}$$

$$|B\rangle := |B, 0, 0\rangle. \tag{19e}$$

In this basis, the Hamiltonian in Eq. (9) takes the form

$$H = \begin{pmatrix} 0 & 0 & \sqrt{2}\hbar g & 0 & 0 \\ 0 & 0 & 0 & \sqrt{2}\hbar g & 0 \\ \sqrt{2}\hbar g & 0 & \frac{1}{2}(E_B + \delta) & 0 & \hbar g \\ 0 & \sqrt{2}\hbar g & 0 & \frac{1}{2}(E_B - \delta) & -\hbar g \\ 0 & 0 & \hbar g & -\hbar g & 0 \end{pmatrix}, \tag{20}$$

where the origin of the energy scale is shifted to the biexciton.

An analytic solution of the full five-level system is complicated and has so far only been presented in the weak coupling limit [30] ($g \ll \kappa$), where only one-way transitions along the paths $|B\rangle \to |X_H\rangle \to |G_H\rangle$ and $|B\rangle \to |X_V\rangle \to |G_V\rangle$ can occur because the photon losses are much faster than the time needed for the reexcitation of higher-energetic dot states. However, to fully benefit from the microcavity, one is often interested in strongly coupled dot-cavity systems [34–36] where the condition $g \ll \kappa$ is not met and other approaches are required.
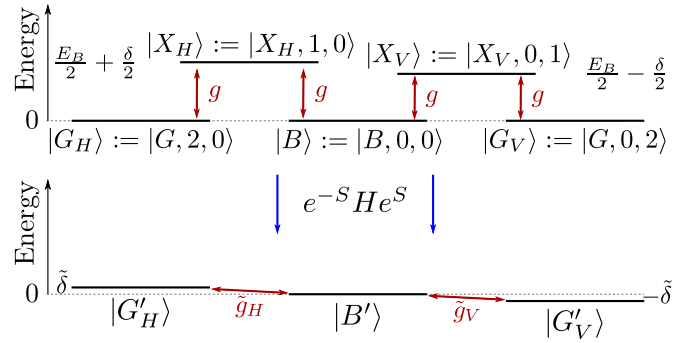

FIG. 2. Sketch of the block diagonalization reducing the dynamics in the five-level system described in Eqs. (19) to a three-level system with states defined in Eqs. (22).

Here, we make use of the fact that in typical quantum dots the biexciton binding energy $E_B \sim 1$–6 meV defines the largest energy scale. Strongly coupled dot-cavity systems typically have couplings on the order of $\hbar g \sim 0.1$ meV, while typical values for the fine structure splitting are in the range of $\delta \sim 0.01$–0.1 meV, so that a perturbative treatment in terms of the small parameters $\lambda := \hbar g/(\frac{1}{2}E_B)$ and δ/E_B is appropriate. For later reference, we also define $\lambda_{H/V} := \hbar g/[\frac{1}{2}(E_B \pm \delta)]$.

In the case considered here, where the cavity modes are in resonance with the two-photon transition to the biexciton state, the comparatively large binding energy suppresses the occupation of the exciton states. Thus one can perform a perturbative block-diagonalization [37,38] (Schrieffer-Wolff transformation) and thereby remove the high-energy states with one exciton and one photon from the dynamics, as sketched in Fig. 2. To this end, a unitary transform $e^{-S}He^S$ is applied to the Hamiltonian H, where $S = S^{(1)} + S^{(2)} + \dots$ is expanded in orders of the perturbing Hamiltonian $H^{(1)}$ consisting of the off-diagonal elements of H in Eq. (20). The matrices $S^{(i)}$ are then obtained by the condition that the matrix elements between high- and low-energy states in $e^{-S}He^S$ vanish up to order $\mathcal{O}((H^{(1)})^{i+1})$ (cf. Refs. [37] or [38] for explicit expressions for $S^{(i)}$). This transformation therefore perturbatively eliminates the couplings between the low-energy ground and biexcitonlike states and the high-energy excitonlike states. After decoupling the low-energy and high-energy states, the latter are disregarded as they are irrelevant for the dynamics.

Up to second order in λ, the block diagonalization yields the effective Hamiltonian

$$H' = \begin{pmatrix} \tilde{\delta} & 0 & \hbar\tilde{g}_H \\ 0 & -\tilde{\delta} & \hbar\tilde{g}_V \\ \hbar\tilde{g}_H & \hbar\tilde{g}_V & 0 \end{pmatrix}, \tag{21}$$

with $\tilde{\delta} = \hbar g(\lambda_V - \lambda_H) \approx \lambda^2 \delta$ and $\tilde{g}_{H/V} = \mp\sqrt{2}\lambda_{H/V}g$ in the basis

$$|G_H'\rangle := (1 - \lambda_H^2)|G_H\rangle - \sqrt{2}\lambda_H|X_H\rangle - \frac{1}{\sqrt{2}}\lambda_H^2|B\rangle, \tag{22a}$$

$$|G_V'\rangle := (1 - \lambda_V^2)|G_V\rangle - \sqrt{2}\lambda_V|X_V\rangle + \frac{1}{\sqrt{2}}\lambda_V^2|B\rangle, \tag{22b}$$

$$|B'\rangle := -\frac{\lambda_H^2}{\sqrt{2}}|G_H\rangle + \frac{\lambda_V^2}{\sqrt{2}}|G_V\rangle - \lambda_H|X_H\rangle + \lambda_V|X_V\rangle$$
$$+ \left(1 - \frac{1}{2}(\lambda_H^2 + \lambda_V^2)\right)|B\rangle. \tag{22c}$$

Thus perturbation theory in λ allows one to reduce the five-level system of the biexciton cascade to an effective three-level system, where the three levels have mostly the character of the ground state of the dot with two horizontally or vertically polarized photons and the biexciton state.

In the three-level basis, the effective coupling $\tilde{g}_{H/V}$ is reduced by a factor $\sim \lambda$ compared with the coupling g in the five-level system. The effective splitting $2\tilde{\delta}$ between the states $|G'_H\rangle$ and $|G'_V\rangle$ is reduced even more compared with the fine structure splitting δ of the excitonic states in the original five-level system because it only appears in second order in λ. When also the Lindblad terms are written in the basis described in Eqs. (22), the biexcitonlike state $|B'\rangle$ acquires the small loss rate $(\lambda_H^2 + \lambda_V^2)\kappa$ and the loss rates for the states $|G'_H\rangle$ and $|G'_V\rangle$ become $2(1 - \lambda_{H/V}^2)\kappa$, which are of the same order of magnitude as the rates κ for the corresponding states $|G_H\rangle$ and $|G_V\rangle$ in the five-level system.

The central insight gained by this transformation is that, due to the renormalization of the coupling, the effective three-level system can be in the weak coupling limit $|\tilde{g}_{H/V}| \ll \kappa$ even when the orignal five-level system describing the biexciton cascade is not ($g \sim \kappa$), as is the case for typical parameters for dot-cavity systems [20]. Due to the weak coupling, the dynamics in the effective three-level system is easily understood. The initial occupations of the biexciton state $|B'\rangle$ are transferred to the ground states $|G'_H\rangle$ and $|G'_V\rangle$ and then decay due to the losses before they can reexcite the biexciton state, yielding an essentially incoherent dynamics. An explicit calculation of the dynamics in the weakly coupled effective three-level system is presented in the Appendix. It is found that the occupation of the biexcitonlike state $|B'\rangle$ decays exponentially with an effective rate

$$\kappa_B = \left(\lambda_H^2 + \lambda_V^2\right)\left(\frac{4g^2}{\kappa} + \kappa\right), \tag{23}$$

where the term propotional to $4g^2/\kappa$ is due to the transitions to the states $|G'_H\rangle$ and $|G'_V\rangle$ and the term proportional to κ originates from the losses due to the admixture of states with a nonvanishing number of photons to the state $|B'\rangle$. The occupations and coherences $\rho_{G'_i G'_j} = \langle(|G'_i\rangle\langle G'_j|)\rangle$ between the states $|G'_H\rangle$ and $|G'_V\rangle$ are found to be

$$\rho_{G'_i G'_j} = \frac{\tilde{g}_i \tilde{g}_j}{\kappa^2}\left(e^{-\kappa_B t} - e^{[-(2 - \lambda_i^2 - \lambda_j^2)\kappa + i(\tilde{\delta}_i - \tilde{\delta}_j)/\hbar]t}\right), \tag{24}$$

with $\tilde{\delta}_{H/V} = \pm\tilde{\delta}$.

The long-time dynamics of $\rho_{G'_i G'_j}$ is determined by the same loss rate κ_B as the biexcitonlike state, whereas the initial increase from zero is governed by a term decaying with $\kappa \gg \kappa_B$. Because the renormalized splitting $\tilde{\delta}$ is very small compared with typical loss rates κ, possible oscillations of $\rho_{G'_H G'_V}$ are overdamped. Furthermore, the second term in Eq. (24) disappears already after a short time $\sim \kappa^{-1}$. Neglecting $\tilde{\delta}$ in the second exponent in Eq. (24) yields the

following simple analytic expression for the concurrence

$$C_{\text{analytic}} = \frac{2|\rho_{G'_H G'_V}|}{\rho_{G'_H G'_H} + \rho_{G'_V G'_V}} \approx \frac{2|\tilde{g}_H \tilde{g}_V|}{\tilde{g}_H^2 + \tilde{g}_V^2} = \frac{E_B^2 - \delta^2}{E_B^2 + \delta^2}. \tag{25}$$

First, we find that, although the density matrix elements change in time, the analytic expression predicts that the concurrence is constant in time. Furthermore, the concurrence depends only on the biexciton binding energy and the fine structure splitting and is indepedent of the dot-cavity coupling g and the cavity loss rate κ.

Because all density matrix elements entering in the expression for the concurrence have virtually the same time dependence, integrating the density matrix elements over the time t yields the same result also for the single-time integrated concurrence

$$\overline{C}_{\text{analytic}} = C_{\text{analytic}} \approx \frac{E_B^2 - \delta^2}{E_B^2 + \delta^2}. \tag{26}$$

Thus our analysis reveals that the single-time integrated concurrence is the same as the concurrence at any point in time and is therefore a measure of the entanglement of formation for the two-photon state generated in the cavity by the biexciton cascade.

B. Numerical results

To check the validity of the analytic results for the concurrence, we now present numerical calculations of the biexciton cascade described by the dot-cavity Hamiltonian in Eq. (9) and the loss term in Eq. (10) in the five-level basis introduced in Eqs. (19). Futhermore, we study the effects of phonons due to the dot-phonon Hamiltonian in Eq. (11), which have been neglected in the derivation of the analytic results, using a numerically exact real-time path-integral method [39–42] described in detail in the supplement of Ref. [42].

If not stated otherwise, we use the following parameters: dot-cavity coupling constant $\hbar g = 0.1$ meV, biexciton binding energy $E_B = 1.5$ meV, cavity loss rate $\kappa = 0.25$ ps^{-1}, and fine structure splitting $\delta = 0.1$ meV. Note that for these parameters ($g/\kappa \approx 0.6$) the system is clearly not in the weak-coupling limit, so that conventional weak-coupling theories are not applicable. For calculations involving the dot-phonon interaction, we use parameters suitable for a 3 nm wide self-assembled InGaAs quantum dot embedded in a GaAs matrix (cf. Ref. [42]). Furthermore, the phonons are assumed to be initially in equilibrium at a temperature $T = 10$ K.

Figure 3 depicts the time evolution of the time-dependent concurrence $C(t)$ and the single-time integrated concurrence $\overline{C}$ determined numerically as well as its analytic value according to Eq. (26). In the absence of dot-phonon interaction, the time-dependent concurrence indeed agrees well with the constant analytic result as well as the single-time integrated concurrence after an initial phase of ~ 40 ps duration, as expected from the analytic results. If phonons are taken into account, $C(t)$ and $\overline{C}$ still agree well after this initial phase, but the stationary value for long times is reduced.

The dependence of the time-averaged concurrence $\langle C \rangle_\infty$ and the single-time integrated concurrence $\overline{C}$ on the fine structure splitting δ is shown in Fig. 4. Here, we consider $\langle C \rangle_\infty$ since it condenses the information contained in $C(t)$ into a
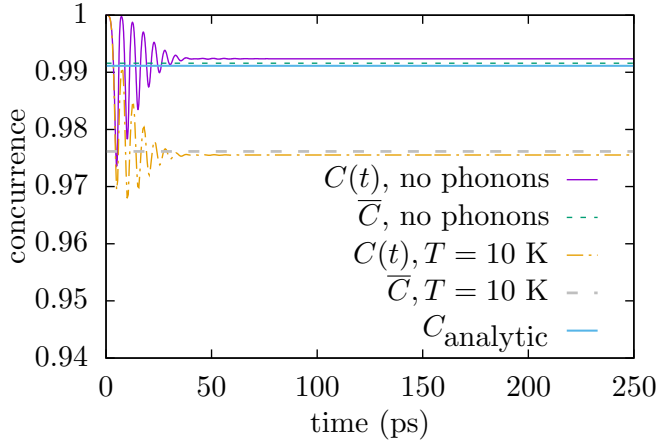
FIG. 3. Time-dependent concurrence $C(t)$ and single-time integrated concurrence $\overline{C}$ calculated numerically without dot-phonon interaction and with phonons at a temperature $T = 10$ K compared with the analytically obtained result C_{analytic} for the phonon-free case.

FIG. 5. Dependence of the time-averaged concurrence $\langle C \rangle_\infty$ and the single-time integrated concurrence $\overline{C}$ with and without dot-phonon interaction on the cavity loss rate κ using a fine structure splitting $\delta = 0.1$ meV. Also shown is the analytically obtained result C_{analytic}.

single number that can be compared with $\overline{C}$. The averaging time $T = 1000$ ps for $\langle C \rangle_\infty$ is chosen such that it is much larger compared with all other timescales in the system. For calculations not accounting for the dot-phonon interaction [Fig. 4(a)], the time-averaged concurrence and the single-time integrated concurrence are in good agreement with the analytic results for the whole range of fine structure splittings. When phonons are taken into account [Fig. 4(b)], both definitions of the concurrence still coincide but yield, in general, significantly lower values than the concurrence obtained by neglecting the dot-phonon interaction. However, at vanishing fine structure splitting $\delta = 0$, the concurrence remains one even in the presence of phonons as predicted in previous studies [30]. This is due to the fact that both paths of the biexciton cascade are completely symmetric in this case. The resulting absence of which-way information makes it possible to get a completely entangled state for all times.
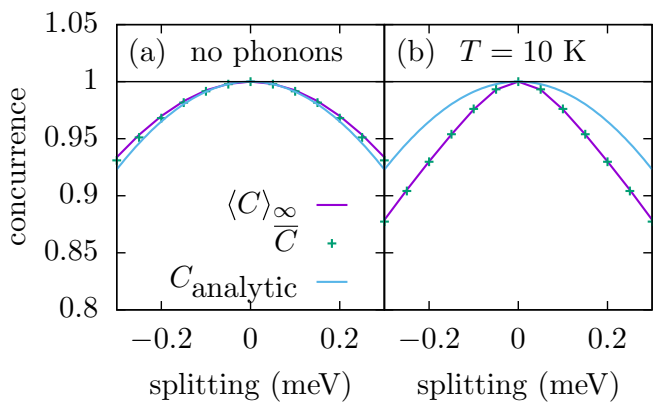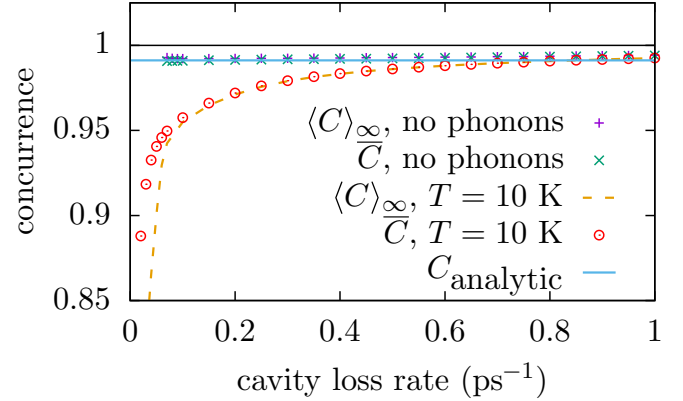

FIG. 4. Dependence of the time-averaged concurrence $\langle C \rangle_\infty$, and the single-time integrated concurrence $\overline{C}$ on the fine structure splitting δ, calculated (a) without dot-phonon interaction and (b) with phonons at a temperature $T = 10$ K. For comparison, the analytically obtained result C_{analytic} for the phonon-free case is displayed in (a) and (b).

It is worth noting that the value of the concurrence remains close to one even for the relatively large fine structure splitting of $\delta = 0.1$ meV. As will be discussed in Sec. IV, the dependence of the double-time integrated concurrence on δ turns out to be completely different. The near independence on δ of the single-time integrated concurrence is easily understood by the argument of Stevenson *et al.* [11] discussed in the introduction according to which there is a high probability for finding the maximally entangled state $|\Psi\rangle = \frac{1}{\sqrt{2}}(|HH\rangle + e^{i\tau\delta/\hbar}|VV\rangle)$. Thus, the time-dependent as well as the single-time integrated concurrence have high values because even for finite δ the system is at any point in time close to a maximally entangled state. This high degree of entanglement can, however, not be uncovered when the system state is reconstructed by collecting data points over an extended τ interval, as is done in the double-time integrated concurrence, because of destructive interference. The remaining observed weak decrease of the single-time integrated concurrence with rising δ reflects the deviation of the actual system state from the idealized pure state $|\Psi\rangle$.

Finally, the dependence of $\langle C \rangle_\infty$ and the single-time integrated concurrence $\overline{C}$ on the cavity loss rate κ is depicted in Fig. 5 for a fine structure splitting $\delta = 0.1$ meV. Again, in absence of dot-phonon interaction, the time-averaged concurrence as well as the single-time integrated concurrence coincide with the analytic result, which is independent of κ. When the interaction between the quantum dot and the phonons is accounted for, it is found that the concurrence increases monotonically with increasing loss rate. At $\kappa = 0$, the concurrence becomes zero (not shown) and for large loss rates, the concurrence approaches the same value as obtained when the dot-phonon interaction is disregarded. This can be explained by the fact that the dot-phonon interaction enables phonon-assisted processes. First of all, given enough time, phonon emission and absorption leads to a thermal occupation of energy eigenstates. Secondly, transitions involving the exciton states $|X_H, 1, 0\rangle$ and $|X_V, 0, 1\rangle$, which are otherwise off-resonant, are enabled by the absorption of phonons with energies close to $E_B/2$. For typical biexciton binding energies in the range of a few meV, this energy is close to the maximum

of typical phonon spectral density [43], so that the phonon-assisted transitions through excitonic states are particularly efficient. In any case, the coherences between the states $|G,2,0\rangle$ and $|G,0,2\rangle$ are strongly reduced by phonon effects, which in turn reduce the concurrence $C(t)$.

However, the phonon-induced loss of coherence requires a finite amount of time and therefore competes with the cavity losses. Note that the latter leads to a uniform decrease of the coherences as well as the occupations of the two-photon state, which appear in the numerator and the denominator in the definition of the concurrence $C(t)$ in Eq. (8), respectively. Therefore the cavity losses do not directly affect the concurrence $C(t)$, which is also the reason why the analytic expression C_{analytic} in Eq. (25) does not depend on κ. In contrast, phonons only marginally affect the occupations but they can strongly reduce the coherences, which results in a reduced concurrence $C(t)$. Thus, if the cavity loss rate κ is small, phonons can suppress the degree of entanglement measured by the concurrence $C(t)$. For large κ, the occupations can decay faster than the time needed for phonon-induced decoherence, so that for very large κ the phonon-free situation is recovered.

To summarize, our numerical calculations of the concurrence in the biexciton cascade in the absence of dot-phonon interaction confirm the validity of the analytic expression for the concurrence in Eq. (25) for a large range of fine structure splittings and cavity loss rates. This supports the core idea of our analytic approach that the biexciton cascade can be discussed in terms of an effective three-level system that, when the biexciton binding energy is large enough, is in the weak-coupling limit ($\tilde{g} \ll \kappa$) even if the original system is not ($g \sim \kappa$). As a consequence of the weak coupling in the effective three-level system, the dynamics of the relevant two-photon density matrix elements is exponentially damped rather than oscillatory, so that an integration over time does not lead to a cancellation of coherences. For this reason, the single-time integrated concurrence $\overline{C}$ agrees very well with the typical value of the time-dependent concurrence $C(t)$ and its average value given by $\langle C \rangle_\infty$ and is therefore a measure for the entanglement of formation of the two-photon state. Numerically exact path integral calculations reveal that the relation $\overline{C} \approx \langle C \rangle_\infty$ still holds when the dot-phonon interaction is accounted for.

However, the quantitative agreement between $\overline{C}$ and the time-averaged concurrence $\langle C \rangle_\infty$ can also be brought to its limits: for systems with small or vanishing biexciton binding energy, $\lambda = \hbar g / (\frac{1}{2} E_B)$ is no longer a small parameter, which has consequences for the time-dependent concurrence as can be seen in Fig. 6. For a small biexciton binding energy, the concurrence $C(t)$ shows pronounced oscillations that persist for more than 100 ps if the influence of phonons is disregarded. When accounting for the dot-phonon interaction the oscillations are damped down much more quickly. These oscillations can be traced back to a coherent Rabi dynamics between the ground and the biexciton state which causes an oscillatory behavior for both the numerator and the denominator in the expression for $C(t)$ given by Eq. (8). If one compares in such a case the long-time limit of the time-averaged concurrence $\langle C \rangle_\infty$, which coincides reasonably well with $C(t)$ for long times, with the single-time integrated concurrence $\overline{C}$, where numerator and denominator are separately averaged over time, it is found that these quantities noticeably deviate.
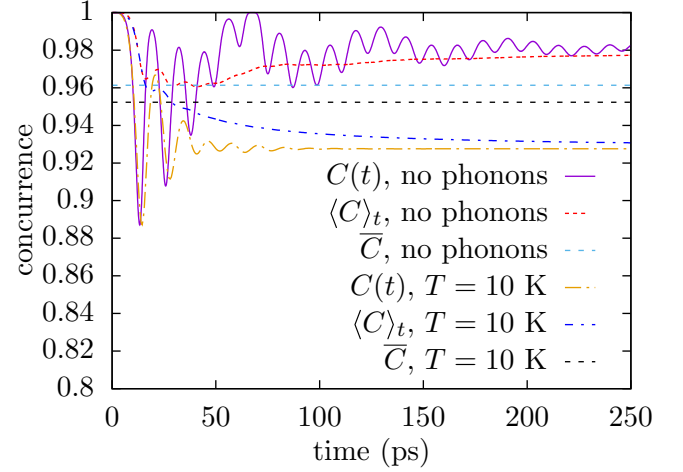

FIG. 6. Time-dependent concurrence $C(t)$ and time-averaged concurrence $\langle C \rangle_t$ as a function of time plotted together with the value of the single-time integrated concurrence $\overline{C}$ for a quantum dot with a small biexciton binding energy $E_B = 0.3$ meV with and without dot-phonon interaction.

IV. DOUBLE-TIME INTEGRATED CONCURRENCE

Having discussed the time-dependent and single-time integrated concurrence, we now move on to the double-time integrated concurrence. To this end, we derive an analytic expression for the double-time integrated concurrence for the biexciton cascade in absence of dot-phonon interaction and subsequently compare it with numerical results.

A. Analytic results

The calculation of the double-time integrated concurrence $\overline{\overline{C}}$ as defined in Eq. (16) requires the knowledge of the two-time correlation function $G^{(2)}_{ij,kl}(t,\tau)$, which can be obtained in the Heisenberg picture by

$$G^{(2)}_{ij,kl}(t,\tau) = \text{Tr}[a_i^\dagger(t) a_j^\dagger(t+\tau) a_k(t+\tau) a_l(t) \hat{\rho}(0)], \quad (27)$$

where $\hat{\rho}(0)$ is the initial density matrix. Introducing the time evolution operator $U(t)$ and rearranging terms yields

$$G^{(2)}_{ij,kl}(t,\tau) = \text{Tr}[a_j^\dagger a_k U(\tau)[a_l U(t)\hat{\rho}(0)U(-t)a_i^\dagger]U(-\tau)]. \quad (28)$$

To obtain the double-time integrated concurrence, we first integrate over the time t and define

$$\begin{aligned} \overline{G}^{(2)}_{ij,kl}(\tau) &= \int_0^\infty dt \, G^{(2)}_{ij,kl}(t,\tau) \\ &= \text{Tr}[a_j^\dagger a_k U(\tau)\tilde{\rho}(0)U(-\tau)] \\ &= \text{Tr}[a_j^\dagger(\tau) a_k(\tau)\tilde{\rho}(0)] = \langle a_j^\dagger a_k(\tau)\rangle_{\tilde{\rho}}, \quad (29a) \end{aligned}$$

with

$$\tilde{\rho}(0) = \int_0^\infty dt \, a_l U(t)\hat{\rho}(0)U(-t)a_i^\dagger = a_l \left[\int_0^\infty dt \, \hat{\rho}(t)\right] a_i^\dagger. \quad (29b)$$

Thus $\overline{G}^{(2)}_{ij,kl}(\tau)$ can be calculated like the average of the operator $a^{\dagger}_j a_k$ at time τ evaluated with a generalized (possibly non-Hermitian) density matrix $\tilde{\rho}$. The initial value of $\tilde{\rho}$ can be obtained from the dynamics of the density matrix elements that have been calculated analytically in the last section. The matrix elements have to be integrated over the time t and the photon operators a_l and $a^{\dagger}_i$ have to be applied from the left and from the right, respectively. Note that to derive Eqs. (29), we have assumed a time evolution given by a unitary operator $U(t)$. In practice, we take into account a Lindblad term in the equations of motion for the description of cavity losses due to the coupling of the light modes within the cavity with a continuum of light modes outside the cavity. Such non-Hamitonian terms give rise to a dynamics that is, in general, not described by a unitary time evolution. However, when the light modes outside the cavity are included in the description, the time evolution of the total system can again be represented by a unitary time evolution operator $U(t)$. Calculating the trace in Eq. (29a) over the field modes outside of the cavity and applying the usual Markovian approximation for the derivation of the Lindblad equations it is straightforward to show that the abovementioned prescription for the calculation of $\overline{G}^{(2)}_{ij,kl}(\tau)$ identically transfers to systems with Lindblad terms such as cavity losses.

As before, it is easy to see that in order to calculate the concurrence, one only needs to account for matrix elements of $\hat{\rho}(t)$ involving the five states defined in Eqs. (19) with exactly two excitations. The application of the operators a_l and $a^{\dagger}_i$ reduces the number of photons and thereby the number of excitations by one. Furthermore, the biexciton state without photons $|B,0,0\rangle$ is removed by the action of a photon destruction operator, leaving only the four relevant states

$$\tilde{G}_H = |G,1,0\rangle, \tag{30a}$$

$$\tilde{X}_H = |X_H,0,0\rangle, \tag{30b}$$

$$\tilde{X}_V = |X_V,0,0\rangle, \tag{30c}$$

$$\tilde{G}_V = |G,0,1\rangle \tag{30d}$$

that have to be accounted for in the calculation of $\tilde{\rho}(\tau)$. Restricted to this basis, the dot-cavity Hamiltonian reads

$$H = \begin{pmatrix} 0 & \hbar g & 0 & 0 \\ \hbar g & \frac{1}{2}(E_B + \delta) & 0 & 0 \\ 0 & 0 & \frac{1}{2}(E_B - \delta) & \hbar g \\ 0 & 0 & \hbar g & 0 \end{pmatrix}. \tag{31}$$

This Hamiltonian represents a system of two decoupled two-level systems, which is diagonalized by the eigenstates

$$\tilde{G}'_i = \cos(\lambda_i)|\tilde{G}_i\rangle - \sin(\lambda_i)|\tilde{X}_i\rangle, \tag{32a}$$

$$\tilde{X}'_i = \sin(\lambda_i)|\tilde{G}_i\rangle + \cos(\lambda_i)|\tilde{X}_i\rangle \tag{32b}$$

with $i \in \{H,V\}$. The complete procedure up to this point is sketched in Fig. 7. In order to get more transparent expressions, we again focus on terms up to second order in λ and approximate $\cos(\lambda_{H/V}) \approx 1 - \frac{1}{2}\lambda^2_{H/V}$ as well as $\sin(\lambda_{H/V}) \approx \lambda_{H/V}$.
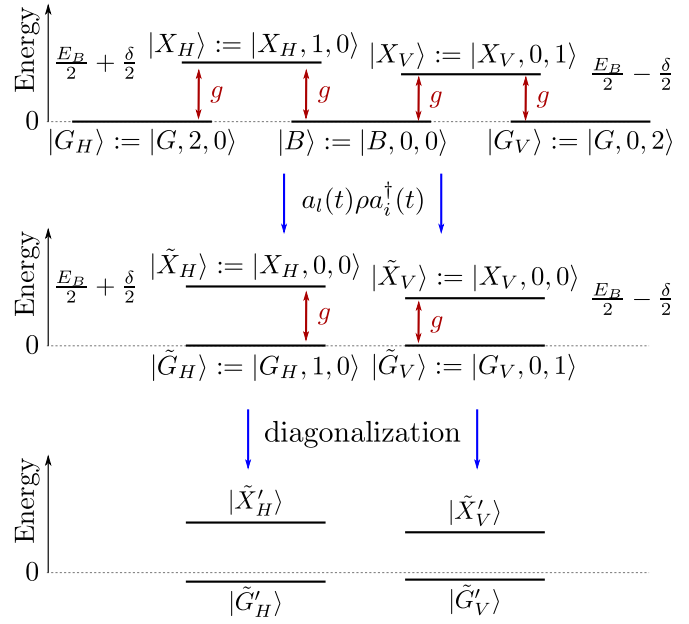

FIG. 7. Sketch of the four-level system for the description of the τ dependence of the two-time correlation function $G^{(2)}_{ij,kl}(t,\tau)$. The application of a_l from the left and $a^{\dagger}_i$ from the right on the density matrix ρ with nonzero elements only for the five states depicted in the top panel results in a generalized density matrix with nonzero elements only for the four states in the middle panel. The resulting four-level system can be decomposed into two decoupled two-level systems and diagonalized analytically.

Then, the energy eigenvalues are

$$E_{\tilde{G}'_i} = -\lambda^2_i \frac{1}{2}(E_B + \delta_i), \tag{33a}$$

$$E_{\tilde{X}'_i} = (1 + \lambda^2_i)\frac{1}{2}(E_B + \delta_i) \tag{33b}$$

with $\delta_{H/V} = \pm\delta$.

Transforming also the Lindblad term into the basis of the states in Eqs. (32), we obtain the equations of motion

$$\frac{\partial}{\partial\tau}\tilde{\rho}_{\tilde{G}'_i\tilde{G}'_j} = \left[\frac{i}{\hbar}(E_{\tilde{G}'_i} - E_{\tilde{G}'_j}) - \kappa\left(1 - \frac{1}{2}(\lambda^2_i + \lambda^2_j)\right)\right]\tilde{\rho}_{\tilde{G}'_i\tilde{G}'_j}$$
$$- \frac{1}{2}\kappa(\lambda_i\tilde{\rho}_{\tilde{X}'_i\tilde{G}'_j} + \lambda_j\tilde{\rho}_{\tilde{G}'_i\tilde{X}'_j}), \tag{34a}$$

$$\frac{\partial}{\partial\tau}\tilde{\rho}_{\tilde{G}'_i\tilde{X}'_j} = \left[\frac{i}{\hbar}(E_{\tilde{G}'_i} - E_{\tilde{X}'_j}) - \frac{1}{2}\kappa\left(1 - \lambda^2_i + \lambda^2_j\right)\right]\tilde{\rho}_{\tilde{G}'_i\tilde{X}'_j}$$
$$- \frac{1}{2}\kappa(\lambda_i\tilde{\rho}_{\tilde{X}'_i\tilde{X}'_j} + \lambda_j\tilde{\rho}_{\tilde{G}'_i\tilde{G}'_j}), \tag{34b}$$

$$\frac{\partial}{\partial\tau}\tilde{\rho}_{\tilde{X}'_i\tilde{X}'_j} = \left[\frac{i}{\hbar}(E_{\tilde{X}'_i} - E_{\tilde{X}'_j}) - \frac{1}{2}\kappa(\lambda^2_i + \lambda^2_j)\right]\tilde{\rho}_{\tilde{X}'_i\tilde{X}'_j}$$
$$- \frac{1}{2}\kappa(\lambda_i\tilde{\rho}_{\tilde{G}'_i\tilde{X}'_j} + \lambda_j\tilde{\rho}_{\tilde{X}'_i\tilde{G}'_j}). \tag{34c}$$

Note that the cross terms introduced by the losses are of minor importance since the slowly changing occupations $\tilde{\rho}_{\tilde{G}'_i\tilde{G}'_j}$ and $\tilde{\rho}_{\tilde{X}'_i\tilde{X}'_j}$ are off-resonantly driven by the fast oscillating (with frequency $\sim \frac{1}{2}E_B/\hbar$) coherences $\tilde{\rho}_{\tilde{G}'_i\tilde{X}'_j}$ and vice versa. This

allows us to neglect these cross terms in the following. Then, the solutions of Eqs. (34) are damped oscillations.

Here, we are interested in the delay-time-integrated matrices

$$\overline{\overline{\rho}}_{ij} = \int_0^\infty d\tau \, \tilde{\rho}_{ij}(\tau), \tag{35}$$

which can be expressed by

$$\overline{\overline{\rho}}_{\tilde{G}'_i \tilde{G}'_j} = \frac{1}{\kappa\left(1 - \frac{1}{2}(\lambda_i^2 + \lambda_j^2)\right) - \frac{i}{\hbar}\left(E_{\tilde{G}'_i} - E_{\tilde{G}'_j}\right)} \tilde{\rho}_{\tilde{G}'_i \tilde{G}'_j}(0), \tag{36a}$$

$$\overline{\overline{\rho}}_{\tilde{G}'_i \tilde{X}'_j} = \frac{1}{\frac{1}{2}\kappa\left(1 - \lambda_i^2 + \lambda_j^2\right) - \frac{i}{\hbar}\left(E_{\tilde{G}'_i} - E_{\tilde{X}'_j}\right)} \tilde{\rho}_{\tilde{G}'_i \tilde{X}'_j}(0), \tag{36b}$$

$$\overline{\overline{\rho}}_{\tilde{X}'_i \tilde{X}'_j} = \frac{1}{\frac{1}{2}\kappa\left(\lambda_i^2 + \lambda_j^2\right) - \frac{i}{\hbar}\left(E_{\tilde{X}'_i} - E_{\tilde{X}'_j}\right)} \tilde{\rho}_{\tilde{X}'_i \tilde{X}'_j}(0). \tag{36c}$$

The final steps to obtain the double-time integrated concurrence are a number of basis transformations of the initial values. First, we have to transform the analytic result for the single-time averaged density matrix in the effective three-level system [basis: G'_i, B' in Eqs. (22)] back into the original five-level system [basis: G_i, X_i, B in Eqs. (19)], then we have to apply the photon annihilation operators [new basis: $\tilde{G}_i, \tilde{X}_i$ in Eqs. (30)] and transform the result to the diagonal basis spanned by the states $\tilde{G}'_i$ and $\tilde{X}'_i$ defined in Eqs. (32) to obtain the initial values for the effective density matrix $\tilde{\rho}_{ij}(0)$. With these initial values, Eqs. (36) are evaluated and the result is transformed back to the basis spanned by $\tilde{G}_i$ and $\tilde{X}_i$.

Keeping only second-order terms, we find the initial values

$$\tilde{\rho}_{\tilde{G}'_i \tilde{G}'_j}(0) \approx \tilde{\rho}_{\tilde{G}_i \tilde{G}_j}(0) = 4(2\delta_{ij} - 1)\frac{g^2}{\kappa^2}\frac{\lambda_i \lambda_j}{\kappa_B}, \tag{37a}$$

$$\tilde{\rho}_{\tilde{G}'_i \tilde{X}'_j}(0) \approx \tilde{\rho}_{\tilde{G}_i \tilde{X}_j}(0) = 2i(2\delta_{ij} - 1)\frac{g}{\kappa}\frac{\lambda_i \lambda_j}{\kappa_B}, \tag{37b}$$

$$\tilde{\rho}_{\tilde{X}'_i \tilde{X}'_j}(0) \approx \tilde{\rho}_{\tilde{X}_i \tilde{X}_j}(0) = (2\delta_{ij} - 1)\frac{\lambda_i \lambda_j}{\kappa_B}. \tag{37c}$$

The double-time integrated density matrix elements entering the concurrence are

$$\overline{\overline{\rho}}_{\tilde{G}_i \tilde{G}_j} \approx \frac{1 - \frac{1}{2}(\lambda_i^2 + \lambda_j^2)}{\kappa\left(1 - \frac{1}{2}(\lambda_i^2 + \lambda_j^2)\right)} \tilde{\rho}_{\tilde{G}_i \tilde{G}_j}(0)$$
$$+ \frac{\lambda_i \lambda_j}{\frac{1}{2}\kappa\left(\lambda_i^2 + \lambda_j^2\right) - \frac{i}{\hbar}\left(E_{\tilde{X}'_i} - E_{\tilde{X}'_j}\right)} \tilde{\rho}_{\tilde{X}_i \tilde{X}_j}(0) \tag{38}$$

because the coherences $\tilde{\rho}_{\tilde{G}'_i \tilde{X}'_j}$ lead to contributions of the order of $\mathcal{O}(\lambda^3)$. Thus the double-time integrated density matrix has two contributions, one from direct transitions through the low-energy eigenstates $\tilde{G}'_i$ and one from transitions through the high-energy excitonlike eigenstates $\tilde{X}'_i$. On the one hand, the contributions from the occupations $\tilde{\rho}_{\tilde{X}'_i \tilde{X}'_j}$ are suppressed by a factor $\sim \lambda^2$ because the projection of $\tilde{X}'_i$ on $\tilde{G}_i$ is $\sim \lambda$. On the other hand, the losses for the excitonlike states $\tilde{X}'_i$ are smaller by a factor $\sim \lambda^2$, so that the time integral yields a larger contribution. All in all, the relative strength of the contributions

from transitions through $\tilde{G}'_i$ and $\tilde{X}'_i$ are determined by the factor $4g^2/\kappa^2$.

It is also interesting that the occupations of the excitonlike states $\tilde{X}'_i$ stem from the projection of the occupations of biexcitonlike eigenstate B' onto $|X_H, 1, 0\rangle$ and $|X_V, 0, 1\rangle$ at the time of the loss of the first photon, i.e., when the first photon annihilation operator is applied. In contrast, the contributions through $\tilde{G}'_i$ have their origin in the occupations of the ground states $|G, 2, 0\rangle$ and $|G, 0, 2\rangle$. This suggests that the latter can be interpreted as a two-photon process in the sense that two excitations are transferred from the quantum dot to the cavity before the first photon is emitted from the cavity, while the former corresponds to a one-photon process. This interpretation is corroborated by the fact that the factor $4g^2/\kappa^2$ is identical to the ratio κ_{2P}/κ_{1P} between cavity-assisted two- and one-photon emission processes discussed in Ref. [19] in the context of the generation of highly polarized (nonentangled) photon pairs.

Using the analytic expressions for the double-time integrated density matrix $\overline{\overline{\rho}}$, the double-time integrated concurrence is found to be

$$\overline{\overline{C}} = \frac{2|\overline{\overline{\rho}}_{G_H G_V}|}{\overline{\overline{\rho}}_{G_H G_H} + \overline{\overline{\rho}}_{G_V G_V}}$$
$$= C_{\text{analytic}} \frac{\left|4\frac{g^2}{\kappa^2} + C_{\text{analytic}}\frac{1}{1-ip}\right|}{4\frac{g^2}{\kappa^2} + 1} \tag{39}$$

with

$$p := \frac{E_{\tilde{X}'_H} - E_{\tilde{X}'_V}}{\hbar\kappa\frac{1}{2}\left(\lambda_H^2 + \lambda_V^2\right)}. \tag{40}$$

Keeping only the lowest-order terms in λ and $\frac{\delta}{E_B}$ in the numerator and in the denominator, we can further simplify this result to

$$p \approx \frac{\delta}{\hbar\kappa\lambda^2} = \frac{\delta E_B^2}{4\hbar^3 \kappa g^2}. \tag{41}$$

Note that the contribution of $\frac{1}{1-ip}$ to the concurrence becomes insignificant for $\delta \gg \hbar\kappa\lambda^2$. Therefore this term only contributes for small splittings δ, for which the value of the concurrence C_{analytic} is nearly one and the double-time integrated concurrence is well described by

$$\overline{\overline{C}}_{\text{analytic}} = C_{\text{analytic}} \frac{\sqrt{\left(4\frac{g^2}{\kappa^2} + \frac{1}{1+p^2}\right)^2 + \left(\frac{p}{1+p^2}\right)^2}}{4\frac{g^2}{\kappa^2} + 1} \tag{42}$$

with p from Eq. (41).

B. Numerical results

In Fig. 8, the numerically calculated double-time integrated concurrence $\overline{\overline{C}}$ for the phonon-free case is depicted as a function of the fine structure splitting δ for $\hbar g = 0.1$ meV, $\kappa = 0.25$ ps^{-1}, and $E_B = 1.5$ meV and compared with the analytic expressions for the time-dependent and double-time integrated concurrence. The analytic expression for the double-time integrated concurrence reproduces the main features of the numerical results quite well. For further comparison we also show in Fig. 8 results for $\overline{\overline{C}}$ accounting for phonons at a temperature $T = 10$ K. The necessary evaluation of two-time
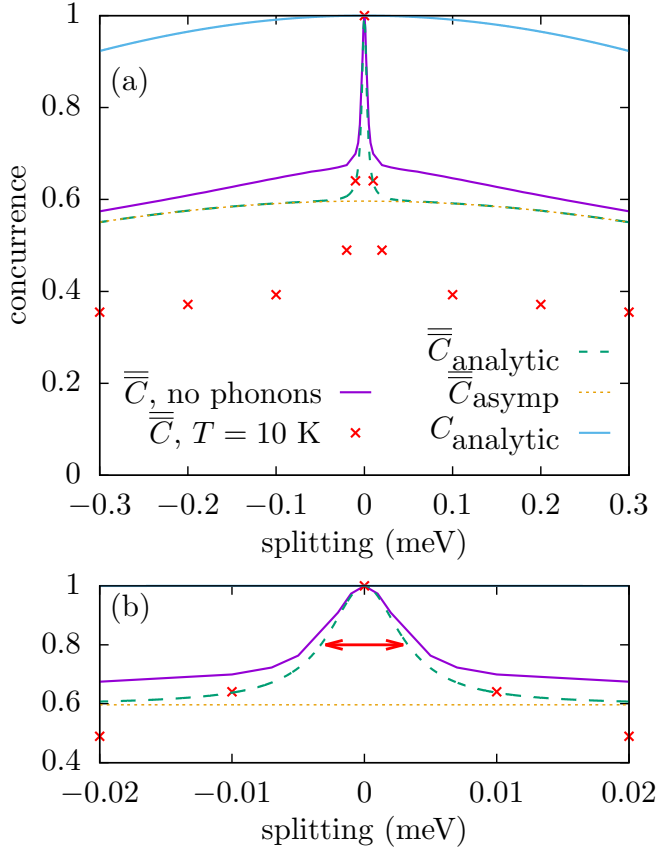
FIG. 8. (a) Double-time integrated concurrence $\overline{\overline{C}}$ as a function of the fine structure splitting δ for the phonon-free case and with phonons for a temperature $T = 10$ K compared with its analytic approximation $\overline{\overline{C}}_{\text{analytic}}$ in the phonon-free case and the corresponding asymptotic behavior $\overline{\overline{C}}_{\text{asymp}}$. Also shown is the analytic result C_{analytic} for the single-time integrated concurrence without phonons. (b) shows a zoom of the central peak where the red double arrow indicates a FWHM of $2\hbar\kappa\lambda^2 = 8\hbar^3\kappa g^2/E_B^2$.

correlation functions in the presence of phonons has been carried out by a numerically exact path integral approach, the details of which will be discussed elsewhere.

Let us first concentrate on the results for the phonon-free case. In contrast to our analytic expression C_{analytic}, which approximates well the time-dependent concurrence $C(t)$ as seen before and which remains close to one even for large fine structure splittings, the double-time integrated concurrence $\overline{\overline{C}}$ typically has a narrow Lorentzian-like peak at splittings close to zero with a width $\sim 10\,\mu$eV and, for larger splittings, reaches a plateau. This qualitative behavior of the double-time integrated concurrence has been reported before in numerical studies [20,29] and is also in agreement with experimental results [8–10]. However, to the best of our knowledge, key quantities, such as the width of the central peak and the height of the plateau, have not yet been explained in terms of the microscopic parameters of the system. Here, the derivation of the analytic expression for the double-time integrated concurrence allows us to identify these key quantities. In particular, recall that the numerator in the analytic expression for the double-time integrated concurrence in Eq. (42) has two

contributions: the terms containing the parameter p originating from transitions through excitonlike energy eigenstates $\tilde{X}_i'$ of the four-level system in Eqs. (30), and another term from the transitions through the lowest energy eigenstates $\tilde{G}_i'$. Because p is proportional to the fine structure splitting δ and the contribution through the excitonlike eigenstates $\tilde{X}_i'$ decays for large values of p as $\frac{1}{p}$, the double-time integrated concurrence for large δ is determined by the contribution through the eigenstates $\tilde{G}_i'$. For $p \to \infty$, one obtains from the analytic expression in Eq. (42),

$$\overline{\overline{C}}_{\text{asymp}} = C_{\text{analytic}} \frac{4g^2}{4g^2 + \kappa^2} = \frac{E_B^2 - \delta^2}{E_B^2 + \delta^2} \frac{4g^2}{4g^2 + \kappa^2}, \quad (43)$$

which is also plotted in Fig. 8.

As can be seen from the figure, the central peak can be attributed to the transitions through the excitonlike eigenstates $\tilde{X}_i'$ and its width is explained as follows: due to the diagonalization of the four-level system, the excitonlike states acquire a finite contribution from states involving the ground state of the quantum dot and one cavity photon. The admixture of these states leads to a mean photon number $n \approx \lambda_{H/V}^2$ for the states $\tilde{X}_i'$. Thereby the excitonlike eigenstates acquire a loss term with a rate $\gamma \approx \kappa\lambda^2$. This loss rate γ of an excitonlike eigenstate coincides with the cavity-assisted single-photon emission rate κ_{1P} from the state $|X_H,0,0\rangle$ to $|G_H,0,0\rangle$ derived in Ref. [19]. For a Lorentzian resonance, the full width at half maximum (FWHM) of the spectrum is related to the exponential decay rate γ by FWHM $= 2\hbar\gamma$, which in our case yields FWHM $= 2\hbar\kappa\lambda^2 = 8\hbar^3\kappa g^2/E_B^2$. This value is indicated in the inset of Fig. 8 as a red double arrow and agrees well with the FWHM of the central peak of the double-time integrated concurrence. Finally, we note that at $\delta = 0$ the double-time integrated concurrence reaches its maximum value $\overline{\overline{C}} = 1$ even when phonons are accounted for and thus agrees in this case with $\overline{C}$. However, introducing a phenomenological pure dephasing of the coherences between electronic configurations has been reported [20,29] to result in lower values of $\overline{\overline{C}}$ at $\delta = 0$.

Phonons have a noticeable impact on the double-time integrated concurrence as can be seen, e.g., from the results (red crosses) shown in Fig. 8 for $T = 10$ K. In particular, phonons drastically reduce the concurrence for larger splittings while for small $\delta \lesssim 0.01\,\mu$eV there is almost no phonon influence. Overall, qualitative trends, like the narrow peak of $\overline{\overline{C}}$ as a function of δ as well as the plateau obtained for larger splittings, remain similar to results obtained without accounting for phonons. This is in line with previous theoretical calculations in Ref. [29] on the basis of master equations in the polaron frame [44].

In the literature [13,31], also the impact of frequency filtering of the emitted photons on the behavior of concurrences evaluated for finite δ has been discussed. It is worthwhile to note that there are cross-relations between frequency filtering and selecting photons according to the delay of their emission. This is best understood by noting that the emission of the cavity tuned in resonance to the two-photon transition from the ground to the biexciton state typically exhibits emission lines at the energies of the dipole-coupled dot transitions as well as at the two-photon transition [19,31]. Emissions via dipole-coupled dot transitions correspond to a cascaded

decay where first a single photon is emitted in a transition from the biexciton to one of the excitons and then, at a later time, a second photon is generated in the decay of an exciton to the ground state. In contrast, the two photons from the direct biexciton-to-ground state transition are generated almost simultaneously with a much narrower spread in the emission time than in cascaded emissions. Thus, filtering the emitted signal at the frequency for the two-photon transition, one collects a subset of photons with a low spread in τ similar to measuring the single-time integrated concurrence. Indeed, for a weakly driven cavity, Ref. [31] reported in this case values near one independent on δ for the single- as well as the double-time integrated concurrences. On the other hand, filtering at frequencies of the dipole-coupled transitions or between the fine-structure split exciton lines results in low values for the double-time integrated concurrence [13,31], while the single-time integrated concurrence stays close to one. Thus, using the already discussed argument of Stevenson *et al.*, according to which simultaneously emitted photon pairs are expected to have higher degrees of entanglement than photon pairs emitted with a delay, all tendencies observed for different frequency filtered emissions can be nicely explained.

Also, the role of the cavity can to some extent be discussed from the perspective that a cavity provides a frequency filter. However, it should be noted that a cavity tuned to the ground-to-biexciton state transition in general filters photons not only at the frequency of the two-photon transition but also at frequencies corresponding to photons emitted in a cascaded decay, as is evident from the corresponding emission spectra [19,31]. The relative weights between two-photon and cascaded emissions is governed by the ratio of the respective emission rates $\kappa_{2P}/\kappa_{1P} = 4g^2/\kappa^2$. Thus, for weakly coupled cavities ($g \ll \kappa$), the cavity essentially filters only the cascaded emission, which should lead to low double-time integrated concurrences. Indeed, we find from our analytic result, Eq. (42),

$$\lim_{g \to 0} \overline{\overline{C}}_{\text{analytic}} = \begin{cases} 1, & \text{for } \delta = 0 \\ 0, & \text{otherwise} \end{cases}, \qquad (44)$$

i.e., a maximally sharp drop of the double-time integrated concurrence as a function of δ. Reaching the limit $g = 0$, however, is for a cavity without driving a highly singular case since, for vanishing g, there is no coupling between the dot levels and the system simply remains in the biexciton state if radiative recombination is disregarded. The above discussion therefore applies for small but finite g. In the opposite limit $g \gg \kappa$, the assumption $g \ll E_B$ made in the derivation of our analytic result may be violated so that, strictly speaking, Eq. (42) can no longer be used. Nevertheless, the tendency expected from our above discussion that, in this limit, the cavity essentially filters only the simultaneous emission and thus the double-time integrated concurrence should approach high values is corroborated by formally taking the limit $g \to \infty$ in Eq. (42), which yields

$$\lim_{g \to \infty} \overline{\overline{C}}_{\text{analytic}} = \overline{C}_{\text{analytic}} = \frac{E_B^2 - \delta^2}{E_B^2 + \delta^2}. \qquad (45)$$

This is in accordance with our expectation as well as the results in Ref. [31] for an emission filtered at the two-photon transition.
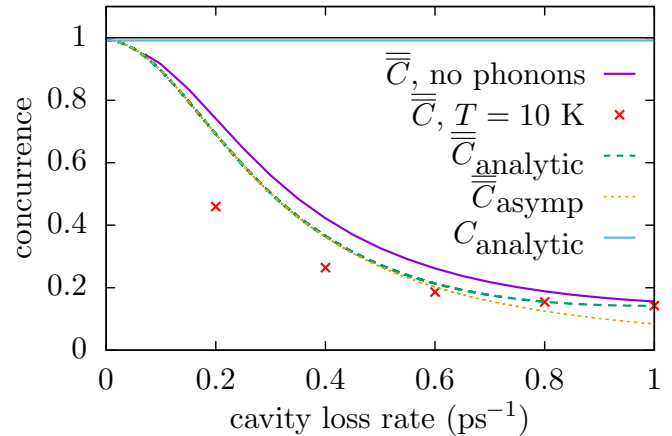

FIG. 9. Double-time integrated concurrence $\overline{\overline{C}}$ for a fine structure splitting $\delta = 0.1$ meV as a function of the cavity loss rate κ without phonons and with phonons at temperature $T = 10$ K compared with the analytic result $\overline{\overline{C}}_{\text{analytic}}$ for the double-time integrated concurrence without phonons and its asymptotic behavior $\overline{\overline{C}}_{\text{asymp}}$. Also shown is the analytic result C_{analytic} for the time-dependent concurrence in the phonon-free case.

Apart from the δ dependence, also the impact of the cavity loss rate κ on the different concurrences compared in this paper is instructive. The dependence of the double-time integrated concurrence $\overline{\overline{C}}$ on κ is depicted with and without phonons in Fig. 9 for the same fine structure splitting $\delta = 0.1$ meV as used in Fig. 5 for the single-time integrated concurrence. While the analytic expression for the time-dependent concurrence C_{analytic} predicts a value close to one and independent of the loss rate, the double-time integrated concurrence in Fig. 9 significantly depends on κ already without phonons: it decreases monotonically with increasing κ and follows the asymptotic expression in Eq. (43) for the height of the plateau. The latter is due to the fact that we are considering here a value of δ where in Fig. 8 already the plateau is reached. While the unnormalized density matrix elements entering the numerator and the denominator in the expression for the single-time integrated concurrence are affected in the same way by a change of κ, this is not the case for the double-time integrated concurrence. Here, the unnormalized density matrix elements reflect, according to Eq. (38), the competition between two-photon and sequential single-photon processes. The cavity loss rate enters the corresponding contributions in two ways: first, the relative weight of two- and single-photon parts is governed by the ratio of the corresponding emission rates $\kappa_{2P}/\kappa_{1P} = 4g^2/\kappa^2 = \tilde{\rho}_{\tilde{G}_i \tilde{G}_j}(0)/\tilde{\rho}_{\tilde{X}_i \tilde{X}_j}(0)$. Second, the two-photon parts decay as a function of τ without oscillations while the sequential single-photon contributions exhibit oscillations reflecting the relative phase between the two involved exciton components. This translates after τ integration into prefactors $\sim 1/\kappa$ and $\sim 1/[\frac{1}{2}\kappa(\lambda_i^2 + \lambda_j^2) - \frac{i}{\hbar}(E_{\tilde{X}_i'} - E_{\tilde{X}_j'})]$. Altogether, in the limit of vanishing κ, the two-photon contribution dominates irrespective of the other parameters due to the $\sim 1/\kappa^3$ singularity and $\overline{\overline{C}}_{\text{analytic}}$ approaches C_{analytic} which is close to one. For small enough κ and finite δ, the concurrence has reached the plateau with respect to its δ dependence and is thus well
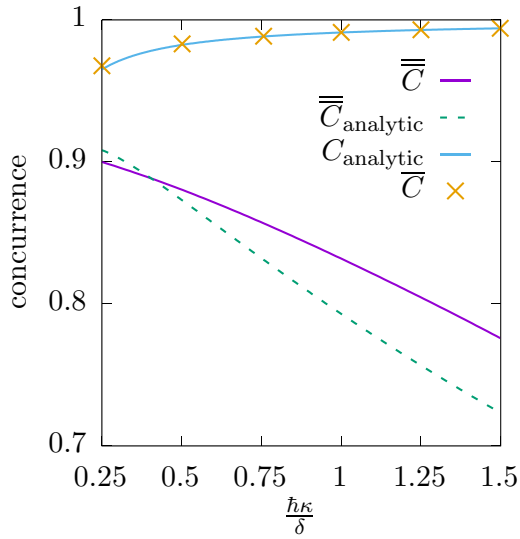
FIG. 10. Single- and double-time integrated concurrences for the phonon-free case plotted vs. $\frac{\hbar\kappa}{\delta}$ for fixed $\hbar\kappa\,\delta = 0.01$ meV^2. Shown are the numerically obtained results together with the corresponding analytic approximations.

described by Eq. (43), indicating a drop with rising κ following a Lorentzian with a FWHM $4g$. We note in passing that when κ is further increased for fixed other parameters the width of the peak in Fig. 8 grows $\sim \kappa$ such that according to Eq. (42) $\overline{\overline{C}}_{\text{analytic}}$ recovers again to the high value C_{analytic} in the limit $\kappa \to \infty$. However, for the parameters used in Fig. 9 this recovery occurs for much larger κ values than covered in the plot.

For $\overline{C}$ as well as $\overline{\overline{C}}$, the interaction with phonons leads to a reduction of the concurrence due to decoherence and because phonons cause the system to be in a mixed state. As discussed before, the phonon impact decreases with increasing cavity loss rate because higher κ values limit the time-window over which the phonon-induced decoherence can take place. For the double-time integrated concurrence this is nicely seen in Fig. 9 where the results with and without phonons approach each other for large κ. Altogether, we find a diminishing phonon influence for rising κ on top of a nearly constant behavior of the single-time integrated concurrence, while for the double-time integrated concurrence this is superimposed on a strong decay. The resulting total effect is a complete trend reversal for finite δ in the presence of phonons: $\overline{C}$ increases with rising κ while $\overline{\overline{C}}$ decreases as long as δ is large enough to be in the plateau in Fig. 8.

Interestingly, while the trend reversal as a function of the cavity loss rate is attributed to the phonon influence, the nonequivalence of $\overline{C}$ and $\overline{\overline{C}}$ can already be demonstrated in the phonon-free case. To this end, we plot $\overline{C}$ and $\overline{\overline{C}}$ as a function of $\frac{\hbar\kappa}{\delta}$ for fixed $\hbar\kappa\,\delta$ in Fig. 10. While $\overline{C}$ is increasing monotonically with rising $\frac{\hbar\kappa}{\delta}$, $\overline{\overline{C}}$ is decreasing. The observation of opposite trends in the single- and double-time integrated concurrences has important implications for the interpretation of the results. When comparing different situations, e.g., cavities with different values κ_1 and κ_2, it may turn out that according to $\overline{C}$ the cavity with κ_1 gives rise to the higher

entanglement while for $\overline{\overline{C}}\kappa_2$ leads to the higher entanglement or vice versa. This clearly demonstrates that $\overline{C}$ and $\overline{\overline{C}}$ cannot be equivalent measures for the same physical quantity, but instead measure two different types of entanglement.

V. CONCLUSION

We have studied the two-photon state generated by the biexciton cascade in a quantum dot embedded in a microcavity. Our main focus is a comparison of dependencies of three different practical definitions of concurrences prevalent in the literature on relevant parameters such as the exciton fine structure splitting and the cavity loss rate. In particular, we compare the time-dependent concurrence $C(t)$ associated with the state of the system at a given time t, which by definition reflects the corresponding entanglement of formation, with concurrences derived from the results of different quantum state reconstruction strategies. These strategies are based on photon coincidence measurements collecting data points either over extended real- and delay-time intervals (double-time integrated concurrence $\overline{\overline{C}}$) or over an extended real-time interval but a narrow delay-time window (single-time integrated concurrence $\overline{C}$). Considering the photons recorded in the two detectors of the coincidence measurements, these concurrences refer to photons with a simultaneous emission time t ($C(t)$), photons resulting from simultaneous emission irrespective of the time t of the emission ($\overline{C}$), and photons resulting from emissions without resolving the emission times of both photons ($\overline{\overline{C}}$).

For a quantum dot with finite biexciton binding energy ($E_B \gg \delta$) in a cavity whose modes are tuned in resonance with the two-photon transition between the ground and the biexciton state, we have derived analytic expressions for the time-dependent, the single-time integrated, and the double-time integrated concurrence in the absence of dot-phonon interaction. Our results are applicable also beyond the weak-coupling limit of the dot-cavity system and we have shown that they agree well with the results obtained from numerical calculations.

The single-time integrated concurrence, which can be accessed experimentally by time-windowing techniques [11] or using vary narrow time bins for the delay time [12], is found to be close to the stationary value of the time-dependent concurrence at long times. This remains true when the dot-phonon interaction is fully taken into account. The reason for this agreement between $\overline{C}$ and $C(t)$ is that, due to the high energetic penalty involved in the occupation of single-exciton states with one cavity photon, the dynamics of the biexciton cascade is essentially incoherent and exponential, even when the coupling g is comparable to the cavity loss rate κ. Because all oscillations between the states with two photons in either the horizontally or the vertically polarized cavity mode are overdamped, the time-integration does not lead to a significant dephasing of coherences between those states. Thus, in the dot-cavity configuration considered here, the information contained in $C(t)$ about the entanglement of formation assigned to two-photon states in the cavity at time t is accessible by the more easily measurable single-time integrated concurrence $\overline{C}$.

In contrast, the double-time integrated concurrence, which in most experiments is the measured quantity since measuring over extended real-time and delay-time intervals provides the highest photon coincidence counts, shows a completely different behavior than either $C(t)$ or $\overline{C}$. First of all, disregarding phonons, $\overline{\overline{C}}$ as a function of the fine structure splitting δ has a narrow peak with a FWHM of approximately 10 μeV and then drops to a plateau that only weakly depends on the value of the splitting. We also obtain analytic expressions for the height of the plateau as well as the FWHM of the central peak and thereby explain the shape of the double-time integrated concurrence as a function of δ. Numerical simulations reveal that phonons do not change this behavior qualitatively and only lead to quantitative corrections, which is in line with previous studies [29]. In contrast, neither with nor without phonons the time-dependent concurrence exhibits a narrow peak as a function of the fine structure splitting which evolves into a plateau for larger splittings. In the phonon-free case, it stays close to one even for splittings as large as ~ 0.1 meV, while phonons lead to a reduction that follows a bell-shaped curve. This different behavior upon variation of the fine structure splitting can be attributed to the fact that, even in the presence of a nonvanishing fine structure splitting, the two emitted photons are strongly entangled at any given time, which is reflected in the time-dependent and the single-time integrated concurrence. However, the integration over the delay time in the double-time integrated concurrence gives rise to destructive interference of the two pathways.

Another qualitative difference between the time-dependent concurrence and the double-time integrated concurrence is the dependence on the cavity loss rate. The analytic expression for $\overline{C}$, which does not account for the effects of phonons, is independent of the cavity loss rate. Taking dot-LA-phonon interactions into account using a numerically exact real-time path-integral method [42] reveals that phonons can lead to a reduction of the concurrence and that the concurrence increases with the cavity loss rate. The reason for this is that the losses limit the time available for dephasing processes, so that for large κ the phonon-induced reduction of the concurrence is suppressed. In contrast, for the considered situation $\overline{\overline{C}}$ decreases with increasing loss rate in the phonon-free case as well as when phonons are taken into account. This κ dependence of $\overline{\overline{C}}$ essentially reflects the competition between two- and single-photon processes.

From these results it clearly follows that upon variation of the cavity loss rate opposite orderings are obtained with respect to the two figures of merit provided by $\overline{C}$ and $\overline{\overline{C}}$, respectively. In addition, already in the phonon-free case, it turns out that $\overline{C}$ and $\overline{\overline{C}}$ exhibit opposite trends when varying the ratio between κ and δ, while keeping the product of these quantities constant. Altogether, this implies that single- and double-time integrated concurrences cannot be equivalent measures for the same physical quantity but instead reflect different aspects of entanglement.

ACKNOWLEDGMENTS

APPENDIX: DYNAMICS IN THE EFFECTIVE THREE-LEVEL SYSTEM

Here, we calculate the dynamics in the weakly coupled three-level system spanned by the states $|G'_H\rangle, |G'_V\rangle$ and $|B'\rangle$ defined in Eqs. (22). To this end, we define the density matrix elements

$$\rho_{\nu'\mu'} := \langle (|\nu'\rangle\langle\mu'|)\rangle, \qquad (A1)$$

with $\nu', \mu' \in \{G'_H, G'_V, B'\}$.

In the subspace spanned by the above states, the Lindblad losses induce transitions to states with lower excitation numbers. However, these states can be disregarded in the equation of motion for $\rho_{\nu'\mu'}$ since they do not couple back to states with higher excitation numbers. Thus the trace of the density matrix ρ in the subspace spanned by $\{G'_H, G'_V, B'\}$ is no longer conserved and we find

$$\frac{\partial}{\partial t}\rho_{\nu'\mu'} = \frac{i}{\hbar}\sum_{\bar{\nu}}\left[H'_{\nu'\bar{\nu}}\rho_{\bar{\nu}\mu'} - \rho_{\nu'\bar{\nu}}H'_{\bar{\nu}\mu'}\right]$$
$$- \frac{\kappa}{2}\sum_{\bar{\nu}}(n_{\nu'\bar{\nu}}\rho_{\bar{\nu}\mu'} + \rho_{\nu'\bar{\nu}}n_{\bar{\nu}\mu'}), \qquad (A2)$$

where $n_{\nu'\mu'} = \sum_{i=H,V}(a_i^\dagger a_i)_{\nu'\mu'}$ is the photon number operator. The equations of motion for the effective three-level system are then

$$\frac{\partial}{\partial t}\rho_{B'B'} = -(\lambda_H^2 + \lambda_V^2)\kappa\rho_{B'B'} - \sum_{i\in\{H,V\}}2\tilde{g}_i\mathrm{Im}(\rho_{G'_iB'}), \qquad (A3a)$$

$$\frac{\partial}{\partial t}\rho_{G'_iB'} = \left(i\frac{\tilde{\delta}_i}{\hbar} - \kappa\right)\rho_{G'_iB'} + i\tilde{g}_i\rho_{B'B'} - \sum_{j\in\{H,V\}}i\tilde{g}_j\rho_{G'_iG'_j}, \qquad (A3b)$$

$$\frac{\partial}{\partial t}\rho_{G'_iG'_j} = \left[i\left(\frac{\tilde{\delta}_i}{\hbar} - \frac{\tilde{\delta}_j}{\hbar}\right) - 2\left(1 - \frac{1}{2}(\lambda_i^2 + \lambda_j^2)\right)\kappa\right]\rho_{G'_iG'_j} + i\tilde{g}_i\rho_{B'G'_j} - i\tilde{g}_j\rho_{G'_iB'}, \qquad (A3c)$$

where we have defined $\tilde{\delta}_{H/V} = \pm\tilde{\delta}$. It is straightforward to see that when the system is initially in the biexciton state, $\rho_{G'_iB'} = \mathcal{O}(\lambda)$ and $\rho_{G'_iG'_j} = \mathcal{O}(\lambda^2)$. Furthermore, we consider the weak-coupling regime in the effective three-level system where $\tilde{g}_i \ll \kappa$. Therefore $\rho_{G'_iG'_j}$ decays fast compared to $\rho_{B'B'}$ due to the losses and can be neglected for the calculation of $\rho_{G'_iB'}$. Then, the coherences $\rho_{G'_iB'}$ are given by

$$\rho_{G'_iB'}(t) = i\tilde{g}_i\int_0^t dt'\, e^{(-\kappa+i\tilde{\delta}_i/\hbar)(t-t')}\rho_{B'B'}(t'). \qquad (A4)$$

Because $\rho_{B'B'}$ changes only on a much longer-time scale [all terms on the right-hand side (r.h.s.) of Eq. (A3a) are of the order $\mathcal{O}(\lambda^2)$] than $\rho_{G'_iB'}$, one can apply the Markov limit consisting of evaluating $\rho_{B'B'}(t')$ at $t' = t$ and setting the lower limit of

the intergral to $-\infty$, so that

$$\rho_{G'_i B'}(t) \approx i \frac{\tilde{g}_i}{\kappa - \frac{i}{\hbar}\tilde{\delta}_i} \rho_{B'B'}(t). \tag{A5}$$

Feeding this result back into the equation for $\rho_{B'B'}$ and dropping terms higher than second order in λ, one finds

$$\rho_{B'B'}(t) \approx e^{-\kappa_B t}, \tag{A6}$$

$$\kappa_B \approx \left(\lambda_H^2 + \lambda_V^2\right)\left(\frac{4g^2}{\kappa} + \kappa\right). \tag{A7}$$

Using again Eq. (A5), one obtains explicit expressions for $\rho_{G'_i B'}$ and its complex conjugate $\rho_{B'G'_i} = (\rho_{G'_i B'})^*$, which are

the source terms necessary for the calculation of $\rho_{G'_i G'_j}$ from Eq. (A3c):

$$\rho_{G'_i G'_j}(t) = \left(\frac{\tilde{g}_i \tilde{g}_j}{\kappa + \frac{i}{\hbar}\tilde{\delta}_j} + \frac{\tilde{g}_i \tilde{g}_j}{\kappa - \frac{i}{\hbar}\tilde{\delta}_i}\right) \int_0^t dt'$$
$$\times e^{[-(2-\lambda_i^2-\lambda_j^2)\kappa + i(\tilde{\delta}_i - \tilde{\delta}_j)/\hbar](t-t')} e^{-\kappa_B t'}. \tag{A8}$$

Integrating over t' and keeping only terms up to second order in the prefactor yields

$$\rho_{G'_i G'_j} = \frac{\tilde{g}_i \tilde{g}_j}{\kappa^2} \left(e^{-\kappa_B t} - e^{[-(2-\lambda_i^2-\lambda_j^2)\kappa + i(\tilde{\delta}_i - \tilde{\delta}_j)/\hbar]t}\right). \tag{A9}$$

[1] N. Gisin, G. Ribordy, W. Tittel, and H. Zbinden, Rev. Mod. Phys. **74**, 145 (2002).

[2] J. L. O'Brian, A. Furusawa, and J. Vučković, Nat. Photonics **3**, 687 (2009).

[3] A. Orieux, M. A. M. Versteegh, K. D. Jöns, and S. Ducci, Rep. Prog. Phys. **80**, 076001 (2017).

[4] A. Zeilinger, Phys. Scr. **92**, 072501 (2017).

[5] M. A. M. Versteegh, M. E. Reimer, K. D. Jöns, D. Dalacu, P. J. Poole, A. Gulinatti, A. Guidice, and V. Zwiller, Nat. Commun. **5**, 5298 (2014).

[6] M. Müller, S. Bounouar, K. D. Jöns, M. Glässl, and P. Michler, Nat. Photon. **8**, 224 (2014).

[7] N. Akopian, N. H. Lindner, E. Poem, Y. Berlatzky, J. Avron, D. Gershoni, B. D. Gerardot, and P. M. Petroff, Phys. Rev. Lett. **96**, 130501 (2006).

[8] R. M. Stevenson, R. J. Young, P. Atkinson, K. Cooper, D. A. Ritchie, and A. J. Shields, Nature **439**, 179 (2006).

[9] A. J. Hudson, R. M. Stevenson, A. J. Bennett, R. J. Young, C. A. Nicoll, P. Atkinson, K. Cooper, D. A. Ritchie, and A. J. Shields, Phys. Rev. Lett. **99**, 266802 (2007).

[10] R. Hafenbrak, S. M. Ulrich, P. Michler, L. Wang, A. Rastelli, and O. G. Schmidt, New J. Phys. **9**, 315 (2007).

[11] R. M. Stevenson, A. J. Hudson, A. J. Bennett, R. J. Young, C. A. Nicoll, D. A. Ritchie, and A. J. Shields, Phys. Rev. Lett. **101**, 170501 (2008).

[12] S. Bounouar, C. de la Haye, M. Strauß, P. Schnauber, A. Thoma, M. Gschrey, J.-H. Schulze, A. Strittmatter, S. Rodt, and S. Reitzenstein, Appl. Phys. Lett. **112**, 153107 (2018).

[13] G. Pfanner, M. Seliger, and U. Hohenester, Phys. Rev. B **78**, 195410 (2008).

[14] C. Sánchez Muñoz, F. P. Laussy, C. Tejedor, and E. del Valle, New J. Phys. **17**, 123021 (2015).

[15] J. D. Mar, J. J. Baumberg, X. L. Xu, A. C. Irvine, and D. A. Williams, Phys. Rev. B **93**, 045316 (2016).

[16] A. J. Bennett, M. A. Pooley, R. M. Stevenson, M. B. Ward, R. B. Patel, A. Boyer de la Giroday, N. Sköld, I. Farrer, C. A. Nicoll, D. A. Ritchie, and A. J. Shields, Nat. Phys. **6**, 947 (2010).

[17] S. Seidl, M. Kroner, A. Högele, K. Karrai, R. J. Warburton, A. Badolato, and P. M. Petroff, Appl. Phys. Lett. **88**, 203113 (2006).

[18] T. Huber, A. Predojević, M. Khoshnegar, D. Dalacu, P. J. Poole, H. Mejedi, and G. Weihs, Nano Lett. **14**, 7107 (2014).

[19] E. del Valle, A. Gonzalez-Tudela, E. Cancellieri, F. P. Laussy, and C. Tejedor, New J. Phys. **13**, 113014 (2011).

[20] S. Schumacher, J. Förstner, A. Zrenner, M. Florian, C. Gies, P. Gartner, and F. Jahnke, Opt. Express **20**, 5335 (2012).

[21] S.-K. Liao, W.-Q. Cai, J. Handsteiner, B. Liu, J. Yin, L. Zhang, D. Rauch, M. Fink, J.-G. Ren, W.-Y. Liu, Y. Li, Q. Shen, Y. Cao, F.-Z. Li, J.-F. Wang, Y.-M. Huang, L. Deng, T. Xi, L. Ma, T. Hu, L. Li, N.-L. Liu, F. Koidl, P. Wang, Y.-A. Chen, X.-B. Wang, M. Steindorfer, G. Kirchner, C.-Y. Lu, R. Shu, R. Ursin, T. Scheidl, C.-Z. Peng, J.-Y. Wang, A. Zeilinger, and J.-W. Pan, Phys. Rev. Lett. **120**, 030501 (2018).

[22] C. H. Bennett, D. P. DiVincenzo, J. A. Smolin, and W. K. Wootters, Phys. Rev. A **54**, 3824 (1996).

[23] M. A. Nielsen and I. L. Chuang, *Quantum Computation and Quantum Information* (Cambridge University Press, Cambridge, 2000).

[24] W. K. Wootters, Quantum Info. Comput. **1**, 27 (2001).

[25] W. K. Wootters, Phys. Rev. Lett. **80**, 2245 (1998).

[26] S. M. Hein, F. Schulze, A. Carmele, and A. Knorr, Phys. Rev. Lett. **113**, 027401 (2014).

[27] D. F. V. James, P. G. Kwiat, W. J. Munro, and A. G. White, Phys. Rev. A **64**, 052312 (2001).

[28] F. Troiani, J. I. Perea, and C. Tejedor, Phys. Rev. B **74**, 235310 (2006).

[29] D. Heinze, A. Zrenner, and S. Schumacher, Phys. Rev. B **95**, 245306 (2017).

[30] A. Carmele and A. Knorr, Phys. Rev. B **84**, 075328 (2011).

[31] E. del Valle, New J. Phys. **15**, 025019 (2013).

[32] J. P. Reithmaier, G. Sek, A. Löffler, C. Hofmann, S. Kuhn, S. Reitzenstein, L. V. Keldysh, V. D. Kulakovskii, T. L. Reinecke, and A. Forchel, Nature (London) **432**, 197 (2004).

[33] S. C. Kuhn, A. Knorr, S. Reitzenstein, and M. Richter, Opt. Express **24**, 25446 (2016).

[34] C. Schneider, P. Gold, S. Reitzenstein, S. Höfling, and M. Kamp, Appl. Phys. B **122**, 19 (2016).

[35] J. P. Reithmaier, Semicond. Sci. Technol. **23**, 123001 (2008).

[36] J. Kasprzak, K. Sivalertporn, F. Albert, C. Schneider, S. Höfling, M. Kamp, A. Forchel, S. Reitzenstein, E. A. Muljarov, and W. Langbein, New J. Phys. **15**, 045013 (2013).

[37] R. Winkler, *Spin-Orbit Coupling Effects in Two-Dimensional Electron and Hole Systems* (Springer, Berlin, 2003).

[38] S. Bravyi, D. P. DiVincenzo, and D. Loss, Ann. Phys. **326**, 2793 (2011).

[39] N. Makri and D. E. Makarov, J. Chem. Phys. **102**, 4600 (1995).

[40] A. Vagov, M. D. Croitoru, M. Glässl, V. M. Axt, and T. Kuhn, Phys. Rev. B **83**, 094303 (2011).

[41] A. M. Barth, A. Vagov, and V. M. Axt, Phys. Rev. B **94**, 125439 (2016).

[42] M. Cygorek, A. M. Barth, F. Ungar, A. Vagov, and V. M. Axt, Phys. Rev. B **96**, 201201(R) (2017).

[43] M. Glässl, A. M. Barth, and V. M. Axt, Phys. Rev. Lett. **110**, 147401 (2013).

[44] A. Nazir and D. P. S. McCutcheon, J. Phys.: Condens. Matter **28**, 103002 (2016).

Publication 13

From strong to weak temperature dependence of the two-photon entanglement resulting from the biexciton cascade inside a cavity

T. Seidelmann, F. Ungar, M. Cygorek, A. Vagov, A. M. Barth, T. Kuhn, and V. M. Axt

From strong to weak temperature dependence of the two-photon entanglement resulting from the biexciton cascade inside a cavity

T. Seidelmann,[1] F. Ungar,[1] M. Cygorek,[2] A. Vagov,[1,3] A. M. Barth,[1] T. Kuhn,[4] and V. M. Axt[1]

[1]*Lehrstuhl für Theoretische Physik III, Universität Bayreuth, 95440 Bayreuth, Germany*
[2]*Department of Physics, University of Ottawa, Ottawa, Ontario, Canada K1N 6N5*
[3]*ITMO University, St. Petersburg, 197101, Russia*
[4]*Institut für Festkörpertheorie, Universität Münster, 48149 Münster, Germany*

We investigate the degree of entanglement quantified by the concurrence of photon pairs that are simultaneously emitted in the biexciton-exciton cascade from a quantum dot in a cavity. Four dot-cavity configurations are compared that differ with respect to the detuning between the cavity modes and the quantum dot transitions, corresponding to different relative weights of direct two-photon and sequential single-photon processes. The dependence of the entanglement on the exciton fine-structure splitting δ is found to be significantly different for each of the four configurations. For a finite splitting and low temperatures, the highest entanglement is found when the cavity modes are in resonance with the two-photon transition between the biexciton and the ground state and, in addition, the biexciton has a finite binding energy of a few meV. However, this widely used configuration is rather strongly affected by phonons such that other dot-cavity configurations, that are commonly regarded as less suited for obtaining high degrees of entanglement, become more favorable already at temperatures on the order of 10 K and above. If the cavity modes are kept in resonance with one of the exciton-to-ground-state transitions and the biexciton binding energy is finite, the entanglement drastically drops for positive δ with rising temperatures when T is below $\simeq 4$ K, but is virtually independent of the temperature for higher T.

I. INTRODUCTION

Entangled photon pairs can be used as the fundamental building blocks for a wide range of applications in quantum communications, quantum cryptography, or quantum computation [1–3]. Furthermore, entanglement can be used to test fundamentals of quantum mechanics, e.g., by revealing violations of Bell's inequality [1,4]. Different devices and protocols for the generation of entangled photon pairs have been proposed. A well-established and especially attractive way of producing (polarization) entangled photon pairs is the emission of photon pairs via the biexciton cascade in semiconductor quantum dots (QDs) inside a microcavity which enhances the light collection efficiency [5–12]. One special advantage of using semiconductor quantum dots is the possibility to generate triggered [5–7] or even on-demand [10,11,13] entangled photon pairs which is of utmost importance for applications.

Entanglement generation from the biexciton cascade is possible since the biexciton can decay via two paths, first into one of the two exciton states and a photon which can be either polarized horizontally (H) or vertically (V). Subsequently, the exciton generated in the first step can further decay to the QD ground state by emitting a second photon with the same polarization as the photon generated in the biexciton decay. Ideally, the two paths are fully symmetric and the corresponding quantum state is a coherent superposition of the respective amplitudes, resulting in a maximally entangled two-photon state. However, when which-path information is introduced by disturbing the symmetry, e.g., by a finite

fine-structure splitting between the intermediate exciton states, the superposition becomes asymmetric and the entanglement decreases. In principle, it is possible to come close to maximal entanglement in current experiments, either by selecting QDs which naturally have a sufficiently small fine-structure splitting [7,10], by tuning the splitting with external fields [5,6,14], or by applying strain [15]. However, these requirements are rather restrictive. Therefore, it has been proposed to look for less demanding conditions which still allow for a high degree of entanglement. A prominent proposal of this type considers QDs with a sizable biexciton binding energy which are embedded in a microcavity. Besides the possibility of an increased light extraction efficiency, a microcavity offers the advantage that the resonance between the cavity modes and electronic transitions in the dot can be used to enhance, e.g., direct two-photon transitions between the biexciton and the ground state compared to sequential transitions from the biexciton to the exciton or from the exciton to the ground state. Since the direct two-photon transitions do not involve the occupation of exciton states, the fine-structure splitting is effectively not probed, leading to drastically reduced which-path information and therefore increased entanglement [16,17]. When the cavity mode is tuned to the two-photon resonance, a finite biexciton binding energy is typically favorable for entanglement since it shifts the sequential single-photon transitions further away from resonance.

In order to systematically compare different configurations of cavity and QD transition frequencies, a measure for the entanglement is required. A widely accepted measure is the

concurrence, which has a one-to-one correspondence to the entanglement of formation [18]. The latter represents the amount of pure-state entanglement that is at least present in a mixed state described by a given density matrix. The concurrence has the advantage that it can be directly calculated from the values of the reduced density matrix of the bipartite system for which the entanglement is to be measured [19]. Here, we focus on the concurrence of simultaneously emitted photon pairs which, albeit yielding lower signals due to filtering only photons with equal emission times from the cavity, typically show the highest degree of entanglement in experiments [20,21], as well as theoretical calculations [17,22].

Phonons are known to have a tremendous impact on the dynamics of QDs in general [23–33] and on QD-cavity systems in particular [34–43]. Since the pure dephasing induced by acoustic phonons is a major source of decoherence in QDs [24–26], phonons might also limit the entanglement of the two-photon states generated in the biexciton cascade. However, in many studies of the entanglement phonons have either been completely disregarded [13,17] or accounted for by a phenomenological pure dephasing rate [16,44,45]. The description based on rates ignores that phonon-induced pure dephasing leads only to a partial loss of coherence which is nonexponential [46,47] and is the origin of many other non-Markovian effects [37,48,49]. Furthermore, with phenomenological rates the temperature dependence of the degree of entanglement cannot be predicted. An explicit treatment of the phonon impact on the concurrence in the biexciton cascade has been presented in Ref. [50]. However, that paper concentrates on the contributions from the sequential decay of the biexciton via intermediate excitons and misses the competition with the direct two-photon decay to the ground state, which is at the heart of the protocol based on resonant two-photon transitions in systems with finite biexciton binding energies proposed in Ref. [16]. The effect of phonons on the concurrence in the case where two-photon transitions dominate the biexciton decay has been analyzed in Ref. [51] where, however, no selection of simultaneously emitted photon pairs has been considered. As mentioned above, the latter is more favorable for obtaining a high degree of photon entanglement.

In this paper, we investigate the phonon impact on the degree of two-photon polarization entanglement obtained after the decay of a biexciton in a cavity as measured by the concurrence of simultaneously emitted photon pairs. We present a comprehensive comparison of representative configurations of cavity and QD transition frequencies referring to physical situations with different relative importance of two-photon and sequential single-photon pathways, respectively. We find that the phonon influence in combination with the competition between two-photon and one-photon processes leads to strikingly different dependences on the exciton splitting as well as strongly different temperature dependences.

Tuning the cavity to the two-photon resonance and considering a quantum dot with a biexciton binding energy of a few meV is likely to be the most widely studied configuration in the literature because it is commonly expected to yield the highest two-photon entanglement at finite fine-structure splitting. Indeed at low temperatures we confirm this expectation. The main result of the present paper is, however, that the

distinction of the two-photon resonant configuration with finite biexciton binding energy to yield the highest concurrence is lost typically already at temperatures as low as $\sim$10 K.

The article is structured as follows. In Sec. II we specify the model and the method used. We discuss the concurrence of simultaneously emitted photon pairs as the measure of choice when high degrees of entanglement are targeted and explain how this quantity is extracted from the numerical calculations. In Sec. III four configurations with different resonance settings and biexciton binding energies are introduced which enable us to analyze most clearly the competition between direct two-photon and sequential single-photon processes and its impact on the degree of entanglement. In Sec. IV we demonstrate that the phonon impact strongly depends on the considered configuration, resulting in substantially different dependences on the fine-structure splitting and the temperature. Deviations from the standard bell shape dependence on the splitting or asymmetries reflect the competition between single- and two-photon processes. Finally, in the Conclusion, Sec. V, we present a brief summary of the main results of this article.

II. THEORETICAL APPROACH

A. Model

We consider a semiconductor QD embedded in a microcavity which is initially prepared in the biexciton state. The dynamics of the statistical operator of the system $\hat{\rho}$ is determined by the Liouville–von Neumann equation

$$\frac{d}{dt}\hat{\rho} = -\frac{i}{\hbar}[\hat{H}, \hat{\rho}] + \mathcal{L}[\hat{\rho}], \tag{1}$$

where [,] denotes the commutator. The Hamiltonian

$$\hat{H} = \hat{H}_{\text{QD-cav}} + \hat{H}_{\text{QD-phon}} \tag{2}$$

takes into account the interaction between the QD and two linearly polarized cavity modes ($\hat{H}_{\text{QD-cav}}$) as well as a pure dephasing type coupling to a continuum of longitudinal acoustic (LA) phonons ($\hat{H}_{\text{QD-phon}}$). The Lindblad operator $\mathcal{L}[\hat{\rho}]$ allows the inclusion of non-Hamiltonian dynamics, i.e., cavity losses due to for example imperfect mirrors. Thus the model contains three parts, which are discussed separately in the following.

The first part describes the coupling between the QD and two linearly polarized cavity modes and is modeled by the Hamiltonian [51]

$$\hat{H}_{\text{QD-cav}} = \hbar\omega_H |X_H\rangle\langle X_H| + \hbar\omega_V |X_V\rangle\langle X_V|$$
$$+ \hbar(2\bar{\omega}_X - \omega_B)|B\rangle\langle B| + \sum_{\ell=H,V} \hbar\omega_\ell^c \hat{a}_\ell^\dagger \hat{a}_\ell + \hat{\mathcal{X}}, \tag{3}$$

where the interaction part is given by

$$\hat{\mathcal{X}} = -g(|G\rangle\langle X_H|\hat{a}_H^\dagger + |X_H\rangle\langle B|\hat{a}_H^\dagger$$
$$+ |G\rangle\langle X_V|\hat{a}_V^\dagger - |X_V\rangle\langle B|\hat{a}_V^\dagger) + \text{H.c.} \tag{4}$$

Here, the four states of the QD are represented by the biexciton state $|B\rangle$, the two possible exciton states $|X_H\rangle$ and $|X_V\rangle$, and the ground state $|G\rangle$. The exciton states as well as the two photon modes are labeled with H (horizontal

polarization) and V (vertical polarization). The bosonic operator $\hat{a}^\dagger_{H/V}$ creates one photon with frequency $\omega^c_{H/V}$ and corresponding polarization H or V and H.c. denotes the Hermitian conjugate. The light-matter coupling strength g is assumed to be equal for all couplings and the dipole approximation as well as the rotating-wave approximation are used. The energies $\hbar\omega_{H/V}$ denote the exciton energies, while the energy of the biexciton is $\hbar(2\bar{\omega}_X - \omega_B)$, where $E_B = \hbar\omega_B$ represents the biexciton binding energy and $\hbar\bar{\omega}_X = \hbar(\omega_H + \omega_V)/2$ is the mean exciton energy. The energy of the ground state is set to zero. When the QD is initially prepared in the biexciton state without any photons present in the two orthogonal cavity modes, the total number of excitations (number of excitons plus number of photons) is initially two. Since without losses the excitation number is conserved, the number of states that are accessible by the coherent QD-cavity coupling is restricted to five states of the form $|\chi, n_H, n_V\rangle$ with χ denoting the QD state and $n_{H/V}$ the number of photons present in the corresponding cavity mode. To be specific, these five states are given by $|B, 0, 0\rangle$, $|X_H, 1, 0\rangle$, $|X_V, 0, 1\rangle$, $|G, 2, 0\rangle$, and $|G, 0, 2\rangle$. States with lower excitation numbers become accessible via cavity losses by removing photons from the system. However, we do not need to consider these states explicitly in our calculations, first, because the corresponding dynamical variables do not couple back to the dynamics of the above five states and, second, only states with at least two photons contribute to the concurrence [19,22], which is the target quantity of our analysis.

In Fig. 1 a schematic sketch of the biexciton cascade with the two cavity modes is shown. Because of the exchange interaction the two exciton states X_H and X_V are split by the fine-structure splitting δ symmetric to the mean exciton energy $\hbar\bar{\omega}_X$. Thus the energy of the horizontally polarized exciton state is $\hbar\omega_H = \hbar\bar{\omega}_X + \delta/2$ and the energy of the vertically polarized exciton state is $\hbar\omega_V = \hbar\bar{\omega}_X - \delta/2$. Furthermore, a possible biexciton binding energy E_B can lower the energy of the biexciton state with respect to $2\hbar\bar{\omega}_X$. In general, the energies of the two orthogonally polarized cavity modes do not match any of the electronic transition energies of the QD.

In addition to the light-matter interaction also a pure dephasing type coupling to a continuum of LA phonons is included in the model via

$$\hat{H}_{\text{QD-phon}} = \sum_{\mathbf{q}} \hbar\omega_{\mathbf{q}}\hat{b}^\dagger_{\mathbf{q}}\hat{b}_{\mathbf{q}} + \sum_{\mathbf{q},\chi} n_\chi(\gamma_{\mathbf{q}}\hat{b}^\dagger_{\mathbf{q}} + \gamma^*_{\mathbf{q}}\hat{b}_{\mathbf{q}})|\chi\rangle\langle\chi|. \tag{5}$$

Here, n_χ denotes the number of excitons in the different QD states $|\chi\rangle$ and $\gamma_{\mathbf{q}}$ is the coupling constant. We account for deformation potential coupling which is known to dominate for GaAs-type QDs [46] and $\hat{b}^\dagger_{\mathbf{q}}$ are bosonic creation operators for phonons with energy $\hbar\omega_{\mathbf{q}}$ in the mode with wave vector $\mathbf{q}$.

Finally, possible cavity losses of photons are taken into account using the Lindblad operator

$$\mathcal{L}_{\text{cav}}[\hat{\rho}] = \sum_{\ell=H,V} \frac{\kappa_\ell}{2}(2\hat{a}_\ell\hat{\rho}\hat{a}^\dagger_\ell - \hat{\rho}\hat{a}^\dagger_\ell\hat{a}_\ell - \hat{a}^\dagger_\ell\hat{a}_\ell\hat{\rho}), \tag{6}$$

which allows the inclusion of non-Hamiltonian dynamics while preserving the physically important properties of the statistical operator [52]. In the following we assume the loss rates for the two differently polarized cavity modes to be equal ($\kappa_H = \kappa_V = \kappa$).

Longitudinal optic (LO) phonons have been shown to affect the two-photon entanglement by multiphonon transitions to the continuum of wetting layer states [53]. This mechanism is, however, negligible for temperatures below ~80 K. Since all major findings of the present paper occur at much lower temperatures, effects of LO phonons can safely be disregarded. Nevertheless, we show in the present paper a few results for temperatures above 80 K in order to illustrate how the contribution of LA phonons behaves at elevated temperatures.

B. Method

Equation (1) is numerically solved by using a real-time path-integral (PI) approach. As almost all modern implementations of the real-time PI concept, also our simulations are based on an iteration scheme for the so called *augmented density matrix* which was introduced in the pioneering work of Makri and Makarov [54,55]. This scheme exploits the finiteness of the environment memory to obtain an efficient algorithm for performing efficiently a numerically complete summation over the paths. A specialization of these general ideas to QDs with a super-Ohmic pure-dephasing coupling to a continuum of phonons has been worked out, e.g., in Ref. [56]. Important for the present investigations are two recent extensions of the standard PI treatment. The first is a translation of the PI method from the usual Hilbert space formulation to Liouville space [57]. In this way, the non-Hamiltonian contributions to the dynamics, like, e.g., Lindblad-type loss rates, can be accounted for in a natural way while still treating the phonons without approximation to the model. The second is a reformulation of the PI algorithm such that now a partially summed augmented density matrix is iterated. This reformulation is described in detail in the supplement of Ref. [58], which in principle contains all information about the actually used PI method. For systems like QDs coupled to cavities the reformulation reduces the numerical demands by many orders of magnitude and thus numerically complete simulations for such systems would not be feasible without it. The numerical efficiency might be
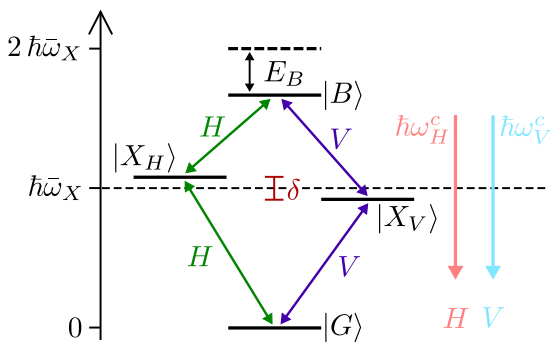

FIG. 1. Schematic sketch of the biexciton cascade with a fine-structure splitting δ between the two exciton states, a mean exciton energy $\hbar\bar{\omega}_X = \hbar(\omega_H + \omega_V)/2$, and a possible biexciton binding energy E_B. In general, both cavity modes can be detuned from the electronic transitions of the QD.
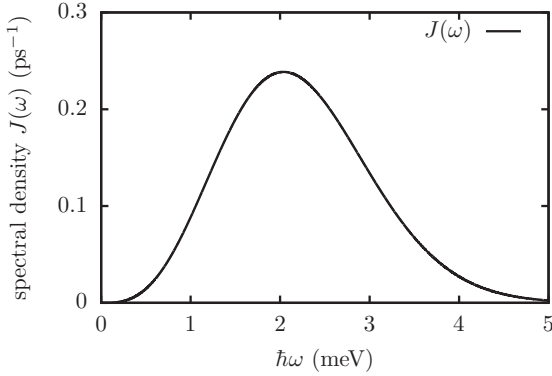
FIG. 2. Phonon spectral density $J(\omega)$ for a spherical GaAs QD with an electron (hole) geometrical confinement length $a_e = 3$ nm ($a_h = a_e/1.15$). The deformation potential constants and the mass density, as well as the sound velocity for a GaAs QD are taken from Ref. [60] and are listed in Table I. An explicit formula for $J(\omega)$ can be found in Ref. [56] or Ref. [57].

further boosted by using recently developed tensor-network techniques [59] which could further extend the applicability of PI methods in future work.

We consider a spherically symmetric GaAs QD with a harmonic oscillator confinement resulting in an electron (hole) confinement length $a_e = 3$ nm ($a_h = a_e/1.15$). The deformation potential constants and the mass density as well as the sound velocity are taken from the literature [60] and enter the phonon spectral density

$$J_{\chi\chi'}(\omega) = n_\chi n_{\chi'} J(\omega), \tag{7}$$

with

$$J(\omega) = \sum_{\mathbf{q}} \gamma_{\mathbf{q}} \gamma_{\mathbf{q}}^* \delta(\omega - \omega_{\mathbf{q}}) \tag{8}$$

appearing in the memory kernels of the PI approach [57]. It is worthwhile to note that all phonon related influences on the dynamics of the QD-photon system enter only via $J(\omega)$. Thus the assumption of a symmetric QD does not entail a loss of generality as long as only the dynamics of QD and photons are concerned, since as shown in Ref. [61] for any QD (not necessarily assuming a symmetric confinement) it is always possible to find a symmetric QD with the same $J(\omega)$.

In Fig. 2 $J(\omega)$ is depicted for the chosen parameters of the QD. For low frequencies $J(\omega)$ approaches zero $\sim\omega^3$ as can be seen from the explicit expression for the deformation potential coupling [46]. We are therefore dealing with a coupling of super-Ohmic type which is responsible for striking non-Markovian effects such as the nonexponential partial loss of coherence [46,47]. Furthermore, we note a pronounced maximum at about 2 meV that is the origin of the resonant structure of the phononic response [24,62].

Assuming that initially the phonons are in thermal equilibrium and the electronic system is prepared in the biexciton state without photons, our PI approach delivers the time dependence of the reduced density matrix $\hat{\bar{\rho}}$ in the subspace spanned by the five states $|B, 0, 0\rangle$, $|X_H, 1, 0\rangle$, $|X_V, 0, 1\rangle$, $|G, 2, 0\rangle$, and $|G, 0, 2\rangle$, where the phonon degrees of freedom have been traced out.

C. Concurrence

As a measure for the degree of entanglement we use the concurrence of simultaneously emitted photons that for brevity will be referred to in the following simply as the *concurrence*. This quantity can be directly calculated from the time-averaged values of the reduced density matrix $\hat{\bar{\rho}}$ of the system [22,45,53]. The time-dependent populations of the two states where two photons are present and the coherences between these states are given by

$$\rho_{mn}(t) = \langle mm|\hat{\bar{\rho}}(t)|nn\rangle, \tag{9}$$

with $m, n \in \{H, V\}$. Here $|HH\rangle := |G, 2, 0\rangle$ is the state with two horizontally polarized photons and $|VV\rangle := |G, 0, 2\rangle$ denotes the state with two vertically polarized photons. The corresponding time-averaged quantities $\bar{\rho}_{mn}$ are calculated according to

$$\bar{\rho}_{mn} = \frac{1}{T_{\text{av}}} \int_0^{T_{\text{av}}} \rho_{mn}(t) dt. \tag{10}$$

From these quantities, the concurrence C is derived as [19,22]

$$C = 2 \left| \bar{\rho}_{HV}^N \right|, \tag{11}$$

where all quantities entering the normalized two-photon coherence

$$\bar{\rho}_{HV}^N = \frac{\bar{\rho}_{HV}}{\bar{\rho}_{HH} + \bar{\rho}_{VV}} \tag{12}$$

are evaluated in the limit $T_{\text{av}} \to \infty$. We average the time-dependent quantities $\rho_{mn}(t)$ until all excitations have left the cavity and the system has reached its ground state $|G, 0, 0\rangle$. Experimentally, the concurrence C is accessible [20,21] by measuring the two-photon correlation function $G_{ij,kl}^{(2)}(t, \tau)$ and extrapolating towards zero delay time $\tau = 0$.

Before presenting the results of our calculations, let us briefly comment on different measures to quantify the entanglement in the biexciton cascade and the impact of the cavity loss rate (a more extended discussion of these issues can be found, e.g., in Ref. [22]). Indeed, for an analysis of polarization entanglement there is a variety of choices for selecting photon pairs for which to calculate the concurrence. Probably the most widely used choice is to inspect the concurrence of all photon pairs that are detected in coincidence measurements without discriminating between the detection times of the two photons. The obvious advantage of this scheme is the high signal yield. For the corresponding theoretical description, the calculation of the two-time two-photon correlation function $G^{(2)}(t, \tau)$ is required [16,22,51,63,64]. Another approach is to consider the concurrence of frequency filtered coincidence measurements [17,63] or for a subsystem of the detected photons, e.g., by only selecting photon pairs with equal emission times from the cavity [17,45]. As stated previously, we follow the latter scheme and focus on the concurrence of simultaneously emitted photon pairs. The reasons behind this choice are presented in the following.

The concurrence calculated for a selected subset of photons is in general quantitatively as well as qualitatively different from the concurrence obtained for another photon subset. For example, it has been found [22] that the concurrence of simultaneously emitted photons shows qualitatively different
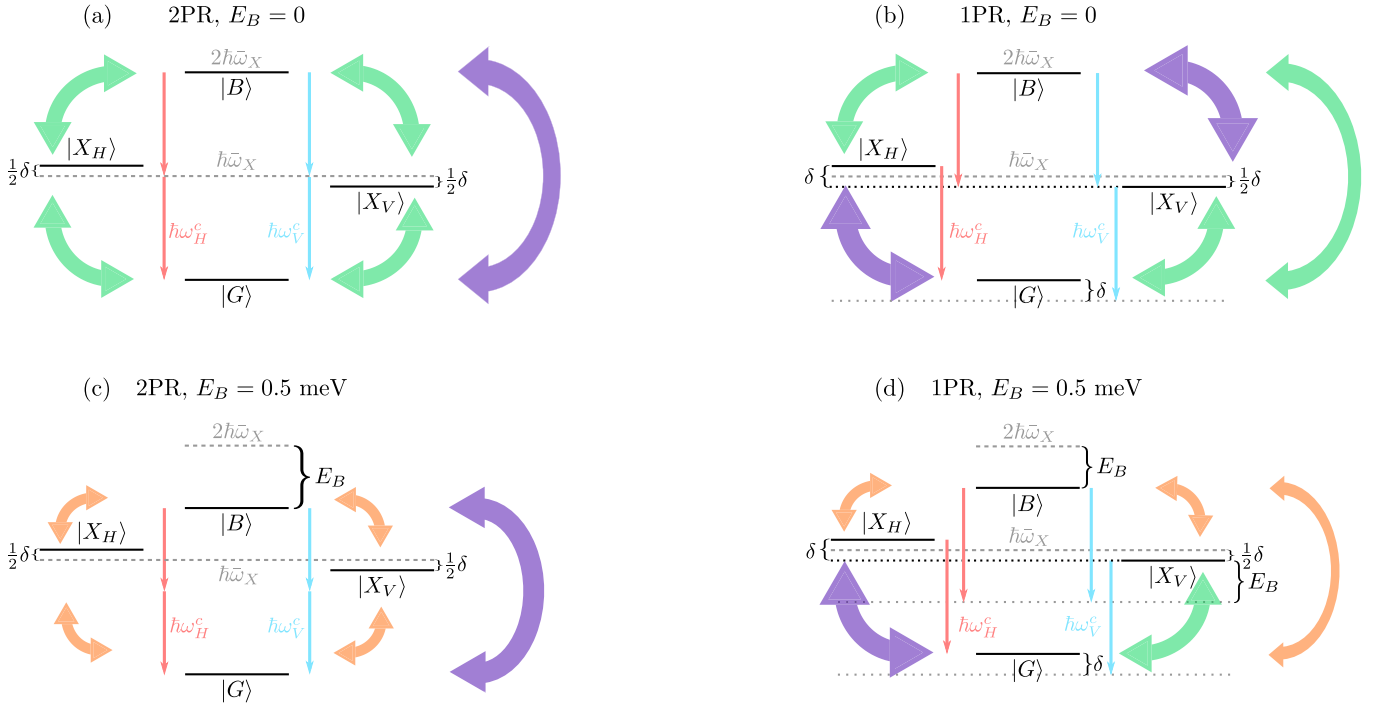
FIG. 3. Schematic sketches of the four different configurations of the QD-cavity system studied in this paper. Big curved purple arrows indicate transitions that are resonant with the corresponding cavity mode. Transitions which are detuned on the order of the fine-structure splitting δ are represented by medium-sized curved green arrows and small curved orange arrows indicate transitions where the detuning is on the order of the biexciton binding energy E_B.

trends with varying cavity losses than observed for photon pairs without selection of the emission time (an increase of the concurrence with rising loss rate is turned into a decrease). Thus these two concurrences calculated for different photon subsets cannot be equivalent measures for the same physical quantity. Nevertheless, in both cases, the phonon impact is reduced with rising loss rate and the concurrence approaches its phonon-free value in the limit of infinite losses [22]. This can be explained by noting that the phonon impact requires a finite time to develop. The loss rate limits the available time window and when the latter becomes too small the phonons cannot efficiently act on the QD degrees of freedom. Besides the different trends regarding the cavity loss rate, experiments [20,21] as well as theory [17,22] indicate that simultaneously emitted photons exhibit a significantly higher degree of entanglement and are much less affected by the which-path information introduced by a finite fine-structure splitting than photon pairs detected without emission time selection. In particular, the concurrence of simultaneously emitted photons represents an upper limit for the achievable degree of entanglement in the latter situation. Since we are interested in the highest possible degree of entanglement for a given QD-cavity configuration we solely concentrate on the concurrence of simultaneously emitted photons. Detecting photon pairs without emission time filtering, on the other hand, would maximize the emission efficiency.

III. DIFFERENT CAVITY CONFIGURATIONS

In this section, four configurations of the QD-cavity system are considered which differ in the value of the biexciton

binding energy E_B as well as in the way the cavity modes are energetically positioned. Throughout this paper, the two orthogonal linearly polarized cavity modes are assumed to have the same frequency ($\omega_H^c = \omega_V^c$). The main difference between the configurations is the position of the cavity modes with respect to the QD transitions. When the cavity modes are kept in resonance with the direct two-photon transition to the biexciton, such that $\omega_{H/V}^c = \bar{\omega}_X - \omega_B/2$, we refer to the configuration as *two-photon resonant* (2PR). In contrast, if the cavity mode frequencies are chosen to match the transition frequency of one of the excitons (without loss of generality we choose the H exciton), such that $\omega_{H/V}^c = \omega_H$, we refer to the configuration as *one-photon resonant* (1PR). In both configurations, we further distinguish between the case of a vanishing biexciton binding energy and a finite value of the latter (in this paper, we consider finite values 0.5 meV $\leqslant$ $E_B \leqslant 6$ meV). Note that if a finite biexciton binding energy is introduced, the energy of the biexciton state is no longer the sum of the energies of the two exciton states.

In Fig. 3 schematic sketches of the 2PR and 1PR configuration with and without a biexciton binding energy are shown. In order to highlight the difference concerning the respective resonance situations, QD transitions are marked by three types of curved arrows in the figure that correspond to different detunings of these transitions from the cavity mode frequency (red or blue straight arrow). Resonant transitions are represented by big curved purple arrows. The medium-sized curved green arrows denote transitions which are detuned on the order of the fine-structure splitting δ and strongly off-resonant transitions with a detuning on the order of the biexciton binding energy E_B (typically

much larger than δ) are indicated by small curved orange arrows.

The special characteristic of the 2PR configurations [Figs. 3(a) and 3(c)] is that the $|G\rangle \leftrightarrow |B\rangle$ transition is resonant with a direct two-photon emission or absorption process, respectively. Therefore, there are two competing channels for the biexciton decay. The biexciton state can decay either via two sequential single-photon emission processes via the exciton states or via a coherent two-photon process from the biexciton state directly to the ground state. For vanishing E_B [Fig. 3(a)] the energies of the exciton states $\hbar\omega_{H/V} = \hbar\bar{\omega}_X \pm \delta/2$ are detuned by $\pm\delta/2$ from the cavity modes which are fixed at $\omega_{H/V}^c = \bar{\omega}_X$. Thus all four electronic transitions involved in the sequential emission paths are weakly detuned by half the value of the fine-structure splitting δ. The direct two-photon processes stay resonant in the 2PR configuration when a finite binding energy E_B is introduced as the cavity modes are changed accordingly. But the four electronic transitions involving an exciton state become strongly detuned on the order of half the biexciton binding energy $E_B/2$ [Fig. 3(c)] when E_B is finite.

In the 1PR configurations [Figs. 3(b) and 3(d)], the $|X_H\rangle \leftrightarrow |G\rangle$ transition is chosen to be resonant with the corresponding cavity mode. Therefore, in the case of a vanishing biexciton binding energy [Fig. 3(b)], the $|X_V\rangle \leftrightarrow |B\rangle$ transition is also resonant, whereas the two remaining cascade transitions as well as the direct two-photon processes are detuned by the value of the splitting δ. Introducing a finite biexciton binding energy does not change the situation for the exciton-to-ground-state transitions but the two transitions between the biexciton state and one of the exciton states as well as the direct two-photon processes are now strongly off resonant and detuned on the order of E_B [cf. Fig. 3(d)].

IV. RESULTS

In this section we analyze how the degree of entanglement between the two states with two photons ($|HH\rangle$ and $|VV\rangle$) is affected by various system parameters. As mentioned before, the system is initially prepared in the biexciton state without any photons and the phonons are assumed to be initially in thermal equilibrium. If not stated otherwise, a light-matter coupling strength $g = 0.1$ meV, a finite exciton splitting $\delta = 0.1$ meV, a biexciton binding energy $E_B = 0.5$ meV, and a cavity loss rate $\kappa = 0.025$ ps^{-1} corresponding to a cavity quality factor $Q \approx 45\,000$ are used. Table I displays these default values and all other material parameters used for the numerical calculations. The given value for the biexciton binding energy E_B is the difference between twice the polaron shifted mean exciton energy and the polaron shifted biexciton energy. In the corresponding phonon-free situation the value for E_B is kept the same in order to compare QD-cavity systems with identical energetic detunings between the cavity modes and the QD transition energies. After quantifying the competition between direct two-photon and sequential single-photon processes in Sec. IV A, the dependence of the concurrence on the exciton fine-structure splitting is investigated in Sec. IV B. Finally, we discuss the temperature dependence of the concurrence for fixed splittings in Sec. IV C.

A. Competition between direct two-photon and sequential single-photon transitions

As pointed out before, e.g., by Schumacher *et al.* [16] or del Valle [17], the competition between the direct two-photon processes from the biexciton state to the ground state and the sequential single-photon processes via the exciton states is of utmost importance for the concurrence. Obviously, by considering configurations with different resonance situations, in particular when switching between 2PR and 1PR configurations, we are comparing situations with different relative importance of two-photon and sequential single-photon processes. To quantify the relative impact of these processes, we introduce the quantity

$$r_{2P/1P} = \frac{|\bar{\rho}_{B,HH}| + |\bar{\rho}_{B,VV}|}{\bar{\rho}_{X_H} + \bar{\rho}_{X_V}}, \tag{13}$$

i.e., $r_{2P/1P}$ is a ratio where the numerator is derived from the coherences $\rho_{B,HH} = \langle B, 0, 0|\hat{\bar{\rho}}|G, 2, 0\rangle$ and $\rho_{B,VV} = \langle B, 0, 0|\hat{\bar{\rho}}|G, 0, 2\rangle$ between the biexciton and the ground state with either two horizontally or vertically polarized photons. The denominator represents the total exciton occupation $\rho_{X_H} + \rho_{X_V}$, where ρ_{X_H} and ρ_{X_V} denote the occupations of the states $|X_H, 1, 0\rangle$ and $|X_V, 0, 1\rangle$, respectively. The bar over these quantities indicates a time averaging as introduced in Eq. (10).

The coherences between the biexciton state and the two states containing the ground state represent a measure for the direct two-photon processes. Note that by inspecting the equations of motion for all elements of the reduced density matrix it becomes apparent that only the equations for these coherences introduce a resonance when the biexciton-to-ground-state transition frequency matches twice the photon frequency. This is the distinctive property of a two-photon process. In contrast, the characteristic feature of sequential single-photon emission processes is the occupation of the intermediate electronic states, in our case the excitons. Thus the total exciton occupation reflects the importance of sequential processes. Altogether, this justifies that the ratio $r_{2P/1P}$ is a possible measure for the relative importance of the direct

TABLE I. Material parameters for the GaAs quantum dot and the default values for the system parameters: light-matter coupling strength g, exciton splitting δ, biexciton binding energy E_B, and cavity loss rate κ. If not stated otherwise these default values are used for the calculations.

| Parameter		Value
Electron geometrical confinement length (nm)	a_e	3.0
Hole geometrical confinement length (nm)	a_h	$a_e/1.15$
Mass density (kg/m^3)	ρ	5370 [65]
Longitudinal sound velocity (m/s)	c_s	5110 [65]
Electron deformation potential constant (eV)	D_e	7.0 [66]
Hole deformation potential constant (eV)	D_h	-3.5 [66]
Light-matter coupling strength (meV)	g	0.1
Exciton fine-structure splitting (meV)	δ	0.1
Biexciton binding energy (meV)	E_B	0.5
Cavity loss rate (ps^{-1})	κ	0.025
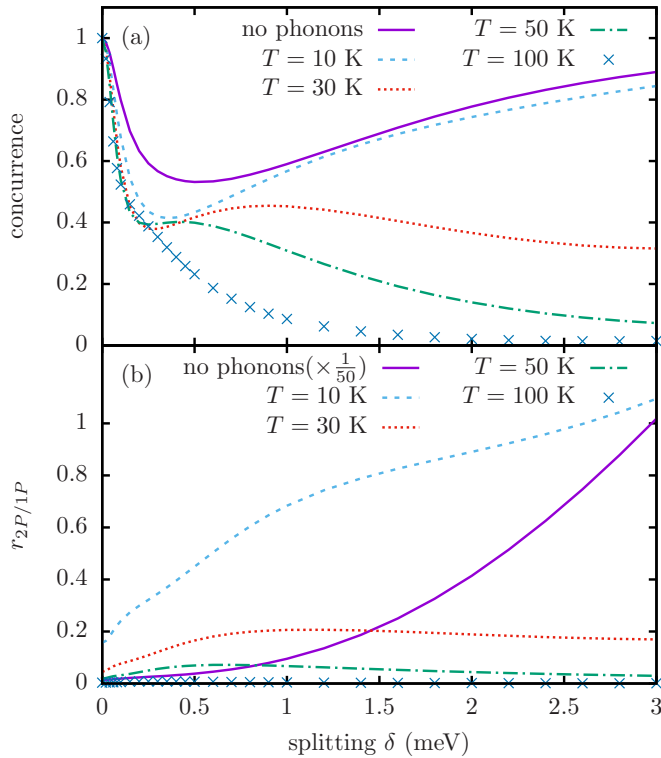
FIG. 4. Comparison of the concurrence [panel (a)] and a measure for the relative importance of two-photon and sequential single-photon processes $r_{2P/1P}$ [panel (b)] as a function of the exciton splitting δ. Different temperatures as well as the limit without phonons are considered. Note that $r_{2P/1P}$ is scaled by the factor $1/50$ in the phonon-free case. The cavity modes are arranged in the 2PR configuration and a vanishing biexciton binding energy is assumed.

two-photon processes compared with the sequential single-photon processes.

Figure 4 displays the concurrence [panel (a)] along with $r_{2P/1P}$ [panel (b)] as a function of δ. The analysis is carried out exemplarily for the 2PR configuration with $E_B = 0$ for four temperatures as well as for the phonon-free case. The plotted range for the fine-structure splitting is chosen larger than usually covered by typical QDs as the role of the two-photon processes can be better highlighted on this extended scale.

As can be seen in Fig. 4(a), the concurrence exhibits a nonmonotonic dependence on the exciton splitting for low temperatures and the phonon-free situation. This behavior can be traced back to the competition between two-photon and sequential single-photon processes. Recalling that in the 2PR configuration the two-photon processes are chosen to be always resonant independent of δ, it follows that any which-path information introduced by the fine-structure splitting affects only the sequential single-photon processes. Figure 4(b) reveals a dominance of sequential emission processes for small exciton splittings. Therefore, the concurrence decreases with rising $|\delta|$ in the small splitting limit since (i) the which-path information is larger for larger $|\delta|$ and (ii) it efficiently affects the concurrence due to the dominance of sequential single-photon processes.

As the splitting increases further, $r_{2P/1P}$ rises because the single-photon processes become more off-resonant and

thus the relative importance of two-photon processes grows, since the latter are always resonant. When either the interaction with the phonons is switched off or the temperature is low enough, $r_{2P/1P}$ increases strongly for larger exciton splittings, indicating a dominance of two-photon processes [cf. Fig. 4(b) for $T = 10$ K]. As a result, the concurrence rises and eventually approaches unity because the which-path information introduced by the exciton splitting is no longer tested. The local maximum of the concurrence seen at higher temperatures of 30 K and 50 K can also be understood with the help of $r_{2P/1P}$ since it shows a similar behavior. Hence the nonmonotonic behavior of the concurrence is a result of the competition between the coherent direct two-photon and sequential single-photon emission processes.

At higher temperatures the relative importance of the sequential emission processes is raised, as can be seen in Fig. 4(b). As the electronic transitions become detuned from the corresponding cavity modes the sequential single-photon processes are assisted by phonon absorption and emission processes to compensate the energy differences, an effect which is enhanced with increasing temperature. In addition, for larger exciton splittings the phonon spectral density is effectively probed at higher values of ω (on the order of δ), resulting in a stronger phonon influence on the system (cf. Fig. 2). Furthermore, coherences, such as the ones relevant for the two-photon processes, are more strongly affected by phonon-induced decoherence than occupations. The combination of these effects explains why $r_{2P/1P}$ decreases for larger splittings at higher temperatures and the concurrence approaches zero.

B. Dependence of the concurrence on the exciton splitting for different configurations

For all four QD-cavity configurations illustrated in Fig. 3, the dependence of the concurrence on the exciton splitting is shown in Fig. 5. First of all, for a vanishing fine-structure splitting, the concurrence is strictly one regardless of the phonon influence since the system is completely symmetric with respect to $H \leftrightarrow V$ so that no which-path information is introduced. This result was also found on the basis of a phenomenological rate equation approach for the phonon-induced pure dephasing [45].

With increasing $|\delta|$ the concurrence decreases, reflecting the increase of which-path information. Furthermore, phonons generally reduce the concurrence for a given splitting, an effect which typically becomes more pronounced at higher temperatures. This can be understood by noting that phonons typically enhance the differences between different pathways and thus increase the which-path information. To see this, we first recall that, when the electronic transitions of the QD are detuned from the corresponding cavity modes, the photon emission processes are assisted by phonon emission and absorption processes to compensate the energy differences. For a finite splitting, depending on the configuration, the two sequential emission paths differ either in the values or the order of the detunings and are therefore influenced differently by the phonons. For example, in the 2PR configuration with $\delta > 0$ and $E_B = 0$, the sequential emission process of two horizontally polarized photons is at first assisted by phonon
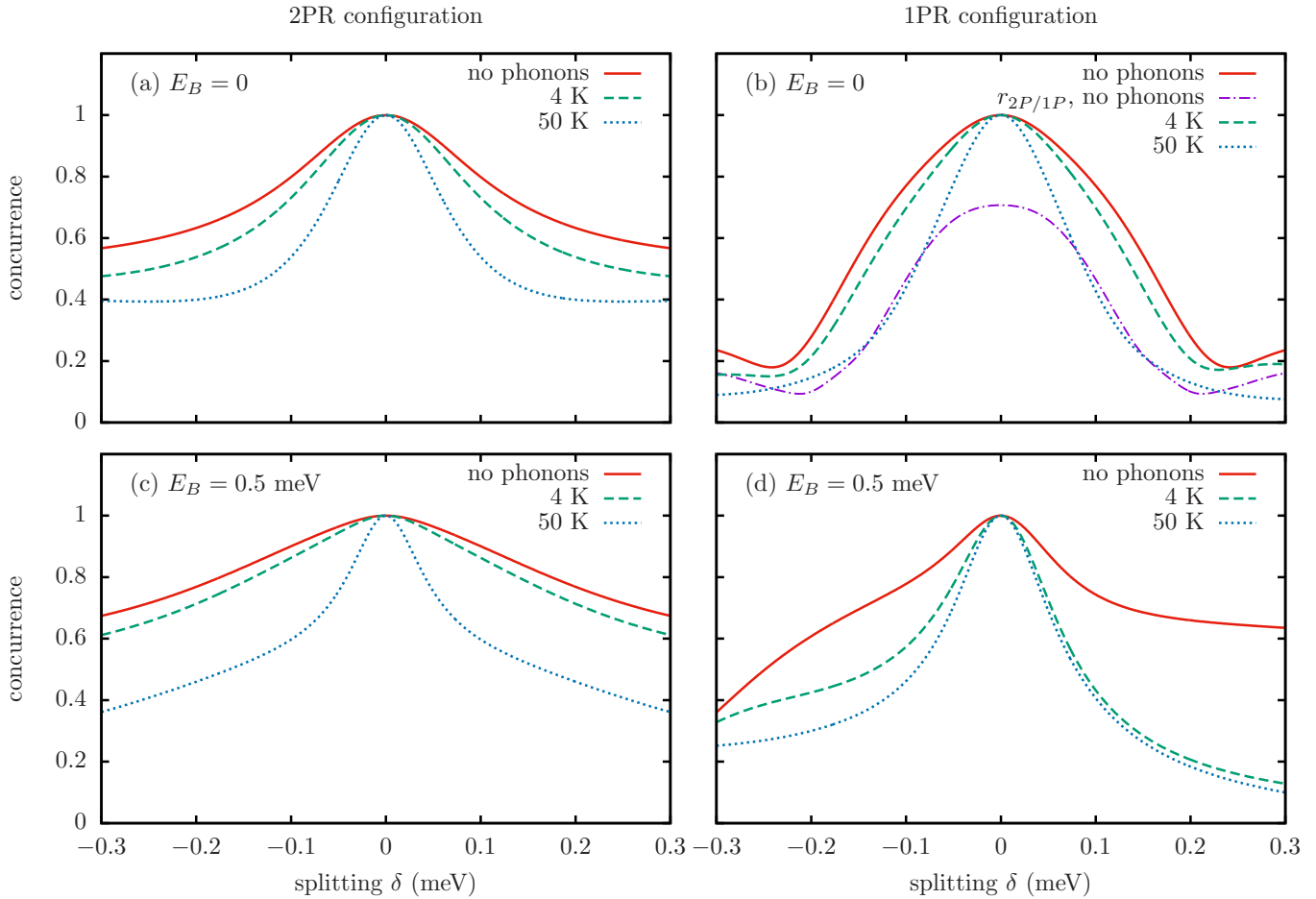
2PR configuration   1PR configuration

FIG. 5. Impact of the exciton splitting δ on the concurrence for all four cavity configurations introduced in Sec. III and depicted in Fig. 3. Results are shown for two different temperatures and without phonons. Panel (b) additionally displays the ratio $r_{2P/1P}$ for the phonon-free case.

absorption and in the second step phonon emission occurs for the exciton-to-ground-state transition. This order is reversed for the sequential emission path for two vertically polarized photons. Obviously, this enhances the difference between both pathways compared with the phonon-free case at least at low temperatures where emission and absorption are noticeably different. In general, as discussed in Sec. IV A, with increasing temperature more phonons are thermally excited and sequential one-photon transitions can be more efficiently bridged by phonon-assisted processes. In combination with the increased phonon-induced decoherence, this leads to a smaller impact of two-photon transitions and therefore a lower concurrence at higher temperatures.

Despite these common tendencies, the detailed dependences of the concurrence on the exciton splitting differ significantly in the respective configurations. For $E_B = 0$, the results for the 2PR configuration [Fig. 5(a)] and the 1PR configuration [Fig. 5(b)] are qualitatively similar for small $|\delta|$ but differ strongly for larger detunings. This can be understood by consulting Fig. 3(a) and Fig. 3(b) which reveals that these configurations become identical in the limit of vanishing splitting. The corresponding concurrences are thus very close to each other for small exciton splittings.

The deviation for larger splittings between the two configurations can be explained by the competition between the

coherent direct two-photon and the sequential single-photon processes. In the 2PR configuration, the relative importance of two-photon processes rises with increasing $|\delta|$ as already discussed in Sec. IV A. However, compared with the 2PR case, the influence of two-photon processes is reduced in the 1PR configuration since they are detuned by the exciton splitting [cf. Fig. 3(b)]. Thus the concurrence in the 2PR configuration is significantly higher for larger $|\delta|$ than in the 1PR configuration.

Nevertheless, the competition between two-photon and single-photon processes also influences the 1PR configuration where the concurrence exhibits a local minimum for low temperatures as well as without phonons, which means that this is not a phonon-induced effect. In fact, phonons cause this minimum to eventually disappear, as can be seen in Fig. 5(b) at 50 K. Figure 5(b) reveals that the nonmonotonic behavior of the concurrence reflects the behavior of $r_{2P/1P}$. Compared with the 2PR configuration [cf. Fig. 4(a)], here the local minima are found already at smaller $|\delta|$ because the electronic transitions of the QD are now detuned by the value of δ, whereas the detuning is only $\delta/2$ in the 2PR configuration. Furthermore, although the value of $r_{2P/1P}$ at vanishing splitting without phonons in Fig. 5(b) is the same as in Fig. 4(b) (note the different scaling in the latter figure), the ratio between two- and one-photon processes is a decreasing function of δ in

the 1PR configuration since a finite splitting also causes a detuning of the direct two-photon transitions in this case. This is in contrast to the 2PR case in Fig. 4, where $r_{2P/1P}$ rises with increasing δ in the phonon-free case.

Next, we consider the results for the 2PR configuration with a finite biexciton binding energy $E_B = 0.5$ meV plotted in Fig. 5(c). In the phonon-free situation and for a temperature of 4 K the concurrence decreases only weakly with increasing $|\delta|$, but at $T = 50$ K it is drastically reduced at finite $|\delta|$. Therefore, a finite biexciton binding energy in the 2PR configuration significantly affects the concurrence [cf. Fig. 5(a)] since it leads to strongly detuned biexciton-to-exciton and exciton-to-ground-state transitions, while the direct two-photon processes remain resonant. Thus, without phonons, the direct two-photon processes are strongly enhanced compared with the sequential single-photon processes, resulting in a significantly higher concurrence that is much less influenced by the splitting.

On the other hand, in the 2PR configuration with finite E_B, phonons with energies $\hbar\omega_{\mathbf{q}} \simeq E_B/2$ are required to bridge the detunings of the sequential transitions. In contrast, for vanishing E_B, the required phonon energies are given by the much smaller value of $|\delta|/2$. At the same time, the relative weight of the phonon influence is proportional to $J(\omega)$. Figure 2 shows that $J(\frac{E_B}{2\hbar}) > J(\frac{\delta}{2\hbar})$ for $E_B = 0.5$ meV and $|\delta| < 0.3$ meV, i.e., the phonon influence and thus the temperature dependence of the concurrence is stronger for a finite biexciton binding energy. This results in the significantly larger difference of the concurrence for 4 K and 50 K in Fig. 5(c) compared with curves for the same parameters but vanishing binding energy in Fig. 5(a). We note in passing that, keeping the splitting in the typical range $|\delta| < 0.3$ meV, for rather high values of the biexciton binding energy the relation $J(\frac{E_B}{2\hbar}) > J(\frac{\delta}{2\hbar})$ is reversed (cf. Fig. 2). However, this limit is usually not reached since typical biexciton binding energies stay below ~ 6 meV.

In contrast to the configurations discussed up to now, the interaction with phonons in the 1PR configuration with a finite biexciton binding energy, depicted in Fig. 5(d), drastically reduces the concurrence already at low temperatures. In this situation, both biexciton-to-exciton-transitions are strongly detuned from the corresponding cavity modes. The horizontally polarized exciton-to-ground-state transition is resonant by definition, while the vertically polarized one is detuned by δ. In addition, also the direct two-photon processes are highly off resonant. As all possible electronic transitions starting from the biexciton state are strongly detuned, the initially prepared occupation of the biexciton state decreases only very slowly when phonons are not accounted for. Hence the occupations of the exciton states and the QD ground state with two photons are always very small. In both the H and V pathway the exciton can be reached by emission of a photon only when a phonon with an energy on the order of $\simeq E_B$ is absorbed. At this energy $J(\omega)$ is even larger than in the 2PR configuration with finite E_B where phonons with energies $\simeq E_B/2$ are required, which explains the dramatic drop of the concurrence from the phonon-free case to the values obtained for 4 K. Furthermore, the concurrence is clearly asymmetric with respect to the exciton splitting in this configuration. Especially in the phonon-free case the concurrence decays much stronger with rising $|\delta|$ for negative than for positive δ.

This is due to the fact that for negative δ one comes closer to the condition that the transition from the biexciton to the H exciton is getting in resonance. Since the decay from the H exciton to the ground state is held in resonance in this configuration, the pathway $|B\rangle \rightarrow |X_H, 1, 0\rangle \rightarrow |G, 2, 0\rangle$ is strongly favored compared with $|B\rangle \rightarrow |X_V, 0, 1\rangle \rightarrow |G, 0, 2\rangle$, resulting in low values of the concurrence. Interestingly, for $\delta > 0$ the concurrence decreases only very little when the temperature is raised further from 4 K to 50 K.

In general, the symmetry with respect to δ is found to be another distinguishing feature between the 2PR and the 1PR configuration. In the 2PR configuration, independent of the biexciton binding energy, the concurrence is a symmetric function of the splitting no matter whether phonons are included or not. In contrast, in the 1PR configuration with a finite binding energy, the concurrence always shows an asymmetric dependence on δ. In this situation, changing the sign of δ changes the absolute value of the detuning between the horizontally polarized cavity mode and the corresponding biexciton-to-exciton transition $\Delta_{B,X_H}(\delta) = E_B + \delta$, while the absolute values of the detunings of the remaining sequential transitions are unaffected. The direct two-photon processes are also detuned by the same value $\Delta E_{2P}(\delta) = E_B + \delta$. Since without phonons the dynamics depends only on the absolute values of the detunings between the electronic transitions and their corresponding cavity modes, an asymmetric concurrence is expected, which is also visible when phonons are accounted for. This asymmetry is stronger at low temperatures since there phonon absorption and emission processes are not equally likely. Turning finally to the 1PR configuration with $E_B = 0$, changing the sign of the exciton splitting no longer changes the absolute values of the detunings. Thus, without phonons, the concurrence is once more symmetric and only a slight asymmetry is observed when phonons are included.

We conclude that the competition between single-photon and two-photon processes plays a decisive role for the concurrence. Furthermore, the arrangement of the cavity modes strongly affects the concurrence as one of the competing processes can be either favored or suppressed. Finally, the values of the various detunings depend on the chosen configuration, resulting in different effective phonon influences and very different dependences of the concurrence on the exciton splitting for each of the considered QD-cavity configurations.

C. Temperature dependence of the concurrence at a finite exciton splitting

After the discussion in the last section it is clear that the temperature dependence of the concurrence also differs for each of the four configurations. In this section we investigate in more detail the concurrence as a function of temperature for different fixed values of the exciton splitting.

Figure 6(a) displays the concurrence as a function of the temperature for a typical value of the exciton splitting $\delta = 0.02$ meV, while a larger value $\delta = 0.1$ meV is used in Fig. 6(b). As expected after the discussion of the 1PR configuration with a finite biexciton binding energy in Sec. IV B, the concurrence drops in this setting steeply for low temperatures followed by a very weak T dependence compared with the other configurations for $T > 4$ K and both splittings. Note that
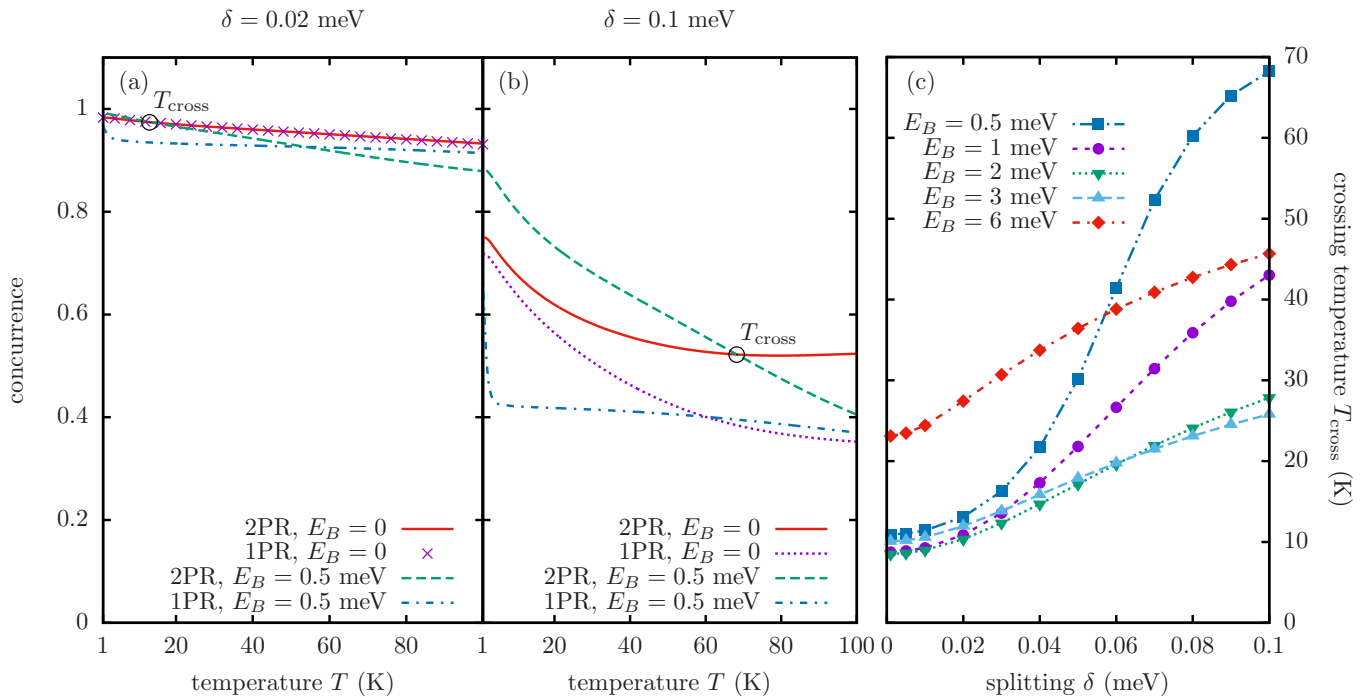
FIG. 6. Concurrence as a function of temperature for a fine-structure splitting $\delta = 0.02$ meV [panel (a)] and $\delta = 0.1$ meV [panel (b)] for all four QD-cavity configurations introduced in Sec. III. Also shown is the crossing temperature T_{cross} of the concurrence in the 2PR configuration with $E_B = 0$ and the concurrence in the 2PR configuration with $E_B > 0$ as a function of δ for several values of the binding energy E_B [panel (c)]. T_{cross} is marked in panels (a) and (b) by a circle.

for $\delta > 0$ in this configuration all sequential processes require the absorption of phonons to bridge the energy mismatches and thus for $T \to 0$ the phonon-free result should be reached. Indeed, as seen in Fig. 6(b), changing the temperature from 1 to 4 K entails a very steep drop of the concurrence before it becomes almost independent of T for $T > 4$ K.

The 2PR configuration with a finite binding energy exhibits a rather strong temperature dependence for both selected values of δ. Because of the weak influence of the exciton splitting in this configuration the concurrence reaches almost one for temperatures close to zero.

The 2PR and 1PR configuration with a vanishing binding energy are, as discussed earlier, almost the same for small δ. Therefore, for $\delta = 0.02$ meV, the concurrence as a function of temperature is nearly identical for both configurations, with the 1PR result being marginally lower. For the larger splitting $\delta = 0.1$ meV these two configurations show a similar temperature dependence at very low temperatures but at higher temperatures the concurrence decreases noticeably stronger in the 1PR configuration.

In the 2PR as well as in the 1PR configuration the sequential single-photon processes are detuned on the order of δ when the biexciton binding energy is zero. Since two-photon processes are more important in the 2PR configuration the corresponding concurrence is higher for all temperatures than in the 1PR configuration when $E_B = 0$. However, this trend reverses for finite E_B at high temperatures.

Let us now compare 2PR results with and without a finite biexciton binding energy. As can be seen in Fig. 6(a) and Fig. 6(b), introducing a finite value for E_B in the 2PR configuration leads to a higher concurrence only below a crossing temperature which depends on δ. In fact, there is a crossing

point of the 2PR concurrence evaluated at finite E_B with each of the three other concurrences considered here. It turns out that the setting with the lowest crossing temperature is the 2PR configuration with vanishing biexciton binding energy. We will denote the corresponding crossing temperature by T_{cross} in the following.

For large splittings, a finite biexciton binding energy can raise the concurrence significantly at low temperatures since the sequential single-photon emission processes become largely detuned and the importance of the two-photon processes is raised. Therefore, in the absence of phonons, a finite binding energy in general results in an increased concurrence, a finding which was already proposed and discussed by Schumacher *et al.* [16].

Above the crossing temperature, however, the pure dephasing coupling to the phonons alters this effect and a finite binding energy in the 2PR configuration reduces the concurrence. As the temperature increases, phonons raise the importance of the detuned single-photon processes because they become assisted by phonon absorption and emission. In the case of a finite binding energy, the cavity modes are more detuned from the electronic transitions involving exciton states. Therefore, the phonon spectral density $J(\omega)$ is probed at larger values so that the effective phonon coupling is stronger compared with the situation without biexciton binding energy. These two effects combined lead to a stronger decrease of the concurrence with increasing temperature for a finite E_B. Thus, above T_{cross}, a finite biexciton binding energy reduces the concurrence and the protection of entanglement in the 2PR configuration is lost.

By comparing Fig. 6(a) and Fig. 6(b), one notices that the crossing point of the concurrence in the 2PR configuration

with and without a finite binding energy moves to lower temperatures for smaller values of the exciton splitting. For the concurrence, this means that the advantage provided by a finite E_B is lost for small δ already at low temperatures $T \sim 10$ K. In Fig. 6(c) this crossing temperature is plotted against δ for several values of E_B. For a given binding energy, T_{cross} exhibits a monotonic increase with increasing exciton splitting and converges to a finite value of about 10 K in the limit $\delta \to 0$ and typical binding energies. Therefore, for typical splittings on the order of several $10 \, \mu$eV, the protection of the entanglement due to a finite binding energy is already lost at quite low temperatures. As can be seen by comparing the results in Fig. 5(a) and Fig. 5(c), the protection of the concurrence due to a finite E_B in the 2PR configuration at temperatures close to zero improves for larger δ. Thus, for larger δ, higher temperatures are needed to destroy this protection and T_{cross} increases with increasing splitting for a given E_B.

Comparing the crossing temperature for different values of the binding energy, a nonmonotonic behavior is found at a given exciton splitting. On the one hand, a higher value of the binding energy results in a better protection of the entanglement at temperatures close to zero. But, on the other hand, the phonon influence and thus the influence of the temperature depends on the energy of the phonons needed to assist the detuned single-photon processes as the phonon spectral density $J(\omega)$ depends (nonmonotonically) on this energy. In the case of the 2PR configuration with finite E_B, this roughly corresponds to half the binding energy. The nonmonotonic behavior of T_{cross} as a function of E_B at a given exciton splitting thus originates from the trade-off between a better protection of the concurrence for higher binding energies at temperatures close to zero and the varying influence of the phonons due to the nonmonotonic behavior of the phonon spectral density. For example, the crossing point temperature in Fig. 6(c) for $E_B = 1$ meV is always higher than for $E_B = 2$ meV. The reason is the much stronger temperature dependence in the latter situation as the phonon spectral density is much higher for a phonon energy of 1 meV than for a value of 0.5 meV (cf. Fig. 2). However, at $\hbar\omega = 1$ meV and $\hbar\omega = 3$ meV the values of $J(\omega)$ are similar, which means that the phonon influence is similar for $E_B = 2$ meV and $E_B = 6$ meV and T_{cross} is always higher in the latter case because of the stronger protection due to the higher binding energy.

V. CONCLUSION

We have analyzed how the competition between two-photon and single-photon emission processes as well as the coupling to LA phonons influences the degree of two-photon entanglement created in a QD-cavity system. To this end we have calculated the concurrence of photon pairs simultaneously emitted in a biexciton-exciton cascade of a QD in a cavity for four different configurations. We account for four electronic states (biexciton, two excitons, and the ground state), two degenerate orthogonally polarized cavity modes that are coupled to the electronic transitions, and cavity losses, as well as for a continuum of LA phonons coupled by the deformation potential interaction to the QD. The numerical simulations are based on a path-integral scheme that allows

the evaluation of quantities of interest without approximation to the model.

The four configurations considered in this paper comprise the two-photon resonant (2PR) and the one-photon resonant (1PR) configuration with a vanishing as well as a finite biexciton binding energy. We find a wealth of interesting results and insights in the physics of the system at hand which we would like to briefly summarize below before we outline our main result at the end.

(a) The competition between two-photon and one-photon processes plays a decisive role for the concurrence and leads to strikingly different dependences on the exciton splitting δ. Among other things, we find, e.g., nonmonotonic dependences and deviations from the standard bell shape in the 2PR as well as in the 1PR configuration. While the 2PR and 1PR configuration without a biexciton binding energy lead to almost the same degree of entanglement for small splittings the 2PR configuration is favorable for larger splittings. These results and the different dependences on the splitting δ can be very well explained by the different relative importance of direct two-photon and sequential single-photon contributions as well as the changing phonon impact when the resonance settings are varied.

(b) The concurrence is in general only symmetric regarding the exciton splitting δ in the 2PR configurations. Additionally, LA phonons affect or even introduce the asymmetry in the 1PR configurations. Because of the characteristics of the phonon coupling this asymmetry is stronger at low temperatures as phonon absorption and emission processes are not equally likely to occur.

(c) The chosen configuration defines the detunings in the quantum dot-cavity system and results in different effective phonon influences and therefore also strongly different temperature dependences of the concurrence. The 2PR and 1PR configuration with a vanishing binding energy have almost the same concurrence value and temperature dependence for the usual exciton splittings of several $10 \, \mu$eV. The concurrence can be virtually independent of the temperature over a wide temperature range, as it is the case in the 1PR configuration with a finite binding energy and positive δ after the concurrence has fallen drastically with rising temperature for T below 4 K.

In order to appreciate our main result, it should be noted that the 2PR configuration with finite biexciton binding energy has attracted a lot of attention [16,17,51] since this configuration has been proposed in order to reach high degrees of entanglement at finite fine-structure splittings. The idea is that two-photon transitions are favored which are much less affected by the which-path information introduced by the fine-structure splitting than sequential single-photon processes. Thus a finite biexciton binding energy protects the entanglement from the destructive impact of the fine-structure splitting by making single-photon processes off-resonant. Indeed, at low temperatures we find the highest degree of entanglement for this configuration which depends only little on the fine-structure splitting. However, the concurrence in the 2PR configuration with finite biexciton binding energy exhibits a steep decrease with rising temperature, which can be explained by an enhanced interaction with phonons resulting from the frequency dependence of the phonon-spectral density combined with

an increase of the importance of sequential single-photon processes at higher temperatures.

This strong temperature dependence is the origin of our most important result that for each of the other three considered configurations there is a finite temperature above which the corresponding concurrence is higher than in the 2PR case with finite biexciton binding energy. Out of the configurations that we compare, the 2PR configuration with vanishing biexciton binding energy has the lowest such crossing temperature T_{cross}, which is found to depend on the fine-structure splitting as well as on the biexciton binding energy. For splittings that are typically found in experiments on the order of several $10\,\mu\text{eV}$ or below and typical biexciton binding energies of few meV, T_{cross} is around or even below 10 K. Thus the special distinction of the 2PR configuration with finite biexciton binding energy in terms of yielding the highest degree of entanglement for finite fine-structure splittings is lost already at rather low temperatures due to the phonon impact and the 2PR configuration with vanishing biexciton binding energy becomes more favorable for achieving the highest value of the concurrence.

[1] N. Akopian, N. H. Lindner, E. Poem, Y. Berlatzky, J. Avron, D. Gershoni, B. D. Gerardot, and P. M. Petroff, Phys. Rev. Lett. **96**, 130501 (2006).

[2] J.-W. Pan, Z.-B. Chen, C.-Y. Lu, H. Weinfurter, A. Zeilinger, and M. Żukowski, Rev. Mod. Phys. **84**, 777 (2012).

[3] A. Orieux, M. A. M. Versteegh, K. D. Jöns, and S. Ducci, Rep. Prog. Phys. **80**, 076001 (2017).

[4] K. D. Jöns, L. Schweickert, M. A. M. Versteegh, D. Dalacu, P. J. Poole, A. Gulinatti, A. Giudice, V. Zwiller, and M. E. Reimer, Sci. Rep. **7**, 1700 (2017).

[5] R. M. Stevenson, R. J. Young, P. Atkinson, K. Cooper, D. A. Ritchie, and A. J. Shields, Nature (London) **439**, 179 (2006).

[6] R. J. Young, R. M. Stevenson, P. Atkinson, K. Cooper, D. A. Ritchie, and A. J. Shields, New J. Phys. **8**, 29 (2006).

[7] R. Hafenbrak, S. M. Ulrich, P. Michler, L. Wang, A. Rastelli, and O. G. Schmidt, New J. Phys. **9**, 315 (2007).

[8] A. Dousse, J. Suffczyński, A. Beveratos, O. Krebs, A. Lemaître, I. Sagnes, J. Bloch, P. Voisin, and P. Senellart, Nature (London) **466**, 217 (2010).

[9] E. del Valle, A. Gonzalez-Tudela, E. Cancellieri, F. P. Laussy, and C. Tejedor, New J. Phys. **13**, 113014 (2011).

[10] M. Müller, S. Bounouar, K. D. Jöns, M. Glässl, and P. Michler, Nat. Photon. **8**, 224 (2014).

[11] R. Winik, D. Cogan, Y. Don, I. Schwartz, L. Gantz, E. R. Schmidgall, N. Livneh, R. Rapaport, E. Buks, and D. Gershoni, Phys. Rev. B **95**, 235435 (2017).

[12] O. Benson, C. Santori, M. Pelton, and Y. Yamamoto, Phys. Rev. Lett. **84**, 2513 (2000).

[13] R. Johne, N. A. Gippius, G. Pavlovic, D. D. Solnyshkov, I. A. Shelykh, and G. Malpuech, Phys. Rev. Lett. **100**, 240404 (2008).

[14] R. M. Stevenson, R. J. Young, P. See, D. G. Gevaux, K. Cooper, P. Atkinson, I. Farrer, D. A. Ritchie, and A. J. Shields, Phys. Rev. B **73**, 033306 (2006).

[15] J. Zhang, J. S. Wildmann, F. Ding, R. Trotta, Y. Huo, E. Zallo, D. Huber, A. Rastelli, and O. G. Schmidt, Nat. Commun. **6**, 10067 (2015).

[16] S. Schumacher, J. Förstner, A. Zrenner, M. Florian, C. Gies, P. Gartner, and F. Jahnke, Opt. Express **20**, 5335 (2012).

[17] E. del Valle, New J. Phys. **15**, 025019 (2013).

[18] W. K. Wootters, Quantum Inf. Comput. **1**, 27 (2001).

[19] W. K. Wootters, Phys. Rev. Lett. **80**, 2245 (1998).

[20] R. M. Stevenson, A. J. Hudson, A. J. Bennett, R. J. Young, C. A. Nicoll, D. A. Ritchie, and A. J. Shields, Phys. Rev. Lett. **101**, 170501 (2008).

[21] S. Bounouar, C. de la Haye, M. Strauß, P. Schnauber, A. Thoma, M. Gschrey, J.-H. Schulze, A. Strittmatter, S. Rodt, and S. Reitzenstein, Appl. Phys. Lett. **112**, 153107 (2018).

[22] M. Cygorek, F. Ungar, T. Seidelmann, A. M. Barth, A. Vagov, V. M. Axt, and T. Kuhn, Phys. Rev. B **98**, 045303 (2018).

[23] J. Förstner, C. Weber, J. Danckwerts, and A. Knorr, Phys. Rev. Lett. **91**, 127401 (2003).

[24] A. Vagov, M. D. Croitoru, V. M. Axt, T. Kuhn, and F. M. Peeters, Phys. Rev. Lett. **98**, 227403 (2007).

[25] A. J. Ramsay, A. V. Gopal, E. M. Gauger, A. Nazir, B. W. Lovett, A. M. Fox, and M. S. Skolnick, Phys. Rev. Lett. **104**, 017402 (2010).

[26] A. J. Ramsay, T. M. Godden, S. J. Boyle, E. M. Gauger, A. Nazir, B. W. Lovett, A. M. Fox, and M. S. Skolnick, Phys. Rev. Lett. **105**, 177402 (2010).

[27] M. Glässl, A. M. Barth, and V. M. Axt, Phys. Rev. Lett. **110**, 147401 (2013).

[28] P.-L. Ardelt, L. Hanschke, K. A. Fischer, K. Müller, A. Kleinkauf, M. Koller, A. Bechtold, T. Simmet, J. Wierzbowski, H. Riedl, G. Abstreiter, and J. J. Finley, Phys. Rev. B **90**, 241404(R) (2014).

[29] V. M. Axt, T. Kuhn, A. Vagov, and F. M. Peeters, Phys. Rev. B **72**, 125309 (2005).

[30] T. Jakubczyk, V. Delmonte, S. Fischbach, D. Wigger, D. E. Reiter, Q. Mermillod, P. Schnauber, A. Kaganskiy, J.-H. Schulze, A. Strittmatter, S. Rodt, W. Langbein, T. Kuhn, S. Reitzenstein, and J. Kasprzak, ACS Photon. **3**, 2461 (2016).

[31] S. Bounouar, M. Müller, A. M. Barth, M. Glässl, V. M. Axt, and P. Michler, Phys. Rev. B **91**, 161302(R) (2015).

[32] D. E. Reiter, Phys. Rev. B **95**, 125308 (2017).

[33] D. P. S. McCutcheon and A. Nazir, New J. Phys. **12**, 113042 (2010).

[34] I. Wilson-Rae and A. Imamoğlu, Phys. Rev. B **65**, 235311 (2002).

[35] U. Hohenester, A. Laucht, M. Kaniber, N. Hauke, A. Neumann, A. Mohtashami, M. Seliger, M. Bichler, and J. J. Finley, Phys. Rev. B **80**, 201311(R) (2009).

[36] K. Müller, K. A. Fischer, A. Rundquist, C. Dory, K. G. Lagoudakis, T. Sarmiento, Y. A. Kelaita, V. Borish, and J. Vučković, Phys. Rev. X **5**, 031006 (2015).

[37] P. Kaer, T. R. Nielsen, P. Lodahl, A.-P. Jauho, and J. Mørk, Phys. Rev. Lett. **104**, 157401 (2010).

[38] P. Kaer, T. R. Nielsen, P. Lodahl, A.-P. Jauho, and J. Mørk, Phys. Rev. B **86**, 085302 (2012).

[39] C. Roy and S. Hughes, Phys. Rev. X **1**, 021009 (2011).

[40] M. Glässl, L. Sörgel, A. Vagov, M. D. Croitoru, T. Kuhn, and V. M. Axt, Phys. Rev. B **86**, 035319 (2012).

[41] C. Roy and S. Hughes, Phys. Rev. B **85**, 115309 (2012).

[42] S. Hughes and H. J. Carmichael, New J. Phys. **15**, 053039 (2013).

[43] J. Iles-Smith, D. P. S. McCutcheon, A. Nazir, and J. Mørk, Nat. Photon. **11**, 521 (2017).

[44] F. Troiani, J. I. Perea, and C. Tejedor, Phys. Rev. B **74**, 235310 (2006).

[45] A. Carmele and A. Knorr, Phys. Rev. B **84**, 075328 (2011).

[46] B. Krummheuer, V. M. Axt, and T. Kuhn, Phys. Rev. B **65**, 195313 (2002).

[47] L. Besombes, K. Kheng, L. Marsal, and H. Mariette, Phys. Rev. B **63**, 155307 (2001).

[48] A. Vagov, V. M. Axt, T. Kuhn, W. Langbein, P. Borri, and U. Woggon, Phys. Rev. B **70**, 201305(R) (2004).

[49] M. Thorwart, J. Eckel, and E. R. Mucciolo, Phys. Rev. B **72**, 235320 (2005).

[50] M. B. Harouni, Laser Phys. **24**, 115202 (2014).

[51] D. Heinze, A. Zrenner, and S. Schumacher, Phys. Rev. B **95**, 245306 (2017).

[52] G. Lindblad, Commun. Math. Phys. **48**, 119 (1976).

[53] A. Carmele, F. Milde, M.-R. Dachner, M. B. Harouni, R. Roknizadeh, M. Richter, and A. Knorr, Phys. Rev. B **81**, 195319 (2010).

[54] N. Makri and D. E. Makarov, J. Chem. Phys. **102**, 4600 (1995).

[55] N. Makri and D. E. Makarov, J. Chem. Phys. **102**, 4611 (1995).

[56] A. Vagov, M. D. Croitoru, M. Glässl, V. M. Axt, and T. Kuhn, Phys. Rev. B **83**, 094303 (2011).

[57] A. M. Barth, A. Vagov, and V. M. Axt, Phys. Rev. B **94**, 125439 (2016).

[58] M. Cygorek, A. M. Barth, F. Ungar, A. Vagov, and V. M. Axt, Phys. Rev. B **96**, 201201(R) (2017).

[59] A. Strathearn, P. Kirton, D. Kilda, J. Keeling, and B. W. Lovett, Nat. Commun. **9**, 3322 (2018).

[60] B. Krummheuer, V. M. Axt, T. Kuhn, I. D'Amico, and F. Rossi, Phys. Rev. B **71**, 235329 (2005).

[61] S. Lüker, T. Kuhn, and D. E. Reiter, Phys. Rev. B **96**, 245306 (2017).

[62] P. Machnikowski and L. Jacak, Phys. Rev. B **69**, 193302 (2004).

[63] G. Pfanner, M. Seliger, and U. Hohenester, Phys. Rev. B **78**, 195410 (2008).

[64] M. Cosacchi, M. Cygorek, F. Ungar, A. M. Barth, A. Vagov, and V. M. Axt, Phys. Rev. B **98**, 125302 (2018).

[65] *Physics of Group IV Elements and III-V Compounds*, edited by O. Madelung, Landolt-Börnstein, New Series, Group III Vol. 17, Pt. a (Springer, Berlin, 1982).

[66] P. E. Selbmann, M. Gulia, F. Rossi, E. Molinari, and P. Lugli, Phys. Rev. B **54**, 4660 (1996).

Publication 14

Phonon-Induced Enhancement of Photon Entanglement in Quantum Dot-Cavity Systems

T. Seidelmann, F. Ungar, A. Vagov, V. M. Axt, M. Cygorek, and T. Kuhn

Phonon-Induced Enhancement of Photon Entanglement in Quantum Dot-Cavity Systems

T. Seidelmann[1], F. Ungar,[1] A. M. Barth,[1] A. Vagov,[1,2] V. M. Axt,[1] M. Cygorek,[3] and T. Kuhn[4]

[1]*Universität Bayreuth, Lehrstuhl für Theoretische Physik III, Universitätsstraße 30, 95447 Bayreuth, Germany*
[2]*ITMO University, St. Petersburg 197101, Russia*
[3]*Department of Physics, University of Ottawa, Ottawa, Ontario, Canada K1N 6N5*
[4]*Institut für Festkörpertheorie, Universität Münster, 48149 Münster, Germany*

We report on simulations of the degree of polarization entanglement of photon pairs simultaneously emitted from a quantum dot-cavity system that demand revisiting the role of phonons. Since coherence is a fundamental precondition for entanglement and phonons are known to be a major source of decoherence, it seems unavoidable that phonons can only degrade entanglement. In contrast, we demonstrate that phonons can cause a degree of entanglement that even surpasses the corresponding value for the phonon-free case. In particular, we consider the situation of comparatively small biexciton binding energies and either finite exciton or cavity mode splitting. In both cases, combinations of the splitting and the dot-cavity coupling strength are found where the entanglement exhibits a nonmonotonic temperature dependence which enables entanglement above the phonon-free level in a finite parameter range. This unusual behavior can be explained by phonon-induced renormalizations of the dot-cavity coupling g in combination with a nonmonotonic dependence of the entanglement on g that is present already without phonons.

The appearance of entangled states is one of the showcase effects that highlights most impressively the dramatic conceptual changes brought forth by going over from classical to quantum physics [1,2]. Moreover, realizations of entangled states, mostly with photons, have paved the way toward many innovative applications [3], e.g., in quantum cryptography [4,5], quantum teleportation [6], quantum information processing [7–10], and photonics [11]. In particular, quantum dot (QD) cavity systems have attracted a lot of attention as sources for triggered entangled photon pairs [12–19], not only because these systems hold the promise of a natural integration in solid-state devices. Embedding a QD in a microcavity enables the manipulation of few-electron and few-photon states in a system with high optical nonlinearities, which can be used for realizing a few-photon logic in quantum optical networks [20]. Furthermore, the cavity boosts the quantum yield due to the Purcell effect [14,21] and, for high cavity quality factors Q, it reduces the detrimental effects of phonons on the photon indistinguishability [22].

The essence of entanglement in a bipartite system is the creation of a state that cannot be factorized into parts referring to the constituent subsystems, which requires the buildup of a superposition state. Polarization entanglement between horizontally (H) or vertically (V) polarized photon pairs is established, e.g., by creating superpositions of the states $|HH\rangle$ and $|VV\rangle$ with two photons with either H or V polarizations exploiting the biexciton cascade [12–18]. Starting from the biexciton, the system can decay first into one of the two excitons and a photon with the corresponding

polarization (H or V). The excitons then decay further to the QD ground state emitting a second photon with the same polarization as in the biexciton decay. Ideally, the resulting quantum state is a coherent superposition and maximally entangled. Which-path information introduced, e.g., by the fine-structure splitting of the excitons, leads to an asymmetric superposition and decreased entanglement. The system can also decay from the biexciton directly to the ground state by simultaneous two-photon emission, a process which is much less affected by which-path information than the sequential single-photon decay [23–25].

Obviously, maintaining a coherent superposition requires stable relative phases between the involved states. However, in a solid-state system, the interaction with the environment unavoidably leads to a loss of phase coherence. In particular, phonons are known to provide a major source of decoherence [26–35], which led to the expectation that phonons should always degrade the entanglement. Indeed, recent simulations [24,36,37] are in line with this expectation.

In this Letter, we demonstrate that the phonon influence is not necessarily destructive. On the contrary, phonons can increase the degree of photon entanglement when the destructive effect resulting from phonon-induced decoherence is overcompensated by phonon-related renormalizations of the QD-cavity coupling that shift the system into a regime of higher photon entanglement. A precondition of this mechanism is a decrease of the degree of entanglement with rising QD-cavity coupling g in the phonon-free case in a finite g range. This is realized,

e.g., in the limit of weak biexciton binding and finite exciton or cavity mode splitting. In both cases, the phonon-induced enhancement is found in a finite range of binding energies and couplings g.

Our studies are based on the Hamiltonian [24,37]:

$$
\begin{aligned}
\hat{H} = &\ \hbar\omega_H |X_H\rangle\langle X_H| + \hbar\omega_V |X_V\rangle\langle X_V| \\
&+ \hbar(\omega_H + \omega_V - \omega_B)|B\rangle\langle B| + \sum_{\ell=H,V} \hbar\omega_\ell^c \hat{a}_\ell^\dagger \hat{a}_\ell \\
&+ \sum_{\mathbf{q}} \hbar\omega_{\mathbf{q}} \hat{b}_{\mathbf{q}}^\dagger \hat{b}_{\mathbf{q}} + \sum_{\mathbf{q},\chi} n_\chi (\gamma_{\mathbf{q}} \hat{b}_{\mathbf{q}}^\dagger + \gamma_{\mathbf{q}}^* \hat{b}_{\mathbf{q}})|\chi\rangle\langle\chi| + \hat{\mathcal{X}},
\end{aligned} \quad (1)
$$

where $|B\rangle$ is the biexciton state with energy $\hbar(\omega_H + \omega_V - \omega_B)$ and a biexciton binding energy $E_B = \hbar\omega_B$, while $|X_{H/V}\rangle$ denote the two exciton states with energies $\hbar\omega_{H/V}$ that couple to H or V polarized cavity modes with destruction (creation) operators $\hat{a}_{H/V}(\hat{a}_{H/V}^\dagger)$ and mode energies $\hbar\omega_{H/V}^c$. $\hat{b}_{\mathbf{q}}(\hat{b}_{\mathbf{q}}^\dagger)$ are operators that destroy (create) longitudinal acoustic phonons with wave vector $\mathbf{q}$ and energy $\hbar\omega_{\mathbf{q}}$. We consider bulk phonons with a linear dispersion and account for the deformation potential coupling $\gamma_{\mathbf{q}}$. n_χ is the number of electron-hole pairs contained in the states $|\chi\rangle \in \{|B\rangle, |X_{H/V}\rangle\}$. Finally, the Jaynes-Cummings type coupling of the cavity modes to the QD with coupling constant g is given by:

$$
\begin{aligned}
\hat{\mathcal{X}} = -g(&|G\rangle\langle X_H|\hat{a}_H^\dagger + |X_H\rangle\langle B|\hat{a}_H^\dagger \\
&+ |G\rangle\langle X_V|\hat{a}_V^\dagger - |X_V\rangle\langle B|\hat{a}_V^\dagger) + \text{H.c.},
\end{aligned} \quad (2)
$$

where H.c. stands for the Hermitian conjugate and $|G\rangle$ is the QD ground state, the energy of which is taken as the zero of energy. In addition, we account for cavity losses with a rate κ by the Lindblad operator:

$$
\mathcal{L}_{\text{cav}}[\hat{\rho}] = \sum_{\ell=H,V} \frac{\kappa}{2}(2\hat{a}_\ell \hat{\rho} \hat{a}_\ell^\dagger - \hat{\rho} \hat{a}_\ell^\dagger \hat{a}_\ell - \hat{a}_\ell^\dagger \hat{a}_\ell \hat{\rho}). \quad (3)
$$

We assume that the system is initially prepared in the biexciton state, without photons and that the phonons are initially in equilibrium at a temperature T. This can be achieved, e.g., by using two-photon resonant or near-resonant excitation with short coherent pulses [16, 38–41], which introduces much less decoherence and time jitter than, e.g., pumping the wetting layer and subsequent relaxation to the biexciton. The dynamics of the reduced density matrix $\hat{\rho}$ is determined by the equation:

$$
\frac{d}{dt}\hat{\rho} = -\frac{i}{\hbar}[\hat{H}, \hat{\rho}]_- + \mathcal{L}_{\text{cav}}[\hat{\rho}], \quad (4)
$$

where $[,]_-$ denotes the commutator. As in Ref. [37], we evaluate $\hat{\rho}$ numerically in the subspace spanned by the five states $|B, 0, 0\rangle$, $|X_H, 1, 0\rangle$, $|X_V, 0, 1\rangle$, $|G, 2, 0\rangle$, and $|G, 0, 2\rangle$, where the numbers $n_{H/V}$ in $|\chi, n_H, n_V\rangle$ denote the number of H/V photons. We use a path-integral approach that does not introduce approximations to the model. This is made possible by recent methodological advances that allow for a natural inclusion of non-Hamiltonian parts of the dynamics (e.g., represented by Lindblad operators) in the path-integral formalism [42] as well as huge improvements of the performance by iterating instead of the augmented density matrix, introduced in the pioneering work of Makri and Makarov [43,44], a partially summed augmented density matrix [45]. We quantify the degree of entanglement by the concurrence, a quantity which has a one-to-one correspondence to the entanglement of formation [46]. To be precise, we use the concurrence of simultaneously emitted photon pairs

$$
C = 2\frac{|\bar{\rho}_{HV}|}{\bar{\rho}_{HH} + \bar{\rho}_{VV}} \quad (5)
$$

(see the Supplemental Material [47] for further details) that can be calculated directly from the time-averaged occupations $\bar{\rho}_{HH}$, $\bar{\rho}_{VV}$ and coherence $\bar{\rho}_{HV}$ of the states $|HH\rangle$ and $|VV\rangle$ [25,37,57]. We focus on simultaneously emitted photon pairs since experiments [58,59] agree with theory [15,37] that this case is favorable for the entanglement.

First, we present results for the situation sketched in Fig. 1(a) where the excitons have a finite fine-structure splitting $\delta = \hbar(\omega_H - \omega_V)$, the biexciton binding energy is zero and both cavity modes are tuned to the two-photon resonance $2\omega_H^c = 2\omega_V^c = \omega_H + \omega_V - \omega_B$. In the situation with phonons, these QD energies denote the polaron-shifted ones. To compare QD-cavity systems with identical energy relations, the energy values are kept the same in the corresponding phonon-free calculations thus keeping the polaron shifts.

Figure 1(b) displays the temperature dependence of the concurrence for three values of the QD-cavity coupling. Only the result for $g = 130\ \mu\text{eV}$ agrees with the common expectation that the entanglement should monotonically decrease with temperature. In contrast, for $g = 60\ \mu\text{eV}$ and $g = 35\ \mu\text{eV}$, unusual nonmonotonic T dependences are found. Most interestingly, for $g = 35\ \mu\text{eV}$, the concurrence is noticeably higher than the corresponding value obtained without phonons in the entire T range that we consider ($T \in [1\ \text{K}, 100\ \text{K}]$); i.e., for certain values of g we find indeed a phonon-induced enhancement of entanglement while in other cases the expectation that phonons reduce the entanglement is confirmed.

The reason for this remarkable behavior becomes apparent when looking at the g dependence of the concurrence in Fig. 1(c). Already without phonons, the concurrence is a nonmonotonic function of g (purple curve) with a pronounced minimum reached roughly for $g \simeq \delta/2$. Dividing Eq. (4) by the coupling strength g and leaving out the coupling to phonons, the system dynamics is described by the rescaled quantities $t' = gt$,
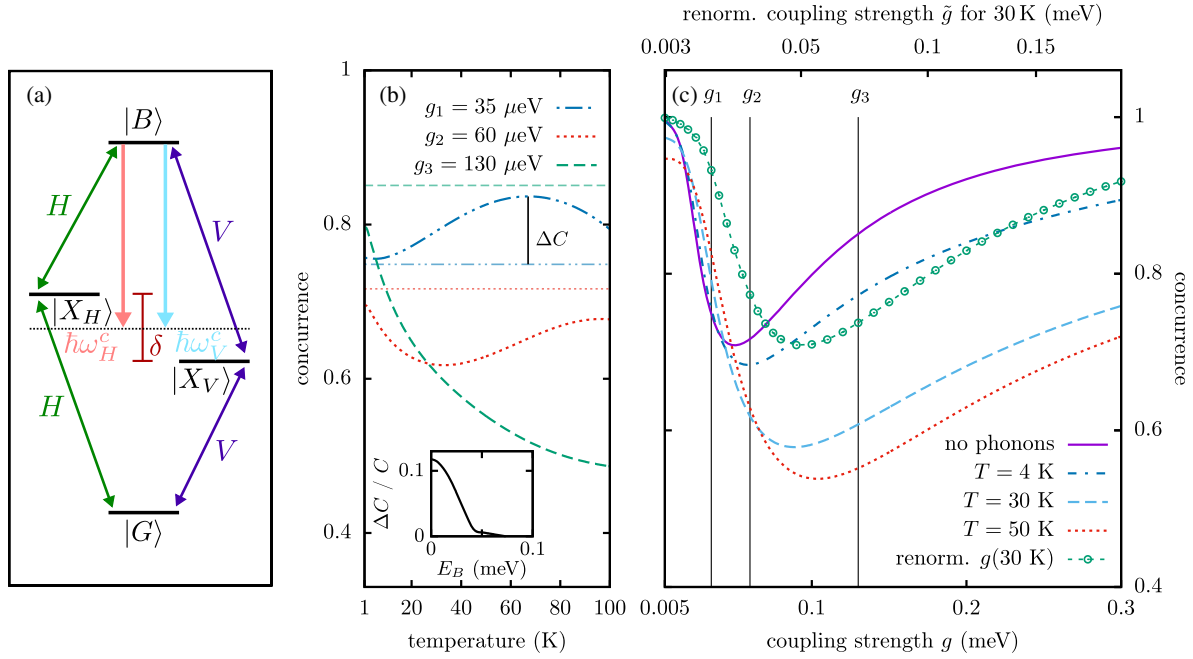
FIG. 1. (a) Sketch of the level scheme of a QD-cavity system with finite fine-structure splitting, zero biexciton binding energy and two-photon resonant cavity modes. (b) Concurrence as a function of the temperature for three selected values of the QD-cavity coupling. The corresponding values obtained without phonons are drawn as straight (faded) lines with the same linetype. Inset: difference ΔC between the maximum concurrence value at finite temperature and the corresponding phonon-free value normalized by the latter as a function of the biexciton binding energy E_B for $g_1 = 35 \mu$eV. (c) Concurrence as a function of the QD-cavity coupling for three temperatures together with the phonon-free result. In addition $C[\tilde{g}(g)]$ is plotted using the phonon-renormalized coupling $\tilde{g}(g)$ for $T = 30$ K (indicated on the upper axis), where $C(g)$ is the phonon-free concurrence. The values of the QD-cavity coupling used in (b) are marked in (c) by vertical lines. Parameters: $\delta = 0.1$ meV, $\kappa = 0.025$ ps^{-1}, electron (hole) confinement length $a_e = 3$ nm, $a_h = a_e/1.15$ where we assume a spherical GaAs-type QD with harmonic confinement. All other parameters, e.g., concerning the phonon coupling, are taken from Ref. [60].

$g' = g/g = 1$, $\delta' = \delta/g$, and $\kappa' = \kappa/g$. Since the concurrence is the asymptotic value of the normalized coherence at long averaging times [37], the rescaling of the time is irrelevant. For large values of g, both parameters δ' and κ' tend to zero. This implies that the concurrence approaches unity for large coupling strengths because the which-path information disappears for a vanishing splitting and thus the concurrence is one [37,57]. For very small QD-cavity couplings, κ' and δ' become arbitrarily large. Therefore, the sequential single photon decay via the intermediate exciton states becomes strongly off-resonant and is thus negligible compared with contributions from a direct two-photon transition, which is always resonant in the present case [25]. Since the which-path information is contained only in the sequential decay, the concurrence approaches unity again. But for finite splittings, the concurrence is smaller than one and thus a minimum must appear at a certain coupling strength g.

When phonons are accounted for, the minimum is lowered and shifted to a higher coupling strength depending on the temperature. We attribute the shift to the well known effect of phonon-induced renormalization of the

light-matter coupling [61]. To support this assignment we have estimated the renormalized coupling $\tilde{g}(g)$ as in Ref. [62] by fitting equations with phenomenological renormalizations of a resonantly driven two-level system to path-integral calculations. The results are shown in the Supplemental Material [47]. If the only effect introduced by phonons was the g renormalization, then the value of the concurrence found without phonons at a particular value of g should be shifted by phonons to $\tilde{g}(g)$. Indeed, in Fig. 1(c) we have plotted $C[\tilde{g}(g)]$ using the phonon-renormalized coupling $\tilde{g}(g)$ for $T = 30$ K, where $C(g)$ is the concurrence in the phonon-free case (green curve with circles). We find that, despite the crudeness of the estimation for $\tilde{g}(g)$, the minimum of the shifted curve agrees even quantitatively well with the minimum found in the full path-integral simulation for this temperature (red dotted curve). Since the shift is larger for higher temperatures, displacing the phonon-free curve necessarily leads to higher values of the shifted curves in regions where the phonon-free concurrence is monotonically decreasing with g. Consequently, in this region, phonon-induced enhancement appears for a finite g range.
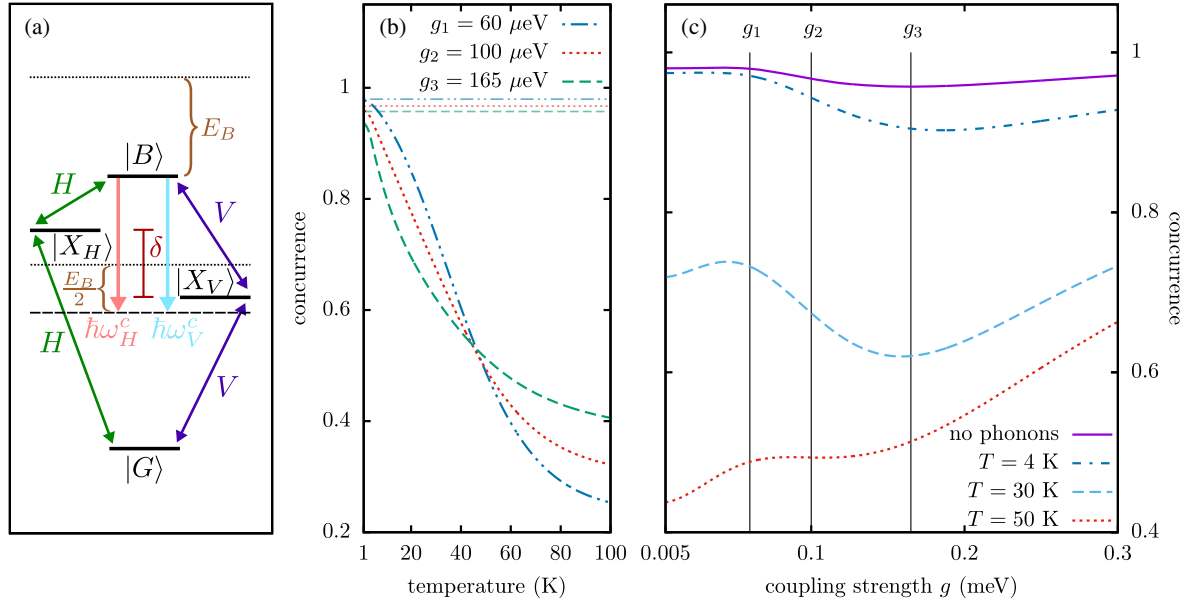
FIG. 2. (a) Sketch of the level scheme of a QD-cavity system with finite fine-structure splitting, biexciton binding energy $E_B = 1$ meV and two-photon resonant cavity modes. (b) Concurrence as a function of the temperature for three selected values of the QD-cavity coupling. The corresponding values obtained without phonons are drawn as straight (faded) lines with the same linetype. (c) Concurrence as a function of the QD-cavity coupling for three temperatures together with the phonon-free result. The values of the QD-cavity coupling used in (b) are marked in (c) by vertical lines. Apart from E_B, the same parameters are used as in Fig. 1.

The total effect of phonons is, however, not merely a shift but also a lowering of the curves with rising temperature, which is indeed due to the dephasing action of phonons. It is important for obtaining a phonon-induced entanglement that the gain in entanglement resulting from the shift of the phonon-free curve due the phonon-induced g renormalization is not destroyed by the overall lowering of the concurrence caused by the decoherence. Figure 1(c) demonstrates that it is indeed possible that the renormalization-induced shift overcompensates the dephasing action. Additionally, when accounting for pure dephasing by introducing a phenomenological rate [23], the phonon-induced enhancement disappears (see the Supplemental Material [47]). This result reaffirms the g renormalization as the main origin of the effect, since it is absent in the phenomenological model.

It is instructive to contrast the above findings with simulations for the more commonly considered situation sketched in Fig. 2(a), where the biexciton binding energy has the finite value $E_B = 1$ meV and the cavity modes are in resonance with the two-photon transition to the biexciton. Again, the phonon-free curve exhibits a minimum which is, however, rather flat [purple line in Fig. 2(c)]. In the limit $g \to \infty$ the concurrence approaches unity since the argument given for the case of vanishing biexciton binding energy applies here as well. For the case that both $g/(\frac{1}{2}E_B)$ and δ/E_B are small parameters, it has been shown analytically in Ref. [37] that the phonon-free concurrence approaches $[(E_B^2 - \delta^2)/(E_B^2 + \delta^2)]$, which is smaller than

one for a finite δ. Including phonons, the reduction of the concurrence for small g values is strongly magnified as seen in Fig. 2(c). Overall, the dephasing action induced by phonons is so strong that the line shape of the concurrence as a function of g is significantly deformed, and the effects related to a renormalization of g cannot be identified. As a consequence, the concurrence monotonically decreases with rising temperature and always stays below the phonon-free calculation for all values of g as exemplarily shown in Fig. 2(b). This demonstrates that the phonon-induced enhancement of entanglement described above can only occur when the g-renormalization effects dominate over the phonon-induced dephasing. The stronger phonon-induced dephasing for E_B on the order of a few meV compared with vanishing E_B has been explained recently [25] by noting that the energies bridged by phonon-assisted processes are closer to the maximum of the phonon spectral density in the former case.

It is worthwhile to note that phonon-induced enhancement of photon entanglement is not restricted to the singular case of vanishing E_B but rather appears for a finite range of binding energies as demonstrated in the inset of Fig. 1(b). The difference ΔC between the maximum concurrence value at finite temperatures and the corresponding phonon-free value is positive clearly for an extended range. Further analysis (shown in the Supplemental Material [47]) reveals that the effect can be observed as long as $E_B \lesssim \delta/2$ holds for our realistic parameters.

We note in passing that the situation considered in Fig. 1 is not the only one where the conditions for phonon-induced entanglement are realized. This phenomenon can also be observed in a system with weak biexciton binding and degenerate excitons where which-path information is introduced by a finite splitting of the cavity modes (see the Supplemental Material [47]). There the concurrence calculated without phonons is again a nonmonotonic function of g, which exhibits even more than one extremum. Also in this case, the phonon-induced renormalization is strong enough to evoke a phonon-induced entanglement for finite parameter ranges.

In conclusion, we demonstrate that phonon-induced renormalizations of the dot-cavity coupling can overcompensate decoherence effects and shift the system to a region of higher entanglement. In combination with a nonmonotonic dependence of the phonon-free concurrence, this can result in a nonmonotonic temperature dependence of the concurrence. Most interestingly, the concurrence can even reach values above the phonon-free level, thus causing phonon-induced photon entanglement.

[1] R. Horodecki, P. Horodecki, M. Horodecki, and K. Horodecki, Rev. Mod. Phys. **81,** 865 (2009).

[2] J. Audretsch, *Entangled Systems: New Directions in Quantum Physics* (Whiley-VCH, Weinheim, 2007).

[3] A. Zeilinger, Phys. Scr. **92,** 072501 (2017).

[4] R. M. Stevenson, R. M. Thompson, A. J. Shields, I. Farrer, B. E. Kardynal, D. A. Ritchie, and M. Pepper, Phys. Rev. B **66,** 081302(R) (2002).

[5] N. Gisin, G. Ribordy, W. Tittel, and H. Zbinden, Rev. Mod. Phys. **74,** 145 (2002).

[6] D. Bouwmeester, J.-W. Pan, K. Mattle, M. Eibl, H. Weinfurter, and A. Zeilinger, Nature (London) **390,** 575 (1997).

[7] J.-W. Pan, Z.-B. Chen, C.-Y. Lu, H. Weinfurter, A. Zeilinger, and M. Żukowski, Rev. Mod. Phys. **84,** 777 (2012).

[8] C. H. Bennett and D. P. DiVincenzo, Nature (London) **404,** 247 (2000).

[9] *Entangled World: The Fascination of Quantum Information and Computation*, edited by J. Audretsch (Whiley-VCH, Weinheim, 2006).

[10] S. C. Kuhn, A. Knorr, S. Reitzenstein, and M. Richter, Opt. Express **24,** 25446 (2016).

[11] J. L. O'Brian, A. Furusawa, and J. Vućković, Nat. Photonics **3,** 687 (2009).

[12] R. M. Stevenson, R. J. Young, P. Atkinson, K. Cooper, D. A. Ritchie, and A. J. Shields, Nature (London) **439,** 179 (2006).

[13] R. Hafenbrak, S. M. Ulrich, P. Michler, L. Wang, A. Rastelli, and O. G. Schmidt, New J. Phys. **9,** 315 (2007).

[14] A. Dousse, J. Suffczyński, A. Beveratos, O. Krebs, A. Lemaître, I. Sagnes, J. Bloch, P. Voisin, and P. Senellart, Nature (London) **466,** 217 (2010).

[15] E. del Valle, New J. Phys. **15,** 025019 (2013).

[16] M. Müller, S. Bounouar, K. D. Jöns, M. Glässl, and P. Michler, Nat. Photonics **8,** 224 (2014).

[17] N. Akopian, N. H. Lindner, E. Poem, Y. Berlatzky, J. Avron, D. Gershoni, B. D. Gerardot, and P. M. Petroff, Phys. Rev. Lett. **96,** 130501 (2006).

[18] A. Orieux, M. A. M. Versteegh, K. D. Jöns, and S. Ducci, Rep. Prog. Phys. **80,** 076001 (2017).

[19] C. Sánchez Muñoz, F. P. Laussy, C. Tejedor, and E. del Valle, New J. Phys. **17,** 123021 (2015).

[20] A. Faraon, A. Majumdar, D. Englund, E. Kim, M. Bajcsy, and J. Vukovi, New J. Phys. **13,** 055025 (2011).

[21] A. Badolato, K. Hennessy, M. Atatüre, J. Dreiser, E. Hu, P. M. Petroff, and A. Imamoğlu, Science **308,** 1158 (2005).

[22] T. Grange, N. Somaschi, C. Antón, L. De Santis, G. Coppola, V. Giesz, A. Lemaître, I. Sagnes, A. Auffèves, and P. Senellart, Phys. Rev. Lett. **118,** 253602 (2017).

[23] S. Schumacher, J. Förstner, A. Zrenner, M. Florian, C. Gies, P. Gartner, and F. Jahnke, Opt. Express **20,** 5335 (2012).

[24] D. Heinze, A. Zrenner, and S. Schumacher, Phys. Rev. B **95,** 245306 (2017).

[25] T. Seidelmann, F. Ungar, M. Cygorek, A. Vagov, A. M. Barth, T. Kuhn, and V. M. Axt, Phys. Rev. B **99,** 245301 (2019).

[26] J. Förstner, C. Weber, J. Danckwerts, and A. Knorr, Phys. Rev. Lett. **91,** 127401 (2003).

[27] A. Vagov, V. M. Axt, T. Kuhn, W. Langbein, P. Borri, and U. Woggon, Phys. Rev. B **70,** 201305(R) (2004).

[28] V. M. Axt, T. Kuhn, A. Vagov, and F. M. Peeters, Phys. Rev. B **72,** 125309 (2005).

[29] P. Machnikowski, Phys. Rev. B **78,** 195320 (2008).

[30] A. J. Ramsay, A. V. Gopal, E. M. Gauger, A. Nazir, B. W. Lovett, A. M. Fox, and M. S. Skolnick, Phys. Rev. Lett. **104,** 017402 (2010).

[31] C. Roy and S. Hughes, Phys. Rev. Lett. **106,** 247403 (2011).

[32] T. Close, E. M. Gauger, and B. W. Lovett, New J. Phys. **14,** 113004 (2012).

[33] P. Kaer and J. Mørk, Phys. Rev. B **90,** 035312 (2014).

[34] D. E. Reiter, Phys. Rev. B **95,** 125308 (2017).

[35] A. Reigue, J. Iles-Smith, F. Lux, L. Monniello, M. Bernard, F. Margaillan, A. Lemaitre, A. Martinez, D. P. S. McCutcheon, J. Mørk, R. Hostein, and V. Voliotis, Phys. Rev. Lett. **118,** 233602 (2017).

[36] M. B. Harouni, Laser Phys. **24,** 115202 (2014).

[37] M. Cygorek, F. Ungar, T. Seidelmann, A. M. Barth, A. Vagov, V. M. Axt, and T. Kuhn, Phys. Rev. B **98,** 045303 (2018).

[38] L. Hanschke, K. A. Fischer, S. Appel, D. Lukin, J. Wierzbowski, S. Sun, R. Trivedi, J. Vucković, J. J. Finley, and K. Müller, npj Quantum Inf. **4,** 43 (2018).

[39] S. Bounouar, M. Müller, A. M. Barth, M. Glässl, V. M. Axt, and P. Michler, Phys. Rev. B **91,** 161302(R) (2015).

[40] D. Huber, M. Reindl, Y. Huo, H. Huang, J. S. Wildmann, O. G. Schmidt, A. Rastelli, and R. Trotta, Nat. Commun. **8,** 15506 (2017).

[41] M. Reindl, K. D. Jöns, D. Huber, C. Schimpf, Y. Huo, V. Zwiller, A. Rastelli, and R. Trotta, Nano Lett. **17,** 4090 (2017).

[42] A. M. Barth, A. Vagov, and V. M. Axt, Phys. Rev. B **94,** 125439 (2016).

[43] N. Makri and D. E. Makarov, J. Chem. Phys. **102,** 4600 (1995).

[44] N. Makri and D. E. Makarov, J. Chem. Phys. **102,** 4611 (1995).

[45] M. Cygorek, A. M. Barth, F. Ungar, A. Vagov, and V. M. Axt, Phys. Rev. B **96,** 201201(R) (2017).

[46] W. K. Wootters, Quantum Inf. Comput. **1,** 27 (2001).

[47] See Supplemental Material at http://link.aps.org/supplemental/10.1103/PhysRevLett.123.137401 for a precise definition of the concurrence of simultaneously emitted photon pairs, details how the renormalization of the coupling g is estimated, some numerical remarks, and for an additional configuration exhibiting phonon-induced entanglement. It also includes Refs. [48–56] in addition to references already cited in the main text. Results obtained using an approximate phenomenological rate model are shown as well as results regarding the dependence on the binding energy.

[48] W. K. Wootters, Phys. Rev. Lett. **80,** 2245 (1998).

[49] G. Pfanner, M. Seliger, and U. Hohenester, Phys. Rev. B **78,** 195410 (2008).

[50] M. Cosacchi, M. Cygorek, F. Ungar, A. M. Barth, A. Vagov, and V. M. Axt, Phys. Rev. B **98,** 125302 (2018).

[51] D. F. V. James, P. G. Kwiat, W. J. Munro, and A. G. White, Phys. Rev. A **64,** 052312 (2001).

[52] M. E. Reimer, M. P. van Kouwen, A. W. Hidma, M. H. M. van Weert, E. P. A. M. Bakkers, L. P. Kouwenhoven, and V. Zwiller, Nano Lett. **11,** 645 (2011).

[53] F. Ding, R. Singh, J. D. Plumhof, T. Zander, V. K ŕápek, Y. H. Chen, M. Benyoucef, V. Zwiller, K. Dörr, G. Bester, A. Rastelli, and O. G. Schmidt, Phys. Rev. Lett. **104,** 067405 (2010).

[54] R. Trotta, P. Atkinson, J. D. Plumhof, E. Zallo, R. O. Rezaev, S. Kumar, S. Baunack, J. R. Schrter, A. Rastelli, and O. G. Schmidt, Adv. Mater. **24,** 2668 (2012).

[55] R. Trotta, E. Zallo, E. Magerl, O. G. Schmidt, and A. Rastelli, Phys. Rev. B **88,** 155312 (2013).

[56] F. Troiani, J. I. Perea, and C. Tejedor, Phys. Rev. B **74,** 235310 (2006).

[57] A. Carmele and A. Knorr, Phys. Rev. B **84,** 075328 (2011).

[58] R. M. Stevenson, A. J. Hudson, A. J. Bennett, R. J. Young, C. A. Nicoll, D. A. Ritchie, and A. J. Shields, Phys. Rev. Lett. **101,** 170501 (2008).

[59] S. Bounouar, C. de la Haye, M. Strau, P. Schnauber, A. Thoma, M. Gschrey, J.-H. Schulze, A. Strittmatter, S. Rodt, and S. Reitzenstein, Appl. Phys. Lett. **112,** 153107 (2018).

[60] B. Krummheuer, V. M. Axt, T. Kuhn, I. D'Amico, and F. Rossi, Phys. Rev. B **71,** 235329 (2005).

[61] A. J. Ramsay, T. M. Godden, S. J. Boyle, E. M. Gauger, A. Nazir, B. W. Lovett, A. M. Fox, and M. S. Skolnick, Phys. Rev. Lett. **105,** 177402 (2010).

[62] A. Vagov, M. Glässl, M. D. Croitoru, V. M. Axt, and T. Kuhn, Phys. Rev. B **90,** 075309 (2014).

Supplement: Phonon-Induced Enhancement of Photon Entanglement in Quantum Dot-Cavity Systems

T. Seidelmann,[1] F. Ungar,[1] A. M. Barth,[1] A. Vagov,[1, 2] V. M. Axt,[1] M. Cygorek,[3] and T. Kuhn[4]

[1] *Universität Bayreuth, Lehrstuhl für Theoretische Physik III,*
Universitätsstraße 30, 95447 Bayreuth, Germany
[2] *ITMO University, St. Petersburg, 197101, Russia*
[3] *Department of Physics, University of Ottawa, Ottawa, Ontario, Canada K1N 6N5*
[4] *Institut für Festkörpertheorie, Universität Münster, 48149 Münster, Germany*

CONCURRENCE OF SIMULTANEOUSLY EMITTED PHOTONS

The concurrence is a widely used measure for the entanglement of a bipartite system. It has a one-to-one correspondence to the entanglement of formation [1] which represents the amount of pure-state entanglement that is at least present in a mixed state described by a given density matrix. Even though the entanglement of formation is more intuitive, the concurrence is usually preferred since it can be extracted directly from the values of the reduced density matrix of the bipartite system for which the entanglement is to be measured [2].

It is worthwhile to note that the photons emitted from the biexciton-exciton cascade can be subdivided in different ways into bipartite subsystems [3]. The associated concurrences are not necessarily equivalent since they may exhibit opposite trends when varying parameters such as, e.g., the cavity losses [3]. Widely used is the concurrence of all photon pairs that are detected in coincidence measurements without discriminating between the detection times of the two photons [3–7]. This choice results in a high signal yield but measurements [8, 9] as well as theoretical considerations [3, 10] indicate that significantly higher degrees of entanglement can be reached by selecting simultaneously emitted photon pairs. For this reason the concurrence of simultaneously emitted pairs is preferred in the present study. The more general expression given in Ref. [2] reduces in our case to

$$C = 2\,|\bar{\rho}_{HV}^{N}|, \tag{S1}$$

where the normalized two-photon coherence

$$\bar{\rho}_{HV}^{N} = \frac{\bar{\rho}_{HV}}{\bar{\rho}_{HH} + \bar{\rho}_{VV}} \tag{S2}$$

is calculated from the time-averaged elements of the reduced density matrix

$$\bar{\rho}_{mn} = \frac{1}{T_{\mathrm{av}}} \int\limits_{0}^{T_{\mathrm{av}}} \langle mm|\hat{\rho}(t)|nn\rangle \, \mathrm{d}t. \tag{S3}$$

Here, $|HH\rangle := |G, 2, 0\rangle$ ($|VV\rangle := |G, 0, 2\rangle$) denotes the state with two horizontally (vertically) polarized photons. The averaging is performed until the time T_{av} is reached where the initially prepared biexciton has fully decayed and the system has reached its ground state without any photons inside the cavity.

In experiments, the two-photon density matrix, from which the concurrence can be derived, is usually reconstructed using quantum state tomography, a technique based on polarization-dependent photon coincidence measurements [11]. This technique gives access to information about the polarization degree of freedom and the delay time between the two detection events. The concurrence of simultaneously emitted photon pairs can be obtained from the reconstructed density matrix elements in the limit where the delay time approaches zero. Typically, in the corresponding experiments, data points are recorded over extended delay time intervals. Here, the limit of zero delay time can be approached by using time-windowing techniques where signals over different delay time windows are recorded and then the data is extrapolated towards zero delay time [8, 9].

RENORMALIZATION OF THE QUANTUM DOT-CAVITY COUPLING

In the main text we argue that the shift of the minimum in the concurrence plotted versus the dot-cavity coupling g is caused by the phonon-induced renormalization of g. This renormalization occurs already in a two-level system

where it is much simpler to analyze than in the five-level system considered in the present manuscript. For vanishing biexciton binding energy and the usually not very large fine-structure splitting, the transitions from the biexciton to the exciton states and from the exciton states to the ground state are similar and their phonon-induced renormalization can be expected to be close to the case of resonant coupling. Therefore, we followed Ref. [12] in order to obtain a simple estimate for the renormalization, i.e., we have performed path-integral calculations for a resonantly driven two-level system with the same dot and phonon parameters as used in the main text but for $\kappa = 0$. For driving with constant amplitude the exciton occupation is well fitted by the expression:

$$\rho_X = \frac{1}{2}\big[1 - e^{-\Gamma t}\cos(\omega t)\big], \tag{S4}$$

where $\Gamma = \Gamma(g, T)$ and $\omega = \omega(g, T)$ are used as fitting parameters. As explained in detail in Ref. [12], the renormalized dot-cavity coupling is related to Γ and ω by:

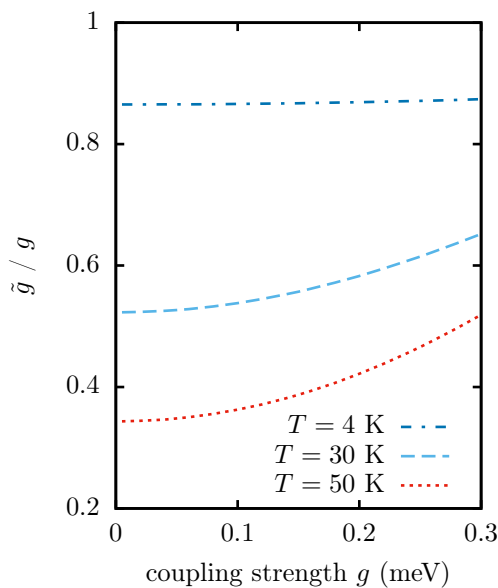$$\tilde{g}(g, T) = [\Gamma^2(g, T) + \omega^2(g, T)]/(4g) \tag{S5}$$

FIG. S1. Renormalized dot-cavity coupling $\tilde{g}(g, T)/g$ as a function of the original coupling g for different temperatures.

Figure S1 displays the resulting renormalized dot-cavity coupling as a function of the original coupling for different temperatures. Clearly, for not too high values of g (which constitutes the typical situation) the phonon renormalization leads to a reduction of the effective coupling. Thus, in order to achieve the same effect with the renormalized g as without renormalization one needs to increase the bare value of g, which explains why the minimum in Fig. 1(c) in the main text is shifted to higher g values.

PHONON-INDUCED ENTANGLEMENT FOR DEGENERATE EXCITONS AND FINITE CAVITY MODE SPLITTING

In this section we present numerical simulations of the concurrence for the situation sketched in Fig. S2(a), i.e., a system with vanishing biexciton binding energy, degenerate excitons and cavity modes with a finite splitting given by $\delta^c = \hbar(\omega_H^c - \omega_V^c)$. Since the excitons are degenerate, which-path information is introduced in this configuration only by the cavity mode splitting.

The concurrence is again a non-monotonic function of g already in the phonon-free case [purple curve in Fig. S2(c)]. However, the situation here is more involved than in Fig. 1(c) in the main text, since instead of a single minimum we now have two well pronounced minima. Accounting for phonons, we observe also in this configuration a clear shift of the curves toward higher g values with rising temperature accompanied by an overall lowering of the curves. As in
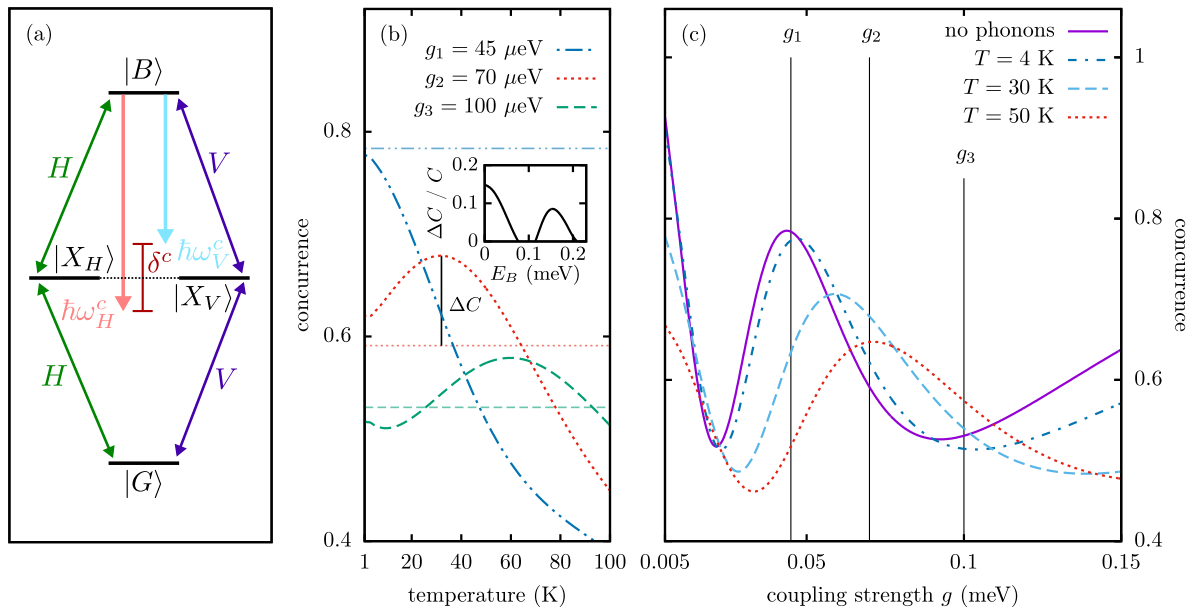
FIG. S2. (a) Sketch of the level scheme of a QD-cavity system with finite cavity mode splitting, zero biexciton binding energy, and degenerate excitons. (b) Concurrence as a function of the temperature for three selected values of the QD-cavity coupling. The corresponding values obtained without phonons are drawn as straight (faded) lines with the same linetype. The inset shows the difference ΔC between the maximum concurrence value at a finite temperature and the corresponding phonon-free value (only positive values are shown) normalized by the latter as a function of the biexciton binding energy E_B for $g_2 = 70$ µeV. In the case of a finite E_B, the cavity modes are adjusted such that their mean energy coincides with the degenerate exciton energy $\hbar\omega_X$: $\hbar\omega^c_{H/V} = \hbar\omega_X \pm \delta^c/2$. (c) Concurrence as a function of the QD-cavity coupling for three temperatures together with the phonon-free result. The values of the QD-cavity coupling used in (b) are marked in (c) by vertical lines. Parameters: $\delta^c = 0.07$ meV, $\kappa = 0.05\,\text{ps}^{-1}$. All other parameters are the same as in Fig. 1 in the main text.

Fig. 1(c) in the main text also here the shift caused by the renormalization is the dominant phonon-induced effect and consequently the temperature dependence of the concurrence depends crucially on the chosen value of g [cf. Fig. S2(b)]. For example, for $g = 45\,\mu\text{eV}$ we find the usually encountered monotonic decrease with rising temperature. In contrast, for $g = 70\,\mu\text{eV}$ and $g = 100\,\mu\text{eV}$ the concurrence exhibits different non-monotonic temperature dependences. In both cases extended ranges for g are found where the concurrence reaches values above the corresponding phonon-free level. This demonstrates that the phenomenon of phonon-induced entanglement as described in the main text can also be observed in a configuration where the cavity modes are split while the excitons are degenerate and the biexciton binding is weak. Again, similar to the configuration discussed in the main text, this effect occurs for a finite range of biexciton binding energies [cf. inset panel (b)]. Here, the effect can be observed even when the binding energy is a few times the value of the splitting δ^c.

DEPENDENCE ON THE BIEXCITON BINDING ENERGY

The effect of phonon-induced enhancement of photon entanglement does not only occur in the singular case of a vanishing biexciton binding energy but rather for a finite range of binding energies depending on the respective splitting. It is worthwhile to note that apart from the natural occurrence of QDs with small biexciton binding energies, the biexciton binding energy can also be tuned into this regime, e.g., by the application of an electrical field [13] or a biaxial strain [14, 15], or both combined [16]. In the main text, the case of a vanishing and a finite (large) E_B value are discussed in detail and presented in Figs. 1 and 2 for a quantum dot-cavity system with finite fine-structure splitting and two photon resonant cavity modes. While in the first case phonon-induced enhancement can be observed this effect does not occur in the latter one. A continuous transition between these two types of behavior is expected.

Figure S3 shows the dependence on the biexciton binding energy E_B of the difference ΔC between the maximum concurrence value at a finite temperature and the corresponding phonon-free value normalized by the latter one. Figure S3(a) displays results for the situation considered in the main text where the cavity modes are degenerate
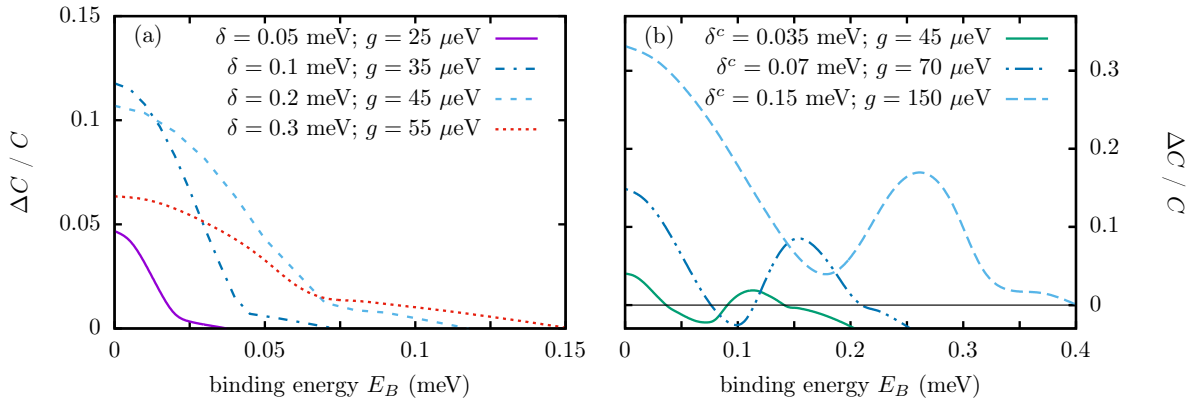
FIG. S3. Difference ΔC between the maximum concurrence value at a finite temperature and the corresponding phonon-free value normalized by the latter as a function of the biexciton binding energy E_B. (a) Results for a QD-cavity system with two-photon resonant cavity modes and cavity loss rate $\kappa = 0.025$ ps^{-1} for four different combinations of finite fine-structure splittings δ and light-matter coupling strengths g. Corresponding level schemes can be found in the main text in Figs. 1 and 2. (b) Results for a QD-cavity system with degenerate excitons and cavity loss rate $\kappa = 0.05$ ps^{-1} for three different combinations of finite cavity mode splittings δ^c and light-matter coupling strengths g. The corresponding level scheme for a vanishing E_B can be found in Fig. S2. In the case of a finite binding energy, the cavity modes are adjusted such that their mean energy coincides with the degenerate exciton energy $\hbar\omega_X$: $\hbar\omega_{H/V}^c = \hbar\omega_X \pm \delta^c/2$.

and the excitons exhibit a finite fine-structure splitting δ, while the curves in Figure S3(b) are obtained for the case described in the previous section where the excitons are degenerate and the cavity modes are split. Different combinations of exciton (cavity mode) splittings δ (δ^c) and coupling strengths g are considered. Indeed, in both QD-cavity configurations discussed in the main text and the supplement, which exhibit phonon-induced enhancement of photon entanglement, this effect occurs for a finite range of binding energies. For both configurations this range is roughly proportional to the respective splitting δ or δ^c. In the case of a QD-system with a finite fine-structure splitting δ and two-photon resonant cavity modes, the effect can be seen until the binding energy reaches approximately half the value of the splitting δ [cf. Fig. S3(a)].

For the second QD-cavity configuration [Fig. S3(b), degenerate exciton energies, finite cavity mode splitting δ^c] the situation is more involved since ΔC turns out to depend non-monotonically on E_B. Nevertheless, also here a finite range of binding energies exists where phonon-induced enhancement of photon entanglement can be found. Again this range is roughly proportional to the splitting δ^c. For some combinations of g and δ^c, the value of ΔC first drops below zero and then phonon-induced entanglement enhancement is recovered at higher values of E_B, while for other combinations the minimum of ΔC as a function of E_B has a positive value. In all cases, phonon-induced enhancement is observed in the E_B range from zero to at least δ^c. After ΔC recovers from its minimum, positive values, indicating the entanglement enhancement compared with the phonon-free case, are found for binding energies approximately up to 2.5 - 4 times the value of the splitting δ^c.

PHENOMENOLOGICAL DEPHASING RATE MODEL

A simple standard approximate method used to model pure dephasing is the introduction of phenomenological pure dephasing rates [5, 17]. Instead of the exact treatment of the continuum of longitudinal acoustic phonons, a Lindblad-type operator is introduced. Here, we follow the methodology of Ref. [5] and use the operator

$$\mathcal{L}_{PD}\left[\hat{\rho}\right] = -\frac{1}{2} \sum_{\substack{\chi, \chi' \\ \chi \neq \chi'}} \gamma_{PD} \, |\chi\rangle\langle\chi|\hat{\rho}|\chi'\rangle\langle\chi'|, \tag{S6}$$

with $\chi, \chi' \in \{G, X_H, X_V, B\}$ and a pure dephasing rate γ_{PD}. Typical values for γ_{PD} correspond to several µeV. In Fig. S4, results are shown for the two configurations discussed in Fig. 1 of the main text and Fig. S2, where phonon-induced enhancement of photon entanglement has been found in simulations fully accounting for phonons on a microscopic level.
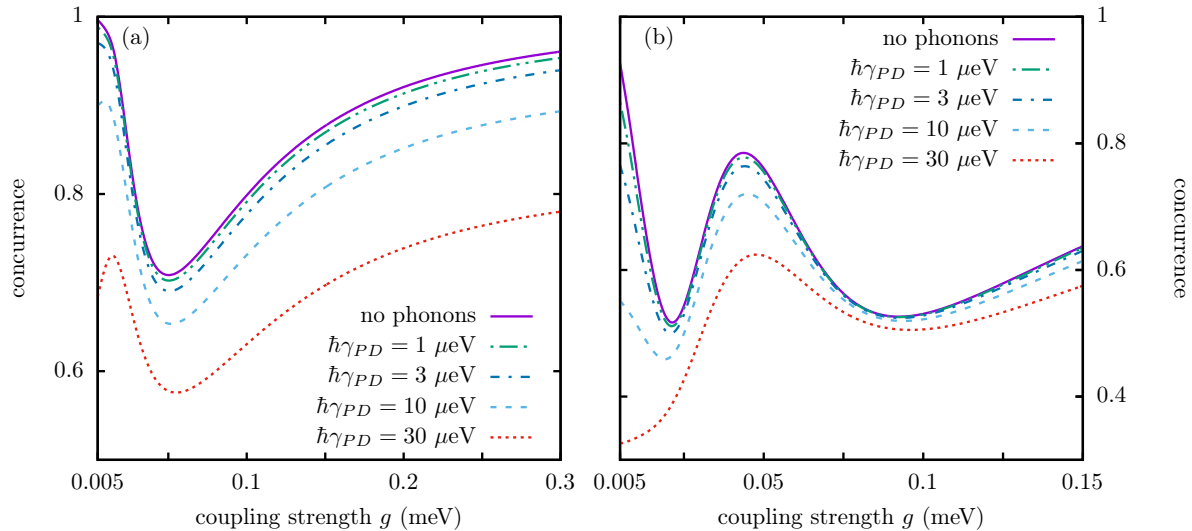
FIG. S4. Results obtained using a phenomenological pure dephasing rate model with different rates γ_{PD} instead of the exact path-integral method. (a) Results for the configuration discussed in Fig. 1 in the main text with parameters $\delta = 0.1$ meV, $\kappa = 0.025$ ps^{-1}. (b) Results for the configuration discussed in Fig. S2 with parameters $\delta^c = 0.07$ meV, $\kappa = 0.05$ ps^{-1}.

Clearly, the effect of phonon-enhanced entanglement does not occur, as the introduction of a pure dephasing rate just leads to a reduction of the concurrence. Furthermore, when one models a higher temperature with a higher loss rate γ_{PD}, an increasing temperature results always in a decreasing degree of entanglement. Thus, the simple phenomenological rate approximation is not sufficient to model the system dynamics in this situation. This finding further strengthens the explanation of the effect given in the main text where we concluded that the phonon-induced enhancement appears because of a renormalization of the light-matter coupling g. This renormalization is, however, absent in the simple rate model and, consequently, the phonon-induced enhancement of photon entanglement does not appear.

NUMERICAL REMARKS

We use for our simulations a recently developed real-time path-integral algorithm to determine the temporal evolution of the reduced density matrix. Two major achievements enable us to obtain numerically complete results for the dynamics of the biexciton cascade coupled to a continuum of longitudinal acoustic phonons. The first is a translation of concepts originally developed in Hilbert space [18, 19] to Liouville space [20], which allows us to account for non-Hamiltonian contributions, like the Lindblad-type losses, to the dynamics. The second is a reformulation of the algorithm to perform the sum over paths. Instead of the widely used iteration scheme worked out by Makri and Makarov [18, 19] for the so called *augmented density matrix*, only a partially summed augmented density matrix is iterated. A detailed derivation and description of this improved iteration scheme can be found in the supplement of Ref. [21]. For systems like quantum dots coupled to cavities and longitudinal acoustic phonons, the numerical demand is reduced by many orders of magnitude in this way. Two parameters, the step size of the time discretization Δt and the number of time steps N_{mem} used to scan the finite memory, determine the quality of the numerical results. These parameters can be well controlled and we speak of *numerically complete results* when no visible change of the results occurs when further decreasing Δt or increasing N_{mem}. For the QD-cavity systems considered in the present paper, numerically converged results are obtained for $\Delta t = 0.5$ ps and $N_{\mathrm{mem}} = 7$.

———————

[1] W. K. Wootters, Quantum Inf. Comput. **1**, 27 (2001).
[2] W. K. Wootters, Phys. Rev. Lett. **80**, 2245 (1998).
[3] M. Cygorek, F. Ungar, T. Seidelmann, A. M. Barth, A. Vagov, V. M. Axt, and T. Kuhn, Phys. Rev. B **98**, 045303 (2018).
[4] G. Pfanner, M. Seliger, and U. Hohenester, Phys. Rev. B **78**, 195410 (2008).

[5] S. Schumacher, J. Förstner, A. Zrenner, M. Florian, C. Gies, P. Gartner, and F. Jahnke, Opt. Express **20**, 5335 (2012).

[6] D. Heinze, A. Zrenner, and S. Schumacher, Phys. Rev. B **95**, 245306 (2017).

[7] M. Cosacchi, M. Cygorek, F. Ungar, A. M. Barth, A. Vagov, and V. M. Axt, Phys. Rev. B **98**, 125302 (2018).

[8] R. M. Stevenson, A. J. Hudson, A. J. Bennett, R. J. Young, C. A. Nicoll, D. A. Ritchie, and A. J. Shields, Phys. Rev. Lett. **101**, 170501 (2008).

[9] S. Bounouar, C. de la Haye, M. Strau, P. Schnauber, A. Thoma, M. Gschrey, J.-H. Schulze, A. Strittmatter, S. Rodt, and S. Reitzenstein, Appl. Phys. Lett. **112**, 153107 (2018).

[10] E. del Valle, New J. Phys. **15**, 025019 (2013).

[11] D. F. V. James, P. G. Kwiat, W. J. Munro, and A. G. White, Phys. Rev. A **64**, 052312 (2001).

[12] A. Vagov, M. Glässl, M. D. Croitoru, V. M. Axt, and T. Kuhn, Phys. Rev. B **90**, 075309 (2014).

[13] M. E. Reimer, M. P. van Kouwen, A. W. Hidma, M. H. M. van Weert, E. P. A. M. Bakkers, L. P. Kouwenhoven, and V. Zwiller, Nano Letters **11**, 645 (2011).

[14] F. Ding, R. Singh, J. D. Plumhof, T. Zander, V. Křápek, Y. H. Chen, M. Benyoucef, V. Zwiller, K. Dörr, G. Bester, A. Rastelli, and O. G. Schmidt, Phys. Rev. Lett. **104**, 067405 (2010).

[15] R. Trotta, P. Atkinson, J. D. Plumhof, E. Zallo, R. O. Rezaev, S. Kumar, S. Baunack, J. R. Schrter, A. Rastelli, and O. G. Schmidt, Advanced Materials **24**, 2668 (2012).

[16] R. Trotta, E. Zallo, E. Magerl, O. G. Schmidt, and A. Rastelli, Phys. Rev. B **88**, 155312 (2013).

[17] F. Troiani, J. I. Perea, and C. Tejedor, Phys. Rev. B **74**, 235310 (2006).

[18] N. Makri and D. E. Makarov, J. Chem. Phys. **102**, 4600 (1995).

[19] N. Makri and D. E. Makarov, J. Chem. Phys. **102**, 4611 (1995).

[20] A. M. Barth, A. Vagov, and V. M. Axt, Phys. Rev. B **94**, 125439 (2016).

[21] M. Cygorek, A. M. Barth, F. Ungar, A. Vagov, and V. M. Axt, Phys. Rev. B **96**, 201201(R) (2017).